Astrophysics and Space Science Library 427

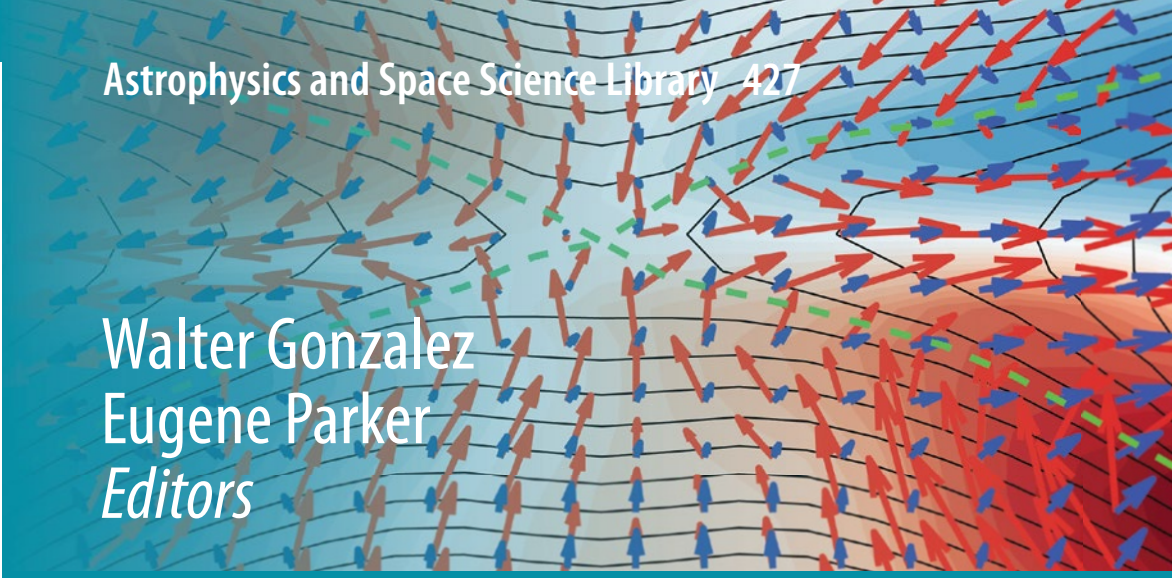

Walter Gonzalez
Eugene Parker
Editors

Magnetic Reconnection

Concepts and Applications

ASSL

Springer

Magnetic Reconnection

Astrophysics and Space Science Library

More information about this series at http://www.springer.com/series/5664

Walter Gonzalez • Eugene Parker
Editors

Magnetic Reconnection

Concepts and Applications

Springer

Editors
Walter Gonzalez
INPE
São José dos Campos, Brazil

Eugene Parker
University of Chicago
CHICAGO
Illinois, USA

ISSN 0067-0057 ISSN 2214-7985 (electronic)
Astrophysics and Space Science Library
ISBN 978-3-319-26430-1 ISBN 978-3-319-26432-5 (eBook)
DOI 10.1007/978-3-319-26432-5

Library of Congress Control Number: 2016931861

Springer Cham Heidelberg New York Dordrecht London

Cover illustration: See Fig. 4.3 in Chapter 4 “Energy Conversion and Inventory of a Prototypical Magnetic Reconnection Layer” by Masaaki Yamada et al. in this book.

Printed on acid-free paper

Springer International Publishing AG Switzerland is part of Springer Science+Business Media (www.springer.com)

Preface

Motivated by the presentations and discussions carried out at the Magnetic Reconnection Workshop, held at the National Institute for Space Research (INPE) of Brazil in March 2014, some of the scientists who attended it thought that it was timely to prepare a new book on magnetic reconnection since previous books on this topic have been published already eight years before or more. Thus, this book deals with a review of fundamental concepts on magnetic reconnection that are still open for research and with applications of this important cosmic plasma process to regions going from the Sun's atmosphere and the Earth's magnetosphere to domains involving heliospheric magnetospheres, stellar atmospheres, turbulent astrophysical plasmas, radiation dominated astrophysical systems, and even quantum systems in which annihilation of quantum magnetic fluxes seems to take place.

This book updates and extends the scope of previous books on magnetic reconnection, especially of those edited by Priest and Forbes (2000) and by Birn and Priest (2007), to which the readers are referred for reviews on fundamental aspects of MHD reconnection and of collisionless reconnection.

Most of the chapters of this book have been prepared having graduate students and postdocs as the main readers in mind, thus providing illustrations and introductory discussions for the addressed topics. However, we believe that all researchers in the field of magnetic reconnection will also profit from the reviews presented in this book since several of the authors have made an effort to incorporate new research material in their reviews. Concerning the units used in this book, because the chapters were written by different authors with some of them preferring the MKS system and some the CGS system, we have not made the effort to present all chapters with only one of these units, also because we assume that the readers are already familiar to find this same situation when reading papers in which the authors prefer to use one system or the other.

In Chap. 1, several of the book authors present opinions about two fundamental questions on magnetic reconnection that still remain unsettled. They refer to the meaning of the generally used expression "magnetic field lines cut and reconnect" as well as to the location and nature of a "diffusion" region of reconnection and to its role in defining the reconnection rate, as compared to that associated with the

global reconnecting system and the boundary conditions. Although one can read about illuminating considerations in the discussions presented in this chapter on such fundamental issues, one can also see that no consensus about them is presently available, thus indicating that the subject of magnetic reconnection remains open for further theoretical, computational, and observational studies.

Although the topic of collisionless reconnection has been reviewed extensively in recent years (Yamada et al. 2010; Mozer and Pritchett 2012; Karimabadi et al. 2013; Treumann and Baumjohann 2013; Hesse et al. 2014), J. Scudder, H. Karimabadi, and B. Daughton present in Chap. 2 of this book a complementary review dealing mostly with the electron physics of reconnection and more particularly with the role of electron demagnetization in collisionless reconnection. From this study the authors present a set of phenomenological parameters that are intended to be used as proxies to locate the electron diffusion region of reconnection, both in 2D and 3D.

The MHD approach to study reconnection still provides important results especially when one deals with global aspects. Thus, E. Priest presents in Chap. 3 a review about the different 3D-MHD structures of reconnection, where the electric current tends to concentrate leading to reconnection-related null points, separators, and quasi-separators. The review also discusses the role of magnetic helicity and of other topological invariants, together with the conditions for flux and field line conservation and for reconnection itself .

In Chap. 4, M. Yamada, J. Yoo, and S. Zenitani present a review on energy conversion and partitioning for a prototypical magnetic reconnection layer, incorporating recent results from laboratory experiments, space observations, and numerical simulations. They conclude that about half of the incident magnetic energy is converted into particle energy, of which 2/3 is ultimately transferred to ions and 1/3 to electrons. They also discuss these results in the context of a systematic variability of the boundary conditions.

The important problem of rapid reconnection and associated changes in field line topology, which has been discussed in several recent publications, is reviewed in Chap. 5 by E.N. Parker and F. Rappazzo. This situation arises where the magnetic stresses drive the plasma and field toward increasing field gradients, so that the current density becomes large without bound, with the plasma dynamics and the kinetics of the thin current sheet controlling the rate of the reconnecting fields. The authors consider where and how the local rapid reconnection phenomenon arises in the overall topology of the surrounding magnetic field and exemplify it with the common bipolar magnetic fields arching above the solar photosphere. Studying the final equilibrium of such a common interlaced field line topology, they conclude that thin current sheets form as intrinsic sites for rapid reconnection.

Magnetopause reconnection has been one of the most studied topics of magnetic reconnection since the initial work by Dungey (1961). In Chap. 6, P.A. Cassak and S.A. Fuselier present an updated review on this topic to give fresh answers to the fundamental questions of where reconnection happens at the magnetopause and how efficient it is as a function of the solar wind driving parameters. The chapter is a pedagogical treatment of magnetopause reconnection, although the authors also try

to incorporate results of recent studies including asymmetries, the diamagnetic drift, and flow shear. For this aim, results from theoretical, observational, and numerical simulations are used.

In Chap. 7, A. Petrukovich, A. Artemyev, and R. Nakamura review the topic of magnetotail reconnection, which also has a long history of theoretical, observational, and modeling efforts. The authors discuss the initiation mechanisms for near-Earth tail reconnection concluding that it still represents one of the major unsolved problems in space physics. They review progress in this research topic during the last decade, especially highlighting variants of overcoming the famous tearing stability problem and discussing with recent multipoint spacecraft observations detailed structures of pre-onset and reconnection zones down to the ion Larmor scale. The latter is argued to support the importance of a self-consistent formation of an unstable state through internal magnetotail reconfiguration.

G. Lapenta , R. Wang, and E. Cazzola give in Chap. 8 a review on reconnection separatrices as studied in recent years for both classical regions of magnetospheric reconnection, dayside and tail. The review primarily focuses on numerical simulations but is supplemented with spacecraft observations. The natural importance of the separatrices lies in the fact that they connect the central region of reconnection with the larger-scale external region that also incorporates the boundary conditions. The authors summarize the average properties of particles and fields in the separatrix regions, also dealing with the various types of instabilities and acceleration processes that tend to occur there. They argue that a significant part of energy conversion takes place in the separatrix regions during reconnection.

Since reconnection is expected to take place also at other planetary magnetospheres, Chap. 9 is devoted to reviewing some reconnection properties for the magnetospheres of Jupiter and Saturn and comparing them with those for the Earth's magnetosphere. Thus, in this chapter, R. Walker and X. Jia present a review especially dealing with plasma transport associated with reconnection in the magnetospheres of these planets. Since observations at the outer planets are sparse, the authors use numerical simulations to give an overall view of plasma transport. The authors claim that solar wind dynamic pressure controls reconnection at Saturn, while both dynamic pressure and the IMF are important at Jupiter. They also present evidence about the importance of Kelvin-Helmholtz waves during transport for the magnetosphere of Saturn.

When studying reconnection at the Sun and at other stellar environments, recent results show an important fractal reconnection scenario that seems to explain several apparently unrelated observations. Thus in Chap. 10, K. Shibata and S. Takasao present a review on this topic using theory and observations. The authors associate a fractal current sheet structure as a source for both small-scale reconnection at the Sun, leading to nano-flares, and to large-scale ones, leading to long-duration flares or giant arcades. They mention that often such reconnection events are closely related with multiple plasmoid ejections from a fractal current sheet. They claim that bursty radio and hard X-ray emissions from flares also suggest fractal reconnection and associated particle acceleration. The authors also discuss about recent findings of many superflares on solar-type stars, which seem to extend the applicability of the

fractal reconnection model of solar flares to a much wider parameter space involving stellar flares.

The topic of turbulent reconnection has received especial attention during recent years with applications mainly in astrophysical systems. In Chap. 11, A. Lazarian, G. Kowal, M. Tamamoto, E.M. De Gouvea Dal Pino, and J. Cho, present a review on this topic using theoretical studies and numerical simulations. The authors claim that magnetic reconnection occurs frequently due to the common and ubiquitous presence of turbulence in cosmic plasmas. They even associate the efficiency and rate of reconnection to the level of turbulence present in the plasma during reconnection. The theory presented in this review is also extended to the relativistic domain.

Since reconnection in astrophysical systems frequently involves radiations there has been increasing efforts trying to incorporate radiation in the reconnection dynamics and energetics in such scenarios. Thus, in Chap. 12, D. Uzdensky reviews this subject, presenting an overview of recent theoretical progress and key high-energy astrophysical applications of radiative reconnection to pulsar wind nebulae, pulsar magnetospheres, black hole accretion-disk coronae, and hot accretion flows in X-ray binaries and active galactic nuclei, with important consequences for the study of relativistic jets, magnetospheres of magnetars, and gamma-ray bursts.

Finally, in Chap. 13, W.D. Gonzalez reviews the very recent topic of annihilation of quantum magnetic fluxes (QMFs) which, although observed to occur until now only in laboratory superconducting systems, is argued to also occur at the superconducting outer core of neutron stars with a probable role in the observed variable dynamics of some neutron stars. The author presents a synthesis of some fundamental aspects associated with QMFs, including the Aharonov-Bohm effect for the phase change of electrons passing in the neighborhood of localized magnetic flux tubes, the Ginzburg-Landau phenomenological theory explaining the origin of QMFs, some laboratory observations of QMFs in superconducting systems, the Treumann et al. (2012) quantum mechanical study of the interaction of oppositely directed QMFs, a quantum field theory approach for the study of the energetics of the annihilation of QMFs and of the emitted radiation, and a discussion about the possible scenario of QMF-annihilation at the superconducting cores of some neutron stars.

The editors would like to thank the efforts done by the contributing authors to this book and expect that its content be useful especially to new researchers in the field of magnetic reconnection.

São José dos Campos, Brazil — Walter D. Gonzalez
Chicago, IL, USA — Eugene N. Parker
September 2015

References

J. Birn, E.R. Priest, *Reconnection of Magnetic Fields: Magnetohydrodynamics and Collisionless Theory and Observations* (Cambridge University Press, New York, 2007)
J.W. Dungey, Phys. Rev. Lett. **6**, 47 (1961)
M. Hesse et al., Space Sci. Rev. (2014). doi:10.1007/s11214-014-0078-y
H. Karimabadi et al., Space Sci. Rev. (2013). doi:10.1007/s11214-013-0021-7
F.S. Mozer, P.L. Pritchett, *Electron Physics of Asymmetric Magnetic Field Reconnection*, in ed. by W. Gonzalez, J. Burch. Key Processes in Solar-Terrestrial Physics (Springer, New York, 2012), pp. 119–143
E. Priest, T. Forbes, *Magnetic Reconnection: MHD Theory and Applications* (Cambridge University Press, New York, 2000)
R.A. Treumann, W. Baumjohann, Front. Phys. (2013). doi:10.3389/fphy.2013.00031
R.A. Treumann, W. Baumjohann, W.D. Gonzalez, Ann. Geophys. (2012). doi:10.5194/angeo-30.1515-2012
M. Yamada, R. Kulsrud, H. Ji, Rev. Mod. Phys. (2010). doi:10.1103/RevModPhys.82.603

Contents

Chapter 1
Fundamental Concepts Associated with Magnetic Reconnection

W.D. Gonzalez, E.N. Parker, F.S. Mozer, V.M. Vasyliūnas, P.L. Pritchett, H. Karimabadi, P.A. Cassak, J.D. Scudder, M. Yamada, R.M. Kulsrud, and D. Koga

Abstract The chapter starts with a discussion about the importance of the concept of magnetic field lines in space plasmas and magnetic reconnection, followed by presentations on: (a) the meaning and validity of empirical constructs related with magnetic reconnection research, such as: "moving" magnetic field lines, "frozen-in" condition and "diffusion region" of reconnection; and (b) experimental evidence of the diffusion region and related energetics. Next, aims to link external (MHD) with internal (non-MHD) regions of reconnection are discussed in association with

W.D. Gonzalez (✉) • D. Koga
National Institute for Space Research (INPE), São José dos Campos, São Paulo 12227-010, Brazil
e-mail: walter.gonzalez@inpe.br

E.N. Parker
Department of Astronomy and Astrophysics, University of Chicago, Chicago, IL 60637, USA

F.S. Mozer
Space Sciences Laboratory, University of California, Berkeley, CA 94720, USA

V.M. Vasyliūnas
Max-Planck-Institut für Sonnensystemforschung, Göttingen 37077, Germany

P.L. Pritchett
Department of Physics and Astronomy, University of California, Los Angeles, CA 90095-1547, USA

H. Karimabadi
SciberQuest, Inc., Del Mar, CA 92014, USA

CureMetrix, Inc., Rancho Santa Fe, CA 92067, USA

P.A. Cassak
Department of Physics and Astronomy, West Virginia University, Morgantown, WV 26506, USA

J.D. Scudder
Department of Physics and Astronomy, University of Iowa, Iowa City, IA 52242, USA

M. Yamada • R.M. Kulsrud
Center for Magnetic Self-Organization, Princeton Plasma Physics Laboratory, Princeton University, Princeton, NJ 08544, USA

W. Gonzalez, E. Parker (eds.), *Magnetic Reconnection*, Astrophysics and Space Science Library 427, DOI 10.1007/978-3-319-26432-5_1

the so-called "Axford conjecture", followed by short presentations on: (a) global equilibria in reconnection; and (b) the role of the separatrices in global aspects of reconnection. In the last section, we present additional discussion about the concept of "diffusion region" and about the two fundamental questions associated with magnetic reconnection reviewed in this chapter.

Keywords Magnetic reconnection concepts • Magnetic field lines • Frozen-in condition • Magnetic diffusion • Generalized Ohm's law • Global equilibria • Magnetic energy transfer • Magnetic reconnection onset • Magnetospheric reconnection • Magnetic reconnection separatrices

1.1 Introduction

Before discussing about magnetic reconnection and its applications in this Book, we review some fundamental concepts associated with magnetic reconnection in a somewhat different perspective from those presented in previous reviews, also trying to incorporate some recently developed ideas about them.

The main motivation for this introductory chapter is the presentation of some updated answers to the following fundamental and long-lasting questions associated with magnetic reconnection:

1. Near the X-line, magnetic field lines "get cut" and later "reconnect" and exit. What does this mean and how does it happen?
2. What defines the reconnection rate, internal processes in the diffusion region or external parameters associated with the overall reconnecting system, or both? What is the role/importance of the separatrices for the study of a combined reconnection rate?

Thus, with respect to Question 1, this Chapter starts in Sect. 1.2 with a review about magnetic field lines (E.N. Parker); followed in Sect. 1.3 by presentations on Empirical Constructs associated with "moving" magnetic field lines, "frozen-in" condition and "diffusion region" of reconnection (F.S. Mozer and P.L. Pritchett), and in Sects. 1.3A and 1.3B, on Experimental evidence of the diffusion region and related energetics (M. Yamada). Concerning Question 2, a discussion about "global aspects of magnetic reconnection and the Axford Conjecture" is given in Sect. 1.4 (V.M. Vasyliūnas); followed by discussions on Global Equilibria in reconnection in Sect. 1.4A (R.M. Kulsrud), and on the Role of Reconnection Separatrices in global aspects of magnetopause reconnection in Sect. 1.4B (W.D. Gonzalez and D. Koga). Finally, Sect. 1.5 presents additional discussion on the concept of "diffusion region" and on Questions 1 and 2, as formulated by some of the other authors.

Most of the Discussion presented in this chapter is done without mentioning much of the relevant references since, being the subject about diverse issues, the list of references would be too extensive.

1.2 Magnetic Field Lines (E.N. Parker)

Magnetic field lines present a graphic picture of the form and topology of the magnetic field, as well as playing a central role in the equilibrium of the field. In particular, it is the field line connections (topology) and the reconnections associated with resistive dissipation of the field, that are the subject of this Book. We consider a large-scale magnetic field embedded in a highly conducting fluid.

A field line is a curve that lies along the magnetic field $B_i(x_k)$ everywhere along its length. Thus the direction cosines of the curve are equal to the direction cosines of the field, and we have

$$\frac{dx_i}{ds} = \frac{B_i}{B}, \tag{1.1}$$

where B is the magnitude of the field and ds represents arc length along the field line. The field line through any point P is defined by the integration of Eq. (1.1) in both directions from P. A nearby point P' defines another field line, etc. and the set of all such points and their associated field lines form a manifold making up the continuous magnetic field $B_i(x_k)$. Neglecting the small resistivity of the fluid for the moment, the magnetic field is carried bodily with the fluid, so we think of the magnetic field lines as moving with the fluid. The connectivity of the fluid lines is preserved by the continuity of the flow velocity. The magnetic field lines play a basic role in the determination of the self-equilibrium of the magnetic stresses. The equilibrium is described by

$$\frac{\partial M_{ij}}{\partial x_j} = 0, \tag{1.2}$$

where

$$M_{ij} = -\delta_{ij}\frac{B^2}{8\pi} + \frac{B_i B_j}{4\pi} \tag{1.3}$$

represents the magnetic stress tensor. The magnetic field exerts an isotropic pressure $B^2/8\pi$ and a tension of twice that amount in the direction along the field lines. As is well known, the equilibrium equation for exact balance between pressure and tension reduces to the form

$$\nabla \times \mathbf{B} = \alpha \mathbf{B}. \tag{1.4}$$

The divergence of the equilibrium equation yields the remarkable result

$$B_j \frac{\partial \alpha}{\partial x_j} = 0, \tag{1.5}$$

stating that the torsion coefficient α is constant along each individual field line no matter what the field line topology. That is to say, the field lines form a family of real characteristics of the equilibrium equation, playing a fundamental role in the structure of the solutions to Eq. (1.4). Then there is the contradictory requirement that the torsion does not vary regardless of how variable may be the writhe of the field line through the region of field. The small set of continuous fields that satisfy this strenuous requirement is characterized by the solutions of the 2D vorticity equation, in which time is replaced by distance along the field. So almost all field line topologies fall outside this special category, providing what are called the *weak solutions* with their combination of current sheets and local domains of the vortex-like solutions. Note finally that each field line in an equilibrium field is subject to the *optical analogy*, that the path of a field line between any two points on a flux surface is identical with the optical ray path on the flux surface in an index of refraction proportional to the field magnitude $B(x_k)$. Thus the field line is described by Fermat's principle and the associated Euler equations (Parker 1991).

Interest lies in large-scale magnetospheric and astrophysical settings where the magnetic field is vigorously swirled by the active convection of the fluid. The evolution of the field is described on those large scales by the familiar MHD induction equation,

$$\frac{\partial B_i}{\partial t} + v_j \frac{\partial B_i}{\partial x_j} = B_j \frac{\partial v_i}{\partial x_j} - B_i \frac{\partial v_j}{\partial x_j} + \eta \nabla^2 B_i, \tag{1.6}$$

where η is the resistive diffusion coefficient, providing a simple example of the dissipation necessary for reconnection. In the absence of resistive diffusion the Cauchy integral for the magnetic field can be set up in terms of the Lagrangian coordinates $x_i(X_k, t)$ at time t of the element of fluid at X_i at $t = 0$, providing

$$\frac{B_i(x_k, t)}{\rho(x_k, t)} = \frac{B_j(X_k, 0)}{\rho(X_k, 0)} \frac{\partial x_i}{\partial X_j}. \tag{1.7}$$

The local tumbling and stretching of the magnetic field is expressed by the progressive tumbling and stretching $\partial x_i / \partial X_j$ of the Lagrangian element of fluid. In the presence of resistive dissipation the connectivity of the field lines is generally not conserved, becoming a function of time. For a brief glimpse of the field line reconnection phenomenon put the fluid at rest so that Eq. (1.6) reduces to the familiar diffusion equation for each of the Cartesian components of the magnetic field,

$$\frac{\partial B_i}{\partial t} = \eta \nabla^2 B_i. \tag{1.8}$$

It follows that the initial magnetic field $B_i(x_k, 0)$ in an infinite space diffuses into

$$B_i(x_k, t) = \frac{1}{(4\pi\eta t)^{3/2}} \int\int\int d^3x'_k B_i(x'_k, 0) \exp\left[-\frac{(x_k - x'_k)^2}{4\eta t}\right] \tag{1.9}$$

in a time t. It is evident from the integration over space that the new field at time t represents a linear superposition of the diverse elements of field from a surrounding neighborhood of characteristic radius $(4\eta t)^{1/2}$. Thus the direction of the local field is perturbed in ways that depend on surrounding fields, thereby changing the path of the forward integration of Eq. (1.1). So the field line fails to connect with the same original field line ahead. And that is the nature of magnetic field line reconnection. It occurs in the presence of dissipation, with our illustrative example based on Ohmic diffusion. We can see that, with the ongoing reconnection, the individual field lines lose their original identity where they pass through a local region of diffusion.

In a field inhomogeneity with scale λ the characteristic reconnection time is comparable to the characteristic diffusion time λ^2/η. On astrophysical scales the diffusion time can be very long indeed, so very little reconnection occurs and can generally be ignored. On the other hand, in situations where the magnetic stresses and/or vigorous fluid motion create strong small-scale variation in the field, the reconnection goes rapidly and becomes a dynamical effect of interest in its own rite, providing such suprathermal phenomena as the aurora and solar flares and intense coronal heating. With these properties of magnetic field lines in mind, we turn to the rapid reconnection phenomenon itself in the active conditions presented by nature.

1.3 Empirical Constructs Associated with Magnetic Reconnection (F.S. Mozer and P.L. Pritchett)

Since the external/global regions associated with reconnection are usually fairly well described by the MHD approximation, in which the concepts "moving" magnetic field lines and "frozen-in" condition are commonly used, in this section we review these concepts together with that known as "diffusion region" of reconnection, considering them only as empirical constructs. Thus, the basic aim of this section is to caution about the validity of their applications.

What is an Empirical Construct?

An empirical construct is a model, concept, or image that exists in the mind that cannot be tested via experiment, so it doesn't exist in the physical world. While empirical constructs are extremely useful for visualizing physical problems, they

can also be applied in domains where their solutions differ from those obtained from Maxwell's equations and Newton's laws of motion. This can lead to confusion and non-physical results. Examples of use and misuse of empirical constructs are the following:

- Moving magnetic field lines
- Frozen-in condition
- The diffusion region of reconnection

Moving Magnetic Field Lines

This is an extremely useful concept for visualizing the temporal evolution of a magnetic field geometry. However, it is also an extremely confusing concept when its application is not well justified. Under what conditions does the empirical construct of moving magnetic field lines produce the same answers as Maxwell's equations and Newton's laws of motion (Newcomb 1958; Longmire 1963)?

Consider the conditions under which field line motion in a plasma causes the magnetic field MAGNITUDE and DIRECTION to evolve in time in a manner consistent with Maxwell's equations and Newton's laws of motion.

Magnitude

In ideal MHD magnetic field lines are not created or destroyed. As the field strength changes, they simply move into or out of the region of interest. Thus, magnetic field lines are conserved.

For an ideal MHD, Ohm's law is $\mathbf{E} + \mathbf{v} \times \mathbf{B}/c = 0$. Thus, Faraday's law gives $\partial \mathbf{B}/\partial t = \nabla \times (\mathbf{v} \times \mathbf{B})$. Then, if we consider a curve C (bounding a surface S) which is moving with the plasma, in a time dt an element $d\mathbf{s}$ of C sweeps out an element of area $\mathbf{v}dt \times d\mathbf{s}$. The rate of change of magnetic flux through C is :

$$\frac{d}{dt}\int_S \mathbf{B} \cdot d\mathbf{S} = \int_S \frac{\partial B}{\partial t} \cdot d\mathbf{S} + \int_C \mathbf{B} \cdot \mathbf{v} \times d\mathbf{s}. \tag{1.10}$$

Thus, as C moves, the flux changes due to the change of $\mathbf{B}$ with time and due to the boundary C moving in space [last term of Eq. (1.10)]. Setting $\mathbf{B} \cdot \mathbf{v} \times d\mathbf{s} = -\mathbf{v} \times \mathbf{B} \cdot d\mathbf{s}$ and applying Stokes's theorem to the last term of Eq. (1.10), we have:

$$\frac{d}{dt}\int_S \mathbf{B} \cdot d\mathbf{S} = \int_S \left(\frac{\partial B}{\partial t} - \nabla \times (\mathbf{v} \times \mathbf{B}) \right) \cdot d\mathbf{S},$$

which is equal to zero in the ideal MHD limit.

Therefore, if the magnetic field lines move with speed $\mathbf{v} = c\mathbf{E} \times \mathbf{B}/B^2$, the magnitude of the magnetic flux is conserved.

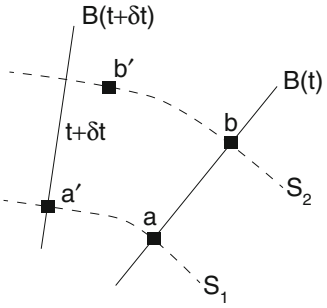

Fig. 1.1 Geometry of moving magnetic field lines (from Mozer 2005)

Velocity

Consider two surfaces, S_1 and S_2, as in Fig. 1.1, that are perpendicular to the magnetic field at times t and $t + \delta t$. At time, t, a magnetic field line intersects the two surfaces at points **a** and **b**. Thus, the vector $(\mathbf{b} - \mathbf{a})$ is parallel to $\mathbf{B}(t)$ and assumed to be $\varepsilon\mathbf{B}(t)$. At the later time, $t + \delta t$, the points **a** and **b** have moved at velocities $c\mathbf{E} \times \mathbf{B}/B^2(\mathbf{a})$ and $c\mathbf{E} \times \mathbf{B}/B^2(\mathbf{b})$ to points $\mathbf{a}'$ and $\mathbf{b}'$. What are the constraints on these motions that cause $(\mathbf{b}' - \mathbf{a}')$ to be parallel to $\mathbf{B}(\mathbf{a}, t + \delta t)$, i.e. $(\mathbf{b}' - \mathbf{a}') \times \mathbf{B}(\mathbf{a}, t + \delta t) = 0$?

From Mozer (2005) one obtains the following two equations:

$$(\mathbf{b}' - \mathbf{a}')/\varepsilon = \mathbf{B} + \mathbf{B} \cdot \nabla(c\mathbf{E} \times \mathbf{B}/B^2)\delta t$$

and

$$\mathbf{B}(\mathbf{a}, t + \delta t) = \mathbf{B} + (\delta\mathbf{B}/\delta t)\delta t + (c\mathbf{E} \times \mathbf{B}/B^2) \cdot \nabla)\mathbf{B}\delta t.$$

Finally, after simplifying to first order in δt, Mozer (2005) obtained the following equation:

$$\mathbf{B} \times (\nabla \times \mathbf{E}_{||}) = 0.$$

Thus, for example, if $\mathbf{E}_{||} = 0$, $c\mathbf{E} \times \mathbf{B}/B^2$ motion causes the field to evolve in a manner consistent with Maxwell's equations. But, if $\mathbf{B} \times (\nabla \times \mathbf{E}_{||}) \neq 0$, Maxwell's equations, together with the other plasma equations, must be solved to find $\mathbf{B}(t)$.

Figure 1.2 shows an example from a particle-in-cell simulation (Pritchett and Mozer 2009) of interacting magnetic fields at the magnetopause in which there are regions (especially those seen in red and blue) where $\mathbf{B} \times (\nabla \times \mathbf{E}_{||}) \neq 0$. For such regions the $c\mathbf{E} \times \mathbf{B}/B^2$ motion can not represent the correct evolution of $\mathbf{B}(t)$.

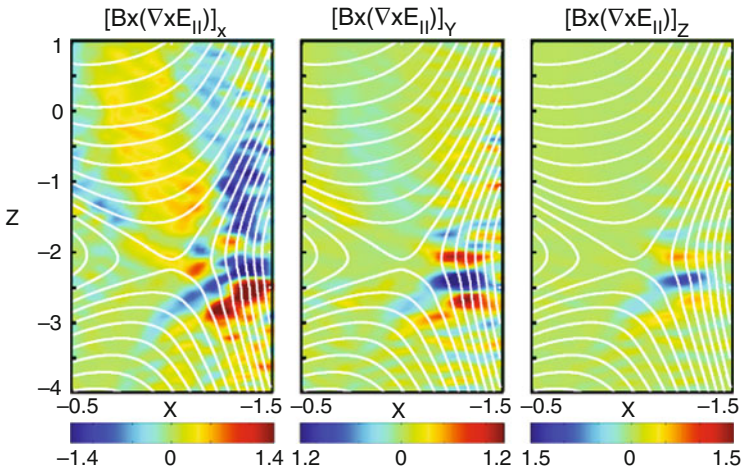

Fig. 1.2 Topology of fields and related quantities for asymmetric reconnection with a guide field (from Pritchett and Mozer 2009). Note that the color scales in all panels are saturated at half the maximum absolute value of the quantity of interest. This particle-in-cell (PIC) simulation was driven by an external E_Y field imposed at the magnetosheath boundary and the total systems size was $L_X \times L_Z = 25.6c/\omega_{pi} \times 25.6c/\omega_{pi}$

Frozen-In Condition

The frozen-in condition states that the plasma and the magnetic field move together at the $c\mathbf{E}\times\mathbf{B}/B^2$ velocity. Alfvén (1942) wrote "the matter of the liquid is fastened to the lines of force", but in 1976 he warned against use of "frozen-in" and "moving" magnetic field lines. Why did he change his mind? Because magnetic field lines cannot be said to move at the $c\mathbf{E} \times \mathbf{B}/B^2$ velocity during the most interesting situations in which the plasma is more complex than ideal MHD, such as at the reconnection-current sheets.

The Generalized Ohm's Law

A more general way of looking for regions where the frozen-in condition is violated is by analyzing the generalized Ohm's law. In two fluid theory, Newton's second law for a unit volume of plasma is:

$$\text{Ions: } n_i m_i(\partial \mathbf{U}_i/\partial t + \mathbf{U}_i \cdot \nabla \mathbf{U}_i) = n_i Ze(\mathbf{E} + \mathbf{U}_i \times \mathbf{B}/c) - \nabla \cdot \mathbf{P}_i + \mathbf{P}_{ie} \tag{1.11}$$

$$\text{Electrons: } n_e m_e(\partial \mathbf{U}_e/\partial t + \mathbf{U}_e \cdot \nabla \mathbf{U}_e) = -n_e e(\mathbf{E} + \mathbf{U}_e \times \mathbf{B}/c) - \nabla \cdot \mathbf{P}_e + \mathbf{P}_{ei} \tag{1.12}$$

where $\mathbf{P}_i$, $\mathbf{P}_e$ are the ion and electron pressure tensors, $\mathbf{P}_{ie}$ ($\mathbf{P}_{ei}$) is the momentum transferred from electrons (ions) to ions (electrons). Multiply Eq. (1.11) by e/m_i and Eq. (1.12) by e/m_e, then subtracting Eq. (1.12) from Eq. (1.11), neglecting quadratic terms, assuming electrical neutrality and ignoring m_e/m_i terms, for $Z = 1$, one gets the generalized Ohm's law:

$$\mathbf{E} + \mathbf{U}_i \times \mathbf{B}/c = \mathbf{j} \times \mathbf{B}/enc - \nabla \cdot \mathbf{P}_e/en + (m_e/ne^2)d\mathbf{j}/dt + (\mathbf{P}_{ie} - \mathbf{P}_{ei}). \quad (1.13)$$

Equivalently, because $(c/ne)\mathbf{j} = \mathbf{U}_i - \mathbf{U}_e$,

$$\mathbf{E} + \mathbf{U}_e \times \mathbf{B}/c = -\nabla \cdot \mathbf{P}_e/en + (m_e/ne^2)d\mathbf{j}/dt + (\mathbf{P}_{ie} - \mathbf{P}_{ei}). \quad (1.14)$$

In Eqs. (1.13) and (1.14) the last terms between parentheses at the right refer to the resistivity of the medium. Figure 1.3b presents a simulation of the components of $\mathbf{E} + \mathbf{U}_i \times \mathbf{B}/c$ and of $\mathbf{E} + \mathbf{U}_e \times \mathbf{B}/c$ for an asymmetric magnetopause (Mozer and Pritchett 2009), and shows locations where these components are different from zero, namely where the magnetic field lines are NOT frozen-in.

The Diffusion Region

The problem with this concept is that it is poorly-defined. If it was well-defined, it might be measurable and would not be an empirical construct. A common view is that the electron diffusion region is a box of size c/ω_{pe} (red rectangle in Fig. 1.3a) in which the electrons are not magnetized. This box is embedded in the ion diffusion region which is a box of size c/ω_{pi} (green rectangle in Fig. 1.3a) within which the ions are not magnetized. Figure 1.3b shows a computer simulation of the ELECTRON diffusion region, in which $\mathbf{E} + \mathbf{U}_e \times \mathbf{B}/c \neq 0$, and of the ION diffusion region, in which $\mathbf{E} + \mathbf{U}_i \times \mathbf{B}/c \neq 0$.

Comparison between Fig. 1.3a,b shows that a definition of the diffusion region as shown in Fig. 1.3a is not useful since, for example, the extension in the X and Z directions of the simulated electron and ion diffusion regions are not clearly different among them and do not resemble the model of Fig. 1.3a with the electron diffusion region clearly imbedded in the ion region.

Summary

One can't think of moving magnetic field lines that simply "get cut and reconnect" at the reconnection region because the concept of moving field lines do not apply there for being a non-MHD region. The concept of "diffusion region" usually adopted in reconnection models does not represent well the related observations and, therefore, needs to be better defined.

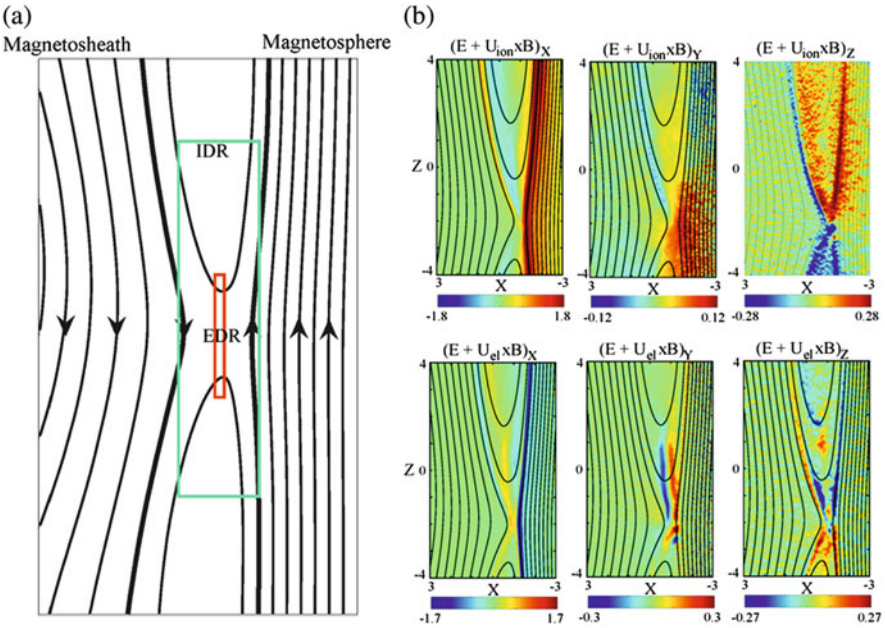

Fig. 1.3 (**a**) Illustration of ion (IDR) and electron (EDR) diffusion region. (**b**) Components of $\mathbf{E} + \mathbf{U}_i \times \mathbf{B}$ and $\mathbf{E} + \mathbf{U}_e \times \mathbf{B}$ (from Mozer and Pritchett 2009). The *red* and *blue* regions in each plot are the locations where the magnitude of the quantity of interest is greater than half of its peak value. This PIC simulation was driven by an external E_Y field imposed at the magnetosheath boundary and the total systems size was $L_X \times L_Z = 25.6c/\omega_{pi} \times 25.6c/\omega_{pi}$

1.3A Experimental Identification of Two-Scale Diffusion Region (M. Yamada)

In the MRX experiment (Yamada et al. 2010), we experimentally identified a two-scale diffusion layer in which an electron diffusion layer resides inside of the ion diffusion layer, the width of which is the ion skin depth (Ren et al. 2008). In this situation we define the ion diffusion layer as the regime of $\mathbf{E} + \mathbf{U}_i \times \mathbf{B}/c \neq 0$ and the electron diffusion layer as the regime of $\mathbf{E} + \mathbf{U}_e \times \mathbf{B}/c \neq 0$. Just outside of the electron diffusion layer, $\mathbf{E} + \mathbf{U}_e \times \mathbf{B}/c = 0$ holds, namely the out of plane reconnection $\mathbf{E}$ field is expressed by $\mathbf{U}_e \times \mathbf{B}/c$, where both $\mathbf{U}_e$ and $\mathbf{B}$ lie within the reconnection plane. It was concluded that Hall effects determine the reconnection rate. Furthermore, it was found that demagnetized electrons are accelerated along the outflow direction and within the reconnection plane, as shown in Fig. 1.4. The width of the electron outflow was shown to scale with the electron skin depth as $5 - 8c/\omega_{pe}$, which is ~3–5 times wider than predicted by 2D numerical simulations (Ji et al. 2008). While the electron outflow seems to slow down due to dissipation in the electron diffusion region, the total electron outflow flux remains independent of the width of the electron diffusion region. We note that even with presence of the

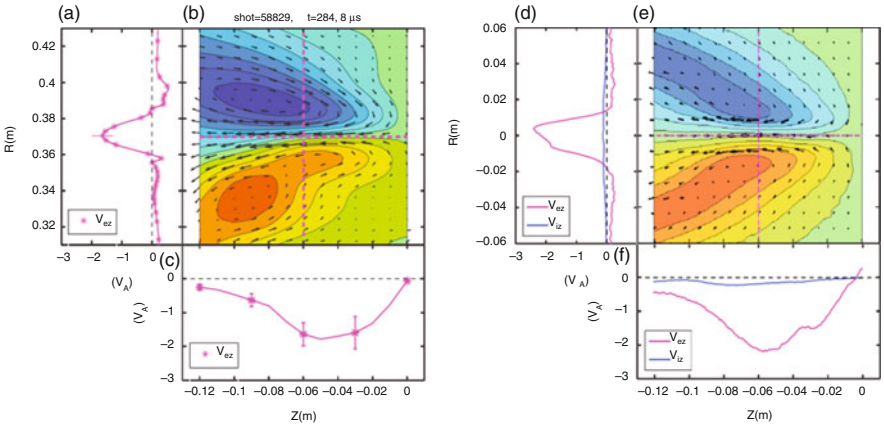

Fig. 1.4 Identification of electron diffusion layer. The *left three panels* (**a–c**) show measured out-of-plane field contours, flow vectors (*black arrows*), and flow velocities in the reconnection plane. Results from a corresponding 2D simulation at a reduced mass ratio are shown in the same format on the three panels (**d–f**) at the *right* using W. Daughton's 2D particle-in-cell code (from Ji et al. 2008; Dorfman et al. 2008)

narrow electron diffusion region, the reconnection rate is still primarily determined by the Hall electric field as was concluded by the GEM challenge (Birn et al. 2001). To our knowledge MRX results are one of the clearest observations of the electron diffusion region within a plasma. When either an externally imposed guide field or inflow asymmetry is applied, the configuration of the electron diffusion layer becomes deformed and changes to a more complex configuration.

1.3B The Energetics of the Two-Fluid Diffusion Layer (M. Yamada)

Our quantitative measurements in the MRX reconnection layer on the acceleration and heating of both electrons and ions demonstrate that half of the incoming magnetic energy is converted to particle energy at a remarkably fast rate (Yamada et al. 2014). In our study we have found that within a collisionless reconnection layer, the energy deposited into the ions is more than twice as large as that deposited into the electrons. Furthermore, a non-negligible amount of magnetic energy flows out the exhaust. It is important to note that when the energy deposition rate to electrons, $\mathbf{j}_e \cdot \mathbf{E}$, is decomposed into $\mathbf{j}_{e\perp} \cdot \mathbf{E}_\perp + \mathbf{j}_{e\parallel} \cdot \mathbf{E}_\parallel$, i.e. separating the inner product into that of the perpendicular and parallel components with respect to the local magnetic field lines, $\mathbf{j}_{e\perp} \cdot \mathbf{E}_\perp$ is measured to be significantly larger than $\mathbf{j}_{e\parallel} \cdot \mathbf{E}_\parallel$. Near the X-point where energy deposition is maximal, $\mathbf{j}_{e\perp} \cdot \mathbf{E}_\perp$ is larger than $\mathbf{j}_{e\parallel} \cdot \mathbf{E}_\parallel$ by more than an order of magnitude. We have observed that the conversion of

magnetic energy occurs across a region significantly larger in area than the narrow electron diffusion region predicted by previous 2D simulations. A saddle shaped electrostatic potential profile is verified to exist within the reconnection plane both in the experiment and simulations and, as a result, ions are accelerated by the resulting electric field at the separatrices (Yoo et al. 2013). This acceleration and heating of ions happens in a wide region extending over an ion skin depth—the so-called ion diffusion region. These accelerated ions are then thermalized by re-magnetization in the downstream region. When the energy deposition rate to ions, $\mathbf{j}_i \cdot \mathbf{E}$, is decomposed into $\mathbf{j}_{i\perp} \cdot \mathbf{E}_\perp + \mathbf{j}_{i\parallel} \cdot \mathbf{E}_\parallel$, the perpendicular component, $\mathbf{j}_{i\perp} \cdot \mathbf{E}_\perp$, is again found to be dominant over $\mathbf{j}_{i\parallel} \cdot \mathbf{E}_\parallel$ in the regions where energy deposition to ions is maximal (Yamada et al. 2015, Chap. 4 of this book).

In Fig. 1.5a, c, it is clearly demonstrated that without guide field or asymmetry, the energy dissipation to electrons and ions occurs primarily due to $\mathbf{j}_{e\perp} \cdot \mathbf{E}_\perp$ and $\mathbf{j}_{i\perp} \cdot \mathbf{E}_\perp$ respectively, that is, the inner products of the perpendicular components of $\mathbf{j}$ and $\mathbf{E}$ with respect to $\mathbf{B}$. This demonstrates a different aspect of broad energy conversion from Mozer and Pritchett's (2011) results on asymmetric reconnection in

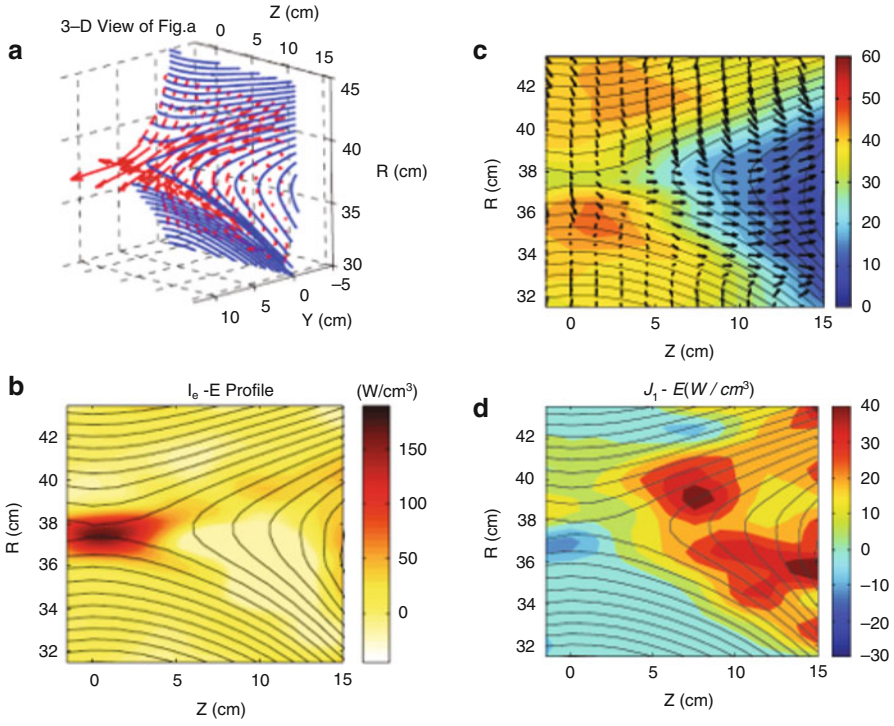

Fig. 1.5 Flow vectors of electron in 3-D views (**a**) and the energy deposition rate to electrons. High energy deposition is primarily due to $\mathbf{j}_{e\perp} \cdot \mathbf{E}_\perp$ which is concentrated in the electron diffusion region (**b**). Flow vectors of ion in the potential well (**c**). The energy deposition to ions occurs across the separatrices and in a much wider region than for electrons (**d**)

which $\mathbf{j}_{e\|} \cdot \mathbf{E}_{\|}$ was emphasized. Based on these results, it would be more appropriate to call these extended energy deposition regions, "energy conversion regions" rather than the "diffusion regions".

1.4 Global Aspects of Magnetic Reconnection and the Axford Conjecture (V.M. Vasyliūnas)

1.4.1 Introduction

Magnetic reconnection can occur only if there are departures from ideal MHD. An obvious question is the extent to which the parameters specifying the non-MHD effects (electrical resistivity, inertial length, gyroradius, etc.) influence the configuration of the system. This question is often stated as: what determines the reconnection rate?. A more specific formulation, applied to a particular system (e.g., the Earth's magnetosphere) is: what determines the amount of open magnetic flux and the rate of magnetic flux transport? These quantitative global parameters can be empirically estimated (from polar-cap area and from cross-polar-cap potential, respectively, among other methods) and have with some success been related to solar-wind parameters. The concept that such global parameters are determined primarily by large-scale MHD dynamics and boundary conditions, with non-MHD effects important mostly for determining properties of local small-scale structures such as boundary layers, was persistently and eloquently argued especially by W.I. Axford and is often called the "Axford conjecture". Recent criticisms of the conjecture are based to a large extent on a misunderstanding of what it means. Unless the Axford conjecture is assumed to be valid at least to some degree of approximation, global MHD simulations of the magnetosphere (most of which do not even pretend to model non-MHD effects adequately) cannot be trusted to give reliable results on anything related to reconnection. Attempts to understand from first principles and derive theoretically the empirically established relations between the solar wind and the global properties of the open magnetosphere (or their proxies in geomagnetic/magnetospheric indices) require careful consideration of the Axford conjecture and related basic assumptions. Global MHD simulations of the magnetosphere, most of which do not even pretend to model non-MHD effects adequately, cannot be trusted to give reliable results on anything related to reconnection, unless the Axford conjecture is assumed to be valid at least to some degree of approximation.

1.4.2 Axford Conjecture

Perhaps the most succinct statement of what we now call the "Axford conjecture" is Axford's own summary of his opening talk at the Workshop on "Magnetic Reconnection in Space and Laboratory plasmas", held at Los Alamos National Laboratory in October 1983 (Axford 1984), Axford summarized his talk in the following way, which we now adopt as the "Axford conjecture":
"*Magnetic reconnection cannot occur unless there is a non-zero electrical resistivity (or some other departure from ideal MHD). However, the large-scale properties of the process are governed primarily by global dynamics and boundary conditions, not by the values of the resistivity or other non-MHD effects*"
(for other, more detailed statements, see Axford 1967, 1969). According to this conjecture, local properties of small-scale regions where the actual reconnection is occurring can depend strongly on resistivity or other non-MHD parameters, but the global configuration of the reconnecting system is largely independent of them. This is not an exact law but a useful approximation (somewhat like MHD itself). A simple analog frequently invoked by Axford is the role of viscosity in aerodynamics: the lift of a plane does not depend on the coefficient of viscosity, but if air were non-viscous then planes could not fly.

Recent criticisms of the Axford conjecture are based to a large extent on a misunderstanding of what it means. Sometimes the conjecture is interpreted as denying any role for the nonideal plasma "diffusion region"; this overlooks Axford's explicit acknowledgement that without nonideal effects there would be no reconnection. An even more extreme interpretation is that, because the solar-wind electric field is the boundary condition for dayside reconnection, the conjecture equates the solar-wind electric field to the magnetopause reconnection electric field; this holds only if any deflection of solar wind flow around the magnetosphere is negligible (a nonsensical assumption, never made by Axford).

1.4.3 Importance of Axford Conjecture

If it is assumed that the Axford conjecture does not hold to any significant degree of approximation, i.e., not only local but also global properties of reconnection are assumed governed primarily by non-MHD effects, then numerical global MHD simulations must be viewed as unreliable on issues involving reconnection (particularly on values of open magnetic flux, reconnection rates, and other quantitative parameters), because their non-MHD aspects are almost always unrealistic and are controlled only in part. Furthermore, it becomes difficult to demonstrate a rational basis for the construction and use of simple empirical coupling functions (driving functions), which relate magnetospheric indices to solar wind bulk parameters without reference to any non-MHD quantities.

When discussing the applicability or otherwise of the Axford conjecture, one should deal with specific defined quantitative physical parameters, not just vague general concepts (such as "reconnection rate") which may be ambiguous and depend on the non-unique definition of "magnetic reconnection". A specific example is discussed in the next section.

1.4.4 Quantitative Properties of an Open Magnetosphere

The simplest configuration of a magnetically open magnetosphere (Fig. 1.6) can be described by three basic quantities: Φ_M = total amount of open magnetic flux, $\mathscr{L}_X$ = length of the dayside reconnection X-line segment, projected along plasma flow streamlines back into the undisturbed solar wind (not the length at the X-line itself), and $\mathscr{L}_{MT}$ = distance between the dayside and the nightside locations of the outer (interplanetary/open) branch of the separatrix, extended into the undisturbed solar wind ("effective length" of the magnetotail). In terms of solar-wind parameters,

$$\Phi_M \simeq \mathscr{L}_X \mathscr{L}_{MT} B_s,$$
$$c\mathscr{E}_d \simeq \mathscr{L}_X V_{sw} B_s,$$
$$(d/dt)\Phi_M = c\mathscr{E}_d - c\mathscr{E}_n,$$

where B_s = reconnecting component of interplanetary magnetic field, and $\mathscr{E}_d$, $\mathscr{E}_n$ = line integrals of electric field along dayside and nightside reconnection segments of

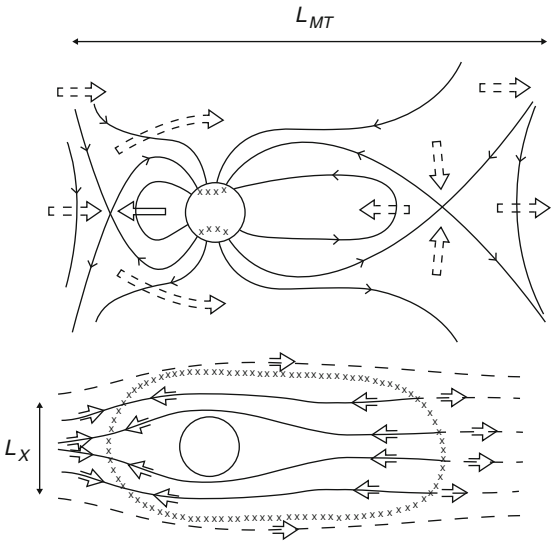

Fig. 1.6 Schematic topological view of magnetically open magnetosphere (from Vasyliūnas 2011). (*Upper*) noon-midnight meridian plane. (*Lower*) equatorial plane. Lines: plasma flow streamlines, x's: (projection of) magnetic X-line = interplanetary/open/closed field line boundary = polar cap boundary

X-line, respectively. In quasi-steady state: $\mathscr{E}_d \simeq \mathscr{E}_n$ = maximum line integral of electric field across polar cap (cross-polar-cap potential, transpolar potential).

The dayside reconnection rate can be specified by

$$c\mathscr{E}_d \simeq \mathscr{L}_X V_{sw} B_s \tag{1.15}$$

It is thus given by known solar wind parameters, plus two numbers to be determined: a length $\mathscr{L}_X$, and an angle that relates B_s to the interplanetary magnetic field B_{SW}. Equation (1.15) represents the electric field integral along a line segment which intersects all interplanetary magnetic field lines, transported by the solar wind, that are going to reconnect with geomagnetic field lines. The essence of the Axford conjecture is that these two numbers are global properties of the flow field, hence governed by the momentum equation and boundary conditions. The reconnection rate given by Eq. (1.15) can also be specified instead by the equivalent line integral along the X-line at the magnetopause and can (in principle!) be calculated from it, provided one knows in detail the extent and path of the reconnecting portion of the X-line and the variation of the electric field along it with local properties—all quantities governed (of course) by local non-MHD effects. (Much recent criticism of the Axford conjecture derives from confusing these two ways of defining the reconnection rate.)

The global calculation of dayside reconnection rate requires solving two coupled flow problems:

1. Magnetosheath (interplanetary field lines): How much solar-wind flow goes around the magnetosphere vs. how much enters the magnetosheath/magnetosphere interaction region?. $\mathscr{L}_X$ is the width in the solar wind of the bundle of streamlines connecting to the interaction region.
2. Magnetosheath/magnetosphere (open field lines): How much plasma entering from the magnetosheath can be accommodated in the diverted post-reconnection flow?. This provides the inner boundary condition necessary to calculate magnetosheath flow and inter alia determine $\mathscr{L}_X$.

The non-MHD-controlled reconnection at and in the immediate vicinity of the X-line (diffusion region) suffices to allow non-zero normal magnetic field and plasma entry elsewhere in the interaction region; the global rate of plasma entry, and hence the value of $\mathscr{L}_X$, should then be controlled primarily by large-scale dynamics of the post-reconnection flow (Axford conjecture in a nutshell!).

Empirical support for this concept may be provided by the observed phenomenon of cross-polar-cap potential saturation (see review by Shepherd 2007 and references therein): for sufficiently large values of the interplanetary electric field, the transpolar potential no longer increases but approaches a constant value. This means that, as the amount of "reconnectable" interplanetary magnetic flux transported by the solar wind increases, the fraction of the incoming flux that actually reconnects with the geomagnetic field (or, equivalently, the value of $\mathscr{L}_X$) decreases. The (increasingly large) remainder must then flow around the magnetosphere without reconnecting. A plausible explanation is that some property or process of post-reconnection flow acts

to limit the amount of magnetic flux that can be transported; mechanisms involving collisional drag in the ionosphere or strong magnetic forces in the magnetosheath have been proposed.

1.4.5 Conclusions

1. Non-MHD terms in the generalized Ohm's law are essential for the occurrence of magnetic field line reconnection, but their direct effects are mainly local, confined to small regions. The primary global consequence is to remove certain constraints, allowing flow and field configurations that otherwise could not occur.
2. These newly allowed flows are subject to the same continuity and momentum balance conditions (Newton's and Maxwell's laws) as any others, hence (Axford conjecture) their large-scale properties should be governed to first approximation by global considerations (note that the Axford conjecture makes no predictions about local properties of non-MHD regions, a point often overlooked in recent criticism).
3. The dayside magnetopause reconnection rate is expected to be constrained primarily by removal of plasma and magnetic flux in (distant) post-reconnection flow. Magnetosheath (pre-reconnection) flow can always adjust itself to any required rate.
4. The observed cross-polar-cap potential saturation may be considered as evidence for the control process described in conclusion (3).

1.4A Global Equilibria (R.M. Kulsrud)

It was shown in the paper of Kulsrud (2011) that during reconnection the global evolution of the surrounding material is, other than its rate, independent of the nature of the processes occurring in the reconnection layer. This statement is valid if the reconnection is slow compared to dynamic times and if the reconnection layer and the separatrix dividing the unreconnected and reconnected regions are very thin. That is to say, one can lay out a series of global equilibria and in each case give the actual geometry and distribution of properties in the unreconnected and reconnected regions. The only dependence on the reconnection processes in the thin layers is the rate at which the global equilibrium progresses through this series.

This statement is based on the variational principle for magnetostatic equilibrium that states that for certain constraints the entire global equilibrium outside of the layers, including the geometry of the different regions, is given by minimizing the total potential energy (Kruskal and Kulsrud 1958; Uzdensky et al. 1996; Kulsrud 2011).

The equilibrium of course satisfies

$$\mathbf{j} \times \mathbf{B} = \nabla p \tag{1.16}$$

inside the two volumes and also the total pressure $P = p + B^2/8\pi$ is the same on each sides of the dividing region.

The constraints are as follows. Denote the unreconnected volume by A and the reconnected volume by B. Let the magnetic fluxes included by the magnetic surfaces in A be ψ_A and in B be ψ_B. Then the constraints which are held fixed under the variation are: the mass functions $M_A(\psi_A)$ and $M_B(\psi_B)$ representing the masses included in the corresponding flux surfaces, the toroidal flux functions $\phi_A(\psi_A)$ and $\phi_B(\psi_B)$ representing the toroidal flux included in the corresponding flux surfaces, and the entropy functions $S_A(\psi_A)$ and $S_B(\psi_B)$ representing the entropies ($S = p/\rho^\gamma$) on the corresponding flux surfaces. (These functions are of interest, because they are preserved during any MHD evolution.)

The variational principle states that of all possible choices of the pressure and magnetic fields that have magnetic surfaces and which satisfy the same constraints, the choice that gives the minimum potential energy

$$\int \left(\frac{p}{\gamma - 1} + \frac{B^2}{8\pi} \right) d^3x$$

where the integral is taken over both A and B, satisfies the magnetostatic equation Eq. (1.16). It also satisfies the continuity of P taken across all the layers. The converse is also true, that any equilibrium state must have a minimum energy under the constraints.

The consequence is that the global equilibrium is uniquely specified by giving the mass functions, toroidal flux functions and the entropy functions.

Now, consider that reconnection after a time dt has removed a flux $d\psi$ from the unreconnected region A, and added it to the reconnected region, B. Since the reconnection layer is very thin the loss of any toroidal flux $d\phi$ in passing from region A to B will be very small and similarly for the Mass dM.

The situation after the reconnection time dt will be that A will have less poloidal flux by an amount $d\psi$, but the functions ϕ, M and S, which are constraints of the motion in MHD, are unchanged over the remainder of the range. In region B the flux $d\psi$ will be added and the range of $d\psi_B$ will be extended by $d\psi$. Again the functions ϕ, M, and S will be unchanged over the original range. However in the extension of its range $d\psi$, the values of the toroidal function and of the mass function will be the same as they were in the last part of its range in A before the infinitesimal reconnection.

However, the entropy will change in the residual range by dissipation processes in the reconnection and separatrix layers. One could imagine that one would have to work out the entropy gain in the reconnection layer in order to complete the function in B. However, if the global region is surrounded by a rigid wall, the total energy must be unchanged. Thus, the value of S in the extended range of the energy is conserved, and the new resulting entropy in the residual flux region of B is determined.

Thus, since the new functions after the infinitesimal reconnection during dt are predetermined once $d\psi$ is known, the new global equilibrium including the changed

geometry is completely determined by global physics alone. Only the amount of flux change in the time dt depends on the actual reconnection physics in the layer.

I have not mentioned the kinetic energy generated in the reconnection process. But under the assumption that reconnection is slow any velocities in region B will be quickly damped by parallel viscosity, which is very large, and the kinetic energy can be considered to be immediately converted to thermal energy and entropy.

Thus, after any reconnection time step all the constraints $(\phi(\psi), M(\psi), S(\psi))$ will be determined in both regions A and B by the amount of reconnected flux, $d\psi$. Therefore, since the global equilibrium is determined by these functions the new equilibrium is established independent of the physics in the narrow layers.

In conclusion, during any sufficiently slow reconnection the sequence of global equilibria will be independently determined by global considerations and not local ones. The role of the reconnection processes is merely to determine the rate at which the global equilibrium proceeds through this series.

1.4B Role of Reconnection Separatrices in Global Aspects of Magnetopause Reconnection (W.D. Gonzalez and D. Koga)

Figure 1.7 illustrates the B-fluxes and plasma flows at the inflow and outflow reconnection regions expected from classical reconnection models, as also claimed below in Sect. 1.5 concerning the needed curvature of the reconnecting B-field topology. The illustrated separatrices (discontinuities separating the non-reconnected from the reconnected B-fluxes) have been found to be rich in plasma and electric field-complex structures, including field-aligned flows, parallel electric fields, density non-uniformities, electron holes, etc (e.g., Lapenta et al., Chap. 8 of this volume). Thus, although from the kinetic point of view the separatrices have plasma and field structures similar to those proper of the diffusion region, from a global view of the overall reconnection region the separatrices can be considered to behave as an interlink between the central diffusion region (black rectangle) and the external large-scale reconnection region. From space and laboratory measurements at the moment we do not know the extension of the separatrices in the large scale reconnection domain, and of its participation in the influence of the external region plasma and field characteristics (boundary conditions) in the physics of the diffusion region, and vice versa. As discussed in Sect. 1.5.1 dealing with the diffusion region, one can also see from these considerations that it is not a simple matter to define spatial limits for the diffusion region since they can become confused with those of the separatrices. The structure of the separatrices should change from case to case according to the selected reconnection scenario for which the boundary conditions and external plasma and field properties can be different, as for example comparing the reconnection case at the dayside magnetopause of the Earth with that at the tail of the magnetosphere. In the former one has a typical asymmetric reconnection with different plasmas and fields entering from the magnetosheath and the magnetosphere to reconnect, the former being influenced by the changing solar wind. On the other hand, at the magnetospheric tail one finds usually a symmetric

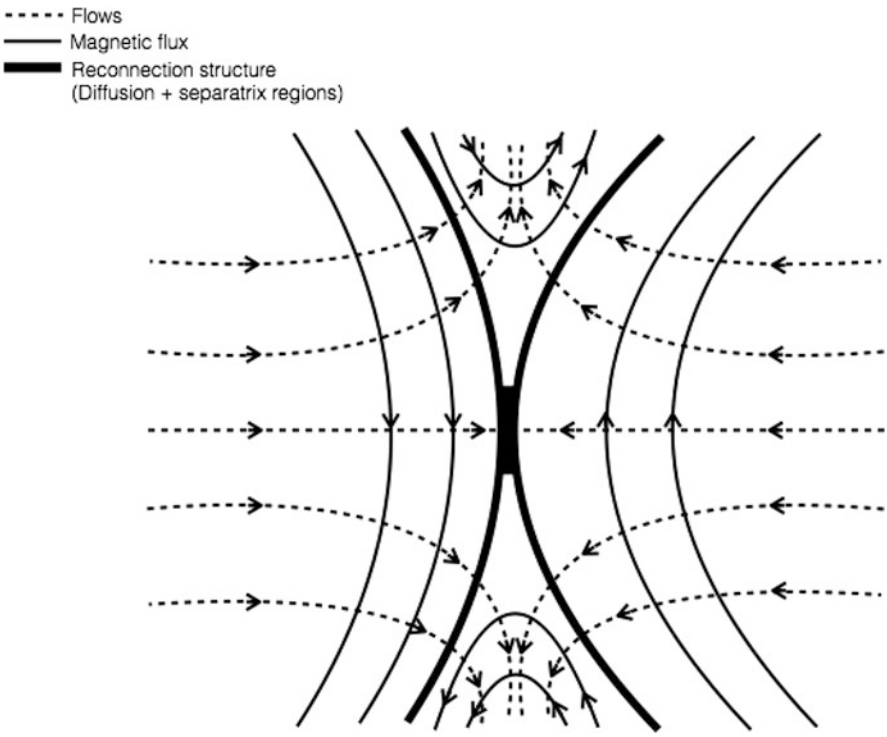

Fig. 1.7 Internal and external regions of the reconnection magnetic field topology and flows

reconnection scenario with plasmas and fields influenced, both, by the solar wind conditions and by the internal dynamics of the magnetosphere.

Figure 1.8 illustrates the expected geometry of the separatrices (dotted curves) between the reconnecting regions at the dayside magnetosphere, as seen on the noon-midnight meridional plane. The approaching solar wind speed, V_{sw}, after the Bow shock becomes decelerated down to the reconnection speed, V_o, close to the magnetopause. After reconnection the reconnected plasma is expected to exit the diffusion region with the local Alfvén speed V_A.

It is expected that the rate of reconnection should be governed both, by the physics of the diffusion region determining the amount of B-flux that this region allows to reconnect and by the properties of the external region, transmitted by the separatrices, determining the amount of reconnected flux that can be supported by the reconnecting system as a whole. Toward this latter understanding it should be necessary to look for the allowed total energy changes in the overall reconnecting system according to a sequence of appropriate states of minimum energy configuration (e.g., Kulsrud, this chapter). As shown in Fig. 1.8, the influence of two important boundary conditions in the overall reconnection process are expected to be considered. One of them refers to the region indicated by the circled number

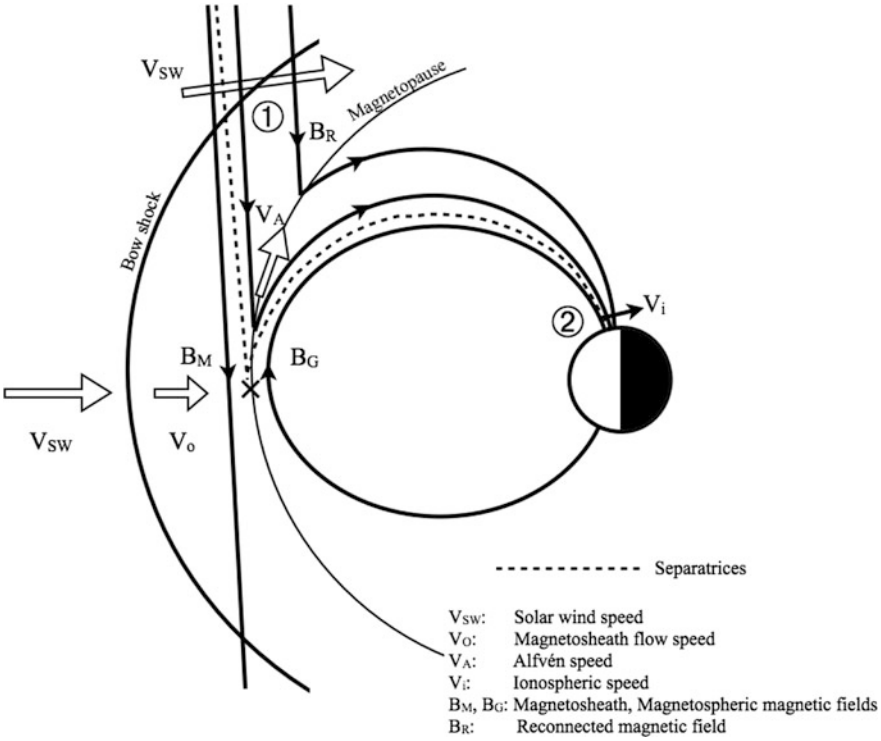

Fig. 1.8 Reconnection separatrices at the magnetosheath and magnetopause of the dayside magnetosphere (details are illustrated for the northern hemisphere assuming that a similar illustration holds for the southern hemisphere)

1, at the top, where the external separatrix finds a magnetosheath plasma with flow speed values that are close to the nominal solar wind speed V_{sw}. The other refers to the region indicated by the circled number 2, where the internal separatrix meets ionospheric plasmas, in which flow speeds associated with the reconnection process can become limited by internal plasma conditions of the ionosphere, such as conductivity, density levels and convection histories. The issue of how these two boundary conditions affect the separatrices and become transmitted down to the diffusion region is at present poorly known due the lack of simultaneous measurements at such separate regions, especially concerning the external separatrix (e.g., Lapenta et al., Chap. 8 of this volume).

With respect to the reconnection energetics associated with the region involving the external separatrix of Fig. 1.8, it is important to realize that the physics of energy transfer from the solar wind to the magnetosphere is expected to be of the dynamo type at high magnetopause latitudes ($\mathbf{E}\cdot\mathbf{J} < 0$), thus allowing transfer of mechanical energy from the solar wind to the magnetospheric tail, to be later transformed in energy supply for storms and substorms (e.g., Gonzalez and Mozer 1974; Gonzalez

et al. 1994). On the other hand, the internal region of reconnection involving the diffusion region is of a load (dissipation) type ($\mathbf{E} \cdot \mathbf{J} > 0$), thus consuming energy from the solar wind rather than transmitting it to the magnetospheric tail. This issue needs to be clearly appreciated when developing the so called "coupling functions" (e.g., Borovsky 2013), since such functions may represent a dissipation region ($\mathbf{E} \cdot \mathbf{J} > 0$) rather than a dynamo region ($\mathbf{E} \cdot \mathbf{J} < 0$), the latter being the necessary type of process to consider in order to compute the energy budget for storms and substorms, as mentioned above.

One important parameter that also needs to be studied to understand the interaction between the diffusion region and the external region of reconnection is the electric field associated with each of these regions. At each of the separatrices, a large-scale electric field is set up by the solar wind and ionospheric flows, respectively, and by the reconnected magnetic field, whereas at the diffusion region, the reconnection electric field is expected to be set up mostly by internal processes (e.g., Scudder et al., Chap. 2 of this volume). We do not know yet how these electric fields get an equilibrium balance in order to compute an overall reconnection rate.

Another important factor to consider in order to find a self consistent solution for the large-scale reconnection problem at the magnetopause is the role of the Bow shock in determining regimes of magnetosheath plasma and magnetic field. For example, it is expected that the reconnection potential becomes saturated for sufficiently large values of the solar wind magnetic field via large-scale currents determined by the Bow shock (e.g., Lopez et al. 2010). On the other hand, during magnetospheric active times, the internal magnetospheric plasma and the plasma sheath are expected to influence the magnetospheric plasma entering in reconnection at the magnetopause (e.g., Borovsky and Denton 2006). With the advent of powerful computers and advanced 3D reconnection models, we may be able to start getting self consistent solutions for the magnetosphere-magnetosheath-Bow shock interaction during magnetopause reconnection, which could be compared with relevant observations to be obtained from the MMS and from other dedicated magnetospheric satellite missions.

1.5 Discussion

1.5.1 What is the "Diffusion Region"?

P.A. Cassak

As discussed in Sect. 1.3, it is challenging to rigorously define the diffusion region, also known as the dissipation region (since the effect allowing magnetic field lines to reconnect need not be of the form of a classical diffusion). The standard way of thinking about the diffusion region is quite operational—outside the diffusion

region, the plasma obeys the frozen-in condition, and inside it does not. However, this operational definition is not precise!

To see why, consider the simplest system we can think of, namely two-dimensional resistive magnetohydrodynamics (MHD) with a uniform resistivity. Suppose we have a magnetic field with a Harris sheet profile,

$$B_X \sim \tanh(Z),$$

which has B_X reversing signs at $Z = 0$. From Ampère's law, this magnetic field has an associated current density profile

$$J_Y \sim \mathrm{sech}^2(Z).$$

Since $\mathrm{sech}(Z)$ is non-zero for all finite Z, the current density J_Y is non-zero for all Z out to infinity. In resistive-MHD with a uniform resistivity, this implies that the resistive electric field $E_Y = \eta J_Y$ is non-zero everywhere out to infinity, and this is true even if the Harris sheet is not undergoing reconnection! Thus, the frozen-in condition is formally broken for all Z, implying that the diffusion region extends over all space. This would be a useless definition of the diffusion region!. Consequently, the idealized picture of having a diffusion region with a sharp boundary outside of which is frozen-in simply does not work, even for the simplest system we could possibly study.

This only means that there is no rigorous definition of the diffusion region, but this does not mean it is not a useful construct. By and large, far from a reconnection site, the departure from the frozen-in condition is relatively small, while near the reconnection site the departure is significant. Therefore, in practice, researchers make an arbitrary choice about where to define the edge of the diffusion region based on when the departure from the frozen-in condition is significant for the application in question. But it is merely a convention, and nature draws no such lines!

Especially with the recent launch of the Magnetospheric Multiscale (MMS) mission, it is important and timely to develop a convention to define the diffusion region, and that this convention should be compared with observations. One very reasonable choice is the location where the convective and non-ideal electric fields are of the same size. Then, inside that location, non-ideal effects are larger and outside the location non-ideal effects are smaller.

Unfortunately, even this simple and logical convention is not without its complications. For example, the scalar part of the gradient of the electron pressure tensor can be non-zero, which leads to the electric field differing from the convective electric field. However, a scalar pressure does not break the frozen-in condition. This has been reported to be an issue at the electron diffusion region in collisionless plasmas. There have been a number of quantities proposed for defining the diffusion region, as will be seen in subsequent sections and chapters of this book.

I think that the key to the issue—whether in 2D or 3D and whether in a fluid or kinetic system—is *dissipation*, which by definition is the irreversible transformation of ordered energy into heat. This is associated with an increase in the entropy of the

plasma. Consequently, I believe a true measure of the diffusion region is where the frozen-in condition is broken *and* entropy is increasing. It would be rather straight-forward to develop a model for this within the confines of resistive-MHD, but in a kinetic system where the entropy is related to a velocity space integral of the structure of the distribution function, it is less obvious how to proceed. The interesting question of how to define the diffusion region will undoubtedly continue!

J.D. Scudder

The diffusion region may have different shapes in different geometries: guide, parallel, symmetric, anti-symmetric and 2D vs 3D. It is almost certainly a place in collisionless reconnection where the thermal electrons become demagnetized. (This is not an if and only if statement however, as we demonstrate in Chap. 2.) We have also documented 5–6 different observable ways to find this condition by "asking" the electrons themselves, i.e. their agyrotropy (Scudder and Daughton 2008). This region needs to be a flux slippage region where $\nabla \times (\mathbf{E} + \mathbf{V} \times \mathbf{B}/c)$ is different from zero. However, since this condition is related to the time scale of disruption of Guiding Center ordering, its size and locale can be inferred by other observable signatures of demagnetization. In 3D this layer is most likely not time independent, spawning ancillary (a) flux ropes and (b) secondary reconnection sites. We will show examples of this in 3D in Chap. 2. The merger of diffusion region concepts such as Vasyliūnas's demagnetization idea with the global conditions (a) squashing and (b) field aligned potential drops have already been demonstrated (Scudder et al. 2015).

H. Karimabadi

The idea of a central diffusion region is most meaningful in simple 2D steady state models in which the reconnection rate can be related to the aspect ratio of the diffusion region. However, this simplification can still be a reasonable idealization in scenarios where there is a well-defined and dominant inflow-outflow region. Unfortunately even in such idealized cases, there is no first principle theory that provides an estimate for the dimensions of the diffusion region. For example, in a collisionless plasma, the width of the electron diffusion region is about one electron skin depth but there is no theory currently that provides an estimate for the length of the diffusion region. An interesting idea that yields an estimate for the aspect ratio of the diffusion region is based on linear theory mode. Since tearing mode is the eigenfunction of a current sheet, one may suppose that a sufficient condition for reconnection is for the tearing to be unstable. The wavenumber for the most unstable tearing mode is given by $k\delta = 2\pi\delta/D \sim 0.5$ or $\delta/D \sim 0.08$ where δ and D are the width and length of the diffusion region. This is in reasonable agreement with the rate of ~ 0.1 which is often observed in various reconnection regimes. Although suggestive, this explanation is not a proof and is not widely adopted. External boundary conditions and system size can also play significant roles in the

rate. For example, if the system is driven, the rate will clearly be affected. Similarly, depending on whether the system has periodic or conducting boundary conditions, the rate would be affected. So, in general, the reconnection rate is determined through a combination of internal and external conditions.

W.D. Gonzalez

Since the initial reconnection papers, considering only the resistive term in the generalized Ohm's law and inserting it in Faraday's equation to follow the time evolution of B, it was clear that the only non ideal term in the equation was of the DIFFUSION type. Thus, from then on people has been calling "diffusion region" to the central/non-ideal reconnection region.

However, from later research dealing mostly with collisionless plasmas we know that there are extra terms in the generalized Ohm's law that need to also be inserted in Faraday's equation creating terms that are not any more of the diffusion type. Thus, trying to keep the same name (diffusion) for the collisionless cases seems to introduce semantic complications with an implicit need of looking for a better name that could represent more appropriately the central region of reconnection for such regimes.

On the other hand, I believe that it will be a difficult task to find a common name for the central region that could represent well all reconnection cases, even in 2D, in which the location, extension and dynamics of the reconnection site can vary depending on the dominant local physics as well as on the different boundary conditions applicable to each case.

In spit of these considerations, calling the central reconnection region a diffusion region, besides having an historical importance, has been helping reasonably well to organize reconnection research and for the time being it may still continue doing it so until, with more advanced observations and models (especially in 3D), we may move towards finding more appropriate nomenclatures, maybe not any more trying to represent just with a single name the whole central region of reconnection, but naming more specific subregions, such as ion Hall region, electron nongyrotropy region(s), and so on.

1.5.2 Comments on Question 1

P.A. Cassak

What does it mean for magnetic field lines to "get cut" and "reconnect"? The overarching answer, I would say, is that there must be some dissipative (irreversible) effect that is important right at the location where field lines get cut and reconnect. In a (theoretical) "ideal" system, there is no reconnection because there are no dissipative effects, and electrons are free to move essentially infinitely fast to short

out any electric fields in the system. In a resistive system, which is relatively easy to understand compared to collisionless systems, resistivity provides the necessary irreversible dissipation to cut the field lines. Much like driving a current through a wire, collisions between electrons and ions prevent the electrons from moving essentially infinitely fast to short out electric fields, so an electric field can exist. From Faraday's law, this electric field allows the field lines to change, and they can undergo the process that appears to observers from afar as magnetic field lines cutting and reconnecting.

In collisionless systems, the same basic picture still holds, in that some dissipative effect allows an electric field to arise. What effect allows this seems to depend on the system parameters. There is pretty broad agreement that for the symmetric case without a guide field, the off-diagonal elements of the electron pressure tensor, effectively an electron viscosity, provide the irreversible dissipation. However, the case with a guide field or with asymmetries has not been studied as much, and there is still much to be learned.

R.M. Kulsrud

The line breaking process is rather simple when viewed from a particle point of view. In a no guide 2D case there is a region near the X-point where the magnetic field is very weak. This region extends out to a distance x where the nominal gyroradius is equal to x. This region is called the betatron radius since the electrons execute betatron orbits rather than gyro-orbits there. In this region they are free to move into the Y direction on betatron orbits. The secret of line breaking is that there is a finite electric field in the Y direction. In any case the rate of line breaking is given by this electric field by Faraday's law. On the other hand such a field will drive a very large current stopping the reconnection and this current is limited by the average speed of the electrons in this betatron region. In normal reconnection this current is limited by collisions (resistivity) which gives the Sweet-Parker reconnection rate. But in the collisionless case the average velocity is the acceleration by the E field during the time τ for the electrons to cross the betatron region, and if τ is shorter than the collision time then one can have a larger E field for the same current (Yamada et al. 2010). This point is difficult to understand from the MHD picture because this process is equivalent to an off diagonal term in the electron pressure term, as also spelled out in the review paper by Yamada et al. (2010).

J.D. Scudder

The "cutting" and "reconnection" short hands are after the effect descriptions, not explanations of how this happens. Maxwell's equations are about the 4-vector potential and that description is smooth in space and time. In the short scaled "diffusion" region it is not longer possible to prove that there is a well defined evolutionary equations for "field lines". If one remains in the dialect of describing

the behavior of magnetic field lines this lapse of an equation of motion for them requires a discontinuity in their causal description, that clever popularizers have dubbed cutting and reconnection. From this vantage point the question "how do they get cut and reconnect" is not a question that theory at that level will ever clarify. If one agrees to go to the 4 vector potentials of Maxwell one does obtain an evolutionary description in space and time that is smooth. While $\mathbf{B}(x, y, z, t)$ as curl of $\mathbf{A}(x, y, z, t)$ at any given time has a definite field line topology, that topology is not predictive of the topology of $\mathbf{B}(x, y, z, t+dt)$. The MHD regimes do not require the 4-vector potential to predict the rearrangement of field lines; at some level the ubiquitous simplifications that MHD can afford, does not serve the student well to predict what can happen when the foundations of MHD are supplanted in strong gradient current channels. It is widely subscribed that the non-ideal corrections to the generalized Ohm's law that preclude field and/or flux preservation under the evolution equations is generally dominated by the agyrotropic electron pressure tensor, with possible corrections from inertial terms. More generally this regime is indicated as sites where the curl of the non-ideal electric field $\mathbf{R}_e = \mathbf{E} + \mathbf{V}_e \times \mathbf{B}/c$ is not equal to zero. An agyrotropic electron pressure tensor generally fulfills this type of violation and microphysically corresponds to the disruption of the magnetization of the bulk of the plasma electrons. Colloquially this implies that the approximations of guiding center theory for electrons are disrupted in these narrow current channels. The most commonly cited approximation involved in guiding center theory is the gyroradius over scale of variation is small. The early work by Vasyliūnas (1975) and the most recent full PIC codes of the process agree that this and other underpinnings of guiding center theory for electrons are disrupted in the electron diffusion region.

W.D. Gonzalez

With respect to the initial reconnection models (Sweet 1958; Parker 1957), if one starts with opposite PLANAR reconnecting magnetic fields (pointing, say, in the Y and $-Y$ directions, approaching $X = 0$ from X and $-X$, with the current sheet in the Z direction), for an incompressible plasma and a stationary situation we have:

$$\nabla \times (\mathbf{V} \times \mathbf{B}) = \eta \Delta \mathbf{B}, \text{ or}$$
$$(\mathbf{B} \cdot \nabla)\mathbf{V} - (\mathbf{V} \cdot \nabla)\mathbf{B} = \eta \Delta \mathbf{B},$$

(with η being the resistive diffusion coefficient at the current sheet). Thus, the X-component of this equation gives:

$$B_Y \partial V_X/\partial Y + B_X \partial V_X/\partial X - V_X \partial B_X/\partial X - V_Y \partial B_X/\partial Y = \eta \Delta B_X.$$

If there is no B_X in the convecting region (planar fields), all the terms in the left hand side of the equation are zero EXCEPT the first, if $B_Y \partial V_X/\partial Y \neq 0$. If so, there must also be a nonzero B_X in the current sheet. However, if $\partial V_X/\partial Y \neq 0$ one can

not continue having a planar **B** field since V_X should change with Y and, assuming a frozen-in condition outside the current sheet, B would become curved. Therefore, in order to have reconnection, reconnecting fields need to have a curved topology near the current sheet, for which $B_X \neq 0$. In reality, of course, the reconnecting fields can present external curvatures, defined by the boundary conditions in each case, as assumed in several models after those by Sweet and Parker (e.g. Petschek 1964; Sonnerup 1970). If one also assumes time-dependence, instabilities in the current sheet, such as the tearing mode (Furth et al. 1963) can provide $B_X \neq 0$, which can facilitate the occurrence of reconnection (Karimabadi et al. 2013).

H. Karimabadi

Reconnection does require formation of a finite normal (to the current sheet) field component (B_X) but a finite B_X does not necessarily imply reconnection. In a simple 2D laminar picture, reconnection requires formation of an X-point which by definition has a finite B_X. If one starts with a current sheet with no imposed perturbation, then the only way it can reconnect is through the tearing mode. The tearing mode has certain wavelength so one can think of a tearing perturbation growing in the sheet. As the size of the perturbation grows due to the growth of tearing, it starts to pinch off the current sheet and create X-lines and trigger reconnection at those points. In some simulations, people impose a GEM-like perturbation which effectively forces the X-point to be at the center of the sheet (Birn et al. 2001) and only a single X-line is formed initially. The generation of finite B_X originates at the X-point. However, in 3D the situation becomes much more complex.

2D steady state MHD models of reconnection present different reconnection solutions as a function of resistivity model. As such they assume B_X. Otherwise there won't be any reconnection. Steady state models by definition don't address generation mechanisms since that involves a time evolving solution requiring dB/dt. The connection to tearing is controversial. If one sees islands forming, then it is clear that tearing is operational, but one can also have reconnection without formation of islands as shown in many simulations. In such cases it is harder to prove tearing as the cause of B_X/reconnection. A good way to think of it is as follows: a current sheet is susceptible to reconnection. This means that any fluctuations in B_X would grow in time and the system would organize itself into an inflow-outflow configuration. This can happen in two ways: (a) since tearing is an eigenfunction of a current sheet, any current sheet that is unstable to tearing would form a finite B_X; (b) one imposes a perturbation in a current sheet that is stable to tearing. This can nonlinearly cause reconnection to occur. It is not clear in such cases where the underlying mechanism becomes nonlinear tearing however. In short, the connection of tearing to reconnection remains controversial.

What causes the field lines to have an open geometry, rather than say something like Sweet-Parker is not understood. Tearing does give the right aspect ratio as required for open field lines but this explanation remains not universally accepted.

Linear tearing has an island chain and if one doesn't impose an X-line perturbation initially, one would form bunch of tearing islands which would coalesce. But if one imposes an X-line perturbation as done in (Birn et al. 2001), then there is only one active X-line (i.e., avoids forming tearing island chains) and one bypasses linear tearing. So the open question that remains in such a case is whether tearing is still playing a role in giving rise to the open geometry.

R.M. Kulsrud

Sweet and Parker implicitly assume incompressibility and replace this with $\nabla \cdot \mathbf{V} = 0$ where $\mathbf{V}$ is the in-plane velocity. This is correct if the transverse field or the ambient pressure is large. If the transverse field is zero, one still has flux freezing out side of the layer, but in the layer the transverse field can slip relative to the velocity, but only by an amount inversely proportionally to the square root of the magnetic Reynolds number. To this extent the global helicity is conserved. (of course it is zero without a transverse field).

M. Yamada

In the classical Sweet-Parker model, there is no flux conservation. All flux is dissipated in the current sheet. B_X is limited to the very narrow region of the current sheet ($d \ll L$). So in this model, we do not discuss the role of B_X in the sheet (it is a black box). As it was analyzed by Priest and Forbes (2000), incoming magnetic energy ($\nabla \cdot (\frac{c}{4\pi}\mathbf{E} \times \mathbf{B})$) is converted to plasma energy, divided usually to internal energy (Enthalpy) and Flow energy $(1/2)mV^2$. Thus there is no outflow of magnetic energy. Only Petschek's model and the two-fluid model can predict magnetic energy outflow.

1.5.3 Comments on Question 2

P.A. Cassak

About how the external MHD region and the internal diffusion region depend on each other and in which circumstances one drives the other, this is a challenging question and it is not clear that we know the answer for naturally occurring systems. One can gain some perspective from simulations. The simplest case is 2D systems, for which much is known. For given system parameters, there is a characteristic rate at which the system would want to reconnect the magnetic flux, quantified by the reconnection electric field. The external system can have its own electric field which need not to be the same. If they are the same, the system will reconnect at

the common rate and will continue to do so steadily for as long as there is more magnetic flux to reconnect.

If, however, the external electric field is larger than the characteristic rate the reconnection would reconnect at and the external electric field is held fixed, then flux is introduced faster than it can reconnect, so it piles up near the diffusion region. This increases the magnetic field strength near the reconnection site, which leads to faster reconnection, so the natural rate of the reconnection would increase. When the reconnection is fast enough to have the same electric field as the external one, a steady state is reached at the external electric field. However, if the external electric field is not fixed, one could imagine that the piled up magnetic field would produce a back pressure on the external field, slowing it down and decreasing the external electric field.

One could make a similar statement if the external electric field is weaker than the reconnection electric field—either the reconnection electric field will decrease when the upstream magnetic field weakens until they are the same, or the external field will increase to supply more flux. The end result is that they should end up at the same electric field. In simulations, the external field is often imposed so the system typically ends up at the imposed external field, but in a real (2D) system, it is not obvious which should dominate. Many believe it is the external field, but I do not think this has been studied sufficiently well.

This is all for 2D, but the situation totally changes for 3D. In 3D, the system has another option—the external flow can simply go around the reconnection site instead of changing the magnetic field at reconnection site, as has been seen in simulations and may take place, for example, at the dayside magnetopause. In such a case, it is not clear whether or how the two are related, and this remains an open question.

J.D. Scudder

This situation is common in boundary layer physics. The diffusion region is a boundary layer that affords a connection between external regions that are increasingly more ideal insofar as MHD approximations are concerned. This problem between LOCAL MHD boundary conditions on the inflow and exhaust is only compounded by the contextual system of external boundary conditions for each reconnection situation. At present this interrelationship should include a list of mechanisms that are capable of (a) changing the time independent assumption of the local MHD boundary conditions usually assumed, or (b) changing the spatial uniformity of the local MHD boundary conditions, such as having undulations in properties that are significant across the 10–100 ion gyroradii scales currently assumed to be planar in 2D. Clearly the physics of these layers becomes more complicated with Kelvin-Helmholtz waves traveling along the current channel for example. To explore these effects requires global modeling of the reconnection current channel together with the external region. This type of modeling is just coming of age.

R.M. Kulsrud

The separatrices are important as the bulk of the mass on the reconnected line crosses the separatrices and has to be accelerated from rest to the outflow velocity. The separatrices are the dividing boundaries between unreconnected and reconnected regions. Roughly speaking the freshly reconnected plasma has to flow along them. Of course they are also moving into the outflow regions and what was freshly reconnected plasma gradually becomes part of the downstream reconnected region. Further, since the field is weaker in the downstream region there is a discontinuity in it and the separatrices are also current regions (Kulsrud 2011).

Acknowledgements W.D. Gonzalez would like to thank the "Conselho Nacional de Pesquisas, CNPq" of Brazil for support, through the Project PQ-303329/2011-4. D.K. would like to thank CAPES for support.

References

H. Alfvén, Nature **150**, 406–407 (1942)
H. Alfvén, J. Geophys. Res. **81**(22), 4019–4021 (1976)
W.I. Axford, Space Sci. Rev. **7**, 149–157 (1967)
W.I. Axford, Rev. Geophys. **7**, 421–459 (1969)
W.I. Axford, Magnetic field reconnection, in *Magnetic Reconnection in Space and Laboratory Plasmas*, ed. by E.W. Hones Jr. AGU Monograph 30 (AGU, Washington, DC, 1984), pp. 1–8
J. Birn et al., J. Geophys. Res. **106**, 3715–3719 (2001)
J.E. Borovsky, J. Geophys. Res. (2013). doi:10.1002/jgra.50110
J.E. Borovsky, M.H. Denton, Geophys. Res. Lett. (2006). doi:10.1029/2006GL026519
S. Dorfman et al., Phys. Plasmas (2008). doi:10.1063/1.2991361
H.P. Furth, J. Killeen, M.N. Rosenbluth, Phys. Fluids **6**, 459–484 (1963)
W.D. Gonzalez, F.S. Mozer, J. Geophys. Res. **79**, 4186–4194 (1974)
W.D. Gonzalez et al., J. Geophys. Res. **99**, 5771–5792 (1994)
H. Ji et al., Geophys. Res. Lett. (2008). doi:10.1029/2008GL034538
H. Karimabadi, V. Roytershteyn, W. Daughton, Y.-H. Liu, Space Sci. Rev. (2013). doi:10.1007/s11214-013-0021-7
M. Kruskal, R.M. Kulsrud, Phys. Fluids, **1**, 265 (1958)
R.M. Kulsrud, Phys. Plasmas (2011). doi:10.1063/1.3628312
C.I. Longmire, *Elementary Plasma Physics* (Interscience Publishers, New York, 1963)
R.E. Lopez et al., J. Geophys. Res. (2010). doi:10.1029/2009JA014597
F.S. Mozer, J. Geophys. Res. (2005). doi:10.1029/2005JA011258
F.S. Mozer, P.L. Pritchett, Geophys. Res. Lett. (2009). doi:10.1029/2009GL037463
F.S. Mozer, P.L. Pritchett, Space Sci. Rev. (2011). doi:10.1007/s11214-010-9681-8
W.A. Newcomb, Ann. Phys. **3**, 347–385 (1958)
E.N. Parker, J. Geophys. Res. **62**, 509–520 (1957)
E.N. Parker, Phys. Fluids B **3**, 2652–2659 (1991)
H.E. Petschek, in *AAS-NASA Symposium on the Physics of Solar Flares*, NASA Special Publications SP-50 (1964), pp. 425–439
E. Priest, T. Forbes, *Magnetic Reconnection MHD Theory and Applications* (Cambridge University Press, New York, 2000)
P.L. Pritchett, F.S. Mozer, Phys. Plasmas (2009). doi:10.1063/1.3206947

Y. Ren et al., Phys. Rev. Lett. (2008). doi:10.1103/PhysRevLett.101.085003
J. Scudder, W. Daughton, J. Geophys. Res. (2008). doi:10.1029/2008JA013035
J.D. Scudder et al., Phys. Plasmas (2015). doi:10.1063/1.4932332
S.G. Shepherd, J. Atmos. Solar-Terr. Phys (2007). doi:10.1016/j.jastp.2006.07.022
B. U. Ö. Sonnerup, J. Plasma Phys. **4**, 161–174 (1970)
P.A. Sweet, in *Proceedings of the International Astronomical Union Symposium on Electromagnetic Phenomena in Cosmical Physics*, Stockholm (1958)
D. Uzdensky, R.M. Kulsrud, M. Yamada, Phys. Plasmas **3**, 1220 (1996)
V.M. Vasyliūnas, Rev. Geophys. Space Sci. **13**(1), 303–336 (1975)
V.M. Vasyliūnas, Space Sci. Rev. (2011). doi:10.1007/s11214-010-9696-1
M. Yamada, R. Kulsrud, H. Ji., Rev. Mod. Phys. (2010). doi:10.1103/RevModPhys.82.603
M. Yamada et al., Nat. Commun. (2014). doi:10.1038/ncomms5774
J. Yoo et al., Phys. Rev. Lett. (2013). doi:10.1103/PhysRevLett.110.215007

Chapter 2
Collisionless Reconnection and Electron Demagnetization

J.D. Scudder

Abstract Observable, dimensionless properties of the electron diffusion region of collisionless magnetic reconnection are motivated and benchmarked in two and three dimensional Particle In Cell (PIC) simulations as appropriate for measurements with present state of the art spacecraft. The dimensionless quantities of this paper invariably trace their origin to breaking the magnetization of the thermal electrons. Several observable proxies are also motivated for the rate of frozen flux violation and a parameter Λ_Φ that when greater than unity is associated with close proximity to the analogue of the saddle point region of 2D reconnection usually called the electron diffusion region. Analogous regions to the electron diffusion region of 2D reconnection with $\Lambda_\Phi > 1$ have been identified in 3D simulations. 10–20 disjoint diffusion regions are identified and the geometrical patterns of their locations illustrated. First examples of associations between local observables based on electron demagnetization and global diagnostics (like squashing) are also presented. A by product of these studies is the development of a single spacecraft determinations of gradient scales in the plasma.

Keywords 3D reconnection • Collisionless reconnection • Demagnetization observables • Diffusion region • Electron demagnetization • Reconnection site

2.1 Introduction

Magnetic reconnection is thought to be made possible by the existence of a "diffusion" region where "physics beyond Alfvén's ideal MHD" facilitates a steep, but smooth, transition between asymptotically sheared magnetic fields. Such a transition effects an interconnection of the previously unlinked, but sheared, magnetic field lines enabling a reorganization of their topology; after reconnection previously skew magnetic field lines pierce the plane of the current sheet. Before reconnection particle populations on either side of the current sheet could not interpenetrate; after

J.D. Scudder (✉)
Department of Physics and Astronomy, University of Iowa, Iowa City, IA, USA
e-mail: jack-scudder@uiowa.edu

W. Gonzalez, E. Parker (eds.), *Magnetic Reconnection*, Astrophysics and Space Science Library 427, DOI 10.1007/978-3-319-26432-5_2

reconnection previously separated plasmas can mix with the advent of components of **B** normal to the current sheet. Prior to steepening such a sheared current channel might be viewed as a classical *tangential discontinuity, (TD)*. As a non-propagating limit of a slow wave, whose normal has become perpendicular to the local magnetic field (Burlaga 1995), this layer is in pressure equilibrium. In nature the current channel of a TD usually occurs with thermal ion gyro radius scales. Theoretically this channel can form a Vlasov equilibrium with scales as small as the electron gyro-scale (Burlaga and Lemaire 1978), although they are usually unstable. Collisionless reconnection can arise in the unstable disruption of such layers (and with the evolution of other initial configurations) when the current channel has narrowed to widths of the order of the electron inertial lengths in the plasma which are the skin depth, $d_e \equiv c/\omega_{pe}$ and the thermal gyro radius, $\rho_e \equiv w_{\perp,e}/\Omega_{ce}$. The electron plasma and cyclotron frequencies are defined by $\omega_{pe}^2 \equiv 4\pi ne^2/m$ and $\Omega_{ce} \equiv eB/mc$, respectively. The j'th species' average rms thermal speed transverse to the magnetic field is denoted $w_{\perp,j} \equiv \sqrt{2kT_{\perp,j}/M_j}$, where M_j is the particles mass and c is the vacuum speed of light. This particle's transverse thermal speed and cyclotron frequency determine its thermal gyro radius $\rho_j = w_{\perp,j}/\Omega_{cj}$.

Alfvén's ideal MHD is an approximation frequently made to simplify the description of plasmas *when they only possess very long spatial scales* $L >> \rho_i$ *and possess very weak time dependence compared to the cyclotron frequencies*. As useful as the ideal MHD approximation can be, it does *not* apply everywhere in a plasma; the physics of magnetic reconnection is only describable by foregoing the simplifications of Alfvén's keen early insight.

While precise mathematical definitions of reconnection have been proposed in 3D geometries, such relationships are usually non-local conditions that are even difficult to verify within simulations, let alone testable with the most advanced, but relatively local, experiments flown on small spacecraft armadas. Even in 2D geometries the mathematical conditions are difficult to experimentally parse, since they define reconnection to be *possible* when not equal conditions of the form $\mathbf{Y} \neq 0$ are fulfilled, where Y is some relationship between flow, electric and magnetic fields. Care should be taken to note that such conditions may be *necessary* for reconnection to ensue, but their satisfaction is generally not *sufficient* to identify reconnection as having been witnessed.

In this chapter the discussion focuses on likely *observable* properties that the inner "diffusion" layer of the reconnection channel might have, while showing that these properties are restatements of, or are rare proxies for the more stringent theoretical definitions. In some circumstances we will argue that necessary conditions of the form $\mathbf{Y} \neq 0$ will need to be strengthened to $|\mathbf{Y}| > a > 0$, with a non-zero value of a before the necessary condition becomes selective enough to identify layers that are actually undergoing magnetic reconnection (cf. Sect. 2.4.1ff).

A commonly cited condition for characterizing magnetic reconnection involves testing for conversion of electromagnetic energy into plasma energy, $J_\parallel E_\parallel > 0$, where the parallel subscript denotes the component along the local magnetic field direction: $G_\parallel \equiv \mathbf{G} \cdot \hat{\mathbf{b}}$. To date no direct measurements of these quantities have ever been made together at the same location in space. Both observables are difficult

measurements; recent progress on $E_\parallel$ detection has been made with long wire booms, but detection of electron inertial scaled $J_\parallel$ layers is exceedingly difficult. Their determination is outside the scope of curlometer approaches, Dunlop and Balogh (2005), with spacecraft flotilla since collision avoidance of the spacecraft keeps the multi-point observations separated on scales broad compared to that of the expected current channels. Direct detection of the current density from particle measurements are impacted by the different time resolutions of electron and ion sensors needed for adequate counting rates and the need to determine 3D number fluxes $n_k\mathbf{V}_k$ for all charged species in the plasma, including those sequential (and, therefore, time aliased) estimates made for different ion species: $\mathbf{J(t)} = \Sigma_k Z_k n_k(t)|e|\mathbf{V}_k(t)$. Even on the recently launched Magnetospheric Multi-Scale (MMS) mission the fastest time scale for determining all necessary contributions from particles for $\mathbf{J}$ is acquired across a total collection time of 10s (South West Research Institute 2010; Fuselier, 2015, private communication). For typical relative motions of the spacecraft such time resolution is still beyond that required at the noon magnetopause to measure $J_\parallel E_\parallel$ directly. Using measured profiles from the magnetometer requires intricate and usually unknown knowledge of the world line of the observations of the profile to *estimate the current density* $\mathbf{J}$. Typically available measurements constrain the integrated change of the current ΔI much more accurately than the current density, that is theoretically required. Accordingly, the desired identification of the reconnection locales must explore other more accessible observables. Unfortunately there are a large number of conceptually critical quantities that are not directly observable. Accordingly, a somewhat indirect approach is required to establish the locales and properties of reconnection layers in space.

Our approach requires the certification of observables that could be made from spacecraft and a description of the electrodynamics that satisfies the theoretician that magnetic reconnection produced the signatures being inventoried. Clearly this argument would be tautological if made using *in situ* data. This chapter profits from using 2 and 3D Particle In Cell (PIC) simulations of reconnection layers which allow internal diagnostics not available to the spacecraft borne observer, which can be used to assure the theoretician that the layers inventoried are signatures of magnetic reconnection. PIC codes can also sidestep the important and troublesome closure problems present in other truncated fluid descriptions of space plasmas such as occur with various forms of MHD. At the same time a subset of PIC output quantities can determine the state of the art spacecraft observables as signatures of the layer. As will become clear in this chapter this inner current channel is distinguished by its effect on electrons, the smallest gyro radii particles in the plasma. Because PIC codes follow the equations of motion of individual electron and ion proxies, the fidelity of the aggregate dynamical picture they allow is clearer than models of reconnection that describe this physics from the reduced fluid pictures of MHD or extended MHD.

We will find it profitable to reframe desirable theoretical quantities from the vantage point of the electrons in the form of the *Generalized Ohm's Law* (Rossi and Olbert 1970). This relationship replaces assumptions like $\mathbf{E} = \eta\mathbf{J}$ with those more appropriate for a wide range of collisionalities, including the troublesome

collisionless regimes commonly occurring in space plasmas. Importantly, the PIC approach allows all of the terms present in this law to be evaluated. The key to detection of reconnection sites will be through electron specific observables and the electric field $\mathbf{R}_e$ reckoned in the rest frame of the bulk of the electrons, which moves in the laboratory frame with velocity $\mathbf{U}_e$. This electric field recurs so often that it is given its own symbol, $\mathbf{R}_e \equiv \mathbf{E} + \mathbf{U_e} \times \mathbf{B}/c$, and its own name, the *Non-Ideal Electric Field*, since its size is above and beyond the common place *Unipolar, or Ideal Electric Field*, caused by motion of the electron fluid relative to the magnetic field: $\mathbf{E}_{ideal} = -\mathbf{U}_e \times \mathbf{B}/c$. This reduced electric field occurs naturally as two of the terms in the Generalized Ohm's Law.

In Alfvén's ideal MHD this unipolar ideal electric field is essentially the *same* as seen in the center of mass frame of the plasma or in any species frame of reference, since by assumption these are weak current regimes and all these frames of reference are the same. For the electron rest frame observer we review below that the apparent time dependence of the magnetic flux is controlled by the $\nabla \times \mathbf{R}_e$. This approach greatly clarifies the physics that is often attempted with extended MHD language; as the current densities increase and the plasma scales reach below the ion inertial lengths this approach provides much needed clarity for the processes that can take place, including reconnection, whether in the collisional or collisionless regimes.

In this chapter we develop an observational program for this inner layer of the current channel that we will refer to below as the *Electron Diffusion Region (EDR)*. We will show that this layer's special character is that it has gradient scales, L, smaller than the thermal electron's gyro radius, ρ_e; this circumstance contradicts that supposed when deriving MHD, where scale lengths are assumed to be much larger than any particle gyro radius ($L >> \rho_i > \rho_e$); thus, it is not surprising that non-MHD phenomena may be caused by such a layer. Observationally layers with these scales are also extremely rare in astrophysics, not being a required part of wave normal modes or discontinuities. Accordingly, *defensible* detections of electron inertial scaled current channels are to be highly prized when seeking to identify sites of collisionless magnetic reconnection. At the same time we address the difficulty of measure spatial scales in moving media, resolving this problem by showing that suitable dimensionless ratios like ρ_e/L are direct observables with modern state of the art plasma observations.

In MHD regimes the gradient scales are assumed to be longer than the gyro radii of either electrons or ions so that the magnetic field strength appears to the individual particle in the plasma to be slowly varying in space and time. These weak variations permit one to predict from classical mechanics that the magnetic moments $\mu_j = w^2_{\perp,j}/B$ of the particles will be adiabatically conserved, with the moment calculated from the particle's circular current formed by its motion transverse to the field. μ_e conservation for the electrons implies that the magnetic flux linked by the gyro orbit is conserved, or loosely, electrons can "follow" a magnetic line of force as it gradually changes strength, direction or becomes slowly time dependent.

With the smallest mass in the plasma, the electron's inability to "follow" a magnetic line of force is much more noteworthy *and rare* than the circumstances where ion's cannot follow the same tube of force. Magnetic moment disruption for

ions is considerably more common because the spatial scale of disruptive gradients need only approach the ion gyro radius for this purpose which occurs in nearly every MHD discontinuity, like *tangential discontinuities (TD), rotational discontinuities (RD), fast and slow shocks, and their wave antecedents*.

Unlike the MHD regime, the electron diffusion region with $L < \rho_e$ is a place where the electrons are said to be *demagnetized*, because the weak gradient premises of this adiabaticity are not realized there. Vasyliunas identified that this demagnetization of electrons was a *necessary* property of symmetric collisionless reconnection layer in 2D (Vasyliunas 1975).

A common misconception is that μ_j conservation/violation occurring in the j'th particles can be ascertained by monitoring the constancy of a moment quantity $kT_{\perp j}/B$ possessing the same units as μ_j. It is easy to construct Vlasov solutions that conserve μ for every particle, but do not conserve the moment related quantity (Scudder et al. 1986). Thus, detection of variability of $kT_{\perp j}/B$ *need not* imply demagnetization of the j'th species.

The signature of the violation of μ_e conservation is that the electron probability distribution in the proper frame, $f_e(\mathbf{w})$, depends *intrinsically* on all three polar variables $|\mathbf{w}|, \theta_w, \phi_w$, where $\mathbf{w} \equiv \mathbf{v} - \mathbf{U_e}$ is the electron velocity relative to the laboratory frame electron bulk velocity, $\mathbf{U}_e$. Making observations that can discern this behavior requires simultaneous sampling of all octants of velocity space, which is possible with the present state of the art of plasma instrumentation; however, measurements that have used spacecraft rotation to build up the gyro-phase distribution of the 3-D velocity distribution are invariably aliased against detecting these signatures. In addition defensible determinations of $\mathbf{U}_e$ in the presence of UV, photo-electrons, spacecraft charging and the time aliasing of data acquisition is a necessary experimental prerequisite for experimental detection of these expected gyro phase dependences within the electron diffusion region.

In this chapter we extend Vasyliunas' original insight into 3D models of reconnection, demonstrating theoretically and with PIC simulations that this inner layer is characterized by demagnetized thermal electrons with observable consequences. While the circumstances of electron demagnetization are expected to be very rare in astrophysical plasmas, not all demagnetized layers are the electron diffusion region; demagnetization will also be shown to occur in other narrow current channels on the separatrices of the overall reconnection layer (where frozen flux violations are very much weaker). Nonetheless, this demagnetization, if perceptible, is a significant sieve for separating resolved two fluid current layers from electron inertial length scaled layers that are potentially reconnecting. *While demagnetization does not define the EDR layer alone, it represents an astrophysically rare, necessary, local, and observable kinetic property for a current layer to be a candidate layer where collisionless magnetic reconnection might be underway.*

Other theoretical considerations of *generalized* magnetic reconnection (GMR) have found it necessary to define its occurrence in 3D in terms of *global attributes* of the process. In this approach magnetic reconnection is defined by *non-local* tests about *the magnetic topology*. Often it is defined as occurring by finding *singular curves/loop integrals* that possess non-zero integrated $E_\parallel$, (Hesse et al. 2005).

Alternately, magnetic reconnection is said to require sheafs of field lines that are initially localized in close proximity, but undergo exponential separation, forming *quasi-separatrix layers*. Field lines that participate in such rapidly separating quasi-separatrix environments have flux tube cross sections that are flattened into highly elliptical cross sections, a global property made quantitative by non-locally determining their *squashing factors*, σ, Titov et al. (2002) and Demoulin et al. (1996). These considerations are amplified in Chap. 3 of this monograph (Priest 2016).

As theoretically useful as such concepts may be, these non-local properties are hard to verify using single spacecraft measurements, or even a flotilla of single spacecraft measurements such as those of Cluster or Magnetospheric Multi-Scale (MMS); they may not even be possible to discern except using global snapshots from 3D simulations. If these non-local criterion are critical for discerning reconnection in the 3D astrophysical context, there would appear to be insurmountable observational difficulties to provide *in situ* experimental closure with spacecraft data of sites where it occurs. A brief discussion of some initial attempts to connect local observables with these global concepts will be discussed in Section 2.9.3 of this chapter.

There is also the thorny issue of whether the enabling site of collisionless reconnection in 3D remains conceptually similar to the compact electron inertial scaled region suggested by the isolated "X" saddle point of the flux function that forms in simple 2D models. In 2D the *flux function* is the component of the vector potential orthogonal to the plane of allowed spatial variations. If this plane of variability is the x-y plane, the flux function $A_z(x, y, t)$ completely determines the variations of the magnetic field in the x-y plane (via the x and y components of $\mathbf{B} = \nabla \times \mathbf{A}$). In 3D analogous flux functions do not exist, making the global inventory of magnetic topology difficult. A very real possibility exists in 3D that reconnection sites might be spawned in some loose association by flux ropes enabled by other sites, with multiple ones coexisting in the same general pattern (Daughton et al. 2011). To observationally characterize how reconnection occurs in this likely situation would appear to require a program based on assaying physical properties of the layers encountered, not seeking to verify preconceived geometrical arrangements using 2D electron diffusion regions as the archetype. *We outline a procedure that appears to find the analogue of the electron diffusion region in 3D PIC simulations with the same methodology that correctly identifies the saddle point region of the 2D simulation where the flux function incontrovertibly has already established the locale of the EDR.*

The technical and mathematical conditions for reconnection in textbooks can be rather challenging to verify. Take for example "... reconnection occurs if there is an electric field, $\mathbf{E}$ along the *separator*, $\hat{\mathbf{S}}$", that is when $\mathbf{E} \cdot \hat{\mathbf{S}} \neq 0$. Other attempts to define locally the process of magnetic reconnection also end up specifying something else that is not zero. Examples are "... magnetic reconnection occurs whenever the *non-ideal electric field* $\mathbf{R}_e \neq 0$". Still others insist that magnetic reconnection occurs in the presence of quasi-separator curves delineated by flux

tube path integrals and $\int_B E_\parallel ds \neq 0$. Recently a theoretician suggested reconnection could be identified by finding the regions where $n_e - n_i \neq 0$. The required *frozen flux violation* for magnetic reconnection takes the form $\nabla \times \mathbf{R}_e \neq 0$. Vasyliunas' arguments (Vasyliunas 1975) suggested the site of 2D symmetric collisionless reconnection to be a place where the thermal electrons were not magnetized, which is yet another *not equal to zero* condition: $\partial f(\mathbf{w})/\partial \phi_w \neq 0$. *Even if all the quantities were measurable for these conditions, they do not suggest how large a violation of zero would confirm the occurrence of magnetic reconnection in the data.*

All the conditions in the previous paragraph are of the form $Y \neq 0$, making Y a *thresholdless variable, usually having dimensions*. Such conditions are experimentally difficult to test. The noise of measurement, ΔY, can always satisfy a thresholdless condition. Surely that is not enough to identify a site of magnetic reconnection. Far better would be to couch the theory in terms of *thresholded and dimensionless* conditions, that establish a minimum $\sigma_Y \neq 0$ for verification that a process, effect or condition had been witnessed. Whenever $Y/\sigma_Y > 1$ and $\Delta Y/\sigma_Y << 1$ one has a non-trivial measure of signal to noise for the decision. Lastly, but most important, the dimensionless test must be framed in terms of what is *observable* with the current state of the art instrumentation; thus, nothing involving delineating separators or measuring space charge densities is in this category at present. For example, in space, there is no local observable Y that determines the rate at which magnetic flux is being dissipated or the violation of the electron's magnetic moment, yet one still wishes to identify layers where this and related properties have transpired to advance and test the present theoretical understanding of reconnection.

This chapter is about reorganizing what is presently known about collisionless magnetic reconnection to produce observable, thresholded, dimensionless tests specific to identifying the electron diffusion region; an observable test is one that can be conducted with presently available state of the art plasma and fields measurements deployed on available spacecraft. As will be clear when our list is formulated, such tests will represent sieves of increasing probability that the electron diffusion region has been transited.

A short tour of frequently cited observables for reconnection that are used in the literature is provided in Fig. 2.1, Scudder (2015); those labeled "P-" are jump conditions from conservations for layers that Pass a mass flux. As indicated by the multiple situations (columns) with "X's" in them, these tests are not specific to the properties of *only* reconnection sites. The A* test is also tailored to identifying torsional transitions, such as Alfvén waves, or *rotational discontinuities (RD's)*, that transmit a mass flux while also shearing the magnetic field between their asymptotic states. Any locally planar disturbance that propagates through the plasma satisfies the "P-" or "A*" property.

While these tests may be necessary to screen discontinuities or waves that pass mass flux as some reconnection models require, they are for such common conditions in the plasma, by themselves they do not possess strong leverage for identifying the layer as a part of the process of magnetic reconnection. Even the frequently cited incidence of *"jetting"* or observations of flow acceleration are not

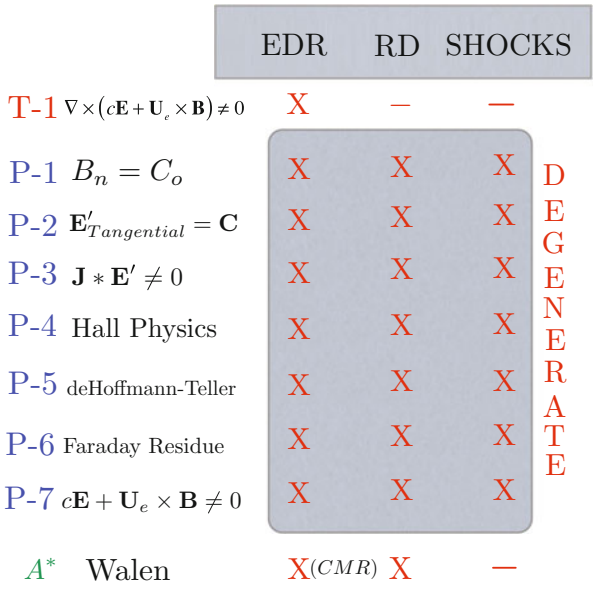

Fig. 2.1 Tests used for magnetic reconnection detection in space plasmas (Scudder 2015). P- are the flux passing test for planar layers (Paschmann and Daley 1998); A* is the Alfvénic or Walén tests used in the literature. The theoretical T−1 test from Faraday's law is discussed in this chapter, but has not been tested in space. Subscripts n and tangential refer to the local plane tangential to the current layer. Primed variables are observed in the rest frame of the current sheet. The deHoffmann-Teller frame test checks for the existence of a frame of reference outside the layer were changes of the fluid velocity and magnetic field are parallel. The Faraday Residue test attempts to identify a non-zero conserved normal component of B_n (Gauss' law) and conserved components of $\mathbf{E}\times\hat{\mathbf{n}}$, which from the $\nabla\mathbf{E} = 0$ implies the layer traversed has a *rest frame* where the transition can be viewed as time stationary. The Faraday residue test is usually performed with a flow proxy $\mathbf{E} = -\mathbf{U}\times\mathbf{B}/c$ and magnetic fields $\mathbf{B}$. The Faraday residue test is an alternate test for non-zero mass flux, best performed with electric and magnetic field observations. The X's in a given row denote the classes of layers where the test applies. When multiple X's are in a row, many different layers can pass such a test. $\mathbf{J}\cdot\mathbf{E}'\neq\mathbf{0}$ corresponds to energy exchanged with the electromagnetic field in the rest frame of the discontinuity, a process that occurs in most MHD transitions, whether involving reconnection or not. This quantity measures the work done by the layer in the rest frame of the layer and is generally partitioned between particles and fields; by contrast the Galilean invariant quantity $J_{\|}E_{\|}$ determines the net energy made available from the fields to the plasma, which if greater than zero reflects one of the hallmarks of magnetic reconnection: a shift of field energy into plasma energy

peculiar to reconnection, but are the hallmark of tangential accelerations that are *the property of Alfvénic structures wherever they are found*. Thus to our point, *the identification of the reconnection site cannot primarily rely on the detection of the P- and A* signatures as a certification of the reconnection layer*. Performing multiple tests successfully in the P- list can not strengthen the experimental case that a reconnection layer has been transited, since any layer that passes a give P- test should pass all of them, if the data quality and calibration are adequate for the test.

2.2 Magnetic Reconnection

If steady 2D magnetic reconnection is described with spatial variations allowed in the x-y plane, a time independent *reconnection* electric field, E_z is required parallel to the current sheet implied by the abutting magnetic fields where $\mathbf{B_1} \cdot \mathbf{B_2} < 0$. In steady state a long way away from the current sheet E_z is determined by the ideal electric field of MHD: $E_z = -\hat{\mathbf{z}} \cdot \mathbf{U_e} \times \mathbf{B}/c$; in this asymptotic regime the plasma is idealized as essentially current and gradient free, as Alfvén's hypothesized, where $\mathbf{U} = \mathbf{U}_i = \mathbf{U}_e$, where $\mathbf{U}$ is the center of mass velocity.

Faraday's equation $\partial \mathbf{B}/\partial t = -c\nabla \times \mathbf{E}$ for the plasma has many different approximations where various terms are assumed important. In the frame where the electrons are at rest (moving with velocity $\mathbf{U}_e$ in the laboratory frame) the left hand side becomes a total derivative and $\mathbf{E}$ is transformed by Galilean effects to become

$$\left.\frac{D\mathbf{B}}{Dt}\right|_{\mathbf{U}_e} = -c\nabla \times \mathbf{R}_e, \tag{2.1}$$

where the total derivative in the frame moving with velocity $\mathbf{W}$ satisfies the operator identity $D/Dt|_{\mathbf{W}} = \partial/\partial t + \mathbf{W} \cdot \nabla$. This rate of change is controlled by the circulation of the *non-ideal electric field* $\mathbf{R}_e$ defined in three equivalent ways:

$$\mathbf{R}_e \equiv \mathbf{E} + \mathbf{U}_e \times \mathbf{B}/c, \quad (I) \tag{2.2}$$

and from the steady state electron momentum equation

$$\mathbf{R}_e = -\frac{1}{en_e}\Big[\nabla \cdot \mathbf{P}_e + \nabla \cdot (mn\mathbf{U}_e\mathbf{U}_e)\Big] + \eta\mathbf{J} + TF(\mathbf{q}_e), \quad (II) \tag{2.3}$$

where the *resistive electric field* $\eta\mathbf{J}$ is defined by

$$\eta\mathbf{J} = -en_e m\nu_{ei}(\mathbf{U}_e - \mathbf{U}_i), \tag{2.4}$$

ν_{ei} is the electron ion coulomb collision rate, and *TF* is emf associated with the thermal force, a friction between electrons and ions that is caused by the pear shaped (skewed) electron distributions that reflect the presence of heat flow (Braginskii 1965).

Finally, a form for $\mathbf{R}_e$ in terms of the *ion* flow velocity can avoid using the electron flow velocity at the expense of including the *Hall emf* in the last term:

$$\mathbf{R}_e \equiv \mathbf{E} + \frac{\mathbf{U}_i \times \mathbf{B}}{c} - \frac{\mathbf{J} \times \mathbf{B}}{nec}. \quad (III) \tag{2.5}$$

Form (III) is often used, but its equivalence to form (I) clearly establishes that the Hall emf is (1) not able to disrupt the magnetic field from being frozen to the *electron rest frame* and that (2) when the Hall emf's are suggested to be necessary

for *fast magnetic reconnection* to occur, their need could be viewed as arguments that *all* the freedom of a two fluid plasma must be permitted to get fast reconnection, including electron pressure gradients and the electron thermal force of version (II). Because the Hall emf is not an agent for disrupting frozen flux as reckoned by the electron rest frame observer, its occurrence in the so called *ion diffusion region*, where Hall electric and magnetic signatures are observed, is not really a signature of the frozen flux violation *for the electron rest frame observer*. Alternately, the evolution equation for magnetic field lines continues to exist throughout the two fluid ion diffusion region, because they are advected there by, and frozen into the rest frame of the electrons (cf. Appendix 2).

2.2.1 Frozen Flux Violation

Consider a comoving, closed, right handed, orientable path C, with outward vectorial area **A** along the local magnetic field direction, with differential normal $\hat{\mathbf{b}}dA$. Using Stokes theorem on Eq. (2.1) determines an equation for the rate of change of magnetic flux, Φ, penetrating **A** for the observer moving with the electron bulk speed $\mathbf{U}_e$ (Priest and Forbes 2000; Schindler 2000), viz:

$$\left.\frac{D\Phi}{Dt}\right|_{\mathbf{U}_e} = -c\oint_C \hat{\mathbf{b}}\cdot\mathbf{R}_e ds. \tag{2.6}$$

The time scale for this frozen flux change can be determined as

$$\nu_\Phi \equiv \tau_\Phi^{-1} = \left|\frac{Dln\Phi}{Dt}\right|_{\mathbf{U}_e}. \tag{2.7}$$

Similar expressions can be determined for departures from *line preservation* with rates for this process indicated by $\nu_\uparrow$ (Birn and Priest 2000; Scudder et al. 2015a).

When the RHS of Eq. (2.6) vanishes *Alfvén's Frozen Flux Theorem of Ideal MHD* is implied. If at time t the magnetic flux is "frozen", it means that the equation of motion for a magnetic field line (a) exists, (b) is locally the same as determined from the electron fluid velocity, and (c) in an increment *dt* that the field line's location may be predicted to have moved *transverse* to itself a distance $d\mathbf{s}(\mathbf{x}) = (\mathbf{U}(\mathbf{x})_e - (\mathbf{U}(\mathbf{x})_e\cdot\hat{\mathbf{b}}(\mathbf{x}))\hat{\mathbf{b}}(\mathbf{x}))dt$, and is well described by the $\mathbf{B}(\mathbf{x}+d\mathbf{s}(\mathbf{x}), dt)$. In this situation there is no lateral slippage between the magnetic tube of force and the local velocity of the electron fluid perpendicular to **B**. This theorem supposes $\nabla\times\mathbf{R}_e \equiv 0$; frequently revered as if it were a law of physics, the theorem loses its predictive power in those physical circumstances, like reconnection, where this precondition is no longer fulfilled. However, since the violations require gradients and a circulation of $\mathbf{R}_e$ the very long scale lengths of variation supposed by Alfvén weaken the possible size of this violation unless $\mathbf{R}_e$ simultaneously became large in such weak gradient regions. However, since $\mathbf{R}_e$ is a "left over" electric field above

and beyond the unipolar **E**, one is hard pressed to suggest a physical system with very large scales where $\mathbf{R}_e$ grows to keep its curl sizable. This is the content of Alfvén's argument when he introduced his frozen in approximation.

When the frozen flux theorem is violated the mental image of field lines being "carried" by the electron flow (in the above sense) is no longer strictly true. Here, too, there is the absence of a threshold: slippage between the electrons and **B** may occur, but be *innocuous*, while at other times the slippage is absolutely essential to the dynamics of the process. Innocuous slippage occurs in many places, since Alfvén's frozen flux theorem is an idealization, akin to the no friction assumptions that are common in first year mechanics problems. "Substantial" frozen flux violations accompany *magnetic topology change*, a process that would not be possible if the motion of magnetic field lines and the average cross field motion of the electrons were always mathematically the same.

2.2.2 "Broken" Field Lines

These considerations are also involved in reconciling the perplexing MHD description of magnetic reconnection as a "cutting and restitching" of magnetic curves. When decisive frozen flux violations occur the rearrangement *over time* of magnetic field lines is not predicted by the electron kinematic description (Schindler 2000; Birn and Priest 2000). Nonetheless, a spatial picture of the magnetic field can be deduced at any "freeze frame", but the *temporal evolution of their rearrangements* is richer than the simple kinematic picture of magnetic field lines as spaghetti advected by the electrons. In this sense the violation of Alfvén's frozen flux approximation reflects the hidden degrees of freedom that the Maxwell-Plasma system has that do not conform to a kinematic picture of the electrons advancing the location of tubes of force in the medium. These violations occur in locations with electron inertial scale spatial gradients far removed from the large scale systems Alfvén had in mind when suggesting the *frozen flux* simplification.

2.2.3 Regimes of Frozen Flux

The *frozen flux condition*

$$\nabla \times \mathbf{R}_e = 0 \tag{2.8}$$

can be satisfied in many ways. Deciding that Eq. (2.8) has been violated has proven to be a vexing problem for experimentalists with spacecraft time series data. Alfvén's *frozen in* condition, $\mathbf{R}_e = 0$, is the simplest condition that implies the *frozen flux* condition is true, but it clearly is not the only one. In the space literature the circumstances of violating the "frozen in condition" are commonly inverted

to suggest that such observations imply violations of the "frozen flux condition." Alfvén's frozen in condition is sufficient, but not necessary, for satisfying the frozen flux condition. Simple counterexamples where $R_e \neq 0$ and the flux remains frozen are $\mathbf{R}_e = \nabla\psi$ where ψ is a scalar function, or $\mathbf{R}_e = -\nabla P_e(n)/(en)$, where P_e is a scalar functional of n. For the theorist this implies that polytrope closures will not allow collisionless reconnection. By such examples, experimental detections of *large* values for $\mathbf{R}_e \neq 0$ have no *necessary* claim on being sites for frozen flux violation. Detection of significant $E_\parallel$ (Mozer 2005), which is clearly part of $\hat{\mathbf{b}} \cdot \mathbf{R}_e \neq 0$, are an inadequate basis for routinely identifying sites of frozen flux violation (Scudder et al. 2008). As seen from Eq. (2.6) Stokes loop integrals of $\hat{\mathbf{b}} \cdot \mathbf{R}_e$, rather than spot readings, are required to be non-zero to show violations of the frozen flux condition. To date such loop integrals have not been produced empirically.

2.3 Taxonomy of Non-ideal Effects

Clearly, violations of frozen flux are required for magnetic reconnection. Although such violations are *necessary* for magnetic reconnection, they are *not always sufficient* indicators of magnetic reconnection. Making decisions of this type will hinge on the time scales τ_Φ of the frozen flux violation [cf. Eq. (2.7)], since Alfvén's suggestion of *ideal MHD* is based on an assumed scale free medium with time scales for slippage assumed infinite; this idealization has frozen flux decaying at an excruciatingly slow time scale, that in first approximation is ignorable.

If magnetic reconnection is to be defined, including a necessary threshold of sufficient frozen flux violation, there must be a way to differentiate locales where magnetic reconnection is dynamically important from those with innocuous slippage that exist when $\mathbf{R}_e$ has finite curls, because the scale lengths of variation are longer than electron inertial scales but still not infinite. We set this as our focus in this chapter.

The theoretical study of magnetic reconnection requires retaining *some non-zero* $\mathbf{R}_e$ *that has a non-vanishing curl*. When $\mathbf{R}_e \neq 0$ is retained in the description of the system it is referred to as a description via *non-ideal MHD*. The separation of the effect of the *ideal* unipolar electric field seen by the observer at rest in the electron frame in the LHS of Eq. (2.6) makes it clear that the electric field contributions retained on the RHS in $\mathbf{R}_e$ are not necessarily retained for their numerical importance relative to the unipolar motional electric field, but are being retained for what processes they structurally enable in the time and space evolution of the magneto-fluid.

To avoid the complexity of the general form for $\mathbf{R}_e$, a considerable literature exists discussing resistive reconnection that explores what may be learned without treating $\mathbf{R}_e$ in its full quantitative form. Some modelers have argued that it does not matter what is used for $\mathbf{R}_e$, so long as it has a curl. Clearly that argument is not

without exceptions, since so called *fast reconnection* with rates near $0.1V_A$ were not recovered until $\mathbf{R}_e$ was modified to include so called *Hall effect terms* that allow two fluid electrodynamics in the current sheet, while spatially uniform resistive terms that treat the fluid as a single entity were ineffective for this purpose.

There is thus a two tiered approach: (1) the ideal processes are always addressed with the LHS of Eq. (2.6), and (2) *selected* forms of $\mathbf{R}_e$ that are retained on the RHS for analysis of possibly new effects. Frankly, some choices in the literature reflect avoiding the serious theoretical roadblocks to entertain more realistic treatments, although this is changing with the advent of full Particle in Cell *PIC* and some multi-fluid simulations that avoid most of these concerns, but contain challenges of their own.

2.3.1 Coulomb Collisional Regime

By far the simplest regime is the *collisional regime* where $\mathbf{R}_e$ is replaced by the *Ohmic emf*:

$$\mathbf{R}_e \simeq \eta \mathbf{J} = \frac{m\nu_{ei}(\mathbf{U}_i - \mathbf{U}_e)}{en_e}, \tag{2.9}$$

but neglecting the *thermal force*, $TF(q)$, which also scales with collision rate and the heat flux. The cgs resistivity is given by $\eta_{cgs} = m\nu_{ei}/(ne^2)$, where ν_{ei} is the electron ion coulomb collision rate. Since the collision rate is proportional to density, the non-constant properties of the resistivity involve its reduction as T_e increases according to the $T_e^{-3/2}$; this dependence can be important as the dissipation heats the electrons in the current sheet. Physically this heating is spatially dependent, but *usually* η is considered as uniform in space and constant in time when studying problems of this type.

The ohmic emf has a curl so that $-c\nabla \times \mathbf{R}_e = \mathscr{D}\nabla^2\mathbf{B}$, where the diffusivity $\mathscr{D}$ (assumed uniform in space and constant in time) is given by $\mathscr{D} = c^2\eta_{cgs}/(4\pi ne^2) = d_e^2\nu_{ei}$. In this resistive approximation Faraday's equation becomes a simple parabolic vector diffusion equation for $\mathbf{B}$ in the comoving frame of the electrons:

$$\tau_{ei}\frac{D\mathbf{B}}{Dt}\Big|_{\mathbf{U}_e} = d_e^2\nabla^2\mathbf{B}, \tag{2.10}$$

where $\tau_{ei}^{-1} = \nu_{ei}$ is the coulomb electron ion mean rate for momentum transfer. The form of Eq. (2.10) shows that the *natural length scale for coulomb resistive diffusion is the electron inertial length, d_e, but the time scale for this process is the time scale for electron-ion collisions*. The origin of the term *electron diffusion region (EDR)* is from this resistive MHD form of the reconnection problem, where the magnetic field profile actually satisfies a mathematical diffusion equation within the current channel. In present usage the EDR refers to the layer where the current is channeled,

regardless of the mathematical form of the equation(s) that determine the transition profile, even if they are not parabolic differential equations.

By neglecting the thermal force *and the T_e dependence of η* this modeling is not hampered by the other limitation of reduced theoretical models of magnetic reconnection: *closure*. Closure is the process that effects a truncation of the infinite number of moments of the kinetic equation for the plasma, that for example might suggest how heat flows when there are gradients in the temperature and density. Actually the neglect of the T_e dependence of η is partially to avoid the closure issues of how to advance the temperature without knowing *a priori* the form of the heat law.

Throughout almost all locales of the current sheet the *ideal* left hand side of Faraday's equation dominates the *non-ideal* right hand side, even in the resistive regime. The ratio of LHS to RHS is the *magnetic Reynolds number, R_m*, that in most astrophysical contexts generally exceeds 10^6; however, the tiny but non-zero non-ideal RHS enables structural changes (including changes in apparent connectedness of asymptotically disconnected lines of force) that the left hand side cannot, no matter how disparate their sizes may be.

2.3.2 *Collisionless Terms of* $\mathbf{R}_e$

The remaining terms of $\mathbf{R}_e$ are the possible *collisionless* causes for magnetic reconnection, since unlike η and *TF* they do not involve the binary collision rate ν_{ei}. These are

$$\mathbf{R}_e^{less} = -\frac{\nabla \cdot \mathbf{P}_e + \nabla \cdot (mn_e\mathbf{U}_e\mathbf{U}_e) + \frac{\partial mn_e\mathbf{U}_e}{\partial t})}{en_e} \tag{2.11}$$

In order, these terms are known as the *diamagnetic*, *dynamic* and *acceleration* terms, although as specific terms in the electron momentum equation they all are forces per unit charge density felt by the electron fluid in the plasma.

We show below that Vasyliunas' argument places the gradient scale of the *diamagnetic* term in the reconnection channels as having a scale $L \simeq \rho_e \equiv \beta_e^{1/2} d_e$ at least at the separator of symmetric 2D reconnection. In the literature arguments appear that the diamagnetic term can be ignored (closure phobia!) by only considering low $\beta_e << 1$; however, the natural progress of collisional and collisionless reconnection raises the electron temperature and weakens B so that the current channel actually occurs in a higher β_e than its value outside the current layer (cf. Fig. 2.9). The diamagnetic term starts to grow on the d_i scale, when the two fluid effects commence with ions and electrons taking different paths through the layer and the diamagnetic pressure forces compensate for the new $\mathbf{J} \times \mathbf{B}$ force that occurs in the one fluid description.

Vasyliunas' assay pertains to the inner electron diffusion region of a symmetric reconnection layer where the electrons are demagnetized. In terms of the electron thermal Mach number, $M_e \equiv U_e/w_{\perp,e}$, the dynamic pressure term is $O(M_e^2)$ times the diamagnetic term. While $M_e << 1$ in traditional MHD, as we develop below it is expected to be order unity within the current sheet. In steady state the acceleration term vanishes, but in dynamic phases it clearly can be the same order as the other terms. In the collisionless regime this term supports displacement current effects in the emf which generally occur with ω_{pe} time scales, that are also frequently ignored, appealing to MHD ordering. At times the anomalous resistance used in modeling is said to reflect effects from this acceleration term. Therefore, in the current sheet of magnetic reconnection the hierarchy of terms in $\mathbf{R}_e$ are (diamagnetic:dynamic) and are expected in the proportion $(1 : M_e^2)$, with the dynamic pressure terms possibly competitive with the diamagnetic terms near the saddle point, where as shown below $M_e \simeq 1$. The diamagnetic and dynamic terms can survive in steady state, while the acceleration term is usually ignored.

2.3.2.1 Scales of Electron Diffusion Region

If steady magnetic reconnection is to be possible one of first two terms in the RHS of Eq. (2.11) must produce an emf, E_z, out of the plane when 2D variations are allowed in the x-y plane. Enforcing this condition at the stagnation point (in 2D) of a symmetric reconnection layer shows that the divergence of the dynamic pressure is not available for this purpose, since it vanishes there in this limit $mn(\mathbf{U}_e \cdot \nabla)\mathbf{U}_e = 0$. The diamagnetic term's divergence of the electron pressure tensor must perform this role (Vasyliunas 1975).

Since in 2D the partial derivatives of the divergence act only in the x-y plane, the E_z component is possible via

$$\hat{\mathbf{z}} \cdot \nabla \cdot \mathbf{P}_e = \frac{\partial P_{e,xz}}{\partial x} + \frac{\partial P_{e,yz}}{\partial y}. \tag{2.12}$$

Assuming that the electrons remain magnetized implies (MacMahon 1965) that the form of $\mathbf{P}_e$ can be given by

$$P_{e,ij}^{gyro} = P_{e,\parallel} b_i b_j + P_{e,\perp}(\delta_{ij} - b_i b_j), \tag{2.13}$$

where $P_{e,k}$ are the three eigenvalues of the pressure tensor, two of which are equal and associated with eigenvectors perpendicular to $\mathbf{B}$. [In the isotropic pressure regime the eigenvectors have no preferred direction.] Components of unit vectors

along the magnetic field are denoted by $b_k = B_k/|\mathbf{B}|$ and δ_{ij} is the well known Kronecker delta. Equation (2.12) may now be evaluated as

$$\hat{\mathbf{z}} \cdot \nabla \cdot \mathbf{P}_e \simeq \hat{\mathbf{z}} \cdot \nabla \cdot \mathbf{P}_e^{gyro} = \mathscr{Q}_I + \mathscr{Q}_{II} + \mathscr{Q}_{III}, \tag{2.14}$$

where

$$\mathscr{Q}_I \equiv \frac{\partial(P_{e,\parallel} - P_{e,\perp})}{\partial x}[b_x]b_z + \frac{\partial(P_{e,\parallel} - P_{e,\perp}}{\partial y}[b_y]b_z \tag{2.15}$$

$$\mathscr{Q}_{II} \equiv (P_{e,\parallel} - P_{e,\perp})\Big[\frac{\partial b_x}{\partial x}\Big]b_z + (P_{e,\parallel} - P_{e,\perp})\Big[\frac{\partial b_y}{\partial y}\Big]b_z \tag{2.16}$$

$$\mathscr{Q}_{III} \equiv (P_{e,\parallel} - P_{e,\perp})bx\Big[\frac{\partial b_z}{\partial x}\Big] + (P_{e,\parallel} - P_{e,\perp})b_y\Big[\frac{\partial b_z}{\partial y}\Big]. \tag{2.17}$$

All the quantities in square brackets, [ ], in Eqs. (2.15)–(2.17) will now be shown to vanish at the separator. As one proceeds to the saddle point (x_o, y_o) of the flux function, $B_x, B_y \to 0$, so that $\mathscr{Q}_I \to 0$. Similarly, since $B_x(x, y_o)$ and $B_y(x_o, y)$ are both minima then $\partial b_x/\partial x, \partial b_y/\partial y \to 0$ and $\mathscr{Q}_{II} \to 0$. Finally, even with a constant guide field $B_z = C$, $\partial b_z/\partial x = \partial b_z/\partial y \to 0$ and $\mathscr{Q}_{III} \to 0$. This calculation shows by contradiction that $\mathbf{P}_e \simeq \mathbf{P}_e^{gyro}$ cannot support the reconnection saddle point of 2-D symmetric reconnection, as it cannot produce the needed E_z dictated by steady state conditions.

Vasyliunas concluded that collisionless magnetic reconnection required a full tensorial $\mathbf{P}_e$, more general than that assumed in Eq. (2.13); this new required generality is sometimes referred to in the literature as the onset of *non-gyrotropy*. Others have adopted the term and symbol *agyrotropy*, $A\emptyset_e$ (Scudder 2008), for this broken cylindrical symmetry, defined by the formula

$$A\emptyset_e = 2\frac{|P_{\perp,e,1} - P_{\perp,e,2}|}{P_{\perp,e,1} + P_{\perp,e,2}}, \tag{2.18}$$

involving the two, possibly different, eigen-values for linearly independent eigenvectors perpendicular to the magnetic field of the tensor given in Eq. (2.35) below. The term *agyrotropy* is a Greek construction that parallels that of *anisotropy*, which is the negation of *isotropy* (Schulz, 2003, private communication); with agyrotropy *an+gyrotropy* collapses to *agyrotropy* since the prefix occurs before a consonant, unlike the case for *an+isotropy*. $A\emptyset_e$ is an observable if the electron pressure tensor is measured in a model independent way with some reports of its detection (Scudder 2008; Scudder et al 2002; Scudder et al. 2012; Lopez 2015; Tang et al. 2013).

Vasyliunas had also noted that achieving an agyrotropic electron pressure tensor would require unusual conditions, since MacMahon (1965) had recently systematized the justification for a gyrotropic pressure tensor provided the electron thermal gyro radius, ρ_e, was small compared to the scale length, L, of gradients in the problem and the time variations of the problem were slow compared to the electron cyclotron period. In the usual MHD ordering, L is presumed much larger than ρ_e; thus the gyrotropic form [Eq. (2.13)] for $\mathbf{P}_e$ assumed in MHD is rarely considered worrisome. However, Vasyliunas' deduction that MacMahon's ordering had to be violated was consistent with his discussing magnetic reconnection where electrons lose their labeling ability of field lines and that magnetic reconnection cannot occur in the relatively weak gradient MHD regimes considered by MacMahon.

Vasyliunas also established that the scale L of the symmetric reconnection layer would be comparable to ρ_e, in order that an agyrotropic $\mathbf{P}_e$ could be understood to naturally occur there. *His analysis made a significant stride in the direction of asserting how MHD's predictions are vacated in the collisionless reconnection layer: disrupt MHD's inherent assumptions about relative scales.* These assumptions are discussed in Sect. 2.4.

In steady state *Vasyliunas's conclusion underscored the importance of measuring short scale lengths in the plasma if reconnection sites are to be identified*. For space measurements this poses serious operational problems (cf. Appendix 3) since the observations are performed in moving media as time series, and are not known along regular cartesian spatial arrays, as are available in a PIC simulation. In addition it is also unknown if the transition is steady, planar, or of a known local orientation. New approaches to this problem are discussed in Sect. 2.4.1 and Appendix 3.

2.3.2.2 Overview Collisionless Description

Since 1975 it has been clear that realizing the correct type of electron pressure tensor to support $\mathbf{R}_{ez}$ at the separator for 2D symmetric reconnection required gradient scale lengths near or under the electron thermal gyro radius. This also meant that the width of the current channel would be of the order of the electron skin depth, since $\rho_e = \beta_e^{1/2} d_e$ and β_e in the current channel is usually $O(1)$. Nearly 25 years later full PIC treatments of the 2D reconnection problem showed from their reconstructed pressure tensors that cylindrical symmetry about the local magnetic field direction was interrupted in the layer thought to be reconnecting (Hesse et al. 1999). As shown in Fig. 2.2 analysis of PIC information also demonstrates that the departure from cylindrical symmetry of the perpendicular eigenvalues $\mathbf{P}_{\perp,e,j}$ of the electron pressure tensor was shown by the enhancements of $A\emptyset_e \neq 0$ near and around X and O points suggested by the projection of field lines from contours of the flux functions; indications of weaker violations of $A\emptyset_e$ along the separatrices are also shown in this figure (Scudder 2008).

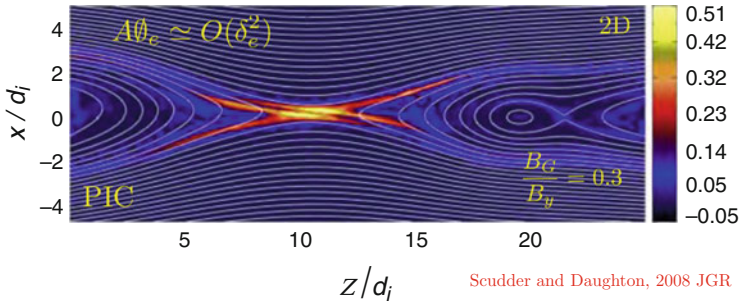

Fig. 2.2 Demonstration of patterns of $A\emptyset_e$ from PIC simulations, demonstrating their ability to label interesting field topologies, indicated with contours of field lines from the flux function. Most intense incidences of $A\emptyset_e$ are shown to radiate from the saddle point. Symmetric weak guide geometry indicated. Nonetheless, enhancements also occur along the separatrices and near O point. *Figure reformatted from* Scudder (2008)

A good portion of the complexity of describing collisionless magnetic reconnection is caused by the theoretically challenging parameter regime of the current channel, possessing kinetic scales: $L_{EDR} < \rho_e \simeq d_e << \rho_i \simeq d_i$. Since the collision times are so long this is also the regime where the plasma transits the scale of the current channel long before coulomb scattering can play a role, making the fluid description and its closure problematic. This parameter regime rules out many traditional descriptions for a plasma, such as two fluid approximations with possible finite Larmor radius corrections, since neither of the species is magnetized. Vlasov fluid treatments simplified by enforcing various invariants along characteristics are also crippled with a heavily restricted number of conserved quantities; for those that can be used they apply only to special geometries. Nothing short of full integration of the self consistent equations of motion for electrons and ions in the evolving electric and magnetic fields is appropriate for theoretical analysis. Fortunately Particle in Cell (PIC) computations are now increasingly being performed in full 3D with modern peta-scale computers. Valiant attempts to extend fluid descriptions into this area have been made, but invariably they are hard pressed to describe the evolution of the pressure tensor well, since the needed *non-local* closures are just not available to truncate these moment hierarchies.

By following the equations of motions of macro electron and proton "particles" and then reassembling their statistical mechanics as a function of space, the PIC approach avoids the irksome problems of closure faced by all reduced closure approaches. The fluid moment equations using the PIC supported plasma moments are then used to understand the phenomena that have been elucidated by eschewing unjustified closure schemes. As with all models there are limitations for PIC models involving number of integration time steps and unwanted collisional effects of macro-particles. With care these limitations can be minimized while making good use of the resolved particle behavior across the narrow current channels.

2.4 2D Reconnection: Training Wheels

In this section thresholded diagnostics are identified for features that can be associated with the inner *electron diffusion region, EDR*. The 2D geometry possesses a built in "ground truth" since it has a flux function that allows the behavior of the in-plane topology of **B** to be interrogated. In particular, the magnetic field in the plane of spatial variations is determined solely by the z component of the vector potential, $A_z(x, y, t)$, which is the flux function. The comoving derivative of A_z in the electron rest frame determines the rate of reconnection (cf. Appendix 1). Contours of $A_z(x, y)$ are field lines (cf. Appendix 1). The description of reconnection in 3D is made more complicated by the *absence* of a flux function when variations in all three dimensions are allowed.

Our approach is to first theoretically show in the controlled 2D PIC environment that *interesting thresholded quantities associated with the defining properties of reconnection are observables*, and then to show visually and statistically that these observable quantities can be used to recover much that the flux function tells the theorist analytically. The advantage is (1) that the physics of these observables is not limited to 2D reconnection, while (2) the leverage of a flux function is a artifice that only works for 2D reconnection modeling, but in 2D it *can* confirm or deny our approach as finding the interesting region where frozen flux is violated. An additional simplification is that the global rate of magnetic reconnection can be determined in 2D geometries from $DA_z/Dt|_{\mathbf{U}_e} = -cR_{ez}$ at the saddle point. In 2D this quantity has been compared favorably (Scudder et al. 2015a) to the frozen flux rate of Eq. (2.7) from Faraday's Law by forming the curls, $\nabla \times \mathbf{R}_e$, directly from PIC variables. While the approach using the curl of $\mathbf{R}_e$ is overkill in 2D, it provides a way in 3D simulations to inventory locales of frozen flux violation where the flux function is not available to help evaluate the value of our thresholded quantities discussed below (Scudder et al. 2015b). As we show in the subsequent sections the observables discussed here also highlight interesting places in 3D and they suggest hints of global conditions of 3D reconnection mentioned in the introduction.

2.4.1 MacMahon and Electron Demagnetization

Vasyliunas' insight suggested that the EDR (in 2D) is a place where MacMahon's systematic expansions for the underpinnings of MHD *fail*. MacMahon's motivation for the commonly used gyrotropic pressure tensor of MHD relied on single particle Guiding Center ordering (Northrop 1963): gyro radius over scale lengths are assumed small and frequencies of time variation described are low compared to the ion cyclotron frequency. In his mathematics there are actually three expansion parameters that are assumed simultaneously small which we will assign the names δ, ϵ and τ. These conditions reduce (MacMahon 1965; Hazeltine and Waelbroeck 1999) to the above casual summary, but *their explicit specification provides one*

immediate benefit: two of them are shown to be observables with the present state of the art instrumentation of space plasma packages.

MacMahon's three assumed small expansion parameters for each species, k, were:

$$\delta_k \equiv \frac{c|\mathbf{E}_{\perp,k} + \mathbf{U}_k \times \mathbf{B}/c|}{w_{\perp,k}B} = \frac{c\left|\mathbf{R}_{k,\perp}\right|}{w_{\perp,k}B} << 1 \tag{2.19}$$

$$\epsilon_k \equiv \frac{2\pi|Z_k e\mathbf{U}_k \cdot \mathbf{E}|}{\Omega_{c,k}kT_k} << 1 \tag{2.20}$$

and

$$\tau_k \equiv \frac{\omega}{\Omega_{c,k}} << 1. \tag{2.21}$$

In the above order these required conditions are that (I) the perpendicular electric force felt in the k'th species rest frame is much smaller than the magnetic force on the thermal speed particle of that species; (II) the energy gain per species gyro period is small compared to the averaged gyrational energy; and (III) the frequency of time variation studied is slow compared to the cyclotron frequency of the k'th species.

Condition III has already been discussed in the beginning of this section, but the ordinary summary for condition I of this regime, $\rho_k/L << 1$, does not explicitly appear in these conditions. Using the electrons as the example, this condition is implied as may be seen by using the leading order term of the Generalized Ohm's law for $en_e\mathbf{R}_e \simeq -\nabla \cdot \mathbf{P}_e$ to restate (I) as

$$\frac{c(I - \hat{\mathbf{b}}\hat{\mathbf{b}}) \cdot \nabla \cdot \mathbf{P}_e}{en_e w_{\perp,e}B} \simeq \frac{< w_{\perp,e}^2 >^{1/2}}{\Omega_{ce}L_\perp} = \frac{\rho_e}{L_\perp}, \tag{2.22}$$

where $L_\perp$ is the cross field scale length has been used to approximate

$$|(I - \hat{\mathbf{b}}\hat{\mathbf{b}}) \cdot \nabla \cdot \mathbf{P}_e| \simeq \frac{n_e m < w_{\perp,e}^2 >}{L_\perp}.$$

It is important to emphasize that relations in Eqs. (2.19)–(2.21) above require the electric field to be measured directly; proxies for the electric field such as $\mathbf{E} \simeq -\mathbf{U_j} \times \mathbf{B}/c$ where the $\mathbf{U_j}$ are either the electron or ion bulk velocity do not contain the information available from a direct, high quality, and calibrated measurement of $\mathbf{E}$. This may be seen since using such an approximation immediately implies that $\delta_j \equiv 0$ yielding the attendant erroneous conclusion that the spatial scales of the system are infinitely large. On the contrary, such an inference is the circular corollary of not introducing ambient information about *all* of $\mathbf{E}$, rather than the ideal

approximations for it that are often used, but contain no sub MHD scale information that characterize plasmas with gradients and reconnection current channels in particular.

Bonus 1: The really good news is that conditions (I, II) *without approximation* are directly measurable with the present state of the art plasma and fields instrumentation in space. Even when $E_\parallel$ is not measured, condition (I) can be determined. Furthermore, δ_k and ϵ_k can be measured *without measuring any lengths, nor determining any geometry as are involved in more traditional length determinations (cf. Appendix 3)*

Bonus 2: This means that *to measure lengths in the plasma one only has to compute the species gyro radius and its form of δ_k, which only requires the measurement of the commonly available $E_\perp$* to infer:

$$L_\perp \simeq \frac{\rho_k}{\delta_k}, \tag{2.23}$$

The hidden sensitivity to length in Eq. (2.23) comes, of course, from having measured the electric field used in δ_k. Accordingly, the length inferred by this process is across the magnetic field. In the ideal MHD limit $\delta_k \rightarrow 0$ and it correctly suggests the scale free MHD world view.

Bonus 3: The form of these dimensionless expansion parameters are interesting for our "thresholdless" problem of the properties that characterize magnetic reconnection, like the violation of the "frozen in condition", $\mathbf{R}_e \neq 0$. The MHD postulates are violated when condition I is violated, which implies

$$\frac{|\mathbf{R}_{e,\perp}|}{B} > \frac{w_{\perp,e}}{c}, \tag{2.24}$$

establishing the values of $|R_{\perp,e}|$ that would seriously violate the *frozen in* condition of MHD. In the solar wind, for example, the RHS of Eq. (2.24) is 0.003. In terms of the wind's thermal Mach number, M_e, we determine

$$|\mathbf{R}_{e,\perp}| > M_e^{-1}|\mathbf{E}_{\perp,sw}| \simeq 10\, mV/m, \tag{2.25}$$

where we have assumed $U = 400\, km/s$, $B = 5\, nT$ and $M_e = 0.2$, which are all typical in the solar wind. In this same regime the perpendicular components of the divergence of $\mathbf{P}_e$ would suggest $|\mathbf{R}_{e,\perp}| \simeq 10^{-7}|\mathbf{E}_{\perp,sw}|$; thus, it would be difficult to satisfy Eq. (2.25) in the solar wind proper. The principal reason for this circumstance is the half AU scale length of the electron pressure in the unstructured solar wind.

Bonus 4: The energy gain expansion parameter ϵ_k constrains parallel and perpendicular parts of $\mathbf{R}_e$, viz

$$\epsilon_k = \frac{4\pi c}{w_{\perp,k}B}\left(\mathbf{M}_{k,\perp}\cdot\mathbf{R}_{k,\perp} + M_{k,\parallel}R_{k,\parallel}\right) << 1 \tag{2.26}$$

where $M_{k,q}$ is the q'th component of the electron thermal mach number of the flow. It should also be noted that with MHD ordering the first term in Eq. (2.26) is formally zero; however, in the EDR this term *can* be important and must be retained for exploration for circumstances where $\epsilon > 1$. (However, if this first term is experimentally found to be important away from current channels there are experimental errors in the observables used, since routinely this quantity should be consistent with experimental zero.)

Equation 2.26 can be rewritten as a condition on how big a parallel electric field can be before violating the MHD ordering. Using k = e for specifics

$$\epsilon_e = 4\pi\delta_e \left| \mathbf{M}_{e,\perp} \cdot \hat{\mathbf{R}}_{e,\perp} + M_{e,\parallel} \frac{E_\parallel}{|\mathbf{R}_{\perp,e}|} \right| << 1. \tag{2.27}$$

Clearly the limit of Eq. (2.27) on $E_\parallel$ is proportional to $|\mathbf{B}|$, being proportional to δ_e^{-1}. Thus, detections of $E_\parallel$ "bigger than my instruments sensitivity level", while interesting, are not sufficient to show that MHD ordering is violated until $\epsilon_e > 1$ is demonstrated. Such limits will be different in the magnetotail than at the forward magnetopause, or auroral zones.

The other insight from this form is that MacMahon's parameters are potentially interdependent when $\delta_e \simeq 1$ and the non-ideal electric field and electron flow are not orthogonal. Within the current channel evidence exist from PIC that ϵ_e and δ_e can be correlated, but generally are not as MHD ordering becomes more prevalent and δ_e relaxes to zero, attended by $\mathbf{E}_\perp \cdot U_{\perp,e} \to 0$.

Bonus 5: For frozen flux slippage to be innocuous its time scale should be slow compared to the electron cyclotron frequency

$$\frac{\nu_\Phi}{\Omega_{ce}} = \left| \frac{-c \oint\!\!\oint_C \hat{\mathbf{b}} \cdot \nabla \times \mathbf{R}_e da}{< B > A\Omega_{ce}} \right| \simeq \rho_e \frac{\delta_e}{L_{\nabla\times}} \simeq \delta_e^\alpha << 1, \tag{2.28}$$

where Eq. (2.23) has been used and the scale of the gradients of the curl indicated by $L_{\nabla\times}$. If this scale is estimated also from the gyro radius and Eq. (2.23) then $\alpha \to 2$ in Eq. (2.28) . If the $L_{\nabla\times}$ saturates at ρ_e, then $\alpha \to 1$. Equation 2.28 is in the form of the τ condition III of MacMahon [cf. Eq. (2.21)]. As shown below in Fig. 2.22 electron agyrotropy has just the same scaling, $A\emptyset_e \propto \delta^\alpha$, flipping between 2 and 1 as agyrotropy intensifies.

Thus, Eq. (2.28) can be rewritten in a form that clearly restates Vasyliunas' insight, but now from the vantage point of 3D:

$$\frac{\nu_\Phi}{\Omega_{ce}} \sim A\emptyset_e. \qquad (3D) \tag{2.29}$$

The arguments leading to Eq. (2.29) also suggest that MacMahon's condition III is also rendered "observable" through $A\emptyset_e$. We define the observable $\Upsilon_{*,\Phi} \equiv \Omega_{ce} A\emptyset_e$ and have calibrated $\Upsilon_{*,\Phi}$ against direct determination of ν_Φ in a 3-D PIC simulation to determine the scaling of Eq. (2.29) to be

$$\nu_\Phi = 0.80 {\Upsilon_{*,\Phi}}^{0.685} \equiv \Upsilon_\Phi(\Omega_{ce}, A\emptyset_e) \tag{2.30}$$

In this way the new quantity Υ_Φ becomes a *calibrated observable proxy in 3D* for the *unobservable* rate ν_Φ of frozen flux violation.

Bonus 6: Another possible measure for thresholding the *strength of the violation of frozen flux* that has recently been used with PIC codes is

$$\Lambda_\Phi \equiv \left| \frac{\nu_\Phi}{Dln\nu_\Phi/Dt|_{\mathbf{U}_e}} \right| \propto \frac{\sqrt{3}\nu_\Phi}{\Omega_{ce}\delta_e M_e cos\Theta\sqrt{2+An_e}} \equiv \Psi_{*,\Phi}. \tag{2.31}$$

In this expression An_e is the electron anisotropy, and $cos\Theta$ is the dot product between unit vectors of the electron's flow and spatial derivatives in the convective derivative in the denominator of the definition of Λ_Φ. The motivation for the form for Λ_Φ is that

$$\Lambda_\Phi \simeq \frac{\nu_\Phi}{\nu_{transit}} = \frac{\tau_{transit}}{\tau_\nu} \tag{2.32}$$

determined by the ratio of the time scale, $\tau_{transit}$, for the electron fluid to transit the scale of the local frozen flux violations to the time scale of the frozen flux violations, τ_ν . The idea behind this condition is that it takes time for the electron mechanics to react to the frozen flux violation which already measures these violations in its rest frame. The natural yardstick for ν_Φ is then the rate $\nu_{transit}$ at which these violations were traversed. It is conceivable that narrow regions of extreme frozen flux violation can be rendered innocuous by passing across them rapidly; or, conversely that slow traverses can enhance slow rates of frozen flux violations. This approach explicitly acknowledges that weak frozen flux violations may not be informative for the location of reconnection sites, where we have shown that frozen flux violations are substantial, that is with $\Lambda_\Phi > 1$.

Finally, theoretically thresholded Λ_Φ is rather difficult to evaluate directly even from PIC variables; by consensus Λ_Φ is unmeasurable using the current state of the space instrumentation (since ν_Φ is). However, the extreme RHS of Eq. (2.31) suggests a test for an *observable* proxy between Λ_Φ and an observable ratio, $\Psi*_\Phi$, given by

$$\Psi_{*,\Phi} = \frac{\sqrt{3}A\emptyset_e}{\delta_e cos\Theta M_e\sqrt{2+An_e}}, \tag{2.33}$$

that does not require curls of $\mathbf{R_e}$ for its evaluation, but requires a well calibrated electron detector on a single spacecraft. Studies of the correlation between $\Psi_{*,\Phi}$

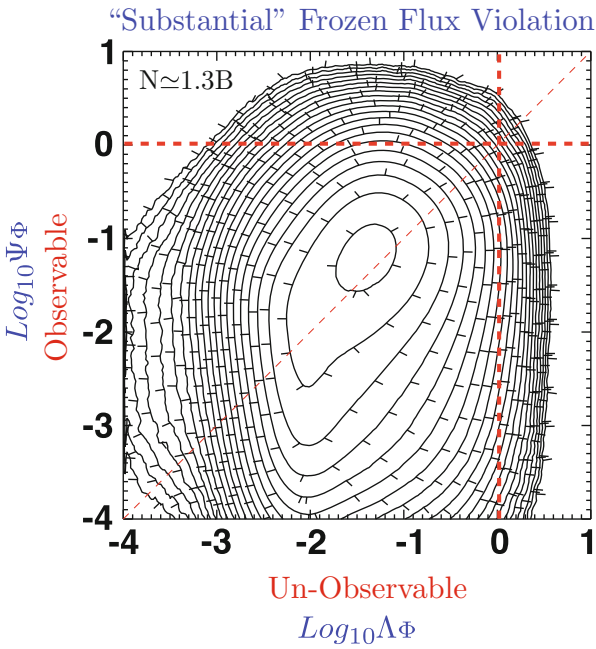

Fig. 2.3 Correlation from 3D PIC between the observable Ψ_Φ and the unobservable Λ_Φ that when greater than unity locally identifies regions of strong frozen flux violation that appear to be necessary at a 3D reconnection site. From forth coming reference Scudder et al. (2015b)

and Λ_Φ using 3D PIC codes have determined the following calibrated form for this proxy:

$$\Psi_\Phi \equiv \left(\frac{\Psi_{*,\Phi}}{18.13}\right)^{1.921} \simeq \Lambda_\Phi, \tag{2.34}$$

which shows that $\Psi_{*,\Phi}$ tends to overestimate the desired size of Λ_Φ; the calibration afforded by Eq. (2.34) can be used with observables to emulate the unmeasurable Λ_Φ. The precise constants of this correlation are specific to the resolution of the PIC simulation used. The correlation between $Log_{10}\Psi_{*,\Phi}$ and $Log_{10}\Lambda_\Phi$ is also very strong, but is not calibrated for determining sites of $\Lambda_\Phi \simeq 1$. The excellent correlation Ψ_Φ, Λ_Φ using Eq. (2.34) is shown in Fig. 2.3 which was performed with over 1.28 billion determinations across the entire 3D PIC simulation discussed below. A flotilla's measurements of Ψ_Φ could help delineate the context of the regime as shown below with Fig. 2.18.

2.4.2 "Observations" in 2D PIC of ν and Λ

An example of using these diagnostics is shown in Fig. 2.4, where color contours of frozen line violation, $\nu_\uparrow$ and thresholded values of $\Lambda_\uparrow$ variation are shown from a 2D anti-parallel PIC simulation. White curves denote projections of magnetic field

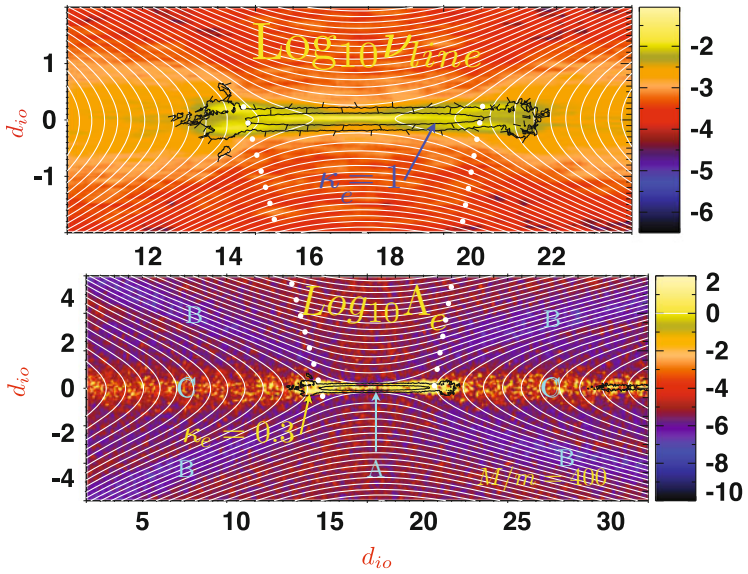

Fig. 2.4 *Top*: Colored contour shows $Log_{10}\nu_{\uparrow}$ with superposed contour (*black*) of $\kappa_e = max\{\delta_e, \epsilon_e\}$ in *black* with downhill direction indicated by flags. (*B*): Same region in larger context, with the same isocontours of κ_e indicated on top of $Log_{10}\Lambda_{\uparrow}$. The *color contours* in *Bottom* are determined by operations that may be performed on 3D simulations. When $\Lambda_{\uparrow} > 1$ this method finds the saddle point (known here in 2D) to be the reconnection locale. The *black contours* also show that MacMahon's assumptions are strongly violated in the same vicinity of the saddle point. The κ_e diagnostic and $\Lambda_{\uparrow}$ reenforce one another's implications. *Reproduced with permission for the November 2015 Phys. Plasmas, **22**, 101204, Copywrite 2015, AIP Publishing LLC* (Scudder et al. 2015a)

lines in the plane of variations. Larger values of both variables are concentrated near the saddle points indicated by the field curves, but extend well away from them in certain directions. Isocontours of $\kappa_e = max\{\delta_e, \epsilon_e\}$ at 0.3 and 1 are superposed in black on the color contours (flags denote the downhill direction); they clearly encircle the saddle point indicated by the pattern of the projections of the magnetic field. The contiguous region of enhanced demagnetization, $\kappa_e > 1$, clearly envelopes the peak region of descending intensity of $\nu_{\uparrow}$ and clearly frames the region of $Log_{10}\Lambda_{\uparrow} > 0$ which is where $\Lambda_{\uparrow} > 1$. The contours of $\Lambda_{\uparrow} = 1$ also clearly differentiate between *innocuous* and significant frozen flux violations, agreeing that the important regions encircle the saddle point from the flux function and pointing to the complementary regions as being innocuous. $\Lambda_{\uparrow}$ out along the separatrices and in the exhaust of the reconnection patterns are several power of 10 below its above unity size near the saddle point. The frozen flux slippages along the separatrices, while present, are thus anecdotal, and do not suffice to identify the separatrices as reconnection sites. *The flux function underscores the correctness of this inference.* Nonetheless, there are *some* hints of demagnetization in the vicinity of the separatrices, reenforcing the insufficiency of reporting

non-zero demagnetization, by itself, for identifying regions where significant frozen flux violations, as is occurring when $\Lambda_{\uparrow} > 1$ about the saddle point. We return to this point in the discussion section.

While the pattern of theoretically interesting color contoured variables in this figure can be determined with PIC variables, they are *presently unobservable* using present state of the art measurements from space platforms. Only the information involving δ_e and ϵ_e that went into determining the black contours of the thresholded demagnetization condition, κ_e, are observables. This figure demonstrates that these observables do provide needed information for diagnosis of such regions; however, even the *topography* of κ_e is not a direct observable. As a scalar $\kappa_e(t)$ would be ready observable; using a flotilla of spacecraft measuring κ_e simultaneously perhaps the variation of $\kappa_e(\mathbf{x})$ might be inferred for limited areas. Being dimensionless and with some background in PIC studies of this type (as a function of guide field strengths and asymmetry) *in situ* diagnosis of regimes may be facilitated.

2.5 Macro Signatures of Demagnetized Electrons

The signatures of electron demagnetization just discussed involve using measurements of the electromagnetic field components in the electron rest frame. The indices of electron demagnetization imply thresholds for the size of $|\mathbf{R}_{e,\perp}|/B$ and $E_{\parallel}/B$. *In this section we deduce further moment level corollaries of demagnetized layers that can be assessed without measuring the electric field* and refer the reader to recent more detailed examples in the literature (Scudder et al. 2015a,b; Scudder 2015).

2.5.1 Agyrotropy $A\emptyset_e$

A way to detect agyrotropic electrons is to compute the symmetric tensor which measures the average velocity space variance of the distribution function perpendicular to the magnetic field direction:

$$\aleph_{ij} = < (\mathbf{w} \times \hat{\mathbf{b}})_i (\mathbf{w} \times \hat{\mathbf{b}})_j >, \tag{2.35}$$

where $\mathbf{w}$ is the electron velocity in the electron rest frame and $<>$ stands for a velocity space average over a temporally unaliased velocity distribution. Such measurements are best performed by detectors that do not wait for the sensors to reorient by one half spin to obtain their full solid angle coverage. This tensor has only two non-zero eigenvalues, since the third vanishes with the magnetic field as its eigenvector. If its two non-zero eigenvalues are not equal the distribution is certainly

not gyrotropic. As shown in Scudder (2008) the two non-zero eigenvalues of $\aleph$ are given by

$$\lambda_{\pm} = \frac{\alpha \pm \sqrt{\alpha^2 - 4\beta}}{2}, \tag{2.36}$$

where $\alpha = Tr\,\aleph$ and

$$\beta = -(\aleph_{xy}^2 + \aleph_{xz}^2 + \aleph_{yz}^2 - \aleph_{xx}\aleph_{yy} - \aleph_{xx}\aleph_{zz} - \aleph_{yy}\aleph_{zz}). \tag{2.37}$$

Then agyrotropy, $A\emptyset_e$ is defined to be

$$A\emptyset_e = 2\frac{|\lambda_+ - \lambda_-|}{\lambda_+ + \lambda_-}, \tag{2.38}$$

which ranges between the gyrotropic limit of 0, and the planar limit of 2. For this measurement to be geophysically interesting its size must routinely be demonstrated to be small and only enhanced in layers with current channels as implied by the magnetic field profile. The experimentally routine values of $A\emptyset_e$ away from current channels reflect the state of calibration of the detection system and *must* be established prior to "detection" of $A\emptyset_e \neq 0$.

An alternative characterization of electron demagnetization is sensed by the size of the irreducibly tensorial part, χ, of the electron pressure tensor, $P_{e,ij}$, defined by the operation

$$\chi \equiv P_{e,ij} - ab_ib_j - \frac{(Tr\mathbf{P}_e - a)}{2}(\delta_{ij} - b_ib_j), \tag{2.39}$$

where $a = \hat{\mathbf{b}} \cdot \mathbf{P}_e \cdot \hat{\mathbf{b}}$. If the plasma is gyrotropic χ is the null matrix. There are many ways to judge the *size* of a matrix. The matrix χ essentially describes the variations of the pressure different from being cylindrically symmetric about $\mathbf{b}$. As a matrix χ contains information about the symmetry breaking in three eigen-directions that have no a priori connection to $\mathbf{b}$. Unless those eigen-directions are computed, inventories of the size of this symmetry breaking are not unique.

A scaled version of the Frobenius norm of χ has also been suggested to estimate the size of χ (Aunai et al. 2013). The Frobenius norm of χ is the square root of the sum of the squares of its eigenvalues and the recently proposed alternative for $A\emptyset_e$ is

$$Au_e = \frac{2\sqrt{\Sigma_k \lambda_k^2}}{Tr\,\mathbf{P}_e}. \tag{2.40}$$

Other equally frame invariant measures that *could* be used to measure the departures represented by χ are the geometric mean of the absolute value of the eigenvalues

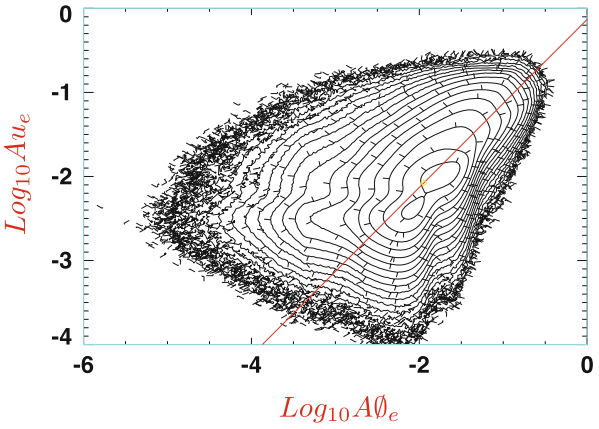

Fig. 2.5 Correlation of $A\emptyset_e$ and Au_e showing that these two apparently different measures are generally in agreement, especially for the bigger values. To guide the eye the *red line* i$y = x + x_o$ is included with origin set by the highest probability point in the 2D histogram. From forthcoming reference Scudder et al. (2015b)

compared to the average eigenvalue of $\mathbf{P}_e$

$$Au_{e2} \propto \frac{3\sqrt[3]{|Det\ \chi|}}{TrP_e} \tag{2.41}$$

or the straight ratio of determinants of χ and that of the entire pressure tensor:

$$Au_{e3} \propto \frac{|Det\ \chi|}{Det\ \mathbf{P}_e}. \tag{2.42}$$

Figure 2.5 shows the correlation of $A\emptyset_e$ and Au_e using over 1.28 billion estimates in a 3D asymmetric guide example (Daughton et al. 2011), showing that the two proposed indices of agyrotropy produce very similar information, especially when the selected observables are largest.

2.5.2 *Electron Thermal Mach Number*

To achieve a narrow, electron inertial scaled current channel the electrons of the plasma must almost exclusively support the out of plane current density, because the ions are not nimble enough to do so. As derived in Scudder et al. (2015a) Ampere's equation implies that the electron thermal Mach number, M_{ez}, in the out of plane current channel should be of order unity, or more precisely

$$M_{ez} \sim \frac{\delta_e}{\beta_e\sqrt{1+S^2}} \tag{2.43}$$

where S is the ratio of guide field to interconnection field strength well away from the current sheet. Equation 2.43 is derived assuming the magnetic profile is linear

near its reversal with a scale L suggested by the crossing orbits of the electrons. The scale of the current has been taken to be $L = \sqrt{d_e \rho_e}$, motivated by Parker's early considerations of particle dynamic studies at current sheets (Parker 1957); the electron β_e in this formula is determined at the scale length L from the null using the reconnecting components of **B** only. Various combinations of $\delta \simeq 1$ and $\beta_e \uparrow 1$ suggest that M_e could be order unity within the current sheet.

For the experimentalist *detection of* $O(1)$ *electron thermal mach numbers represent a truly unusual circumstance*, since even the *supersonic* solar wind only has $M_e \simeq 0.2$, and that value is reduced upon entering the sheath as the flow speed is reduced and the thermal speed increased. (Here too, the routine agreement of $\mathbf{U}_e \simeq \mathbf{U}_i$ must be experimentally demonstrated for comparable density and temperature regimes before the detection of large M_e is defensible.) In the one resolved electron diffusion region reported to date $M_e > 1$ was reported (Scudder et al. 2012) as reproduced below in Fig. 2.13.

2.5.3 Convergent Electric Fields

Models of reconnection invariably have converging electric fields caused by the *unmeasurable* space charge in the layers that exist to induce the ions to come towards the separator. These electric fields are concentrated normal to the current sheet and are perpendicular to the guide and interconnection magnetic field components. These fields are usually strong as compared with MHD electric fields, but their ability to demagnetize electrons depends on $\delta_e > 1$. This demagnetizing condition becomes $E_\perp > B(nT) w_{\perp,e}/c$, which in observational units implies

$$E_\perp(mV/m) > 0.55 B(nT) \sqrt{T(eV)}. \tag{2.44}$$

At the magnetopause this condition becomes (with 50 nT and 100 eV) a threshold for demagnetization of approximately $E_\perp > 275\, mV/m$, while the MHD inflow reconnection electric field at $U_{in} \simeq 0.1 M_A$ has a size of $E_{recon} \simeq 2.5\, mV/m$. Macroscopically, the convergent pattern (cf. inset (c) Fig. 2.8) is unusual correlative information. Before reaching their peak strengths such fields will cause electric drifts in the electrons, until disrupted by their demagnetization.

As distinctive as the convergent electric field pattern may be, the inference of electron demagnetization from this asymmetric pattern would require measuring values of $E_\perp$ more than 100 times the reconnection MHD electric field. In the presence of asymmetric reconnection with $B_{sh} < [1 - 4] B_{sp}$ the measured normal electric field is also asymmetric with $|E_{x,sh}| < |E_{x,sp}|$. The observations are consistent with comparable, but very small, demagnetization on the two sides of the current channel. Below, symmetric and asymmetric current layers are illustrated that show this range of asymmetries in the converging electric field strengths.

2.5.4 *Electron Anisotropy*

In the layers adjoining the low density side of the electron diffusion region there is a zone where the electrons, though still magnetized, are bouncing back and forth in a parallel electrical potential, gaining energy from the parallel electric field while moving into a weakening magnetic field. Conservation of the first adiabatic invariant causes rather large electron anisotropies to occur *while the electrons still remain magnetized*, again because the numerator of μ is increased while the denominator decreased. Electron anisotropies as high as 8–10 are seen in PIC simulations (Le et al. 2009; Egedal et al. 2012). A recent resolved EDR gave evidence for electron temperature anisotropy of nearly 8 (Scudder et al. 2012) shown in Fig. 2.13 below.

2.6 Overview of Observables

The relationship of our thresholded observables and theoretical quantities of magnetic reconnection are identified in Fig. 2.6; in addition, the logical progression of these techniques from 2D into 3D geometries is also shown. Proceeding from left to right we have shown that the comoving time rate of change of the flux function, $\frac{DA_z}{Dt}|_{\mathbf{U}_e}$, agrees with the reconnection rate determined from Eq. (2.7) in 2D simulations (Scudder et al. 2015a). With 2D simulations we can determine the rate using the 2D peculiar flux function approach and via the $\nabla \times \mathbf{R}_e$ and Eq. (2.7), which is available in either 2 or 3 dimensions. We then show that the region of enhanced ν_Φ agrees with the saddle point of the flux function. We also see that this same

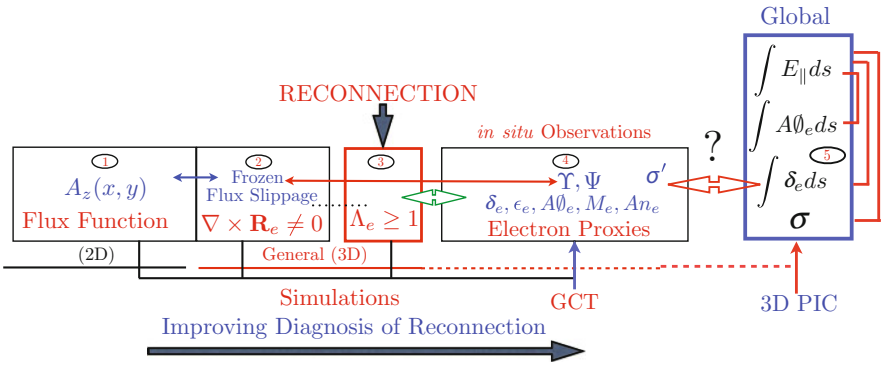

Fig. 2.6 The links between theoretically interesting quantities (boxes 1–3), and observable ones including the new ones (box 4), Υ and Ψ proposed in Scudder et al. (2015a) to generalize the determination of the local rate of frozen flux violation and its significance in 3D. Far *right rectangle* (5) suggests some *global* theoretical diagnostics of interest, including the squashing index σ that we suggest has an observable proxy, σ', in this chapter. See text. *From forthcoming article* Scudder et al. (2015b)

region is one where δ_e and ϵ_e are misordered, showing that the thermal electrons are demagnetized there. In box 3 we explore with Λ what is the necessary threshold for ν_Φ to be big enough to be "dynamically important" and thus indicative that the observer is in the region like the X point region of 2D reconnection. Box 4 correlates the evidence for the primary and secondary signatures of electron demagnetization with this conclusion both in 2D and 3D simulations. In box 5 we briefly touch on local signatures of global squashing σ properties that are beginning to be explored with 3D PIC simulations.

2.7 Benchmarking Thresholded Observable Quantities

In 2D simulations the flux function conveniently summarizes the changing topology of **B** projected on the 2D plane of variations. With the flux function information (available in PIC) as a backdrop, we now look at the thresholded *observable* spacecraft diagnostics deduced from PIC simulations to show that they, too, can find what the flux function knows all too well. The idea is that in 3D there is no flux function, so these new diagnostics (which do not depend on the dimensionality of the reconnection layer being studied) have the potential to supply auxiliary information (usually provided by the flux function in 2D) that can be accessed when studying 3D sites occurring in PIC or nature. In addition, the ability to locally determine ν_Φ via the $\nabla \times \mathbf{R}_e$ gives us a control (like the flux function) that can be determined in 3D simulations to have an idea where frozen flux violations are taking place and, by transitivity, to evaluate the thresholded quantity Λ_Φ's ability to label regimes where demagnetization is dynamically important.

Our approach in this initial sub-section analyzes frames from 2D PIC simulations of anti-parallel reconnection, where a flux function is available, to show that $\delta, \epsilon, \Lambda$ contain information similar to that reflected in the flux function.

2.7.1 2D Anti-Parallel

The thresholded guiding center theory expansion variables of Eqs. (2.19)–(2.21) for an anti-parallel simulation are shown in Fig. 2.7 with the 2D *projections* of the magnetic field lines (white) superposed. This column of contours is framed at the top by the *unobservable* rate of frozen line violation $\nu_\uparrow$ and its dimensionless variant, $\Lambda_\uparrow$ (bottom). The domain of vigorous frozen line violation occurs when $Log_{10}\Lambda_\uparrow > 0$. In the top panel black contours of $\kappa_e = \max\{\delta_e, \epsilon_e\} = [0.3, 1]$ are superposed with flags that point "down" hill. These contours, indicative of strong electron demagnetization, neatly enclose the region of maximum $\nu_\uparrow$, as well as the yellow regions in the bottom panel where $\Lambda_\uparrow > 1$. According to our 3D capable approach the bottom panel suggests that dynamically important frozen flux violations occur where $\Lambda_\uparrow > 1$ in precisely the same locations where the observable

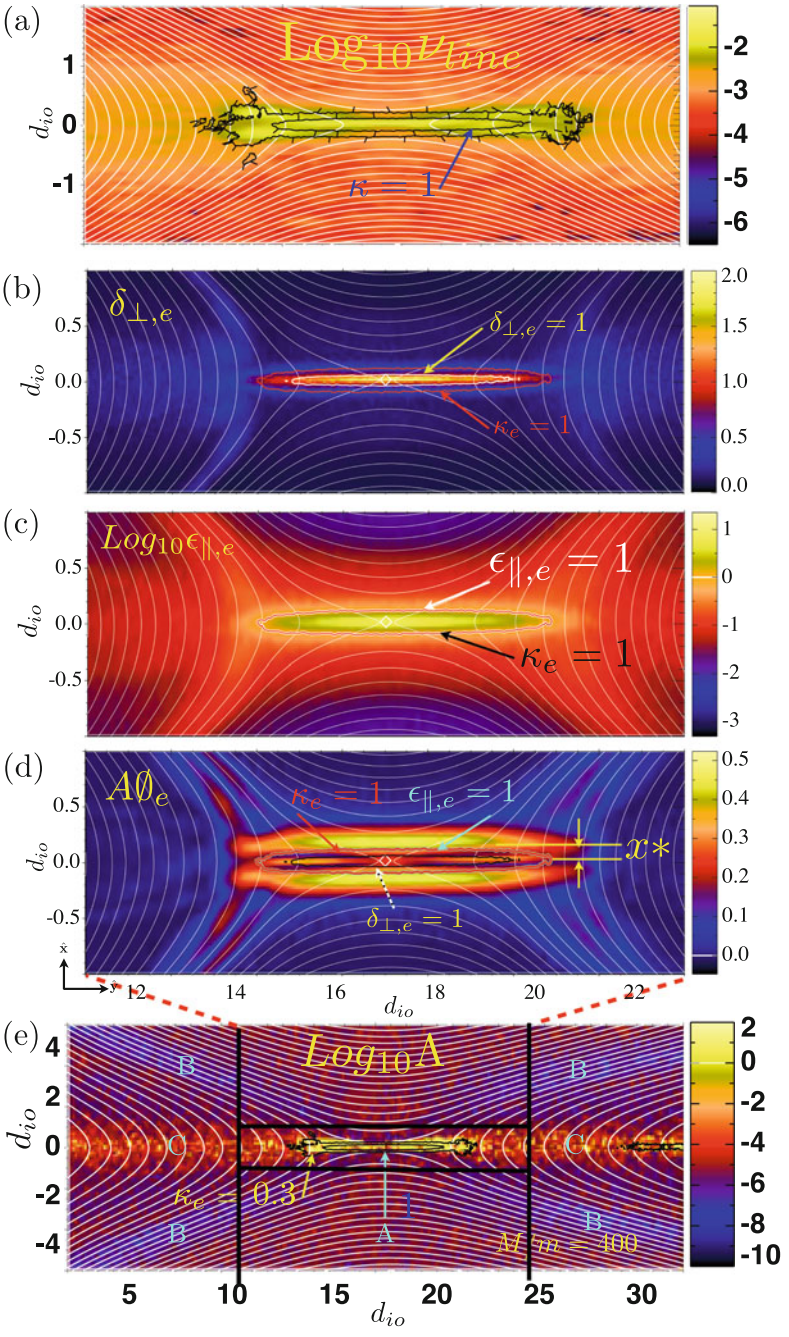

Fig. 2.7 Microscopic signatures of electron demagnetization from reference Scudder et al. (2015a). See text for description. Note the differential compression 6:1 of the horizontal and vertical axes. Anti-parallel, open PIC simulation of reconnection with $d_{io} = 20d_{eo}$. Separate panels discussed in text. *Reproduced with permission for the November 2015 Phys. Plasmas,* ***22****, 101204, Copywrite 2015, AIP Publishing LLC* (Scudder et al. 2015a)

MacMahon indices of demagnetization are significant, and in a saddle point region of the 2D available flux function.

The middle three panels of Fig. 2.7 are all *observables*: MacMahon's first two perturbation parameters clearly show they are not small compared to unity in the saddle point region. The third panel is visual proof of Vasyliunas' deduction that agyrotropic $\mathbf{P}_e$ is required in this saddle point area for collisionless reconnection to occur. The double ribbon pattern of $A\emptyset_e$ seems to reflect a spatial localization of demagnetization as if the outer ribbons are turning points in orbits that concentrate agyrotropic disruptions of phase space density. The channel of large δ, for example, is narrower than is the double ribbon of $A\emptyset_e$. Since the channel has scales well under the gyro radius the consequences for the fluid moments and the pressure tensor will be felt over a broader spatial scale commensurate with where the electrons begin to sense the field again. This can be seen better in Fig. 2.9 where the true maximum peak of the ribbons of $A\emptyset_e$ occur rather precisely when $\kappa_e < 1$, which reflects the increasing magnetization of the disrupted electrons leaving this inner area.

These data support the idea that the saddle point area where significant frozen flux violation is occurring (using $\nabla \times \mathbf{R}_e$) are places where the electrons are indeed demagnetized, while identifying the same locale where the flux function has a saddle point.

Manifestations at the macroscopic moment level of underlying circumstances where the electrons are demagnetized are shown in Fig. 2.8. The top panel shows the strongly varying electron thermal mach number, peaking near $M_e \sim O(1)$, that reflects the electron inertial scaled current channel and that the ions cannot contribute significantly to the drift. This signal is so extraordinary that it should be routinely expected if a case is to be made that the EDR has been traversed; such a strong signature is not known to occur elsewhere where *in situ* samples of astrophysical plasmas have been made; even through shock waves $M_e << 1$ is typical. The anisotropy signature (e) is not directly that of demagnetization of the electrons, but the reverse: it reflects the manipulation of the pressure anisotropy by the strong parallel electric field along the separatrices coupled with electrons cooling as they move into weaker magnetic fields. The principal signature is the unusually large pressure anisotropies compared to that more typically seen in well sampled locales such as the solar wind, magnetosheath or magnetosphere, where electron anisotropies are rarely outside of the range $0.5 < An_e < 2$. If larger electron anisotropies than this range are encountered when crossing current channels indicated by **B**, they should be evaluated for evidence of an exit from a demagnetized region. In the antiparallel geometry, as here, these layers can be seen on both "sides" of the current sheet, whereas they occur preferentially on the low density side of asymmetric reconnection layers, especially favoring low β_e and guide geometries (cf. Sect. 2.7.2, Fig. 2.10). The middle three panels illustrate other features of the layer: (1) their departure from charge neutrality (b), although this is not presently thought to be observable; (2) the pattern of converging electric fields along the inflow normals which has been observed (c). These converging electric fields owe their size to the space charge in the layer, but they appear also to be causative of the agyrotropy seen in the electrons (which is contoured on top of the colored E profile).

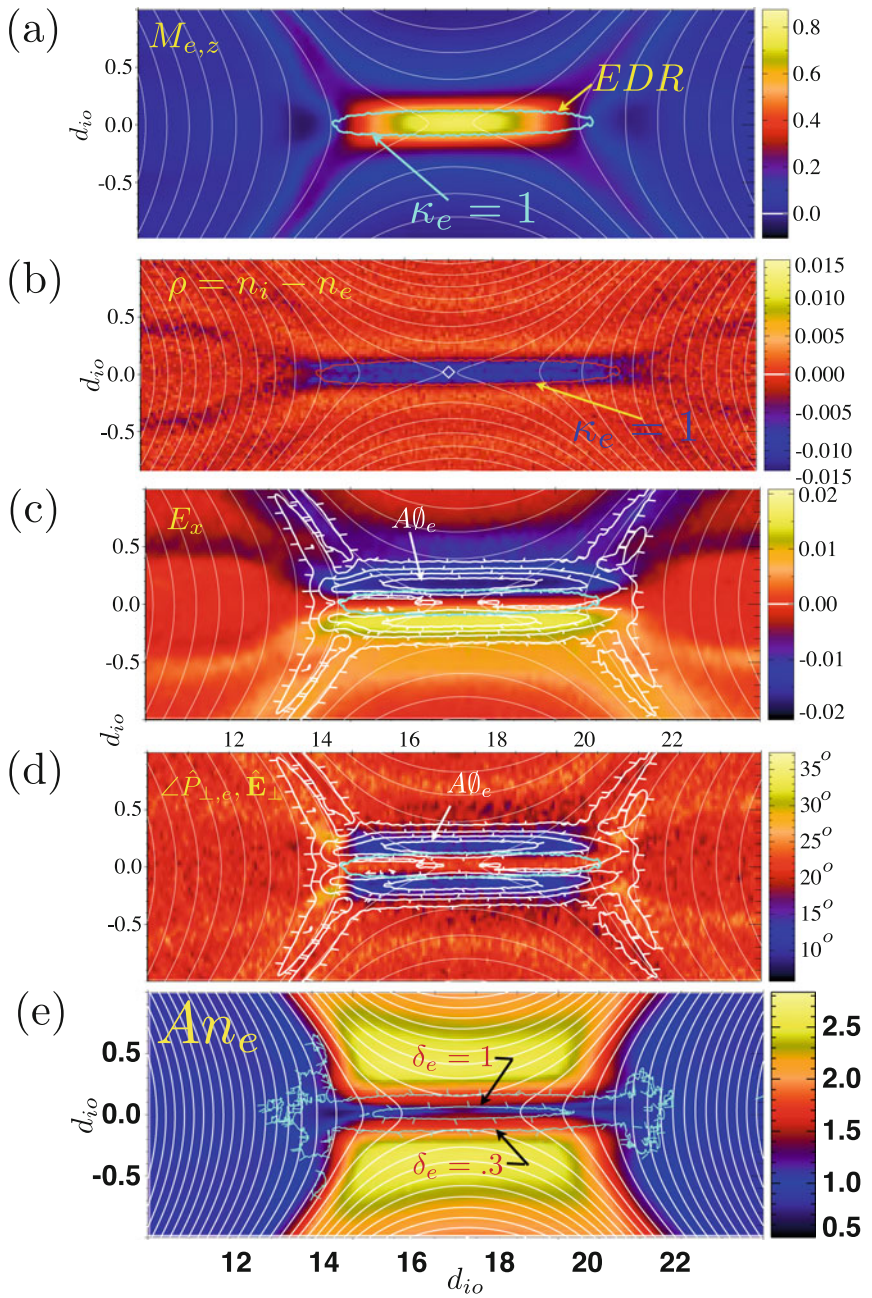

Fig. 2.8 Macroscopic observables associated with the reconnection layer as discussed in the text; same data as in Fig. 2.7. *Reproduced with permission for the November 2015 Phys. Plasmas, **22**, 101204, Copywrite 2015, AIP Publishing LLC* (Scudder et al. 2015a)

The short scales of the transition and the strong electric field allow this electric field to do work on the gyro motions of the electrons. Ordinarily crossed **E** and **B** fields cause electrons to $\mathbf{E} \times \mathbf{B}$ drift, provided the electrons remain magnetized which they do not across the EDR. In such a regime all components of **E** can do net work on the electrons and contribute to ϵ_e.

An observable indication of this effect at work is to compute the angle θ between the perpendicular electric field and the nearest perpendicular eigenvector of pressure tensor (d). Commonly $\theta << 25°$ in regions when $A\emptyset_e$ is seen to be enhanced. This same condition allows the perpendicular electric field to enhance ϵ_e, thus keeping this index high, reflective of it being disordered with respect to MacMahon's assumptions. (See Scudder 2008 for more details.)

The simultaneous profiles of the reconnection layer along the inflow and outflow symmetry lines are provided in Fig. 2.9. Comparing the top and bottom panels allows the ratio of inflow to outflow region of demagnetization to be determined for this symmetric anti-parallel case. Using $\kappa_e \simeq 1$ one determines a ratio of integrated full widths for inflow to outflow to be $1.75d_e : 48d_e$, which is $1.75d_e : 2.4d_i$, where local skin depths have been used to account for the variation of the density across the profile. The abrupt decrease in the $\kappa_e < 1$ along the exhaust signals the remagnetization of the electrons in the exhaust. This accompanies a strong braking of the electron's exhaust flow speed as they must now *respect and gyrate* about the strengthening normal magnetic field across the exhaust. This braking also causes some electron heating to occur (not shown) and is the cause of the two zone picture of the outflow region of the EDR (Karimabadi et al. 2007).

2.7.2 2D Symmetric Guide Geometry Diagnostics

Diagnostics for the 2D symmetric guide geometry are also shown in the panels of Fig. 2.10, where a guide field 0.5 that of the interconnecting magnetic field is used with mass ratio 360. The out of plane guide field adds a new asymmetry to the electrodynamics that is especially clear across the exhausts where a *preferred* separatrix line occurs, so that of the two lines that define the separatrices, one of them becomes preferred and negatively charged as a result of the newly remagnetized electrons in the exhaust feeling a $-|e|\mathbf{U}_e \times \mathbf{B}_{guide}/c$ force that rather promptly encourages the electrons in the exhaust to veer up against the preferred separator. This process leaves the full width of the exhaust with a non-uniform character, with more electrons to one side than the other. The ions are not as magnetized in the exhaust, nor are they travelling initially as fast as the electrons, so there is a polarization of charge. This separation of charges causes a secondary electric field across the exhaust, which with the guide field, produces a large scale component of E×B along the exhaust that assists in bring the ions up to their terminal Alfvén speed as they become demagnetized. The exhaust channel for the electrons is asymmetrically confined to the vicinity of, but inside of, this preferred separatrix arm whose location is delineated by the flux function.

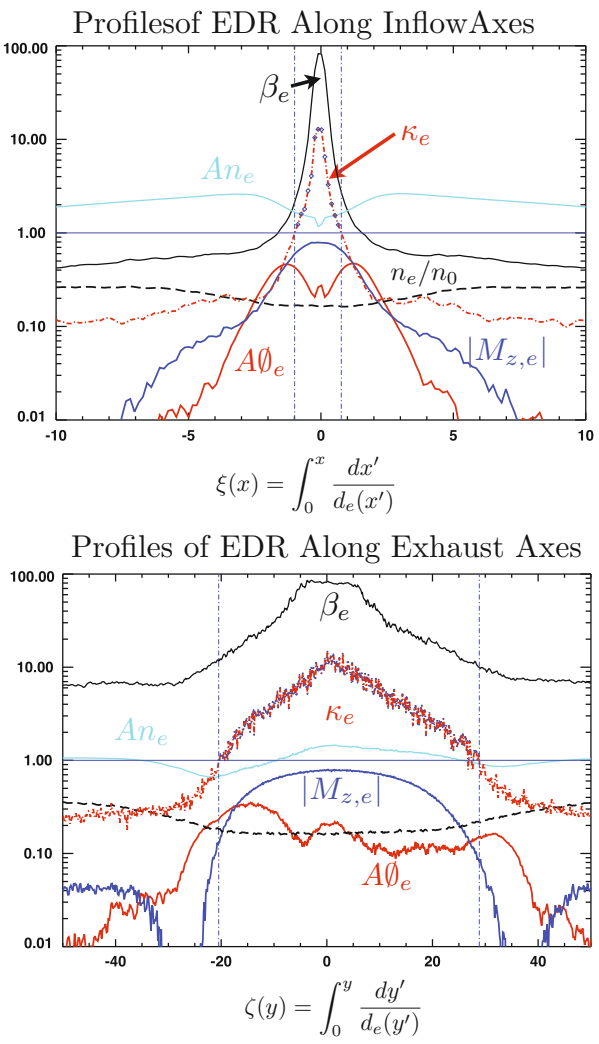

Fig. 2.9 *Top* Diagnostic profiles on inflow symmetry axis; *Bottom* on exhaust symmetry axis of Fig. 2.8. *Reproduced with permission for the November 2015 Phys. Plasmas, **22**, 101204, Copywrite 2015, AIP Publishing LLC* (Scudder et al. 2015a). $d_{io} = 20d_{eo}$ in this simulation

The presentation shows a mixture of diagnostic quantities across the plane (Fig. 2.10) and then focuses in Fig. 2.11 on statistically histogrammed properties found in the layer (defined by the dotted lines in Fig. 2.10d) inside the exhaust separatrix known from the flux function.

The statistics show that peak values of MacMahon's $\epsilon_e > \delta_e$, but that there is a strong demagnetizing spike near the center of the preferred arm superposed on a generally enhanced demagnetization along the preferred arm, including general enhancements of $A\emptyset_e$. Throughout and along the preferred arm significant frozen flux slippage is seen as in our LHDI simulation in Fig. 2.14 below. In agreement with the flux function's assessment of the topology, our thresholded level Λ remains

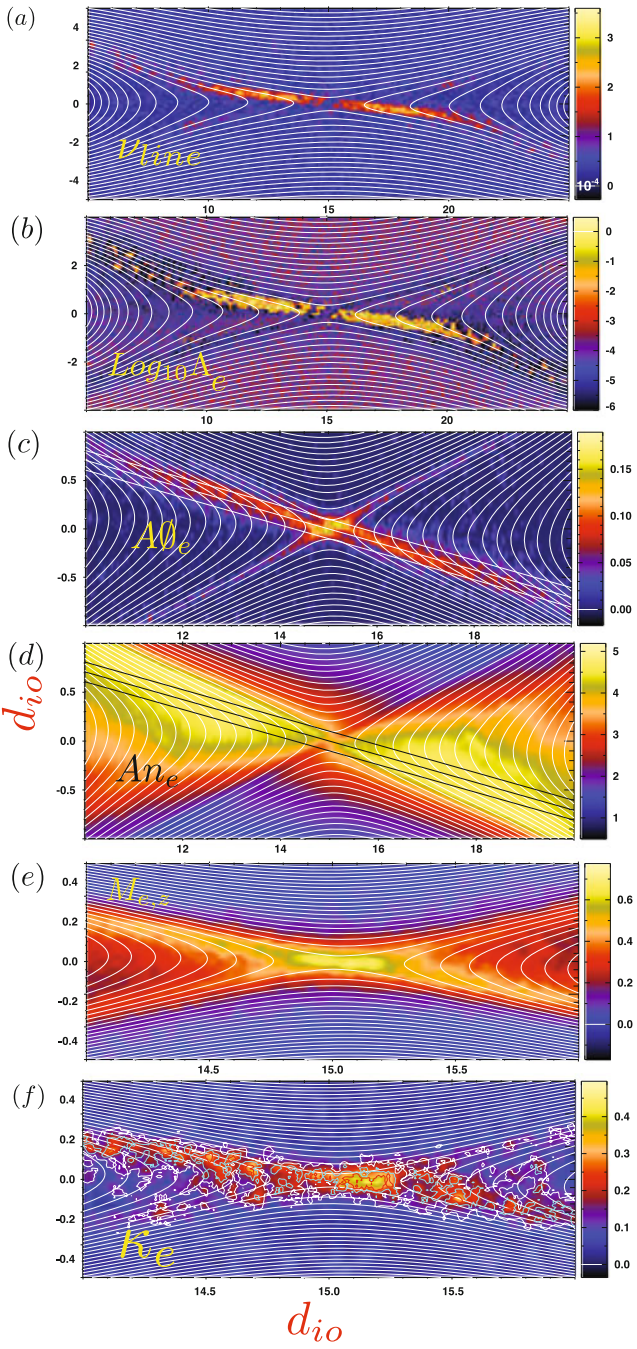

Fig. 2.10 Diagnostics of 2D Guide geometry S=0.5 as discussed in the text. Diagonal lines indicate region where further details and diagnostics are presented in Fig. 2.11. *Reproduced with permission from the November 2015 Phys. Plasmas,* ***22****, 101204, Copywrite 2015, AIP Publishing LLC* (Scudder et al. 2015a)

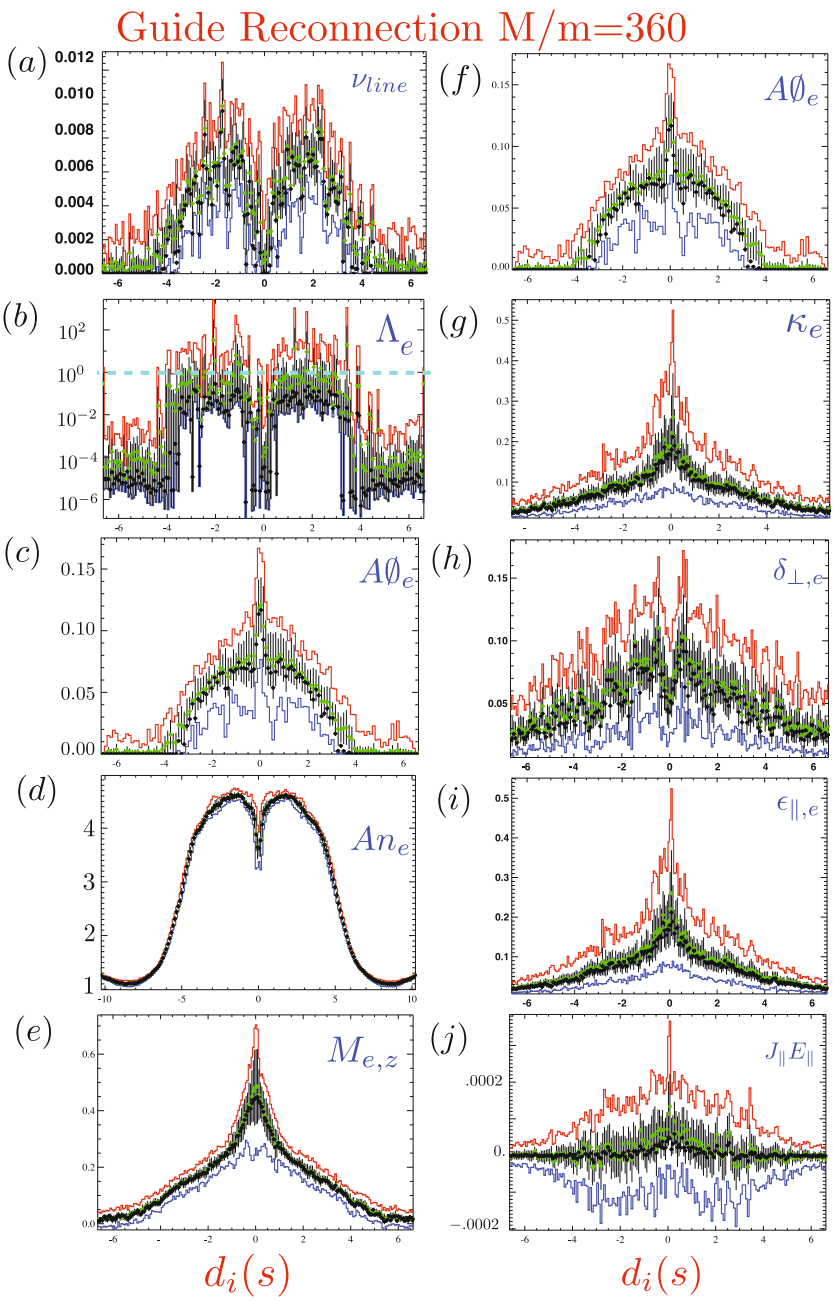

Fig. 2.11 Symmetric Guide $B_z = 0.5B_y$ (Daughton et al. 2006). *Insets* discussed in the text. Colors refer to harmonic (*green*), max(*red*), min(*blue*), variances (*black bar*) about mean (*black dot*) cf. text. Distance d is measured along the center diagonal line in Fig. 2.10c,d, in units. Fig. 2.10d in units of the *local* ion skin depth. *Dashed cyan line* in inset (**b**) is the cross over regime for $\Lambda_e \simeq 1$. *Reproduced with permission from November 2015 Phys. Plasmas, **22**, 101204, Copyright 2015, AIP Publishing LLC* (Scudder et al. 2015a)

below unity along this arm and does not suggest that frozen flux slippage is at the level of a reconnection site. The preferred arm's slippage has a rather pronounced termination at $\pm 4 d_{io}$ along the preferred arm; it also has a significant depression near the center of the arm that is caused by the symmetry of this layer (cf. Scudder et al. 2015a).

A sequence of simulations were done with variable guide field strengths, keeping the interconnection fields the same. While the reconnection rates were observed to be about the same, the level of demagnetization seen at the separator systematically decreased with increasing guide field. In the guide field geometry the conserved reconnection electric field has a strong parallel component, that essentially is an imposition by MHD of $E_{\|}$ much stronger that usual. In addition, the magnetic field has a component along the desired direction of the current channel, giving the current density in the sheet a significant parallel component. In this sense the guide field geometry requires less demagnetization while forming the narrow current channel of the desired intensity, as compared with an anti-parallel geometry. It appears to be the case that less agyrotropy was actually needed to gain access in the solution to the out of plane current needed by the boundary conditions. Nonetheless, Vasyliunas' insight still holds, agyrotropy was still required to support the layer, it was just not as strong as it is in the anti-parallel case. In this sense the anti-parallel geometry while simplest to analyze may be the most complicated as far as gyro orbits. Graphs of these effects are illustrated elsewhere (Scudder et al. 2015a).

2.7.3 2D Guide Asymmetric

Most magnetopause crossings are observed with field strengths and particle densities asymmetric about the current sheet. A fortuitous crossing allowed the EDR to be resolved with the Polar spacecraft that has been diagnosed with the approaches of this chapter (Scudder et al. 2012). Despite the actual 3D geometry of the encounter a 2D asymmetric guide (S = 1) simulation was conducted. It was not possible to achieve the full density asymmetry witnessed in terms of density contrast. A profile through the simulation was found that agreed well with the size and spatial ordering of the observable MacMahon expansion parameters determined from the Polar data that analyzed **E**, **B** and plasma data. The simulation was post processed in terms of the above observable parameters and a pseudo time line was created to move through the spatial mesh of the simulation to gather a possible time series to compare with the spacecraft time series. The fortuitous encounter occurred at very low relative speed (1.6 km/s) and knowledge of this speed and geometrical determinations allowed time intervals to be converted into spatial intervals, providing length scale assignments for event durations. The ordering of the features recorded in the pseudo traverse of the layer in the simulation had many features seen in the data including a large angle shearing of the magnetic field with (different) but electron inertial scale length linear ramps in the magnetic field profile. The profile from the simulation is shown in Fig. 2.12.

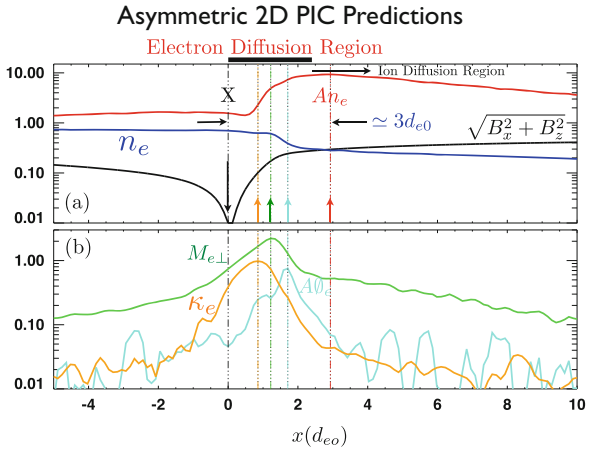

Fig. 2.12 Profiles of in plane magnetic field strength $\sqrt{B_x^2+B_z^2}$, density n_e, and electron anisotropy An_e in panel (**a**) and electron thermal Mach number $M_{e,\perp}$, index of electron demagnetization κ_e and electron agyrotropy $A\emptyset_e$ in panel (**b**) for diagnostic quantities across an asymmetric 2D simulation used for the identification of the resolved EDR in Scudder et al. (2012). Note (in panel **b**) that the $A\emptyset_e$ profile is asymmetrically situated relative to the mach number's indication of the maximum current layer. The anisotropy is on the lower density side of the EDR of the asymmetric layer and its size is anti-correlated with the decrease of $A\emptyset_e$ from its layer peak value. Figure adapted from reference Scudder et al. (2012)

As mentioned before the very low β_e on the magnetospheric side led to an expectation of very high electron pressure anisotropy (> 8), that was recorded by the Polar Hydra instrument, as was significant agyrotropy (> 1) and $M_e > 1.3$. In addition, significant electron heating was found in the reconnection layer. The high anisotropy seen in the simulation was used as an ordering parameter to shuffle the time appearance of the observations as a time series to become a spatially ordered portrait of the layer. This is reproduced in Fig. 2.13, showing the strong quantitative correspondence between the variables observed and expected in the simulation using the reordered data's traverse (Scudder et al. 2012). Particularly extraordinary were the high electron anisotropy$An_e > 7$, *electron* thermal mach number, $M_e > 1.3$, and agyrotropy $A\emptyset_e > 1.2$. These values are previously unheard of extremes for electrons sampled *in situ* in an astrophysical plasma, yet their sizes were corroborated by the PIC simulations. Prominent electron heating is also observed in this crossing, that is clearly different from the thermal state of the plasma on either side of the density transition.

2.7.4 Calibrating Λ_Φ in 2D

Since Λ_Φ is our only thresholded indicator of serious frozen flux violation in 3D, it is important to certify in controlled 2D simulations that the theoretically defined $\Lambda_\Phi > 1$ is properly calibrated so that $\Lambda_\Phi > 1$ and $\Lambda_\Phi < 1$ can be relied upon

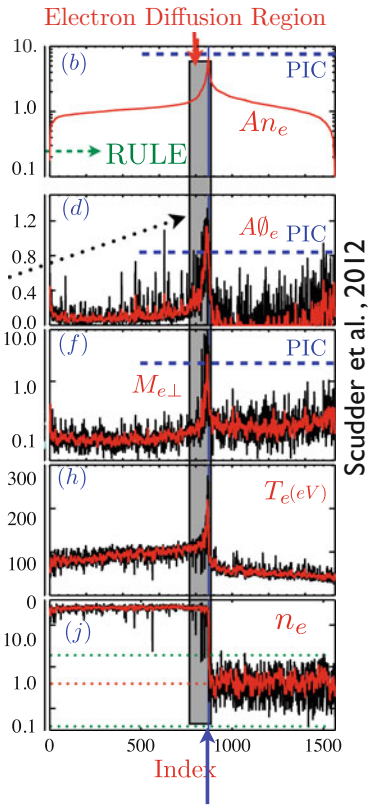

Fig. 2.13 First experimentally resolved electron diffusion region in space plasma that was located between vertical *black line* and vertical *blue line* (Scudder et al. 2012). The *black line* is the experimental location of the separator, the *blue* is the exit into the magnetized inflow region on the magnetospheric sensed by the abrupt decrease of the density indicated in panel (j) (Scudder et al. 2012). Peak PIC suggested values indicated by *dotted horizontal lines* in each panel. Mach number, anisotropy, $A\emptyset_e$, and strong electron heating in panels (f), (b), (d), and (h), respectively of the layer meet or exceed PIC levels expected. Figure adapted from Scudder et al. (2012)

to make the distinction between significant and innocuous frozen flux violations. So far this calibration has been done by comparing with the rates from the flux function, ν_Φ.

A 2D simulation was designed (Scudder et al. 2015a) to assure that our interpretation of Λ_Φ was calibrated, with 1 as the numerical value that signifies "significant frozen flux violation" as at a 2D saddle point which would be called the EDR. A 2D current sheet geometry was initialized with anti-parallel fields perpendicular to the x-y plane that contained all spatial variations; a sinuous, but narrow current interface possessing electron inertial scales separated the two regions of oppositely oriented fields. Had a third direction of variation been allowed this layer would have commenced reconnecting; by the dimensionality of the simulation reconnection was geometrically precluded. For this geometry the spatially varying exhaust arising out of a possible stagnation point would have had to flow along the out of plane (symmetry) direction where no gradients where allowed. The time dependence observed in the simulation was vigorous since the regime was Lower Hybrid Drift unstable. As shown in Fig. 2.14 the subsequent evolution included non-zero frozen flux violations with detectable enhanced variations of Λ_Φ centered on the current ribbon, very large $A\emptyset_e > 1$, and narrow, enhanced $\delta_e \simeq 1$ (not shown),

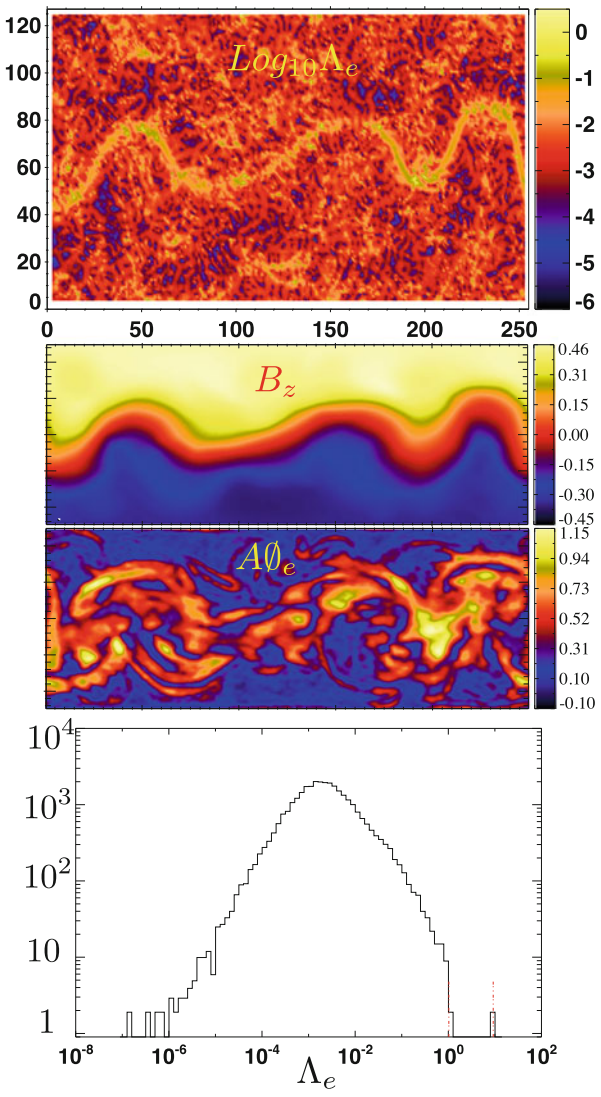

Fig. 2.14 LHDI simulation designed to test Λ_Φ interpretation (Scudder et al. 2015a). 2D simulation conducted in geometry where magnetic reconnection and "significant frozen flux violation" *cannot* occur. The output of the test is what values does the computation of Λ_Φ produce, summarized in histogram form in the *bottom panel*, and spatially in the *uppermost panel*. *Middle panels* show the variation of the component of **B** that would be the interconnecting component if the geometry would allow this process. Spatial variation of $A\emptyset_e$ demonstrates that prominent demagnetization occurs in the narrow channel. But $\Lambda_\Phi \leq 1$ for essentially all grid points, showing that the absence of $\Lambda_\Phi > 1$ is indeed consistent with this simulation where magnetic reconnection is geometrically prohibited. *Reproduced with permission for the November 2015 Phys. Plasmas, 22, 101204* (Scudder et al. 2015a)

confirming the electron inertial scales of the current channels. As shown in the bottom panel of Fig. 2.14 Λ_Φ was generally not zero, but its distribution from all 32,768 cells of the simulation terminated rather precisely at unity; *with only* 0.02 *% of cells indicating mild violations of this threshold*. Of these eight offending cells, only one had an adjacent cell in its eight surrounding cells that also exceeded unity. This lack of reenforcement suggests that this level of violation of the threshold could be viewed as noise in calculating Λ_Φ since the calculation is dependent on the *ratio* of two computed numbers in each cell that involve curls and gradients of curls.

From this test it is concluded that the $\Lambda_\Phi > 1$ threshold is a consistent approach to use when looking for "interesting" locations in 3D simulations, especially given its proofing (cf. Fig. 2.4) to locate saddle points in 2D simulations where reconnection was known to be underway. Below,in Sects. 2.8.1 and 2.8.2, we demonstrate *within* 3D simulations that Λ_Φ and Ψ_Φ are appropriately thresholded.

2.8 3D Reconnection: Exploring Reality

With the loss of the flux function in 3D, Λ_Φ becomes the major model independent tool when looking with computer simulations to identify frozen flux violations. Unfortunately direct measurements in space of Λ_Φ are impractical, even from a suite of spacecraft such as Cluster or Magnetospheric Multi-Scale (MMS). Above we have suggested an observational proxy that may fill this gap. However, for theoretically benchmarking thresholded diagnostics in 3D within PIC simulations Λ_Φ becomes our reference of choice; for the time being it assumes a similar theoretical importance for 3D that the flux function has for 2D modeling.

A recently discussed 3D PIC simulation with guide field equal to the asymptotic reconnection field strength that is asymmetric (Daughton et al. 2014) is used to further study the role of the proposed diagnostics and Λ for finding the interesting layers that could be detected by state of the art spacecraft instrumentation. This simulation was initialized as a Harris sheet and spans the intervals $35d_i \times 85d_i \times 85d_i$ in the x, y, z directions respectively; it used a mass ratio of 100 and was initialized with a profile invariant along the guide (z) field direction. The longer directions of the simulation were along the nominal exhaust (y) and guide field (z) directions with the narrower (x) dimension along the inflow. Higher values of x are initially at weaker density and stronger magnetic fields, providing asymmetric boundary conditions for the current channel formation that is much like what occurs at planetary magnetopauses.

The variation of the current density in the (x-y) inflow-outflow plane (half way along the guide field's z domain) is color coded in Fig. 2.15 at four different times in the evolution. Gross changes to the current density structure occur during this limited time. The superposed yellow contour boundaries were determined for each slice using detailed information in the PIC solution in the form of *tagged tracer electrons* followed during the simulation (Daughton et al. 2011, 2014). The mean value of the tracer tags of all the particles in a cell reflects the dominant origin of the particles, since the tracers from "outside" of the initial Harris sheet carry an immutable tag value of 1 or -1 depending on their initially being on one side or the other of the Harris current sheet. The yellow contours correspond to the mean value of this label being $\mathscr{F}_e = \pm 0.99$, effectively delineating (within the code) the evolution with time of where the "initial electrons on opposite sides" of the current sheet have come to be mixed as enabled by the magnetic reconnection occurring *somewhere* in the simulation, including the possibility that this mixing occurred at some other locale different from the cell possessing this average value. However,

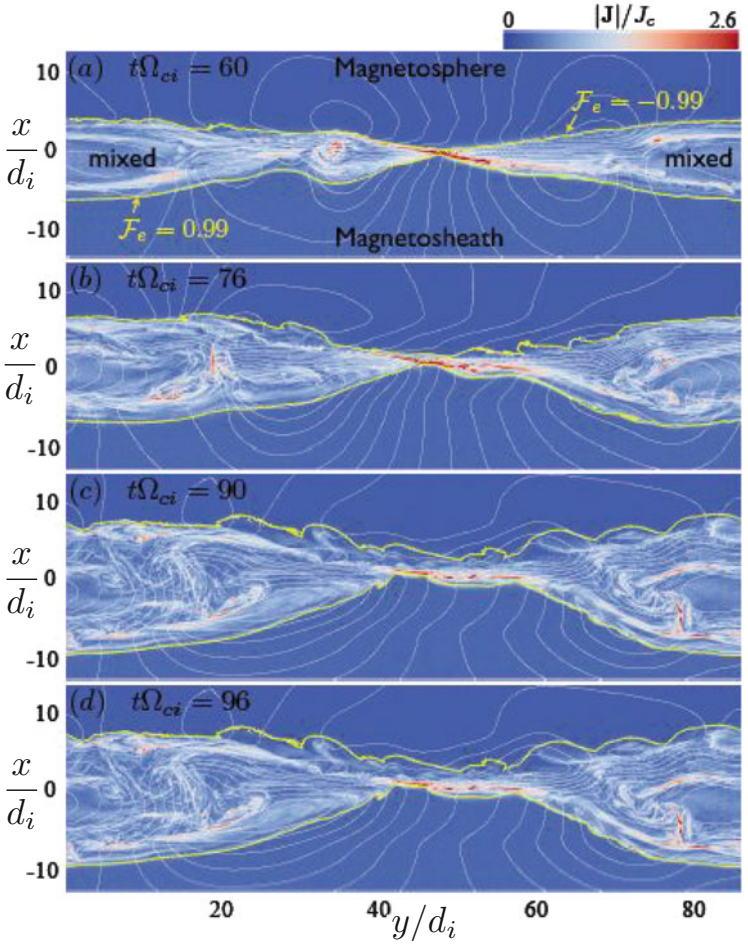

Fig. 2.15 Time evolution of |**J**| from 3D solution viewed in the inflow-outflow plane midway along the guide field direction at four indicated times (Daughton et al. 2014). *Yellow contours* delineate mixing boundaries determined from IC electrons tagged by their spatial positions at t = 0, cf. text discussion. While this boundary is *unobservable*, its determination within PIC does delineate the boundary between unconnected flux regions (*above* and *below* this curve) and interconnected flux tubes between the *yellow curves* where electron mixing is in evidence. In this sense these curves are analogous to the *unobservable* 2D separatrices and should be the boundaries between classes of observables, where interesting *observable* kinetic signatures might be expected. It should be noted that these yellow curves do not necessarily indicate mixing where the curves are seen, but that plasma on either side of these boundaries have been mixed "somewhere" prior to being seen where they are inventoried. *Reproduced with permission from May 2014 Phys. Physics of Plasmas,* ***21****, 052037. Copyright 2014, AIP Publishing LLC*

a mitigating factor is choosing the contour values with absolute value so close to unity, since at 0.99 this represents only a small admixture from the opposite side of the initial current sheet of 1 % of electrons in the cell; this makes such a location near to where mixing is first apparent. The smaller the value of $|\mathscr{F}_e|$ contours, the less direct is the inference of the possibility that such a contour is a site of *local* exchange between the two regimes; conversely small values of $|\mathscr{F}_e|$ indicate more extensive mixing of the initially segregated sides of the Harris current sheet.

Across the four time steps the regions of enhanced current density have evolved and the yellow hour-glass contours have widened perceptively with time, indicative of more integrated electron mobility over its past dynamics. This labeling has been quantitatively used (Daughton et al. 2014) to determine a fast reconnection rate for the simulation, further proofing its capability to differentiate unconnected flux (outside the yellow curves) from interconnected flux inside the hour glass. That calculation gave confidence for using the yellow curves as a separatrix in this 3D geometry, a property deduced in 2D from the flux function alone. Interestingly, in either geometry the separatrices, being topological, are not local observables.

For a given time step one should imagine determining the yellow contours on each 2D x-y plane of the 3D simulation. At the grid resolution the union of all such contours sweep out two surfaces, that crudely look like the two sheets of a hyperbolic cylinder, with its cylindrical axis generally along the guide field direction. The hyperbolic shape is generally correct in each plane along the guide direction, but the surface is more nuanced in the guide direction than found in a formal cylinder swept out by a hyperbolic cylinder of two sheets.

While tagged electrons are certainly *undetectable* in space, their delineation of the yellow "hyperbolic cylinder" in this study with the other results of this simulation can check the reliability of our approach: does $\Lambda_e > 1$ continue to work in 3D as the identifier of where significant frozen flux violations occur, and only inside these yellow boundaries as places? If it does, then finding observable corollaries with $\Lambda_e > 1$ in the code becomes increasingly viable as an observational strategy for identifying 3D reconnection sites in space *without* an *a priori* geometrical template of how it is actually organized (as is provided by the yellow boundaries and tracer tags, which are clearly artificial and not knowable from state of the art spacecraft measurements).

The discretized cylinder $|\mathscr{F}_e| = 0.99$ provides a generalized label for the "inside" versus the outside of the current channel "wedge" of the reconnection pattern. With time the current channel grows, filaments and becomes distorted, even in the plane presented in this picture. There is even evidence that there may be more than one intense current channels, aka "electron diffusion region(s)" present in the system. It is distinctly possible that unlike 2D the union of all sites that are reconnecting may neither be compact, interconnected, or organized in a planar arrangement predetermined by the geometry of the initial conditions. The detection of flux ropes in these 3D simulations (Daughton et al. 2011, 2014) that are forbidden in 2D makes it highly likely that the generalization of *the* EDR in actual 3D circumstances may not be a deformed, but still compact, geometrical version of

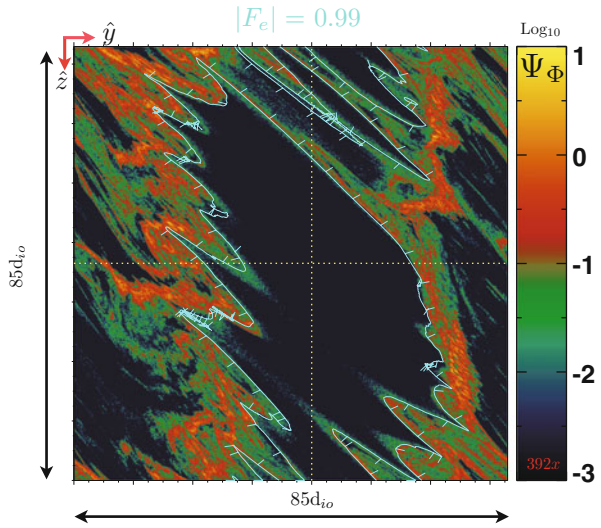

Fig. 2.16 Outflow-guide section of 3-D simulation contrasting *unobservable* level contours of $|\mathscr{F}_e| = 0.99$ (*cyan*) (determined within PIC by following individual macro-particles) with *observable* contours of Ψ_Φ, the proxy for "strong" local violations of frozen flux defined by Λ_Φ (Scudder et al. 2015b). Regions with $|\mathscr{F}_e| < 0.99$ are indicated by the downhill flags on the cyan contours. Consistency is shown in the plane along the guide field direction of Λ_Φ and Ψ_Φ being large only in the regions where $|\mathscr{F}_e| < 0.99$, even when this geometry is rather intricate. See text. From forthcoming paper Scudder et al. (2015b)

the EDR witnessed in 2D, but formed with disconnected sites in its proximity. We will show examples of this below.

2.8.1 Does $\Lambda_\Phi \simeq \Psi_\Phi$ Agree with $\mathscr{F}_e$ Boundaries?

Having traced the mixing of the macro particle electrons within PIC we can contrast the generalized cylinder boundary defined above by $|\mathscr{F}_e| = 0.99$ with the regions of the simulation where $\Lambda_\Phi > 1$ and $\Lambda_\Phi < 1$ which tests the conceptual importance of Λ_Φ for finding locales of different aggregate mixing in the simulation. Since $\Lambda_\Phi \simeq \Psi_\Phi$ the unobservable $|\mathscr{F}_e = 0.99|$ boundaries and the topology of Ψ_Φ are contrasted in Fig. 2.16. An outflow guide (y-z) cut of the simulation results for $\Psi(x_o, y, z)$ are color contoured, with superposed cyan isocontours of $|\mathscr{F}_e| = 0.99$. The plane of this section of the 3-D simulation is $4.4d_{io}$ behind the narrowest thinning of the generalized cylinder. This section of the cylinder defined by $|\mathscr{F}_e| = 0.99$ alternately cuts into the exhausts at either y extreme and is in the inflow regime near the middle of the y domain shown. The wrinkled 3-D nature of the cylindrical surface of mixing defined by $|\mathscr{F}_e| = 0.99$ implies a rather complicated system of cyan contour curves. On each contour the direction "downhill" (towards more mixing) is indicated by the

flags pointing locally perpendicular to the isocontour. Of particular importance is that downhill is the direction to "inside" the 3D wrinkled cylinder; inside according to $|\mathscr{F}_e|$ is the domain of electrons having been (locally or non-locally) mixed from their initial separated states of the Harris initial state of the simulation. Within such a mapped perimeter one should find those possible regions where $\Lambda_\Phi \simeq \Psi_\Phi$ should show up as enhanced. This figure shows that the colored *observable* contours of $Log_{10}\Psi_\Phi > 0$ respect the cyan pattern, with essentially no significant occurrence in the darkest "outside" regions of $|\mathscr{F}_e|$ and all the enhanced values of $\Psi_\Phi \geq 1$ inside the boundary painstakingly defined by following the tags of electron mixing. Further, the colored contours outside (in the inflow) are all weak, i.e. innocuous. It should be also noted that the Ψ_Φ also shows gradations of values with similar shapes as implied by $|\mathscr{F}_e|$ despite the two measures having no direct mathematical contact except through being diagnostics of the single vs aggregates of equations of motion followed by the PIC simulations. Many sections of the 3D simulation have been viewed by the authors in this way, showing the strong reproducibility of the domain of mixing $|\mathscr{F}_e| < 0.99$ (as here) of electrons using the *observable* proxy $\Psi_\Phi > 1$ as a marker for the same condition; conversely, "outside" regions invariably have values of $\Psi_\Phi < 1$. Note that innocuous frozen flux violations also can occur "inside" the mixing cylinder boundary where the frozen flux violations may be strong or innocuous.

2.8.2 Does $\Lambda_\Phi \simeq \Psi_\Phi$ Makes Sense in 3D?

To finish the validation of the concept of Λ we present statistical summaries over the entire 3D simulation frame of the correspondence permitted by comparing with painstaking maps made possible with $|\mathscr{F}_e|$. Using one time slice of the 3D simulation the probability distributions of thresholded frozen flux violations Λ_Φ are illustrated in Fig. 2.17; the red distribution for regions outside the yellow cylinder are more compact in extent than the distribution for the inner region (indicated in black). Using over one billion determinations the red distribution has $P(\Lambda_\Phi) > 1$ only 0.04 % of the time and a most probable value of $0.02 << 1$. The "inside" black distribution of $P(\Lambda_\Phi)$ has a higher mean value although it, too, is still less than unity. However, a significant fraction (1.8 %) of inside cells have $\Lambda_\Phi > 1$. Three points are important here: first, the fraction of outside points with $\Lambda_\Phi > 1$ is very nearly the same as the 0.02 % seen in the 2-D LHDI simulation where reconnection was geometrically prevented. Secondly, $\Lambda_\Phi > 1$ in the inside volume is still rare, occurring with a filling factor of 1:55. Thirdly, Λ_Φ is not a binary indicator, possessing plausible variations and *a continuum of values throughout the simulation* that are typically well below unity; this realization reenforces the need for a finite threshold value (like $\Lambda_\Phi > 1$ for "dynamically interesting frozen flux violations" for use when hunting for the electron diffusion region.

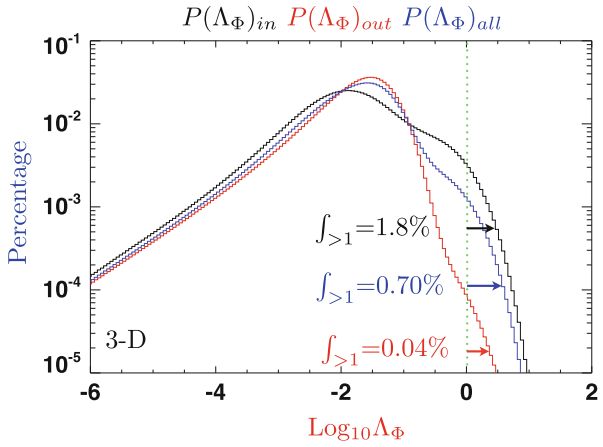

Fig. 2.17 Percentage Probability of occurrence of Λ_Φ segregated by cells outside (*red*), versus inside (*black*), the *yellow* "separatrix" boundaries of Fig. 2.15 (Scudder et al. 2015b). Inventory of the 1.1 billion cells showing the rareness of the condition $\Lambda_\Phi > 1$. A visual presentation of this scarcity in a given plane is presented in Figs. 2.15 and 2.18 below. This figure is from a forthcoming paper Scudder et al. (2015b)

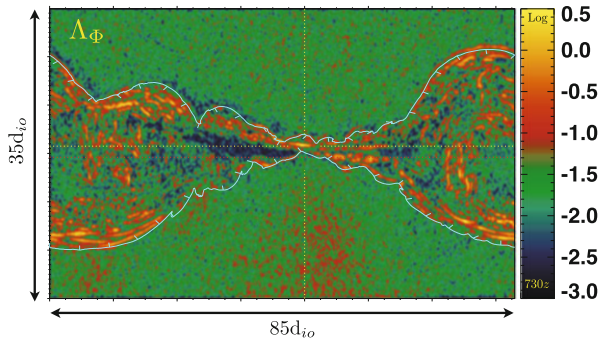

Fig. 2.18 Λ_Φ in section of 3D simulation (inflow-outflow plane) showing regions where $Log_{10}\Lambda_\Phi > 0$; $\Lambda_\Phi > 1$ indicative of a serious level of frozen flux violation as has been witnessed in 2D at saddle points of the flux function (Scudder et al. 2015b). These *bright yellow arcs* are generally in the regions of the hourglass boundaries (*light cyan curve*) of Fig. 2.15 and are candidate layers where reconnection could be identified. This figure is from a forthcoming paper Scudder et al. (2015b)

The inflow-outflow plane's spatial structure for $\Lambda_\Phi(x, y, z_o)$ (Fig. 2.18) illustrates new complexity in the 3-D inflow-outflow plane analogous to that mapped in the 2-D geometry of the bottom inset of Fig. 2.4. Not only are there locations of significant $\Lambda_\Phi > 1$ at the narrowest constriction of the $|\mathscr{F}_e|$ contours, there are many other locales where $\Lambda_\Phi > 1$ in other localized regions both along the separating cyan curves, but also well inside these curves. This contour section was made midway in the simulation volume along the guide axis. This figure also shows

the continuum character of this diagnostic; the "outside" region generally has *non-zero, but innocuous frozen flux slippage levels* with $\Lambda_\Phi < 1$; these regions have longer scales that those at a 2D electron diffusion region, but the scales in the inflow are not infinite, and the curl operation that analyzes the $\mathbf{R}_e(x, y, z)$ sense these finite scales. As in 2D the weak frozen flux violations that occur in these regions are not dynamically important. This is a clear situation where thresholded parameters are required to make decisions.

The inner region of the cylinder shows a higher *mean* value of Λ_Φ for at least two reasons: (1) as a confined region two of its scale lengths are shortened by being spatially confined between the yellow hyperbolas; (2) there are regions within the yellow cylinder (but not outside) where there are "significant frozen flux violations". The probability distribution above shows that in a given plane these violations appear sparse, yet they clearly occur in groupings near the cyan boundary and at places where O points would have occurred in 2D reconnection. [Topological work using this simulation has also identified a separator near the narrowest constriction of the $|\mathscr{F}_e|$ surface and O points inside the expanding wedge of the cylinder (Dorelli, 2014, private communication)]. In addition, there is a new population in the sample comprised of $\Lambda_\Phi > 1$ with values as high a 10–12 with a smooth probability up to those values. Note these regions also include the narrowed down region of the two hyperbolas, that would be the remnant of the initially loaded "separator" line. Statistically this argues that on average as few as 1.8 % of the cells in three dimensional "wedge" region between the yellow cylinder have strong frozen flux slippage. Clearly, there are smaller domains within the wedge where this fraction is significantly higher. Thus the average "filling factor" for $\Lambda_\Phi > 1$ is misleading.

Visually one can see in Fig. 2.18 that the brightest values of $Log\,\Lambda_\Phi > 0$, i.e. $\Lambda_\Phi > 1$, occur within a general hour glass shape, with a large number of order unity arcs found along, but inside, the hour glass shape, although not exclusively. These bright arcs are often in interrupted lanes *in this projection*, but their overarching property is that the frozen flux violation is extraordinarily high in these localized regions. These enhancements are reminiscent of Fig. 2.4 of the 2D guide situation, where enhancements of Λ_Φ are coherent and rising out of the background along (but inside of) the preferred guide separatrices (delineated by the flux function); however, along the mathematical separatrices in 2D we showed that Λ_Φ was still way below unity and strongly contrasted it with the central EDR region where the $\Lambda_\Phi > 1$, the flux function topology displayed the X point geometry, and guiding center parameters were all misordered. However, in 3D this morphology is different with enhancement of Λ_Φ just within the cyan mixing curves as large or higher as occurs at the nominal remnant of the initial Harris sheets separator line seen in this figure.

The lane structure of Λ_Φ *in this plane* is often comprised of curvilinear segments that are often not continuous. It should be kept in mind that any 2D contour presentation is of the signatures apparent in only this plane of the 3D solution. Any three dimensional structures, or curves, that are not parallel to the inflow-outflow plane (of this picture) can appear to start and stop where the otherwise continuous curves pass through the chosen plane for contouring. Further, a ribbon when piercing

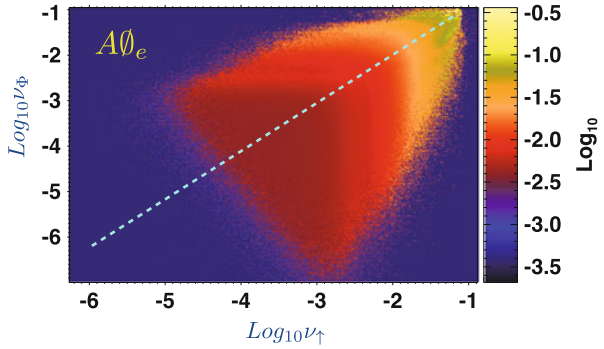

Fig. 2.19 Correlations of the *observable* $A\emptyset_e$ proxy for the *theoretically important, but unobservable* rates of frozen flux: ν_Φ and $\nu_\uparrow$ (Scudder et al. 2015b). Note the wide dynamic rate of frozen flux/line violations across the simulation. Sites of frozen flux/line violation *cannot* be defined in a yes–no binary way. Summary of 1.1 Billion cells in 3D simulation. From forthcoming article Scudder et al. (2015b)

the presentation plane could leave a curvilinear track that reflects more its angle of attack to the presentation plane than its true length. From this vantage point the possible patterns of Λ_Φ when contouring in the plane can have patterns that can generally include dots, line segments and even longer curves depending on this angle of inclination.

2.8.3 $A\emptyset_e$ Organizes ν_j in 3D

In the 2D geometry we have argued that Vasyliunas' insight led to suggesting that the rate of frozen flux violation $\nu_\Phi/\Omega_{ce} \simeq A\emptyset_e$. We argued that this same result remains in 3D, assuming that electron demagnetization is the common enabling concept in 2D and 3D. In this section we show that this relationship is maintained in 3D simulations. Figure 2.19 shows with over 1 billion readings in a 3D histogram that strong $A\emptyset_e$ organizes both strong line $\nu_\uparrow$ and flux ν_Φ violations. The graph illustrates with its color the mean value of $A\emptyset_e$ that occurred in the pixel with coordinates $[\nu_\uparrow, \nu_\Phi]$. Clearly there is general agreement that the rate of frozen flux and line violation increases with increased size of $A\emptyset_e$.

Figure 2.20 uses a two dimensional histogram of occurrence between ν_Φ and Υ to support the expected linear correlation based on arguments above. $[\nu_\Phi, \Omega_{ce}A\emptyset_e]$. For larger values the best fit power law for the suggested relation is 1.1. Given the curls of $\mathbf{R}_e$ involved in ν_Φ vs the local electron pressure tensor eigenvalue calculations for the agyrotropy, this is very good agreement. It should also be noted that ν_Φ is not an observable with the present state of the art space measurements, while the vertical axis involving $A\emptyset_e$ and Ω_{ce} is an observable

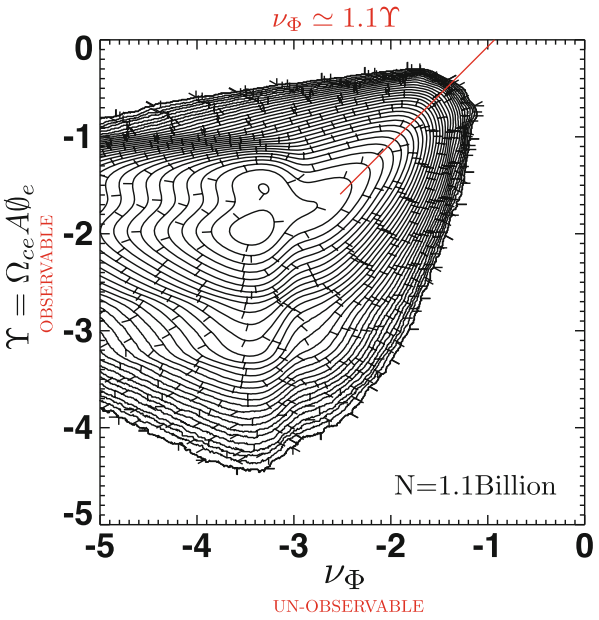

Fig. 2.20 Inventory from 1.1 billion pixels in 3D PIC showing $\nu_\Phi \sim A\emptyset_e$ as a correlation between an "unobservable" ∼ "proxy" appears reasonable, especially when the signals are strongest (Scudder et al. 2015b). *Red* segment shows correlation when signals are strong. From forthcoming article Scudder et al. (2015b)

We suggest that the variable combination Υ:

$$\Upsilon = \Omega_{ce} A\emptyset_e \simeq \nu_\Phi \tag{2.45}$$

produces an observable proxy for the theoretically important, but unobservable *unscaled* rate of frozen flux violation, ν_Φ. Figure 2.21 visually makes this point in two panels, with the top one from the 3D PIC variables giving a direct spatial portrait of $\nu_\Phi(x, y)$, while the bottom panel shows the suggested proxy using other PIC variables that are presently within the state of the art from space observations (such as on MMS). Close replication of details and structures are seen in observable proxy Υ that are seen in the theoretically more direct map from $\nu_\Phi(x, y)$.

2.8.4 $A\emptyset_e \propto \delta^{1\leftrightarrow 2}$ in 3D

While MacMahon suggested that the irreducibly tensorial parts of **P** should scale like δ^2, for weak δ, Fig. 2.22 shows (on either sides of the peak probability) suggestions of two red power laws, scaling as δ_e^2 for frequent, but smaller than peak amplitudes, to δ_e^1 scaling at higher than peak values. A similar trend is also seen in a large collection of estimates from data (Rodriguez et al. 2008; Lopez 2015) Thus the scaling reported in Fig. 2.20 of $\nu_\phi \propto \Upsilon_e^{1.1} \simeq A\emptyset_e^{1.1}$, at the largest values of ν_Φ takes precedence over the small amplitude expectation that $\nu_\Phi \propto \delta_e^2$.

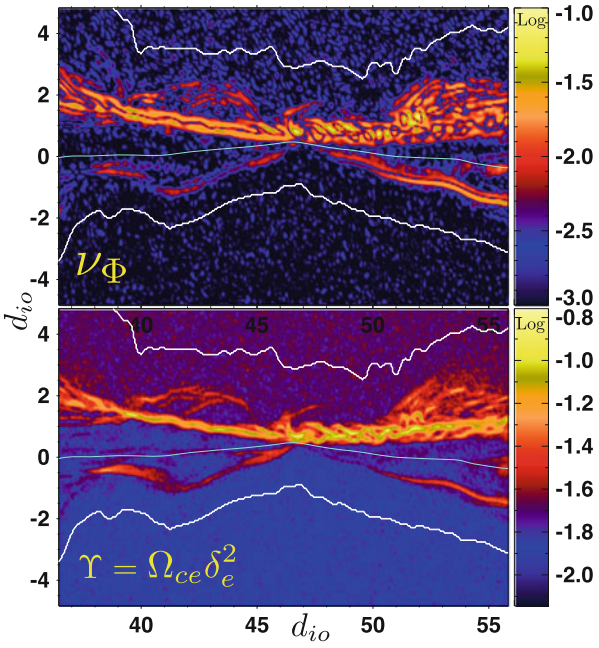

Fig. 2.21 *Top* Close up 2D section near separator of 3D simulation using ν_Φ determined from the $\nabla \times \mathbf{R}_e$ versus *Bottom* the Υ proxy for ν_Φ that is presently routinely observable; from forthcoming paper Scudder et al. (2015b)

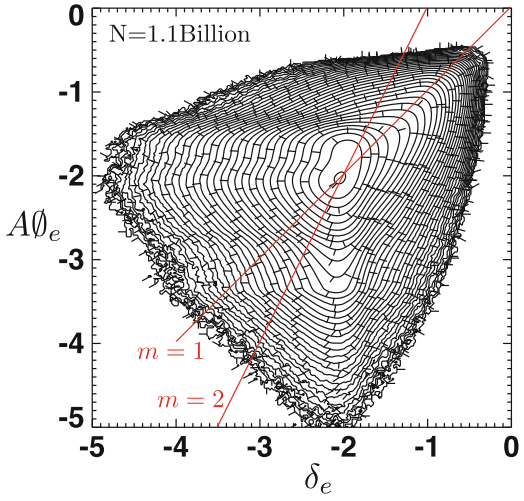

Fig. 2.22 Log–Log correlation of $A\emptyset_e$ scaling with δ_e makes transition from quadratic to linear dependence as δ_e increases (Scudder et al. 2015b). *Red lines* are power laws of index 2 and 1 through the peak of the occurrence distribution. Near and just below the occurrence peak the organization favors quadratic dependence as suggested by MacMahon, but for larger values than at the peak a clear break occurs toward $A\emptyset_e \simeq \delta_e$. From forthcoming paper Scudder et al. (2015b)

2.9 Reconnection Layers in 3D

The variation of the intensity within the 3D PIC solution where $0.001 < \Lambda_\Phi < 3$ is shown by the color contours in three orthogonal isometric sections in Fig. 2.23, with insets a–c corresponding to inflow-outflow, guide-outflow and guide-inflow sections, respectively. The sections are made along dotted lines indicated in their

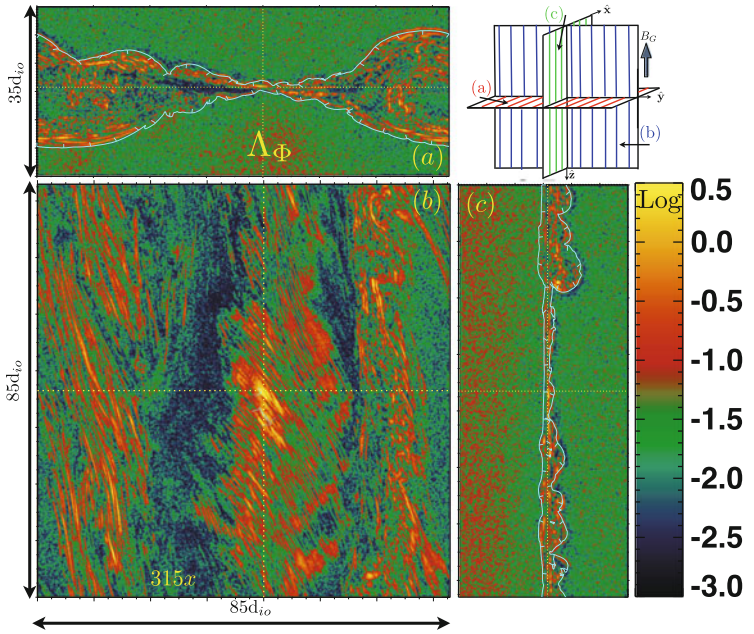

Fig. 2.23 3D Isometric, orthogonal sections of $Log_{10}\Lambda_\Phi$ passing near to the original Harris separator line (x = 315). Geometry of panels (a-c) as extracted from the 3-D simulation cube as indicated in the isometric inset. Note localized enhancement of $\Lambda_\Phi > 1$ shown most clearly in inset (**b**). Also clearly shown is the localization of this region in the guide direction and that the curve of maximum dissipation is inclined to the simulation coordinates. From forthcoming article Scudder et al. (2015b)

orthogonal insets. The contours are color coded according to the common logarithm and the striking variations of color indicate the significant range of variation of this index. Bright yellow regions indicate locales where $\Lambda_\Phi > 1$ and are candidate regions for being reconnection sites. Care should be exercised when interpreting the size of the reconnection layer until three orthogonal projections about a given locale is inventoried. The location of the $|\mathscr{F}_e| = 0.99$ boundaries were pierced by these planes are indicated by light cyan curves. The inset in the upper right hand corner shows the relation of the three sections of the solution shown in the three panels that surround it.

The upper rectangle (inset a) is the inflow-outflow variation as available from a 2D simulation, but here it is literally a horizontal slice of the 3D solution made perpendicular to the guide field direction, color coded by the variation of Λ_Φ. The square panel shows a planar cut that includes the outflow direction on the horizontal and the guide field direction on the vertical. The tall rectangular panel (c) under the inset represents a cross section whose horizontal axis is along the inflow (or thin dimension of the 3D rectangle) and the vertical along the guide field direction. All three sections are isometric sections so that squares in any view contain the same

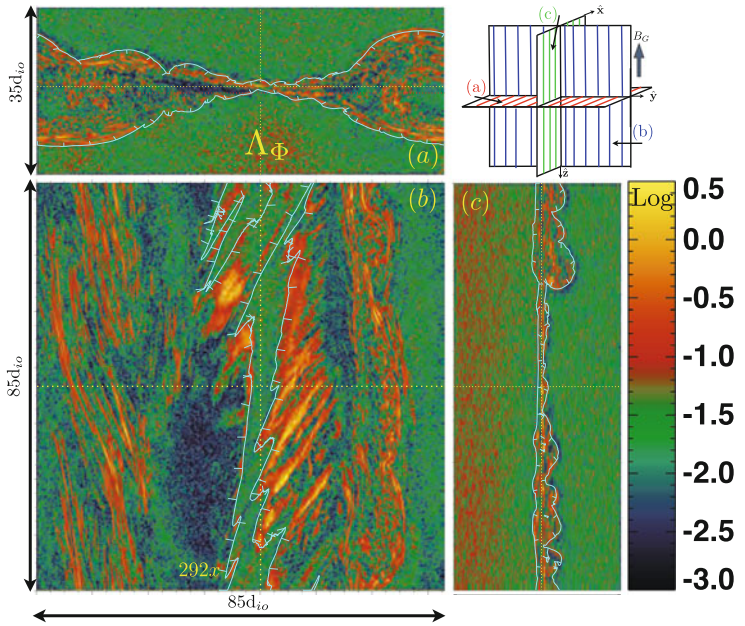

Fig. 2.24 3D Isometric, orthogonal sections of $Log_{10}\Lambda_\Phi$ along cut plane slightly displaced into the high density region, showing the banded enhancements of Λ_Φ on the mixing-separatrix surfaces being cut in both exhausts. Geometry of panels (a-c) as extracted from the 3-D simulation cube as indicated in the isometric inset. From forthcoming article Scudder et al. (2015b)

area. The outflow axes of these cuts is near to the initial separator of the Harris sheet and slightly displaced toward the low density side behind the separator of the Harris sheet.

From these three views we immediately see that the enhanced locations of Λ_Φ are largely near, (1) but inside, the quasi-cylindrical boundary mapped by particle tags indicated here by cyan curves where it cuts the planes of these sections where electrons show evidence of local or non-local mixing (during their prior history) with the outside regime; and (2) occur in a pattern across the rectangular section, with undulations that are organized in a chevron pattern at nearly 45° to the guide field direction. From the side view of the vertical rectangle the high Λ_Φ regions occur all up and down the guide field direction, but the width of the layers of significant frozen flux violation layer that are non-uniform along the guide direction, even showing locales of deep circulation into the low density side.

A 3D section slightly displaced towards the inflow region on the high density side (in front of the Harris separator) is shown in Fig. 2.24, that clearly shows the surface wave type undulations in Λ_Φ that occur generally on the cylindrical boundary determined by $|\mathscr{F}_e|$. Note that the chevron markings are inclined in the opposite direction in this view relative to that previously. The undulations are particularly pronounced on the low density side of the transition (larger x side of cylinder)

where they have been shown to be consistent with LHD waves. The striations in Λ_Φ that follow the ridge wave pattern suggest that large amplitude LHD waves in 3D can induce reconnection in periodic patterns as seen in the yellow regions of enhancements of Λ_Φ. This phenomena cannot happen in 2D simulations and may be the cause for spawning flux ropes that have been reported with this 3D simulation (Daughton et al. 2011, 2014).

In both of these 3D sectional views it is clear that many disjoint sites where reconnection is taking place must be considered. No simple model for the occurrence of the strong frozen flux sites can be anticipated with this level of dynamical freedom. Well inside the cylindrical mixing surface, there is evidence of multiple strands of strong frozen flux violations largely parallel to the guide field direction, but showing evidence of weak helical twists. These layers are in the general areas associated with the O lines identified previously (Dorelli, 2014, private communication).

Even within these exceptional sites of frozen flux violation, there are intensity variations of nearly an order of magnitude. These sections also reflect strands of high Λ_Φ that are rather narrow, but organized obliquely to the plane of these sections. Some evidence for this type of structuring can be seen in the chevron pattern in the square inset (b) of this figure.

A careful inspection of this figure reveals the significant number of sites where $\Lambda_\Phi > 1$ occur; these sites are clearly not localized at the initial separator of the initial conditions, although there is a clear spine of $\Lambda_\Phi > 1$ running down panel (b) that mimics the current patterns and is in the region identified with a separator in this solution (Dorelli, 2014, private communication).

2.9.1 3D Geometry of the Sites of Strong Frozen Flux Violation: Multiple Disjoint EDRs

In this section we examine the locales where $\Lambda_\Phi(\mathbf{X}) > 1$ occur in the simulation, using this scalar as a measure of the intensity of the serious frozen flux violation. It has proven useful to compute the polar angles Θ, Φ about a central point $\mathbf{X}_o$ of the code which we determine as the average of all pixels where $\Lambda_\Phi > 2$. We have chosen to divide the millions of these locales into four groups based on their minimum value of Λ_Φ successively exceeding $j = \{1, 2, 3, 4\}$ Fig. 2.25 depicts the location of the polar angles Φ_j, Θ_j painted with a color reflective of its j value, that in order are (1) gray, (2) cyan, (3) green and (4) red. These locales are painted onto the graph in numerical order so that the nesting of successively stronger regions can be seen. Together they give an overall impression of the ordered geometrical distribution of the sites of very strong frozen flux violations. The branch cut of the Φ_j is at 180°, so that in this coordinate system the nominal outflow jets have $\Phi_{exhaust} \sim \pm 90°$, while the inflow axes are along $\Phi_{inflow} \sim 0, 180 - \epsilon, -180 + \epsilon$, as angles measures in the x-y plane. Θ is the standard polar latitude angle from the $\hat{\mathbf{z}}$ direction of the code which is along the guide field direction.

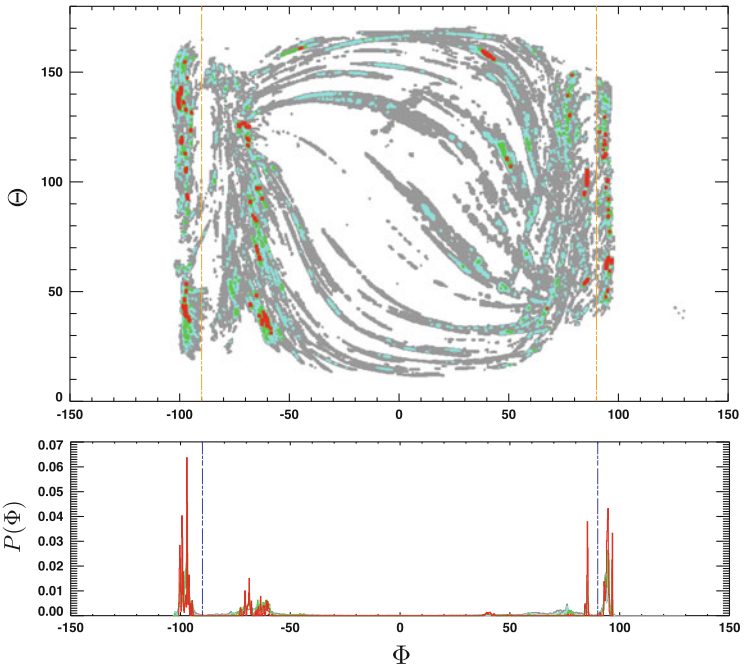

Fig. 2.25 *Top* Loci of polar angles of pixels (about center of pattern) where $\Lambda_\Phi > 1$ *grey*; > 2 *cyan*; > 3 *green*; > 4 *red*. Note predominance of strong signatures in four bands at nearly constant Φ values on either side of $\Phi = \pm 90°$ indicated by *vertical orange lines*. *Bottom* The identification of these four nearly straight *ridges* is facilitated by the probability distributions in Φ constructed by ignoring the Θ values of the pixels in the *top panel*. These ridges correspond to the inner and outer edges of the mixing regions that bound the general exhaust for the central reconnection layer. From forthcoming article Scudder et al. (2015b)

This figure shows that $\Lambda_\Phi > 1$ sites are highly structured in their polar angle locales. Even the weakest signatures (painted in grey) give evidence for lanes of enhanced frozen flux violation with rather intricate patterns. There are two classes of these structures: (i) those that occur with high probability in regions of approximately constant Φ about $\Phi = \pm 90°$, that correspond nicely with the flaring boundaries of the "mixing" boundaries used above to delineate inside and out of the current layer and (ii) a second group of traces/lanes that reach *between* the two disjoint areas of class (i). The lanes of class (ii) appear to radiate from and converge on "poles" with Φ_*, Θ_* coordinates of $(-70°, 125°)$ and $(75°, 50°)$. As the threshold get larger the regions become more compact, but the regions of highest Λ_Φ are increasingly concentrated in four layers of nearly constant Λ_Φ that correspond to half planes from $\mathbf{X}_o$ corresponding to the approximate asymptotes of the mixing boundaries seen in yellow curves in Fig. 2.15 The probability of occurrence of each group with phase angle Φ_j is shown in the bottom panel of this figure. The strongest $\Lambda_\Phi > 4$ grouping gives the sharpest probability profile that is nevertheless consistent with the probability constructed with a lower thresholds.

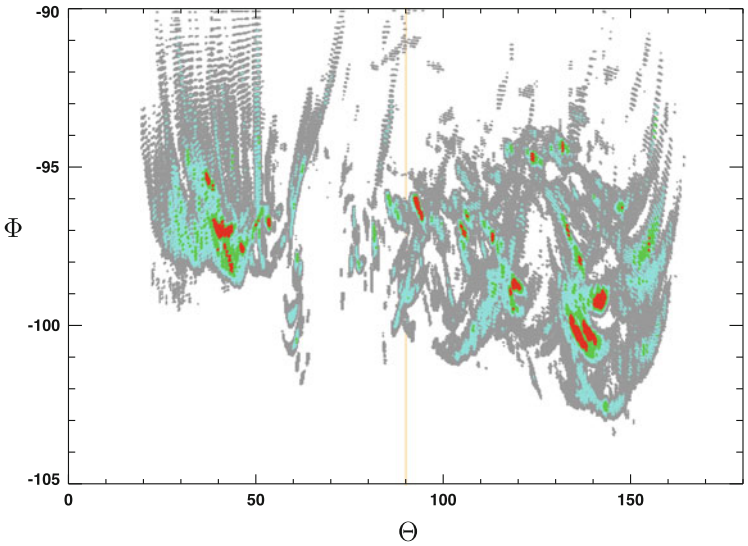

Fig. 2.26 Expanded view of contributions in narrow region of $\Phi < -100°$ for one mixing edge on the high density side of the layer to the *left of center*, showing the striations of occurrence as widely dispersed in Θ but very narrow in Φ. Ray patterns in *grey* suggest undulations/waves causing migration *above* and *below* $\Lambda_\Phi = 1$ thresholds. Rays appear to converge in angle to regions where $\Lambda_\Phi > 4$. There are clearly a large number of disjoint hot spots, *identified as candidate analogues of the EDR in 3D*. From forthcoming article Scudder et al. (2015b)

By focusing ones attention on one of these indicated azimuthal planes where there is high occurrence probability further insight can be achieved of the geometrical distribution of these large Λ_Φ sites. If $\Phi = \Phi_* \sim -100°$, then the selected points can be vernierly segregated in Φ in the vicinity of $-100°$ to show the angular structure and strands that will be suppressed below when trying to inventory the spatial distribution of these regions. Figure 2.26 depicts a high resolution slice of the $\Phi(\Theta)$ distribution found in the near vicinity of the $< \Phi < -100°$ region. This picture gives evidence for structures entering and leaving the region of $\Phi = -100°$ as would be expected with the curved mixing boundary shown above.

Given the thresholding used to make this picture one can see clearly periodic disturbances in Φ interrupted by white as would occur with a wave "train" whose Λ_Φ was oscillatory with peak amplitudes near $1 + \Delta$ where Δ is small. These "trains" have spatial widths of a few degrees in Θ, but can extend $10 - 20°$ in Φ before becoming lost in other signatures of a slightly different orientation.

Curiously, many of these "trains" appear to converge on even stronger Λ_Φ regions highlighted in cyan, green and even red. The closer these trains get to the red regions of intense Λ_Φ the less likely are distinct trains to be seen silhouetted on the white background, as if the $\Lambda_\Phi > 4$ regions were the spatial "source" for these trains? Certainly the most intense regions of $\Lambda_\Phi > 3$ are seen to be disjoint at this resolution. The red zones with $\Lambda > 4$ generally extend a few degrees in either polar

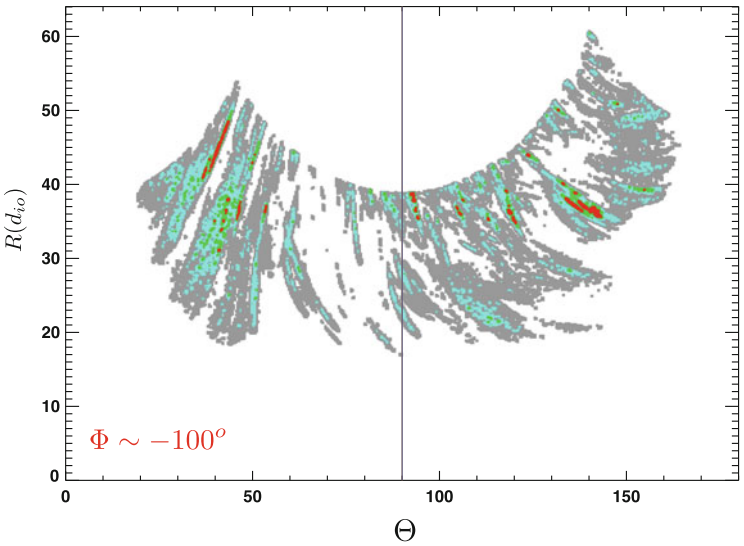

Fig. 2.27 This figure illustrates the latitudinal dependence of the radial distance $R(\Theta)$ for strong violations of frozen flux as color coded by the intensity of Λ_Φ. Multiple ribbons of enhanced violations are shown with typical lengths of $10 - 20d_{io}$. Orderly termination of arcs at maximum radius reflects the variation of the distance to the edge of the simulation box along different Θ values. Strongest violations of frozen flux (*red*) are well removed from simulation boundary. In this plane the location of the Λ_Φ violations range from $20 - 50d_{io}$ from the simulation center. From forthcoming article Scudder et al. (2015b)

angle and tend to be rather compact. In this single half plane there are over 15 such compact very intense frozen flux regions.

Suppressing the $\pm 6^\circ$ spread in Φ in Fig. 2.26 we construct a spatial portrait in Fig. 2.27 of these regions based on the radius, R, and elevation angle, Θ of the pixel. In this figure the horizontal axis is Θ and the vertical axis is the distance R in ion skin depth units from the assumed center of the 3D occurrence of these flux violations. The first impression with this format is that there are many ribbons $R(\Theta, \Phi_*)$ of *reconnection curves*, with lengths of order $5 - 20d_{io}$. In the longer arcs there is usually a $\Lambda_\Phi > 4$ region. The arcs are separated in angle by $> 10^\circ$, which at their distances from $\mathbf{X}_o$ imply spatial separations at times of order $5 - 15d_{io}$ apart.

The upper radial curvilinear boundary to these arcs is caused by the finite simulation box, and serves to show where the strongly enhanced regions of Λ_Φ occur; generally the ribbons and strings enhancements are well away from the simulation's boundary and generally more than $20d_{io}$ away from the center of the simulation rectangle$(35 \times 85 \times 85)d_{io}$. These layers primarily occur along the flaring portion of the "mixing" boundary and correspond to examples of enhanced lanes of $\Lambda_\Phi > 1$ seen in Fig. 2.18 just inside the cyan mixing boundary.

Given our demonstration in this chapter that $\Lambda_\Phi > 1$ is a well calibrated index of the saddle point region in 2D simulations, and correctly predicts LHDI models

are not reconnecting when they are geometrically prohibited to reconnect, and given the agreement between mixed and unmixed plasmas for predicting the incidence of strong frozen flux signatures, it would appear that *there is little room but to suggest that the ribbon like structures with $\Lambda_\Phi > 1$ reported in Figs. 2.25, 2.26, and 2.27 are the analogue in 3D of the EDR of 2D magnetic reconnection.* These structures appear to be present in rather large numbers in restricted regions of the current channel, be $10 - 20 d_{io}$ in length and be concentrated on the mixing boundary that has been previously identified (Daughton et al. 2011).

2.9.2 EDR Closeup

A close up of a strong Λ_Φ region near the narrowest constriction of the mixing boundary is shown in Fig. 2.28. The narrow feature depicted in the projected (a) plane is actually approximately $7 d_{io}$ in length, canted along the guide field direction with an angle similar to those seen in the chevron strips of Λ_Φ shown above. The layer remains thin in cross section in the dimensions transverse to this length. In 3D the signatures of diagnostics in a given plane can look sporadic *in that plane* even though the structures are elongated out of the chosen plane. One has the impression that much of the disjointed curvilinear segments of Λ_Φ seen in plane (a) section

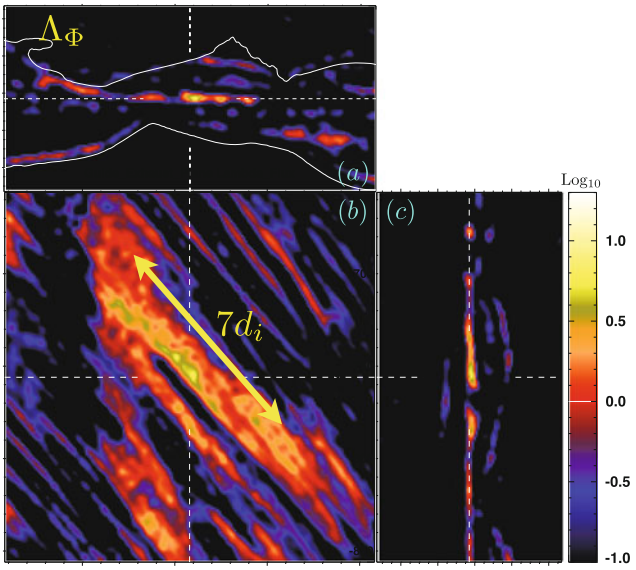

Fig. 2.28 Close up slightly behind separator site of reconnection: orthographic Λ_Φ. Linear dimensions of the square is $11.64 d_{io}$; thin dimension of *top* and *side* sections are $4.79 d_{io}$. Geometry of panels (a–c) as extracted from the 3-D simulation cube as indicated in the isometric inset. From forthcoming article Scudder et al. (2015b)

of the orthographic projections represent such projection effects of structures (as shown immediately above in Fig. 2.25, 2.26, and 2.27) that are smoother when seen in their "natural" geometry where the elongations are in some optimal plane.

2.9.3 *Hints at Local: Global Diagnostics in 3D*

The theoretical underpinnings of magnetic reconnection in 3D involves global properties that clearly challenge an inventory from spacecraft. However, our internal verifications have begun to show some correspondences between what *can* be sampled versus the global quantities that figure in the theory.

One idea is that *quasi-separatrix layers* are the generalization of the separator line which can be defined in 2D reconnection that emanates from the saddle point and is perpendicular to the two dimensional plane where variation is allowed. A property of these layers is that initially close magnetic lines that comprise these layers undergo rapid separation from one another in these locations. The implication is that the cross section of these tubes if they started as circles would become highly elliptical, that is "squashed" in the process (Demoulin et al. 1996; Titov et al. 2002). The measure of this squashing involves integrals (cf. Scudder et al. 2015b; Finn et la. 2014) along field lines over distances comparable to the simulation size, making this assay decidedly non-local and not directly accessible to even a flotilla of spacecraft making current state of the art measurements. In the top panel of Fig. 2.29 values

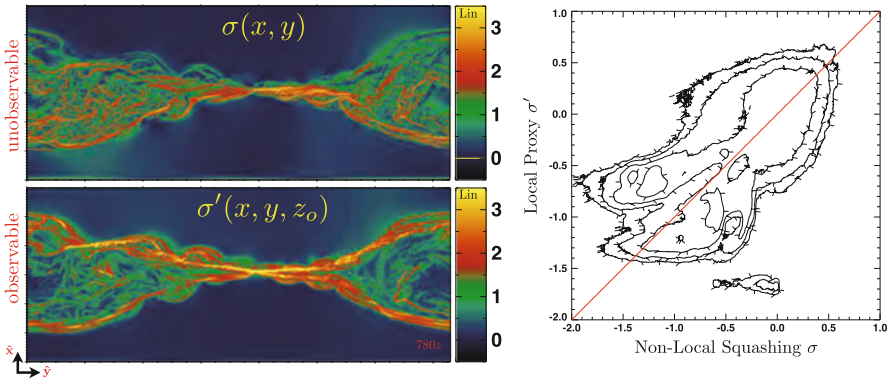

Fig. 2.29 *Top* Global PIC Squashing parameter σ, *Bottom* Local inference of squashing σ' that could be deduced by state of the art spacecraft instrumentation and using a local Harris sheet model to estimate the non-local effects (Private Communication William Daughton, 2015; Scudder et al. 2015b). *Color contours* are shown with linear scales. Some apparent differences on linear scale are present. (*Right*) inset shows the correlations between unobservable global index and local proxy: $[Log_{10}\sigma, Log_{10}\sigma']$, showing their correlation with one another. Note the wide dynamic range of this correlation on Log_{10} graph deemphasizes the color distinctions that appear in the contour comparison using linear scale. From forthcoming article Scudder et al. (2015b)

for the squashing parameter $\sigma(x, y)$ *determined from the full 3D variation of the PIC code* are shown (Daughton, private communication, 2014), while the bottom panel illustrates the proxy value $\sigma'(x, y)$ determined locally using the properties of a *local Harris sheet* model to estimate what value might be expected there. This approach requires use of δ_e summarized above as well as making local determination of normal and guide field geometry along the space track. This figure shows there is a coarse correspondence between the actual line integrals performed within the PIC and local approximations to the squashing factor. The principal assumption of this approach is that the local Harris characterization of the magnetic field at the observer is the dominant determinant of the squashing factor. Other global local connections have been identified (Scudder et al. 2015b).

2.10 Big Picture About Finding Site(s) of Magnetic Reconnection

Our approach to finding reconnection sites with such elusive properties is a form of using sieves of increasing fineness to find documentable sites where collisionless magnetic reconnection is underway. A measure of the fineness of the sieve is how many unwanted objects pass the sieve including your objective. In Fig. 2.1 many structures pass these sieves that are not reconnection sites, but just structure that pass a mass flux—which a reconnection layer does also. Ideally the electron diffusion region would be identified based on there is "no other interpretation" possible for the data.

We have argued in this chapter that electron demagnetization is sufficiently rare in the domain of sampled astrophysical plasmas, that it should be used as a necessary sieve in such identifications *after* the same sieve on almost all other plasmas has determined negligible levels of demagnetization. We have also argued that another macroscopic sieve would involve detecting electron thermal mach number $M_e \simeq 1$; such mach numbers are totally unknown in space plasmas except as theoretically expected in reconnection. Figure 2.1 shows that there are many objects beyond layers thought to be involved in reconnection that pass the sieve represented by these tests. The status quo approach can be markedly improved with these new electron specific sieves. Figure 2.30 gives an overview of the relationships of these sieves, with the coarser jump conditions of Fig. 2.1 well removed from identifying the EDR and with more surgical sieves involving electron kinetic properties as one gets closer to clear identifications. At present the sieves discussed in this chapter are technically possible and would appear to be an exceedingly attractive way to reap the investments of so many research dollars represented by the Magnetospheric Multiscale Mission which seeks to critique experimentally how collisionless magnetic reconnection "really works" in nature.

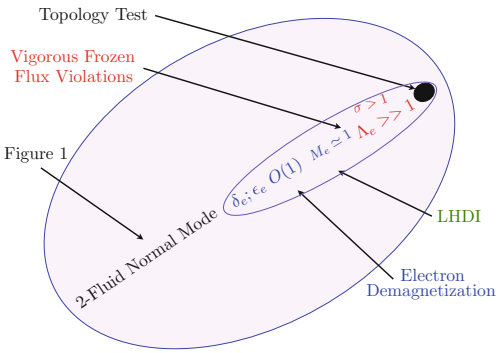

Fig. 2.30 The telescope of scales involved in finding layers certifiably involved in collisionless magnetic reconnection (Scudder 2015). Outside the frame of this figure are 1 fluid jump conditions as summarized in Fig. 2.1 of this chapter. Proximity to the EDR in this figure requires tests of increasing sophistication beyond Hall signatures that are commonplace two fluid features. Careful assays will require electron specific properties certified by the electrons in the plasma. Without evidence to show that the measured thermal electrons are demagnetized, there will be no convincing evidence that the innermost expected current layer of magnetic reconnection has been traversed. From forthcoming article Scudder (2015)

Appendix 1: Role of $R_{ez} \neq 0$ in 2D Flux Slippage

The electric field in terms of the potentials takes the form

$$\mathbf{E} = -\nabla\phi - \frac{1}{c}\frac{\partial \mathbf{A}}{\partial t}. \tag{2.46}$$

For the observer moving with the electrons, the partial derivative becomes an advective derivative and **E** transforms via Galilean relativity while the scalar potential is not modified yielding

$$\frac{d\mathbf{A}}{dt}\Big|_{\mathbf{U}_e} = -c\Big(\mathbf{R}_e + \nabla\phi\Big). \tag{2.47}$$

Since the gradient only has components in the (x-y) plane of the 2D simulation, the total time evolution of A_z is determined by the z component *alone* of the non-ideal electric field:

$$\frac{dA_z}{dt}\Big|_{\mathbf{U}_e} = -c\mathbf{R}_{e,z}. \tag{2.48}$$

Since the components of **B** in the x-y plane set the reconnection topology, and $B_x = \frac{\partial A_z}{\partial y}$ and $B_y = -\frac{\partial A_z}{\partial x}$, the time evolution in 2D of the reconnection topology is controlled only by the non-zero "out of plane component" of the violation of Alfven's "frozen in" condition. While a parallel electric field generally makes

$\mathbf{R}_e \neq 0$, unless $E_\parallel \hat{\mathbf{b}} \cdot \hat{\mathbf{z}} \neq 0$ its violation of Alfvén 's frozen in condition does not affect the slippage of flux in 2D.

A side benefit of the existence of the vector potential is that the isocontours of $A_z(x, y)$ have local normals given by $\mathbf{n} \propto (\frac{\partial A_z}{\partial x}, \frac{\partial A_z}{\partial y})$. Such normals are always perpendicular to the components of $\mathbf{B}$ in the x, y plane, since $\mathbf{n} \cdot \mathbf{B} \equiv 0$ everywhere in the x-y plane. Accordingly contours of A_z provide a simple way for exhibiting the topology of magnetic field lines, without having to integrate the three differential equations for field lines to find out where they go. In 3D the answer to such questions cannot be provided in this way since there is no flux function available.

Appendix 2: The Origin of Two Scales About the Reconnection Site

The mass asymmetry in a hydrogen plasma shows that the electron momentum equation is a natural way to discuss the factors that control the electric field and gives its physics to the Generalized Ohm's law. For those who have learned MHD as a one fluid description of magnetized plasmas, there is a path to seeing that nothing has been lost developing our picture of the current channel with electron myopia. In the so called one fluid picture that underlies MHD the scales of the system are long, the currents are weak, so that it is actually true that $\mathbf{U}_e \simeq \mathbf{U}_i \simeq \mathbf{U}$ where

$$\mathbf{U} \equiv \frac{n_e m \mathbf{U}_e + n_i M \mathbf{U}_i}{n_e m + n_i M} \simeq \mathbf{U}_i. \tag{2.49}$$

In this context Alfvén's ideal approximation shows up in the literature as the assertion that the magnetic fields is displaced by where the Center Of Mass (COM) go, which in this approximation is the same as where the ions or electrons go! This physics is often summarized that the field moves with the ions since they essentially determine the COM. However, as the scales being explored are no longer infinite, gradients and current densities occur and are supported by relative motion between electrons and ions $\mathbf{J} = en_e(\mathbf{U}_i - \mathbf{U}_e)$ and MHD is exported into regions where the density becomes lower and the binary rate ν_{ei} for binary collisions also drops. The plasma still has many other scales regulated by the density and the magnetic field strength that keep the system well organized, especially the gyro scales at right angles to the magnetic field. The time periodicity caused by gyrating about the magnetic field permits certain adiabatic concepts like μ conservation and Guiding Center Drifts to be useful in the description of the medium. The decreased collision rate allows the electrons and ions to become uncoupled thermally, promoting the idea that perhaps it is attractive to forego the single fluid concept because there are no longer thermally exchanging internal energy efficiently by copious collisions. If the ions become demagnetized $\rho_i/L \geq 1$ the currents that they might represent can generate emf's of the Hall variety, that show up in the one fluid's variant of

the Generalized Ohm's Law as $\mathbf{J} \times \mathbf{B}$ forces, that have come to be known as Hall emf's. Hall emf's always occur in the one fluid extended MHD picture when the underlying physics has become two fluid in character.

A similar situation occurs when describing a shock wave: the momentum laden ions hurtle across the shock layer, while the agile electrons do an intricate detour along the shock surface until they cross the shock layer at a different location than the ions did. In a very real way the magnetized electron's agile side step carried the magnetic field along the surface of the shock and delivered it into the magnetosheath some distance from where the demagnetized solar wind ion had pierced the shock. The relatively abrupt, but magnetized motion of the electrons allowed them to label and advect the magnetic field through the shock layer, while the protons, with convected gyro radii thicker than the shock ramp, became demagnetized there, lost there hold on their solar wind field line and propagate downstream in the magnetosheath gyrating about another magnetic field line. Because the ion gyro radius is larger than the electrons, it loses its ability to follow changes in direction of $\mathbf{B}$ more readily than do the electrons. Central to the idea of particles labeling or advecting a field line is that the species can "hold on to", gyrate about, and label the line in question. Clearly ions have more trouble with this than electrons. The earth's bow shock layer is a large amplitude standing whistler wave, a high frequency extension off of the Alfvén wave dispersion branch with wavelengths intermediate between $\rho_e < \lambda < \rho_i$. A whistler is a collective mode (wave) in the magnetized plasma that owes its existence to the distinctly different mobility of the electrons at frequencies approaching the electron cyclotron frequency, which is well above the traditional regime for ideal MHD. It is an example of plasma behavior enabled in the two fluid regime.

However, all is not as nice as it was with large scale one fluid MHD with strong collisions. What happens along field lines with gradients of finite scale? What happens to Alfvén's picture of the magnetic field frozen into the motion of the plasma when the plasma decides to have a split personality with electrons writhing to a different drummer than the ions? There was a degenerate situation for Alfvén's ideal MHD, with three fluid velocities essentially the same because he surmised very weak gradients, very weak current and very low frequencies for such a theory, making the electrodynamics and the mathematics very simple. In fact Alfvén could have announced his frozen flux theorem for ideal MHD by remarking that the electron, or ion or fictional center of mass (COM) fluid carried the magnetic field—since in his postulated regime there was essentially no difference between the three possible fluids. But as the frequencies go up and the scale lengths become *finite* it is no longer true that the preservation of flux is equally true for the observers at rest in the COM frame, the ion frame and the electron. Can the concept of frozen flux persist in the two fluid domain?

The derivation of Eq. (2.6) shows it can be retained until circumstances that cause $\nabla \times \mathbf{R}_e \neq 0$ to occur, at which point the electron flow can no longer presage where magnetic field lines go.

If the same type of derivation were done with the ion momentum equation a similar equation, of equal truthfulness, would be

$$\frac{D\mathbf{B}}{Dt}|_{\mathbf{U}_i} = -c\nabla \times \mathbf{R}_i, \tag{2.50}$$

where the ion's non-ideal electric field is given by

$$\mathbf{R}_i = \frac{\nabla \cdot \mathbf{P}_i + \nabla \cdot (n_i M \mathbf{U}_i \mathbf{U}_i) + \frac{\partial n_i M \mathbf{U}_i}{\partial t}}{en_i}. \tag{2.51}$$

By inspection $\mathbf{R}_i$ can have scales as short as the ion gyro and inertial lengths, ρ_i and d_i. At the shock when the shock layer is thinner than the convected ion inertial length $L = U/\Omega_{ci}$ there will be non-zero contributions from all of these ion terms. Certainly the ion pressure tensor is non-gyrotropic on this scale through the layer, and *Eq. (2.50) correctly indicates that the magnetic flux will no longer be viewed by the ion rest frame observer as being conserved.* At the same place the electrons remain magnetized, its dynamic term is quadratically smaller by M_e^2, and the electron rest observer confidently assays that magnetic flux is being conserved and not slipping in his frame!

While either ion or electron observer's description *of their perception* is technically "correct", the electron observer's description can perceive conservation of magnetic flux down to shorter scales than the ion observer and thus over a wider range of scales of change, essentially because $d_e = d_i/42.84$. Thus the electron observer's decision of frozen flux violation is in some sense the last word because there is no lighter species able to more agilely follow the contortions of **B**. Fortunately, the physicist can pick which frame gives the most information.

A similar situation happens for the plasma as it approaches a reconnection current sheet. Far away from the layer (like electrons and protons in the solar wind way in front of the shock) both species agree the magnetic flux is frozen in their respective frames. However as the plasma approaches the current channel the larger ion gyro radii "feel" the upcoming gradients earlier than the electrons and their $\mathbf{R}_i$ becomes structured with ion gyro scale and inertial scale length structures, that cause the flux to appear to be slipping in the ion frame of reference. Meanwhile the electrons, still well removed in units of *their* inertial scales from the current sheet, experience weak gradients with $\rho_e/L << 1$ so that they remain magnetized and are able to label and advect the magnetic field and deduce that the magnetic flux is essentially frozen in the electron rest frame until coming within several electron gyro radii of the reconnection channel. This is the physical reason for expecting a two zone layer upon approaching the reconnection current sheet.

Confusingly for students this outer layer, where the ions see the magnetic field as slipping with respect to U_i, is referred to as the *ion diffusion region*. The confusion is that according to the electron rest frame observer throughout this outer region, the magnetic field remains totally frozen to the electron bulk motion. None of the mysterious processes that cloud how reconnection happens takes place in this ion

layer, despite some who title papers about this region as about the "diffusion region", leaving the adjective "ion" out of the title. In this sense there is no intrinsic loss of field line identity taking place in this outer, ion layer.

That the ion rest observer makes such a statement says more about his glasses than what is happening! *It is a two fluid regime.* However, this ion inertial layer is a place where ions are making adjustments that electrons are not making. The ions are starting to deflect up and around the obstacle, while the electron are undeterred. This differential response represents a current that implies a $\mathbf{J} \times \mathbf{B}$ Hall electric field is seen by the ion rest frame and COM observers. In this regime pressure gradients of ions and electrons start to form. The electrons remain magnetized as they ExB and diamagnetic drift, and as they do they carry the magnetic field with it, creating the "Hall magnetic patterns" foreseen in theory (Sonnerup 1979) and found in superposed epoch modeling with spacecraft data (Eastwood et al. 2007).

It is only within the electron inertial scaled innermost region of the current channel that the electron rest frame observer detects intense frozen flux slippage; here magnetic reconnection will take place. If anywhere this is the collisionless "diffusion" region. It is increasingly common to see this inner region termed the *electron diffusion region (EDR)*, with the "electron adjective" retained. Although historically in resistive MHD this was a diffusive layer and the solution of a diffusion equation, there is no guarantee from the Generalized Ohm's law that this inner "electron diffusion region" will have profiles that mathematically satisfy parabolic diffusion equations.

This discussion has an experimental corollary relevant for those who would document the behavior of collisionless magnetic reconnection in nature: the phenomenology of the outer ion scale that is called the ion diffusion region is rather common in nature, occurring whenever two fluid behavior is allowed or required. It may be necessary for collisionless reconnection, but the detection of Hall signatures by themselves is exceedingly common. The Hall effects restate that two fluid effects are "in play" in the plasma. In fact, nearly any current system that is identified in space will have such Hall effects attending their occurrence. The behavior of the electrons and ions within shock waves hinge on this differential behavior. The current that flows is caused by the different paths of the ions and electrons as they cross the shock. The out of plane Hall magnetic signature in the reconnection context, is also a well documented feature of the shock layer, representing an out of the coplanarity perturbation (Goodrich and Scudder 1984).

Appendix 3: Traditional Techniques for Measuring Lengths in Space Plasmas

Even the most basic conversion of a time interval Δt on a given spacecraft to a length $|\Delta \mathbf{x}|$ traversed along the normal to the structure,

$$\Delta x = \Delta t \hat{\mathbf{n}} \cdot \mathbf{W}_{rel}, \tag{2.52}$$

involves two unknown *vectors*: $\mathbf{W}_{rel}$, the relative velocity of the s/c sensor to the layer, and $\hat{\mathbf{n}}$, the local normal to the surface whose thickness Δx is desired. (Both vectors are required to be known in a common coordinate system.) Alternately, consider two spacecraft, sampling the "transition" at times t_1 and t_2 separated by a known vectorial distance $\Delta\mathbf{X} = \mathbf{X}(t_1) - \mathbf{X}(t_2)$. By cross correlation the times of the "same" structure may be found t_1, t_2, allowing $\Delta\mathbf{x} = \hat{\mathbf{n}} \cdot \Delta\mathbf{X}$. Such a determination still requires an experimental determination of the surface normal and that the front being encountered is without *spatial* variation direction transverse to the determined normal to the surface; also hidden in this approach is the assumption that the structures are not evolving in time between t_1, t_2 and do not have some wave numbers that support the structure possessing more time independent than others! The final painful fact is that the scales expected are short, with $\rho_e \simeq 1\,km$ at the forward magnetopause. To forestall time evolution between observations, the spacecraft must be rather closely collocated, which they might not be for key signatures that require geometrical characterization. With relative motions of order the Alfvén speed likely, the *time resolution for either of these approaches must be much better than 20 ms* and external knowledge of the surface normal and its local planarity are required to get a well constrained determination. The approaches using Eq. (2.19) offer a much more direct approach for obtaining scale information that only involve scalars.

Acknowledgements This paper summarizes work made possible from a fruitful collaboration over many years with William Daughton, Homa Karimabadi and Vadim Roytershteyn. We gratefully acknowledge NSF Grant No. ATM 1153817, NASA NNX 13AG08G at Iowa, and NASA Heliophysics Theory Program at LANL and SciberQuest. NSF has supported our calculations at Ranger and Kraken and NASA has supported this work through the High-End Computing (HEC) Program through the NASA Advanced Supercomputing (NAS) Division at Ames Research Center. We thank Walter Gonzalez for organizing the symposium celebrating Eugene Parker's contributions to the Physics of Magnetic Reconnection, held at São José dos Campos, Brazil, in March 2014. We also celebrate Gene Parker's contributions in many other areas including mentoring D.A. Tidman as a post-doc who became one of our thesis advisors and Gene's collegial interactions during his long career with our other teachers: B. Coppi, S. Olbert, L. Burlaga and D. Papadopoulis. Editorial comments from SED and computer support from R. Holdaway at University of Iowa are also acknowledged.

References

N. Aunai, M. Hesse, M. Kuznetsova, Phys. Plasma **20** (2013). doi:10.1063/1.4820953
J. Birn, E. Priest, *Reconnection of Magnetic Fields* (Cambridge University Press, Cambridge, 2000)
S.I. Braginskii, *Advance of Plasma Physics*, vol. I (Academic, New York, 1965), pp. 1–97
L.F. Burlaga, *Interplanetary Magnetohydrodynamics* (Oxford University Press, New York, 1995)
L.F. Burlaga, J.L. Lemaire, J. Geophys. Res. **83**, 5157 (1978)
W. Daughton, J. Scudder, H. Karimabadi, Phys. Plasma **13**, 072101 (2006)
W. Daughton, V. Roytershteyn, H. Karimabadi, L. Yin, B.J. Albright, B. Bergen, K.J. Bowers, Nat. Phys. **7**, 539D (2011)

W. Daughton, T.K.M. Nakamura, H. Karimabadi, V. Roytershteyn, B. Loring, Phys. Plasma **21**, 052307 (2014)
P. Demoulin, J.C. Henoux, E.R. Priest, C.H. Mandrini, Astrophysics **308**, 643 (1996)
M.W. Dunlop, A. Balogh, Ann. Geophys. **23**, 901 (2005)
J.P. Eastwood, T.-D. Phan, F.S. Mozer, M.A. Shay, M. Fujimoto, A. Retino, M. Hesse, A. Balough, E.A. Lucek, I. Dandouras, J. Geophys. Res. **112**, A06235 (2007)
J. Egedal, W. Daughton, A. Le, Nat. Phys. **8**, 321–324 (2012). doi:10.1038/nphys2249
J.M. Finn, Z. Billey, W. Daughton, E. Zweibel, Plasma Phys. Controlled Fusion **56**, 064013 (2014)
C.C. Goodrich, J.D. Scudder, J. Geophys. Res. **89**, 6654 (1984)
R.D. Hazeltine, F. Waelbroeck, *The Framework of Plasma Physics* (Perseus, Reading, MA, 1999)
M. Hesse, K. Schindler, J. Birn, M. Kuznetsova, Phys. Plasmas **6**, 1781 (1999); P. Pritchett, J. Geophys. Res. **106**, 3783 (2001); M. Hesse, M. Kuznetsova, J. Birn, Phys. Plasmas **11**, 5387 (2004); P. Ricci, J.U. Brackbill, W. Daughton, G. Lapenta, Phys. Plasmas **11**, 4102 (2004); W. Daughton, J.D. Scudder, H. Karimabadi, Phys. Plasmas **13**, 072101 (2006); L. Yin, W. Daughton, H. Karimabadi, B.J. Albright, K.J. Bowers, J. Margulies, Phys. Rev. Lett. **101**, 125001 (2008)
M. Hesse, T. Forbes, J. Birn, Astrophys. J. **631**, 1227H (2005)
H. Karimabadi, W. Daughton, J.D. Scudder, Geophys. Res. Lett. **34**, L13104 (2007)
A. Le, J. Egedal, W. Daughton, W. Fox, N. Katz, Phys. Rev. Lett. **102**, 85001 (2009)
J.Y. Lopez, Ph.D. Thesis, University of Iowa, 2015
A. MacMahon, Phys. Fluids **8**(10), 1840 (1965)
F.S. Mozer, J. Geophys. Res. **110**, A12 (2005)
T.G. Northrop, *Adiabatic Motion of Charged Particles* (Wiley, New York, 1963)
E.N. Parker, Phys. Rev. **107**, 924 (1957)
G. Paschmann, P.W. Daley, *Analysis Methods for Multi-Spacecraft Data*, ISSI, **SR-001** (1998)
E. Priest, Chapter 3 in *Magnetic Reconnection: Concepts and Applications*, ed. by W.D. Gonzalez, E.N. Parker (Springer, Berlin, 2016)
E. Priest, T. Forbes, *Magnetic Reconnection* (Cambridge University Press, Cambridge, 2000); D. Biskamp, *Magnetic Reconnection in Plasmas* (Cambridge University Press, Cambridge, 2000)
S.L. Rodriguez, J.D. Scudder, F.S. Mozer, C.T. Russell, EOS, 2008AGUFMSM31A1701R (2008)
B. Rossi, S. Olbert, *Introduction to the Physics of Space* (McGraw-Hill, New York, 1970)
K. Schindler, *Physics of Space: Plasma Activity* (Cambridge University Press, Cambridge, 2000)
J.D. Scudder J. Geophys. Res. (2015, in preparation)
J.D. Scudder, W. Daughton, J. Geophys. Res. **113**, A06222 (2008)
J.D. Scudder, A. Mangeney, C. Lacombe, C.C. Harvey, T.L. Aggson, R.R. Anderson, J.T. Gosling, G. Paschmann, C.T. Russell, J. Geophys. Res. **91**, 11019 (1986)
J.D. Scudder, F.S. Mozer, N.C. Maynard, C.T. Russell, J. Geophys. Res. **107**, SMP13-1 (2002)
J.D. Scudder, R.D. Holdaway, R. Glassberg et al., J. Geophys. Res. **113**, A10208 (2008)
J.D. Scudder, R.D. Holdaway, W. Daughton, H. Karimabadi, V. Roytershteyn, C.T. Russell, J.Y. Lopez, Phys. Rev. Lett. **108**, 225005 (2012)
J.D. Scudder, H. Karimabadi, W. Daughton,V. Roytershteyn, Phys. Plasmas **22**(10), 101204 (2015a, in preparation)
J.D. Scudder, W. Daughton, H. Karimabadi, V. Roytershteyn, Phys. Plasmas **22**(10), 101204 (2015b, submitted)
B.U.O. Sonnerup, *Solar System Plasma Processes*, vol. 3, ed. by L.J. Lanzerotti, C.F. Kennel, E.N. Parker (North-Holland, Washington, DC, 1979), p. 45
South West Research Institute, 10160.17-BADCO-01, B.A.D.C.O. for MMS Mission, 5 (2010)
X. Tang, C. Cattell, J. Dombeck, L. Dai, L. Wilson, A. Breneman, A. Hupbach, THEMIS observations of the magnetopause electron diffusion region: large amplitude waves and heated electrons. Geophys. Res. Lett. **40**(12), 2884–2890 (2013)
V.S. Titov, G. Hornig, P. Demoulin, J. Geophys. Res. **107**, SH3-1 (2002)
V.M. Vasyliunas, Rev. Geophys. Space Phys. **13**, 303 (1975)

Chapter 3
MHD Structures in Three-Dimensional Reconnection

E. Priest

Abstract This review of three-dimensional reconnection focusses on the MHD aspects of the process. It describes the different structures where current tends to concentrate and so lead to reconnection, namely, *null points* (where the magnetic field vanishes), *separators* (which are magnetic field lines joining null points) and *quasi-separators*. Then the role of topological invariants such as *magnetic helicity* (which describes the twist and linkage of magnetic structures) is described, together with the conditions for flux and field-line conservation and for reconnection itself. The surprising and crucial differences between 2D and 3D reconnection are highlighted and finally the different regimes for 3D reconnection are summarised.

Keywords Magnetic fields • Magnetic reconnection • Magnetic topology • Magnetohydrodynamics • Plasma physics • Solar activity • Solar flares

3.1 Introduction

Most of the Sun behaves like an ideal medium, in which plasma elements preserve their magnetic connections and the magnetic field is said to be *frozen to the plasma*. Here Ohm's law (generalised or otherwise) reduces to

$$\mathbf{E} + \mathbf{v} \times \mathbf{B} = \mathbf{0}, \tag{3.1}$$

Magnetic flux and field-line connections are both conserved, and there is no reconnection, so that the magnetic topology is conserved. The term *magnetic topology* refers here to any property that is preserved by an ideal displacement, such as the linkage and knottedness of the field.

However, there exist small *localised regions* of length L, say, much smaller than the global length scale (L_e) where nonideal effects such as magnetic diffusion are important and the magnetic connectivity breaks down. Here the plasma is non-ideal

E. Priest (✉)
Mathematics Institute, University of St Andrews, St Andrews, KY16 9SS, UK
e-mail: eric.r.priest@gmail.com

W. Gonzalez, E. Parker (eds.), *Magnetic Reconnection*, Astrophysics and Space Science Library 427, DOI 10.1007/978-3-319-26432-5_3

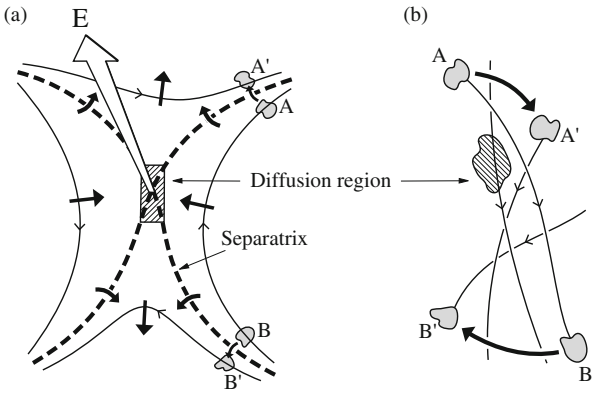

Fig. 3.1 General nature of (**a**) two-dimensional and (**b**) three-dimensional reconnection, in which initial plasma elements A and B are located in an ideal region and are joined by a magnetic field line; they then move to locations A' and B', where they are no longer joined magnetically, since the field line through A' no longer links to B'

(either collisionless or collisional) and the generalised Ohm's law has the form

$$\mathbf{E} + \mathbf{v} \times \mathbf{B} = \mathbf{N}, \tag{3.2}$$

where $\mathbf{N}$ represents any nonideal term. Then the condition $\mathbf{B} \times (\nabla \times \mathbf{N}) = \mathbf{0}$ implies *magnetic field-line conservation*, namely, that, if any two plasma elements are initially joined by a magnetic field line, they will continue to be joined. On the other hand, $\nabla \times \mathbf{N} = \mathbf{0}$ implies *magnetic flux conservation*, namely, that the magnetic flux through any closed curve that moves with the plasma remains constant during the evolution of the field. Thus, line conservation and flux conservation are not equivalent, since, although flux conservation implies field-line conservation, the reverse is not true (Sect. 3.5).

Magnetic reconnection may be defined as a *change of magnetic connectivity of plasma elements* due to the presence of a *localised region of non-idealness* (i.e., a *diffusion region*), where the magnetic field may diffuse through the plasma, whether in 2D (Fig. 3.1a) or in 3D (Fig. 3.1b). However, when localised nonideal plasma effects are important, several classes of magnetic field evolution arise that satisfy Faraday's law

$$\frac{\partial \mathbf{B}}{\partial t} = -\nabla \times \mathbf{E} \tag{3.3}$$

and Maxwell's equation

$$\nabla \cdot \mathbf{B} = 0 \tag{3.4}$$

as indicated in Fig. 3.2 (Hornig 2001). The largest subclass conserves electromagnetic flux

$$\int_{S(t)} \mathbf{B} \cdot d\mathbf{s} + \int_{S(t)} \mathbf{E} \cdot d\mathbf{l}\, dt = const,$$

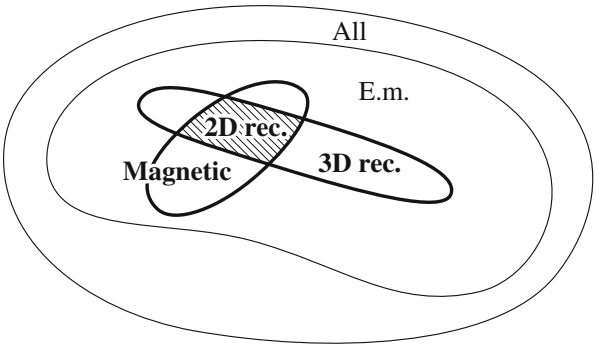

Fig. 3.2 The different classes of evolution of a magnetic field. Within all possible types of evolution (indicated as "All"), there is a large class that conserves electromagnetic flux (called "E.m."). In turn, entirely within that class is a family of three-dimensionally reconnecting situations (called "3D rec") and a second family that conserves magnetic flux (called "Magnetic"). Two-dimensional reconnection (called "2D rec") is a special case of 3D reconnection that also conserves magnetic flux

where $S(t)$ is a surface bounded by a curve that moves with the plasma. Within this, one subclass of solutions conserves magnetic flux by itself ($\int_{S(t)} \mathbf{B} \cdot d\mathbf{s} = const$), while another represents 3D reconnection. Also, the subclass of 3D reconnection that preserves magnetic flux represents 2D reconnection.

For many purposes, the behaviour of plasma and magnetic fields is well described by magnetohydrodynamics (MHD for short) but this chapter is focussing on the MHD of 3D magnetic reconnection. Non-MHD aspects have been discussed in chapter 2 and in Birn and Priest (2007). Resistive MHD with classical ohmic dissipation works well in the solar interior and the low solar atmosphere, but, in the outer corona, Hall MHD with a two-fluid approach or a kinetic model are more appropriate. Nevertheless, even in the latter case, an MHD approach can capture much of the essence of the process and provide an overall macroscopic picture or mould within which the detailed micro-plasma physics operates.

In resistive MHD, the non-ideal term on the right of Eq. (3.2) has the form

$$\mathbf{N} = \eta \boldsymbol{\nabla} \times \mathbf{B},$$

where

$$\eta = \frac{1}{\mu\sigma}$$

is the *magnetic diffusivity*, where μ is the magnetic permeability and σ the electrical conductivity. When η is uniform, Eqs. (3.2) and (3.3) reduce to the standard *induction equation*

$$\frac{\partial \mathbf{B}}{\partial t} = \boldsymbol{\nabla} \times (\mathbf{v} \times \mathbf{B}) + \eta \nabla^2 \mathbf{B}, \tag{3.5}$$

which expresses the magnetic field change in time at a fixed point in space due to a combination of advection (in which the magnetic field is carried with the plasma) and diffusion (in which it slips through the plasma). The ratio of the first (advection) term to the second (diffusion) term on the right is the *magnetic Reynolds number*

$$R_m = \frac{L_e v_e}{\eta},$$

where L_e is the typical global length-scale for variations in plasma properties and v_e is a typical plasma velocity. Thus, the fundamental process of MHD reconnection occurs in an almost-ideal resistive plasma whose magnetic Reynolds number is much larger than unity ($R_m \gg 1$).

The other main equation for steady-state MHD (when the dominant forces are a pressure gradient and a magnetic force) is the equation of motion

$$\rho(\mathbf{v}\cdot\boldsymbol{\nabla})\mathbf{v} = -\boldsymbol{\nabla}p + \mathbf{j}\times\mathbf{B}, \tag{3.6}$$

$$= -\boldsymbol{\nabla}p + (\boldsymbol{\nabla}\times\mathbf{B})\times\mathbf{B}/\mu,$$

$$= -\boldsymbol{\nabla}[p + B^2/(2\mu)] + (\mathbf{B}\cdot\boldsymbol{\nabla})\mathbf{B}/\mu, \tag{3.7}$$

where ρ is the plasma density and p the plasma pressure. These are supplemented by an energy equation and the continuity equation

$$\boldsymbol{\nabla}\cdot(\rho\,\mathbf{v}) = 0,$$

which for an incompressible plasma reduces to $\boldsymbol{\nabla}\cdot\mathbf{v} = 0$.

Reconnection may be fast or slow (in a sense defined below), although in many dynamic phenomena such as solar flares it is fast.

The usual principal effects of magnetic reconnection are:

(i) to convert some of the magnetic energy into heat by ohmic dissipation;
(ii) to accelerate plasma by converting magnetic energy into bulk kinetic energy;
(iii) to generate strong electric currents, current filamentation and shock waves, all of which may be associated with strong electric fields that accelerate fast particles;
(iv) to change the global connections of the field lines and so affect the paths of fast particles and heat, which are directed mainly along the magnetic field.

This chapter summarises three-dimensional MHD reconnection, which is very much a matter of current research. To start with, there is a brief history (Sect. 3.1.1), followed in Sect. 3.3 by a description of the different types of geometrical and topological structures where electric current may accumulate and give rise to 3D reconnection, namely, null points (at which the magnetic field vanishes), separators (field lines that join two null points) and quasi-separators, which are the intersections of two *quasi-separatrix layers (QSLs)*, across which the mapping of magnetic field lines changes continuously but extremely rapidly, whereas across

a true separatrix surface it changes discontinuously. Then Sect. 3.4 discusses magnetic helicity and turbulent relaxation, while Sect. 3.5 gives an account of other topological invariants and some braiding experiments. Section 3.2 describes basic concepts that are crucial for 3D reconnection, such as flux and field-line conservation, conditions for reconnection, and differences between 2D and 3D reconnection. Finally, Sect. 3.6 summarises different regimes of 3D reconnection and magnetic braiding experiments.

This brief overview deals with many of the general properties of 3D reconnection, and touches on its applications to the Sun. It also focuses on the single-fluid MHD aspects, although many of the general results are equally relevant for multiple-fluid and kinetic theories. More details and applications to the magnetosphere and turbulent plasmas can be found in books (Priest and Forbes 2000 or Birn and Priest 2007) and reviews such as Schindler et al. (1988); Hornig (2001, 2004); Hesse et al. (2005); Hornig and Wilmot-Smith (2008). For those who are accustomed to two-dimensional reconnection, a surprising feature is that many of the two-dimensional properties do not carry over into three dimensions, and so new tools and techniques need to be developed (Sect. 3.2.3). Thus, the topology of a 3D field can be highly complex and needs to be understood and modelled. Furthermore, the different regimes of reconnection are much richer and are only just being explored. Whereas reconnection in 2D takes place at an X-point, in 3D it can occur at null points, separators or quasi-separators. Again, the concept of a flux velocity, which is so useful in 2D, fails completely in 3D and implies that field lines continuously change their connections while passing through a localised diffusion region rather than only at the X-point.

3.1.1 Brief History

In 2D, reconnection can occur only at a 2D X-type null point (a null point, near which the magnetic field lines have hyperbolic shapes). The reconnection rate (or inflow plasma speed) for the original *Sweet-Parker model* (Sweet 1958; Parker 1957) is $v_i = v_{Ai}/R_m^{1/2}$, where v_{Ai} is the inflow Alfvén speed and $R_m = Lv_{Ai}/\eta \gg 1$ is the magnetic Reynolds number based on the length L of the sheet. This is much too slow for solar flares and is referred to as *slow reconnection*. Subsequently, Petschek (1964) proposed the first model for *fast reconnection* at a rate of typically $v_i/v_{Ai} = 0.01 - 0.1$, with four standing slow-mode shock waves extending from a tiny central diffusion region. Later, Priest and Forbes (1986) discovered a whole family of *Almost-Uniform* solutions for *fast reconnection*, including the solution of Petschek as a special case.

After a period of debate and numerical experiment it has now been well established that fast reconnection (Almost-Uniform or Petschek) may occur in three distinct circumstances:

(i) when the magnetic diffusivity is enhanced at the X-point, due to for example micro-turbulence (Baty et al. 2009a,b; Baty 2012);
(ii) in collisionless reconnection when the Hall effect is included (Drake et al. 1994; Shay et al. 1998; Birn et al. 2001; Huba 2003);
(iii) by turbulent reconnection due to secondary tearing in current sheets (Forbes and Priest 1987; Loureiro et al. 2007; Bhattacharjee et al. 2009; Daughton et al. 2009; Huang and Bhattacharjee 2010).

The emphasis is now focussed on 3D reconnection, which is completely different from 2D reconnection in several ways (Priest et al. 2003) (Sect. 3.2.3). Landmark papers by Schindler et al. (1988) and Hesse and Schindler (1988) proposed a concept of *General Magnetic Reconnection*, in which reconnection can occur either at null points or in the absence of null points whenever an electric field ($E_\parallel$) parallel to the magnetic field is produced by any region of local nonidealness. The condition for reconnection to occur is simply that

$$\int E_\parallel \, ds \neq 0,$$

evaluated along a magnetic field line that passes through the region of local non-idealness: indeed, the maximum value of this integral gives the rate of reconnection (Sect. 3.2.4).

Basic concepts for the nature of flux and field-line conservation and conditions for reconnection have now been clarified (Hornig 2004; Hornig and Wilmot-Smith 2008) (Sect. 3.2.1). Also, in a key development, new topological invariants have been discovered and their importance revealed in magnetic braiding experiments that are probably relevant to coronal heating (Yeates et al. 2010; Yeates and Hornig 2011b, 2013, 2014; Wilmot-Smith et al. 2010, 2011; Russell et al. 2015) (Sect. 3.5). Several different types of 3D reconnection have been studied, namely, null-point reconnection (Priest and Titov 1996; Priest and Pontin 2009; Pontin et al. 2011b, 2013), separator reconnection (Longcope and Cowley 1996; Longcope 2001; Parnell et al. 2010a; Stevenson et al. 2015), and quasi-separator reconnection (Priest and Démoulin 1995) (Sect. 3.6). Thus, *torsional spine or fan reconnection* occurs when rotational motions concentrate the current along the spine or fan of a null point, *spine-fan reconnection* when shearing motions concentrate it along both (Sect. 3.6.1); and *separator reconnection* when the current is concentrated along a separator field line that joins two null points and represents the intersection of two separatrix surfaces (Sect. 3.6.2). In the absence of null points, *quasi-separator reconnection* can occur at a quasi-separator (Sect. 3.6.3).

3.2 Basic Concepts

Several basic concepts are important to discuss before describing the different regimes of reconnection. These include the subtle difference between flux and field-line conservation and their conditions for existence, the conditions for reconnection

to take place, the surprising differences between 2D and 3D reconnection, and the way to classify reconnection.

3.2.1 Magnetic Flux and Field-Line Conservation

Magnetic flux and field lines are both conserved in ideal MHD and the flux and field-line velocities are equal to the plasma velocity. In nonideal MHD, however, flux and field-line conservation are no longer equivalent (Hornig and Schindler 1996), while flux and field-line velocities are not unique (Sect. 3.2.1.2). These are part of a deeper concept of electromagnetic flux conservation (Fig. 3.2), in which the different kinds of magnetic field evolution may be categorised in a way that distinguishes between conservation of electromagnetic flux, magnetic flux and magnetic field lines (Hornig 2001).

3.2.1.1 An Ideal Plasma

The induction equation for an ideal plasma is

$$\frac{\partial \mathbf{B}}{\partial t} = \nabla \times (\mathbf{v} \times \mathbf{B}), \tag{3.8}$$

and Ohm's law reduces to

$$\mathbf{E} + \mathbf{v} \times \mathbf{B} = 0. \tag{3.9}$$

Alfvén's theorem then implies:

(a) conservation of magnetic flux (the flux through a closed curve moving with the plasma);
(b) conservation of magnetic field lines (so that, if two plasma elements are initially joined by a field line, they remain so);
(c) conservation of magnetic topology (all features of the magnetic field that are preserved under an ideal motion).

Furthermore, the components of plasma velocity ($\mathbf{v}_\perp$), flux velocity [$\mathbf{w}_\perp$, defined to satisfy Eq. (3.12)] and field-line velocity [$\mathbf{w}_{L\perp}$, defined to satisfy Eq. (3.15)] perpendicular to the magnetic field are all equal:

$$\mathbf{v}_\perp = \mathbf{w}_\perp = \mathbf{w}_{L\perp} = \frac{\mathbf{E} \times \mathbf{B}}{B^2}. \tag{3.10}$$

Magnetic Flux Conservation implies that plasma elements initially forming a flux tube will continue to do so, while *Magnetic Field-Line Conservation* means that two plasma elements initially joined by a field line will always remain joined.

3.2.1.2 A Non-ideal Plasma

Here Ohm's law has the form

$$\mathbf{E} + \mathbf{v} \times \mathbf{B} = \mathbf{N}, \tag{3.11}$$

where the nonideal term on the right is written $\mathbf{N} = \eta \nabla \times \mathbf{B}$ for classical resistivity.

A magnetic field variation is then *flux-preserving* if there exists a magnetic flux velocity ($\mathbf{w}$) satisfying

$$\frac{\partial \mathbf{B}}{\partial t} = \nabla \times (\mathbf{w} \times \mathbf{B}). \tag{3.12}$$

However, for an Ohm's Law of the form (3.11), Faraday's equation implies

$$\mathbf{N} = \mathbf{u} \times \mathbf{B} + \nabla \Phi, \tag{3.13}$$

in terms of a *slippage velocity* $\mathbf{u} = \mathbf{v} - \mathbf{w}$ and a potential (Φ).

Then, if $\mathbf{u} \cdot \mathbf{B} = 0$, the flux velocity may be written

$$\mathbf{w} = \mathbf{v} + \frac{(\mathbf{N} - \nabla \Phi) \times \mathbf{B}}{B^2}, \tag{3.14}$$

where in general both $\Phi(\mathbf{r}, t)$ and therefore the flux velocity ($\mathbf{w}$) are not unique.

In contrast, magnetic field variations conserve magnetic field lines if there exists a magnetic field-line velocity ($\mathbf{w}_L$) and a scalar function of position (λ_L) that satisfy

$$\frac{\partial \mathbf{B}}{\partial t} = \nabla \times (\mathbf{w}_L \times \mathbf{B}) + \lambda_L \mathbf{B}. \tag{3.15}$$

Thus, by picking the particular case where $\lambda_L = 0$ and $\mathbf{w}_L = \mathbf{w}$, we see that flux conservation (3.12) implies field-line conservation (3.15). However, the reverse is not true, since there are many solutions for a non-ideal plasma that conserve field lines but don't conserve flux (i.e., all those for which $\lambda_L \neq 0$).

A field-line velocity ($\mathbf{w}_{L\perp}$) may be defined if and only if Ohm's Law can be transformed into the form

$$\mathbf{E} + \mathbf{w}_L \times \mathbf{B} = \mathbf{a}, \tag{3.16}$$

where $\nabla \times \mathbf{a} = -\lambda_L \mathbf{B}$. Thus,

$$\mathbf{w}_{L\perp} = (\mathbf{E} - \mathbf{a}) \times \mathbf{B}/B^2,$$

which is not unique, since $\mathbf{a}$ is not unique.

3.2.2 Conditions for Reconnection to Occur

Before describing the different 3D regimes, we need to mention some subtleties about the differences between diffusion and reconnection so as to understand reconnection in three dimensions. In many respects 3D reconnection is very different indeed from the concept of 2D reconnection that we are accustomed to. Diffusion describes slippage of field lines relative to the plasma, whereas reconnection involves a change in magnetic connectivity of plasma elements, but, as we shall see, the two are not identical, since you can have slippage of field lines while given plasma elements can remain connected by field lines.

The nature of the nonideal term in Ohm's law determines whether there will be simple slippage of field lines or 2D reconnection or 3D reconnection. In 2D, a *flux velocity* is a useful concept, but in 3D it fails. Nevertheless, it can be replaced by a so-called *dual flux velocity* (Sect. 3.2.3). Here, we also summarise differences between 2D and 3D reconnection and discuss the way reconnection can be defined and classified (Sect. 3.2.4).

Whether or not reconnection occurs depends on the nature of the non-ideal term $\mathbf{N}$ in Ohm's law

$$\mathbf{E} + \mathbf{v} \times \mathbf{B} = \mathbf{N}. \tag{3.17}$$

If it can be written in the form

$$\mathbf{N} = \mathbf{u} \times \mathbf{B} + \nabla \Phi,$$

the curl of Ohm's law becomes

$$\frac{\partial \mathbf{B}}{\partial t} = \nabla \times (\mathbf{w} \times \mathbf{B}),$$

where $\mathbf{w} = \mathbf{v} - \mathbf{u}$ is a flux velocity and $\mathbf{u}$ is the slippage velocity. Thus, the magnetic field behaves as if it moves with a velocity $\mathbf{w}$ and we can deduce:

(a) if $\mathbf{N} = \mathbf{u} \times \mathbf{B} + \nabla \Phi$ and $\mathbf{u}$ is smooth, then there is slippage of magnetic field but no reconnection;
(b) if $\mathbf{N} = \mathbf{u} \times \mathbf{B} + \nabla \Phi$ and $\mathbf{u}$ is singular, then there is 2D reconnection;
(c) if $\mathbf{N} \neq \mathbf{u} \times \mathbf{B} + \nabla \Phi$, then there is reconnection in 2.5D or 3D.

Furthermore, an implication of Eq. (3.17) is that $\mathbf{E} \cdot \mathbf{B} = \mathbf{N} \cdot \mathbf{B}$.

Thus, reconnection implies diffusion, since reconnection involves diffusion in an isolated region, but diffusion does not necessarily imply reconnection since diffusion can occur without reconnection. Furthermore, *fast outflow jets* are sometimes but not always accelerated during 3D reconnection, whereas they are invariably present in slow or fast 2D reconnection.

In two-dimensional MHD, $\mathbf{E}$ and $\mathbf{N}$ are perpendicular to $\mathbf{B}$ and $\mathbf{E} + \mathbf{w} \times \mathbf{B} = \mathbf{0}$. Three possible types of behaviour are then possible:

(a) If $\mathbf{B} \neq \mathbf{0}$, then $\mathbf{w}$ is smooth everywhere and there is slippage of the magnetic field, which is *flux-conserving* in a strong sense;
(b) If $\mathbf{B} = \mathbf{0}$ at some point and the neighbouring magnetic field is elliptic, then $\mathbf{w}$ becomes infinite with a divergent singularity and magnetic flux is destroyed or generated at the null;
(c) If $\mathbf{B} = \mathbf{0}$ at some point and the neighbouring magnetic field is hyperbolic, then $\mathbf{w}$ becomes infinite with a hyperbolic singularity and there is *magnetic flux reconnection*, with the flux conserved in the weak sense that $\mathbf{w}$ is regular except at one point.

In 3D, for an isolated nonideal region, a flux conservation velocity ($\mathbf{w}$) does not in general exist (Priest et al. 2003) and so the concept of a single flux velocity fails. However, it can be replaced by a dual flux velocity (Sect. 3.2.3).

3.2.3 Surprising Differences Between 2D and 3D Reconnection

Many new features appear in 3D that make 3D reconnection completely different from 2D reconnection.

2D reconnection has the following basic properties:

(i) It can occur only at an X-type null point;
(ii) A flux velocity ($\mathbf{w}$) satisfying Eq. (3.12) exists everywhere except at null points; it has a hyperbolic singularity at an X-point; the magnetic flux moves at the velocity ($\mathbf{w}$) and slips through the plasma (which moves at $\mathbf{v}$);
(iii) The mapping of field lines near an X-point from one part of a boundary to another is discontinuous as a footpoint crosses a separatrix (Fig. 3.12a);
(iv) While they are in the diffusion region, field lines generally preserve their connections; the exception is the X-point, where the field lines break and their connections are changed;
(v) When two flux tubes are about to reconnect, they approach the diffusion region with velocity $\mathbf{w} = \mathbf{v}$, and then they break and rejoin perfectly to form two new flux tubes that are moving out at $\mathbf{w} = \mathbf{v}$ (Fig. 3.3a);
(vi) When a flux tube is partly in a diffusion region, both parts of the tube that are outside have $\mathbf{w} = \mathbf{v}$, whereas the segment that lies inside has $\mathbf{w} \neq \mathbf{v}$; in other words, the two wings of the tube outside the diffusion region are moving

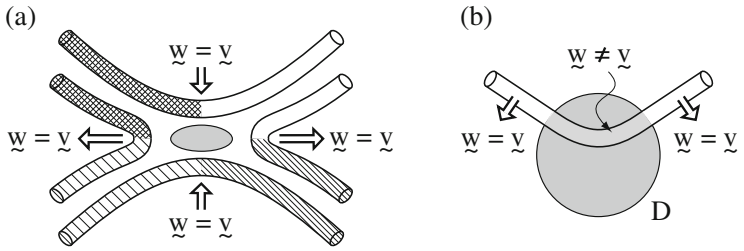

Fig. 3.3 In 2D reconnection, (**a**) two flux tubes break and rejoin perfectly and (**b**) a flux tube slips through most of the diffusion region while preserving its connection

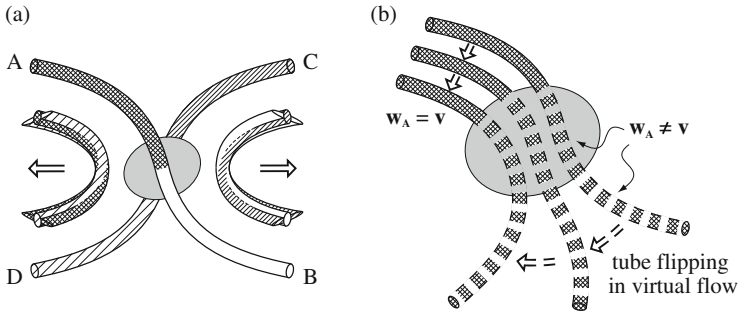

Fig. 3.4 In 3D reconnection (**a**) two flux tubes break and partly rejoin and (**b**) the projection of a flux tube slips through the diffusion region and flips in a virtual flow

with the plasma, while the central segment is slipping through the plasma (Fig. 3.3b).

For the following reasons, none of these properties carry over into three dimensions, and so the nature of 3D reconnection is profoundly different from 2D reconnection. In 3D the properties of reconnection are as follows:

(i) It can take place in 3D either at null points or in the absence of nulls (e.g., at *quasi-separators*, Sect. 3.3.4);
(ii) A flux tube velocity (**w**) does not in general exist in 3D (Hornig and Priest 2003);
(iii) For regions without a null point, the mapping of field lines from one part of a boundary to another is in general continuous (e.g., Fig. 3.12b);
(iv) While in a 3D diffusion region, field lines continually change their connections;
(v) Two flux tubes don't usually break and reform perfectly to give two flux tubes; instead, each section of the original tubes joins to a different part (Fig. 3.4a);
(vi) When two flux tubes are partly in the diffusion region, during the process of reconnecting they split into four parts, each of which flips differently (Fig. 3.4b); if field lines forming a flux tube are projected through a diffusion

region, beyond the diffusion region they move with a velocity that is completely different from the plasma velocity: such a *virtual flow* (with which the tube is flipping) is a manifestation of the non-existence of a flux-conserving velocity (Hornig and Priest 2003).

Since a flux velocity $\mathbf{w}$ is nonunique, it is usually fixed by assuming $\mathbf{w} = \mathbf{v}$ in the ideal region. Although in 2D a single $\mathbf{w}$ exists (and is singular), in 3D reconnection no single velocity $\mathbf{w}$ exists satisfying Eq. (3.12) and the constraint that $\mathbf{w} = \mathbf{v}$ in the ideal region. A resolution of the difficulty is to describe the behaviour of field lines in 3D by introducing a *dual flux velocity* pair ($\mathbf{w}_{in}, \mathbf{w}_{out}$) since they continually change their connections while they are passing through the diffusion region. Consider a set of field lines whose directions point in towards a diffusion region and which are attached to moving plasma elements; their instantaneous positions can be calculated and hence their velocities ($\mathbf{w}_{in}$, say), including their continuations through the diffusion region into an ideal region, where they are no longer attached to plasma elements but exhibit flipping. Similarly, the velocities ($\mathbf{w}_{out}$) of a set of field lines can be calculated from the other side of the diffusion region whose directions point out from the diffusion region. In 3D $\mathbf{w}_{in} \neq \mathbf{w}_{out}$, but in 2D $\mathbf{w}_{in} = \mathbf{w}_{out}$.

3.2.4 Definition and Classification of Reconnection

MHD reconnection always involves a change of magnetic connectivity of plasma elements due to the presence of a localised diffusion region where ideal MHD breaks down. In 2D, it occurs at an X-point, the electric field ($\mathbf{E}$) is normal to the plane, and there is a flow of plasma across the separatrices. A landmark paper by Schindler et al. (1988) asked the question "which of these properties is robust enough to form the basis for a definition of reconnection in 3D?" They realised that reconnection can occur in the absence of nulls and separatrices, and so they suggested that a change of magnetic connectivity be used as the fundamental definition of *"General Magnetic Reconnection"*. Their concept includes all effects of local nonidealness that produce a component ($E_{||}$) of the electric field along a particular magnetic field line, and they suggested

$$\int E_{||}\, ds \neq 0, \tag{3.18}$$

as a necessary and sufficient condition for general magnetic reconnection, where the integral is along that particular magnetic field. In conditions where MHD (with a generalised Ohm's Law) is not valid, such as auroral acceleration, this definition is not appropriate.

An equivalent condition is that the magnetic helicity (Sect. 3.4) change in time, which may be proved as follows. The relative magnetic helicity (Sect. 3.4.1) may be written $H = \int_V (\mathbf{A} + \mathbf{A}_0) \cdot (\mathbf{B} - \mathbf{B}_0)\, dV$, where $\mathbf{B}_0$ is the magnetic field at time (t_0)

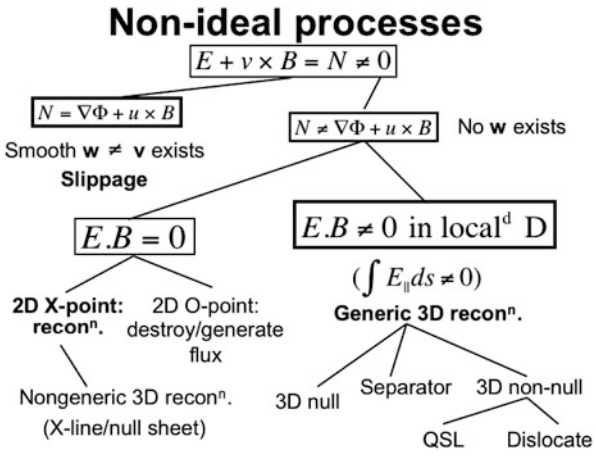

Fig. 3.5 Classification of non-ideal processes. Other 3D non-null examples of reconnection include kink instability and braided fields

and $\mathbf{A}_0$ is the corresponding vector potential. Using $\mathbf{E} = -\nabla\Phi - \partial\mathbf{A}/\partial t$ then leads to

$$\frac{dH}{dt} = -2\int_V \mathbf{E}\cdot\mathbf{B}\, dV - \int_S \mathbf{n}\cdot[(\mathbf{B}-\mathbf{B}_0)\Phi + \mathbf{E}\times(\mathbf{A}-\mathbf{A}_0)]\, dS.$$

Assuming that $\mathbf{E} = \mathbf{0}$ and $\mathbf{B} = \mathbf{B}_0$ on S and remembering that $\mathbf{E}\cdot\mathbf{B} = 0$ outside the diffusion region D_R, this reduces to

$$\frac{dH}{dt} = -2\int_{D_R} \mathbf{E}\cdot\mathbf{B}\, dV = -2\int_{D_R} E_{\|}B\, dV.$$

Non-ideal processes for which $\mathbf{E} + \mathbf{v}\times\mathbf{B} = \mathbf{N}$ (Fig. 3.5) may be divided into those for which $\mathbf{N} = \mathbf{u}\times\mathbf{B} + \nabla\Phi$ (when a smooth finite flux velocity ($\mathbf{w}$) exists and there is slippage) and those for which $\mathbf{N} \neq \mathbf{u}\times\mathbf{B} + \nabla\Phi$, when no $\mathbf{w}$ exists and there are two classes:

(i) $\mathbf{E}\cdot\mathbf{B} = 0$ and there is either a 2D X-point topology (classical 2D reconnection) or a 2D O-point (where magnetic flux may be destroyed or generated).
(ii) generic 3D reconnection with a localised diffusion region ($\mathbf{E}\cdot\mathbf{B} \neq 0$), so that $\int E_{||}\, ds \neq 0$, whose maximum value gives the reconnection rate. This includes 3D null reconnection and 3D non-null reconnection. Null reconnection includes spine-fan reconnection, torsional reconnection and separator reconnection, depending on whether the current concentrates along the spine, fan or separator (Sect. 3.2.2). Non-null reconnection includes reconnection at QSLs (Sect. 3.2.4) and flux-tube disconnection (Wilmot-Smith and Priest 2007).

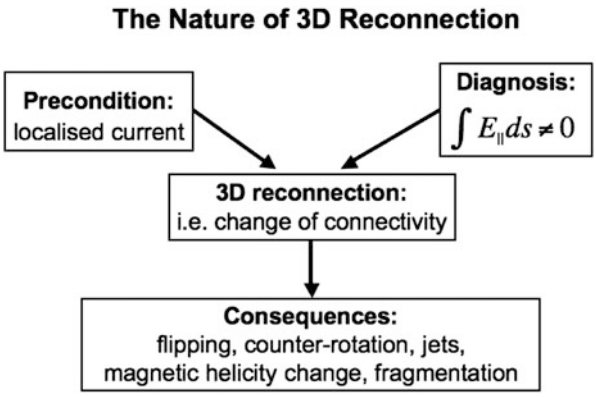

Fig. 3.6 The precondition for, diagnosis and consequences of 3D reconnection

3D reconnection occurs when there is a change of magnetic connectivity of plasma elements and is diagnosed by the condition $\int E_{||}\, ds \neq 0$ (Fig. 3.6). The precondition for this is the formation of a localised current concentration at a natural location where strong currents tend to grow, namely, a null, separator or quasi-separator. Reconnection does not occur just precisely at such locations, but rather everywhere throughout the finite diffusion regions located around them.

Consequences of reconnection include: magnetic flipping and counter-rotation associated with a small change of magnetic helicity; jets of plasma, naturally accelerated by the Lorentz forces in the current concentrations; and fragmentation of the current that arises either by a resistive or ideal instability or by the action of jets from one reconnection region interacting with the surroundings.

3.3 Geometrical and Topological Structures That Are Important for Reconnection

Key features of 3D topology include null points and separatrix surfaces. Separatrices originate at null points or bald patches, and in a complex field they make up a web of surfaces called a *topological skeleton* (Priest et al. 1996; Haynes and Parnell 2010) that is crucial for understanding the structure of the field (Longcope 2005; Parnell et al. 2010b; Platten et al. 2014).

Complex magnetic configurations include both laminar field lines (lying on flux surfaces) and chaotic field lines that are space-filling. Laminar fields form a skeleton of separatrix surfaces (Sect. 3.3.2) and a *quasi-skeleton* of quasi-separatrix layers (QSLs) (Sect. 3.3.4). The intersections of pairs of separatrices are known as *separator curves* (Lau and Finn 1990), whereas the intersections of QSLs are *quasi-separators* (sometimes called *hyperbolic flux tubes*). Titov (2007); Titov et al. (2009) introduced the term *structural skeleton* to denote the sum of the topological

and quasi-skeleton (i.e., both the separatrices and QSLs), which are best identified by Titov's Q-factors (Titov 2007; Titov et al. 2009).

The importance of null points, separators and quasi-separators (Sects. 3.2.3 and 3.2.4) is that they are natural locations where strong currents tend to concentrate as sheets, which then rapidly dissipate by reconnection.

3.3.1 3D Null Points

A null point is a location where the magnetic field vanishes, and so the field near a null point usually increases linearly with distance from it. An example of such a linear null has field components

$$(B_x, B_y, B_z) = (x, y, -2z),$$

or in cylindrical polars $(B_r, B_\theta, B_z) = (r, 0, -2z)$, so that $\nabla \cdot \mathbf{B} = 0$ is satisfied identically.

Two families of field lines, the *spine* and *fan* (Priest and Titov 1996), link to a linear null (Lau and Finn 1990). A spine curve is an isolated field line in Fig. 3.7a approaching or receding from the null along the z-axis. Its neighbouring field lines form two bundles that spread out as they approach the fan surface (the xy-plane).

In general, the magnetic field of a linear null possesses nine constants, three for each field component. By using $\nabla \cdot \mathbf{B} = 0$, normalising and rotating axes, Parnell et al. (1996) showed that they may be reduced to four constants, two of which (a, b) have no clear physical meaning, while the other two $(j_\parallel, j_\perp)$ represent the current along and perpendicular to the spine. The resulting magnetic field components are

$$\begin{pmatrix} B_x \\ B_y \\ B_z \end{pmatrix} = \begin{pmatrix} 1 & \frac{1}{2}(b - j_\parallel) & 0 \\ \frac{1}{2}(b + j_\parallel) & a & 0 \\ 0 & j_\perp & -a - 1 \end{pmatrix} \begin{pmatrix} x \\ y \\ z \end{pmatrix}. \tag{3.19}$$

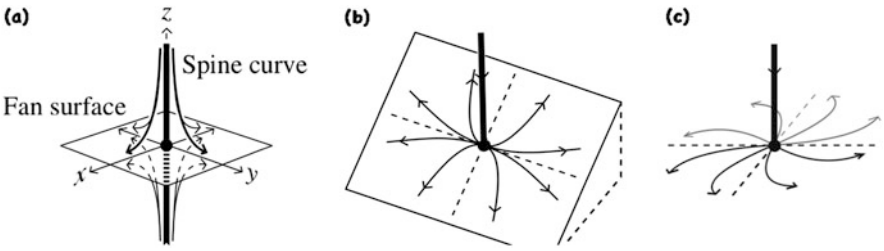

Fig. 3.7 (**a**) Structure of the field lines near a 3D null point with a spine and fan, (**b**) skeleton of an oblique null ($j_\perp \neq 0$) and (**c**) a spiral null, for which $j_\parallel$ exceeds a critical value

When there is a current ($j_\perp$) normal to the spine, the fan surface becomes inclined to the spine at an angle not equal to $\frac{1}{2}\pi$, and we have an *oblique null* (Fig. 3.7b). On the other hand, when the current ($j_\parallel$) along the spine exceeds a critical value, the eigenvalues of the matrix in Eq. (3.19) are no longer all real and it gives rise to a *spiral null*, with the field lines in the fan spiralling into or out of the null (Fig. 3.7c).

3.3.2 Separatrix Surfaces and Separator Field Lines

Solar coronal magnetic field generally enters or leaves the corona through the photosphere in locations that may be considered sources or sinks of magnetic flux as far as the corona is concerned. When modelled as a two-dimensional region, the corona contains *separatrix field lines* that separate the plane into topologically distinct regions, since all the field lines in one region start at a particular source and end at a particular sink (Fig. 3.8a, b).

In the corona two types of 2D separatrix curve are found. One originates at an *X-point*, where the field vanishes and is locally hyperbolic, while the other simply touches the boundary in a so-called *bald patch* (Titov et al. 1993). In 2D, reconnection occurs at an X-point by the breaking and rejoining of field lines and the transferring of flux across the separatrices from one topological region to another.

In 3D, complex configurations have similar properties, with *separatrices* now being surfaces of field lines across which their mapping jumps discontinuously. Again, there are two types of separatrix: firstly, a *separatrix fan surface*, which is an extension of the fan surface of a null point (Fig. 3.10); and secondly a *bald-patch separatrix*, which touches a boundary in a curve known as a *bald patch* (see Sect. 3.3.3 and Fig. 3.11).

Since separatrix surfaces consist of magnetic field lines, they intersect in a special field line called a *separator*, which ends at null points or on the boundary (Fig. 3.8c) (Priest and Titov 1996; Longcope and Cowley 1996; Longcope 2005; Parnell et al. 2010a). The spines of each null lie in the fans of the other null. The fans form sheets which intersect in a *single separator* field line, going from one null to the other, and the fans are finite in the transverse direction, being bounded by the spines of the opposite nulls.

Null points are always created in pairs by a *bifurcation* (i.e., a change in topology) (Brown and Priest 2001). In many numerical experiments, such as those on coronal heating or flux emergence, null points can be highly numerous and form like beads on a string or chain, joined in multiple ways by short separators (Parnell et al. 2010b; Haynes and Parnell 2010). Thus, separators tend to occur as either tiny *intracluster separators* joining nulls within a cluster or as much longer *intercluster separators* linking to distant nulls or joining separate clusters.

The topological structure of the magnetic field (i.e., the form that is preserved by ideal motions) can be found in several ways: from a map of changes of footpoint connectivity (e.g., Parnell and Galsgaard 2004; Longcope et al. 2007;

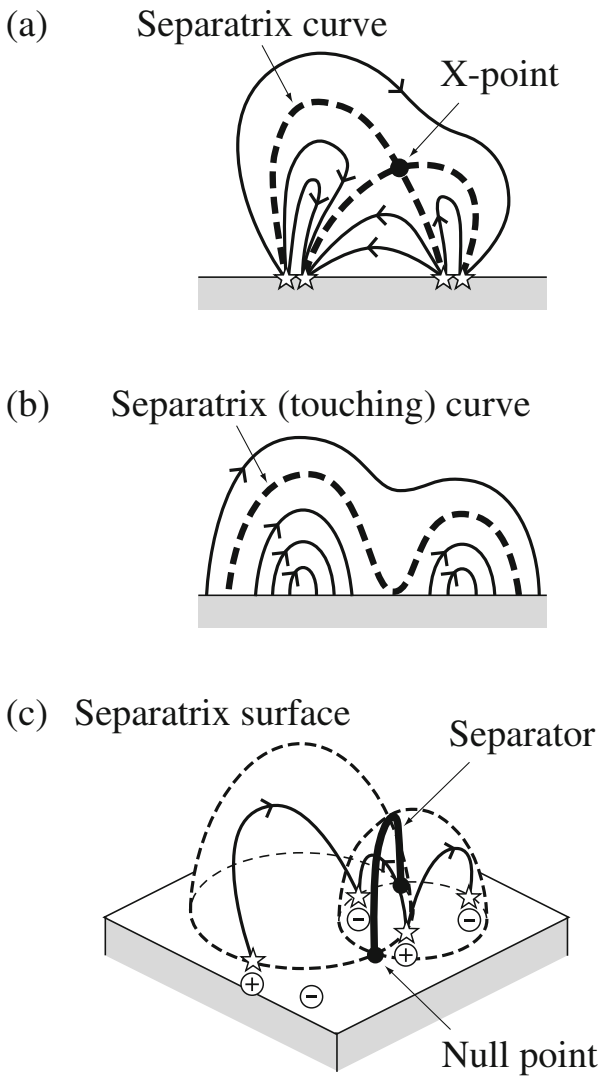

Fig. 3.8 Two-dimensional separatrix curves that (**a**) intersect at an X-point or (**b**) touch the boundary in a bald patch. (**c**) Three-dimensional separatrix surfaces (due to four starred sources) that intersect in a separator (and that may instead touch the boundary)

Haynes et al. 2007; Parnell et al. 2010b); from a map of the discontinuities in footpoint connectivity by calculating the skeleton from nulls and bald patches (Titov et al. 2011); or from the squashing factor (Q, Sect. 3.3.4), which reveals both separatrices and QSLs but does not distinguish precisely between them, apart from the separatrices appearing generally as thinner structures in practice (e.g., Titov 2007; Titov et al. 2012; Masson et al. 2012).

3.3.3 Topological Skeletons in the Solar Corona

The incredibly complex solar corona is created from myriads of magnetic flux sources that poke through the photosphere into the overlying atmosphere. These sources are concentrated by convection in many intense flux tubes and are joined through the corona to many other sources. In addition, in the corona there are many null points whose fans spread out to form a complex web of separatrices. The topology of such complex fields can be understood by constructing the *skeleton* of the field, namely, the set of separatrix surfaces that originate both in the fans of null points and in bald patches (Priest et al. 1996). The coronal skeleton due to two unbalanced photospheric sources consists of a separatrix surface in the shape of a dome encircling the weaker source (Fig. 3.9). From this may be built up the topological properties of the building blocks of complex fields created by a finite number of sources.

In the *magnetic charge topology* approach, clumps of magnetic flux are approximated as point sources; this is commonly adopted for modelling coronal magnetic field arising from photospheric flux distributions (Longcope 2005). The coronal skeleton includes several important elements, which make up, e.g., *pseudo-streamers* (Titov et al. 2011):

* *separatrix domes* spread out from the fans of coronal nulls and close down to the photosphere, enclosing a region of parasitic polarity (Fig. 3.10a);
* *separatrix curtains* also originate as the fans of coronal nulls, but they are more vertical and form open sheets that project out into the solar wind, either as closed separatrices or open separatrices (Fig. 3.10b);
* *bald-patch separatrices* touch the solar surface at bald patches (Fig. 3.11);
* *streamer separatrices* separate closed field of bipolar regions from open field;
* *closed separators* are the intersections of separatrix curtains and either separatrix domes or bald-patch separatrices;

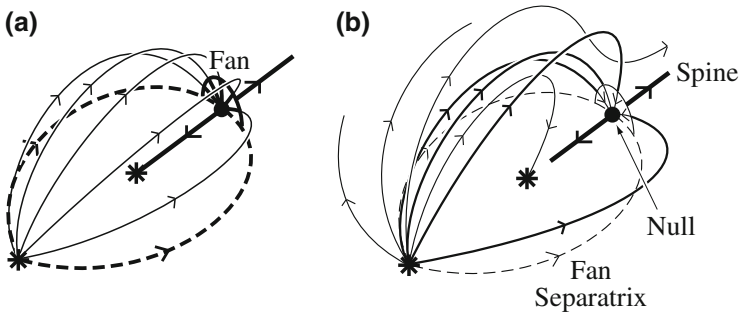

Fig. 3.9 (**a**) Magnetic field lines for the separatrix dome skeleton of the coronal field due to two unbalanced sources (*stars*), in which the fan of a null (*a large dot*) arches over the weaker source. (**b**) The field lines above and below the separatrix dome

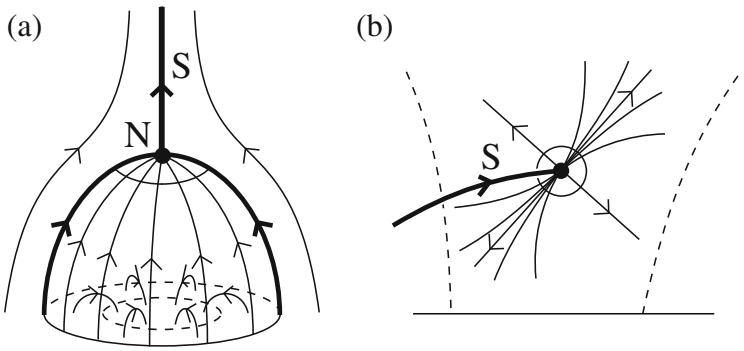

Fig. 3.10 Two of the three building blocks of coronal topology arising from coronal nulls with spines (S) and fans (indicated by a *circle*): (**a**) a separatrix dome formed when the null-point fan closes down to the solar surface and (**b**) a separatrix curtain, when the null-point fan is open into the high corona

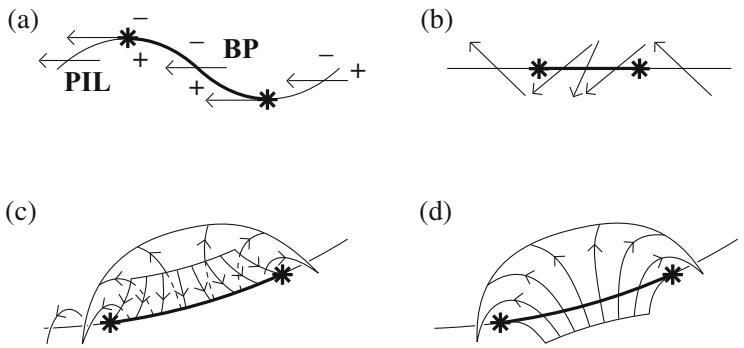

Fig. 3.11 The third building block of coronal topology, namely a bald-patch separatrix surface, showing (**a**) the field-line directions across a curved polarity-inversion line (PIL), a segment of which is a bald patch (BP), with a strong overlying field having a uniform direction (**b**) the field-line directions when the PIL is straightened out, and the field lines in the bald-patch separatrix surface viewed (**c**) from the side and (**d**) from above

* *open separators* are the intersections of separatrix curtains and streamer separatrices.

A bald patch (Titov et al. 2011) is a segment of a polarity-inversion line (PIL) where the direction of the horizontal field is abnormal in the sense that it is directed from the negative polarity side. Bald patches are rather numerous in practice. They tend to occur when the polarity-inversion line of a highly sheared field snakes through an active region, or below a large-scale magnetic flux rope (e.g., around a prominence), or when the large-scale background field is oppositely directed to

and stronger than the small-scale field that is trying to close down across a polarity-inversion line.

3.3.4 *Quasi-Skeletons*

Across separatrix surfaces, the magnetic connectivity of plasma elements jumps discontinuously and reconnection can occur at the intersections of separatrices, namely separators. However, across *quasi-separatrix layers* (QSLs), the connectivity has a steep but finite gradient. QSLs are remnant separatrices and form a quasi-skeleton. They intersect in *quasi-separators*, at which *quasi-separator reconnection* (Priest and Démoulin 1995) may take place just as readily as at separators. The core process inside a QSL is magnetic flipping (Priest and Forbes 1992), whereby magnetic field lines flip past one another in opposite directions. Application to solar flares was soon developed, where flipping in quasi-separator reconnection was instead called *slip-running reconnection* by Aulanier et al. (2006). Furthermore, it was found that current sheets tend to form spontaneously along quasi-separators in response to any smooth and large-scale footpoint motion (Aulanier et al. 2005).

At a 2D null point, reconnection is associated with a discontinuity in the field-line mapping from one footpoint to another. For the simple X-point field

$$B_x = x, \quad B_y = -y, \tag{3.20}$$

a point $(x_0, 1)$ on the top boundary ($y = 1$) will map to $(1, y_1)$, say, on the side boundaries ($y = \pm 1$) in such a way that, when $(x_0, 1)$ crosses a separatrix, the point $(1, y_1)$ suddenly jumps in location to $(-1, y_1)$ (Fig. 3.12a).

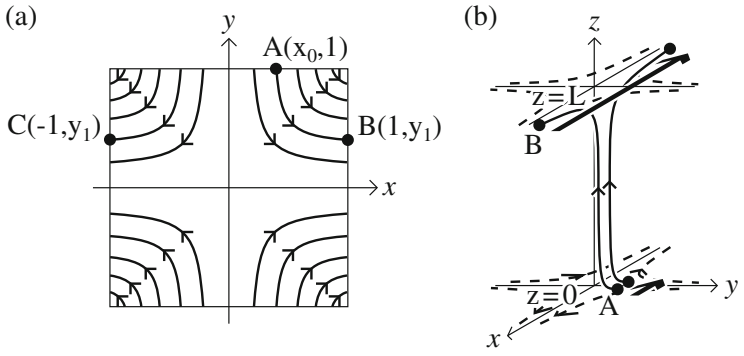

Fig. 3.12 Mapping along magnetic field lines of footpoints for (**a**) a 2D X-field from the top or bottom boundary of a square to the side boundary and (**b**) a 3D sheared X-field from the plane $z = 0$ to the plane $z = L$

Such a mapping discontinuity is present also in 3D at the separatrix surfaces that spread out from nulls or bald patches. When nulls or bald patches are absent, there are no separatrices and the mapping of one footpoint to another is continuous (Schindler et al. 1988). However, Priest and Démoulin (Priest and Démoulin 1995) realised that, even in the absence of separatrices, there often exists a web of quasi-separatrix layers, which we call *quasi-topology*.

Suppose a 3D configuration is surrounded by a closed surface S. Then the mapping of field-line footpoints from one part of S to another may be calculated. For instance, if a small component ($B_z = l \leq 1$) is added to Eq. (3.20) to create a sheared X-field, the mapping becomes continuous, so that, as the point $\mathrm{A}(x_0, y_0)$ crosses the y-axis in the plane $z = 0$, the other end $\mathrm{B}(x_1, y_1)$ in the plane $z = 1$ moves continuously (Fig. 3.12b).

Quasi-separatrix layers may be identified as sheets where the gradients of the mapping are very large. This definition of a QSL involves a mapping to a boundary and therefore refers to global properties of a configuration. The concept of a QSL may be defined formally by splitting the surface S into parts S_0 and S_1 where the field lines enter and leave the volume, respectively, and set up orthogonal coordinates (u, v) in S and w normal to S. Then field lines map (u_0, v_0) in S_0 to (u_1, v_1) in S_1. Next, form the *displacement gradient tensor*

$$\mathscr{F} = \begin{pmatrix} s_1 \partial u_1/\partial u_0 & s_2 \partial u_1/\partial v_0 \\ s_3 \partial v_1/\partial u_0 & s_4 \partial v_1/\partial v_0 \end{pmatrix} \tag{3.21}$$

from the gradients of the mapping functions $u_1(u_0, v_0)$ and $v_1(u_0, v_0)$ and the scaling factors s_i and evaluate the expression

$$N = \sqrt{\left(s_1 \frac{\partial u_1}{\partial u_0}\right)^2 + \left(s_2 \frac{\partial u_1}{\partial v_0}\right)^2 + \left(s_3 \frac{\partial v_1}{\partial u_0}\right)^2 + \left(s_4 \frac{\partial v_1}{\partial v_0}\right)^2}. \tag{3.22}$$

Finally, define a quasi-separatrix layer as the region where $N \gg 1$.

A quasi-separatrix layer (where $N \gg 1$) is associated with a large expansion along one direction and a large compression along the other, such that N is approximately equal to the largest eigenvalue of the matrix in Eq. (3.21) ($N \approx \lambda_{max}$).

A better way of diagnosing a QSL was discovered by normalising N^2 to give a *squashing factor* (Titov 2007)

$$Q = -\frac{N^2}{B^*_{z-}/B_{z+}}, \tag{3.23}$$

where N is calculated by mapping along a field line from one end where the normal field is B_{z+} to the other end where it is B^*_{z-}. Then Q is independent of the direction of mapping and a QSL is a layer where $Q \gg 1$. If a flux tube has one footpoint rooted in a small circular patch and the other in a distorted ellipse, then Q measures the aspect ratio of the ellipse. Titov et al. (2009) extended the concept further by

defining slip-forth and slip-back squashing factors (Q_{sf} and Q_{sb}), which identify the *reconnection fronts* of field lines that have been or are about to be reconnected in an evolving configuration.

3.4 Magnetic Helicity

Magnetic helicity is a topological quantity with an intimate relation to 3D reconnection. It measures *self-helicity* (twisting and kinking of a flux tube) and *mutual helicity* (the linkage between different flux tubes). It may be shown to be a global invariant that cannot be changed in an ideal medium and decays very slowly (over the global magnetic diffusion time τ_d) in a weakly resistive medium (Berger and Field 1984). Reconnection on times much smaller than τ_d cannot, to a first approximation, destroy magnetic helicity but only convert it from one form to another. Thus, conservation of magnetic helicity provides an important constraint on the final state produced by reconnection. It has so far proved invaluable in analysing the complex topologies observed in the solar atmosphere and in determining the nature and causes of twisted structures that are so important in solar flares.

During 3D reconnection, there is, however, a tiny change in magnetic helicity whose presence is essential to the occurrence of reconnection (Sect. 3.2.4). Other concepts have also been developed more recently, such as the *topological degree*, *topological entropy* and *topological flux function* (Yeates et al. 2010; Yeates and Hornig 2013), which are important in measuring topology and their changes during reconnection (Sect. 3.5).

The lowest-energy state that conserves the total magnetic helicity is a linear force-free field (Woltjer 1958). For example, laboratory machines called reversed-field pinches are so turbulent that magnetic surfaces break down by multiple reconnections and spread the magnetic helicity uniformly throughout the configuration to create a linear force-free state (Taylor 1974). Magnetic helicity is also important in dynamo theory (Moffatt 1978).

The first to realise the importance of magnetic helicity for the solar corona were Heyvaerts and Priest (1984), who developed Taylor's theory (Taylor 1974) to allow magnetic flux to thread the photosphere and suggested that coronal magnetic fields are in a state of MHD turbulence with energy fed into the corona by photospheric motions, so that the corona is continually heated by turbulent reconnection as it evolves through a series of linear force-free states. They also suggested that, if the magnetic helicity becomes too great, it may be expelled in a coronal mass ejection. It is now widely applied to understand coronal evolution (Berger 1999; Pevtsov et al. 2001, 2003). An important development was the idea of relative helicity and its evolution (Berger and Field 1984), and another is the generalisation of the Heyvaerts-Priest theory of coronal relaxation to include constraints other than magnetic helicity (Amari and Luciani 2000), such as the topological degree of the mapping from one footpoint to another (Yeates et al. 2010; Yeates and Hornig 2011a; Pontin et al. 2011a).

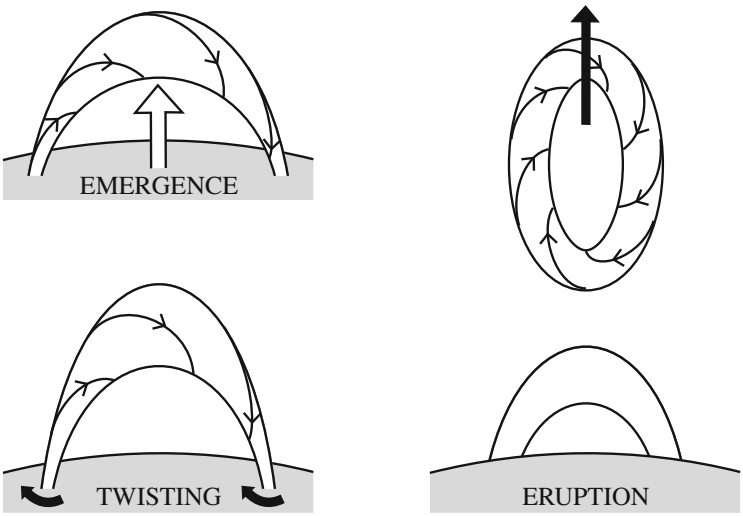

Fig. 3.13 Magnetic helicity changes due to flux emergence from below the photosphere (*shaded*), twisting of the photospheric footprints of a coronal flux tube or an eruption

In the solar atmosphere the continual motion of photospheric magnetic footpoints tends to build up magnetic helicity until it is ejected by magnetic eruptions. Thus, magnetic helicity in the atmosphere can change either by the emergence of twisted or linked structures from the solar interior or by twisting (or untwisting) footpoint motions of coronal loops. Magnetic helicity of a coronal loop can also be decreased by the detachment and ejection of magnetic structures from the solar surface (as in prominence eruptions) (Fig. 3.13).

3.4.1 Magnetic Helicity and Turbulent Relaxation

In a closed volume (V), bounded by a surface S, magnetic helicity is defined to be

$$H_0 = \int_V \mathbf{A} \cdot \mathbf{B}\, dV, \tag{3.24}$$

where $\mathbf{A}$ is the vector potential such that $\mathbf{B} = \nabla \times \mathbf{A}$. H_0 is gauge invariant if the volume is magnetically closed, but not if magnetic field lines enter or leave it.

Relative magnetic helicity is

$$H = \int_{V_\infty} \mathbf{A} \cdot \mathbf{B} - \mathbf{A}_0 \cdot \mathbf{B}_0\, dV, \tag{3.25}$$

and has the advantage of being gauge-invariant (Berger and Field 1984). Here $\mathbf{B}_0 = \nabla \times \mathbf{A}_0$ is a field that is potential inside V, is the same as $\mathbf{B}$ outside V and satisfies $\mathbf{A} \times \mathbf{n} = \mathbf{A}_0 \times \mathbf{n}$ on S. Berger and Field (1984) realised that the difference in helicity integrated over all space (V_∞) of any two fields that differ only inside V is independent of the field outside V, and that a particularly useful reference field inside V is a potential field, since it is completely determined by $\mathbf{B} \cdot \mathbf{n}$ on S.

Magnetic helicity changes in time at a rate

$$\frac{dH}{dt} = -2 \int_V \mathbf{E} \cdot \mathbf{B} \, dV + 2 \int_S \mathbf{A}_p \times \mathbf{E} \cdot \mathbf{n} \, dS,$$

where a gauge ($\mathbf{A}_p$) has been chosen that satisfies $\nabla \cdot \mathbf{A}_p = 0$ and has $\mathbf{A}_p \cdot \mathbf{n} = 0$ on S. If there is no slippage on the boundary and the resistive Ohm's Law ($\mathbf{E} = -\mathbf{v} \times \mathbf{B} + \mathbf{j}/\sigma$) holds, this becomes

$$\frac{dH}{dt} = -2 \int_V \mathbf{j} \cdot \mathbf{B}/\sigma \, dV + 2 \int_S (\mathbf{B} \cdot \mathbf{A}_p)(\mathbf{v} \cdot \mathbf{n}) - (\mathbf{v} \cdot \mathbf{A}_p)(\mathbf{B} \cdot \mathbf{n}) \, dS. \tag{3.26}$$

Here the internal helicity dissipation is represented by the first term and the flow of helicity across the boundary by the surface integral.

Thus, if the magnetic field varies on a length-scale (L), equating dH/dt to the first term with $j \sim A/(\mu L^2)$ implies that the time-scale for magnetic helicity dissipation is the global diffusion time ($\tau_d = L^2/\eta$). Also, on time-scales much shorter than τ_d, changes of helicity are given by the surface term. Thus, for example, if the volume is closed, with $\mathbf{B} \cdot \mathbf{n} = \mathbf{v} \cdot \mathbf{n} = 0$, the helicity is conserved. But, if instead footpoint motions along the surface are prescribed, the resulting injection or extraction of helicity may be deduced as follows.

For a plane surface ($z = 0$), magnetic helicity evolution may be written

$$\frac{dH}{dt} = 2 \int \int (\mathbf{B} \cdot \mathbf{A}_p) v_z - (\mathbf{v} \cdot \mathbf{A}_p) B_z \, dxdy, \tag{3.27}$$

in the ideal limit, where the integration is over the xy-plane. The first term represents the effect of the emergence of structures carrying helicity through the surface, while the second term represents injection by footpoint shuffling of helicity into fields already present in the volume. In particular, if a plane surface S is threaded by the footpoints of N thin flux tubes of magnetic flux $F_{m(i)}$, and, if the motion of each footpoint consists of a translation plus a uniform rotation at a rate ω_i, the rate change of magnetic helicity is

$$\frac{dH}{dt} = -\frac{1}{2\pi} \left[\sum_{i=1}^{N} \omega_i F_{m(i)}^2 + \sum_{i=1}^{N} \sum_{j=1}^{N} \dot{\theta}_{ij} F_{m(i)} F_{m(j)} \right], \tag{3.28}$$

where $\dot{\theta}_{ij}$ is the time derivative of the relative angle (θ_{ij}) between footpoints i and j (Berger 1984). The first term arises because footpoint rotation injects one unit of twist into a flux tube every $2\pi/\omega$ seconds. The second term measures the rate at which footpoints circle each other and braid the flux tubes.

When twisting and linking is built up from an initially potential field that has widely separated, untwisted tubes, the helicity may be deduced from Eq. (3.28). It consists of the self-helicity (H_s) of each tube due to its own internal twist, and the mutual helicity (H_m) due to linking of the tubes, namely,

$$H = \sum_{i=1}^{N} H_{si} + \sum_{\substack{i,j=1 \\ i<j}}^{N} H_{mij},$$

where the ith flux tube has *self-helicity* $H_{si} = \Phi_{T_i} F_{m(i)}^2/(2\pi)$ in terms of its twist Φ_{T_i} (or $2\pi \times$ number of turns) and magnetic flux $F_{m(i)}$, and the *mutual helicity* is

$$H_{mij} = 2L_{ij} F_{m(i)} F_{m(j)} \tag{3.29}$$

in terms of the *linking number* L_{ij}, which is a topological parameter describing two curves that does not change as the curves are distorted without crossing through each other. Each curve is given a direction, and reversing one of the directions changes L_{ij} by -1. Each crossing has a sign $+1$ or -1, depending on whether the first curve is in front of or behind the other, and the linking number is just half the sum of the signed crossings.

The helicity of a straight flux tube of uniform twist is

$$H = \frac{\Phi_T}{2\pi} F_m^2. \tag{3.30}$$

More generally, if the axis of the tube is itself twisted or kinked, then the self-helicity is increased by the *writhing number* due to the shape of the axis.

3.5 Other Topological Invariants and Braiding Experiments

The Taylor hypothesis (Taylor 1974) suggests that during turbulent magnetic reconnection and relaxation the only constraint is the global magnetic helicity, which measures the second-order linkage of field lines, so that the final state is the linear force-free field that preserves the total magnetic helicity. This explains well the final observed state in a reversed-field pinch, and it was suggested that, after generalising the hypothesis to include field lines entering or leaving the region, it could also be applied to solar coronal structures (Heyvaerts and Priest 1984; Dixon et al. 1989). Two other modifications to the hypothesis were also suggested,

namely, to give: *intermediate relaxation* to a state with an energy above that of a linear force-free field when the driving time is not long enough to allow complete relaxation; or *partial relaxation* in which open fields eject magnetic helicity into the solar wind and are close to potential, while closed fields relax to a linear force-free state (Vekstein et al. 1993). In addition, it was suspected that higher-order invariants may play a role (Bhattacharjee et al. 1980).

Determining the allowed final state after turbulent relaxation is important for the coronal heating and solar flare problems, since it limits the amount of energy release that is available. A recent discovery in numerical simulations of relaxation of braided fields is that the final state can sometimes be far from a Taylor state even though the total magnetic helicity is conserved (Amari and Luciani 2000; Wilmot-Smith et al. 2010).

For example, Wilmot-Smith, Hornig and Pontin have constructed a series of braided magnetic fields and studied the way they relax (Wilmot-Smith et al. 2009a,b, 2010, 2011; Pontin et al. 2011a; Pontin and Hornig 2014). They first show how to construct a braided magnetic field analytically to use as a starting point, and develop a numerical method to relax it towards a force-free equilibrium (Wilmot-Smith et al. 2009a). When they start with a highly braided field with zero total magnetic helicity, no net current and a uniform normal field component at the two ends, Taylor's hypothesis would imply relaxation to a uniform field throughout the volume (Wilmot-Smith et al. 2010; Pontin et al. 2011a). However, they find instead that the final state is a nonlinear force-free field with no small-scale currents and consisting of two flux tubes having opposite twist (Fig. 3.14). The magnetic field remains smooth during the relaxation with only large-scale current structures, but the integrated parallel electric current has a highly filamentary structure with extremely short length-scales and a myriad of thin current sheets, so that the magnetic flux reconnects multiple times (Pontin et al. 2011a).

Yeates et al. (2010) have solved the puzzle of the absence of a Taylor state in the braiding experiments by proposing an extra topological invariant, called *the topological degree*, which can prevent the system reaching the Taylor state when the initial value of the topological degree differs from its value in the Taylor state. They suppose that all field lines link from the lower boundary (D_0) to the top boundary (D_1), and consider a mapping $\mathbf{x}_1 = \mathbf{f}(\mathbf{x}_0)$ along field lines from a point $\mathbf{x}_0$ on D_0 to a point $\mathbf{x}_1$ on D_1 (Fig. 3.15). The field line mapping has several points ($\mathbf{x}_0^p$) (called *periodic orbits*) where $\mathbf{f}(\mathbf{x}_0) = \mathbf{x}_0$ and which represent *fixed points* of the mapping $\mathbf{f} - \mathbf{I}$ (where $\mathbf{I}$ is the identity map). Each such point is characterised by a *fixed point index* (*index* ($\mathbf{x}_0^p$)), which is $+1$ when the field lines near the fixed point are elliptic in shape and -1 when they are hyperbolic (assuming the fixed points are generic, structurally stable and isolated). Then the *topological degree*,

$$T = \sum_{\mathbf{x}_0^p} index(\mathbf{x}_0^p), \tag{3.31}$$

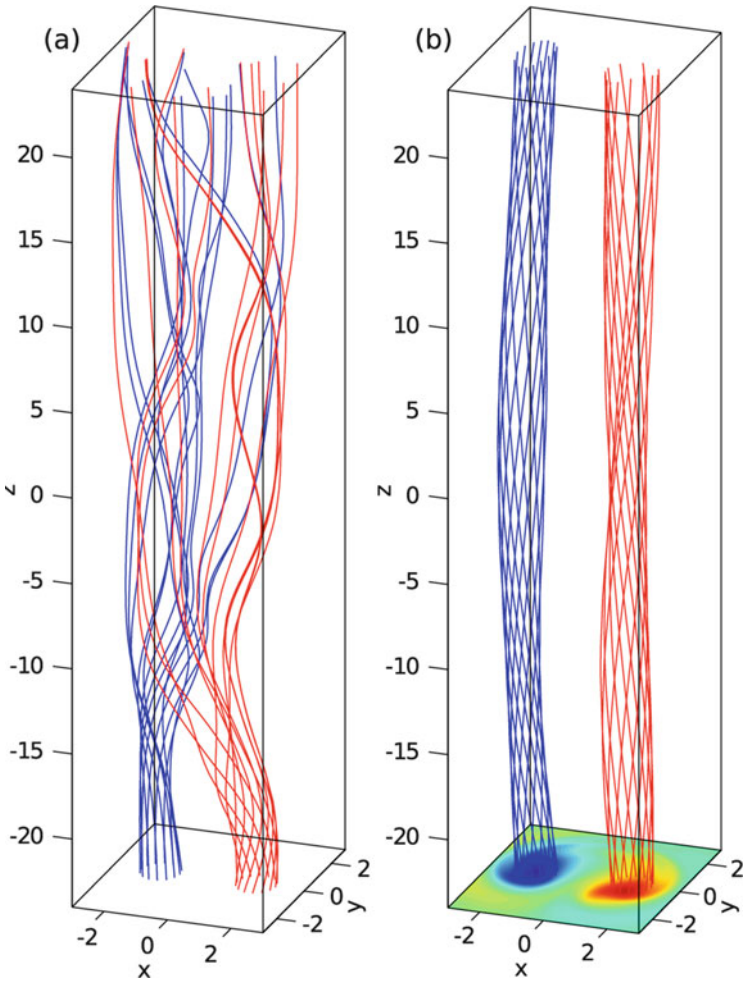

Fig. 3.14 Magnetic field lines in a braiding experiment for (**a**) the initial state and (**b**) the final relaxed state after 290 Alfvén times. Field lines are traced from the same starting points on the bottom boundary in both cases. (Reprinted with permission from Yeates and Hornig (2011a); copyright (2011) by the Institute of Physics)

is simply the sum of the fixed point indices over all such fixed points. By the Lefschetz-Hopf theorem (Brown 1971), which requires only that the mapping be continuous, this is a conserved quantity provided no periodic orbits cross the side boundary of the domain. Thus, fixed points can be created or annihilated only in pairs of opposite index.

One way to compute the topological degree is to construct a colour map. Each point $\mathbf{x}_0 = (x_0, y_0)$ on the lower boundary is allocated one of four colours, depending on its mapping $\mathbf{f}(\mathbf{x}_0) = (f_x, f_y)$ to the top boundary. Thus, dark grey

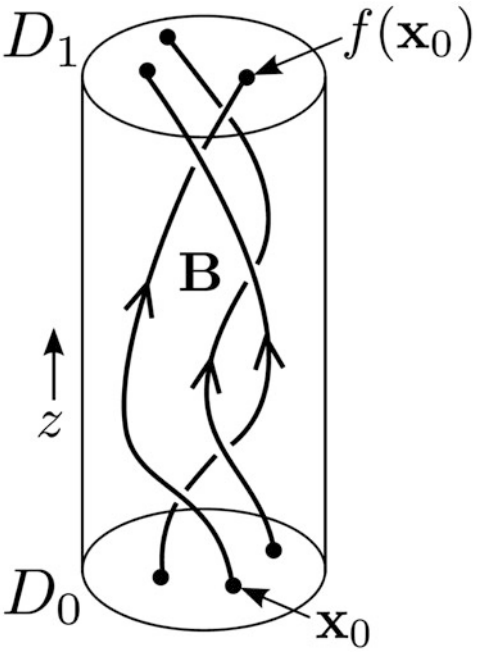

Fig. 3.15 The nomenclature for a mapping $\mathbf{x}_1 = \mathbf{f}(\mathbf{x}_0)$ of field lines from the lower boundary (D_0) to the upper boundary (D_1). (Reprinted with permission from Yeates and Hornig (2011a); copyright (2011) by the Institute of Physics)

corresponds to $f_x > x_0$ and $f_y > y_0$, white to $f_x < x_0$ and $f_y > y_0$, light grey to $f_x < x_0$ and $f_y < y_0$ and black to $f_x > x_0$ and $f_y < y_0$. It turns out that isolated generic fixed points are points where all four colours meet. If the sequence of colours on a small anticlockwise circle around a point is darkgrey-white-lightgrey-black, then it transpires that we have an elliptic point with index $+1$, but if the sequence is darkgrey-black-lightgrey-white we have a hyperbolic point with index -1 (Yeates and Hornig 2011a). Thus, to determine the topological degree, either sum the individual indices or simply record the sequence of colours around the boundary of D_0. For example, the colour maps for the relaxation experiment of Fig. 3.14 show that initially there are 12 fixed points with index $+1$ and 10 with index -1, giving a topological degree of 2. During relaxation, reconnection changes the topology and eliminates fixed points in pairs, leaving just two elliptical fixed points at the end (Fig. 3.16).

Yeates and Hornig (2011a) developed the analysis to include a general periodic flux tube (such as in a toroidal system), and showed how the sum of indices over all interior fixed points is invariant for any continuous evolution inside the tube, which may be turbulent and/or dissipative. The original definition of the index assumed there are no fixed points on the side boundary, but they extended this to allow such points. Assuming ideal evolution on the side boundary, the total index of the fixed points there is fixed, and so the total index of the fixed points in the interior (where the mapping evolves) is also fixed.

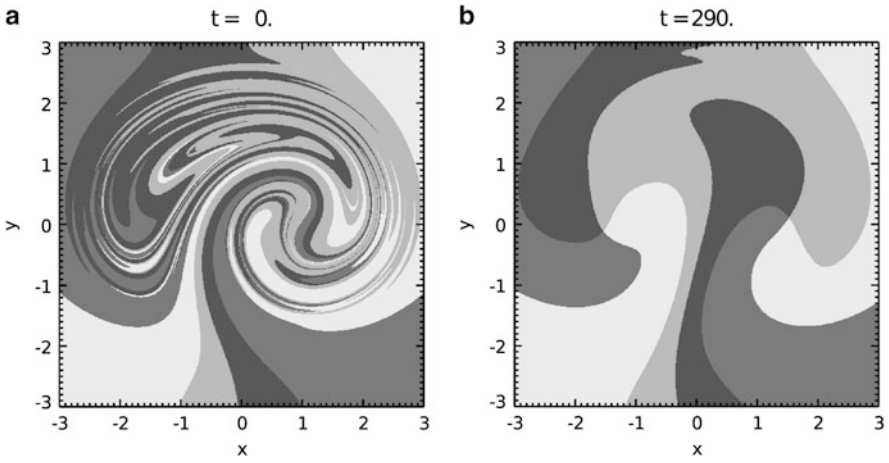

Fig. 3.16 The "colour" maps at the start and end of the relaxation experiment in Fig. 3.14, where the different "colours" are dark grey, black, light grey and white. (Reprinted with permission from Yeates and Hornig (2011a); copyright (2011) by the Institute of Physics)

Yeates and Hornig (2011b) generalise the familiar 2D concept of a flux function to a 3D magnetic field connecting two boundaries. There are two ways of measuring reconnection rates in 3D, namely using the integral along field lines of the parallel electric field (Sect. 3.2.4) or by counting the flux transfer between distinct flux domains. They therefore (i) use the hyperbolic fixed points to define a partition of the flux and (ii) measure the rate of transfer of fluxes in this partition. This reconnection rate with respect to the partition is called a *partition reconnection rate*. It captures only the processes that change fluxes between the flux domains and not those within each domain.

In 2D the separatrix field lines from X-points give a natural partition of the field (Fig. 3.17), and the flux in each domain is given by the difference in the values of the flux function (A) at neighbouring null points, so that the global reconnection rate may be calculated from the changes in flux measured by the changes in A at the nulls, even in turbulent 2D fields with many nulls. Two important properties of A, where $B_x = \partial A/\partial y$ and $B_y = -\partial A/\partial x$, are: A is constant along field lines ($\mathbf{B}\cdot\nabla A = 0$); and, for ideal evolution, A is invariant ($\partial A/\partial t + \mathbf{v}\cdot\nabla A = 0$). Furthermore, reconnection occurs only at X-points and so a global *partition reconnection rate* can be defined as the sum of changes in the values of A at the X-points ($\mathbf{x}_p$), namely,

$$\Delta\phi_P = \sum_{\mathbf{x}_p} \left| \frac{dA(\mathbf{x}_p)}{dt} \right| . \tag{3.32}$$

In 3D, a natural partition arises in terms of separatrix surfaces that originate at fans of 3D null points or at bald patches, but complications arise from the possibility of chaotic regions. Yeates and Hornig (2011b, 2013) consider a simply

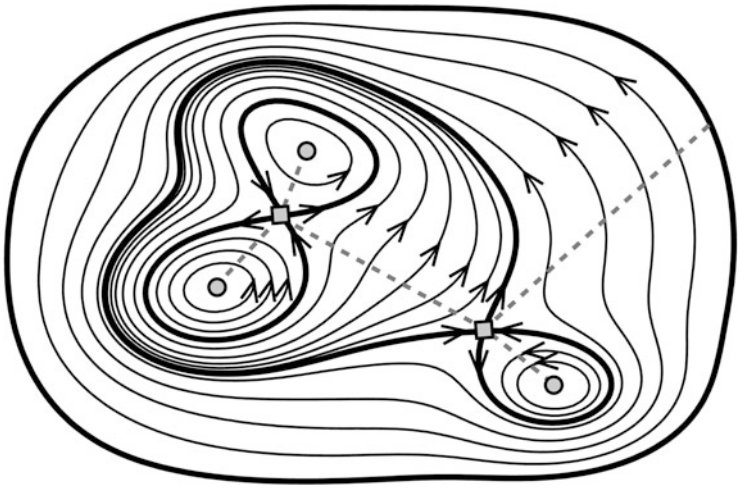

Fig. 3.17 An example of a 2D magnetic field with hyperbolic nulls (*squares*), elliptic nulls (*circles*) and separatrices (*thick curves*). Partition fluxes may be measured as differences in A across the *dashed lines*. (Reproduced with permission from Yeates and Hornig (2011b); copyright (2011) AIP Publishing LLC)

connected domain with all field lines connecting two boundaries and construct a *topological flux function* ($\mathscr{A}(x, y)$) that retains several properties of the 2D flux function ($A(x, y)$). It is defined simply by integrating the vector potential $\mathbf{A}$ along magnetic field lines from the lower boundary ($z = 0$, say) to the upper boundary ($z = 1$), namely,

$$\mathscr{A} = \int_{z=0}^{z=1} \mathbf{A} \cdot d\mathbf{s} = \int_0^1 \frac{\mathbf{A} \cdot \mathbf{B}}{B_z} dz. \tag{3.33}$$

Gauge invariance is ensured by imposing on the boundary $\mathbf{n} \times \mathbf{A} = \mathbf{n} \times \mathbf{A}_{ref}$, where $\mathbf{A}_{ref} = \frac{1}{2} r\, \mathbf{e}_\phi$ is the vector potential of a reference field ($\mathbf{e}_z$) that matches $\mathbf{B}$ on the boundary (Yeates and Hornig 2013).

The relative magnetic helicity may be written in terms of $\mathscr{A}(x, y)$ as an integral over the lower boundary

$$H_r = \int_{z=0} \mathscr{A} B_z \, dxdy, \tag{3.34}$$

so that the topological flux function is a helicity density per unit magnetic flux or a helicity per field line; it is called a *field line helicity* by Berger (1988). It also measures the average poloidal flux around any given field line and from the above equation its integral over the cross-section gives the relative magnetic helicity. The final state of the braiding experiment shown in Fig. 3.14 possesses equal regions

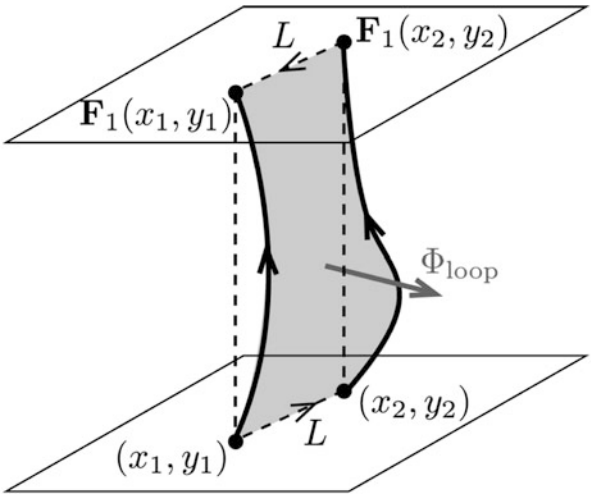

Fig. 3.18 The flux Φ_{loop} through the surface defined by two fixed points (x_1, x_2) is measured by $\mathscr{A}(x_2, y_2) - \mathscr{A}(x_1, y_1)$. (Reproduced with permission from Yeates and Hornig (2011b); copyright (2011) AIP Publishing LLC)

of positive and negative $\mathscr{A}(x, y)$, which is an example of how the topological flux function contains more information about the topology than the magnetic helicity.

Yeates and Hornig (2013) define a *braid* as being a magnetic field in which all the field lines join one plane to another, so that two braids are topologically equivalent if one can be distorted to the other by an ideal evolution with no flow on the boundaries. They show that $\mathscr{A}(x, y)$ uniquely characterises the topology of a magnetic braid so that two braids are topologically equivalent if and only if their topological flux functions are identical. More generally they (Yeates and Hornig 2014) show that the topological flux function uniquely characterises field line mapping and hence magnetic topology.

They partition the 3D magnetic flux by considering the field lines from neighbouring fixed points, as indicated in Fig. 3.18, since the integrals along the lines L on the top and bottom boundaries are equal and opposite, so that the flux through the surface is given by the difference of the topological flux functions at the two fixed points (Yeates and Hornig 2011b). They show that, even with chaotic fields, the partition fluxes are defined, as in the 2D case, by the values of $\mathscr{A}(x, y)$ at the fixed points, even though the partition of space into different regions need not be well defined. Also, the global partition reconnection rate is found by summing over the hyperbolic fixed points $\mathbf{x}_p$ as

$$\Delta\phi_P = \sum_{\mathbf{x}_p} \left| \frac{d\mathscr{A}(\mathbf{x}_p)}{dt} \right|. \tag{3.35}$$

They also prove that

$$\frac{\partial \mathscr{A}}{\partial t} + \mathbf{w} \cdot \nabla \mathscr{A} = \int_{\mathbf{x}_0}^{\mathbf{x}_1} \mathbf{E} \cdot d\mathbf{s}, \tag{3.36}$$

where $\mathbf{w}$ is the flux velocity and the integral is taken along a field line through a fixed point. Thus, the rate of change of $\mathscr{A}(x, y)$ along a fixed point field line is the same as the integrated parallel electric field. However, a global reconnection rate found from integrating $\mathbf{E}_\parallel$ may differ from the global partition reconnection rate, since the latter sums reconnection at separators, whereas the former may also include reconnection at other locations.

It should be noted that Eq. (3.36) holds only in a particular gauge where the electrostatic potential (Φ such that $\partial \mathbf{A}/\partial t = -\mathbf{E} - \nabla \Phi$) cancels the $\mathbf{w} \cdot \mathbf{A}$ term. More generally, Russell et al. (2015) have replaced Eq. (3.36) by

$$\frac{\partial \mathscr{A}}{\partial t} + \mathbf{w} \cdot \nabla \mathscr{A} = \int_{\mathbf{x}_0}^{\mathbf{x}_1} \mathbf{E} \cdot d\mathbf{s} + [\mathbf{w} \cdot \mathbf{A} - \Phi]_{\mathbf{x}_0}^{\mathbf{x}_1}, \tag{3.37}$$

Since the right-hand side of Eq. (3.36) is the decay rate of total helicity, the extra terms in Eq. (3.37) are necessary for the field-line helicity to be re-organised more rapidly than the total helicity decays.

3.6 Regimes for Three-Dimensional Reconnection

Null points, separators and quasi-separators are natural weak spots in a magnetic field where current can easily build up and reconnection will tend to occur. We therefore describe here models for reconnection at such locations.

3.6.1 Null Point Reconnection

A study of the kinematics of steady ideal flows in the neighbourhood of a null point or separator suggested three distinct types of 3D reconnection, depending on whether the current focuses along a spine, fan or separator (Priest and Titov 1996). Later, the nature of the flow in the diffusion region was studied and computational experiments set up, leading to a categorisation of null-point reconnection into three modes (Priest and Pontin 2009): *spine-fan reconnection* and *torsional spine reconnection* are driven by twisting motions, but the generic mode observed in numerical experiments in response to shearing motions possesses a strong fan-aligned current with flow across both spine and fan; it is in some sense a combination of spine and fan reconnection, and so we call it *spine-fan reconnection* (Sect. 3.6.1.3).

The kinematic effect of an isolated 3D diffusion region was modelled by Hornig and Priest (2003) by solving

$$\mathbf{E} + \mathbf{v} \times \mathbf{B} = \eta\, \mathbf{j}, \tag{3.38}$$

where $\nabla \times \mathbf{E} = \mathbf{0}$, $\mathbf{j} = \nabla \times \mathbf{B}/\mu$ and $\nabla \cdot \mathbf{B} = 0$. A sufficiently simple magnetic field was imposed that both the field's mapping and its inverse could be found analytically. Writing $\mathbf{E} = \nabla \Phi$, the integral of the component of Eq. (3.38) parallel to $\mathbf{B}$ determines Φ everywhere as an integral along field lines

$$\Phi = \int \frac{\eta\, \mathbf{j} \cdot \mathbf{B}}{B}\, ds + \Phi_e, \tag{3.39}$$

in terms of values (Φ_e) at one end of the field lines and the distance s along them.

The reconnection region may be isolated by choosing a form of η that is localised. So-called *pure* solutions have $\Phi_e \equiv 0$ and can produce counter-rotating (or flipping) flows of field lines that link the diffusion region. The rate of reconnection of flux is then calculated by evaluating the integral

$$\frac{dF_m}{dt} = \int E_\parallel ds \tag{3.40}$$

along a field line through the diffusion region (Schindler et al. 1991; Hesse et al. 2005). Then the flow normal to the field lines is determined by the component of Eq. (3.38) perpendicular to $\mathbf{B}$ as

$$\mathbf{v}_\perp = \frac{(\nabla \Phi - \eta\, \mathbf{j}) \times \mathbf{B}}{B^2}. \tag{3.41}$$

Numerical experiments have been conducted which go beyond the constraints of analytical theory and shed more light on the nature of reconnection at a 3D null. Galsgaard et al. (2003) rotated field lines around the spine and found *torsional fan reconnection* with the current concentrated in the fan plane. Pontin and Galsgaard (2007) instead rotated the field lines near a fan plane and produced *torsional spine reconnection* with strong currents along the spine. Pontin et al. (2007) also investigated *spine-fan reconnection*, with the formation and dissipation of a current sheet in response to shearing the spine (Fig. 3.19).

3.6.1.1 Torsional Spine Reconnection

The above formalism may be applied to steady kinematic behaviour of an isolated cylindrical diffusion region of radius a and height $2b$ containing a spiral null of the form

$$(B_R, B_\phi, B_z) = \frac{B_0}{L_0}\left(R, \tfrac{1}{2}\bar{j}_0 R, -2z\right) \tag{3.42}$$

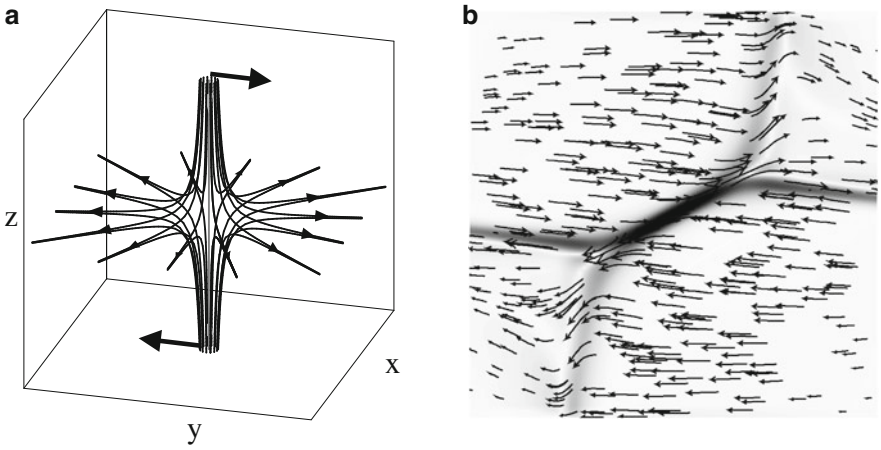

Fig. 3.19 (**a**) A shearing motion of the field lines near a spine that is originally located along the z-axis. (**b**) The resulting collapse of spine and fan to form *spine-fan reconnection*, showing the current-density contours (*shaded*) and flow velocity arrows in the $x = 0$ plane (reprinted with permission of David Pontin)

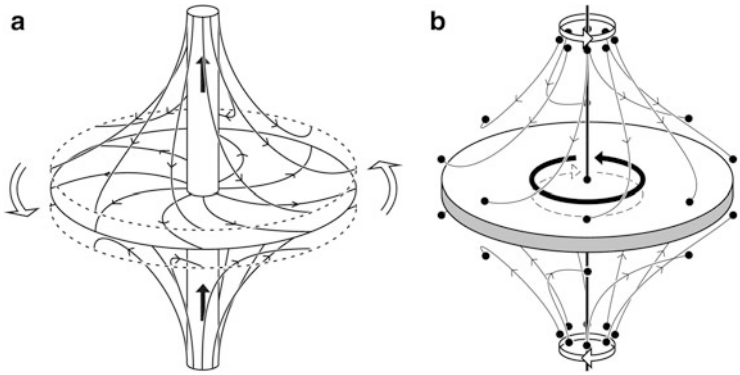

Fig. 3.20 Rotational motions (*open arrows*) of: (**a**) the fan, driving torsional spine reconnection with a strong spine current (*solid arrows*); (**b**) the spine, driving torsional fan reconnection with a strong fan current and slippage of field lines (*solid arrow*)

in cylindrical polars (Pontin et al. 2004), with the spine and current directed along the z-axis, where $\bar{j}_0$ is a dimensionless current density. A rotation of the fan plane drives a current along the spine and creates twisting flows about the spine (Pontin and Galsgaard 2007). Inside the spine current tube, there is rotational slippage, with the field lines becoming disconnected and rotating around the spine (Fig. 3.20a).

The core of such reconnection is a pure elementary solution, with zero flow outside the volume defined by the 'envelope' (F) of flux that threads the diffusion region. Inside F, the flow and flux velocities are purely rotational (i.e., in the ϕ-direction), so that there is no flow across either spine or fan. The reconnection rate

($\int E_\parallel dl$ along the spine) measures the rate of rotational mis-matching of the flux velocities of field lines entering and leaving the diffusion region. Any ideal solution (Φ_{id}) may be added to this, such as a stagnation-point flow ($\Phi_{id} = \phi_0 x_0 y_0$), which brings flux into F and carries it out again. The result is a transition from O-type to X-type flow near the null when ϕ_0 exceeds a critical value.

3.6.1.2 Torsional Fan Reconnection

Here a rotation of field lines near the spine in opposite directions above and below the fan builds up a fan current sheet. In the sheet, field lines experience rotational slippage in the opposite sense above and below the fan (Fig. 3.20b), but there is no flow across either spine or fan. The counter-rotation (above and below the fan) builds up a double-spiral structure near the null point, with a radial current and an axial current that reverses sign at the fan plane.

Such reconnection may be modelled as above for a *double-spiral null* with

$$(B_R, B_\phi, B_z) = \frac{B_0}{L_0}\left(R,\ 2\bar{j}_0 \frac{z^{2M+1}R^{N-1}}{b^{2M+N-1}},\ -2z\right)$$

and M and N positive integers. The magnetic diffusivity inside the diffusion region (D) is $\eta = \eta_0(1 - R^m a^m)(1 - z^n b^n)$, which peaks at the null point and vanishes on the boundary of D when m and n are positive and n is even. As before, the pure non-ideal solution may be calculated and a wide range of ideal solutions added.

3.6.1.3 Spine-Fan Reconnection

Pontin et al. (2005) has applied the same approach to a disc-shaped diffusion region (D) containing a null point with a uniform fan-aligned current $[B_0\bar{j}_0/(\mu L_0)]$ in the x-direction and field components

$$(B_x, B_y, B_z) = \frac{B_0}{L_0}(x, y - \bar{j}_0 z, -2z).$$

Inside the diffusion region [$R_1 < a$, $|z| < b$, where $R_1^2 = x^2 + (y - \bar{j}_0 z/3)^2$], the magnetic diffusivity decreases smoothly and monotonically from the null to zero at its boundary, outside which it vanishes.

In general, if the driving motions shear a null point rather than rotate it, the result will be *spine-fan reconnection*, with the shear distortion focussing in the weak-field region near the null point, forming a localised current sheet (Fig. 3.21). The resulting plasma flow crosses both the spine and fan of the null. Field lines traced from footpoints anchored in the fan-crossing flow flip up and down the spine, whereas those that are traced from the top and bottom of the domain flip around the spine in the fan plane. The reconnection rate is again given by an integral of the form (3.40), taken along the fan field line parallel to the direction of current flow (here the x-

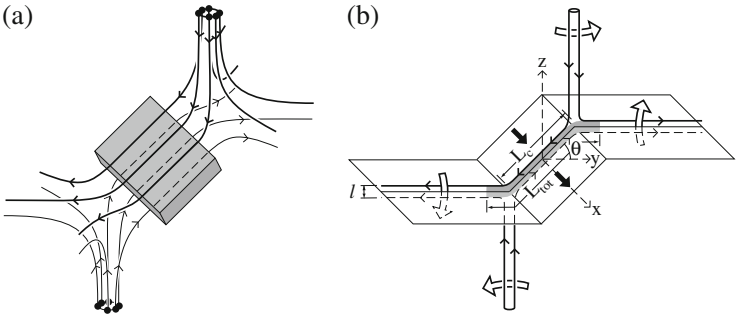

Fig. 3.21 (**a**) The structure of spine-fan reconnection, showing field lines and the (*shaded*) diffusion region. (**b**) Corresponding motion of flux across spine and fan (*large light arrows*). The sheet current flows in the *x*-direction (*large dark arrows*): it has width *l*, total length L_{tot} (in the *yz*-plane), and length L_c common to spine and fan

axis): it equals the rate of flux transport across the fan (separatrix) surface (Pontin et al. 2005).

It is the flux transfer across both spine and fan that distinguishes spine-fan reconnection. Furthermore, the current concentration is in the form of a localised sheet that is inclined at an intermediate angle between the spine and fan. Note that reconnection always occurs at a current sheet of nonzero dimensions rather than at a single point, and so there is a transfer of flux through the current sheet and hence across the fan, although this will generally be smaller than the flux transfer across the more extensive current sheets that can form along separators as follows.

3.6.2 Separator Reconnection

When two nearby null points are present, their two fans will in the generic (structurally stable) case intersect in a *separator* (Fig. 3.22), which is a natural location for the formation of a current sheet and therefore for reconnection. This was demonstrated in a pioneering numerical experiment by Galsgaard and Nordlund (1997) on the response of a periodic force-free equilibrium containing eight null points to footpoint shearing on two boundaries. They discovered that current sheets develop along the separators joining nearby nulls, with Alfvénic jets of plasma ejected out of the sides of the sheets. Then Parnell and Galsgaard (2004); Parnell et al. (2008) modelled coronal reconnection driven by the motion of a pair of opposite-polarity photospheric fragments in an overlying horizontal field. They discovered that the main dissipation mechanism is separator reconnection at multiple separator current sheets in *recursive reconnection*, where the dissipation is enhanced by the same flux being recycled and undergoing reconnection many times. Furthermore, when the separator current is strong enough, the field in transverse planes changes from X-type to O-type.

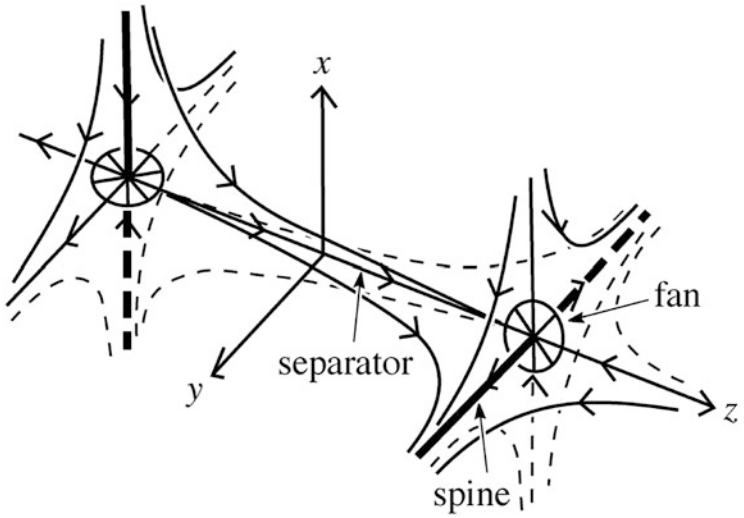

Fig. 3.22 Configuration of magnetic field lines near two nulls including a separator joining one null to the other

Longcope has also developed the idea of the formation and dissipation of separator current sheets (Longcope and Cowley 1996; Longcope 2001) and applied it to coronal heating (Priest et al. 2005). He generalised the two-dimensional theory for current sheet formation in a quadrupolar field (Priest and Raadu 1975) to show how in three dimensions the current and energy storage are related to the change in magnetic flux (Longcope et al. 1998; Longcope and Magara 2004). The ideas have also been applied to the evolution and brightening of an active region (Longcope et al. 2005) and to flares (Longcope and Silva 1998; Longcope and Beveridge 2007). Separator reconnection is probably important in coronal heating, and it may also play a role in accelerating the slow solar wind according to the S-Web model and in releasing energy in solar flares.

3.6.3 Quasi-Separator Reconnection

A region in a magnetic field where the gradient of the footpoint mapping is large is called a Quasi-Separatrix Layer (QSL), the best measure being the *squashing factor, Q* [Eq. (3.23)]. Suppose the field-line velocity components $v_{\perp 1x}$ and $v_{\perp 1y}$ are imposed at a point $(x_1, y_1, 1)$ on the top side $(z = 1)$ of a cube, and deduce the function $\Phi(x_1, y_1)$ together with $\mathbf{E}$ and $\mathbf{v}_\perp$ throughout the cube. The resulting electric field on the base $(z = 0)$ of the cube has components

$$E_{x0} = -\frac{\partial \Phi}{\partial x_1}\frac{\partial x_1}{\partial x_0} - \frac{\partial \Phi}{\partial y_1}\frac{\partial y_1}{\partial x_0}, \qquad E_{y0} = -\frac{\partial \Phi}{\partial x_1}\frac{\partial x_1}{\partial y_0} - \frac{\partial \Phi}{\partial y_1}\frac{\partial y_1}{\partial y_0}, \tag{3.43}$$

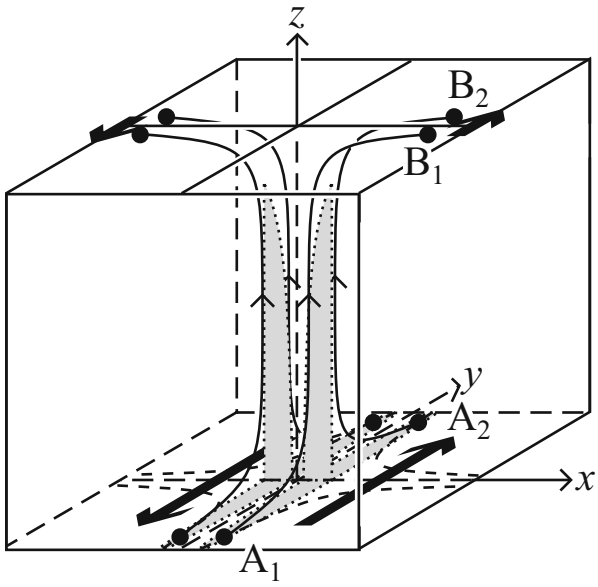

Fig. 3.23 Quasi-separatrix layer (*shaded*) due to large field-line displacement on the bottom of a cube caused by a small displacement on the top. The magnetic field is that of uniform field in the z-direction superposed on the field of an X-point in planes parallel to the xy-plane

which depend partly on the electric field components on the top ($E_{x1} = -\partial\Phi/\partial x_1$, $E_{y1} = -\partial\Phi/\partial y_1$) and partly on the gradients of the mapping functions [$x_1(x_0, y_0)$ and $y_1(x_0, y_0)$]. Thus, $\mathbf{E}_0$ is large where the gradients of the mapping are large, namely in a QSL. This is the crux of why they are so important and why reconnection tends to occur in quasi-separators, namely the intersection of two QSLs, which are essentially the remnants of separatrices.

As an example, suppose we impose on the top ($z = 1$) and side ($x = 12$) of a cube $v_{\perp 1x} = 0, \quad v_{\perp 1y} = v_0 x_1$ and $v_{\perp 1x} = 0, \quad v_{\perp 1y} = \frac{1}{2}v_0$ (Fig. 3.23). Then the base velocity ($z = 0$) along the x-axis ($y = 0$) peaks at $x_0 = \frac{1}{2}\epsilon$ with a value of $v_0/(2\epsilon)$. If this peak exceeds the Alfvén speed, there will exist two diffusive layers centred on $x_0 = \pm\frac{1}{2}\epsilon$, where the field lines are unfrozen and so flip rapidly through the plasma. In other words, the field lines move quicker than the plasma and become disconnected from it.

Any smooth photospheric motion of the footpoints tends to produce strong currents at QSLs. Démoulin et al. (1996) considered an initially potential field $\mathbf{B}_0 = b(X_0, Y_0)\nabla X_0 \times \nabla Y_0$, where (X_0, Y_0) are the horizontal coordinates for the field-line footpoint in the positive flux. They displaced the footpoints by a small amount to give a force-free field ($\mathbf{B}_0 + \mathbf{B}_1$), where $\mathbf{B}_1 = U\nabla X_0 + V\nabla Y_0 + W\nabla S_0$ in terms of

functions (U, V, W) of (X_0, Y_0, S_0). When $W \equiv 0$, the footpoint displacement $(\mathbf{d}_1)$ has the form

$$\mathbf{d}_1 = U \int \frac{\nabla X_0}{B_0} dS + V \int \frac{\nabla Y_0}{B_0} dS, \tag{3.44}$$

where the integrals are taken along field lines. At QSLs, the integrals change their values rapidly with (X_0, Y_0), and so do U and V if $\mathbf{d}_1$ is assumed to vary smoothly. But $\mathbf{j}_1 \times \mathbf{B}_0 = \mathbf{0}$ implies $\mu \mathbf{j}_1 = \alpha(X_0, Y_0)\mathbf{B}_0$, where $\mu \mathbf{j}_1 = \nabla \times \mathbf{B}_1$ in turn implies $\alpha = \partial V / X_0 - \partial U / \partial Y_0$. Thus, the rapid variation of U and V with X_0, Y_0 means that intense currents are generated along the QSLs. Later, Titov et al. (2003) showed how boundary motions that create a stagnation point near the quasi-separator make currents build up exponentially along it, while Aulanier et al. (2005) demonstrated the effect in a resistive MHD experiment.

3.7 Conclusion

The study of reconnection in three dimensions is very much in its infancy. General properties and consequences have been studied and have highlighted just how different this process is in three dimensions, with many new features that are absent in two dimensions. In three dimensions the process is much richer and more varied, and a range of different regimes has been identified, including separator reconnection, quasi-separator reconnection and three different types that occur at null points, the most common being spine-fan reconnection. What they have in common is that they occur after the current density has intensified in the neighbourhood of a null, separator or quasi-separator, and then they occur throughout the resulting diffusion region, with field lines continually changing their connections as they pass through.

In future, many basic questions remain to be answered, such as determining the rates of reconnection for the different regimes, the dimensions of the diffusion region and the conditions for triggering reconnection, as well as the nature of the resulting particle acceleration when the diffusion regions are collisionless. In this task, a combination of sophisticated computational experiment, physical intuition and analytical modelling will continue to be essential.

References

T. Amari, J.F. Luciani, Phys. Rev. Lett. **84**, 1196 (2000)
G. Aulanier, E. Pariat, P. Démoulin, C.R. Devore, Sol. Phys. **238**, 347 (2006)
G. Aulanier, E. Pariat, P. Démoulin, Astron. Astrophys. **444**, 961 (2005)
H. Baty, Phys. Plasmas **19**(9), 092110 (2012). doi:10.1063/1.4752744
H. Baty, T.G. Forbes, E.R. Priest, Phys. Plasmas **16**, 012102/1 (2009a)
H. Baty, E.R. Priest, T.G. Forbes, Phys. Plasmas **16**, 060701/1 (2009b)

M.A. Berger, Geophys. Astrophys. Fluid Dyn. **30**, 79 (1984)
M.A. Berger, Astron. Astrophys. **201**, 355 (1988)
M.A. Berger, in *Magnetic Helicity in Space and Laboratory Plasmas*, ed. by M.R. Brown, R.C. Canfield, A.A. Pevtsov (American Geophysical Union, Washington, 1999), pp. 1–11
M.A. Berger, G. Field, J. Fluid Mech. **147**, 133 (1984)
A. Bhattacharjee, R.L. Dewar, D.A. Monticello, Phys. Rev. Lett. **45**, 347 (1980). doi:10.1103/PhysRevLett.45.347
A. Bhattacharjee, Y.M. Huang, H. Yang, B. Rogers, Phys. Plasmas **16**(11), 112102 (2009)
J. Birn, E.R. Priest, *Reconnection of Magnetic Fields: MHD and Collisionless Theory and Observations* (Cambridge University Press, Cambridge, 2007)
J. Birn, J.F. Drake, M.A. Shay, B.N. Rogers, R.E. Denton, M. Hesse, M. Kuznetsova, Z.W. Ma, A. Bhattacharjee, A. Otto, P.L. Pritchett, J. Geophys. Res. **106**, 3715 (2001)
R.F. Brown, *The Lefschetz Fixed Point Theorem* (Scott Forman, London, 1971)
D.S. Brown, E.R. Priest, Astron. Astrophys. **367**, 339 (2001)
W. Daughton, V. Roytershteyn, B.J. Albright, H. Karimabadi, L. Yin, K.J. Bowers, Phys. Plasmas **16**(7), 072117 (2009). doi:10.1063/1.3191718
P. Démoulin, J. Henoux, E.R. Priest, C.H. Mandrini, Astron. Astrophys. **308**, 643 (1996)
A.M. Dixon, M.A. Berger, E.R. Priest, P.K. Browning, Astron. Astrophys. **225**, 156 (1989)
J.F. Drake, R.G. Kleva, M.E. Mandt, Phys. Rev. Lett. **73**, 1251 (1994)
T.G. Forbes, E.R. Priest, Rev. Geophys. **25**, 1583 (1987)
K. Galsgaard, Å. Nordlund, J. Geophys. Res. **102**, 231 (1997)
K. Galsgaard, E.R. Priest, V.S. Titov, J. Geophys. Res. **108**(A1), SSH 10.1 (2003)
A.L. Haynes, C.E. Parnell, Phys. Plasmas **17**(9), 092903 (2010)
A.L. Haynes, C.E. Parnell, K. Galsgaard, E.R. Priest, Proc. R. Soc. Lond. **463**, 1097 (2007)
M. Hesse, K. Schindler, J. Geophys. Res. **93**, 5539 (1988)
M. Hesse, T.G. Forbes, J. Birn, Astrophys. J. **631**, 1227 (2005). doi:10.1086/432677
J. Heyvaerts, E.R. Priest, Astron. Astrophys. **137**, 63 (1984)
G. Hornig, in *An Introduction to the Geometry and Topology of Fluid Flows*, ed. by R.L. Ricca (Kluwer, Dordrecht, 2001), pp. 295–313
G. Hornig, in *Tubes, Sheets and Singularities in Fluid Dynamics: Fluid Mechanics and Its Applications*, ed. by K. Bajer, H.K. Moffatt (Kluwer, Boston, 2004), p. 133
G. Hornig, E.R. Priest, Phys. Plasmas **10**, 2712 (2003)
G. Hornig, K. Schindler, Phys. Plasmas **3**, 781 (1996)
G. Hornig, A. Wilmot-Smith, in *European Solar Physics Meeting*, vol. 12, ed. by H. Peter (2008), p. 3
Y.M. Huang, A. Bhattacharjee, Phys. Plasmas **17**(6), 062104 (2010). doi:10.1063/1.3420208
J.D. Huba, in *Space Simulations*, ed. by M. Scholer, C. Dum, J. Büchner (Springer, New York, 2003), pp. 170–197
Y.T. Lau, J.M. Finn, Astrophys. J. **350**, 672 (1990)
D.W. Longcope, Phys. Plasmas **8**, 5277 (2001)
D.W. Longcope, Living Rev. Sol. Phys. **2**, 1 (2005)
D.W. Longcope, C. Beveridge, Astrophys. J. **669**, 621 (2007)
D.W. Longcope, S.C. Cowley, Phys. Plasmas **3**, 2885 (1996)
D.W. Longcope, T. Magara, Astrophys. J. **608**, 1106 (2004)
D.W. Longcope, A.V.R. Silva, Sol. Phys. **179**, 349 (1998)
D.W. Longcope, G.H. Fisher, A.A. Pevtsov, Astrophys. J. **507**, 417 (1998)
D.W. Longcope, D. McKenzie, J. Cirtain, J. Scott, Astrophys. J. **630**, 596 (2005)
D.W. Longcope, C. Beveridge, J. Qiu, B. Ravindra, G. Barnes, S. Dasso, Sol. Phys. **244**, 45 (2007)
N.F. Loureiro, A.A. Schekochihin, S.C. Cowley, Phys. Plasmas **14**(10), 100703 (2007)
S. Masson, G. Aulanier, E. Pariat, K.L. Klein, Sol. Phys. **276**, 199 (2012)
H.K. Moffatt, *Magnetic Field Generation in Electrically Conducting Fluids* (Cambridge University Press, Cambridge, 1978)
E.N. Parker, J. Geophys. Res. **62**, 509 (1957)
C.E. Parnell, K. Galsgaard, Astron. Astrophys. **428**, 595 (2004)

C.E. Parnell, J. Smith, T. Neukirch, E.R. Priest, Phys. Plasmas **3**, 759 (1996)
C.E. Parnell, A.L. Haynes, K. Galsgaard, Astrophys. J. **675**, 1656 (2008)
C.E. Parnell, A.L. Haynes, K. Galsgaard, J. Geophys. Res. **115**(A14), 2102 (2010a)
C.E. Parnell, R.C. Maclean, A.L. Haynes, Astrophys. J. Lett. **725**, L214 (2010b)
H.E. Petschek, in *AAS-NASA Symposium on the Physics of Solar Flares* (NASA Spec. Publ. SP-50, Washington, 1964), pp. 425–439
A.A. Pevtsov, R.C. Canfield, S.M. Latushko, Astrophys. J. **549**, L261 (2001)
A.A. Pevtsov, V. Maleev, D.W. Longcope, Astrophys. J. **593**, 1217 (2003)
S.J. Platten, C.E. Parnell, A.L. Haynes, E.R. Priest, D.H. Mackay, Astron. Astrophys. **565**, A44 (2014). doi:10.1051/0004-6361/201323048
D.I. Pontin, K. Galsgaard, J. Geophys. Res. **112**, A03103 (2007)
D.I. Pontin, G. Hornig, ArXiv e-prints (2014)
D.I. Pontin, G. Hornig, E.R. Priest, Geophys. Astrophys. Fluid Dyn. **98**, 407 (2004)
D.I. Pontin, G. Hornig, E.R. Priest, Geophys. Astrophys. Fluid Dyn. **99**, 77 (2005)
D.I. Pontin, A. Bhattacharjee, K. Galsgaard, Phys. Plasmas **14**, 052106 (2007)
D.I. Pontin, A.L. Wilmot-Smith, G. Hornig, K. Galsgaard, Astron. Astrophys. **525**, A57 (2011a)
D.I. Pontin, A.K. Al-Hachami, K. Galsgaard, Astron. Astrophys. **533**, A78 (2011b)
D.I. Pontin, E.R. Priest, K. Galsgaard, Astrophys. J. **774**, 154 (2013). doi:10.1088/0004-637X/774/2/154
E.R. Priest, P. Démoulin, J. Geophys. Res. **100**, 23,443 (1995)
E.R. Priest, T.G. Forbes, J. Geophys. Res. **91**, 5579 (1986)
E.R. Priest, T.G. Forbes, J. Geophys. Res. **97**, 1521 (1992)
E.R. Priest, T.G. Forbes, *Magnetic Reconnection: MHD Theory and Applications* (Cambridge University Press, Cambridge, 2000)
E.R. Priest, D.I. Pontin, Phys. Plasmas **16**, 122101 (2009)
E.R. Priest, M.A. Raadu, Sol. Phys. **43**, 177 (1975)
E.R. Priest, V.S. Titov, Philos. Trans. R. Soc. Lond. **355**, 2951 (1996)
E.R. Priest, D.P. Lonie, V.S. Titov, J. Plasma Phys. **56**, 507 (1996)
E.R. Priest, G. Hornig, D.I. Pontin, J. Geophys. Res. **108**(A7), SSH 6.1 (2003)
E.R. Priest, D.W. Longcope, J. Heyvaerts, Astrophys. J. **624**, 1057 (2005)
A.J.B. Russell, A.R. Yeates, G. Hornig, A.L. Wilmot-Smith, Phys. Plasmas **22**, 032106 (2015)
K. Schindler, M. Hesse, J. Birn, J. Geophys. Res. **93**, 5547 (1988)
K. Schindler, M. Hesse, J. Birn, Astrophys. J. **380**, 293 (1991)
M.A. Shay, J.F. Drake, R.E. Denton, D. Biskamp, J. Geophys. Res. **103**, 9165 (1998). doi:10.1029/97JA03528
J.E.H. Stevenson, C.E. Parnell, E.R. Priest, A.L. Haynes, Astron. Astrophys. **573**, A44 (2015). doi:10.1051/0004-6361/201424348
P.A. Sweet, in *Electromagnetic Phenomena in Cosmical Physics*, ed. by B. Lehnert (Cambridge University Press, Cambridge, 1958), pp. 123–134
J.B. Taylor, Phys. Rev. Lett. **33**, 1139 (1974)
V.S. Titov, Astrophys. J. **660**, 863 (2007)
V.S. Titov, E.R. Priest, P. Démoulin, Astron. Astrophys. **276**, 564 (1993)
V.S. Titov, K. Galsgaard, T. Neukirch, Astrophys. J. **582**, 1172 (2003)
V.S. Titov, T.G. Forbes, E.R. Priest, Z. Mikić, J.A. Linker, Astrophys. J. **693**, 1029 (2009)
V.S. Titov, Z. Mikić, J.A. Linker, R. Lionello, S.K. Antiochos, Astrophys. J. **731**, 111 (2011)
V.S. Titov, Z. Mikic, T. Török, J.A. Linker, O. Panasenco, Astrophys. J. **759**, 70 (2012)
G.E. Vekstein, E.R. Priest, C.D.C. Steele, Astrophys. J. **417**, 781 (1993)
A.L. Wilmot-Smith, E.R. Priest, Phys. Plasmas **14**, 102903 (2007)
A.L. Wilmot-Smith, G. Hornig, D.I. Pontin, Astrophys. J. **696**, 1339 (2009a)
A.L. Wilmot-Smith, G. Hornig, D.I. Pontin, Astrophys. J. **704**, 1288 (2009b)
A.L. Wilmot-Smith, D.I. Pontin, G. Hornig, Astron. Astrophys. **516**, A5 (2010)
A.L. Wilmot-Smith, D.I. Pontin, A.R. Yeates, G. Hornig, Astron. Astrophys. **536**, A67 (2011)
L. Woltjer, Proc. Natl. Acad. Sci. U. S. A. **44**, 489 (1958)
A.R. Yeates, G. Hornig, J. Phys. A **44**(26), 265501 (2011a)

A.R. Yeates, G. Hornig, Phys. Plasmas **18**(10), 102118 (2011b). doi:10.1063/1.3657424
A.R. Yeates, G. Hornig, Phys. Plasmas **20**(1), 012102 (2013). doi:10.1063/1.4773903
A.R. Yeates, G. Hornig, J. Phys. Conf. Ser. **544**(1), 012002 (2014). doi:10.1088/1742-6596/544/1/012002
A.R. Yeates, G. Hornig, A.L. Wilmot-Smith, Phys. Rev. Lett. **105**(8), 085002 (2010)

Chapter 4
Energy Conversion and Inventory of a Prototypical Magnetic Reconnection layer

M. Yamada, J. Yoo, and S. Zenitani

Abstract A comparative review study is made to find basic mechanisms of energy conversion and partitioning in a prototypical magnetic reconnection layer. The recent results from three different disciplines, laboratory experiments, space observations, and numerical simulations, are reviewed. Our quantitative studies of the acceleration and heating of both electrons and ions in the MRX (Magnetic Reconnection Experiment) laboratory experiment and our supporting numerical studies demonstrate that a half of the incoming magnetic energy is converted to particle energy with a remarkably fast speed. Comparing the results from numerical simulations and the MRX experiments, a systematic study is made on the effects of boundary conditions on the energy inventory. In our studies of a relatively wide range of monitoring box sizes in both MRX and 2D simulations, it is observed that 50 % of the inflowing magnetic energy is converted to particle energy, of which 2/3 is ultimately transferred to ions and 1/3 to electrons. These results are also consistent with the recent space measurements in the magnetotail reconnection layer by Eastwood et al. (Phys. Rev. Lett. **110**, 225001, 2013)

Keywords Conversion of magnetic energy • Electron diffusion region • Energy inventory • Energy partitioning • Magnetic reconnection • Particle heating

An important characteristic of magnetic reconnection is that energy is converted from the reconnecting magnetic field to plasma particles through acceleration and heating processes. This paper addresses key unresolved questions on the energetics of magnetic reconnection: How is magnetic energy converted to plasma kinetic energy? How is the converted energy partitioned to ions and electrons?

M. Yamada (✉) • J. Yoo
Princeton Plasma Physics Laboratory, Princeton University, P.O. Box 451, Princeton, NJ 08543, USA
e-mail: myamada@pppl.gov; jyoo@pppl.gov

S. Zenitani
National Astronomical Observatory of Japan, 2-21-1 Osawa, Mitaka, Tokyo 181-8588, Japan

W. Gonzalez, E. Parker (eds.), *Magnetic Reconnection*, Astrophysics and Space Science Library 427, DOI 10.1007/978-3-319-26432-5_4

4.1 Introduction

In most astrophysical plasmas, magnetic field lines are considered to be frozen into the plasma as they move. For instance, in the solar corona or solar winds, the flux freezing allows lines of force to be wound up tightly, thereby storing a large amount of magnetic energy. The process that breaks this frozen-in condition is magnetic reconnection; it allows the field lines to break, to change their topology, and to reconnect, releasing stored magnetic energy. Research on magnetic reconnection, which started with observations of solar flares (Giovanelli 1946), was dominated by analytical theory in the early phase (Parker 1957; Petschek 1964). Recent progress in understanding the physics of magnetic reconnection has been made through the analysis of results from all three research fronts: space and astrophysical observations, laboratory experiments, and theory and numerical simulations; (Zweibel and Yamada 2009; Yamada et al. 2010). Space and astrophysical observations have provided evidence that magnetic reconnection plays an important role in natural plasmas and have strongly motivated fundamental reconnection research. Theory and numerical simulations provide insights into the complex reconnection process by breaking it down into a set of simpler subprocesses. Each subprocess can be independently studied and analyzed in depth in order to improve fundamental physics understanding. Laboratory experiments dedicated to the study of the fundamental reconnection physics measure several key plasma parameters simultaneously at a large number of points across the reconnection region. In contrast, space satellites can provide data only at a few select points. As a result, dedicated laboratory experiments are well suited to quantitatively cross-checking theoretically proposed physics mechanisms and models thereby providing a bridge between space observations and theoretical models.

In the early stage of reconnection research, the main focus was on the rate of reconnection, which was known to occur much faster than predicted by the classical resistive MHD models (e.g. Parker 1957; Biskamp 2000). Over the last two decades, two-fluid effects were found to play an important role in facilitating fast reconnection in collisionless plasmas. This was verified by a close comparison of various theoretical models (e.g. Ma and Bhattacharjee 1996; Birn et al. 2001; Uzdensky and Kulsrud 2006) with space plasma observations (e.g. Nagai et al. 2001; Øieroset et al. 2001; Mozer et al. 2002; Phan et al. 2004) and laboratory results (Yamada 2007; Zweibel and Yamada 2009). Recently, conclusive experimental evidence for two-fluid effects, the quadrupole Hall magnetic field, was found within the reconnection layer (Ren et al. 2005; Yamada et al. 2006; Brown et al. 2006). Simultaneously, non-MHD effects such as the effects of plasma micro-turbulence and kinetic physics were extensively studied. Experimental data was compared with 2D numerical computations using both two-fluid and fully kinetic simulation codes (Murphy and Sovinec 2008; Ji et al. 2008; Dorfman et al. 2008; Daughton et al. 2009; Roytershteyn et al. 2010, 2013), pushing these codes to plasma regimes and system sizes which are closer to realistic conditions in the present day experiments.

In the most recent stage of reconnection research, one of the major goals is to investigate the key mechanisms of energy conversion from the magnetic field to particle kinetic energy across reconnection regions of various scale sizes. This is one of the most important issues in magnetic reconnection research, since it is the energetic aspect of reconnection that are often of primary interest in applying reconnection to astrophysics. This is especially important in heliospheric and astrophysical applications where reconnection is widely invoked as a mechanism underlying explosive and violent energy release phenomena, often powering spectacularly high-energy activity such as solar and stellar flares. An important aspect of the plasma energization during reconnection is the acceleration of a large number of nonthermal particles to very high, sometimes relativistic, energies as determined by the observed signatures in high energy radiation. Particle heating and acceleration during magnetic reconnection have been directly observed in space and laboratory plasmas. A well-known example of energetic particle generation due to magnetic reconnection is solar flares (e.g. Lin 2011). Hard x-ray measurements reveal the generation of energetic electrons up to the MeV range, while Gamma ray measurements indicate the existence of ions up to the GeV range. Surprisingly, some observations show that a significant fraction (up to 50 %) of the released magnetic energy is deposited in energetic particles in solar flares (Lin and Hudson 1976; Lin et al. 2003; Emslie et al. 2005; Krucker et al. 2010). Sometimes a positive correlation was observed between $>$ 300 keV electrons and $>$ 30 MeV protons (Shih et al. 2009). It still remains unknown how such a large number of particles in solar flares become accelerated to non-thermal (tail) energy regimes, although many mechanisms have been suggested for their generation (for a more extensive review, see Zharkova et al. 2011).

Ion acceleration associated with magnetic reconnection has been widely observed both in space and laboratory plasmas. In the Earth's magnetosphere, ion jets close to the local Alfvén velocity (V_A) have been attributed to reconnection outflows (e.g. Paschmann et al. 1979; Gosling et al. 1986; Phan et al. 2000; Øieroset et al. 2001). In the laboratory, ion flow close to V_A was observed during spheromak merging experiments (Brown et al. 2008; Ono et al. 1996, 2011). The in-plane (Hall) electric field has been identified as the cause of the ion bulk acceleration (e.g. Shay et al. 1998) and this mechanism has been verified in a laboratory reconnection layer (Yoo et al. 2013).

Ion heating during reconnection has been observed in the magnetosphere. In space satellite observations, various non-Maxwellian ion distributions have been measured (Hoshino et al. 1998; Wygant et al. 2005). It was pointed out that the strong Hall electric field generates non-Maxwellian distributions inside the separatrices, thereby increasing the effective ion temperature (from the second moment of distributions) significantly (Wygant et al. 2005; Drake et al. 2009). Recently, Phan et al. (2014) reported that the ion internal energy increase is about 20 % of the total incoming magnetic energy via a statistical survey of magnetopause events. Significant ion temperature increase associated with a reconnection event has been measured in laboratory fusion experiments such as in reversed-field pinch (RFP) devices (Fujisawa et al. 1991; Scime et al. 1992; Gangadhara

et al. 2007; Fiksel et al. 2009; Magee et al. 2011), as well as in controlled reconnection experiments (Ono et al. 1996; Hsu et al. 2000; Stark et al. 2005; Ono et al. 2011; Yoo et al. 2013). Recently, Yoo et al. (2013) pointed out that ion heating is caused by the Hall electric field and that a thermalization process called remagnetization occurs in the exhaust region due to stochastic motion of ions and finite collisionality. It is yet to be resolved how ions are thermalized in fully collisionless plasmas. Other mechanisms such as anomalous scattering by a stochastic magnetic field and/or waves have been suggested (Gekelman et al. 1982; Fiksel et al. 2009).

Electron heating related to magnetic reconnection has also been observed both in space and laboratory. In the Earth's magnetotail, a statistical survey on electron thermal temperature as a function of distance from the X point was conducted by Imada et al. (2005). It is interesting that electron heating is observed to occur in the downstream regions somewhat away from the X point. Phan et al. (2013) surveyed magnetopause reconnection exhausts to identify the amount of electron heating and found that only a small fraction ($\sim$2.5 %) of the incoming magnetic energy was converted to electron internal energy. In an early laboratory experiment with a large guide field, magnetic energy conversion to electron thermal energy was studied and the observed heating was attributed to an anomalous resistivity (Stenzel et al. 1982). With one-dimensional (1D) profile measurements of the upstream electron temperature, Ji et al. (2004) reported an anomalous electron heating, and concluded that the observed heating was due to non-classical Ohmic heating beyond the Spitzer resistivity based value (Spitzer 1962). This result has been confirmed by Yoo et al. (2014a) with detailed 2D measurements of the electron temperature. Also the energy in the electron flow was found to be much smaller than the thermal energy (Eastwood et al. 2013; Yamada et al. 2014), while the electron outflow exceeds the Alfvén velocity (Ren et al. 2008b). Despite these numerous measurements, the mechanisms responsible for non-classical electron heating remain unknown.

In this paper, in addition to reviewing detailed mechanisms of ion acceleration and heating, we discuss the overall energy inventory during collisionless magnetic reconnection. A quantitative analysis is carried out in order to determine how much of the incoming magnetic energy is converted to different forms of outgoing energy. We compare space and laboratory measurements with numerical simulations and discuss which mechanisms dictate the energy partitioning and inventory.

In Sect. 4.2, the fundamental energy transport equations are derived and used to briefly review energy conversion in the Sweet-Parker model as well as in two-fluid reconnection. In Sect. 4.3, recent laboratory measurements of energy conversion are presented. In Sect. 4.4, recent space measurements relevant to the energy inventory are discussed. In Sect. 4.5, results from 2D numerical simulations are presented. Finally, in Sect. 4.6, we discuss the current understanding regarding the energy inventory during collisionless reconnection.

4.2 Energy Inventory Analysis

4.2.1 Energy Transport Equations

Fundamentally, the transport and conversion of electromagnetic field energy is governed by Poynting's theorem:

$$\frac{\partial}{\partial t}\left(\frac{B^2}{2\mu_0}+\frac{\epsilon_0 E^2}{2}\right)+\nabla\cdot\mathbf{S}=-\mathbf{J}\cdot\mathbf{E}, \tag{4.1}$$

where $\mathbf{S}=(\mathbf{E}\times\mathbf{B})/\mu_0$ is the Poynting flux. In non-relativistic plasmas, the electric field energy ($\epsilon_0 E^2/2$) is usually neglected. The neglect of inductive electric fields is a valid approximation for the evolution of macroscopic magnetic fields provided that the characteristic timescale is much longer than the light crossing time. In plasmas, the electrostatic field energy may also be neglected due to the assumption of quasineutrality. The term on the right-hand side stands for the work done by the electric field per unit time and unit volume. In a plasma, this term accounts for the energy transfer between the field and the plasma. The condition $\mathbf{J}\cdot\mathbf{E}>0$ and $\mathbf{J}\cdot\mathbf{E}<0$ are referred to as the load and dynamo effects, respectively.

The one-fluid (MHD) energy transport equation is

$$\frac{\partial}{\partial t}\left(u+\frac{\rho}{2}V^2\right)+\nabla\cdot\left[(u+p)\mathbf{V}+\frac{\rho}{2}V^2\mathbf{V}\right]=\mathbf{J}\cdot\mathbf{E}, \tag{4.2}$$

where $p=n_eT_e+n_iT_i$ is the pressure, $u=(3/2)p$ is the internal energy density, $\rho=m_en_e+m_in_i$ is the mass density, and $\mathbf{V}$ is the single-fluid velocity. By combining (4.1) and (4.2), the following energy transport equation can be derived (Birn and Hesse 2005):

$$\frac{\partial}{\partial t}\left(\frac{B^2}{2\mu_0}+u+\frac{\rho}{2}V^2\right)+\nabla\cdot(\mathbf{S}+\mathbf{H}+\mathbf{K})=0, \tag{4.3}$$

where $\mathbf{H}=(u+p)\mathbf{V}$ is the enthalpy flux, and $\mathbf{K}=(\rho/2)V^2\mathbf{V}$ is the flow energy flux.

For two-fluid dynamics, (4.2) and (4.3) are modified to include the microscopic heat flux, $\mathbf{q}$ and the scalar pressure, p, is generalized to the total pressure tensor, $\overline{\mathbf{P}}$:

$$\frac{\partial}{\partial t}\left(u_s+\frac{\rho_s}{2}V_s^2\right)+\nabla\cdot(\mathbf{H}_s+\mathbf{K}_s+\mathbf{q}_s)=\mathbf{J}_s\cdot\mathbf{E}, \tag{4.4}$$

$$\frac{\partial}{\partial t}\left[\frac{B^2}{2\mu_0}+\sum_{s=e,i}\left(u_s+\frac{\rho_s}{2}V_s^2\right)\right]+\nabla\cdot\left[\mathbf{S}+\sum_{s=e,i}(\mathbf{H}_s+\mathbf{K}_s+\mathbf{q}_s)\right]=0. \tag{4.5}$$

Here, u_s is derived from the pressure tensor, $u_s = \mathrm{Tr}(\overline{\mathbf{P}}_s)/2$ and $\mathbf{H}_s = u_s\mathbf{V}_s + \overline{\mathbf{P}}_s \cdot \mathbf{V}_s$ is the enthalpy flux for spices s,

In this form, the only term added to the MHD energy transport equation (2.2) is the divergence of the microscopic heat flux of each species, $\mathbf{q}_s$. If the heat flux at the boundary is negligible and the diagonal terms of the pressure tensor are dominant for both electrons and ions, the two-fluid energy transport equation (4.4) reduces to the MHD energy transport equation (4.2).

With either (4.2) or (4.4), the change in a certain form of energy inside a volume of plasma can be calculated by analyzing the corresponding energy fluxes through the boundary of that volume. Assuming that the system is in steady state, energy of one form must be converted to (from) other forms of energy if the outgoing flux is smaller (larger) than the incoming flux. For example, the efficiency of magnetic reconnection with regards to the conversion of magnetic energy can be estimated by measuring the Poynting flux at each surface on the boundary of the diffusion region. The energy inventory of the other forms of energy (e.g. flow and thermal) can be also obtained by measuring corresponding fluxes through the boundary surfaces.

For the energy inventory analysis in a reconnection layer, it is important to choose a properly sized volume since the energy conversion process occurs not only over the ion diffusion region but also as at so-called reconnection fronts where plasma jets originating from an active reconnection site interact with the background plasmas (Angelopoulos et al. 2013). The energy conversion process at the reconnection front inevitably depend on the boundary conditions there. To exclude effects from a specific choice of boundary conditions, we set the volume size for the energy inventory analysis such that it covers most of the ion diffusion region but not the reconnection fronts. With this limited volume size, the overall energy inventory is somewhat independent from the boundary condition (Yamada et al. 2015).

4.2.2 *Energy Conversion in the Sweet-Parker Model*

The Sweet-Parker model is based on assumptions of steady state, 2D geometry and incompressibility (Sweet 1958; Parker 1957). Under these assumptions, the inflow (V_{in}) and outflow (V_{out}) velocities are calculated based on force balance and mass conservation $LV_{in} = \delta V_{out}$ with L and δ being the half length and half width of the layer respectively, as illustrated in Fig. 4.1. A straightforward calculation (e.g. Priest and Forbes 2000) leads to $V_{out} = V_A$, $\delta = L/\sqrt{\mathcal{L}_q}$, and $V_{in} = V_A/\sqrt{\mathcal{L}_q}$, where $\mathcal{L}_q = \mu_0 L V_A/\eta_{spit}$ is the Lundquist number[1] and η_{spit} is the Spitzer resistivity.

[1]To avoid confusion with the Poynting vector ($\mathbf{S}$), we use $\mathcal{L}_q$ instead of the conventional S to denote the Lundquist number.

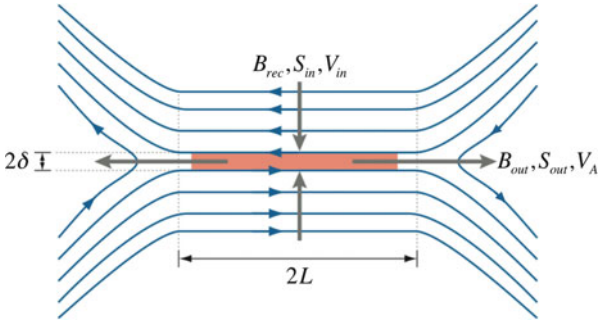

Fig. 4.1 Magnetic geometry for the Sweet-Parker model. Oppositely directed field lines are brought together and reconnect in a diffusion region (*red color*). Figure from Zweibel and Yamada (2009)

Subsequently, the incoming Poynting (S_{in}), flow energy (K_{in}), and enthalpy (H_{in}) flux of reconnection layer are expressed by

$$S_{in} = E_{rec}B_{rec}/\mu_0 = (B_{rec}^2/\mu_0)V_{in}, \tag{4.6}$$

$$K_{in} = \rho V_{in}^3/2 = (1/2\mathcal{L}_q)S_{in}, \tag{4.7}$$

and

$$H_{in} = (5/2)p_{in}V_{in} = (5/4)\beta S_{in}. \tag{4.8}$$

Here E_{rec} is the reconnection (out-of-plane) electric field, B_{rec} is the reconnecting magnetic field, p_{in} is the upstream pressure, and β is the ratio of upstream plasma pressure to magnetic pressure. When $\mathcal{L}_q \gg 1$ and $\beta \ll 1$ as is typical of magnetized astrophysical plasmas, the total incoming flux is dominated by the Poynting flux.

The outgoing fluxes can also be expressed in terms of the incoming magnetic energy flux, S_{in}. Since the reconnection electric field is uniform over the layer from the steady-state assumption, we have that

$$E_{rec} = V_{in}B_{rec} = V_A B_{out}, \tag{4.9}$$

where B_{out} is the magnetic field strength in the exhaust region. The outgoing Poynting (S_{out}) and flow energy (K_{out}) fluxes are given by

$$S_{out} = E_{rec}B_{out}/\mu_0 = S_{in}/\sqrt{\mathcal{L}_q}, \tag{4.10}$$

and

$$K_{out} = \rho V_A^3/2 = (\sqrt{\mathcal{L}_q}/2)S_{in}. \tag{4.11}$$

The outgoing enthalpy flux (H_{out}) can be obtained using (4.2). With the steady-state assumption and the divergence theorem, the relation between the incoming and outgoing fluxes is

$$(S_{in} + H_{in} + K_{in})L = (S_{out} + H_{out} + K_{out})\delta. \tag{4.12}$$

With this relation, and Eqs. (4.6)–(4.11), H_{out} is found to be

$$H_{out} = \left[\left(\frac{1}{2} + \frac{5}{4}\beta\right)\sqrt{\mathcal{L}_q} - \frac{1}{2\sqrt{\mathcal{L}_q}}\right] S_{in}. \tag{4.13}$$

The above equations indicate that most of the incoming electromagnetic energy is dissipated within the rectangular-shaped diffusion region and that the energy is equally split into plasma flow and thermal energy. The change in the magnetic energy (ΔW_M) inside the diffusion region per unit time and unit length along the out-of-plane direction is given by

$$\Delta W_M = -4(LS_{in} - \delta S_{out}) = -4LS_{in}(1 - 1/\mathcal{L}_q). \tag{4.14}$$

The outgoing magnetic energy is smaller than the incoming energy by a factor of $1/\mathcal{L}_q$. Since $\mathcal{L}_q \gg 1$ for most astrophysical and large laboratory plasmas, the outgoing magnetic energy is negligible, which means that most of the incoming magnetic energy is dissipated within the diffusion region by resistivity. Similarly, the changes in the flow (ΔW_K) and enthalpy (ΔW_H) energy are

$$\Delta W_K = 4(LK_{in} - \delta K_{out}) = 2LS_{in}(1 - 1/\mathcal{L}_q) = -\Delta W_M/2, \tag{4.15}$$

$$\Delta W_H = 4(LH_{in} - \delta H_{out}) = 2LS_{in}(1 - 1/\mathcal{L}_q) = -\Delta W_M/2. \tag{4.16}$$

Thus, there is an equipartition between the flow and thermal energy gain in the Sweet-Parker model (Priest and Forbes 2000). This equipartition means that half of the incoming magnetic energy must be converted to flow energy in order to achieve the required Alfvénic outflow.

4.2.3 *Energy Conversion in Two-Fluid Reconnection*

Because electron and ion dynamics are quite different in the two-fluid regime, a quantitative analysis of the energy partition in a two-fluid reconnection layer is

difficult to carry out. In fact, this difficulty is closely related to the fact that there is presently a lack of a general theory of two-fluid reconnection. Such a theory should be able to self-consistently predict key reconnection parameters such as the reconnection rate, plasma outflow velocity, layer aspect ratio, as well as energy deposition. It is known that the reconnection mechanisms can depend on many factors including the boundary condition, asymmetry in upstream parameters, and the strength of the guide field. Here we assume a 2D anti-parallel geometry and describe how the energy inventory in the two-fluid reconnection layer (Fig. 4.2) is qualitatively different from that in the Sweet-Parker model.

Figure 4.2 illustrates a schematic diagram of two-fluid reconnection. Since the ion skin depth is larger than the electron skin depth, ions are demagnetized first and form a large ion diffusion region (gray color). Electrons are frozen to the field lines and convected through the ion diffusion layer until they reach the small electron diffusion region (orange color). This two-scale diffusion layer has been experimentally identified (Ren et al. 2008b) by checking where the ideal condition, $\mathbf{E} + \mathbf{V}_s \times \mathbf{B} = 0$ for $s = e, i$, is violated. Outside the electron diffusion region, $\mathbf{E} + \mathbf{V}_e \times \mathbf{B} = 0$ mostly holds; namely the out-of-plane reconnection electric field is balanced by $\mathbf{V}_e \times \mathbf{B}$.

Energy deposition to electrons occurs mostly within the electron diffusion region (EDR) and at the separatrices (black dashed lines in Fig. 4.2) (Pritchett 2010; Yoo et al. 2014a). Energy conversion in the EDR can be discussed via a Sweet-Parker-type scaling analysis. Since the EDR is relatively small compared to the ion scale, the incompressible assumption of the Sweet-Parker model is generally valid. As a result, the electron outflow $V_{e,out} \sim (L_e/\delta_e)V_{e,in}$, where L_e and δ_e are the half length and half width of the EDR, respectively, and $V_{e,in}$ is the electron inflow speed. From (4.9), one can show that the outgoing magnetic energy is $(L_e/\delta_e)^2$ times smaller than the total incoming magnetic energy into the EDR. Since $(L_e/\delta_e) \gg 1$,

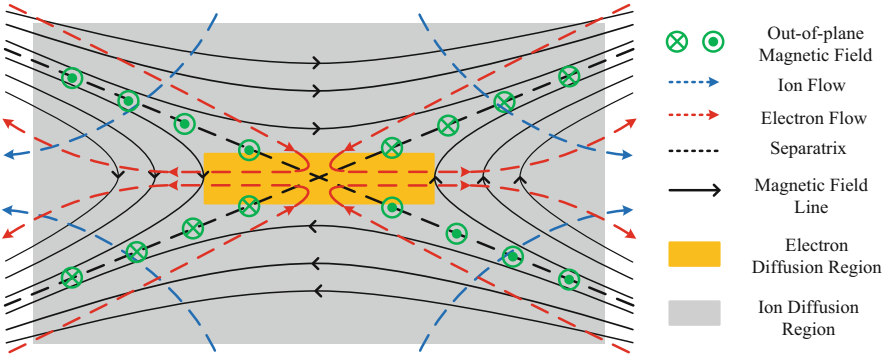

Fig. 4.2 Schematic picture of two-fluid reconnection. Ions decouple from electrons in the ion diffusion region (*gray color*). Electrons are frozen to the field lines until they reach to the electron diffusion region (*orange color*). The electron flow pattern creates the quadrupole out-of-plane magnetic field, a signature of the Hall effect. Figure from Yamada et al. (2015)

the outgoing magnetic energy is negligible. Then, the ratio between the electron flow energy gain, ΔW_{Ke} and the incoming magnetic energy to the electron diffusion region, ΔW_{Me} becomes

$$\frac{\Delta W_{Ke}}{\Delta W_{Me}} = \frac{1}{2}\left(\frac{V_{e,out}}{V_{Ae}}\right)^2 = \frac{1}{2}\left(\frac{L_e}{\delta_e}\right)^2\left(\frac{m_e}{m_i}\right)^2\left(\frac{V_{e,in}}{V_A}\right)^2, \tag{4.17}$$

where $V_{Ae} = B_{rec}/\sqrt{\mu_0 m_e n_e}$ is the electron Alfvén velocity. The electron outflow velocity is generally less than V_{Ae} (e.g. Daughton et al. 2006; Ren et al. 2008a), which means that the flow energy increase is less than half of the incoming magnetic energy into the EDR.

For a more quantitative discussion, both the half length (L_e) and width (δ_e) of the electron diffusion region need to be specified. Many simulations (e.g. Daughton et al. 2006; Shay et al. 2007; Karimabadi et al. 2007; Pritchett 2010; Zenitani et al. 2011a) and experiments (Ren et al. 2008a) show that L_e is on the order of several ion skin depths ($d_i = c/\omega_{pi}$). On the other hand, there is a long-standing discrepancy in δ_e between simulations and experiments; δ_e is much larger in experiments (6–10d_e; $d_e = c/\omega_{pe}$, electron skin depth) than in kinetic simulations (1–2d_e) (Dorfman et al. 2008; Ji et al. 2008; Roytershteyn et al. 2010, 2013). As a result, the electron outflow velocity in experiments is about $0.1V_{Ae}$ (Ren et al. 2008a), smaller than the values in 2D simulations. Therefore, the electron flow energy increase in MRX is only about 5 % of the total energy gain and the rest of the energy is converted to electron enthalpy or comes out as the heat flux (Yoo et al. 2014a).

A Sweet-Parker-type scaling analysis can be also applied for a qualitative discussion on energy conversion in the ion diffusion region (IDR). However, the incompressible assumption is not generally valid there; density in the exhaust region is higher than that in the inflow region (e.g. Ji et al. 1998; Hesse et al. 2001; Pritchett 2001; Shay et al. 2001; Daughton et al. 2006; Dorfman et al. 2008). After considering the density difference, mass conservation yields

$$V_{i,out} \sim \frac{L_i}{\delta_i}\frac{n_{in}}{n_{out}}V_{i,in}, \tag{4.18}$$

where L_i and δ_i are the half length and width of the IDR, n_{in} and n_{out} are the density in the inflow and outflow region, and $V_{i,in}$ and $V_{i,out}$ are the ion inflow and outflow speed, respectively. The typical aspect ratio (L_i/δ_i) of the IDR is 3–5, and the density ratio (n_{in}/n_{out}) is 0.3–0.5, depending on the boundary condition (e.g. Hesse et al. 2001; Daughton et al. 2006; Dorfman et al. 2008; Yoo et al. 2013). The inflow ion speed, $V_{i,in}$ in collisionless (two-fluid) reconnection ranges from 0.1–0.2 V_A (e.g. Birn et al. 2001). With these values, the ion outflow becomes smaller than the Alfvén velocity, typically about $0.5V_A$ in particle-in-cell (PIC) simulations and experiments (e.g. Shay et al. 2001; Karimabadi et al. 2007; Zenitani et al. 2013; Yoo et al. 2013, 2014b). As a result, the ion flow energy gain, ΔW_{Ki} is only about 10 % of the total incoming magnetic energy to the IDR, W_{Mi}, which means that the ion energy gain is

dominated by an enthalpy increase (Aunai et al. 2011; Eastwood et al. 2013; Yamada et al. 2014).

Another interesting feature of energy conversion in the IDR is that the outgoing magnetic energy is not negligible due to the relatively small aspect ratio. From (4.7), the outgoing magnetic field is determined by the ratio between ion inflow and outflow speeds. Unlike in the Sweet-Parker model, B_{out} is not negligible since the inflow and outflow speeds are not strongly separated. Moreover, there is also an outgoing Poynting flux associated with the Hall fields, i.e. the out-of-plane magnetic field and in-plane electric field. For reconnection with a negligible guide field, this outgoing flux (S_{Hall}) is larger than the conventional (MHD) outgoing Poynting flux associated with B_{out} and E_{rec}, S_{MHD} (Shay et al. 2011; Eastwood et al. 2013; Yamada et al. 2014).

One natural question regarding energy conversion in two-fluid reconnection is the ratio of the electron energy gain to ion energy gain. This is non-trivial because two-fluid reconnection involves several internal structures on different scales such as the EDR, the IDR, and the separatrix region. For example, a $\mathbf{j}_e \cdot \mathbf{E}$ profile shows that it is strongly positive inside the EDR, becomes negative just outside the EDR where the electron outflow speed exceeds the local $\mathbf{E} \times \mathbf{B}$ velocity, and is mostly positive but structured along the separatrices (Pritchett 2010).

Regardless of aforementioned complications, an important aspect of energy conversion in two-fluid reconnection is that ions can gain more energy than electrons. The energy conversion inside the IDR but outside the EDR is dominated by ion energy gain due to the large Hall electric field. The incoming magnetic energy to the EDR and the IDR is proportional to L_e and L_i, respectively. Since L_i ($> 10d_i$, unless limited by the system size or boundary condition) is 3–10 times larger than L_e, the total ion energy gain can easily exceed the total electron energy gain. In the following sections, more quantitative discussions on energy conversion and partitioning in two-fluid reconnection are presented, based on observations in laboratory, space, and numerical simulations.

4.3 Recent Quantitative Study of Energy Conversion Processes in a Laboratory Reconnection Layer

Heating and acceleration of plasma particles during magnetic reconnection processes have been observed in many fusion plasma devices as well as in laboratory experiments dedicated to the fundamental study of magnetic reconnection (Yamada et al. 2010). For example, in a reversed field pinch (RFP) device, a relaxation phenomenon occurs and global magnetic structures are reorganized into a lower magnetic energy state (Taylor 1986). During this self-organization process, it is observed that the magnetic energy is converted to plasma particles, ions particularly gain considerable energy, due to reconnection process. Despite these clear observations, it is difficult from these measurements to identify and describe the

energy flow pattern because the heating mechanisms are not well understood. Furthermore, as with any discussion of temperature, the non-trivial global transport and confinement of particles must be considered. In experiments dedicated to reconnection research, energy transfer from magnetic to plasma thermal energy was observed during the merging of two toroidal plasmas in the TS-3 experiment (Yamada et al. 1990; Ono et al. 1996). A violent plasma acceleration was seen in the toroidal direction as the field lines contract after the merging and bulk plasma acceleration and ion heating were documented. The SSX experiment was also utilized to study ion heating and acceleration during merging (Kornack et al. 1998). More recently, a significant local heating of electrons and global ion heating has been observed in the MAST experiment (Ono et al. 2015). While these results are very interesting and unique, the exact mechanisms of energy conversion have not yet been identified.

In this section, we present recent results from a laboratory experiment in which a well-defined reconnection layer is generated in a controlled manner. This allows energy conversion mechanisms and the partitioning of energy flow to be quantitatively studied and documented. In MRX, the energy conversion and inventory have been extensively studied for the past several years in a nearly collision-free reconnection layer (Yoo et al. 2014a; Yamada et al. 2014, 2015). This has enabled MRX to produce the first map of energy conversion processes within the ion diffusion region, as well as a quantitative analysis on the energy inventory within a well-defined reconnection layer.

Figure 4.3 shows a schematic of the MRX apparatus (a) together with the measured flow of electrons and ions in the reconnection layer (b), wherein two oppositely directed field lines merge and reconnect. Each flux core (darkened section in Fig. 4.3a) contains both toroidal field (TF) and poloidal field (PF) coils. By pulsing both PF and TF coil currents in a controlled manner, a proto-typical reconnection layer is generated and a detailed energy inventory study is carried out (Yamada et al. 2015). For standard conditions of $n_e \sim 2\text{–}6 \times 10^{13}$ cm^{-3}, $T_e = 5 - 15$ eV, $B = 0.1 - 0.3$ kG, $\mathcal{L}_q > 400$; the electrons are well magnetized ($\rho_e \ll L$; ρ_e is the electron gyro-radius) while the ions are not. The mean free path for electron-ion Coulomb collisions is in the range of 5–20 cm ($>$ the layer thickness), and, as a result, the reconnection dynamics are dominated by two fluid and kinetic physics (Yamada 2007; Yamada et al. 2010). We employ a coordinate system (R, Y, Z) where B_z is reconnecting field component and Y is the out of plane axis.

For this study, all available MRX diagnostics were utilized including magnetic probes which measure all three components of the magnetic field, Mach probes measuring ion flows, an array of triple Langmuir probes for measuring electron temperature and density, and ion dynamics spectroscopy probes (IDSPs) to measure ion temperature (Fiksel et al. 1998). The electron flow vectors are derived by the current density profile measured by fine scale magnetic probes. That is, $\mu_0 \mathbf{J} = \nabla \times \mathbf{B}$ and $\mathbf{V}_e = \mathbf{V}_i - \mathbf{J}/n_e e$.

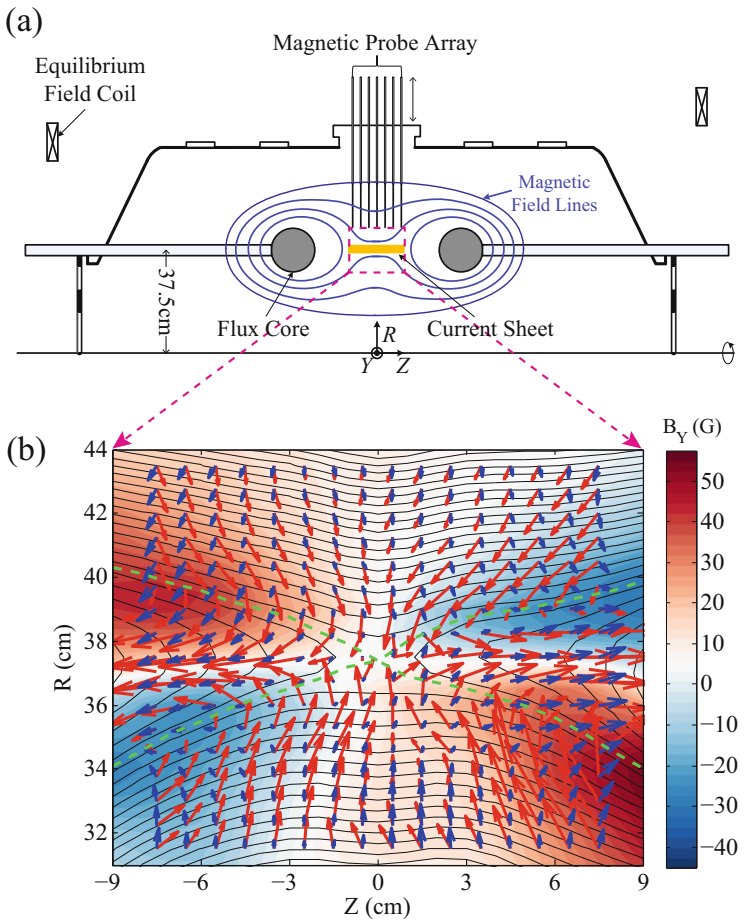

Fig. 4.3 (**a**) MRX apparatus and reconnection drive. (**b**) Measured flow vectors (length represent velocity) of electrons (*red arrows*) and ions (*blue*) in the full reconnection plane together with poloidal flux contours (which represent reconnecting field line components projected in the reconnection plane) and out of plane field contours; 1 cm vector length stands for about 2×10^6 cm/s, color contours represent out-of-plane field strength, and *green broken lines* depict (experimentally identified) separatrix lines. A toroidal symmetry is assumed. Figure from Yamada et al. (2015)

4.3.1 Electron Dynamics and Heating in the Two-Fluid Reconnection Layer

Figure 4.3b depicts the flow vectors of ions (in blue) and electrons (red) across the whole reconnection plane together with poloidal flux contours (black lines, representing magnetic field lines) and colored contours of the out-of-plane magnetic field component. One can see the typical reconnection features in which the

magnetic field strength weakens near the X point, the electron drift flow velocity in the reconnection plane becomes very large near the X point and electrons flows out to the exhaust region. Figure 4.4a presents measurements of the electron flows in a 3D view along one half of the reconnection plane. Ions, which become demagnetized as they enter the ion diffusion region (whose width is $\sim d_i \sim 5$–6 cm), are accelerated and flow outwards along the exhaust direction, as seen in Fig. 4.3b. In contrast, the magnetized electrons flow inwards towards the X point across the field lines. The quadrupole out-of-plane magnetic field profile, a signature of the Hall effect, is clearly visible in the color contours of Fig. 4.3b.

As the incoming field lines are convected inwards, they are stretched along the Y direction (out-of-plane) due to the Hall effect, as shown in Fig. 4.4a. Once entering the EDR, magnetic field lines break and electrons quickly flow out along the exhaust direction. In the upstream (inflow) section of the MRX reconnection layer, the electron inflow velocity is measured to be small ($V_e \sim V_i \ll V_A$) as expected, however the electron outflow velocity is measured to be much faster ($\sim 5V_A$). One can observe that electrons flow out almost orthogonal to magnetic field lines (Fig. 4.4a) near the X point. Further away from the X point, electrons appear to pull newly reconnected field lines towards the exhaust in the outflow region.

The energy deposition rate on electrons, $\mathbf{j}_e \cdot \mathbf{E}$, is concentrated near the X point as seen in Fig. 4.4b. This measured energy deposition region is significantly broader ($\sim 10d_e$) than predicted by numerical simulations (e.g. Pritchett 2010). The MRX data indicates that electron heating also takes place in the wide exhaust region, as seen in Fig. 4.4c. It is noteworthy that when $\mathbf{j}_e \cdot \mathbf{E}$ is decomposed into $\mathbf{j}_{e\perp} \cdot \mathbf{E}_\perp$ and $j_{e\parallel}E_\parallel$, $\mathbf{j}_{e\perp} \cdot \mathbf{E}_\perp$ is found to be more than an order of magnitude larger than $j_{e\parallel} \cdot E_\parallel$ near the X point where energy deposition is maximal. Here parallel and perpendicular directions are defined with respect to the local magnetic field, $\mathbf{B}$. While an electron temperature rise was measured near the X point, the extent of the high temperature region is even wider than the electron diffusion region as can be seen Fig. 4.4c. The measured 2D electron temperature profile indicates that fast electron heat conduction occurs along the magnetic field lines in the exhaust. We note that Ohmic dissipation based on the perpendicular Spitzer resistivity accounts for less than 20 % of the required heating power.

4.3.2 Ion Acceleration and Heating in the Potential Well of the Reconnection Layer

Within the ion diffusion region, electrons flow differently from ions. This flow of magnetized electrons generates strong electric fields within the reconnection plane, especially near the separatrices, as shown in Fig. 4.5a. It has been experimentally demonstrated that this strong electric field is equivalent to the saddle shaped electric potential profile formed in the reconnection plane in order to balance the Lorentz force on the electron flow (Yoo et al. 2013). This potential structure gets wider and

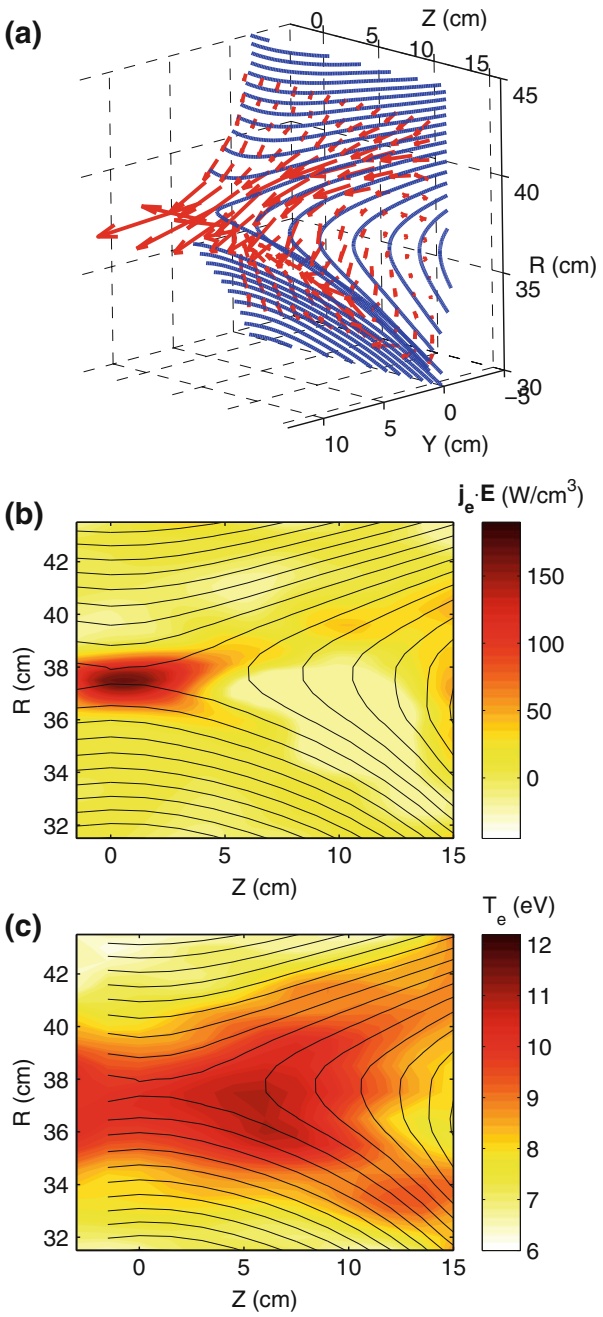

Fig. 4.4 (**a**) Measured flow vectors of electrons in a half reconnection plane in its bird's eye view in 3D geometry. (**b**) and (**c**) While the energy deposition to electrons, $\mathbf{j}_e \cdot \mathbf{E}$, is concentrated near the X point (**b**), strong electron temperature rise is observed in the wide area of the exhaust region (**c**). Figure from Yamada et al. (2015)

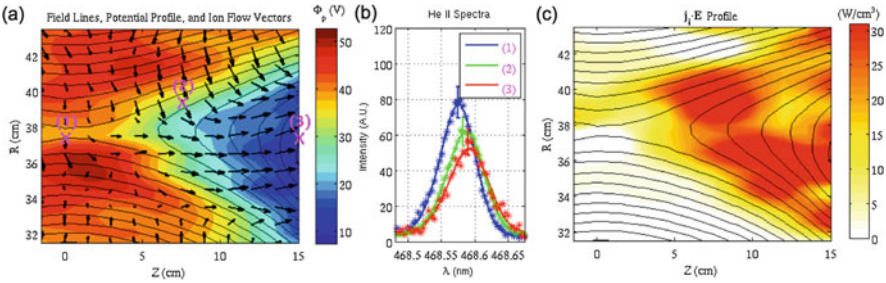

Fig. 4.5 (**a**) Measured potential profile of one half of the two-fluid reconnection layer together with ion flow vectors (length represent velocity) measured by Mach probes. (**b**) He II 4686 Å spectra at three locations marked with X in (**a**). Broadening and shifting in the downstream region indicate ion heating and acceleration. (**c**) 2D profile of the ion energy gain, $\mathbf{j}_i \cdot \mathbf{E}$. Energy conversion to ions occurs throughout the downstream region. Figure from Yamada et al. (2015)

broader downstream of the X point. The MRX potential profile is consistent with measurements by the CLUSTER spacecraft (Wygant et al. 2005), which showed a narrow potential well near the X point with a half width in the range of 60–100 km (3–5 d_e), and a deeper and wider well towards the exhaust region. The in-plane Hall electric field, (i.e. potential drop) is mostly perpendicular to the local magnetic field lines, and is strongest across the separatrices. As clearly seen in Fig. 4.5a, the electric potential is seen to be nearly constant along a poloidal flux contour (or the magnetic field line). In this figure, it should be noted that a large electric field across the sepratrices extends to a significantly larger area of the reconnection layer ($L \gg d_i$) than the region in which field line breaking and reconnection occur. A typical magnitude of the in-plane electric field E_{in} is $\sim$ 700 V/m, which is much larger than the reconnection electric field $E_{rec} \sim 200$ V/m.

Figure 4.5a also shows the 2-D profile of the ion flow vectors. From this data, it is clear that ion flows change directions at the separatrices and are accelerated in both the Z and the R directions. Figure 4.5b depicts the spectrum of the 4686Å line of helium ions measured by the IDSP probes at three locations. This spectrum profile represents the local velocity distributions of ions versus V_Z. The spatial resolution of the IDSP probes is 4 cm. Shifted Maxwellian distributions are observed at three typical positions, as shown in Fig. 4.5b. Electrostatic acceleration of ions occurs at the separatrix area and converts magnetic energy to ion kinetic energy. Figure 4.5c presents the profile of the energy deposition to ions $\mathbf{j}_i \cdot \mathbf{E}$. Comparing with Fig. 4.4b where the energy deposition rate to electrons is shown, the energy deposition to ions occurs across a much broader region of the ion diffusion region.

Ion heating is observed downstream along the exhaust. It was noted that ions must lose considerable momentum as they pass though the downstream region and are subsequently thermalized. The cause of this anomalously fast slowdown of ions, together with the ion heating, is thought to be due to "remagnetization" of the exiting ions. Downstream, the reconnected field lines pile up and so the local magnetic field strength is quite large, allowing ions to become magnetized. Two dimensional

kinetic simulations have been carried out to verify this remagnetization and to understand how ions are heated downstream (Yoo et al. 2014b). A reasonably good agreement between the observed ion temperature profile and numerical simulation was obtained only when realistic collision frequencies were used, indicating that ion thermalization is due to remagnetization with the addition of finite collisionality in the downstream region.

4.3.3 *Inventory of Converted Energy in the Two-Fluid Reconnection Layer*

During the two-fluid reconnection processes, it was found that the energy conversion to electrons and ions occurs across very different regions and via quite different mechanisms. Now let us identify how much of the magnetic energy is transferred to plasma particles.

The energy inventory is calculated by monitoring the changes of magnetic energy and the enthalpy of ions and electrons, while measuring the incoming and outgoing magnetic flux, enthalpy flux, and bulk flow flux (kinetic energy flux), and additional loss such as heat conduction loss. All of these quantities are measured within and along the well-defined boundary shown in Fig. 4.6. This boundary encloses a plasma volume, $\mathcal{V}_b$, and is given by $31.5 \leq R \leq 43.5\,\text{cm}$, and $0 \leq Z \leq 15\,\text{cm}$. An assumption of symmetry is made with respect to the major axis of the MRX plasma (i.e. along the out-of-plane direction). All key parameters are measured locally with typical error bars of 10–15 %. Here we define the incoming Poynting flux, $S_{in} = (E_Y B_Z/\mu_0)e_R$ to be associated with the reconnection electric field and reconnecting magnetic field whereas the outgoing Poynting flux is divided into

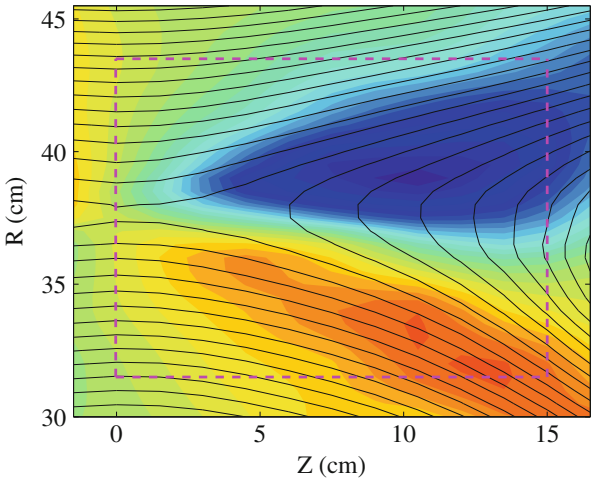

Fig. 4.6 Boundary for the MRX energy inventory analysis. The *dashed magenta box* ($\sim 2d_i \times 2d_i$) shows the region where the energy inventory analysis is conducted. The *color* indicates out-of-plane quadrupole field, and the *black lines* are the poloidal flux contours that represent the magnetic field lines

the MHD component, $S_{MHD} = -(E_Y B_R/\mu_0)e_Z$ and the Hall field component, $S_{Hall} = (E_R B_Y/\mu_0)e_Z - (E_Z B_Y/\mu 0)e_R$. An isotropic pressure is assumed in this calculation, just as was done by Birn and Hesse (2005). This assumption can be justified in our plasma where only a small anisotropy was observed and only within in a limited region near the X point.

We estimate the energy loss rate of each species by considering the electron and ion heat flux, electron energy loss by impurity radiation, and ion energy loss to neutrals by charge-exchange collisions. The heat flux loss through the boundary was estimated by the formulation in Braginskii (1965). The radiation losses are assumed to be due solely to oxygen radiation, as justified by spectral measurements made using the IDSPs. In Fig. 4.7, all quantities are normalized by the rate of incoming of magnetic energy, 1.9 MW. The outgoing Poynting flux is sizable in MRX due to the two-fluid reconnection physics. This outgoing Poynting flux is primarily due to the Hall fields. It is also quantitatively evaluated how much of the magnetic energy is converted to thermal and flow (kinetic) energy of electrons and

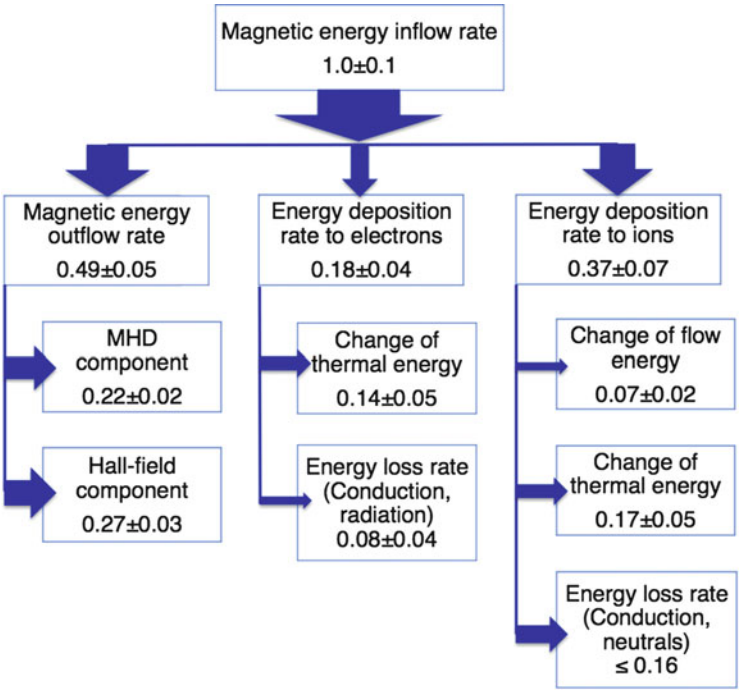

Fig. 4.7 Partitioning of the converted magnetic energy in the MRX reconnection layer. All quantities are normalized to the rate of energy inflow, $W_{M,in} = 1.9$ MW. The outgoing Poynting flux is sizable in MRX where two-fluid reconnection occurs because of outgoing energy associated with the Hall field components. Our quantitative measurements show that a half of the incoming magnetic energy is converted to particle energy with a remarkably fast speed, $\sim 0.2(B^2/2\mu_0)V_A$. Figure from Yamada et al. (2014)

ions in the volume $\mathcal{V}_b$. In our local energy flux inventory, about half of incoming magnetic energy is converted to particle energy, 1/3 of which goes to electrons and 2/3 to ions. Our quantitative measurements show that half of the incoming magnetic energy is converted to particle energy at a remarkable fast rate, $0.2(B^2/2\mu_0)V_A$. This value is larger than the value calculated by the classical Sweet-Parker rate, $(B^2/2\mu_0)V_A/\sqrt{\mathcal{L}_q} = 0.03(B^2/2\mu_0)V)A$ for $\mathcal{L}_q = 900$. If we apply our results to space and astrophysical plasmas with much larger $\mathcal{L}_q$, the difference would become significantly larger.

We note here that the final temperatures of plasma particles after reconnection should depend both on the energy deposition rate and the loss rate of for each component. For example, in plasma fusion devices the ion confinement time is generally longer than that of electrons. When magnetic reconnection occurs, the magnetic energy is transferred to ions and electrons through acceleration and dissipation mechanisms, and their final temperatures are determined by the balance of both the energy deposition and loss. Such an example is shown in Fig. 4.8 (Magee 2011). During magnetic reconnection in an RFP devise, a notable change was observed in the magnetic field equilibrium together with a large reduction of the stored magnetic energy as seen in Fig. 4.8a. While the ion temperature increase is significant, the electron temperature actually decreases, as seen in Fig. 4.8b. This is thought to be due to increased electron losses as a result of the reconnection process. Generally about 20–30 % of magnetic energy is observed to be transferred to ion thermal energy in RFP relaxation events. The above MRX results in which

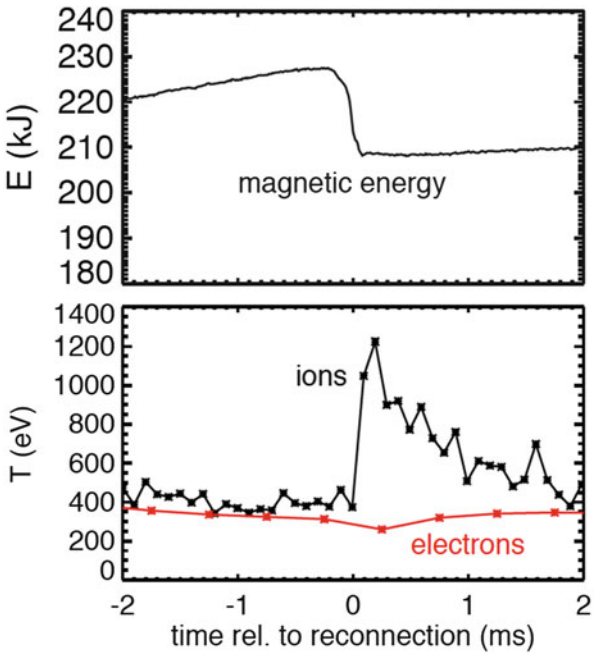

Fig. 4.8 Time evolution of total magnetic energy (*upper panel*) and the temperature of ion (*black*) and electrons (*red*) versus time (ms) re-normalized to the time of relaxation (*lower panel*). Figure from Magee (2011)

30–35 % of magnetic energy is transferred to ion enthalpy in a typical reconnection layer, is consistent with the general energy inventory of relaxation phenomena in RFP devices. However, more quantitative analysis are required in order to reveal the detailed characteristics of the RFP relaxation phenomena.

In magnetosphere plasmas, the measured ion temperature is generally observed to be about six times higher than that of electrons. This characteristic could be explained by fast electron heat conduction loss from the reconnection area, similarly as observed in the above laboratory experiments, while the ion energy confinement time is much longer than that of electrons.

4.4 Measurements of Energy Conversion in Space

It is difficult to obtain the complete energy inventory for a reconnection event in space, since the number of satellites is limited and the proximity to the X point is hard to determine. It would be even harder to evaluate the energy inventory in a well defined reconnection layer. Thus, recent space results relevant to the energy inventory mostly came from statistical surveys of reconnection events.

The most extensive quantitative analysis on the energy inventory in space was conducted by Eastwood et al. (2013). There, a collection of 18 Cluster encounters with anti-parallel reconnection events in the magnetopause is examined in order to measure the partition of outgoing energy fluxes such as Poynting (S_x) and enthalpy fluxes of plasma particles. They used the ion outflow velocity ($v_{i,x}$) as an important proxy for evaluating the distance of the satellite from the X point. They evaluated quantitatively the amount of the Poynting flux, electron and ion flow energy ($K_{e,x}$ and $K_{i,x}$), enthalpy ($H_{e,x}$ and $H_{i,x}$), and heat ($Q_{e,x}$ and $Q_{i,x}$) fluxes for antiparallel symmetric reconnection in the Earth's magnetotail.

Figure 4.9 shows the normalized absolute energy fluxes as a function of the normalized outflow velocity. The positive (negative) normalized outflow means that the satellite is on the earthward (tailward) side. The electron kinetic flux is negligible compare to others, and the ion heat flux is about one order of magnitude smaller than the electron heat flux. The MHD Poynting flux, S_{MHD} is the outgoing Poynting flux associated with the reconnection electric field and the normal magnetic field, such that $S_{MHD} = E_y B_z/\mu_0$. It is worth noting that the outgoing Poynting flux associated with the Hall fields, $S_{Hall} = -E_z B_y/\mu_0$ is larger than S_{MHD}, since the total Poynting flux is one order of magnitude larger than S_{MHD}, as shown in Fig. 4.9. There are also clear asymmetries between earthward and tailward fluxes especially in the electron heat flux and ion enthalpy flux.

Although the incoming energy fluxes also need to be specified in order to perform a complete analysis of the energy inventory, most of them could not be measured due to the low plasma density in the lobe (inflow) region. The only measured quantity in the inflow region is the lobe magnetic field (B_L), which is closely related to the incoming magnetic energy. The incoming energy flux is dominated by the Poynting flux since $\beta \ll 1$ and $\mathcal{L}_q \gg 1$. Both incoming flow energy and enthalpy fluxes are

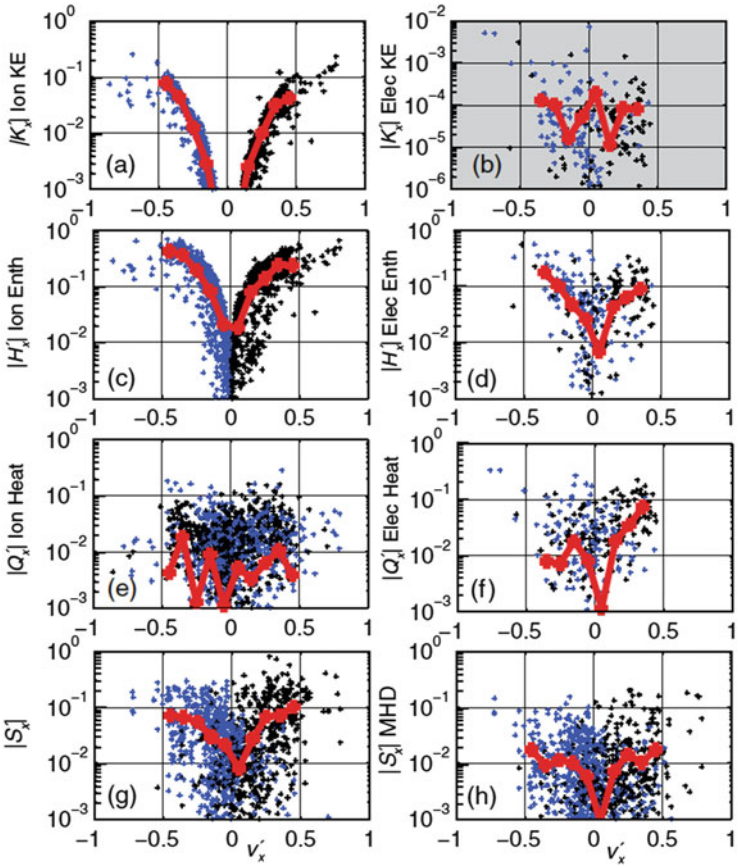

Fig. 4.9 Normalized absolute outgoing energy fluxes as a function of the normalized outflow velocity; (**a**) ion flow energy, (**b**) electron flow energy, (**c**) ion enthalpy, (**d**) electron enthalpy, (**e**) ion heat, (**f**) electron heat, (**g**) Poynting, and (**h**) Poynting flux corresponding to the Hall fields, respectively. Figure from Eastwood et al. (2013)

Table 4.1 Average normalized energy fluxes during magnetic reconnection in the magnetotail

	$K'_{i,x}$	$H'_{i,x}$	$H'_{e,x}$	$Q'_{e,x}$	$S'_{e,x}$
Earthward	0.04	0.24	0.09	0.09	0.10
Tailward	−0.08	−0.43	−0.18	−0.01	−0.07

Two normalized energy fluxes, $H'_{e,x}$ and $Q'_{e,x}$ are calculated for $\pm 0.35 v'_{i,x}$, while others for $\pm 0.45 v'_{i,x}$. Table from Eastwood et al. (2013)

estimated to be negligible compared to the corresponding outgoing fluxes because the plasma temperature in the inflow region is low.

Table 4.1 shows the normalized outgoing energy fluxes during reconnection in the magnetotail. Numbers in the first and second rows are quantities in the earthward and tailward direction, respectively. The authors assume that the outflow is along the

x direction of the GSM coordinate system. The results summarized in Table 4.1 are completely different from those in the Sweet-Parker model described in Sect. 4.2.2. The outgoing flux is dominated by ion and electron enthalpy fluxes, and the ion enthalpy flux is about factor of 2.5 larger than the electron enthalpy flux. There is no equipartition between the ion flow and enthalpy flux, as the ion flow energy flux is much smaller. The outgoing Poynting flux is not negligible, which is consistent with previous measurements (Shay et al. 2011; Eastwood et al. 2010). Both the electron flow energy and ion heat fluxes are insignificant, while the electron heat flux is comparable to the Poynting flux. There are notable differences between earthward and tailward fluxes, which may be caused by the different boundary conditions or by the effects of the solar wind on the global geometry.

Results in Table 4.1 show that the energy conversion is very efficient and that the ion energy gain is about twice as much as the electron energy gain. Since the outgoing magnetic energy is 13 % of the incoming magnetic energy, 87 % of the incoming magnetic energy seems to be converted into other forms of energy in the diffusion region. While the measurements are expected to have relatively large errors, the total ion energy gain ($\sim \Delta W_{Hi} + \Delta W_{Ki}$) is more than half of the incoming energy, and the total electron energy gain ($\sim \Delta W_{He} + \Delta W_{Qe}$) is about 30 %.

Recently, Phan et al. (2013) and Phan et al. (2014) studied bulk electron and ion heating during reconnection by surveying about 80 reconnection exhausts at the dayside magnetopause. Reconnection at the dayside magnetopause, where the solar wind plasma interacts with the magnetospheric plasma, is characterized by asymmetry in upstream plasma parameters as well as in the magnetic field across the current sheet (e.g. Mozer and Pritchett 2011). Therefore, the incoming magnetic energy per ion-electron pair, $m_i V_{AL,asym}^2$ is used to represent the available magnetic energy. Here, $V_{AL,asym}^2$ is the hybrid Alfvén velocity defined in Cassak and Shay (2007) and Phan et al. (2013).

Phan et al. (2013) showed that only 1.7 % of the incoming magnetic energy is converted to bulk electron heating after taking the asymmetric plasma parameters

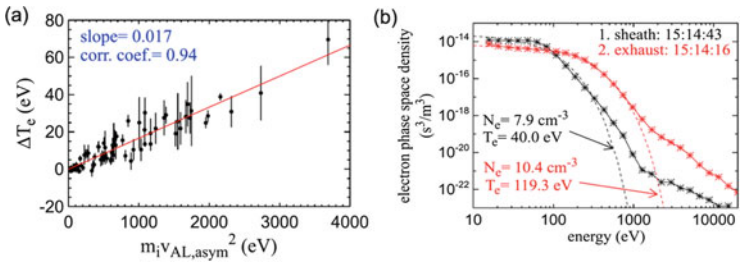

Fig. 4.10 (**a**) Electron energy increase as a function of the total incoming magnetic energy per electron-ion pair, $m_i V_{AL,asym}^2$, which is the ratio of incoming Poynting fluxes to incoming particle fluxes. The bulk electron temperature is proportional to the total incoming magnetic energy. (**b**) Example of electron energy distribution functions and fitting to the Maxwellian function. Figure from Phan et al. (2013)

into account, as shown in Fig. 4.10a: ($\Delta T_e \approx 0.017 m_i V_{AL,asym}^2$). The electron temperature increase is defined as the difference in $T_e = p_e/n_e$ between the exhaust region and the magnetosheath. Since the plasma population in the exhaust region is dominated by the higher-density magnetosheath plasma, ΔT_e can represent the bulk electron temperature increase. In this case, the corresponding electron enthalpy increase accounts for only 4.3 % of the incoming magnetic energy, which is quite different from the results (∼20 %) of Eastwood et al. (2013) that were obtained in the magnetotail. Furthermore, a recent study via 2D numerical simulations also shows that the electron temperature increase is about 3.3 % of the total incoming magnetic energy (Shay et al. 2014). This may be caused by the difference in boundary conditions between the magnetotail and magnetopause and/or errors in measurements, but more statistical surveys are required to understand this discrepancy.

From a similar statistical survey, Phan et al. (2014) reports that the ion temperature increase is about 13 % of the incoming magnetic energy, ($\Delta T_i \approx 0.13 m_i V_{AL,asym}^2$), as shown in Fig. 4.11. This result is consistent with the previous research by Drake et al. (2009), where 22 solar wind exhaust encounters were examined. The corresponding ion enthalpy increase is about 33 %, which is somewhat smaller than the result of Eastwood et al. (2013). In this research, the ion temperature is defined with the second moment of distributions ($T_i = p_i/n_i$). This is because strongly non-Maxwellian ion distributions are common inside the ion diffusion region (e.g. Hoshino et al. 1998; Wygant et al. 2005) due to interaction between ions and the Hall electric field. This effective temperature does not represent true ion heating as defined by a broadening of a Maxwellian distribution function. However, the effective temperature includes effects from non-thermal ions and represents the average ion energy in the ion rest frame.

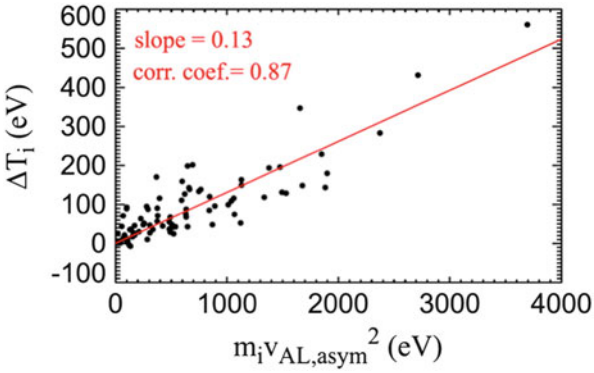

Fig. 4.11 Ion temperature increase as a function of the total magnetic energy per electron ion pair. The ion energy increase is about 13 % of the incoming magnetic energy per electron-ion pair. Figure from Phan et al. (2014)

4.5 Study of Energy Inventory by 2D Numerical Simulations

4.5.1 Fluid Simulations

The energy budget in resistive MHD reconnection has been extensively studied by Birn and his colleagues (Birn and Hesse 2005; Birn et al. 2008; Birn and Hesse 2009, 2010; Birn et al. 2010). Birn and Hesse (2005) showed that magnetic energy is predominantly transferred into internal energy during magnetotail reconnection. In the context of asymmetric reconnection, Birn et al. (2008) showed that the outflow energy flux is mainly carried by the enthalpy flux. They further demonstrated that the energy transfer to internal energy is dominant by integrating (4.3) over the reconnection region. The enthalpy flux is also significant during solar flare reconnection $\Delta W_H > 0$ (Birn and Hesse 2009) as well as during guide-field reconnection (Birn and Hesse 2010). These analysis lead to the compressible MHD theory of asymmetric reconnection (Birn et al. 2010). Figure 4.12 shows the energy balance during an MHD simulation of symmetric reconnection (Birn et al. 2010). We see that the magnetic energy (ΔS, corresponding ΔW_M in Sect. 4.2.1) is converted to an equal amount of both enthalpy (ΔH, corresponding ΔW_H in Sect. 4.2.1) and bulk flow energy (ΔK, corresponding ΔW_K in Sect. 4.2.1) in the low β case (Fig. 4.12a), while the enthalpy flux becomes dominant in the high β case (Fig. 4.12b).

4.5.2 Kinetic Simulations

One of the earlier attempts to understand the energy transfer mechanisms using 2D particle-in-cell (PIC) simulations was carried out by Horiuchi and Sato (1997). In their work, the current was decomposed into the separate contributions from ions and electrons, $\mathbf{J} = \mathbf{j}_e + \mathbf{j}_i$, while the electric field was decomposed into the elec-

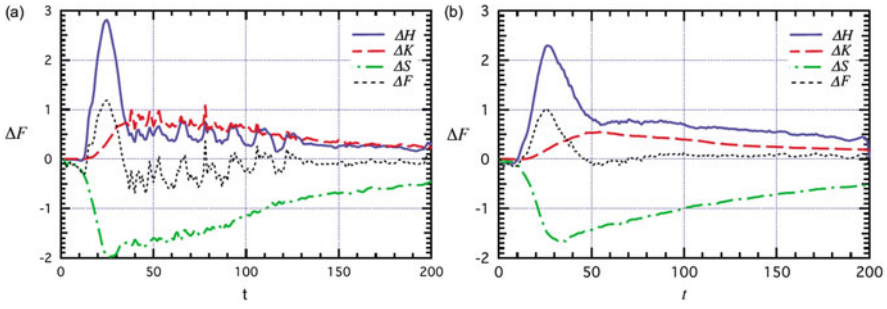

Fig. 4.12 Energy balance during symmetric MHD reconnection (**a**) for $\beta = 0.1$ and (**b**) for $\beta = 1$. Figure from Birn et al. (2010)

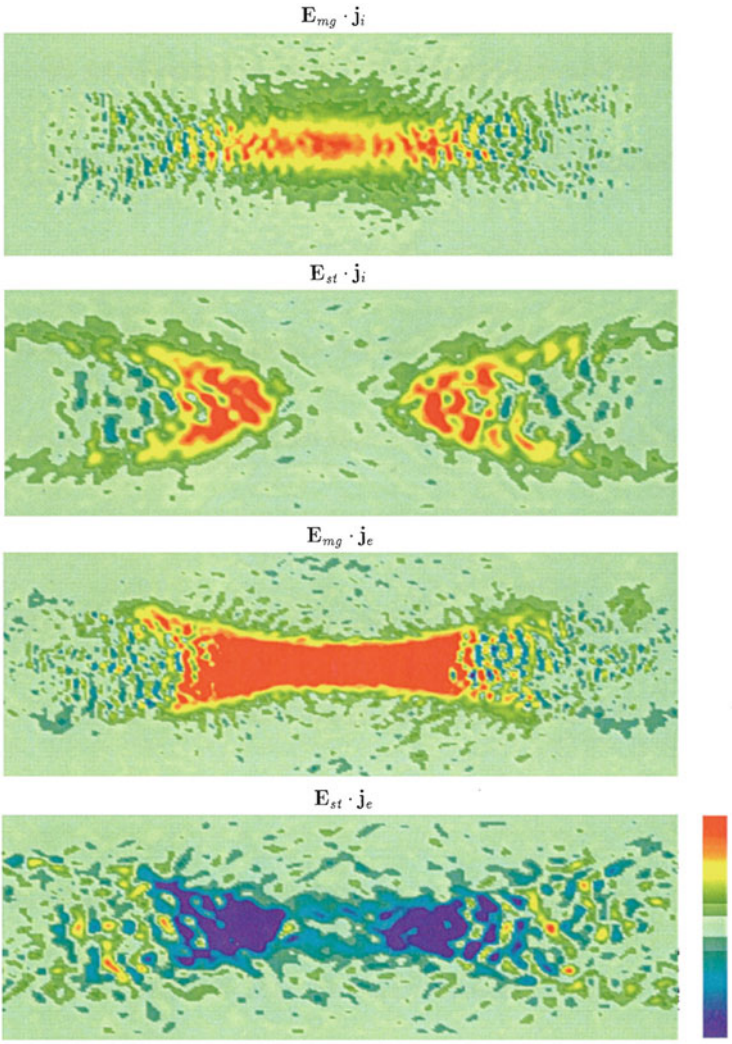

Fig. 4.13 Profiles of $\mathbf{j}_i \cdot \mathbf{E}_{mg}$, $\mathbf{j}_i \cdot \mathbf{E}_{st}$, $\mathbf{j}_e \cdot \mathbf{E}_{mg}$, and $\mathbf{j}_e \cdot \mathbf{E}_{st}$ in 2D PIC simulation. Figure from Horiuchi and Sato (1997)

tromagnetic and electrostatic components, $\mathbf{E} = \mathbf{E}_{mg} + \mathbf{E}_{st}$. These decompositions allowed for the detailed investigation of the energy transfer from the fields to the plasma as shown in Fig. 4.13. They found that the electrons mostly gain their energy from $\mathbf{E}_{mg}$ near the X point, and that the electrons later lose their energy to $\mathbf{E}_{st}$, although the exact scale lengths of energy deposition was not clearly shown. On the other hand, the ions gain energy by $\mathbf{E}_{st}$. The time evolution of the electron velocity distribution function suggests that the energy is transferred to bulk kinetic energy first, and later converted to electron thermal energy. This is supported by a recent

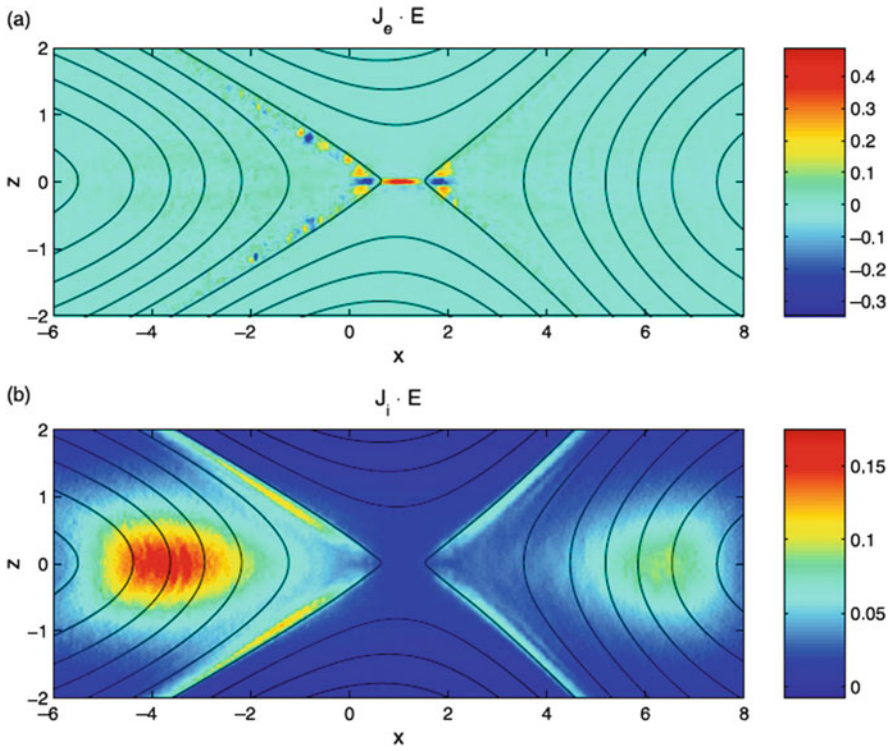

Fig. 4.14 Profiles of $\mathbf{j}_e \cdot \mathbf{E}$ (**a**) and $\mathbf{j}_i \cdot \mathbf{E}$ (**b**) in 2D PIC simulation with a realistic mass ratio ($m_i/m_e = 1600$). Figure from Pritchett (2010)

analysis (Lu et al. 2013), which shows that the electron bulk flow energy is converted to thermal energy around the diffusion region. Similar 2D profiles of $\mathbf{j}_e \cdot \mathbf{E}$ and $\mathbf{j}_i \cdot \mathbf{E}$ are obtained in simulations with a realistic mass ratio ($m_i/m_e = 1600$), as shown in Fig. 4.14 (Pritchett 2010). The electron energy gain is localized near the X point, while the ion energy gain occurs across the separatrices and throughout the exhaust region. These observations agree with the aforementioned laboratory measurements in Sect. 4.3.

It has been argued that the enhanced energy conversion localized near the X point is a good indicator of the central reconnection site (Birn and Hesse 2005; Zenitani et al. 2011b). However, this electron energy loading condition ($\mathbf{j}_e \cdot \mathbf{E} > 0$) does not positively identify the central reconnection site, or the electron diffusion region, since the $\mathbf{j}_e \cdot \mathbf{E} > 0$ condition can be found in other places away form the electron diffusion region, especially during asymmetric reconnection with a guide field (Pritchett and Mozer 2009).

While intense, localized energy dissipation occurs in the electron diffusion region, the overall size of this region (few d_e) is quite small due to the light electron mass. Thus, the total energy dissipation in the electron diffusion region is small.

Furthermore, it is well known that the electron diffusion region and associated structures are quite complex (e.g. Karimabadi et al. 2007; Shay et al. 2007; Zenitani et al. 2011a) and sensitive to slight parameter changes (Le et al. 2013). Due to these complications, it is more meaningful to examine the energy inventory on the ion scale where Hall physics is dominant.

Surprisingly, the number of works on the kinetic energy budget beyond the electron-scale region is limited. Aunai et al. (2011) carried out hybrid simulations and evaluated the energy budget over the reconnection region and throughout their simulations. They found that more than half of the incoming electromagnetic energy was transferred to the ion internal energy during the quasi-steady reconnection period. Since the electron temperature is set be constant in these hybrid simulations, energy conversion to electrons is not included. This large ion enthalpy energy increase is consistent with both of the aforementioned space and laboratory observations.

Ion heating is also studied in fully kinetic PIC simulations. Drake et al. (2009) reported that the ion heating mechanism in the exhaust is similar to a pick-up process. Once an individual ion enters into the exhaust, it travels along a field line until it reaches the midplane where the Speiser motion (Speiser 1965) reverses its trajectory. The ion temperature increase from this pick up process is estimated to be $m_i V_{out}^2/3$, which is proportional to the ion mass. However, space observations of the solar wind exhaust show that the temperature increments are consistently smaller than the prediction.

Shay et al. (2014) systematically studied electron heating in the exhaust. They found that electrons are preferentially heated in the parallel direction and that the increase in the electron temperature is proportional to the incoming magnetic energy, $\Delta T_e \sim 0.033 m_i V_A^2$. They evaluated the electron temperature across the exhaust and near the electron jet front, but even farther downstream the results appear to be unchanged.

Unfortunately, there is no consensus on the ion-scale structure, such that it is difficult to discuss the energy inventory in the ion diffusion region quantitatively. Many simulations have reported an ion-scale current layer at the center of the exhaust (e.g. Lottermoser et al. 1998; Liu et al. 2012; Le et al. 2014), which resembles, in our opinion, a kinetic model by Hill (1975). Outside the central current layer, incoming ions bounce back and forth due to the potential well and counter-streaming ion beams along the field-lines are generated, thereby increasing the ion parallel temperature significantly (Liu et al. 2012; Higashimori and Hoshino 2012; Le et al. 2014). In order to understand the energy inventory in the ion diffusion region, it is first necessary to understand these kinetic features of ions.

The energy conversion in the downstream region also depends on the boundary condition imposed in the simulations. It has been observed that $\mathbf{j}_i \cdot \mathbf{E} > 0$ (Sitnov et al. 2009; Pritchett 2010) in the exhaust. However, when periodic boundary conditions are used, it is often observed that there is instead energy loss to the field ($\mathbf{J} \cdot \mathbf{E} < 0$), because the plasma flows compress the magnetic fields in the piled-up region (Ma et al. 2012; Lapenta et al. 2014). Furthermore, as the piled-up field pushes the downstream plasma sheet, magnetic energy is again converted to

plasma energy near the dipolarization front (Pritchett 2008; Lapenta et al. 2014). These complexities indicate that the overall energy inventory is also affected by the boundary conditions of the system. These boundary effects on the energy inventory have not been addressed so far.

4.5.3 Case Studies

To obtain deeper insights into the energy budget in fully kinetic simulations, we examine two examples of recent PIC simulations—one with periodic boundary conditions and the other with open boundary conditions. The first simulation is from Zenitani et al. (2013). The simulation is initialized with a Harris-like current sheet, whose thickness is 0.5 in the reference ion inertial length, d_{i0} that is computed with the reference density n_0. The background plasma density is $0.2n_0$, the mass ratio (m_i/m_e) is 100, the temperature ratio T_i/T_e is 5. In the x-z plane, we use 2400 × 1600 grid cells for the $76.8 \times 38.4d_{i0}$ domain with periodic (x) and reflecting (z) boundaries. We use 1.7×10^9 particles.

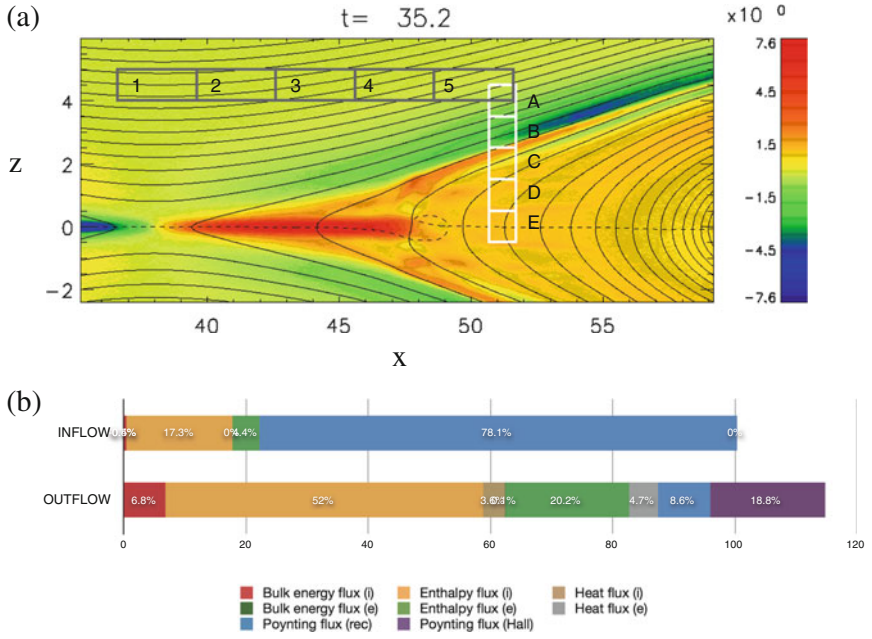

Fig. 4.15 2D PIC simulation results, taken from Zenitani et al. (2013). (**a**) The electron outflow velocity (V_{ex}) and selected domains for our energy inventory analysis. (**b**) Composition of the incoming and outgoing energy fluxes

Figure 4.15a shows the electron outflow velocity V_{ex} averaged over $0.25/\Omega_{ci}$. In order to discuss the energy budget in the Hall-physics region, we evaluate the energy flux in the ten boxes shown. The fluxes are accumulated both in the inflow and outflow regions as shown in Fig. 4.15b and they are normalized by the total incoming energy flux. The incoming energy flux and the total outgoing flux do not match, which indicate that the system is not in a perfect steady state (the reconnection rate is slowly decreasing around this time).

As shown in Fig. 4.15b, the Poynting flux is the dominant incoming energy flux. Assuming an isotropic plasma and the ideal condition, $E_{rec} = V_{in}B_{rec}$, we obtain $(H_{i,in} + H_{e,in})/S_{MHD} = 5\beta_{in}/4$, where the subscript 'in' denotes inflow quantities and $S_{MHD} = E_{rec}B_{rec}/\mu_0$. With an upstream β of 0.2, S_{MHD} carries 80 % of the incoming energy. The ratio of the ion enthalpy flux to the electron's also stems from the initial configuration of $T_i/T_e = 5$. Similarly, assuming $V_{in} \sim 0.1V_A$, we obtain $K_{i,in}/S_{MHD} = 0.5(V_{in}/V_A)^2 = 0.005$, which is negligible. The electron bulk kinetic flux is even smaller than ion bulk kinetic flux by a factor of m_i/m_e. Therefore, the incoming bulk flow energy is negligible.

On the other hand, the ion enthalpy flux is the largest among the outgoing energy fluxes. This is largely because the ion outflow speed is sub-Alfvénic, $V_{i,out} < 0.5V_A$ (Zenitani et al. 2013). Strictly speaking, it is difficult to define V_i near the midplane, because the ions are highly nongyrotropic. For example, the velocity distribution function in the box E contains multiple subcomponents, as shown in Fig. 5 in Zenitani et al. (2013). The ion heat flux may be an outcome of the nongyrotropic velocity distribution. Due to the light mass, the electron bulk energy flux is negligible. On the other hand, the electron enthalpy flux is significant. Some amount of electron heat flux is attributed to local electron-scale structures in boxes B and C, such as the field-aligned electron inflows near the separatrix and narrow outgoing jets. Their contributions are, however, small compared with the large scale fluxes. It should also be noted that the Hall component of the Poynting flux, S_{Hall}, is significant in this case. As reconnection proceeds, the Hall magnetic field B_y and the in-plane Hall electric field generate the outgoing Poynting flux.

The second example is taken from a PIC simulation in Le et al. (2013), and these results are further analyzed by Yamada et al. (2015). The simulation is also initialized with a Harris-like current sheet with the sheet thickness of $0.5d_{i0}$, where d_{i0} is the ion skin depth evaluated with n_0. The mass ratio is 1836, T_i/T_e is 5 in the current sheet and 6.6 in the background, and the background density is $0.23n_0$. Due to computational constraints, $\omega_{pe}/\Omega_{ce} = 2$ and the domain size is $20 \times 20d_{i0}$ with open boundaries (Daughton et al. 2006). The simulation has 5120×5120 cells with $\sim 10^{10}$ particles per species. Figure 4.16a shows the 2D profile of the out-of-plane current and demonstrates the geometry of the box inside which the energy inventory is analyzed.

Figure 4.16b shows the energy budget as a function of the size of the box in the PIC simulation. It should be noted that the box size L is normalized to the upstream ion skin depth $d_i \sim 2d_{i0}$, rather than the reference skin depth d_{i0} for better comparison to the experimental results presented in Sect. 4.3. The energy inventory is relatively insensitive to the box size L, as long as it is larger than $1.5d_i$ and

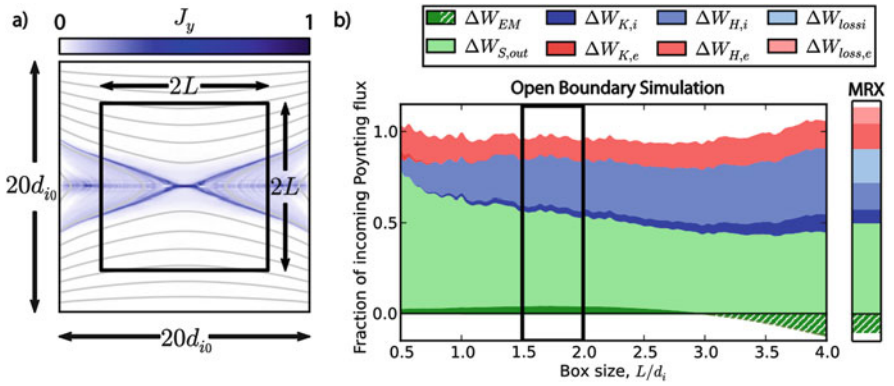

Fig. 4.16 (**a**) Simulation geometry with the box inside which the energy inventory is analyzed. The *color* shows the out-of-plane current density. (**b**) Energy inventory as a function of the box size, L. The energy inventory is relatively insensitive to L, when $1.5d_i \lesssim L \lesssim 4d_i$. Figure is from Yamada et al. (2015)

smaller than $4d_i$. If the box size becomes close to the total system size of $5d_i$, effects from the boundary play a role. Overall, the energy inventory is consistent with that of MRX (shown separately on the side). The outgoing magnetic energy, $\Delta W_{S,out}$ (green) is about 50 % of the incoming magnetic energy. The electron flow energy $\Delta W_{K,e}$ (red) is negligible. The electron enthalpy increases of electrons, $\Delta W_{H,e}$ (light red) accounts for about 10 % of the incoming magnetic energy. The ion flow energy gain, $\Delta W_{K,i} \sim 5\,\%$ (blue) is significantly smaller than the ion enthalpy increase, $\Delta W_{H,i} \sim 25\,\%$ (light blue). The energy deposited to ions is about 2–3 times larger than that to electrons.

Since the mass ratio is different in these two cases, the electron kinetic structures are different in size. In the $m_i/m_e = 100$ case, the half-length of the electron jet is $\sim 10d_{i0}$, as shown in Fig. 4.15. This corresponds to $\sim 4.5d_i$, where $d_i = 2.23d_{i0}$ is the initial upstream ion skin depth. In the $m_i/m_e = 1836$ case, the full-length of the central electron current layer appears to be $\sim$ 2–$3d_{i0} \sim d_i$, as shown in Fig. 4.16. Given that the electron-scale structure scales like the typical electron skin depth $d_e \propto \sqrt{m_e}$, the electron region in the $m_i/m_e = 1836$ case will be 4.3 times smaller than that in the $m_i/m_e = 100$ case. Therefore, these two numerical results are reasonable. Figure 4.15b tells us that the electron heat flux is a minor energy carrier in collisionless PIC simulations. Since it is related to the electron-scale structure near the separatrix, the electron heat flux is less and less important on a larger scale. This justifies our assumption to ignore the heat flux in the $m_i/m_e = 1836$ case.

In both simulations, the contribution from the Hall fields (the out-of-plane quadrupole magnetic field and the in-plane electrostatic field) to the outgoing Poynting flux is not negligible, which agrees with space and laboratory observations in Sects. 4.3 and 4.4. This Poynting flux, S_{Hall} may eventually vanish on the MHD scale, however, this large-scale physics has not been addressed in kinetic simulations and it is unclear when the Hall fields become negligible.

4.6 Summary and Discussion

We have carried out a comparative study in order to find the basic mechanisms of energy conversion and partitioning in a typical magnetic reconnection layer. The results from three different studies in laboratory experiments, space observations, and numerical simulations, have been reviewed.

Our quantitative measurements in the MRX reconnection layer regarding the acceleration and heating of both electrons and ions demonstrate that half of the incoming magnetic energy is converted to particle energy with a remarkably fast speed. The ion energy gain is about twice larger than the electron energy gain, and a non-negligible amount of magnetic energy flows out to the exhaust.

For electrons, we have observed that the conversion of magnetic energy occurs across a region significantly larger than the narrow electron diffusion region in earlier 2D simulations. The broad electron diffusion region observed in MRX indicates non-classical electron heating (Yoo et al. 2014a), but exact mechanisms for this anomalous electron heating have not been identified. It is also important to note that when energy deposition rate to electrons, $\mathbf{j}_e \cdot \mathbf{E}$, is decomposed to $\mathbf{j}_{e\perp} \cdot \mathbf{E}_\perp + j_{e\parallel} E_\parallel$, $\mathbf{j}_{e\perp} \cdot \mathbf{E}_\perp$ is found to be significantly larger than $j_{e\parallel} E_\parallel$ near the X point. This is because electrons gain energy mostly from the out-of-plane reconnection electric field and this electric field is perpendicular to the magnetic field near the X point as there is a negligible guide field for this study (<5 % of the reconnecting magnetic field).

Ion acceleration and heating occurs throughout the ion diffusion region. A saddle-shaped electrostatic potential profile is verified to exist in the reconnection plane both in the experiment and simulations, and ions are accelerated by the resulting electric field at the separatrices. These accelerated ions are then thermalized by re-magnetization in the downstream region. Similarly, when energy deposition rate to ions, $\mathbf{j}_i \cdot \mathbf{E}$, is decomposed to $\mathbf{j}_{i\perp} \cdot \mathbf{E}_\perp + j_{i\parallel} E_\parallel$, $\mathbf{j}_{i\perp} \cdot \mathbf{E}_\perp$ is also found to be dominant over $j_{i\parallel} E_\parallel$ across the separatrices where the ion energy gain is strongest. The ions gain energy mostly from the in-plane electrostatic field, which is mostly perpendicular to the magnetic field both near the separatrices and in the exhaust region.

This dominance of $\mathbf{J}_\perp \cdot \mathbf{E}_\perp$ over $J_\parallel E_\parallel$ in energy conversion to plasma continues to exist even during asymmetric reconnection with a moderate guide field ($\sim$30 % of B_{rec}) (Pritchett and Mozer 2009). We expect that this trend changes with the presence of a significant guide field ($> B_{rec}$), where the reconnection electric field has a larger parallel component.

The partitioning of the outgoing energy fluxes was recently measured from multiple encounters of the Cluster satellite with the Earth's magnetotail reconnection site. The observed energy partition is qualitatively consistent with the MRX data, namely, more than 50 % of the incoming magnetic energy flux is converted to the particle energy flux, which is dominated by the ion enthalpy flux. The electron enthalpy and heat flux are evaluated and found to be smaller than the ion enthalpy flux. Although it is difficult to determine the exact size of their boundary due to the limited number of measurement points (spacecraft) and the motion of the X point, the half length

of the tail reconnection layer was estimated to be 2000–4000 km, about 3–6 ion skin depths. The normalized scale length of this measurement is thus very similar to the MRX case of $L \sim 3d_i$. In both measurements, significantly more energy is converted to ions than to electrons .

We have also carried out a systematic study of the effects of the size of boundary on the energy inventory by comparing the results from numerical simulations and laboratory experiments using different boundary sizes. It is concluded that for a relatively broad range of boundary sizes, about 50 % of the inflowing magnetic energy is converted to particle energy and that ion energy gain is more than twice of electron energy gain. Furthermore, numerical simulations with open boundary conditions conclude that the above features of energy conversion and partitioning do not strongly depend on the size of the analysis region, at least, over the tested range of scales.

Our comparative study has found implications for the scaling of the energy inventory with respect to the Lundquist number. When we compare our results from plasmas of $\mathcal{L}_q < 1000$ with that of the magnetosphere where the Lundquist number is significantly larger ($> 10^8$), we have found a similar energy flow pattern, which indicates the energy conversion processes do not strongly depend on the Lundquist number. This is consistent with our expectation that two-fluid physics, rather than the classical MHD physics, plays the dominant role in both the magnetosphere and MRX where the electron mean free path is comparable with the scale of the current sheet.

We have made a comparative review of the recent studies on the energetics of magnetic reconnection in space and laboratory plasmas in order to find common characteristics of energy conversion and partitioning in the reconnection layer. In spite of these similar results among 2D PIC simulations, laboratory experiments, and space observations, there exist major questions: why are the results from different plasmas with different boundary box sizes similar? Why do these 2D simulation agree with the MRX results which should intrinsically include 3D effects? At the moment, there is no definite answer, but their agreement may imply that the primary energy conversion mechanisms and the partitioning of energy are determined fundamentally by two-dimensional Hall MHD physics.

Acknowledgements The authors thank Jonathan Jara-Almonte for his valuable comments.

References

V. Angelopoulos, A. Runov, X.-Z. Zhou, D.L. Turner, S.A. Kiehas, S.-S. Li, I. Shinohara, Electromagnetic energy conversion at reconnection fronts. Science **341**(6153), 1478–1482 (2013)

N. Aunai, G. Belmont, R. Smets, Proton acceleration in antiparallel collisionless magnetic reconnection: kinetic mechanisms behind the fluid dynamics. J. Geophys. Res. **116**, 09232 (2011)

J. Birn, M. Hesse, Energy release and conversion by reconnection in the magnetotail. Ann. Geophys. **23**(10), 3365–3373 (2005)
J. Birn, M. Hesse, Reconnection in substorms and solar flares: analogies and differences. Ann. Geophys. **27**(3), 1067–1078 (2009)
J. Birn, M. Hesse, Energy release and transfer in guide field reconnection. Phys. Plasmas **17**(1), 012109 (2010)
J. Birn, J.F. Drake, M.A. Shay, B.N. Rogers, R.E. Denton, M. Hesse, M. Kuznetsova, Z.W. Ma, A. Bhattacharjee, A. Otto, P.L. Pritchett, Geospace environmental modeling (GEM) magnetic reconnection challenge. J. Geophys. Res. **106**, 3715 (2001)
J. Birn, J.E. Borovsky, M. Hesse, Properties of asymmetric magnetic reconnection. Phys. Plasmas **15**(3), 032101 (2008)
J. Birn, J.E. Borovsky, M. Hesse, K. Schindler, Scaling of asymmetric reconnection in compressible plasmas. Phys. Plasmas **17**(5), 052108 (2010)
D. Biskamp, *Magnetic Reconnection in Plasmas* (Cambridge University Press, New York, 2000)
S.I. Braginskii, Transport processes in a plasma, in *Reviews of Plasma Physics*, vol. 1, ed. by M.A. Leontovich (Consultants Bureau, New York, 1965), pp. 205–311
M.R. Brown, C.D. Cothran, J. Fung, Two fluid effects on three-dimensional reconnection in the swarthmore spheromak experiment with comparisons to space data. Phys. Plasmas **13**(5), 056503 (2006)
M.R. Brown, C.D. Cothran, D.H. Cohen, J. Horwitz, V. Chaplin, Flow dynamics and plasma heating of spheromaks in SSX. J. Fusion Energy **27**, 16–19 (2008)
P.A. Cassak, M.A. Shay, Scaling of asymmetric magnetic reconnection: general theory and collisional simulations. Phys. Plasmas **14**(10), 102114 (2007)
W. Daughton, J. Scudder, H. Karimabadi, Fully kinetic simulations of undriven magnetic reconnection with open boundary conditions. Phys. Plasmas **13**(7), 072101 (2006)
W. Daughton, V. Roytershteyn, B.J. Albright, H. Karimabadi, L. Yin, K.J. Bowers, Influence of coulomb collisions on the structure of reconnection layers. Phys. Plasmas **16**(7), 072117 (2009)
S. Dorfman, W. Daughton, V. Roytershteyn, H. Ji, Y. Ren, M. Yamada, Two-dimensional fully kinetic simulations of driven magnetic reconnection with boundary conditions relevant to the magnetic reconnection experiment. Phys. Plasmas **15**(10), 102107 (2008)
J.F. Drake, M. Swisdak, T.D. Phan, P.A. Cassak, M.A. Shay, S.T. Lepri, R.P. Lin, E. Quataert, T.H. Zurbuchen, Ion heating resulting from pickup in magnetic reconnection exhausts. J. Geophys. Res. **114**, 05111 (2009)
J.P. Eastwood, T.D. Phan, M. Øieroset, M.A. Shay, Average properties of the magnetic reconnection ion diffusion region in the Earth's magnetotail: the 2001–2005 cluster observations and comparison with simulations. J. Geophys. Res. **115**(A8), 08125 (2010)
J.P. Eastwood, T.D. Phan, J.F. Drake, M.A. Shay, A.L. Borg, B. Lavraud, M.G.G.T. Taylor, Energy partition in magnetic reconnection in Earth's magnetotail. Phys. Rev. Lett. **110**, 225001 (2013)
A.G. Emslie, B.R. Dennis, G.D. Holman, H.S. Hudson, Refinements to flare energy estimates: a followup to "energy partition in two solar flare/CME events" by A.G. Emslie et al. J. Geophys. Res. **110**(A11), 11103 (2005). ISBN:0148-0227
G. Fiksel, D.J.D. Hartog, P.W. Fontana, An ical probe for local measurements of fast plasma ion dynamics. Rev. Sci. Instrum. **69**(5), 2024–2026 (1998)
G. Fiksel, A.F. Almagri, B.E. Chapman, V.V. Mirnov, Y. Ren, J.S. Sarff, P.W. Terry, Mass-dependent ion heating during magnetic reconnection in a laboratory plasma. Phys. Rev. Lett. **103**, 145002 (2009)
A. Fujisawa, H. Ji, K. Yamagishi, S. Shinohara, H. Toyama, K. Miyamoto, Anomalous ion temperature and plasma resistance due to MHD fluctuations in Repute-1 reversed field pinch plasmas. Nucl. Fusion **31**(8), 1443 (1991)
S. Gangadhara, D. Craig, D.A. Ennis, D.J.D. Hartog, G. Fiksel, S.C. Prager, Spatially resolved measurements of ion heating during impulsive reconnection in the madison symmetric torus. Phys. Rev. Lett. **98**, 075001 (2007)
W. Gekelman, R.L. Stenzel, N. Wild, Magnetic field line reconnection experiments, 3. Ion acceleration, flows, and anomalous scattering. J. Geophys. Res. **87**, 101–110 (1982)

R. Giovanelli, A theory of chromospheric flares. Nature **158**(4003), 81–82 (1946)
J.T. Gosling, M.F. Thomsen, S.J. Bame, C.T. Russell, Accelerated plasma flows at the near-tail magnetopause. J. Geophys. Res. **91**(A3), 3029–3041 (1986)
M. Hesse, J. Birn, M. Kuznetsova, Collisionless magnetic reconnection: electron processes and transport modeling. J. Geophys. Res. Space Phys. **106**(A3), 3721–3735 (2001)
K. Higashimori, M. Hoshino, The relation between ion temperature anisotropy and formation of slow shocks in collisionless magnetic reconnection. J. Geophys. Res. **117**(A1), 01220 (2012)
T.W. Hill, Magnetic merging in a collisionless plasma. J. Geophys. Res. **80**(34), 4689–4699 (1975)
R. Horiuchi, T. Sato, Particle simulation study of collisionless driven reconnection in a sheared magnetic field. Phys. Plasmas **4**(2), 277–289 (1997)
M. Hoshino, T. Mukai, T. Yamamoto, S. Kokubun, Ion dynamics in magnetic reconnection: comparison between numerical simulation and geotail observations. J. Geophys. Res. **103**, 4509–4530 (1998)
S.C. Hsu, G. Fiksel, T.A. Carter, H. Ji, R.M. Kulsrud, M. Yamada, Local measurement of nonclassical ion heating during magnetic reconnection. Phys. Rev. Lett. **84**, 3859–3862 (2000)
S. Imada, M. Hoshino, T. Mukai, Average profiles of energetic and thermal electrons in the magnetotail reconnection regions. Geophys. Res. Lett. **32**(9), 09101 (2005)
H. Ji, M. Yamada, S. Hsu, R. Kulsrud, Experimental test of the Sweet-Parker model of magnetic reconnection. Phys. Rev. Lett. **80**, 3256–3259 (1998)
H. Ji, S. Terry, M. Yamada, R. Kulsrud, A. Kuritsyn, Y. Ren, Electromagnetic fluctuations during fast reconnection in a laboratory plasma. Phys. Rev. Lett. **92**, 115001 (2004)
H. Ji, Y. Ren, M. Yamada, S. Dorfman, W. Daughton, S.P. Gerhardt, New insights into dissipation in the electron layer during magnetic reconnection. Geophys. Res. Lett. **35**(13), 13106 (2008)
H. Karimabadi, W. Daughton, J. Scudder, Multi-scale structure of the electron diffusion regions. Geophys. Res. Lett. **34**, 13104 (2007)
T.W. Kornack, P.K. Sollins, M.R. Brown, Experimental observation of correlated magnetic reconnection and Alfvénic ion jets. Phys. Rev. E **58**, 36–39 (1998)
S. Krucker, H.S. Hudson, L. Glesener, S.M. White, S. Masuda, J.-P. Wuelser, R.P. Lin, Measurements of the coronal acceleration region of a solar flare. Astrophys. J. **714**(2), 1108 (2010)
G. Lapenta, M. Goldman, D. Newman, S. Markidis, A. Divin, Electromagnetic energy conversion in downstream fronts from three dimensional kinetic reconnections. Phys. Plasmas **21**(5), (2014)
A. Le, J. Egedal, O. Ohia, W. Daughton, H. Karimabadi, V.S. Lukin, Regimes of the electron diffusion region in magnetic reconnection. Phys. Rev. Lett. **110**, 135004 (2013)
A. Le, J. Egedal, J. Ng, H. Karimabadi, J. Scudder, V. Roytershteyn, W. Daughton, Y.-H. Liu, Current sheets and pressure anisotropy in the reconnection exhaust. Phys. Plasmas **21**(1), 012103 (2014)
R.P. Lin, Energy release and particle acceleration in flares: summary and future prospects. Space Sci. Rev. **159**, 421–445 (2011)
R.P. Lin, H.S. Hudson, Non-thermal processes in large solar flares. Sol. Phys. **50**, 153–178 (1976)
R.P. Lin, S. Krucker, G.J. Hurford, D.M. Smith, H.S. Hudson, G.D. Holman, R.A. Schwartz, B.R. Dennis, G.H. Share, R.J. Murphy, A.G. Emslie, C. Johns-Krull, N. Vilmer, Rhessi observations of particle acceleration and energy release in an intense solar gamma-ray line flare. Astrophys. J. Lett. **595**(2), 69 (2003)
Y.-H. Liu, J.F. Drake, M. Swisdak, The structure of the magnetic reconnection exhaust boundary. Phys. Plasmas **19**(2), 022110 (2012)
R.-F. Lottermoser, M. Scholer, A.P. Matthews, Ion kinetic effects in magnetic reconnection: hybrid simulations. J. Geophys. Res. **103**(A3), 4547–4559 (1998)
S. Lu, Q. Lu, C. Huang, S. Wang, The transfer between electron bulk kinetic energy and thermal energy in collisionless magnetic reconnection. Phys. Plasmas **20**(6), 061203 (2013)
Z.W. Ma, A. Bhattacharjee, Role of photospheric footpoint shear in the impulsive dynamics of the solar corona. Geophys. Res. Lett. **23**(21), 2955–2958 (1996). ISBN:0094-8276
Z.W. Ma, H.E. Sun, L.C. Lee, A.T.Y. Lui, Energy transformation in a reconnection site. Phys. Plasmas **19**(3), 032904 (2012)

R.M. Magee, Ion energization during tearing mode magnetic reconnection in a high temperature plasma. Ph.D. thesis, University of Wisconsin-Madison, 2011

R.M. Magee, D.J. Den Hartog, S.T.A. Kumar, A.F. Almagri, B.E. Chapman, G. Fiksel, V.V. Mirnov, E.D. Mezonlin, J.B. Titus, Anisotropic ion heating and tail generation during tearing mode magnetic reconnection in a high-temperature plasma. Phys. Rev. Lett. **107**, 065005 (2011)

F.S. Mozer, P.L. Pritchett, Electron physics of asymmetric magnetic field reconnection. Space Sci. Rev. **158**(1), 119–143 (2011)

F.S. Mozer, S.D. Bale, T.-D. Phan, Evidence of diffusion regions at a sub solar magnetopause crossing. Phys. Rev. Rett. **89**, 015002 (2002)

N.A. Murphy, C.R. Sovinec, Global axisymmetric simulations of two-fluid reconnection in an experimentally relevant geometry. Phys. Plasmas **15**(4), 042313 (2008)

T. Nagai, I. Shinohara, M. Fujimoto, M. Hoshino, Y. Saito, S. Machida, T. Mukai, J. Geophys. Res. 106, 25929 (2001). doi:10.1029/2001JA900038

M. Øieroset, T.-D. Phan, M. Fujimoto, R.P. Lin, R.P. Lepping, *In situ* detection of collisionless reconnection in the Earth's magnetotail. Nature **412**, 414–417 (2001)

Y. Ono, M. Yamada, T. Akao, T. Tajima, R. Matsumoto, Ion acceleration and direct ion heating in three-component magnetic reconnection. Phys. Rev. Lett. **76**, 3328–3331 (1996)

Y. Ono, H. Tanabe, Y. Hayashi, T. Ii, Y. Narushima, T. Yamada, M. Inomoto, C.Z. Cheng, Ion and electron heating characteristics of magnetic reconnection in a two flux loop merging experiment. Phys. Rev. Lett. **107**, 185001 (2011)

Y. Ono, H. Tanabe, T. Yamada, K. Gi, T. Watanabe, T. Ii, M. Gryaznevich, N. Scannell, R. Conway, B. Crowley, C. Michael, High power heating of magnetic reconnection in merging tokamak experiments Phys. Plasmas **22**(5), 055708 (2015)

E.N. Parker, Sweet's mechanism for merging magnetic fields in conducting fluids. J. Geophys. Res. **62**(4), 509–520 (1957)

G. Paschmann, B.U.Ö. Sonnerup, I. Papamastorakis, N. Sckopke, G. Haerendel, S.J. Bame, J.R. Asbridge, J.T. Gosling, C.T. Russell, R.C. Elphic, Plasma acceleration at the Earth's magnetopause: evidence for reconnection. Nature **282**, 243–246 (1979)

H.E. Petschek, Magnetic field annihilation. NASA Spec. Pub. **SP-50**, 425 (1964)

T.D. Phan, L.M. Kistler, B. Klecker, G. Haerendel, G. Paschmann, B.U.Ö. Sonnerup, W. Baumjohann, M.B. Bavassano-Cattaneo, C.W. Carlson, A.M. DiLellis, K.-H. Fornacon, L.A. Frank, M. Fujimoto, E. Georgescu, S. Kokubun, E. Moebius, T. Mukai, M. Oieroset, W.R. Paterson, H. Reme, Extended magnetic reconnection at the Earth's magnetopause from detection of bi-directional jets. Nature **404**(6780), 848–850 (2000). ISBN:0028-0836

T.D. Phan, M.W. Dunlop, G. Paschmann, B. Klecker, J.M. Bosqued, H. Rème, A. Balogh, C. Twitty, F.S. Mozer, C.W. Carlson, C. Mouikis, L.M. Kistler, Cluster observations of continuous reconnection at the magnetopause under steady interplanetary magnetic field conditions. Ann. Geophys. **22**(7), 2355–2367 (2004)

T.D. Phan, M.A. Shay, J.T. Gosling, M. Fujimoto, J.F. Drake, G. Paschmann, M. Oieroset, J.P. Eastwood, V. Angelopoulos, Electron bulk heating in magnetic reconnection at Earth's magnetopause: dependence on the inflow alfvén speed and magnetic shear. Geophys. Res. Lett. **40**(17), 4475–4480 (2013)

T.D. Phan, J.F. Drake, M.A. Shay, J.T. Gosling, G. Paschmann, J.P. Eastwood, M. Oieroset, M. Fujimoto, V. Angelopoulos, Ion bulk heating in magnetic reconnection exhausts at Earth's magnetopause: dependence on the inflow Alfvén speed and magnetic shear angle. Geophys. Res. Lett. **41**(20), 7002–7010 (2014)

E. Priest, T. Forbes, *Magnetic Reconnection - MHD Theory and Applications* (Cambridge University Press, New York, 2000)

P.L. Pritchett, Collisionless magnetic reconnection in a three-dimensional open system. J. Geophys. Res. **106**(A11), 25961–25977 (2001)

P.L. Pritchett, Energetic electron acceleration during multi-island coalescence. Phys. Plasmas **15**(10), 102105 (2008)

P.L. Pritchett, Onset of magnetic reconnection in the presence of a normal magnetic field: realistic ion to electron mass ratio. J. Geophys. Res. **115**(A10), 10208 (2010)
P.L. Pritchett, F.S. Mozer, Asymmetric magnetic reconnection in the presence of a guide field. J. Geophys. Res. **114**(A11), 11210 (2009)
Y. Ren, M. Yamada, S. Gerhardt, H. Ji, R. Kulsrud, A. Kuritsyn, Experimental verification of the Hall effect during magnetic reconnection in a laboratory plasma. Phys. Rev. Lett. **95**, 055003 (2005)
Y. Ren, M. Yamada, H. Ji, S. Dorfman, S.P. Gerhardt, R. Kulsrud, Experimental study of the Hall effect and electron diffusion region during magnetic reconnection in a laboratory plasma. Phys. Plasmas **15**, 082113 (2008a)
Y. Ren, M. Yamada, H. Ji, S.P. Gerhardt, R. Kulsrud, Identification of the electron-diffusion region during magnetic reconnection in a laboratory plasma. Phys. Rev. Lett. **101**, 085003 (2008b)
V. Roytershteyn, W. Daughton, S. Dorfman, Y. Ren, H. Ji, M. Yamada, H. Karimabadi, L. Yin, B.J. Albright, K.J. Bowers, Driven magnetic reconnection near the dreicer limit. Phys. Plasmas **17**(5), 055706 (2010)
V. Roytershteyn, S. Dorfman, W. Daughton, H. Ji, M. Yamada, H. Karimabadi, Electromagnetic instability of thin reconnection layers: comparison of three-dimensional simulations with MRX observations. Phys. Plasmas **20**(6), (2013)
E. Scime, S. Hokin, N. Mattor, C. Watts, Ion heating and magnetohydrodynamic dynamo fluctuations in the reversed-field pinch. Phys. Rev. Lett. **68**, 2165–2167 (1992)
M.A. Shay, J.F. Drake, R.E. Denton, D. Biskamp, Structure of the dissipation region during collisionless magnetic reconnection. J. Geophys. Res. **103**(A5), 9165–9176 (1998). ISBN:0148-0227
M.A. Shay, J.F. Drake, B.N. Rogers, R.E. Denton, Alfvénic collisionless magnetic reconnection and the hall term. J. Geophys. Res. Space Phys. **106**(A3), 3759–3772 (2001)
M.A. Shay, J.F. Drake, M. Swisdak, Two-scale structure of the electron dissipation region during collisionless magnetic reconnection. Phys. Rev. Lett. **99**, 155002 (2007)
M.A. Shay, J.F. Drake, J.P. Eastwood, T.D. Phan, Super-Alfvénic propagation of substorm reconnection signatures and poynting flux. Phys. Rev. Lett. **107**, 065001 (2011)
M.A. Shay, C.C. Haggerty, T.D. Phan, J.F. Drake, P.A. Cassak, P. Wu, M. Oieroset, M. Swisdak, K. Malakit, Electron heating during magnetic reconnection: a simulation scaling study. Phys. Plasmas **21**(12), 122902 (2014)
A.Y. Shih, R.P. Lin, D.M. Smith, Rhessi observations of the proportional acceleration of relativistic >0.3 mev electrons and >30 mev protons in solar flares. Astrophys. J. Lett. **698**(2), 152 (2009)
M.I. Sitnov, M. Swisdak, A.V. Divin, Dipolarization fronts as a signature of transient reconnection in the magnetotail. J. Geophys. Res. Space Phys. **114**(A4), 04202 (2009)
T.W. Speiser, Particle trajectories in model current sheets: 1. Analytical solutions. J. Geophys. Res. **70**(17), 4219–4226 (1965)
L. Spitzer, *Physics of Fully Ionized Gases*, 2nd edn. (Interscience Publishers, New York, 1962)
A. Stark, W. Fox, J. Egedal, O. Grulke, T. Klinger, Laser-induced fluorescence measurement of the ion-energy-distribution function in a collisionless reconnection experiment. Phys. Rev. Lett. **95**, 235005 (2005)
R.L. Stenzel, W. Gekelman, N. Wild, Magnetic field line reconnection experiments, 4. Resistivity, heating, and energy flow. J. Geophys. Res. **87**(A1), 111–117 (1982)
P. Sweet, *Electromagnetic Phenomena in Cosmical Physics* (Cambridge University Press, New York, 1958), p. 123
J.B. Taylor, Relaxation and magnetic reconnection in plasmas. Rev. Mod. Phys. **58**, 741–763 (1986)
D.A. Uzdensky, R.M. Kulsrud, Physical origin of the quadrupole out-of-plane magnetic field in hall-magnetohydrodynamic reconnection. Phys. Plasmas **13**(6), 062305 (2006)

J.R. Wygant, C.A. Carttell, R. Lysak, Y. Song, J. Dombeck, J. McFadden, F.S. Mozer, C.W. Carlson, G. Parks, E.A. Lucek, A. Balogh, M. Andre, H. Reme, M. Hesse, C. Mouikis, Cluster observations of an intense normal component of the electric field at a thin reconnecting current sheet in the tail and its role in the shock-like acceleration of the ion fluid into the separatrix region. J. Geophys. Res. **110**, 09206 (2005)

M. Yamada, Progress in understanding magnetic reconnection in laboratory and space astrophysical plasmas. Phys. Plasmas **14**(5), 058102 (2007)

M. Yamada, Y. Ono, A. Hayakawa, M. Katsurai, F.W. Perkins, Magnetic reconnection of plasma toroids with cohelicity and counterhelicity. Phys. Rev. Lett. **65**, 721–724 (1990)

M. Yamada, Y. Ren, H. Ji, J. Breslau, S. Gerhardt, R. Kulsrud, A. Kuritsyn, Experimental study of two-fluid effects on magnetic reconnection in a laboratory plasma with variable collisionality. Phys. Plasmas **13**(5), 052119 (2006)

M. Yamada, R. Kulsrud, H. Ji, Magnetic reconnection. Rev. Mod. Phys. **82**, 603–664 (2010)

M. Yamada, J. Yoo, J. Jara-Almonte, H. Ji, R.M. Kulsrud, C.E. Myers, Conversion of magnetic energy in the magnetic reconnection layer of a laboratory plasma. Nature communications **5**, 4474 (2014)

M. Yamada, J. Yoo, J. Jara-Almonte, W. Daughton, H. Ji, R.M. Kulsrud, C.E. Myers, Study of energy conversion and partitioning in the magnetic reconnection layer of a laboratory plasma. Phys. Plasmas **22**(5), 056501 (2015)

J. Yoo, M. Yamada, H. Ji, C.E. Myers, Observation of ion acceleration and heating during collisionless magnetic reconnection in a laboratory plasma. Phys. Rev. Lett. **110**, 215007 (2013)

J. Yoo, M. Yamada, H. Ji, J. Jara-Almonte, C.E. Myers, Bulk ion acceleration and particle heating during magnetic reconnection in a laboratory plasma. Phys. Plasmas **21**(5), 055706 (2014a)

J. Yoo, M. Yamada, H. Ji, J. Jara-Almonte, C.E. Myers, L.-J. Chen, Laboratory study of magnetic reconnection with a density asymmetry across the current sheet. Phys. Rev. Lett. **113**, 095002 (2014b)

S. Zenitani, M. Hesse, A. Klimas, C. Black, M. Kuznetsova, The inner structure of collisionless magnetic reconnection: the electron-frame dissipation measure and hall fields. Phys. Plasmas **18**(12), 122108 (2011a)

S. Zenitani, M. Hesse, A. Klimas, M. Kuznetsova, New measure of the dissipation region in collisionless magnetic reconnection. Phys. Rev. Lett. **106**, 195003 (2011b)

S. Zenitani, I. Shinohara, T. Nagai, T. Wada, Kinetic aspects of the ion current layer in a reconnection outflow exhaust. Phys. Plasmas **20**(9), 092120 (2013)

V.V. Zharkova, K. Arzner, A.O. Benz, P. Browning, C. Dauphin, A.G. Emslie, L. Fletcher, E.P. Kontar, G. Mann, M. Onofri, V. Petrosian, R. Turkmani, N. Vilmer, L. Vlahos, Recent advances in understanding particle acceleration processes in solar flares. Space Sci. Rev. **159**, 357–420 (2011)

E.G. Zweibel, M. Yamada, Magnetic reconnection in astrophysical and laboratory plasmas. Annu. Rev. Astron. Astrophys. **47**(1), 291–332 (2009)

Chapter 5
Rapid Reconnection and Field Line Topology

E.N. Parker and A.F. Rappazzo

Abstract Rapid reconnection of magnetic fields arises where the magnetic stresses push the plasma and field so as to increase the field gradient without limit. The intent of the present writing is to show the larger topological context in which this commonly occurs. Consider an interlaced field line topology as commonly occurs in the bipolar magnetic regions on the Sun. A simple model is constructed starting with a strong uniform magnetic field B_0 in the z-direction through an infinitely conducting fluid from the end plate $z = 0$ to $z = L$ with the field lines tied at both end plates. Field line interlacing is introduced by smooth continuous random turbulent mixing of the footpoints at the end plates. This configuration is well suited to be modeled with the reduced magnetohydrodynamic (MHD) equations, with the equilibria given by the solutions of the 2D vorticity equation in this case. The set of continuous solutions to the "vorticity" equation have greatly restricted topologies, so almost all interlaced field topologies do not have continuous solutions. That infinite set represents the "weak" solutions of the vorticity equation, wherein there are surfaces of tangential discontinuity (current sheets) in the field dividing regions of smooth continuous field. It follows then that current sheets are to be found throughout interlaced fields, providing potential sites for rapid reconnection. That is to say, rapid reconnection and nanoflaring are expected throughout the bipolar magnetic fields in the solar corona, providing substantial heating to the ambient gas. Numerical simulations provide a direct illustration of the process, showing that current sheets thin on fast ideal Alfvén timescales down to the smallest numerically resolved scales. The asymmetric structure of the equilibria and the interlacing threshold for the onset of singularities are discussed. Current sheet formation and dynamics are further analyzed with dissipative and ideal numerical simulations.

E.N. Parker (✉)
Department of Physics, University of Chicago, Chicago, IL 60637, USA
e-mail: parker@oddjob.uchicago.edu

A.F. Rappazzo
Advanced Heliophysics, Pasadena, CA 91106, USA
e-mail: franco.rappazzo@gmail.com

W. Gonzalez, E. Parker (eds.), *Magnetic Reconnection*, Astrophysics and Space Science Library 427, DOI 10.1007/978-3-319-26432-5_5

Keywords Coronal heating • Field line topologies • Flares • Interlaced field lines • Magnetic equilibrium equation • Numerical simulations • Rapid reconnection • Rate of reconnection • Singular flux surfaces

5.1 Introduction

Rapid reconnection of magnetic field arises where the magnetic stresses drive the plasma and field toward increasing field gradients, so that the current density becomes large without bound. In the real world the increasing field gradients are limited by the slight resistivity of the plasma, of course. That is to say, the gradient increases to the point where resistive dissipation eats up the field fast enough to prevent further gradient increase. This quasi-steady dissipation progresses across the field at a speed at least as fast as the Alfvén speed C divided by the square root of the Lundquist number R_L for the overall field (Parker 1957; Sweet 1958a,b). In other words the rapid reconnection phenomenon is a mechanical process, driven by the magnetic forces so as to increase the field gradients and enhance the resistive dissipation. It occurs where two nonparallel field components are actively squashed together, expelling plasma and field from between them and approaching more closely so as to increase the field gradient and current density. The plasma dynamics and the kinetics of the thin intense current sheet control the rate of reconnection of the fields.

Note then that the basic resistive reconnection rate $C/R_L^{1/2}$ is nowhere near the explosive field reconnection rate in a solar flare or in a substorm in the geomagnetic tail, motivating serious consideration of the precise form of the reconnection site and the effective rate of dissipation. Petschek (1964) made the important point that the dissipation and reconnection site need not extend the full width of the field. He provided plausible arguments for the reconnection speed to be as large as $C/\ln R_L$ and comparable to the reconnection rates in nature. Others noted that the electron conduction speeds in the current sheet may be as large as the ion thermal velocity or greater, exciting plasma turbulence and creating "anomalous resistivity". Then it became clear that the expected central concentration of anomalous resistivity favored the shortening of the current sheet, automatically providing the Petschek mode. It was recognized that the current sheet may be subject to island formation, with the Hall effect involved to further enhance the dissipation rate. And then it was realized that the current sheet is often so thin at the large Lundquist numbers encountered in tenuous plasmas that the ions may decouple from the magnetic field. So the simple resistive MHD current sheet must be replaced by a treatment in plasma kinetics (Biskamp and Drake 1994; Drake et al. 1994, 2005; Biskamp et al. 1997). The result is a further enhancement of the theoretical dissipation rate with a central concentration that automatically favors the Petschek mode. The reader is referred to the review by Yamada (2011) to fill in some of the details of this fundamental work. One can expect reconnection in nature at the observed rates of 0.01–0.1 C at active moments, interspersed with quiet periods of ongoing reconnection perhaps as slow

as the basic resistive rate $C/R_L^{1/2}$. Remote observations generally pick up only the active moments, of course.

Finally, Yamada and coworkers have set up the rapid reconnection phenomenon in the laboratory for quantitative measurements. In particular, they have studied conditions for reconnection at the basic rate $C/R_L^{1/2}$ compared to conditions for the faster Petschek reconnection mode, reviewed in Yamada et al. (2010) and Yamada (2011). The reader is referred to the several papers (and references therein) on the reconnection rate presented in this Volume and to the alternative approach developed by Ng and Bhattacharjee (1998).

The present writing considers where and how the local rapid reconnection phenomenon arises in the overall topology of the surrounding magnetic field. The vigorous convective motions and very large Lundquist numbers found in astrophysical settings suggest that field line topology may be complicated. To consider a basic example, note the common bipolar magnetic fields arching above the solar photosphere. Both ends of the bipolar field are rooted in the turbulent convective photosphere, so the photospheric footpoints of the field are continually intermixed on scales of a few hundred km by the convective granules. It follows that the field lines connecting between the two ends of the bipolar field are interlaced in random patterns along their length, sketched in Fig. 5.1. We investigate the final equilibrium of such a common interlaced field line topology, starting from an initial smooth, continuous, and bounded interlaced field with no further deformations introduced from outside the region, and letting the magnetic stresses in the field topology alone determine the final equilibrium state. The result is that current sheets, i.e., internal sites for rapid reconnection, are intrinsic to interlaced field line topologies wherever they occur (Parker 2012a,b).

In particular it has long been proposed that with vanishing electrical resistivity the current sheets reduce to true mathematical tangential discontinuities. The investigation of singularities in fluid equations poses grand mathematical, physical and computational challenges (Gibbon 2008). While there is no doubt that from a variety of initial conditions of interest to solar and stellar coronae the electric current will in general grow rapidly forming current sheets, a mathematically rigorous proof of the development of a singularity (that remains open also for the 3D Euler and Navier-Stokes equations) may require new methods (e.g., see Tao 2015), while numerical simulations cannot currently follow the unlimited steepening of

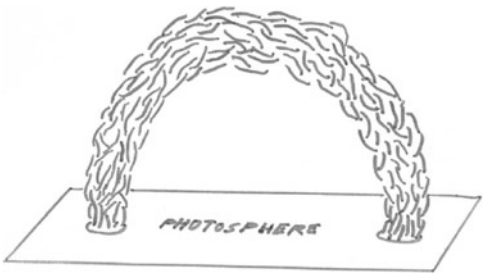

Fig. 5.1 Sketch of interlaced magnetic field line topology of a bipolar solar magnetic field rooted in the convective solar photosphere

the field gradients below the numerical resolution set by computational power and machine precision. It seems that a clearer understanding may be attained by a combination of analytical and numerical investigations, and the development of novel computational and mathematical techniques.

5.2 2D Neutral Points

We begin with a brief review of the field line topology associated with the ongoing field gradient increase and rapid reconnection, so that we can better understand the physical ramifications of the general mathematics of the interlaced field line topology.

It is well known (Parker 1957, 1979; Syrovatskii 1971, 1978, 1981) that a 2D X-type neutral point is the setting for rapid reconnection. Pick a point P in the field $\mathbf{B}(\mathbf{r})$. Set up a Cartesian coordinate system with its origin at P and the z-axis tangent to $\mathbf{B}(P)$. The x and y-axes are perpendicular to $\mathbf{B}(P)$ of course, so $B_x(P) = B_y(P) = 0$. Thus the transverse field in the xy-plane has a 2D neutral point at P. The neutral point is either X-type or O-type.

A pure X-type neutral point arises in the absence of torsion ($\mathbf{B} \cdot \nabla \times \mathbf{B} = 0$), i.e., in a 2D potential field. With suitable orientation of the xy coordinates, the local field in the near neighborhood of P can be written as

$$B_x \simeq \beta y, \quad B_y \simeq \beta x, \tag{5.1}$$

where β is a constant and the scalar potential is βxy. This field can be expressed in terms of the local vector potential in the z-direction,

$$A \simeq \frac{1}{2}\beta \left(y^2 - x^2\right). \tag{5.2}$$

The hyperbolic field lines are given by $A = constant$, sketched in Fig. 5.2 (*left*).

The pure O-type neutral point is represented by the field

$$B_x \simeq +\gamma y, \quad B_y \simeq -\gamma x, \tag{5.3}$$

where γ is a constant. This field can be expressed in terms of the vector potential

$$A \simeq \frac{1}{2}\gamma \left(x^2 + y^2\right) \tag{5.4}$$

in the z-direction. The field lines form concentric circles and the curl of the field is -2γ.

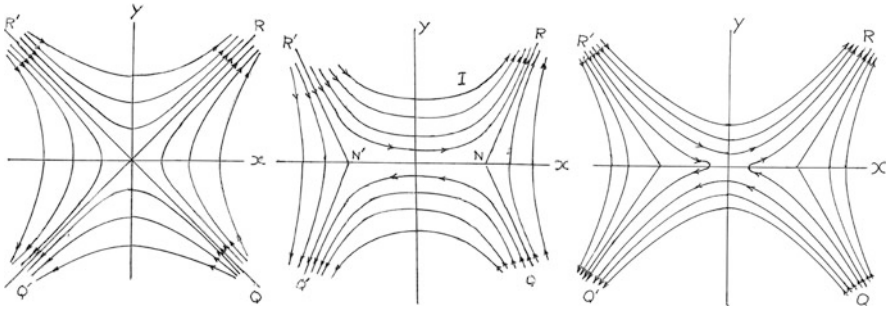

Fig. 5.2 *Left*: 2D X-type neutral point in a curl-free magnetic field. *Center*: Current sheet $N'N$ formed by squashing the X-type neutral point. *Right*: Resistive reconnection of magnetic field across the current sheet $N'N$

When both fields are present,

$$B_x \simeq (\beta + \gamma)y, \quad B_y \simeq (\beta - \gamma)x, \tag{5.5}$$

with

$$A \simeq \frac{1}{2}\left[(\beta + \gamma)y^2 - (\beta - \gamma)x^2\right]. \tag{5.6}$$

Thus the field lines $A = constant$ are a family of hyperbolas when $(\beta + \gamma)$ $(\beta - \gamma) > 0$ and ellipses when $(\beta + \gamma)(\beta - \gamma) < 0$. That is to say, we have an oblique X-type neutral point when $\beta^2 > \gamma^2$ and an elliptical O-type neutral point when $\beta^2 < \gamma^2$. For $\beta = +\gamma$ the magnetic field is $B_x \simeq 2\beta y$, $B_x \simeq 0$, while $\beta = -\gamma$ gives $B_x \simeq 0$, $B_y \simeq 2\beta x$. Obliquity is generally expected in nature.

Reconnection is associated with the X-type neutral point. For if the field in $y > 0$ in Fig. 5.2 (*left* panel) is pushed downward and the field in $y < 0$ is pushed upward, the field sectors in $x > 0$ and $x < 0$ are squeezed right and left out of the picture. The field sectors in $y > 0$ and $y < 0$ squash together at the x-axis, sketched in Fig. 5.2 (*center* panel). The X-type neutral point has been split into two opposite facing Y-type neutral points, marked N and N' in Fig. 5.2 (*center* panel). The tails of the Y-type neutral points join to form a current sheet $N'N$ between the opposite fields in $y > 0$ and $y < 0$. In an infinitely conducting fluid the field at the current sheet is $B_y = 0$ while B_x is discontinuous, reversing sign across the current sheet.

Field line reconnection requires the introduction of some slight resistive diffusivity η. If the fluid did not move, the width of the current sheet profile across the x-axis would evolve with the characteristic thickness $(4\eta t)^{1/2}$ in a time t, increasing at the declining rate $(\eta/t)^{1/2}$. Figure 5.2 (*right* panel) is a sketch of the field after a small time t, showing the reconnection of field across the segment $N'N$ of the x-axis. It is obvious from the figure that the tension in the field ejects fluid out each end of the current layer $N'N$. What is more, B_x changes sign across the x-axis and therefore vanishes on the x-axis, thereby reducing the total magnetic pressure. So pressure

equilibrium, $p + B^2/8\pi = constant$, across the current sheet is maintained with enhanced fluid pressure. The enhanced fluid pressure, together with the magnetic tension, eject field and fluid out each end of the current sheet. The ejection of fluid thins the current sheet and increases the field gradient, so that the rate at which resistivity dissipates magnetic field is maintained at the greatly elevated rate $C/R_L^{1/2}$ or more that we call rapid reconnection.

The next step is to look at the 3D picture of the simple 2D rapid reconnection described so far. The tension in $B(P)$, i.e. B_z, plays no role in the 2D picture, but in 3D the variation with z puts B_z in a central role. To explore the variation in the z-direction along the field $B(P)$ we turn to the optical analogy.

5.3 The Optical Analogy

The optical analogy applies to potential fields, $B_i = \partial\varphi/\partial x_i$. The direction cosines of a field line are given by

$$\frac{dx_i}{ds} = \frac{1}{B}\frac{\partial\varphi}{\partial x_i}, \tag{5.7}$$

where B is the field magnitude and ds is an element of length along the field line.

Consider an electromagnetic wave $\exp i\psi$ in a medium with index of refraction n. The direction cosines of a ray path are

$$\frac{dx_i}{ds} = \frac{\partial\psi/\partial x_i}{|\partial\psi/\partial x_k|}. \tag{5.8}$$

The Eikonal equation, $|\partial\psi/\partial x_k|^2 = n^2$, reduces this to

$$\frac{dx_i}{ds} = \frac{1}{n}\frac{\partial\psi}{\partial x_i}. \tag{5.9}$$

Comparing Eqs. (5.7) and (5.9) it is evident that a field line in a potential field follows the same path as an optical ray in a medium with index of refraction n proportional to the field magnitude B.

We apply this to a field in force-free equilibrium, for which

$$\nabla \times \mathbf{B} = \alpha\mathbf{B}. \tag{5.10}$$

Consider, then, a field line in a flux surface S. The 2D field in the flux surface is a potential field, hence the optical analogy is applicable to the field lines in every flux surface in a force-free field (Parker 1989a,b, 1991, 1994).

Given the optical analogy, it follows that the field line extending between points J and K is subject to Fermat's principle, that the optical path length is an extremum,

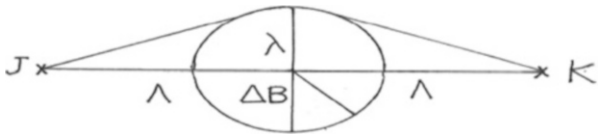

Fig. 5.3 Sketch of a region (scale λ) of enhanced magnetic pressure $\mathbf{B} \cdot \Delta\mathbf{B}/4\pi$ midway between the anchor points J and K of a field line of length 2Λ

and usually a minimum. Thus

$$\delta \int_J^K ds\, B(s) = 0, \tag{5.11}$$

along with the associated Euler equations. It follows that in the neighborhood of a local maximum, the field lines are concave toward the maximum. That is to say, the field lines tend to pass around, rather than through, a region of increased field in order to minimize the "optical" path length. In other words the field lines tend to be squeezed out of regions of high magnetic pressure. The increased magnetic pressure displaces the field line away from the high pressure, while the tension in the displaced field line tends to pull the field line back. The net effect is described by the optical analogy. Figure 5.2 (*center* panel) shows a 2D cross section through the region of maximum field.

Figure 5.3 is a sketch of a simple example, wherein a local increase ΔB in field strength above the ambient B has a characteristic scale λ. The example treats a field line extending a large distance 2Λ between two anchor points ($\Lambda \gg \lambda$). For simplicity the local maximum is placed at the center point of the line connecting the anchor points. Thus a field line skirting the maximum is inclined to the line by an angle of the order of λ/Λ, and the optical path length between anchor points J and K is $2B\Lambda(1 + \lambda^2/2\Lambda^2)$ to lowest order in λ^2/Λ^2. On the other hand, the optical path length straight over the top of the maximum is of the order of $2B\Lambda[1+(\Delta B/B)(\lambda/\Lambda)]$. It follows that the optical path length around the maximum is shorter than the path length through the maximum when

$$\frac{\Delta B}{B} > \frac{\lambda}{2\Lambda}. \tag{5.12}$$

Thus an increase $\Delta B/B$ of this amount squeezes the field out of the region of ΔB, creating a gap in the flux surface S. The gap appears as $N'N$ in Fig. 5.2 (*center* panel), where magnetic flux on one side of $N'N$ comes into contact with magnetic flux on the other side. The two fluxes are oppositely inclined to the z-axis so they produce the current sheet $N'N$. The resistive rapid reconnection across $N'N$ is maintained as fluid is ejected out both ends of the current sheet. Figure 5.4 is

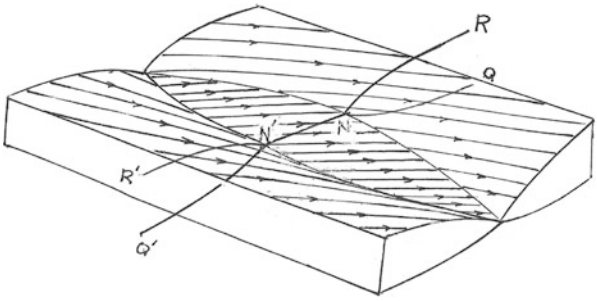

Fig. 5.4 Cutaway sketch of expulsion of magnetic field from magnetic pressure region, including the cross section sketched in the *center panel* of Fig. 5.2

a sketch of the whole 3D picture, including the cross section sketched in Fig. 5.2 (*center* panel).

It should be noted that the essential fluid motions creating the current sheet are the transverse displacements of the field, pushing the quadrants RNQ and $R'N'Q'$ (Fig. 5.2, *center* panel) aside so that the field in $R'N'NR$ comes in contact with the oppositely directed field in $Q'N'NQ$.

Incidentally, we note that the discontinuity of the magnetic field across $N'N$ slightly displaces the fields extending away from the region along the separatrices dividing the four sectors. The displacements are not the same on the two sides of each separatrix, resulting in surfaces of discontinuity (current sheets) along the separatrices shown in Fig. 5.2 (*center* and *right* panels).

Thus far we have considered the effect of local squeezing of the magnetic field to provide the current sheets, sketched in Fig. 5.2 (*center* and *right* panels). In fact there are initial field line topologies in continuous fields wherein the magnetic stresses create current sheets as an intrinsic part of the equilibrium of that field topology. As already noted, the commonly occurring interlaced field, sketched in Fig. 5.1, represents an important astrophysical example of the formation of current sheets as a direct consequence of the field topology.

5.4 Interlaced Field Line Topology

To show the universal formation of current sheets in interlaced fields we turn to the equilibrium equation (5.10) to show that almost all of the interlaced field line topologies naturally form internal surfaces of field discontinuity, i.e. current sheets, thereby providing rapid reconnection sites as an intrinsic part of their equilibria.

Consider, then, the mathematics of the static equilibrium of an interlaced topology. The interlacing topology is best defined relative to the topology of a uniform field. So consider a uniform magnetic field B extending in the z-direction through an infinitely conducting (dissipationless) cold plasma extending from an

infinitely conducting end plate at $z = 0$ to another such end plate at $z = L$. At time $t = 0$ the fluid is set in motion with the transverse 2D incompressible form

$$v_x = +kz\frac{\partial \psi}{\partial y}, \quad v_y = -kz\frac{\partial \psi}{\partial x}, \quad v_z = 0, \tag{5.13}$$

where $\psi = \psi(x, y, kzt)$ represents a bounded, continuous, differentiable function of its arguments. It is readily shown from the MHD induction equation that this fluid motion deforms the magnetic field into

$$B_x = +Bkt\frac{\partial \psi}{\partial y}, \quad B_y = -Bkt\frac{\partial \psi}{\partial x}, \quad B_z = B. \tag{5.14}$$

This deformation corresponds to holding the footpoints of the field fixed at $z = 0$ while introducing an arbitrary swirling and mixing of the footpoints at $z = L$, thereby creating an interlaced field line topology throughout $0 < z < L$, sketched in Fig. 5.5. The function $\psi(x, y, kzt)$ defines the interlaced topology. Note that the interlaced field is everywhere bounded, continuous, and differentiable.

Switch off the swirling $\psi(x, y, kzt)$ at time $t = \tau$, when the interlacing is well developed on a characteristic scale $l\,(<< L)$ in the transverse x and y-directions, and wound up tightly enough that the scale in the z-direction (along the mean field) is comparable to l. That is to say, the field components B_x, B_y, B_z are comparable in magnitude. Then hold fixed the footpoints of the field at $z = 0, L$ while releasing the fluid throughout $0 < z < L$ to move in response to the Lorentz force exerted by the interlaced field. Introduce a small viscosity into the fluid (plasma) so that the motions decline asymptotically to zero as the magnetic field relaxes to the lowest available magnetic energy state.

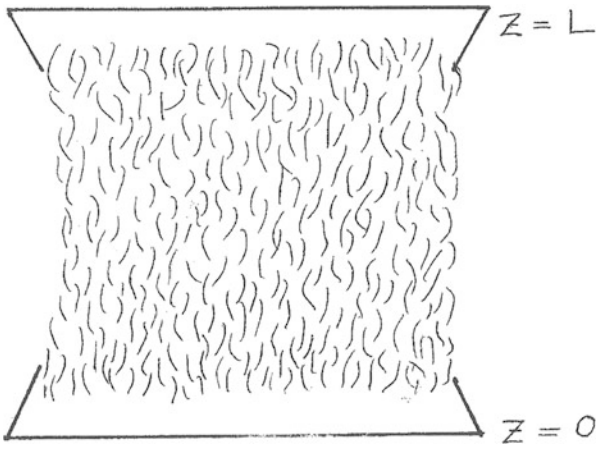

Fig. 5.5 Sketch of the interlaced magnetic field extending between the end plates $z = 0$ and $z = L$

It is important to note that, with the magnetic field attached at both ends $z = 0$ and $z = L$, the field cannot escape. Escape would mean stretching the field in opposition to the tension along the field lines. So with the passage of time the magnetic field, no matter what its interlaced topology, has no choice but to settle into a stable equilibrium. That is to say, there exists a formal mathematical solution to Eq. (5.10) for each and every interlaced field line topology. This fact plays a basic role in the interpretation of the equilibrium equations for the field.

5.5 Equilibrium of the Interlaced Field

In the absence of plasma pressure variations, the final equilibrium conforms to the familiar force-free field equation (5.10)

$$\nabla \times \mathbf{B} = \alpha \mathbf{B}$$

where the scalar function α is the torsion coefficient, given by

$$\alpha = \frac{\oint d\mathbf{s} \cdot \mathbf{B}}{\int d\mathbf{S} \cdot \mathbf{B}} \tag{5.15}$$

at any point P. Here the integration is over a small circle around $\mathbf{B}(P)$ centered on P, $d\mathbf{s}$ is an element of arc length along the circle, and $d\mathbf{S}$ is an element of area enclosed by the circle. The torsion coefficient is equal to the magnetic circulation around any small circle divided by the magnetic flux enclosed by that circle.

The force-free equation (5.10), having mixed characteristics, is unlike other field equations with which we are familiar. This may be seen from the curl of Eq. (5.10),

$$\mathbf{B} \times \nabla\alpha = \nabla^2 \mathbf{B} + \alpha^2 \mathbf{B}, \tag{5.16}$$

wherein the Laplacian operator indicates two families of complex characteristics. Equation (5.16) is a quasilinear elliptic equation. In contrast the divergence of Eq. (5.10) yields

$$\mathbf{B} \cdot \nabla\alpha = 0, \tag{5.17}$$

asserting that α is constant along each individual field line. Thus the field lines represent a family of real characteristics, so that the topology of the field enters directly into the solution of Eq. (5.10), that has both real and complex characteristics, and we may expect solutions of unfamiliar form.

The first point to consider is the assertion that the torsion coefficient α is constant along each field line regardless of how the interlacing topology involves field lines writhing their way from $z = 0$ to $z = L$ through the surrounding interlaced magnetic field. It is not obvious how a constant α can be accomplished along the

line, particularly if the line writhes in opposite senses at different locations along the field. And yet there must be a resolution of this seeming contradiction because, as already noted, a solution to Eq. (5.10) exists for every interlacing topology.

To explore the question, reduce the mathematics to its basic form for the given field line topology by dilating the system, stretching the region $0 < z < L$ in the z-direction by a large factor $1/\epsilon$, with $\epsilon \ll 1$. The dilatation preserves the topology, of course, and reduces the transverse field components to the order of ϵB, while the z-component is not much affected. So write

$$B_x = \epsilon B b_x, \quad B_y = \epsilon B b_y, \quad B_z = B\left(1 + \epsilon^2 b_z\right), \quad \alpha = \epsilon a, \tag{5.18}$$

with

$$\nabla \cdot \mathbf{B} = 0. \tag{5.19}$$

The term first order in ϵ in B_z can be included but turns out to be zero, as we would expect from the fact that the magnetic pressure fluctuations associated with b_x, b_y and b_z are all comparable and, hence, second order in ϵ.

Equation (5.17) becomes

$$\frac{\partial a}{\partial z} + \epsilon\left(b_x \frac{\partial a}{\partial x} + b_y \frac{\partial a}{\partial y}\right) = 0. \tag{5.20}$$

So to lowest order in ϵ we have

$$\frac{\partial a}{\partial z} = 0. \tag{5.21}$$

This proclaims that the torsion coefficient a is constant along the unperturbed field lines. It is a highly restrictive condition on the magnetic field topology (Parker 1972, 1979) and foreshadows the more precise result worked out by van Ballegooijen (1985), who noted that $\partial/\partial z$ is small to $O(\epsilon)$ compared to $\partial/\partial x$ and $\partial/\partial y$ in the stretched field. Take this into account by introducing the coordinate $\zeta = \epsilon z$, so that

$$\frac{\partial}{\partial z} = \epsilon \frac{\partial}{\partial \zeta}, \tag{5.22}$$

and $\partial/\partial\zeta$ is of the same order as the transverse derivatives $\partial/\partial x$ and $\partial/\partial y$. Equation (5.20) becomes

$$\frac{\partial a}{\partial \zeta} + \left(b_x \frac{\partial a}{\partial x} + b_y \frac{\partial a}{\partial y}\right) = 0, \tag{5.23}$$

representing Eq. (5.17) computed along the perturbed field lines, i.e., the actual field lines when expressed in terms of Eq. (5.18).

Now Eq. (5.16) provides the three equations for the local relations between a and the three field components, with

$$-\frac{\partial a}{\partial y} = \frac{\partial^2 b_x}{\partial x^2} + \frac{\partial^2 b_x}{\partial y^2}, \tag{5.24}$$

$$+\frac{\partial a}{\partial x} = \frac{\partial^2 b_y}{\partial x^2} + \frac{\partial^2 b_y}{\partial y^2}, \tag{5.25}$$

$$\epsilon\left(b_x\frac{\partial a}{\partial y} - b_y\frac{\partial a}{\partial x}\right) = \frac{\partial^2 b_z}{\partial x^2} + \frac{\partial^2 b_z}{\partial y^2} + \epsilon a^2. \tag{5.26}$$

to lowest order in ϵ. For present purposes however it is easier to work with the components of Eq. (5.10) because they are one order lower in spatial derivatives. Again neglecting terms second order in ϵ compared to one, we have

$$\frac{\partial b_z}{\partial y} - \frac{\partial b_y}{\partial \zeta} = a b_x, \tag{5.27}$$

$$\frac{\partial b_x}{\partial \zeta} - \frac{\partial b_z}{\partial x} = a b_y, \tag{5.28}$$

$$\frac{\partial b_y}{\partial x} - \frac{\partial b_x}{\partial y} = a. \tag{5.29}$$

Equation (5.19) reduces to

$$\frac{\partial b_x}{\partial x} + \frac{\partial b_y}{\partial y} = 0, \tag{5.30}$$

neglecting terms second order in ϵ compared to one.

Now, it follows from Eq. (5.30) that there exists a function $\Theta(x, y, \zeta)$ such that

$$b_x = +\frac{\partial \Theta}{\partial y}, \quad b_y = -\frac{\partial \Theta}{\partial x}. \tag{5.31}$$

Equation (5.30) is automatically satisfied, and Eq. (5.23) becomes

$$\frac{\partial a}{\partial \zeta} = \frac{\partial \Theta}{\partial x}\frac{\partial a}{\partial y} - \frac{\partial \Theta}{\partial y}\frac{\partial a}{\partial x}. \tag{5.32}$$

Equation (5.29) is written

$$a = -\left(\frac{\partial^2}{\partial x^2} + \frac{\partial^2}{\partial y^2}\right)\Theta. \tag{5.33}$$

Equations (5.32) and (5.33) together determine the possible variations of a and Θ. It is obvious by inspection that Eq. (5.26) provides an equation for b_z once a and Θ are known.

Van Ballegooijen (1985) pointed out that the two Eqs. (5.32) and (5.33) are the exact mathematical analog of the 2D time dependent vorticity (Euler) equation for an inviscid incompressible fluid with time t replaced by ζ. The torsion coefficient a corresponds to the vorticity ω, and the field components b_x and b_y correspond to the fluid velocity components v_x and v_y, the stream function being Θ in both realizations. Unfortunately van Ballegooijen misinterpreted the mathematics, failing to recognize that the infinitely many solutions to the vorticity equation form a topological set only of zero measure compared to all possible field line topologies (see the penultimate paragraph of Appendix B, Janse et al. 2010). So he concluded that all topologies can be accommodated by the vorticity solutions and there is no reason to expect discontinuities. Nonetheless his analogy with vorticity is correct and important. The fact is that $\psi(x, y, kzt)$ represents all possible interlacing field line topologies, and, with all field lines anchored at both ends, every topology has a stable equilibrium. On the other hand, the only continuous equilibrium solutions are the solutions to the vorticity equation (5.23), representing 2D turbulence with the enstrophy analog cascading toward small scales and the kinetic energy analog cascading toward large-scales along the field. But almost all interlaced topologies lack such unique cascading topology. That is to say, a member of the topological set of continuous solutions is a rarity within the set of all topologies. It follows that almost all interlaced field line topologies fail to have continuous equilibrium solutions, i.e., almost all solutions contain one or more surfaces of tangential discontinuity (current sheets). The spaces between the discontinuities are filled with continuous vorticity solutions.

5.6 Structure of Reduced MHD Equilibria and Dynamics

Further insight into the dynamics and the structure of the equilibria has been recently gained with numerical simulations and a quantitative analysis of the equilibria axial asymmetry (Rappazzo and Parker 2013; Rappazzo 2015). A coronal loop is modeled, as in previous work (Rappazzo et al. 2007, 2008), with a simplified cartesian geometry, uniform density ρ, and a *strong and homogeneous axial magnetic field* $\mathbf{B}_0 = B_0\,\hat{\mathbf{e}}_z$ threading the system: a configuration well suited to be studied in the reduced MHD regime (Zank and Matthaeus 1992). At leading order the dynamic velocity and magnetic fields are solenoidal ($\nabla \cdot \mathbf{u} = \nabla \cdot \mathbf{b} = 0$) and have only orthogonal components $\mathbf{u} \cdot \mathbf{B}_0 = \mathbf{b} \cdot \mathbf{B}_0 = 0$. They are linked to the corresponding potentials φ and ψ by $\mathbf{u} = \nabla\varphi \times \hat{\mathbf{e}}_z$, and $\mathbf{b} = \nabla\psi \times \hat{\mathbf{e}}_z$, while vorticity and current density are given by $\omega = -\nabla_\perp^2\varphi$ and $j = -\nabla_\perp^2\psi$ (pointing in the z direction, where $\nabla_\perp^2 = \partial_x^2 + \partial_y^2$). With this notation the nondimensional

reduced MHD equations (Kadomtsev and Pogutse 1974; Strauss 1976) are written as:

$$\frac{\partial \psi}{\partial t} = [\varphi, \psi] + B_0 \frac{\partial \varphi}{\partial z} + \eta_n \nabla_\perp^{2n} \psi, \tag{5.34}$$

$$\frac{\partial \omega}{\partial t} = [j, \psi] - [\omega, \varphi] + B_0 \frac{\partial j}{\partial z} + \nu_n \nabla_\perp^{2n} \omega, \tag{5.35}$$

where the Poisson bracket of functions g and h is defined as $[g, h] = \partial_x g\, \partial_y h - \partial_y g\, \partial_x h$ (e.g., $[j, \psi] = \mathbf{b} \cdot \nabla j$). To render the equations nondimensional the magnetic field has been first expressed as an Alfvén velocity ($b \to b/\sqrt{4\pi\rho}$), and then all velocities have been normalized with $u^* = 1\,\mathrm{km\,s^{-1}}$, a typical value in photospheric convective granules. The domain spans $0 \le x, y \le L_\perp$ and $0 \le z \le L_z$, with $L_\perp = 1$ and $L_z = 10$ in all calculations. Magnetic field lines are line-tied to a motionless photosphere at the top and bottom plates ($z = 0$ and 10), where a vanishing velocity $\mathbf{u} = 0$ is in place. In the perpendicular (x-y) directions a pseudo-spectral scheme with periodic boundary conditions and isotropic truncation de-aliasing is used (*2/3-rule*) (Canuto et al. 2006), while along z a second-order finite difference scheme is implemented. The CFL (Courant-Friedrichs-Levy) condition is satisfied through an adaptive time-step (for a more detailed description of the model and numerical code see Rappazzo et al. 2007, 2008).

Reduced MHD equilibria are given by $\mathbf{B} \cdot \nabla j = 0$, obtained by neglecting velocity and diffusion terms in Eqs. (5.34)–(5.35). Since the total magnetic field is given by $\mathbf{B} = B_0 \hat{\mathbf{e}}_z + \mathbf{b}(x, y, z)$, the equilibrium condition can be written as:

$$\frac{\partial j}{\partial z} = -\frac{\mathbf{b}}{B_0} \cdot \nabla j, \tag{5.36}$$

where both sides correspond to different Lorentz force components orthogonal to $\mathbf{B}_0$: the right-hand side term corresponds to $\mathbf{b} \cdot \nabla \mathbf{b}$, and the left hand side to the $B_0 \partial_z \mathbf{b}$ field line tension. Assigned $\mathbf{b}$ in an x-y plane, e.g., at the boundary z=0 $\mathbf{b}(x, y, z = 0) = \mathbf{b}_{bd}(x, y)$, the integration of this equation for $z > 0$ allows to compute the corresponding equilibrium in the whole computational box $0 \le z \le L_z$.

The reduced MHD equilibrium equation (5.36) is *identical* to the 2D Euler equation

$$\frac{\partial \omega}{\partial t} = -\mathbf{u} \cdot \nabla \omega, \tag{5.37}$$

(with $\nabla \cdot \mathbf{u} = 0$, $\mathbf{u}(x, y, t) = \nabla \phi(x, y, t) \times \hat{\mathbf{e}}_z$, and vorticity $\omega = -\nabla^2 \phi$, with ϕ the velocity potential) under the *mapping*

$$t \to z, \qquad \mathbf{u} \to \frac{\mathbf{b}}{B_0}, \tag{5.38}$$

and consequently $\omega \to j/B_0$.

The physics and solutions of the 2D Euler equation have been studied extensively, including in the laboratory, in the framework of 2D hydrodynamic turbulence (Kraichnan and Montgomery 1980; Tabeling 2002; Boffetta and Ecke 2012). It is among the few partial differential equations for which a theorem proves the existence and uniqueness of its solutions: given a smooth initial condition $\mathbf{u}_0(x, y)$ at time $t = 0$, the 2D Euler equation admits a *unique and regular solution* at $t > 0$ (Rose and Sulem 1978; Chemin 1993; Bertozzi and Constantin 1993; Majda and Bertozzi 2001).

The dynamics of its solutions differ substantially from those of MHD and 3D hydrodynamics. In 2D besides energy also *enstrophy* $\Omega = \int \mathrm{d}a\ \omega^2$ (i.e., integrated square vorticity) is conserved. The presence of this additional ideal invariant strongly limits the development of a direct energy cascade (a transfer of energy toward smaller scales), since the conservation of both $E = \int \mathrm{d}k\ E(k)$ and $\Omega = \int \mathrm{d}k\ k^2 E(k)$ favors the transfer of energy at larger scales (corresponding to smaller k), i.e., an inverse cascade. Kraichnan (1967) and Batchelor (1969) first proposed this inverse energy cascade phenomenology (now supported also by numerical simulations and laboratory experiments, see Boffetta and Ecke (2012) and references therein), where energy develops a spectrum $E_k \propto k^{-5/3}$ following a phenomenology similar to that proposed by Kolmogorov (1941) (that does not depend on the direction of the cascade; Rose and Sulem 1978), with *eddy turnover time* approximately given by

$$t_\ell \sim \frac{\ell}{u_\ell}, \tag{5.39}$$

with a possible logarithmic correction that we neglect (Kraichnan 1971). For a configuration made of vortices of scale ℓ and velocity u_ℓ, t_ℓ is the *timescale* over which such a vortex (eddy) experiences significant distortions due to the relative motion of its components, transferring its energy approximately from the scale ℓ to the scale of double size 2ℓ (schematically drawn in the left panel of Fig. 5.6).

The mapping (5.38) between the solutions of the 2D Euler equation and the reduced MHD equilibria allows to connect the inverse energy cascade *in time* of the solutions of the 2D Euler equation to the asymmetric structure *in space* of the reduced MHD equilibria along the axial direction z (Fig. 5.6), with the caveat that *eddies* are vortices in the hydrodynamic case and magnetic islands in reduced MHD. In particular given a magnetic field $\mathbf{b}_{bd}(x, y)$ at the boundary $z = 0$, made of magnetic islands of scale $\sim \ell$, the unique and regular reduced MHD equilibrium solution $\mathbf{b}_{eq}(x, y, z)$ for which $\mathbf{b}_{eq}(x, y, z = 0) = \mathbf{b}_{bd}(x, y)$ undergoes an increasingly stronger *inverse cascade in space* in the x-y planes for higher values of z (see Fig. 5.6, right panel), with the orthogonal magnetic field length-scale ℓ getting progressively larger up to doubling its value in the plane $z \sim z_\ell$, with

$$z_\ell \sim \frac{B_0}{b_{bd}}\,\ell. \tag{5.40}$$

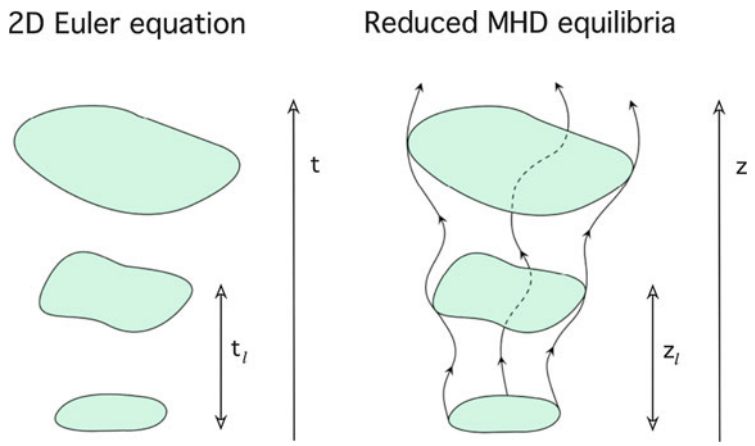

Fig. 5.6 *Left*: Diagram of the inverse energy cascade *in time* of the solution of the 2D Euler equation, characterized by the eddy turnover time $t_\ell \sim \ell/u_\ell$ (Eq. (5.39)). *Right*: Structure of the reduced MHD equilibria *in space*. Its asymmetry in the axial direction z is measured by the variation length-scale $z_\ell \sim B_0\ell/b$ (Eq. (5.40)). Images adapted from Rappazzo (2015)

The variation length-scale z_ℓ is derived from Eq. (5.39) through the mapping (5.38). If the magnetic field is characterized by a scale of order ℓ at $z = 0$ it will have its energy at scale $\sim 2\ell$ at $z = z_\ell$, corresponding respectively to magnetic islands of scales ℓ and 2ℓ in the x-y planes $z = 0$ and $z = z_\ell$.

Therefore the reduced MHD equilibria can be *strongly asymmetric* in the axial direction if the variation length-scale (Eq. (5.40)) is small compared to the loop length $z_\ell < L_z$, or *quasi-invariant* if the variation lenght-scale is larger than the loop length $z_\ell \gtrsim L_z$.

On the other hand the dynamic solutions of the reduced MHD equations (5.34)–(5.35) do not generally develop strong spatial variations along the axial direction, particularly in the case of interest here of footpoint shuffling at the boundaries $z = 0$ and L_z. Indeed the linear terms $\propto B_0\partial_z$ in Eqs. (5.34)–(5.35) give rise to a Alfvén wave propagation at the fast speed B_0 of any perturbation along the axial direction. Consequently the fields do not develop strong variations along z, as confirmed by numerical simulations (e.g., Galsgaard and Nordlund 1996; Dmitruk and Gómez 1999; Rappazzo et al. 2008; Wilmot-Smith et al. 2011; Dahlburg et al. 2012). Since in general the magnetic field rms is approximately invariant along z, we will drop the "boundary" subscript in Eq. (5.40) hereafter, indicating the variation length-scale simply as $z_\ell \sim \ell B_0/b$.

As discussed in the next section, numerical simulations suggest that the loop length L_z is a *critical length* for the variation scale z_ℓ. For initial configurations with magnetic fields invariant along z and intensities stronger than $b > \ell B_0/L_z$, the corresponding equilibria have variation length-scales $z_\ell < L_z$ and therefore are strongly asymmetric and cannot be accessed dynamically. The strong initial deviation from equilibrium sets the plasma in motion, with nonlinear dynamics

generating quickly current sheets (Rappazzo and Parker 2013). In the dissipative case energy is then dissipated, and in this relaxation process energy continues to be dissipated and decrease until the variation length-scale grows up to the critical length $z_\ell \sim L_z$, when an equilibrium quasi-invariant along z can be asymptotically accessed. Hence magnetic fields for which $z_\ell < L_z$ necessarily have to dissipate energy, requiring current sheets to form and magnetic reconnection to occur. *On the contrary*, for magnetic fields with intensities approximately smaller than $b \lesssim \ell B_0/L_z$, the corresponding equilibria have variation length-scales larger than approximately the loop length $z_\ell \gtrsim L_z$, the equilibria are then quasi-invariant along z at the loop scale. The initial magnetic field can in this case adapt quasi-statically to the very close equilibrium with a negligible, if any, energy dissipation.

In summary an initial magnetic field invariant along z will always decay toward an equilibrium. But for intensities larger than $b > \ell B_0/L_z$ the corresponding equilibrium cannot be accessed because it is strongly asymmetric ($z_\ell < L_z$), therefore current sheets will form and magnetic reconnection occur so that a lower energy equilibrium quasi-invariant along z, with variation length-scale $z_\ell \sim L_z$ and magnetic field intensity $b \sim \ell B_0/L_z$, can be accessed.

In the aforementioned discussion we have always considered initial magnetic fields not in equilibrium, i.e., that do not satisfy Eq. (5.36). Solar photospheric motions have a very low frequency ($1/t_c$, with $t_c \sim 5$–8 m) compared to the fast crossing time of Alfvén waves along the loop axis $t_c \gg t_A$, where for typical values of L_z and B_0, e.g., with $L_z \sim 4{\times}10^4$ km and $B_0 \sim 2{\times}10^3$ km/s, we obtain $t_A = L_z/B_0 \sim 20$ s. The configurations most of interest to the Sun are those with $\partial_z j \sim 0$, but with $\mathbf{b} \cdot \nabla j \neq 0$, i.e., with the orthogonal component of the magnetic field out-of-equilibrium in the x–y planes due to the disordered and turbulent nature of photospheric convection. Therefore it is important to remark that the configurations considered here are not unstable. Classic unstable equilibria, e.g., kink (other unstable configurations can be found in Parker (1983); Longcope and Strauss (1993) and references therein), can be recovered in the limit $\mathbf{b} \cdot \nabla j \to 0$ with $b \neq 0$ in Eq. (5.36), that implies also $\partial_z j \to 0$. In this limit the highly symmetric fields of unstable configurations are recovered, but they are outside the scope of this paper.

Since the dynamics are not driven by instabilities, but rather by nonlinear dynamics developing as soon as photospheric motions twist the field lines beyond the critical intensity threshold $b > \ell B_0/L_z$ (see also Eq. (5.12)), current sheets formation clearly stems from the nonlinear dynamics developing due to the magnetic field striving to relax while continuously set out of equilibrium by photospheric motions at its footpoints.

An alternative model for coronal heating had been proposed by van Ballegooijen (1986). Because in his view the magnetic field evolution should be restricted to a continuous quasi-static relaxation to nearby equilibria, he conjectured that successive uncorrelated steps of the magnetic field line footpoints random walk would shred the coronal magnetic field thus producing small-scale current sheets (necessary to heat the corona) uniformly distributed in the loop volume. This kinematic "cascade" of magnetic energy would originate from magnetic field lines

passively tracing their footpoints shuffled in random directions by photospheric motions. This mechanism would lead to current sheet formation on timescale longer than photospheric convection (several random walk steps would be required). The relaxation simulations by Rappazzo and Parker (2013) unquestionably rule out this mechanism, since current sheets form on ideal timescales while the footpoints are fixed at the photospheric plates where no motions are in place (and therefore no footpoint random walk occurs).

On the other hand earlier 2D (Einaudi et al. 1996; Dmitruk and Gómez 1997) and later reduced MHD numerical simulations (Dmitruk and Gómez 1999; Dmitruk et al. 2003; Rappazzo et al. 2007, 2008) have pointed out the connection of the dynamics of this system with MHD turbulence (with similar dynamics also shown in the cold plasma regime (Hendrix and van Hoven 1996) and fully compressible MHD simulations (Galsgaard and Nordlund 1996; Dahlburg et al. 2012)) such as the formation of energy spectra with power-law behavior, the formation of current sheets distributed intermittently in space and time, and the power-law behavior in total energy, peak dissipation and duration of the bursts of dissipation, that correspond to the formation and dissipation of current sheets, that exhibit indexes not far from those determined observationally in X-rays (Georgoulis et al. 1998; Dmitruk et al. 1998). Nevertheless the turbulent regime for this system is very distinct from the corresponding 3D hydrodynamic case (Frisch 1995), and it is overall best characterized as magnetically dominated MHD turbulence. Indeed not only velocity fluctuations $\mathbf{u}$ are generally smaller than magnetic fluctuations $\mathbf{b}$, but energy transfers across scales are determined by the magnetic field. Energy flows between different scales have long been tracked for the hydrodynamic Navier-Stokes equations (Frisch 1995), and more recently they have been studied numerically also in MHD at relatively high resolutions (Dar et al. 2001; Alexakis et al. 2005). A recent investigation of the energy flows toward small scales in a high-resolution boundary driven reduced MHD simulation (Rappazzo and Velli 2011) has allowed to determine which nonlinear terms drive the nonlinear cascade and thus the formation of current sheets. As schematically drawn in Fig. 5.7 energy across different scales of the velocity field (indicated with T_{uu}) have been found to be negligible. In other words the term $\mathbf{u} \cdot \nabla \mathbf{u}$ (corresponding to the term $[\omega, \varphi]$ in Eq. (5.35)), that generates all nonlinear dynamics in the Navier-Stokes equations, gives a negligible contributions to the energy fluxes in this problem. As a result, the magnetic field is in "dynamical non-equilibrium" (Parker 1972, 1988, 1994, 2012b) at all scales, and it creates and shapes the small velocity field along the inertial range (through the Lorentz force terms $\mathbf{b} \cdot \nabla \mathbf{b}$ and $B_0 \partial_z \mathbf{b}$), that in turn create small scales in the magnetic field by distorting it and pushing field lines together, with an overall energy flux toward smaller scales akin to that put forward by Kolmogorov (1941) but for which the eddies that get distorted are magnetic islands.

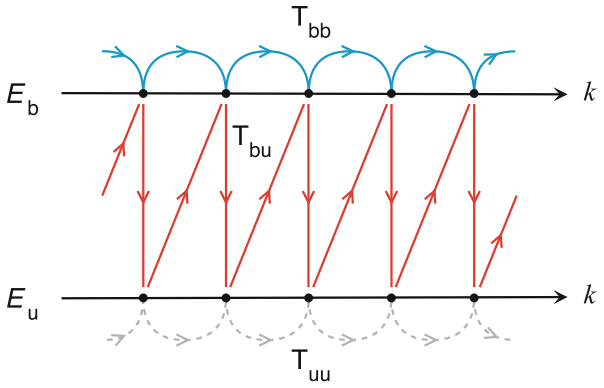

Fig. 5.7 Diagram of energy flows between fields and scales in the inertial range (at scales intermediate between the larger scales where photospheric convection injects energy into the corona and the smaller scales where dissipation occurs). Spectral fluxes are indicated with, e.g., T_{bu} for the flux between different scales of magnetic and velocity fields, and analogously for other fields permutations. Image adapted from Rappazzo and Velli (2011)

5.6.1 Numerical Simulations (Dissipative)

In this section we briefly summarize the dissipative numerical simulations carried out in Rappazzo and Parker (2013) and Rappazzo (2015). Initial conditions at $t = 0$ have a vanishing velocity $\mathbf{u} = 0$ everywhere in the computational box, and a uniform and homogeneous guide field $B_0 = 10^3$. The initial perpendicular magnetic field component $\mathbf{b}_0$, with several intensities b_0 considered, consists of *large-scale* Fourier modes, with orthogonal wave-numbers in the range $3 \leq n_\perp \leq 4$, and example of which is shown in Fig. 5.10 (top left panel). In the parallel direction z initial magnetic fields differ for the number of parallel Fourier modes present at time t = 0. Since the photospheric convection frequency is low compared to the fast Alfvén transit time along coronal loops, the magnetic field is not expected to have strong variations along the loop axis, therefore we consider at first initial conditions invariant along z with $\partial_z = 0$, that have only the parallel mode m=0. Additionally we consider also initial magnetic fields with only the parallel mode m $= 1$, apt for longer loops on the Sun and other active stars where the Alfvén crossing time becomes of the order of the convective timescale or faster, and finally also initial conditions with all parallel modes $m \in [0, 4]$ with a dominant m=0 mode are considered. As remarked in the previous section all magnetic fields at time t $= 0$ are out of equilibrium, in particular for all simulations $\mathbf{b}_0 \cdot \nabla j \neq 0$ initially, because the magnetic field brought about by the turbulent and disordered solar convection lacks the symmetry required to make the corresponding Lorentz force component vanish.

Results of numerical simulations with initial magnetic field invariant along z are shown in Fig. 5.8. All simulations have line-tying boundary conditions in the photospheric-mimicking plates z=0 and 10 (where field lines are rooted in

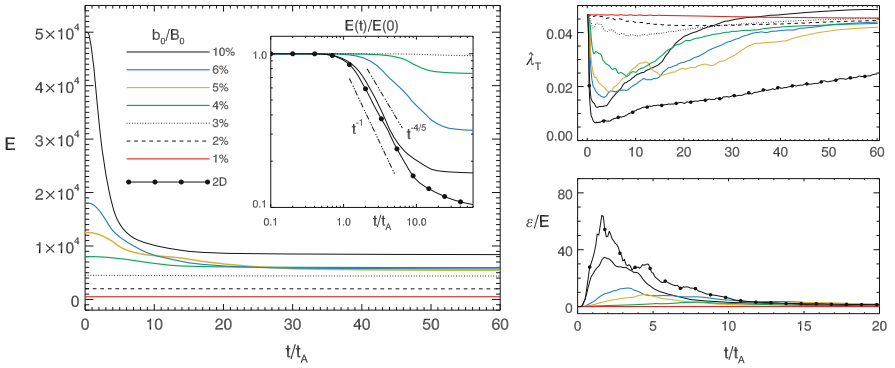

Fig. 5.8 Reduced MHD simulations with initial magnetic field invariant along z ($\partial_z \mathbf{b} = 0$, only parallel mode m = 0 present). *Left*: Total energy vs. time (in logarithmic scale in the *inset*) for line-tied simulations with different values of b_0/B_0 and a 2D simulation with $b_0/B_0 = 10\,\%$. *Right*: Taylor microscale λ_T and normalized energy dissipation rate ϵ/E ($\epsilon = dE/dt$) vs. time. Images adapted from Rappazzo and Parker (2013)

a motionless plasma where $\mathbf{u} = 0$), and periodic boundary conditions in the orthogonal x–y planes. Additionally also results from a 2D simulation are shown (in dotted-continuous black line). As discussed more in detail in Rappazzo and Parker (2013) and Rappazzo (2015) the 2D simulation corresponds to use periodic boundary conditions also in the axial direction z (because the initial condition is invariant along z, no variations are developed in this direction in time), and is used here as a reference case to compare with line-tied simulations. Furthermore the 2D case is appropriate to model the central part of long loops far from the boundaries, where line-tying has a weak influence.

As shown in Fig. 5.8 (left panel) the relaxation of the 2D magnetic field is similar to 2D turbulence decay simulations (Hossain et al. 1995; Galtier et al. 1997; Biskamp 2003), decaying in time approximately as the power-law t^{-1}, even though no velocity field is present in the initial condition and the velocity developed by the out-of-equilibrium magnetic field remains much smaller than magnetic fluctuations the entire time (while in turbulence simulations the velocity field is in approximate equipartition with the magnetic field the whole time). As shown in the right panel of Fig. 5.8 the energy decay corresponds to the rapid formation of small scales, as indicated by the initial sharp decrease of the Taylor micro-scale $\lambda_T = \left(\langle b^2\rangle/\langle j^2\rangle\right)^{1/2}$ that measures the average length-scale of magnetic gradients (Matthaeus et al. 2005), while magnetic reconnection leads to coalescence of magnetic islands that become increasingly larger (corresponding to an inverse cascade of magnetic energy in Fourier space). As detailed in Rappazzo and Parker (2013) and Rappazzo (2015) the solutions of the 2D equations with different initial magnetic field intensities b_0 are self-similar in time, i.e., $\mathbf{b}'(t) = \mathbf{b}(t \cdot b_0'/b_0)\ b_0'/b_0$. While the time evolution is rescaled with the relative intensity b_0'/b_0, the decay exhibits the same power-law behavior t^{-1} with same index for all intensities, current sheets will form and the

inverse cascade occur at rescaled times as for $b_0/B_0 = 10\,\%$, as shown in Fig. 5.8 (see Rappazzo 2015 for corresponding snapshots of the fields in physical space).

Line-tied simulations with differing intensities of the initial magnetic field (Fig. 5.8) depart from the 2D behavior more substantially the smaller the ratio b_0/B_0. For $b_0/B_0 = 10\,\%$ the dynamics are similar, although less small scales are formed, as shown by the slightly larger value of the Taylor micro-scale and smaller dissipative peak, so that a smaller fraction of energy is dissipated (see inset in the left panel of Fig. 5.8). For increasingly smaller values of b_0/B_0 Taylor microscale becomes increasingly larger, while the peak in the dissipation rate strongly decreases, so that increasingly less energy is dissipated and a smaller inverse cascade of magnetic energy occurs. In particular for $b_0/B_0 \lesssim 3\,\%$ barely any dynamics are detected.

The results of these numerical simulations are consistent with the heuristic phenomenology and the structure of the equilibria summarized in the previous section and described in greater detail in Rappazzo and Parker (2013); Rappazzo (2015). The asymmetry along z of the solutions of the reduced MHD equilibrium equation (5.36) can be estimated with the axial variation length-scale $z_\ell \sim \ell B_0/b$ (Eq. (5.40), see also Fig. 5.6), where ℓ is the perpendicular characteristic scale (in the x–y plane) of the magnetic field component $\mathbf{b}$. The dynamical solutions of the reduced MHD equations (5.34)–(5.35) generally do not exhibit strong asymmetries along z. On the other hand the equilibria are strongly asymmetric for $z_\ell < L_z$ or quasi-invariant for $z_\ell \gtrsim L_z$, depending on the relative value of the axial variation scale z_ℓ respect to the loop axial length L_z, with the *critical length* given by $z_\ell \sim L_z$ (corresponding to the critical intensity $b \sim \ell B_0/L_z$). As shown in Fig. 5.8 below the threshold $b_0/B_0 \lesssim 3\,\%$ no substantial energy is dissipated for the line-tied 3D runs, minimal dynamics occurs as the field slightly readjusts to the close equilibrium quasi-invariant along z. In this case the initial magnetic field has a perpendicular scale $\ell \sim L_\perp/3.87 \sim 1/3.87$ (the averaged wavenumber of the initial condition is 3.87 and $L_\perp = 1$), so that the threshold corresponds to a variation length-scale for the initial magnetic field of about $z_\ell = \ell B_0/b_0 \gtrsim 100/(3 \times 3.87)$, i.e., $z_\ell \gtrsim L_z$ since $L_z = 10$.

On the contrary for larger intensities of the initial magnetic field $b_0/B_0 > 3\,\%$ the corresponding equilibria, computed from Eq. (5.36) have a small variation length-scale $z_\ell < L_z$ and are therefore strongly asymmetric along z. Since the initial magnetic field has only the parallel m=0 mode, it is invariant along z and it cannot therefore access the strongly asymmetric equilibrium. Nonlinear dynamics must develop current sheets and dissipate energy via magnetic reconnection for the system to decay to a lower energy state close to an accessible equilibrium quasi-invariant along z. As confirmed by the simulations shown in Fig. 5.8, in the cases when decay occurs, i.e., for initial conditions with $b_0/B_0 > 3\,\%$, the magnetic field relaxes to a new equilibrium that approximately satisfies the condition $b/B_0 \sim 3\,\%$ and $z_\ell \sim L_z$.

Initial conditions with only the parallel mode m $= 1$ decay for any value of the magnetic field intensity b_0/B_0 no matter how small its value (see Rappazzo 2015 for a more extended discussion), in stark contrast with the evolution of initial magnetic

field with only parallel mode m=0 for which no decay is observed for $b_0/B_0 \lesssim 3\,\%$ (Fig. 5.8). This behavior is consistent with the structure of the equilibria outlined previously. Indeed since the only equilibria accessible dynamically must be quasi-invariant along z, i.e., the parallel mode m=0 is the larger parallel mode, if the initial magnetic field has only the mode $\mathrm{m} = 1$ it can only decay. Furthermore the nonlinear dynamics developing during the decay must transfer a fraction of the energy into a parallel m=0 mode for the system to relax to a non-vanishing equilibrium with $\mathbf{b} \neq 0$. In fact this is what happens, and in Fig. 5.9 (middle) the relaxed magnetic field with a structure strongly elongated in the axial direction is shown for the numerical simulation with $b_0/B_0 = 10\,\%$.

Initial magnetic fields with all modes $m \in [0, 4]$ excited, where m=0 is the largest mode, show a behavior similar to that of initial fields with only the mode m=0 (shown in Fig. 5.8), but with a higher fraction of energy dissipated while decaying, and a small but clearly discernible energy dissipation occurs also for very small ratios of b_0/B_0. Again, in agreement with the structure of the equilibria discussed above the magnetic field must decay to a configuration quasi-invariant along z. Therefore all excess energy, particularly in modes higher than zero ($m \geq 1$), must be dissipated and/or partially transferred to the parallel mode m=0, so that the system decays to a lower energy configuration quasi-invariant along z with magnetic field intensity $b \lesssim \ell B_0/L_z$ ($\lesssim 3\,\%$ in this case) and variation length-scale larger than the loop length $z_\ell \gtrsim L_z$.

Finally Fig. 5.9 shows that no matter what the exact structure of the initial magnetic field is (the initial magnetic field has only the modes m=0 in the top panel, only $\mathrm{m} = 1$ in the middle panel, and all modes $m \in [0, 4]$ in the bottom panel), the relaxed magnetic field is quasi-invariant along the axial direction z with its structure dominated by the m=0 mode.

5.7 Continuous Solutions and Weak Solutions

The mathematical studies of the vorticity equation (5.32) have established two important restrictive principles associated with the vorticity ω being constant along each streamline, i.e., the torsion coefficient a being constant along each field line. First, the enstrophy ω^2 cascades to small scales with the passage of time, while the kinetic energy cascades to large scales. That is to say, a^2 cascades with increasing ζ to small scales, while the magnetic energy density $b_x^2 + b_y^2$ cascades to large scales.

The essential point here is that the field line interlacing topology, described by the choice of $\psi(x, y, kzt)$, does not generally exhibit the topology associated with the cascading properties prescribed by the vorticity equation (5.32). That is to say, the special topologies required by the continuous vorticity solutions are contained somewhere within the set of all possible topologies prescribed by $\psi(x, y, kzt)$, but their special nature, necessary to maintain a constant torsion coefficient along each field line, makes them a topological set of measure zero compared to the set of all possible interlacing topologies. Thus almost all topologies prescribed by $\psi(x, y, kzt)$

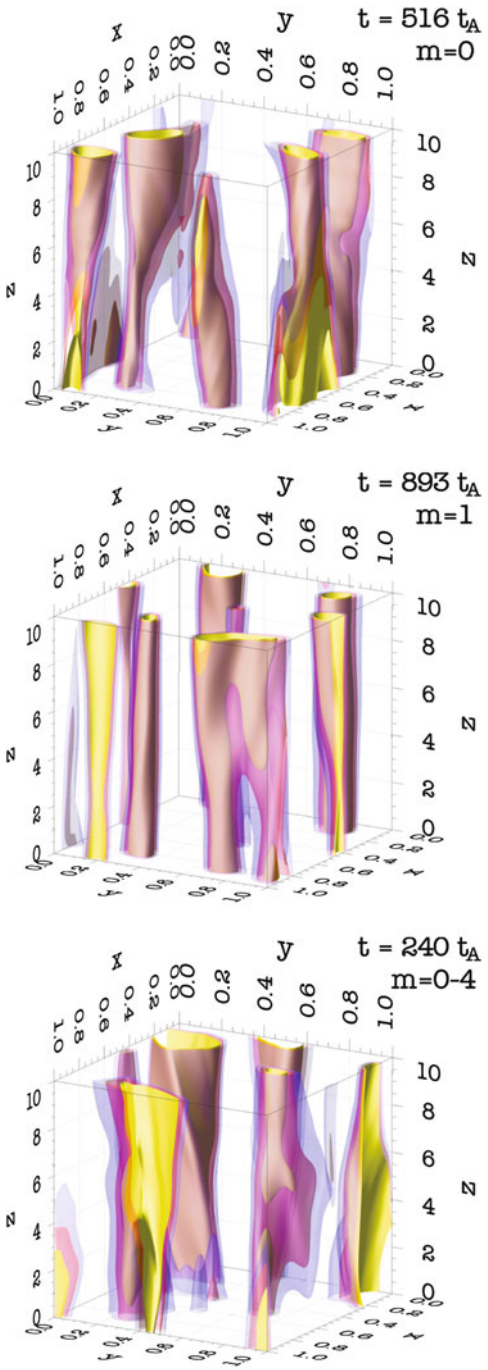

Fig. 5.9 Isosurfaces of the magnetic potential ψ in the asymptotic regime, when the magnetic field has relaxed. The *initial* magnetic field has intensity $b_0/B_0 = 10\,\%$, and it has a different structure along the z direction for the three simulations. This is determined by the parallel modes present at t = 0, respectively only the single parallel modes m = 0, m = 1 and all modes m ∈ [0, 4]. The elongated structure of ψ along z in the asymptotic regime shows that the fields relax into an equilibrium with a strong parallel m = 0 mode for all the initial conditions considered, including the initial condition with only parallel mode m = 1 (where no m = 0 mode is initially present). The computational box has been rescaled for an improved visualization, but the axial length is ten times longer that the perpendicular cross section length. During the decay energy decreases considerably for the initial conditions with $b_0/B_0 = 10\,\%$, as shown in Fig. 5.8 for the initial condition with m = 0, and in Rappazzo (2015) for initial conditions with m = 1 and m ∈ [0, 4] (than display a similar decay rate). Images adapted from Rappazzo (2015)

do not have the very special evolution toward larger or smaller characteristic lengths associated with a continuous solution to Eq. (5.32).

So the vorticity equation (5.32) provides the set of all continuous equilibrium solutions for which the torsion coefficient is constant along each field line, and the continuous solutions exist only for that set of restricted field line topologies. Yet as already noted there is equilibrium for all field line topologies described by the function $\psi(x, y, kzt)$. Thus almost all of the equilibrium solutions are not to be found among the continuous solutions. Recall that specification of the unknown function—the torsion α in this case—on any one characteristic curve of Eq. (5.10), i.e., on any one field line, in no way affects the unknown function on any of the neighboring characteristic curves, i.e., field lines. Thus there may be a discontinuous jump in the unknown function between two contiguous characteristic curves, in the present case a discontinuous jump in the torsion coefficient and in the field between two contiguous field lines. In particular one expects a surface of tangential discontinuity (TD) along a flux surface, with the field direction jumping discontinuously across the TD where the field magnitude is continuous. Neither the field nor the torsion coefficient is defined on the TD, so the troublesome equation (5.10) is inapplicable on the TD. Thus, when the constant torsion along a field line does not fit continuously against the contiguous flux bundles, there is created a TD. Almost all interlaced topologies fail to conform to the requirements dictated by the vorticity equation (5.32). So almost all field line topologies possess one or more TD's as an intrinsic part of their equilibrium (Parker 1972, 1994, 2007). These solutions to the field equation (5.10) are the so called weak solutions (Courant and Hilbert 1980), analogous to the shock solutions familiar in hydrodynamics.

Now conservation ($\nabla \cdot \mathbf{j} = 0$) of current that is everywhere parallel to $\mathbf{B}$ implies that a TD can terminate only at the end plates, $z = 0, L$. Thus a TD created by the field line interlacing at one location extends through successive uncorrelated interlacing patterns elsewhere along the field (Parker 1994). So a succession of independent interlacing patterns provides TD's with diverse orientations. TD's intersect laterally, generally forming an irregular cell structure with continuous solutions of the vorticity equation (5.32) filling the spaces between the TD's.

We emphasize that TDs are an intrinsic part of the mathematics of the equilibrium equation (5.10); they do not arise arbitrarily or independently. They are subject to the field line topology and they form the cell structure into which the continuous vorticity-like solutions are fitted. Each cell writhes along with the field lines, and the solution of Eq. (5.32) fits within its writhing TD boundaries. In this connection note that Eq. (5.16) determines the variation of α in the direction perpendicular to B, while Eq. (5.17) states that α does not vary in the direction of B. These two conditions are made mathematically compatible by the fact that Eq. (5.16) is a quasi-linear elliptic equation, indicated by the linear position of the Laplacian in the equation. Hence, there is a solution of Eq. (5.16) for every possible simply-connected boundary shape. The formal mathematical solution of Eqs. (5.16) and (5.17) is difficult because the precise form and location of the TD's must be worked out simultaneously with the construction of the continuous field that fits within those TD's. Low (2015) has explored the mathematical structure of the

equilibrium equations, providing a formal view far beyond the brief remarks given here.

5.8 Formation of TD's and Rapid Reconnection

The initial interlacing of the magnetic field, described by $\psi(x, y, kzt)$ provides a field, Eq. (5.14), that is everywhere continuous, but not in equilibrium. The TD's form as the asymptotic limit of the relaxation to equilibrium, driven by the Lorentz force of the initial nonequilibrium field, while preserving the field line topology of course. The field gradient is caused to steepen as the Lorentz force squeezes plasma and field out from between two regions of nonparallel field. It is the diminishing separation of the two fields that provides the increasing field gradient and current density. The ultimate equilibrium, with its TD's, arises only in an infinitely conducting (dissipationless) fluid of course. The slightest resistive dissipation prevents the fields reaching that ultimate equilibrium state. We recognize the relaxation process as the formation of rapid reconnection sites. Rapid reconnection, then, is a ubiquitous phenomenon in actively interlacing magnetic fields, e.g., the bipolar magnetic fields of active regions on the Sun and other stars.

Following this proof of existence of the ubiquitous rapid reconnection, the next step in the theoretical development of rapid reconnection in interlaced topologies is to follow the dynamical relaxation of the initial nonequilibrium magnetic field described by Eq. (5.14). So far we have described only the final equilibrium state, made up of weak solutions, in which the continuous solutions of the vorticity equation (5.32) are fitted in among the TD's. Noting that the equilibrium state involves the mathematics of the 2D vorticity equation, for which there are only a few limited analytic solutions (Kraichnan and Montgomery 1980), it is evident that the dynamical evolution toward that state must be pursued by numerical methods. Numerical efforts have been made using the seemingly plausible algorithm that the velocity of the plasma is everywhere equal to a constant times the Lorentz force. Those numerical experiments found no evident trend toward forming TD's. More recently Low (2013) has pointed out that the algorithm is unphysical, i.e., unable to hold the field fixed at the end plates because vanishing plasma velocity requires vanishing Lorentz force. There is also the unphysical effect that neutral points do not move because the Lorentz force vanishes there.

The preferred algorithm assumes a uniform viscosity, so that $\nabla^2\mathbf{v}$ is equal to a small constant times the Lorentz force, and the velocity can be maintained at zero at the end plates. The formation of current layers of monotonically declining thickness is immediately evident in the relaxation of the initial non-equilibrium magnetic field in the reduced MHD regime, illustrated in Fig. 5.10, reprinted from Rappazzo and Parker (2013). In this case an initial magnetic field invariant in the axial direction was considered, and the analyticity-strip method (Sulem et al. 1983; Frisch et al. 2003; Krstulovic et al. 2011; Bustamante and Brachet 2012; Brachet et al. 2013) used to track current sheet thinning. Indicating with δ the distance from the real

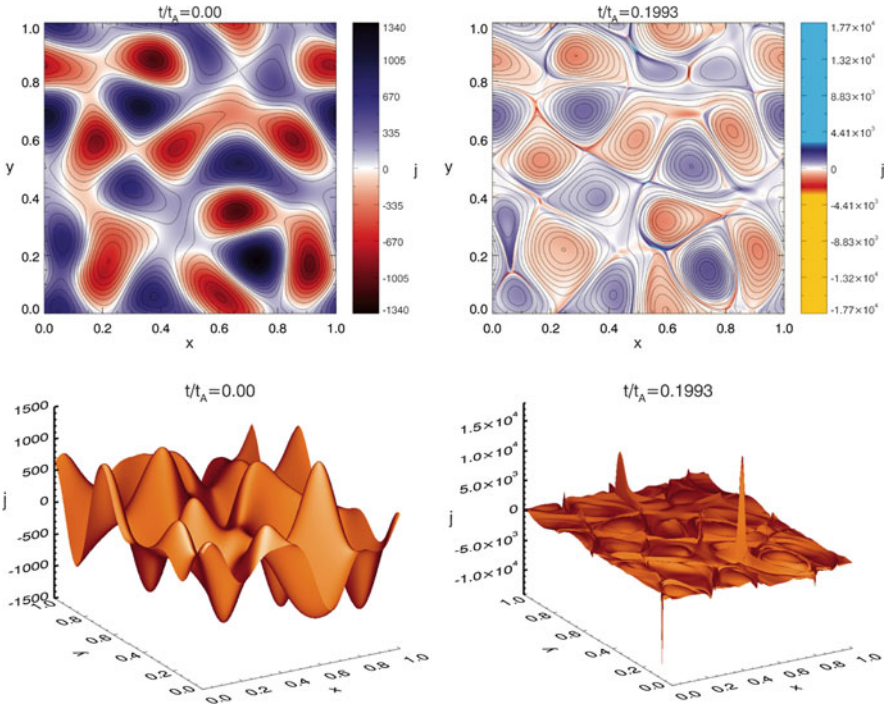

Fig. 5.10 Midplane section through interlaced magnetic field, reproduced from Rappazzo and Parker (2013), showing the initial continuous current density j and then the subsequent concentrated current sheets at time $t = 0.1993\ t_A$ in the relaxation toward stable static equilibrium. *Top panels* show j and the magnetic field lines of the orthogonal magnetic field component **b**

domain of the nearest complex space singularity, this corresponds to an exponential fall-off in Fourier space at large k for the total energy spectrum power-law (of the real solutions):

$$E(k,t) = C(t)\, k^{-n(t)}\, e^{-2\delta(t)k}. \tag{5.41}$$

The width in time of the thinnest current sheet is therefore measured by $\delta(t)$, determined by fitting the total energy spectra with Eq. (5.41) at different times (Fig. 5.11, left panels). The intensification of the current sheets proceeds to the limit of the numerical resolution, as shown in Fig. 5.11 (right panels), where δ decreases down to the smallest admissible scale (fixed at 2 meshes: $2/k_{\max}$, with $k_{\max} = 1364$), while the current and vorticity maxima increase exponentially. One can see the formation of the rapid reconnection site from the beginning. Figure 5.12 shows the current density and field lines of the orthogonal magnetic field for the ideal simulations with initial magnetic field made of all parallel modes $m \in [0, 4]$. It shows that the strongest current in the mid-plane does not overlap with an X-point, a result present also in line-tied dissipative reduced MHD simulations (Rappazzo

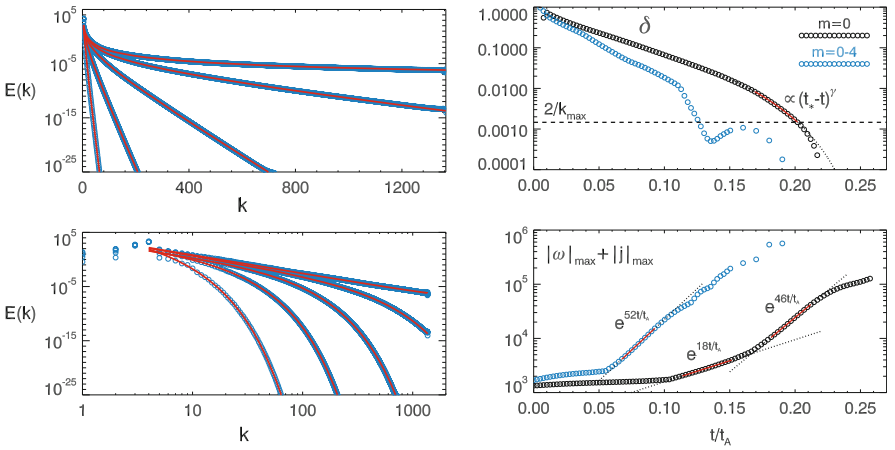

Fig. 5.11 *Left*: Fits of total energy spectra at selected times to Eq. (5.41) in linear-logarithmic scale (*top panel*) and double logarithmic scale (*bottom panel*). *Right*: Linear-logarithmic plot vs. time of the analyticity strip width δ (*top panel*) and of the sum of the current density and vorticity (moduli) maxima (*bottom panel*), for two ideal simulations with respectively only mode m $=$ 0 and all modes m $=$ 0–4 present. The *dashed line* is the resolution scale set at $2/k_{max}$. *Right panel* image adapted from Rappazzo and Parker (2013)

et al. 2008, 2010), for which it has been shown that the X-points of the orthogonal magnetic field are often displaced from current sheets both in periodic and line-tied systems (Zhdankin et al. 2013; Wan et al. 2014), with the higher reconnection rates occurring when both overlap. Linear and nonlinear investigations (Pucci and Velli 2014; Tenerani et al. 2015; Landi et al. 2015) have shown that an exponentially thinning current sheet is unstable to tearing, with its growth rate increasing for smaller thicknesses, reaching fast "ideal" Alfvén values ($\gamma\tau_A \sim 1$) for thicknesses $\delta/L \sim S^{-1/3}$ (where L is the current sheet length, and S the Lundquist number), leading to the formation of many magnetic islands and X-points and developing the complex dynamics of so-called super-tearing or plasmoid instability (Bulanov et al. 1978; Biskamp 1986; Loureiro et al. 2007; Lapenta 2008; Bhattacharjee et al. 2009).

Several authors have pursued the formation of current sheets in diverse initial field line topologies, finding the formation of current sheets, TD's, to be ubiquitous in complex topologies. Rappazzo has pursued an interlaced field three "stitches" long to obtain a first estimate of the threshold for the onset of TD's. Kumar et al. (2013, 2014) have investigated periodic fields containing 3D nulls. Kumar et al. (2014) use a novel representation of B in terms of Euler potentials, so that the computation follows flux surfaces rather than the field itself, to some advantage. They show that TD's are ubiquitous, but do not originate at 3D null points.

This success with numerical methods opens up the possibility to pursue a variety of questions. For instance, in the reduced MHD regime it has been shown that intense current sheets form only above the magnetic field intensity $b \gtrsim \ell B_0/L_z$,

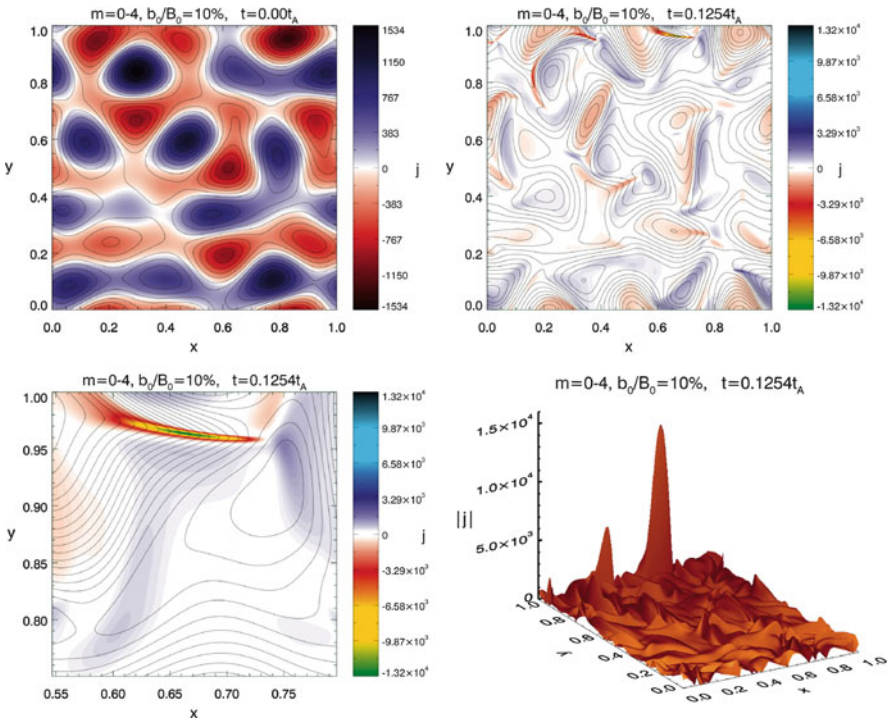

Fig. 5.12 Current density j in the mid-plane z $=$ 5 for the simulation with m $=$ 0–4, at t $=$ 0 (*top left panel*) and at $t \sim 0.125\ \tau_A$ (all other panels). The color scale reveals thin sheets with strong current enhancements, just before δ crosses the resolution scale (see Fig. 5.11). Field lines of the orthogonal magnetic field are overdrawn as continuous lines

corresponding to an equilibrium axial variation scale smaller than the coronal loop length $z_\ell \lesssim L_z$ (Sects. 5.6 and 5.6.1). What is the precise threshold for the strength of the interlacing if it is to develop TD's for magnetic configuration not limited to the reduced MHD regime? Then what is the number of TD's that might form as a consequence of each independent stitch in the interlacing along the field. With the local correlation length l it follows that a field line extends through $O(L/l)$ independent eddies along its path from $z = 0$ to $z = L$. So are there as many as $O(L/l)$ TD's in each characteristic area $/x/$ at the end plate? On the other hand, TD's can join laterally (Parker 1994) reducing the number of separate TD's. It would be interesting to have a look at the irregular cell structure formed by the TD's. Each cell is filled with a solution of the vorticity equation (5.32).

Then there are questions about the final asymptotic field line topology arising from the ongoing rapid reconnection in an arbitrary initial topology $\psi(x, y, kzt)$. Presumably reconnection ceases when the topology is reduced to the threshold for the formation of TD's.

Turning to the Sun consider the interlaced magnetic fields arching up over the convective photosphere into the corona of the Sun. We expect that there is ongoing coronal heating by the basic minimum rapid reconnection rate, of the order of $C/R_L^{1/2}$. This minimum rate is maintained indefinitely along each TD by the active convective interlacing to provide an ongoing low level heating of the ambient plasma. Evidently the minimum rapid reconnection does not always keep up with the active interlacing of the field, with the result that the interlacing may increase in intensity with the passage of time, providing stronger TD's. The growth in the strength of the magnetic TD's in a tenuous gas would be expected occasionally to push the local reconnection rate toward the explosive speed 0.01–0.1 C, producing nanoflares along the TD. The flaring soon dissipates the local interlacing and is sustained for a time by the propagation of interlacing (as Alfvén waves) into the flaring region from the interlacing elsewhere along the field. The individual flare is estimated to be small, of course, perhaps of the order of 10^{24} ergs or less (Parker 1988, and references therein). One can only turn to solar observations of flares, microflares, nanoflares and perhaps picoflares (Katsukawa 2003) for quantitative information. We have suggested (Parker 1988, 1994) that it is such localized small-scale flaring in the interlaced topology of bipolar magnetic filaments that heats the transient filaments of X-ray emitting gas on the Sun, and we expect that most late main sequence stars produce X-rays through the same process.

Acknowledgements It is a pleasure to thank the organizers of the "Parker Workshop on Magnetic Reconnection" for their work and invitations. This research has been supported in part by NASA through a subcontract with the Jet Propulsion Laboratory, California Institute of Technology, and NASA LWS grants number NNX15AB89G and NNX15AB88G. Computational resources supporting this work were provided by the NASA High-End Computing (HEC) Program through the NASA Advanced Supercomputing (NAS) Division at Ames Research Center.

References

A. Alexakis, P.D. Mininni, A. Pouquet, Phys. Rev. E **72**(4), 046301 (2005)
G.K. Batchelor, Phys. Fluids **12**, 233 (1969)
A.L. Bertozzi, P. Constantin, Commun. Math. Phys. **152**, 19 (1993)
A. Bhattacharjee, Y.-M. Huang, H. Yang, B. Rogers, Phys. Fluids **16**, 112102 (2009)
D. Biskamp, Phys. Fluids **29**, 1520 (1986)
D. Biskamp, *Magnetohydrodynamic Turbulence* (Cambridge University Press, Cambridge, 2003)
D. Biskamp, J.F. Drake, Phys. Rev. Lett. **73**, 971 (1994)
D. Biskamp, E. Schwarz, J.F. Drake, Phys. Plasmas **4**, 1002 (1997)
G. Boffetta, R.E. Ecke, Ann. Rev. Fluid Mech. **44**, 427 (2012)
M.E. Brachet, M.D. Bustamante, G. Krstulovic, P.D. Mininni, A. Pouquet, D. Rosenberg, Phys. Rev. E **87**(1), 013110 (2013)
S.V. Bulanov, S.I. Syrovatskii, J. Sakai, J. Exp. Theor. Phys. Lett. **28**, 177 (1978)
M.D. Bustamante, M. Brachet, Phys. Rev. E **86**(6), 066302 (2012)
C. Canuto, M.Y. Hussaini, A. Quarteroni, T.A. Zang, *Spectral Methods* (Springer, Berlin, 2006)
J.Y. Chemin, Ann. Sci. l'École Normale Supérieure **26**(4), 517 (1993)

R. Courant, D. Hilbert, *Methods of Mathematical Physics*, vol. 2 (Interscience , New York, 1980), pp. 635–636
R.B. Dahlburg, G. Einaudi, A.F. Rappazzo, M. Velli, Astron. Astrophys. **544**, L20 (2012)
G. Dar, M.K. Verma, V. Eswaran, Phys. D Nonlinear Phenom. **157**, 207 (2001)
P. Dmitruk, D.O. Gómez, Astrophys. J. **484**, L83 (1997)
P. Dmitruk, D.O. Gómez, Astrophys. J. **527**, L63 (1999)
P. Dmitruk, D.O. Gómez, E.E. DeLuca, Astrophys. J. **505**, 974 (1998)
P. Dmitruk, D.O. Gómez, W.H. Matthaeus, Phys. Plasmas **10**, 3584 (2003)
J.F. Drake, R.G. Kleva, M.E. Mandt, Phys. Rev. Lett. **73**, 1251 (1994)
J.F. Drake, M.A. Shay, W. Thongthai, M. Swisdak, Phys. Rev. Lett. **94**(9), 095001 (2005)
G. Einaudi, M. Velli, H. Politano, A. Pouquet, Astrophys. J. **457**, L113 (1996)
U. Frisch, *Turbulence. The Legacy of A. N. Kolmogorov* (Cambridge University Press, Cambridge, 1995)
U. Frisch, T. Matsumoto, J. Bec, J. Stat. Phys. **113**(5–6), 761 (2003)
K. Galsgaard, Å. Nordlund, J. Geophys. Res. **101**, 13445 (1996)
S. Galtier, H. Politano, A. Pouquet, Phys. Rev. Lett. **79**, 2807 (1997)
M.K. Georgoulis, M. Velli, G. Einaudi, Astrophys. J. **497**, 957 (1998)
J.D. Gibbon, Phys. D Nonlinear Phenom. **237**, 1894 (2008)
D.L. Hendrix, G. van Hoven, Astrophys. J. **467**, 887 (1996)
M. Hossain, P.C. Gray, D.H. Pontius Jr., W.H. Matthaeus, S. Oughton, Phys. Fluids **7**, 2886 (1995)
Å.M. Janse, B.C. Low, E.N. Parker, Phys. Plasmas **17**(9), 092901 (2010)
B.B. Kadomtsev, O.P. Pogutse, Sov. J. Exp. Theor. Phys. **38**, 283 (1974)
Y. Katsukawa, Publ. Astron. Soc. Jpn. **55**, 1025 (2003)
A. Kolmogorov, Akad. Nauk SSSR Dokl. **30**, 301 (1941)
R.H. Kraichnan, Phys. Fluids **10**, 1417 (1967)
R.H. Kraichnan, J. Fluid Mech. **47**, 525 (1971)
R.H. Kraichnan, D. Montgomery, Rep. Prog. Phys. **43**, 547 (1980)
G. Krstulovic, M.E. Brachet, A. Pouquet, Phys. Rev. E **84**(1), 016410 (2011)
D. Kumar, R. Bhattacharyya, P.K. Smolarkiewicz, Phys. Plasmas **20**(11), 112903 (2013)
S. Kumar, R. Bhattacharyya, P.K. Smolarkiewicz, Phys. Plasmas **21**(5), 052904 (2014)
S. Landi, L. Del Zanna, E. Papini, F. Pucci, M. Velli, Astrophys. J. **806**, 131 (2015)
G. Lapenta, Phys. Rev. Lett. **100**, 235001 (2008)
D.W. Longcope, H.R. Strauss, Phys. Fluids B **5**, 2858 (1993)
N.F. Loureiro, A.A. Schekochihin, S.C. Cowley, Phys. Fluids **14**, 100703 (2007)
B.C. Low, Astrophys. J. **768**, 7 (2013)
B.C. Low, Sci. China Phys. Mech. Astron. **58**, 015201 (2015)
A.J. Majda, A.L. Bertozzi, *Vorticity and Incompressible Flow* (Cambridge University Press, Cambridge, 2001)
W.H. Matthaeus, S. Dasso, J.M. Weygand, L.J. Milano, C.W. Smith, M.G. Kivelson, Phys. Rev. Lett. **95**(23), 231101 (2005)
C.S. Ng, A. Bhattacharjee, Phys. Plasmas **5**, 4028 (1998)
E.N. Parker, J. Geophys. Res. **62**, 509 (1957)
E.N. Parker, Astrophys. J. **174**, 499 (1972)
E.N. Parker, *Cosmical Magnetic Fields: Their Origin and Their Activity* (Oxford University Press, New York, 1979)
E.N. Parker, Astrophys. J. **264**, 635 (1983)
E.N. Parker, Astrophys. J. **330**, 474 (1988)
E.N. Parker, Geophys. Astrophys. Fluid Dyn. **46**, 105 (1989a)
E.N. Parker, Geophys. Astrophys. Fluid Dyn. **45**, 159 (1989b)
E.N. Parker, Phys. Fluids B **3**, 2652 (1991)
E.N. Parker, *Spontaneous Current Sheets in Magnetic Fields* (Oxford University Press, New York, 1994)
E.N. Parker, *Conversations on Electric and Magnetic Fields in the Cosmos* (Princeton University Press, Princeton, 2007)

E.N. Parker, *Field Line Topology and Rapid Reconnection*. Astrophysics and Space Science Proceedings, vol. 33 (Springer Berlin Heidelberg, 2012a), pp. 3–9
E.N. Parker, Plasma Phys. Controlled Fusion **54**(12), 124028 (2012b)
H.E. Petschek, NASA Spec. Publ. **50**, 425 (1964)
F. Pucci, M. Velli, Astrophys. J. **780**, L19 (2014)
A.F. Rappazzo, Astrophys. J. **815**, 8 (2015). arX iv.1505.04370 [astro-ph, SR]
A.F. Rappazzo, E.N. Parker, Astrophys. J. **773**, L2 (2013)
A.F. Rappazzo, M. Velli, Phys. Rev. E **83**(6), 065401 (2011)
A.F. Rappazzo, M. Velli, G. Einaudi, R.B. Dahlburg, Astrophys. J. **657**, L47 (2007)
A.F. Rappazzo, M. Velli, G. Einaudi, R.B. Dahlburg, Astrophys. J. **677**, 1348 (2008)
A.F. Rappazzo, M. Velli, G. Einaudi, Astrophys. J. **722**, 65 (2010)
H.A. Rose, P.L. Sulem, J. Phys. Fr. **39**(5), 441 (1978)
H.R. Strauss, Phys. Fluids **19**, 134 (1976)
C. Sulem, P.L. Sulem, H. Frisch, J. Comput. Phys. **50**, 138 (1983)
P.A. Sweet, in *Electromagnetic Phenomena in Cosmical Physics*, ed. by B. Lehnert. IAU Symposium, vol. 6 (1958a), p. 123
P.A. Sweet, II Nuovo Cimento **8**(2), 188 (1958b)
S.I. Syrovatskii, Sov. J. Exp. Theor. Phys. **33**, 933 (1971)
S.I. Syrovatskii, Sol. Phys. **58**, 89 (1978)
S.I. Syrovatskii, Annu. Rev. Astron. Astrophys. **19**, 163 (1981)
P. Tabeling, Phys. Rep. **362**, 1 (2002)
T. Tao (2015). arXiv:1402.0290 [math.AP]
A. Tenerani, A.F. Rappazzo, M. Velli, F. Pucci, Astrophys. J. **801**, 145 (2015)
A.A. van Ballegooijen, Astrophys. J. **298**, 421 (1985)
A.A. van Ballegooijen, Astrophys. J. **311**, 1001 (1986)
M. Wan, A.F. Rappazzo, W.H. Matthaeus, S. Servidio, S. Oughton, Astrophys. J. **797**, 63 (2014)
A.L. Wilmot-Smith, D.I. Pontin, A.R. Yeates, G. Hornig, Astron. Astrophys. **536**, A67 (2011)
M. Yamada, Space Sci. Rev. **160**, 25 (2011)
M. Yamada, R. Kulsrud, H. Ji, Rev. Mod. Phys. **82**, 603 (2010)
G.P. Zank, W.H. Matthaeus, J. Plasma Phys. **48**, 85 (1992)
V. Zhdankin, D.A. Uzdensky, J.C. Perez, S. Boldyrev, Astrophys. J. **771**, 124 (2013)

Chapter 6
Reconnection at Earth's Dayside Magnetopause

P.A. Cassak and S.A. Fuselier

Abstract Magnetic reconnection at Earth's dayside magnetopause plays a crucial role in space weather-related phenomena. The response of the magnetosphere to input from interplanetary space differs greatly depending on where reconnection happens and how efficiently it reconnects magnetic flux from interplanetary space. This chapter is a pedagogical treatment of dayside reconnection. Introductory topics include a guide to the magnetosphere for the uninitiated and a brief history of the field. Technical topics include qualitative properties of dayside reconnection, such as where reconnection occurs and what it looks like, and how reconnection quantitatively depends on ambient conditions, including the effect of asymmetries, the diamagnetic drift, and flow shear. Both observational and theoretical aspects are discussed. The chapter is closed with a discussion of open questions and the outlook for the future of dayside reconnection research.

Keywords Asymmetric reconnection • Dayside reconnection • Diamagnetic effects • Reconnection history • Reconnection location • Reconnection with flow-shear

6.1 Introduction

Earth's magnetosphere is the region of influence of Earth's magnetic field. The dayside magnetopause is the boundary of the magnetosphere on the side of Earth closest to the sun. The chapter gives an introduction to magnetic reconnection at the dayside magnetopause. Reconnection on the nightside of the magnetosphere is discussed in the following chapter.

P.A. Cassak (✉)
West Virginia University, Morgantown, WV, USA
e-mail: Paul.Cassak@mail.wvu.edu

S.A. Fuselier
Southwest Research Institute, San Antonio, TX, USA

University of Texas at San Antonio, San Antonio, TX, USA
e-mail: sfuselier@swri.edu

W. Gonzalez, E. Parker (eds.), *Magnetic Reconnection*, Astrophysics and Space Science Library 427, DOI 10.1007/978-3-319-26432-5_6

Reconnection in the magnetosphere in general, and at the dayside magnetopause in particular, is especially important for a number of reasons. One reason is that it is the place closest to Earth where reconnection occurs naturally. It is accessible to in situ measurements using satellite observations, so it can be studied observationally with the greatest detail of any naturally occurring reconnection setting. In concert with directed laboratory studies of reconnection and its study in magnetically confined fusion devices, theoretical and numerical studies, and remote observations of the sun, the magnetospheres of other planets, and the heliosphere, there have been great strides in understanding the reconnection process.

A second reason dayside reconnection is so important is because of its direct impact on Earth through its role in space weather. In an idealized universe without reconnection, the transfer of material and energy from interplanetary space to the magnetosphere would be minimal, so Earth's magnetic field would largely protect Earth from the charged particles in space. However, reconnection changes the picture: by changing the connectivity of magnetic fields, reconnection is directly involved with allowing the transfer of material and energy from interplanetary space to the magnetosphere. This material is known to potentially cause many problems for us on Earth, including power outages, satellite failures impacting navigation [because global positioning system (GPS) technology is satellite-based] and communication (through cell phones and pagers), increased drag on satellites, harm to astronauts, and impacting airline communication for planes on polar routes. The efficiency of reconnection at the dayside, therefore, plays a crucial part of determining how strongly the input from interplanetary space couples to the magnetosphere. Therefore, predicting space weather to the level where it can be mitigated requires a thorough understanding of reconnection at the dayside magnetopause.

The material in this chapter is intended as an introduction to many exciting developments in the field in the last 15–20 years. Technical terms are in bold font when introduced. By necessity, the treatment is incomplete and represents the biases of the authors. The reader is referred to a number of books and review articles about dayside magnetic reconnection (Hughes 1995; Phan et al. 2005; Dorelli and Bhattacharjee 2007; Trattner et al. 2007b; Lavraud et al. 2011; Paschmann et al. 2013) and reviews on particular facets of dayside reconnection including some covered here (Semenov 1998; Lui et al. 2005; Dorelli et al. 2007; Paschmann 2008; Dorelli and Bhattacharjee 2008; Chisham et al. 2008; Fuselier et al. 2011; Mozer and Pritchett 2011; Moore et al. 2013). This chapter does not further discuss particulars of space weather; the interested reader is referred to review articles (Pulkkinen 2007; Eastwood 2008). The material in the present chapter was chosen to emphasize topics for which significant work has been done both observationally and theoretically, so topics such as the microphysics of reconnection are not emphasized since most satellites do not directly go through reconnection sites.

In order to understand reconnection at the dayside magnetopause, one must have basic knowledge of the magnetosphere; the remainder of Sect. 6.1 is devoted to background information to make the presentation self-contained, including relevant terminology, typical conditions at the dayside magnetopause, and a brief history

of dayside reconnection. (Those knowledgeable about the magnetosphere can skip this section without loss of continuity.) In Sect. 6.2, a number of qualitative properties of dayside reconnection are discussed, including why it occurs, when it occurs, what it looks like, and where it occurs. In Sect. 6.3, quantitative aspects of dayside reconnection are treated, including the dependence of dayside reconnection on ambient conditions at the magnetopause. Finally, Sect. 6.4 gives the authors' thoughts on some open questions concerning dayside reconnection and the future of its study. For each topic, both observational and theoretical perspectives are discussed.

6.1.1 A Brief Introduction to Earth's Magnetosphere

To a zeroth order approximation, if Earth was isolated the magnetic field would approximately be that of a magnetic dipole. However, its position in the solar system modifies this simple picture. Here, relevant terminology and coordinate systems used to describe the magnetosphere are discussed.

6.1.1.1 Terminology

Figure 6.1 shows Earth's magnetosphere as determined in numerical simulations (Komar 2015). The lines show representative magnetic field lines and the background color is the out-of-plane current density (blue for out of the page, red for into the page). For magnetospheric applications, it is standard to measure distances in units of the radius of Earth R_E, which is approximately 6371 km. These figures will be used to put relevant terminology in context.

- **The solar wind:** material that escapes the region near the sun's surface and goes out through interplanetary space. It is almost completely ionized and is made up predominantly of protons and electrons. In Fig. 6.1, the sun would be far to the right of the figure (near 23,500 R_E), and the solar wind comes in from the right.
- **The interplanetary magnetic field (IMF):** the magnetic field in interplanetary space, which is entrained to the solar wind and is therefore carried away from the sun. The yellow magnetic field lines on the right in Fig. 6.1 stretching from the top to the bottom of the plotted domain represent the IMF.
- **The IMF clock angle θ_{IMF}:** the angle the IMF makes relative to the terrestrial dayside magnetic field. The terrestrial magnetic field points mostly from geographic south to geographic north between the sun and Earth. A clock angle of 0° means that the two magnetic fields are aligned, while a clock angle of 180° means they are anti-aligned corresponding to a mostly southward IMF. Panel (a) of Fig. 6.1 is for a due southward IMF ($\theta_{\mathrm{IMF}} = 180°$) and panel (b) is for a due northward IMF ($\theta_{\mathrm{IMF}} = 0°$). Note, the two plots are extremely different! This difference is explained in Sect. 6.1.3.

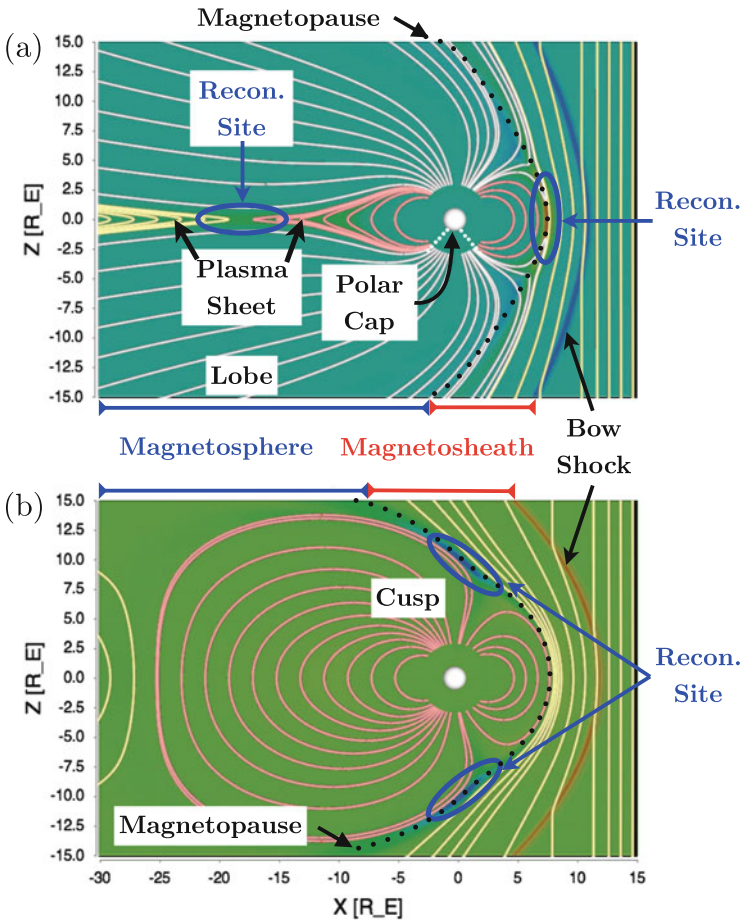

Fig. 6.1 Magnetic field lines of Earth's magnetosphere and the surrounding environment from simulations with no dipole tilt with due (**a**) southward and (**b**) northward interplanetary magnetic field. Earth is the white sphere at the origin and the sun is to the right. The *background color* is the out-of-plane current density, with *blue* out of the page and *red* into the page. Reconnection occurs at the *blue ovals*. The image is from Komar (2015) and is used with permission from C. M. Komar

- **The bow shock:** As the solar wind expands, Earth's magnetic field acts like an obstacle. As with water in a stream going around a rock, the solar wind is deflected around the magnetosphere. However, a typical solar wind speed when it approaches Earth is $\geq$400 km/s, which is faster than typical waves in the solar wind, such as the fast magnetosonic speed. Consequently, unlike water going around a rock, a shock self-consistently forms upstream of the obstacle. At the shock (technically a "fast mode" or "switch-on" shock), the flow abruptly decreases over a short distance (comparable to the ion gyroradius for the solar wind), with a concomitant increase in plasma density, temperature, and magnetic

field strength. For solar wind speeds far exceeding the magnetosonic speed, the solar wind speed decreases by a factor of 4 while the density and magnetic field strength increase by the same factor. Due to the shape of the magnetosphere, the shock is curved forming a characteristic bullet shape, as labeled in Fig. 6.1.

- **The magnetosheath:** the region between the bow shock and the magnetopause (the outer edge of the magnetosphere), as labeled in Fig. 6.1. (The magnetopause and magnetosphere are also labeled in the figure.) The shocked solar wind continues to flow towards Earth's magnetosphere in the magnetosheath.
- **The subsolar point:** The outermost point of the dayside magnetopause, where the shocked solar wind first encounters the magnetosphere. In Fig. 6.1a, the subsolar point is inside the blue oval on the right.
- **The polar cusps:** The regions of the magnetosphere where Earth's dipolar magnetic field fans out from the magnetic poles. The cusps are labeled in Fig. 6.1b, slightly closer to Earth than the two blue ovals.
- **The polar cap:** In Fig. 6.1a, the magnetic field lines are color coded according to their topology. Red magnetic field lines are **terrestrial**, meaning they pierce Earth's surface twice. White magnetic field lines pierce the Earth's surface on one side, but extend to interplanetary space on the other. These are called **open** field lines. The polar cap is the locus of points just above Earth's surface where the magnetic field lines piercing it are open, as shown in Fig. 6.1a.
- **The magnetotail:** As seen most clearly in Fig. 6.1a, one consequence of the interaction of Earth's magnetosphere with the solar wind is the dayside terrestrial magnetic field gets compressed, while the nightside magnetosphere (on the left) gets stretched out. The latter is the magnetotail.
- **The plasma sheet:** The magnetic field in the magnetotail points towards Earth in the northern hemisphere and away from Earth in the southern hemisphere. From Ampère's law, this is supported by a current (not present for a dipole field). The sheet of current in the magnetotail is the plasma sheet, as labeled in Fig. 6.1a.
- **The lobes:** the regions in the magnetotail between the plasma sheet and the nightside magnetopause, as labeled in Fig. 6.1.
- **The flanks:** the region of the magnetopause near the equatorial plane tailward of Earth around the sides of the magnetosphere (out of the planes of Fig. 6.1).
- **The ionosphere:** the layer of Earth's atmosphere consisting of particles ionized by radiation from the sun. It is much denser than the outer magnetospheric and solar wind plasma. Terrestrial and open magnetic field lines map to the ionosphere, so dynamics of the magnetopause affect, and be affected by, it.
- **The plasmasphere:** a relatively cold, dense layer of plasma just outside the ionosphere.
- **The dipole tilt:** In Fig. 6.1, the Earth's dipole moment was chosen to point due southward. However, there is actually an offset between Earth's rotation axis and the direction of Earth's dipole moment by $\simeq 10°$. This is the dipole tilt.

The blue ovals in each figure show where the magnetic field is anti-parallel, which nominally shows the expected location where reconnection occurs for these systems. Further discussion of the location of reconnection is in Sect. 6.2.4.

6.1.1.2 Magnetospheric Coordinate Systems

There are a few common coordinate systems used to describe magnetospheric phenomena. As used previously, the terms *northern* and *southern* hemisphere give positions relative to the equator. To describe the longitudinal position, note the points on Earth's surface directly between the sun and Earth would have their watches read **noon**. The opposite point on the nightside would be **midnight**. Similarly, **dawn** and **dusk** are used to refer to 6 a.m. and 6 p.m., respectively. Earth rotates counterclockwise when looking down from the north pole, so when looking from the sun to Earth, dawn is on the left and dusk is on the right. One can give the longitude in terms of times; this is called **local time (LT)**. If instead of using latitude and longitude relative to Earth's rotation axis, the lines are arranged relative to Earth's magnetic field, the same names for timing can be used; this is called **magnetic local time (MLT)**. This is sketched in Fig. 6.2a.

The most common coordinate system used to describe magnetospheric phenomena is the **Geocentric Solar Magnetic (GSM)** coordinate system, sketched in Fig. 6.2a. The origin is at the center of Earth. The x direction is toward the sun, so that positive x is the dayside and negative x is the nightside. The y direction is perpendicular to Earth's dipole moment, and points from dawn to dusk. The z direction is normal to both in a right-handed sense. The magnetic moment is in the xz plane, and aligns with the z axis when there is no dipole tilt.

Finally, a commonly used coordinate system for local (as opposed to global) properties of the dayside magnetopause are **boundary normal coordinates**. In the absence of reconnection, the magnetopause separates the magnetosheath and magnetosphere, shown as the solid lines in Fig. 6.2b. The outward pointing normal is called the N direction. At a location where reconnection occurs, there is a component of the magnetic field in the N direction, as shown by the dashed field lines; indeed, the measurement of a non-zero normal magnetic field B_N was early evidence for reconnection, as discussed in Sect. 6.1.3. This can be found from observational data by finding the coordinate system that minimizes the change in a component of the magnetic field; this is called **minimum variance analysis** (Sonnerup and Cahill 1967). The direction corresponding to the component of the

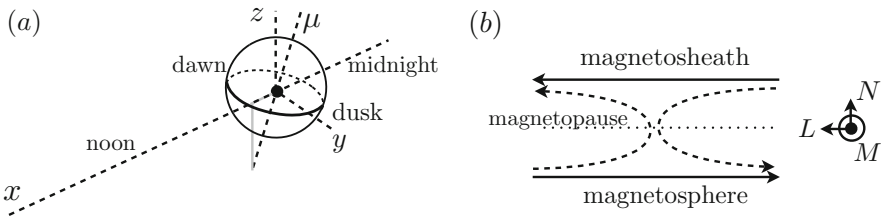

Fig. 6.2 (**a**) Geocentric solar magnetic (GSM) coordinate system with labels for magnetic local time (MLT), where μ is the axis of Earth's magnetic dipole. (**b**) Boundary normal coordinate system

magnetic field that changes maximally is called the L direction, and M completes the right-handed coordinate system. The boundary normal coordinates LMN are often thought to map to the dayside reconnection geometry with L in the outflow direction, N in the inflow direction, and M in the out-of-plane direction. However, while true for some magnetic configurations, this need not be true and should be applied to reconnection with caution (Mozer et al. 2008b).

6.1.2 Typical Conditions at Earth's Dayside Magnetopause

The location of the dayside magnetopause is essentially set by pressure balance. Quantitatively, the ram pressure in the solar wind $\rho_{SW} v_{SW}^2$, where ρ is mass density, v is speed, and the SW subscript means quantities evaluated in the solar wind just outside of the bow shock, is comparable to the magnetic pressure at the magnetosphere $B_{ms}^2/2\mu_0$ just inside the magnetopause, where B_{ms} is the magnetospheric magnetic field. (SI units are used here and throughout.) Equating the two implies $B_{ms} \propto (\rho_{SW} v_{SW}^2)^{1/2}$. Treating Earth's magnetic field as a dipole, one has $B \propto r^{-3}$, implying that the distance to the magnetopause r_{mp} is proportional to $(\rho_{SW} v_{SW}^2)^{-1/6}$. A commonly used semi-empirical result including the coefficient of proportionality between the two is (see, e.g. Walker and Russell 1995)

$$r_{mp} = 107.4 (n_{SW} v_{SW}^2)^{-1/6}, \tag{6.1}$$

where n_{SW} is the solar wind number density, and the above expression is normalized so that using n_{SW} in cm^{-3} and v_{SW} in km/s gives r_{mp} in R_E. Using a mean solar wind density of $8.7\,cm^{-3}$ and speed of 468 km/s (Gosling 2007), one finds the magnetopause location, also called the **standoff distance**, to be $r_{mp} = 9.64\,R_E$.

This allows the estimation of the typical magnetospheric magnetic field. The dipole magnetic field at this position is obtained from $B = B_E (R_E/r)^3$, where $B_E \simeq 2.5 \times 10^4$ nT is the approximate surface magnetic field at the equator. This gives $B \simeq 28$ nT. However, this is merely the dipole magnetic field strength. For this to be the magnetopause location, the IMF is effectively canceling out the field outside of the magnetopause, so the dipole field inside the magnetopause is effectively doubled. Therefore, a typical magnetospheric magnetic field strength is $B_{ms} \simeq 56$ nT. Observations reveal a standoff distance close to 10 R_E and a magnetospheric field in the 50–60 nT range, showing that these calculations give reasonable results.

As conditions in interplanetary space change, the location of the magnetopause follows suit; the magnetopause is said to be **breathing**. This aspect of magnetospheric dynamics makes studying reconnection challenging, as it is a highly coupled nonlinear system. For example, in simulations, changing the conditions in the solar wind also changes the plasma parameters at the magnetopause by altering pressure balance, so it is difficult to show a direct effect on reconnection of a single changed variable. In observations, it is difficult to determine if the magnetosphere

Table 6.1 Typical plasma parameters at the magnetospheric side of Earth's subsolar magnetopause: density n, magnetic field strength B, ion temperature T_i, Alfvén speed c_A, and plasma beta β

Magnetospheric parameter	Typical value
$n_{\rm ms}$ (cm^{-3})	0.1
$B_{\rm ms}$ (nT)	56
$T_{i,\rm ms}$ ($\times 10^5$ K)	2.4×10^3
$c_{A,\rm ms}$ (km/s)	3.9×10^3
$\beta_{\rm ms}$	0.27

Table 6.2 Typical plasma parameters at the magnetosheath side of Earth's subsolar magnetopause as in Table 6.1 derived from solar wind data and models as described in the text

Subsolar magnetosheath parameter (Derived)	Mean	Most probable	Median	5–95 % range start	5–95 % range stop
$n_{\rm sh}$ (cm^{-3})	34.8	20	27.6	12	80
$B_{\rm sh}$ (nT)	24.8	20.4	22.4	8.8	39.6
$T_{i,\rm sh}$ ($\times 10^5$ K)	12	5	9.5	1	30
$c_{A,\rm sh}$ (km/s)	92	99	93	55 (21)[a]	97 (250)[a]
$\beta_{\rm sh}$	2.4	0.8	1.8	0.5	5.3
$\Delta\beta$	2.1	0.5	1.5	0.2	5.0

The last line gives the change in plasma beta across the magnetopause $\Delta\beta = \beta_{\rm sh} - \beta_{\rm ms}$ using $\beta_{\rm ms}$ from Table 6.1

[a]The Alfvén speeds in parenthesis are derived assuming anti-correlation between the solar wind density and interplanetary magnetic field strength

is breathing since the magnetopause motion is typically slower than the spacecraft speed.

The typical ambient conditions at the dayside magnetopause, both on the magnetosheath and magnetospheric sides, are important for reconnection. The conditions in the solar wind are perpetually changing. However, the typical plasma parameters on the magnetospheric side do not vary by a huge amount. The rows in Table 6.1 give typical values at the magnetospheric side (with an "ms" subscript) of the magnetopause for the plasma number density n, the total magnetic field strength B, and the ion temperature T_i at the subsolar region of the magnetosheath. Derived quantities including the Alfvén speed $c_A = B/(\mu_0 m_i n)^{1/2}$ and the plasma beta $\beta = 2\mu_0 n k_B T_i/B^2$ are also provided. The electron temperature is typically about 5 times smaller than the ion temperature (Wang et al. 2012), so it is not included in the β calculation for simplicity. The given magnetic field strength is determined from pressure balance as described earlier.

Table 6.2 provides the same plasma parameters for the magnetosheath (with "sh" subscript) at the subsolar magnetopause. In constructing this table, the density, magnetic field strength, and ion temperature are derived from average properties of the solar wind (Gosling 2007) and the assumptions that:

1. the bow shock is a strong, super-critical, quasi-perpendicular shock, across which the density and magnetic field strength increase by a factor of 4,
2. the solar wind ion temperature increases by a factor of 10 across the bow shock;

3. there is no further change in the shocked solar wind plasma as it convects from downstream of the bow shock to the subsolar magnetopause.

These derived quantities are in good agreement with previously discussed observationally determined values (e.g., Phan et al. 1994).

The columns in Table 6.2 give, from left to right, the mean value, most probable value, median value, and the 5–95 % range for these parameters. The mean, most probable, and median values for the Alfvén speed and β represent the typical ambient conditions at the subsolar magnetopause. However, the 5–95 % range for these derived values is probably not as broad as seen in observations. The density and magnetic field magnitude are typically out of phase with one another in the solar wind. Therefore, if the lowest density is paired with the highest magnetic field and vice-versa, then the Alfvén speed range increases significantly to a range from 21 to 250 km/s. The last line of Table 6.2 gives $\Delta\beta$, the change in β across the subsolar magnetopause: $\Delta\beta = \beta_{sh} - \beta_{ms}$ using the magnetospheric data in Table 6.1. This parameter will be useful in Sect. 6.3.2 when the role of diamagnetic effects on dayside reconnection is discussed.

It is worth pointing out that, while the magnetospheric parameters tend to not change greatly, there are events where cold, dense material from the plasmasphere can reach the dayside reconnection site, leading to a much different plasma density. These events and their effect on dayside reconnection are discussed in Sect. 6.3.4.

6.1.3 A Brief History of Dayside Reconnection

Even before spacecraft were launched initiating the "Space Age" in 1957, information about the space environment that is now called the magnetosphere could be obtained from the ground. It was known that the ionosphere near the poles supported an electric field $\mathbf{E}_{PC}$, or equivalently, a scalar potential ϕ_{PC}, where the "PC" subscript denotes "polar cap." Equipotentials at the northern hemisphere's polar cap during times with strong aurora, from Dungey (1961), are sketched in Fig. 6.3. The southern hemisphere's polar cap has a similar structure, but the polarity of the electric potential is reversed when viewed from above the surface.

The electric field, when combined with the magnetic field pointing into the page in the figure, is consistent with an $\mathbf{E}_{PC} \times \mathbf{B}$ flow directed from the dayside towards the magnetotail over the poles, and back around to the dayside around the perimeter of the polar cap. This is now called **magnetospheric convection**. An early idea on its cause is that the flow of the solar wind around the magnetosphere, where the plasma is essentially at rest, leads to a flow shear across the magnetopause. In this flow shear layer, viscosity becomes important, which drives the magnetospheric plasma to move, thereby convecting the magnetic field.

The understanding of this process changed from an unlikely set of occurrences. Ronald Giovanelli, an Australian of Italian descent, studied solar flares in his spare time while making optical glass for the war effort during World War II (Piddington 1985). He learned that flares are associated with sunspots (Giovanelli 1939) and

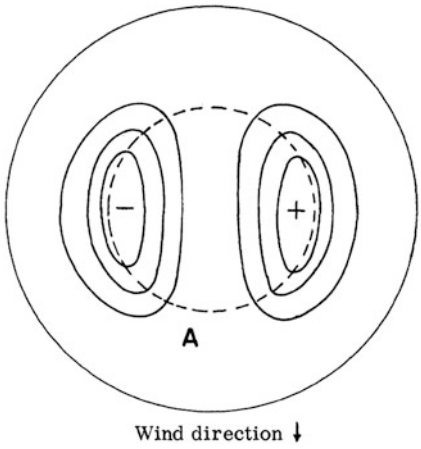

Fig. 6.3 Equipotentials at the northern hemisphere's polar cap during times of strong aurora from Dungey (1961). The x direction points up in the figure. Reprinted figure with permission from [J. W. Dungey, Phys. Rev. Lett., 6, 47, 1961.] Copyright (1961) by the American Physical Society

developed an idea of why this is the case. He realized that the magnetic field near a sunspot, consisting of the sum of the background magnetic field and the magnetic field from the sunspot, had a "neutral point" where the magnetic field goes to zero (Giovanelli 1947). This insight was critical because turned the study of solar flares from hydrodynamic to electromagnetic. Giovanelli proposed that an electric field at neutral point would freely accelerate charged particles, giving the high energies needed to explain flares. (It is now largely believed that this effect happens, but the region is too small to give the amount of observed energization.)

After the war, Giovanelli traveled to England to share his findings with Fred Hoyle, who realized that Giovanelli's insight was important not just for solar flares but also as a potential mechanism to accelerate particles during aurora (Hoyle 1949). Hoyle gave the problem of figuring out what happens at a magnetic neutral point and implications for aurora to his graduate student, James Dungey (1983). It was Dungey who developed the basic premise of reconnection as a change of topology of the magnetic field where it changes directions (Dungey 1953), which was part of his thesis in 1950. In his model, the frozen-in condition of ideal-magnetohydrodynamics (ideal-MHD) breaks down when there is dissipation. As with driving a current through a wire, dissipation allows an electric field. This electric field allows for a change to the magnetic field in the reference frame of the plasma, manifested as an effective breaking of magnetic field lines, which cross-connect in the standard picture of reconnection presented earlier in this book.

It took another decade for Dungey to figure out the implications for the magnetosphere; he describes the circumstances of his key insight as occurring (Dungey 1983) "while preparing for a talk, in a classic place: I was sitting at a sidewalk café in Montparnasse." He realized that when the IMF points southward, it is oppositely directed to the Earth's northward pointing dipole magnetic field, so there is a neutral point and reconnection can occur (Dungey 1961). The newly reconnected field line is now open, and is convected tailward by the solar wind. The flow from the solar wind stretches the open magnetic field lines, providing strong

coupling of the energy in the solar wind to the magnetosphere. In the magnetotail, the magnetic fields are again oppositely directed, as shown in Fig. 6.1a, leading to reconnection in the magnetotail. A newly closed terrestrial field line retracts towards Earth, where it gets redirected around the Earth either in the dawnward or duskward direction, and comes back to the dayside. It is this breaking or "disconnecting" on the dayside and "re-connecting" of the field line on the nightside that prompted Dungey to coin the phrase "magnetic reconnection." Dungey realized that the resultant convection pattern of the magnetic fields would produce the polar cap potential in Fig. 6.3 that had been previously observed and attributed to viscosity.

Dungey also realized that magnetopause reconnection also happens when the IMF is directed northward, as depicted in Fig. 6.1b, but it looks very different. At the subsolar point, the IMF and terrestrial magnetic fields are parallel, so reconnection does not occur. The solar wind flow far from Earth continues to drag the magnetic field away from the sun, so the IMF drapes over the magnetopause. When the draped IMF abuts against the terrestrial field at the nightside magnetopause, the two are oppositely directed in the cusp region, and reconnection can occur, as shown by the blue ovals in the figure. The field lines produced by this reconnection process are again disconnected from Earth, so they continue convecting away from the sun. Without much energy transfer from the solar wind to terrestrial magnetic fields, solar wind-magnetospheric coupling for northward IMF is much weaker than for southward IMF.

A handful of researchers engaged the problem of reconnection. Peter Sweet, who had previously been a student of Fred Hoyle, applied Dungey's reconnection idea to the solar flare problem (Sweet 1958), and Gene Parker, after seeing a talk by Sweet, performed a scaling analysis of the rate at which the magnetic field reconnects (Parker 1957). However, he quickly realized that it was not fast enough to explain observations (Parker 1963). Harry Petschek, an aeronautical engineer by training working on shocks and magnetospheric physics, was introduced to the problem about the rate of reconnection by Arthur Kantrowitz. He realized that the straightening of bent magnetic field lines contributes to the acceleration of the plasma (Petschek 1964), making the reconnection faster. Depending on the upstream conditions, the acceleration could either happen at a **slow shock**, a boundary layer where the magnetic field gets weaker while the flow gets faster and the density and pressure increase, or a **rotational discontinuity**, a boundary layer where the magnetic field rotates and the flow gets faster without change to the plasma density and pressure. (However, see Liu et al. 2011a,b, 2012 for how this changes in a kinetic approach, as opposed to the fluid approach by Petschek.) Petschek and colleagues addressed how the process occurs at the dayside magnetopause (Levy et al. 1964; Petschek 1966; Petschek and Thorne 1967). But by and large, despite evidence in the early 1960s that reconnection played a role in fusion devices (Furth et al. 1963), reconnection did not gain widespread acceptance and was, in Dungey's words, "regarded as an entertaining fiction" (Dungey 1983) in the years following the early work. Undoubtedly, this attitude was aided by the objections to reconnection by Hannes Alfvén, who had strong objections to the description

of magnetic field line motion inherent in reconnection (Williams and Moorehead 1987).

This began to change with an increase in indirect observational evidence from the magnetosphere supporting the reconnection scenario. It was shown that the direction of the IMF is correlated with auroral and geomagnetic activity (Fairfield and Cahill 1966); a southward IMF gives rise to magnetospheric erosion (Aubry et al. 1970), meaning that the magnetopause shifts inward; energetic particles from the sun reach the magnetic field lines anchored at the polar cap first (Fennell 1973). Each of these is consistent with Dungey's model. Around this time, there was an important review paper (Vasyliunas 1975) summarizing the observations and unifying competing reconnection models. Then, the most solid observational evidence for reconnection to date was found using the ISEE satellites. An event where plasma was accelerated at a rotational discontinuity, as would be expected from Petschek's model, was found (Paschmann et al. 1979). Then an event for which there was a non-zero component of the magnetic field normal to the magnetopause was identified (Sonnerup 1981), an indication that reconnection occurred, as pointed out in Fig. 6.2b. These led to more of a widespread belief in Dungey's reconnection model.

Research on reconnection, both observational and theoretical, has continued since these early successes. Modern observations have been able to investigate magnetospheric reconnection with incredible detail. A graphic showing the NASA's fleet of satellites, called the Heliophysics System Observatory, as a function of time is shown in Fig. 6.4. A number of satellite missions have measured direct or indirect effects of reconnection in the magnetosphere, including Polar, Cluster, THEMIS/ARTEMIS, and TWINS. Most recently, a dedicated mission called Magnetospheric Multiscale (MMS), was launched on March 12, 2015, to study the **dissipation region** (the region where ideal-MHD breaks down and field lines can break) of magnetic reconnection in the magnetosphere. It will spend time both at the dayside and in the magnetotail. The expected impact of MMS is discussed in Sect. 6.4.3.

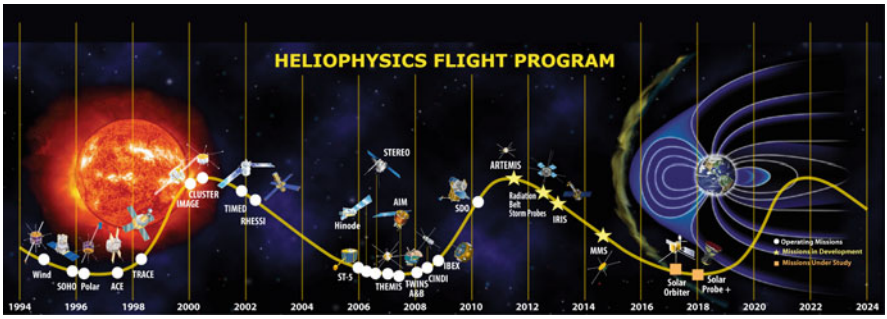

Fig. 6.4 The satellite missions comprising the Heliophysics system observatory, shown as a function of time with the solar cycle overplotted. Image courtesy of NASA

6.2 Properties of Reconnection at Earth's Dayside Magnetopause

Here, qualitative properties of dayside reconnection are summarized; a more quantitative treatment is in Sect. 6.3. This section discusses why, when, and where reconnection at the dayside magnetopause occurs and what it looks like. Two focuses are how reconnection at the dayside differs from other settings and the standard models.

6.2.1 When Dayside Reconnection Occurs

The best evidence from observations and simulations indicate that reconnection at the dayside *always* occurs somewhere. The location where reconnection happens and the local efficiency at which magnetic flux from the solar wind is reconnected can vary with conditions in the solar wind, and there are conditions for which reconnection can be locally suppressed as discussed in Sects. 6.3.2 and 6.3.3, but there is no scenario in which reconnection is not happening somewhere at the dayside at all times.

That dayside reconnection always occurs differs greatly from other settings where reconnection is intermittent. For example, in the solar corona, solar flares are associated with the liberation of up to 10^{32} ergs of magnetic energy. Before a flare, this energy must be stored in the system, so large-scale magnetic energy release through reconnection cannot be occurring. Similarly, in the magnetotail, the reconnected flux at the dayside is convected to the nightside, especially when the IMF has a southward component. There, it can accumulate without significant energy release. The standard picture is that magnetotail reconnection begins when some local condition related to the thickness of the plasma sheet and the structure of the magnetotail magnetic field is met.

6.2.2 Why Dayside Reconnection Occurs

The solar wind convects the interplanetary magnetic field away from the sun, so the IMF is essentially pushed into the magnetosphere. Thus, dayside reconnection is often thought of as "forced." Consider a due southward IMF, as seen in Fig. 6.1a. For southward IMF, the solar wind flow is in the inflow ($-x$) direction at the reconnection site, driving the magnetic fields together where they can reconnect.

However, when the IMF is due northward, as seen in Fig. 6.1b, the solar wind flow around the magnetosphere is nearly parallel to the magnetic field. It is less clear that reconnection is driven in this case. The alternative is that reconnection can generate its own inflow. When magnetic field lines break and cross-connect, the

result is two bent magnetic field lines. They want to straighten to release their energy but, to do so, the energy released by the reconnected field lines must overcome the energy it takes to bend the magnetic fields that have not yet reconnected. If the drive to straighten the magnetic field is large enough, the process will continue even in the absence of forcing. This is the mechanism behind the tearing mode (Furth et al. 1963), which is the linear phase of magnetic reconnection. In other words, reconnection is related to an instability, so it tends to occur naturally if it is energetically favorable to do so. An example of this is reconnection in the magnetotail, where a leading mechanism for the onset of reconnection is thought to be tearing.

For arbitrary IMF clock angle, it is challenging to delineate whether reconnection is predominantly forced or is happening spontaneously. This is because if there is a steady input from the solar wind, the local plasma parameters at the reconnection site adjust to ensure that the external flow seamlessly joins the reconnection inflow to the reconnection site, and it does so in a way that both the solar wind and reconnection site are steady. This topic is very much related to an open question about whether reconnection is set by global or local conditions at the magnetopause, which is the topic of Sect. 6.4.1. Note that reconnection need not be steady even if the solar wind is steady; this is discussed further in Sect. 6.2.3.4.

6.2.3 What Dayside Reconnection Looks Like

This section gives a summary of what dayside reconnection looks like, mostly from a qualitative perspective. In situ observations have been invaluable for developing an understanding. Their main limitation is that they provide plasma parameters on the trajectory of the satellites, which give at most a few one-dimensional (1D) traces of data. Simulations, on the other hand provide a full 2D or 3D picture of a numerical idealization of the process. Much of our visualization of magnetopause reconnection comes from simulations. We start with a description of 2D reconnection at the dayside magnetopause, and briefly address 3D effects.

First and foremost, the reconnection process is very sensitive to the mechanism that breaks the frozen-in condition of ideal-MHD. In particular, if the dissipation is provided by classical ion-electron Coulomb collisions, then the reconnection is relatively slow (Daughton and Roytershteyn 2012; Huang et al. 2011; Ji and Daughton 2011; Cassak and Drake 2013). If the plasma is collisionless, then the reconnection proceeds faster and the reconnected magnetic fields have a wider opening angle (in 2D).

To see what form reconnection takes on, consider the generalized Ohm's law, which is the electron equation of motion written in terms of the electric field **E** (Vasyliunas 1975):

$$\mathbf{E} + \mathbf{v} \times \mathbf{B} = \frac{\mathbf{J} \times \mathbf{B}}{ne} - \frac{\nabla \cdot \mathbf{p}_e}{ne} + \frac{m_e}{e} \frac{d(\mathbf{J}/ne)}{dt} + \eta \mathbf{J}, \tag{6.2}$$

where $\mathbf{v}$ is the bulk flow single-fluid velocity (that arises in MHD), $\mathbf{B}$ is the magnetic field, $\mathbf{J} = \nabla \times \mathbf{B}/\mu_0$ is the current density, n is the number density (assumed equal for ions and electrons), e is the proton charge, $\mathbf{p}_e$ is the electron pressure tensor, m_e is the electron mass, and η is the resistivity. In the electron inertia term (the one proportional to m_e), the electron velocity $\mathbf{v}_e$ is replaced by $-\mathbf{J}/ne$ since the term is only important at small scales where ion bulk motion is relatively unimportant. When the right side is negligible, one recovers ideal-MHD. When the resistive term dominates, one gets collisional reconnection, which is described by the Sweet-Parker model (Parker 1957) for Lundquist numbers $S = \mu_0 L c_A/\eta$ below 10^4, where L is a characteristic system size length scale, and is modified by secondary islands for larger values (Daughton et al. 2009a; Cassak and Drake 2009; Huang and Bhattacharjee 2010). When the resistive term is not dominant, typically the other three terms all can be important at various scales, leading to collisionless reconnection.

To determine which is dominant, one can compare the length scales associated with each term; the largest is the first to become important. When the magnetic fields are anti-parallel and the electron pressure gradient is assumed to be a scalar, a comparison of the convection term $\mathbf{v} \times \mathbf{B}$ and the Hall term $\mathbf{J} \times \mathbf{B}/ne$ reveals that the critical length scale for the Hall term to be important is the **ion inertial length** $d_i = c/\omega_{pi} = (\epsilon_0 m_i c^2/nq_i^2)^{1/2}$ where q_i is the ion charge (typically e in the solar wind), also called the **ion skin depth**. This is equivalent to the gyroradius of an ion traveling at the Alfvén speed, $d_i = c_A/\Omega_{ci}$, where $\Omega_{ci} = q_i B/m_i$ is the ion cyclotron frequency. Using the typical values given in Tables 6.1 and 6.2 reveals

$$d_{i,\mathrm{sh}} = \left(\frac{\epsilon_0 m_i c^2}{n_{\mathrm{sh}} e^2}\right)^{1/2} \simeq 39\ \mathrm{km} \quad \text{and} \quad d_{i,\mathrm{ms}} = \left(\frac{\epsilon_0 m_i c^2}{n_{\mathrm{ms}} e^2}\right)^{1/2} \simeq 721\ \mathrm{km}. \quad (6.3)$$

It is noted in passing that if reconnection has a very strong out-of-plane magnetic field (also called a **guide field**), the Hall effect couples to the ion pressure in the momentum equation to maintain pressure balance, and the length scale becomes the ion Larmor radius $\rho_s = c_s/\Omega_{ci}$ based on the ion acoustic speed $c_s = [(\gamma_e k_B T_e + \gamma_i k_B T_i)/m_i]^{1/2}$, where γ_j is the ratio of specific heats and T_j is the temperature for species j (Zakharov and Rogers 1992; Kleva et al. 1995; Rogers et al. 2001). The two length scales are related by $\rho_s = (\beta/2)^{1/2} d_i$. For intermediate guide field strengths, one expects a smooth transition between the scales ρ_s and d_i.

For collisional reconnection, the half-thickness δ_{SP} of the Sweet-Parker layer is $\delta_{SP} \simeq (\eta L/\mu_0 c_A)^{1/2}$, where L is the half-length of the dissipation region in the outflow direction (Parker 1957). This is an upper bound, since the layer is thinner if secondary islands are playing a role (Shibata and Tanuma 2001; Daughton et al. 2009b; Cassak et al. 2009). Assuming classical (Spitzer) collisions (Spitzer and Härm 1953) are responsible for the resistivity, we get $\eta = (e^2 \ln \Lambda/3\epsilon_0^2 m_e)(m_e/2\pi k_B T_e)^{3/2} = 2.2 \times 10^{-5}\ \Omega \cdot \mathrm{m}$ for the magnetosheath and $7.75 \times 10^{-9}\ \Omega \cdot \mathrm{m}$ for the magnetosphere (using $\ln \Lambda \simeq 20$ and assuming $T_e = T_i/5$). Assuming L is comparable to 1/8 of the circumference of the magnetopause (of

radius R approximately 10.4 R_E), then $L \simeq (1/8)2\pi R \simeq 7.85\ R_E \simeq 52 \times 10^6$ m. Then, δ_{SP} is

$$\delta_{SP,\mathrm{sh}} \simeq \left(\frac{\eta_{\mathrm{sh}} L}{\mu_0 c_{A,\mathrm{sh}}}\right)^{1/2} \simeq 100\,\mathrm{m} \quad \text{and} \quad \delta_{SP,\mathrm{ms}} \simeq \left(\frac{\eta_{\mathrm{ms}} L}{\mu_0 c_{A,\mathrm{ms}}}\right)^{1/2} \simeq 0.32\,\mathrm{m}. \tag{6.4}$$

These are orders of magnitude smaller than the Hall scale d_i! Consequently, collisionless effects become important long before collisional effects, and the reconnection is expected to be collisionless. For comparison, the ion inertial scale and Sweet-Parker thickness in the solar corona are both on the order of 1 m (Priest and Forbes 2000; Cassak et al. 2005; Uzdensky 2007)!

6.2.3.1 The Standard (2D) Picture of Collisionless Reconnection

The standard picture of 2D collisionless reconnection and its relevance for the dayside magnetopause is discussed first. A sketch of the dissipation region and its surroundings is given in Fig. 6.5 from Mozer et al. (2002). The white parts to the left and right have oppositely directed magnetic fields with the northward pointing magnetosphere to the right and the southward pointing magnetosheath to the left. In

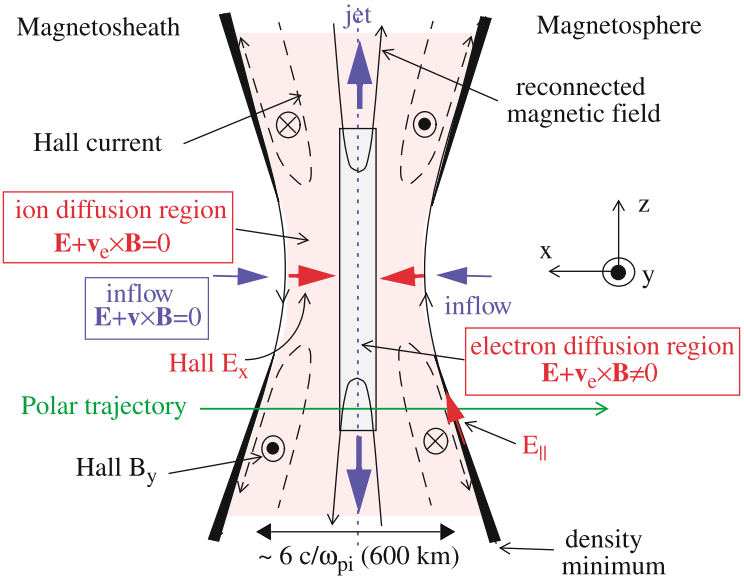

Fig. 6.5 Sketch of the region around the magnetic reconnection site for a symmetric system from Mozer et al. (2002). The *green line* shows the approximate trajectory of the Polar satellite for an observed event shown in Fig. 6.6. Reprinted figure with permission from [F. S. Mozer, S. D. Bale, and T. D. Phan, Phys. Rev. Lett., 89, 015002, 2002.] Copyright (2002) by the American Physical Society

this **upstream** region, the ideal-MHD Ohm's law is approximately satisfied. When reconnection is transpiring, there is a flow towards the magnetopause [in the normal (x) direction] convecting the reconnecting magnetic fields inward. The dominant contribution to the electric field in this region from Eq. (6.2) is the $-\mathbf{v} \times \mathbf{B}$ term; $-v_x B_z$ gives rise to an electric field in the $+y$ direction. The out-of-plane electric field is called the **reconnection electric field**.

When the ions, gyrating around the magnetic fields, reach a distance of their gyroradius (between d_i and ρ_s depending on the guide field) away from the magnetopause, they decouple from the magnetic field as they undergo Speiser orbits (Speiser 1965). However, the electrons remain frozen to the magnetic field ($\mathbf{E} + \mathbf{v}_e \times \mathbf{B} \simeq 0$) because their gyroradius is typically smaller than that of the ions. The region where the ions are not frozen-in but the electrons are is often called the **ion dissipation region** or the **ion diffusion region** even though neither dissipation nor diffusion are actually taking place in this region. (Both terms are acceptable; this chapter employs the former.) In the ion dissipation region, the ions have very little bulk motion because of their Speiser orbits while the electrons continue to have a directed bulk flow towards the magnetopause, so since $\mathbf{J} = q_i n \mathbf{v}_i - en\mathbf{v}_e$ there is a net current directed away from the magnetopause in the ion dissipation region. Consequently, the Hall term $\mathbf{J} \times \mathbf{B}/ne$ in Eq. (6.2) has the dominant role contribution to the reconnection electric field. Indeed, $J_x B_z$ gives rise to an electric field in the y direction, in the same direction as the convective electric field in the upstream region.

The in-plane current density produces an out-of-plane magnetic field (Sonnerup 1979). From Ampère's law, this current is associated with a magnetic field wrapping around it, pointing out of the page on the upper right and lower left and into the page on the lower right and upper left. This out-of-plane magnetic field with a quadrupole structure is called the **Hall magnetic field**. The observational detection of the Hall magnetic fields in the magnetosphere was a key confirmation of the collisionless reconnection model (Nagai et al. 2001; Øieroset et al. 2001; Deng and Matsumoto 2001; Mozer et al. 2002). An equivalent explanation of the Hall magnetic fields is that the current consistent with the reversed magnetic fields (from the right hand rule) is pointing out of the page. This corresponds to electrons carrying the current into the page since $\mathbf{J} \simeq -ne\mathbf{v}_e$. These electrons drag the reconnecting magnetic field out of the page, which introduces an out-of-plane component of the magnetic field with the same quadrupole structure (Mandt et al. 1994).

When the inflowing electrons get within a distance of their gyroradius of the magnetopause, they decouple from the magnetic field. It is in this region that dissipation becomes important, and the magnetic field lines can break and cross-connect, the key part of reconnection. This is widely thought to be associated with the off-diagonal elements of the electron pressure tensor, giving an effective viscosity (Hesse et al. 1999), as discussed in other chapters. This region has a thickness on the order of the electron inertial length $d_e = c/\omega_{pe} = (\epsilon_0 m_e c^2/ne^2)^{1/2}$, which is $(m_i/m_e)^{1/2} \simeq 43$ times thinner than the ion dissipation region. This is often called the **electron dissipation region** where $\mathbf{E} + \mathbf{v}_e \times \mathbf{B} \neq 0$, and is depicted by the inner rectangle in Fig. 6.5. In this region, electrons are accelerated in the

$-y$ direction by the reconnection electric field and gyrate around the reconnected magnetic fields that point in the $\pm x$ direction. This leads to directed flow in the $\pm z$ direction. This flow exits the electron dissipation region at the *electron* Alfvén speed $c_{Ae} = B/(\mu_0 m_e n)^{1/2}$ in the form of outflow jets, going out the top and bottom in Fig. 6.5. In the ion dissipation region, a similar effect directs ions in the $\pm z$ direction, exiting at the (ion) Alfvén speed. Electrons are faster than ions in the ion dissipation region, but slow down as ions speed up, so they nominally exit the ion dissipation region at the same speed. Beyond this point is the **downstream** region consisting of reconnected magnetic fields.

The current produced by the bulk flow of electrons in the ion dissipation region is the **Hall current**, shown as the dashed curve in Fig. 6.5. From the non-zero $J_z B_y$, an electric field in the x direction is produced. This **Hall electric field** is sketched in the figure, pointing toward the magnetopause on either side of the magnetopause.

Determining the extent of the dissipation regions in the outflow direction is complicated. The big picture is that the magnetic field must be divergence free, so the size of the normal component B_x compared to the reconnecting component B_z should be comparable to the width δ over the length L of the dissipation region. As will be discussed in Sect. 6.3, this ratio is typically about 0.1, so a nominal expectation is $L \sim 10\delta$. However, thinking on this has changed, as will be returned to shortly.

The point at the middle of the electron dissipation region, where the magnetic field lines change topology, is called either the **X-point** or the **X-line** because of the shape made by the field lines. In 2D symmetric reconnection, it has to be in the center of the dissipation region by symmetry. The location where the inflow goes to zero is called the **stagnation point**, and is also at the center of the dissipation region. The magnetic field lines forming the boundary between the upstream plasma and the dissipation region (in this 2D picture) are called **separatrices**, which intersect at the X-line. The separatrices are important for reconnection at the dayside magnetopause because they segregate the region into areas with different constituent plasmas. A satellite flying near a reconnection site would see a region of magnetosheath plasma, a region where the plasmas are mixed, and a region with magnetospheric plasma.

Sample data from satellite observations from Mozer et al. (2002) are shown in Fig. 6.6. Each plot shows a plasma parameter on a pass through the magnetopause reconnection site sketched as the green line in Fig. 6.5, with the magnetosheath coming first in time and the magnetosphere coming later. The top plot in Fig. 6.6 shows the electron number density; it is a little higher in the sheath than the magnetosphere, but not by a huge amount. The second plot shows the magnetic field magnitude, and the following three show the three components of the magnetic field in GSM coordinates. In particular, B_z shows the magnetic field reversal, going from about -80 to 80 nT. The B_y entry shows a bipolar deflection; this is consistent with one branch of the quadrupolar Hall magnetic field. Note, it peaks at about 50 nT; it is typical for the Hall magnetic field to be about 0.4 times the strength of the reconnecting (z) component in symmetric reconnection (as determined from magnetotail observations) (Eastwood et al. 2010). The trace for the reconnected magnetic field B_x shows that it is small, on the order of a few nT at most. The

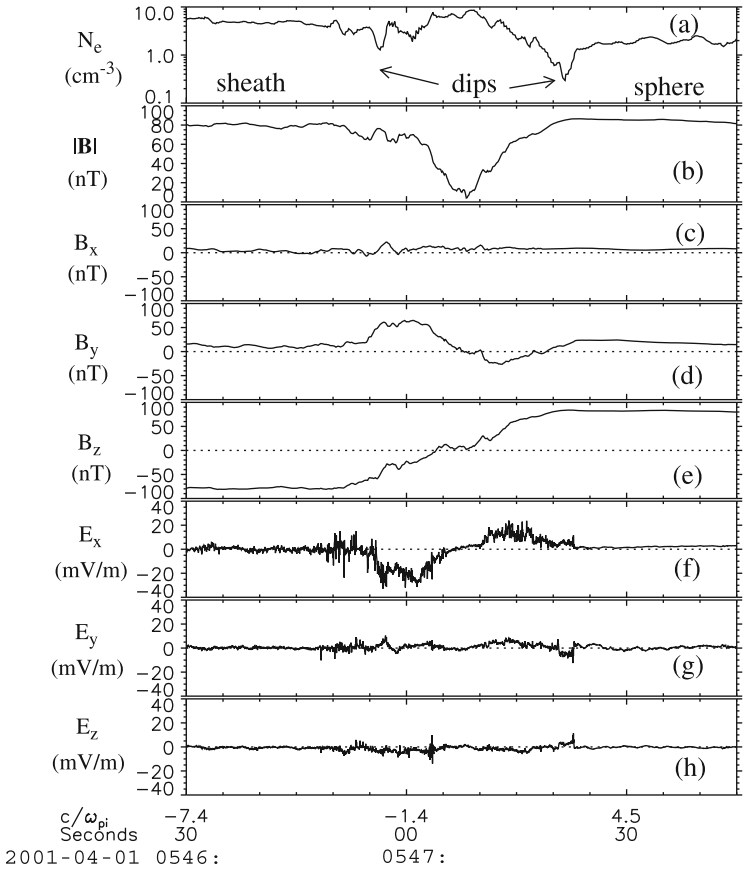

Fig. 6.6 Data from an observed magnetopause reconnection event from Mozer et al. (2002). Shown are electron density N_e, magnetic field magnitude $B = |\mathbf{B}|$, the three components of the magnetic field (in GSM coordinates), and the three components of the electric field (in GSM coordinates). Reprinted figure with permission from [F. S. Mozer, S. D. Bale, and T. D. Phan, Phys. Rev. Lett., 89, 015002, 2002.] Copyright (2002) by the American Physical Society

theoretical prediction is $0.1B_z \simeq 8\,\text{nT}$, in reasonable agreement with the data although it is difficult to carefully assess. The final three plots show the three components of the electric field (in GSM coordinates). In E_x, one sees the bipolar structure of the Hall electric field. The reconnection electric field E_y is relatively small. In summary, the data shows that the collisionless reconnection model is represented in the data quite well, at least for this event.

While not a focus of this chapter, the dissipation region structure noted above, with outflow direction extent about 10 times longer than its thickness, is oversimplified. While the 2D picture in Fig. 6.5 was informed by numerical simulations, they were in relatively small domains. As supercomputers got faster and simulations were used to investigate larger systems, it was found that the electron dissipation

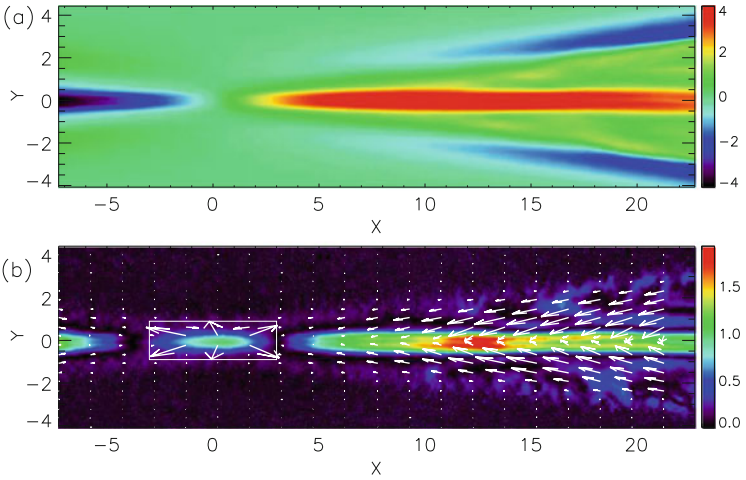

Fig. 6.7 Simulation results showing the two-scale structure of the electron dissipation region: (**a**) Electron outflow velocity, (**b**) departure from idealness of electrons with momentum flux vectors from Shay et al. (2007). Reprinted figure with permission from [M. A. Shay, J. F. Drake, and M. Swisdak, Phys. Rev. Lett., 99, 155002, 2007.] Copyright (2007) by the American Physical Society

region was not limited to an extent of 10 d_e in the outflow direction (Shay et al. 2007; Karimabadi et al. 2007). Figure 6.7 shows (a) the electron outflow velocity and (b) ratio of the departure from idealness $|(\mathbf{E} + \mathbf{v}_e \times \mathbf{B})_M|$ to the reconnection electric field $\mathbf{E}_M$ with momentum flux vectors overplotted for one of these simulations. (Note, the axis labels differ from the convention used here.) This reveals a two-scale structure of the electron dissipation region. The traditional one has been called the **inner electron dissipation region**, and the one that extends into the exhaust is the **outer electron dissipation region**. The outer one can extend 10 s of *ion* inertial lengths (hundreds of d_e) into the downstream region. This alters the structure of the Hall magnetic field; it fills the downstream dissipation region instead of remaining localized near the separatrices as previously thought. This was subsequently identified in satellite observations of reconnection in the magnetosheath (Phan et al. 2007). It was later shown that, while the electrons in the outer electron dissipation region slip with respect to the ions and the magnetic field, they are actually frozen-in (Hesse et al. 2008; Zenitani et al. 2011), with the diamagnetic drift explaining the departure from idealness. This structure calls into question our understanding of the electron and ion dissipation regions, but since the outer electron dissipation region is not dissipative much of our understanding persists. There have been studies into the outer electron dissipation region when a guide field is present (Goldman et al. 2011).

The electron dissipation region is important because the reconnection electric field is in a region where the magnetic field is weak. This allows particles to freely accelerate and gain energy. (In contrast, where the magnetic field is significant, an electric field leads to an $\mathbf{E} \times \mathbf{B}$ drift which leads to no net energy gain.) However,

the electron dissipation region is relatively small, so the reconnection electric field is not thought to be the main source for particle acceleration. Also, direct crossings through the electron dissipation region are rare, so it has been difficult to study. This topic will be addressed again in Sect. 6.4.3.

6.2.3.2 The Effect of Asymmetries

The event studied in Mozer et al. (2002) was significant because it was a clean demonstration of collisionless effects in magnetospheric reconnection. However, in a followup study, it was shown that less than 1 % of dayside reconnection events showed the canonical Hall magnetic field quadrupole structure (Mozer and Retinó 2007). The reason for this is that the event had a particularly strong magnetosheath magnetic field, so the event was nearly "symmetric," meaning that the magnetosheath and magnetospheric parameters were comparable. However, as has long been known (Levy et al. 1964) and is exemplified in the data in Tables 6.1 and 6.2, typical magnetopause parameters make the reconnection **asymmetric**. In particular, the densities on either side typically differ by a factor of more than 100, and the magnetic field changes by a factor of around 2 across the magnetopause.

The presence of asymmetries in magnetic field and/or density changes some details of the reconnection region for symmetric reconnection, though the same qualitative properties persist. One change is that the X-line can be displaced in the inflow direction (Cassak and Shay 2007). This is because if the magnetic field on one side of the dissipation region is much stronger than the other, then it is energetically favorable for the X-line to move toward the strong field rather than the strong field bending to move toward the X-line. This is the cause of magnetospheric erosion. It is often important to move into the reference frame of the X-line because theories are often (tacitly) performed in this frame. In 2D steady-state reconnection in the lab frame, there is a different reconnection electric field $E_{\rm sh}$ and $E_{\rm ms}$ on the two sides of the dissipation region. The frame of the X-line is one in which these two fields are the same; this can be found using the reference frame moving at speed $(E_{\rm sh} - E_{\rm ms})/(B_{\rm sh} + B_{\rm ms})$ (Mozer et al. 2002); the reconnection electric field in this frame is $E = (E_{\rm sh}B_{\rm ms} + E_{\rm ms}B_{\rm sh})/(B_{\rm sh} + B_{\rm ms})$ (Cassak and Shay 2009).

Another change is that the dissipation region takes on an asymmetric structure in the inflow direction. In 2D and in a steady state, conservation of magnetic flux implies that the convective electric field $(-\mathbf{v}\times\mathbf{B})$ on either side must be the same, so the stronger reconnecting magnetic field convects in more slowly (Cassak and Shay 2007). One might think that this means the X-line shifts to the strong magnetic field (magnetospheric) side, but this is not true. The rate at which magnetic energy enters is proportional to the inflow speed times the magnetic energy, so the flux of magnetic energy is larger from the strong magnetic field side even though its flow is slower. This means that the X-line is displaced from the center of the dissipation region towards the weak magnetic field side (the magnetosheath). The stagnation point, on the other hand, is offset towards the side with the smaller mass flux into the dissipation region, given by the side with the smaller ratio of mass density

to magnetic field ρ/B (Cassak and Shay 2007). This is the magnetospheric side for typical conditions. Thus, the X-line and stagnation point are not necessarily co-located for asymmetric reconnection (Priest et al. 2000). This implies that there is an in-plane flow at the X-line during asymmetric reconnection, typically from the magnetosheath to the magnetosphere.

These predictions have been confirmed in observations and simulations. It is consistent with recent observations of reconnection at the polar cusp (Muzamil et al. 2014). Additional observational confirmation for this is discussed in Sect. 6.3.4. In simulations, flow through the X-line had been seen in global MHD simulations (Siscoe et al. 2002; Dorelli et al. 2004). It was originally questioned whether this was a physical result because both simulations used unrealistically high dissipation. However, it is now understood that this is physical, and it had not been seen previously because reconnection was not sufficiently resolved in global simulations (which often rely on grid scale dissipation to allow reconnection) (Cassak and Shay 2009).

A related effect is that the reconnected magnetic field lines at the top and bottom of Fig. 6.5 are asymmetric, as well. The reconnected magnetic field grows preferentially toward the weak magnetic field side (the magnetosheath) because it is easier to bend the weak fields than the strong fields. This is apparent in particle-in-cell (PIC) simulations from Malakit et al. (2013) shown in Fig. 6.8a, where they grow toward the weak magnetic field side at the top of the plot.

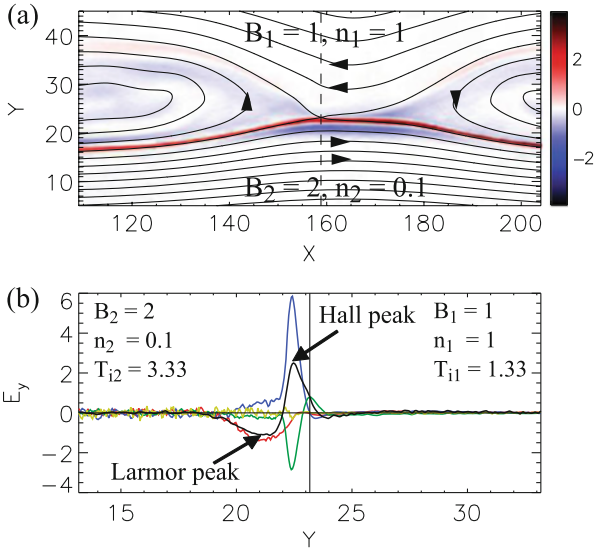

Fig. 6.8 Simulation of reconnection in an asymmetric dayside magnetopause configuration. (**a**) Vertical electric field, with magnetic field lines overplotted. (**b**) Contributions to the vertical electric field along the *dashed line* in panel (**a**). Figure adapted with permission from Malakit et al. (2013). Copyrighted by the American Physical Society

Another interesting impact of upstream asymmetries is the effect on the Hall magnetic and electric fields. While quadrupolar and bipolar, respectively, for symmetric reconnection, they become more bipolar and unipolar for asymmetric reconnection, as has been identified in simulations (Karimabadi et al. 1999; Nakamura and Scholer 2000; Swisdak et al. 2003; Tanaka et al. 2008; Pritchett 2008; Huang and Ma 2008; Malakit et al. 2010, 2013) and observations (Øieroset et al. 2004; Retinó et al. 2006; Mozer et al. 2008a,b; Mozer and Pritchett 2010). For typical conditions, the Hall magnetic field on the magnetosheath side dominates its magnetospheric counterpart, giving a bipolar appearance. The Hall electric field on the magnetospheric side dominates the magnetosheath side. This is shown in simulation results in Fig. 6.8; the red part in panel (a) is the magnetospheric Hall electric field. (Note the axes are labeled differently than the convention employed here; their x corresponds to z and their y corresponds to x.) It has been suggested that the structure of the Hall magnetic field is dictated by the location of the X-line and stagnation point (Malakit 2012).

It was recently shown that asymmetric reconnection for dayside magnetopause parameters has an additional electric field structure, which has been referred to as the **Larmor electric field** (Malakit et al. 2013). As with the Hall electric field, it is an in-plane (normal, in the x direction) electric field. While the Hall electric field points toward the magnetopause on both sides, the Larmor electric field only appears on the magnetospheric side and points away from the boundary layer. It is visible in simulations, shown in Fig. 6.8, as the blue region below the X-line in panel (a) and is labeled in the cut shown in panel (b). It was recently reported to be observed in Polar data (Koga et al. 2014).

Another important property of asymmetric magnetopause reconnection is the expected appearance of an electron pressure anisotropy in the region upstream of the dissipation region, chiefly on the magnetospheric side (Egedal et al. 2011). This electric field arises from the out-of-plane electric field having a component parallel to the out-of-plane (Hall) magnetic field, producing a parallel electric field. This field accelerates electrons along the field, giving rise to a higher parallel temperature than perpendicular temperature. The region of the electron pressure anisotropy is correlated with the region with the Larmor electric field (Malakit 2012).

The characteristic thickness of the reconnecting current sheet is also affected by asymmetries. Indeed, with no guide field the thickness is the ion inertial scale d_i; for asymmetric reconnection, it is not clear which density to use. It has been suggested that the thickness of the layer in asymmetric reconnection in terms of magnetosheath (sh) and magnetospheric (ms) parameters is Cassak and Shay (2009)

$$d_{i,\mathrm{asym}} = \frac{1}{2}\left(\sqrt{\frac{B_{\mathrm{sh}}}{B_{\mathrm{ms}}}} + \sqrt{\frac{B_{\mathrm{ms}}}{B_{\mathrm{sh}}}}\right) d_{i,\mathrm{out}}, \tag{6.5}$$

where $d_{i,\mathrm{out}} = (\epsilon_0 m_i c^2/e^2)^{1/2}[(B_{\mathrm{sh}} + B_{\mathrm{ms}})/(n_{\mathrm{sh}}B_{\mathrm{ms}} + n_{\mathrm{ms}}B_{\mathrm{sh}})]^{1/2}$. For typical parameters from Tables 6.1 and 6.2, $d_{i,\mathrm{asym}} = 49\,\mathrm{km}$, intermediate between $d_{i,\mathrm{sh}}$ and $d_{i,\mathrm{ms}}$. This prediction was tested numerically, but not observationally.

Another interesting difference due to the asymmetry is the physics causing the dissipation. In symmetric collisionless reconnection without a guide field, the dissipation allowing the magnetic fields to change topology is the off-diagonal elements of the electron pressure tensor. For asymmetric reconnection, the term that dominates at the X-line is the electron inertia term (Hesse et al. 2014).

Note that reconnection at the dayside is also likely to be asymmetric in the outflow direction. For due southward IMF and without a dipole tilt, the system is north-south symmetric so no such asymmetry would occur, but for any less symmetric system this is expected to be important (Komar 2015). Reconnection that is asymmetric in the outflow direction has been addressed (Murphy et al. 2010), though more work is necessary for magnetopause applications.

6.2.3.3 The Effect of Magnetosheath Flow

Upstream flow at Earth's magnetopause can also affect reconnection. While Earth's rotation causes the plasma near it to corotate, this typically does not extend out to the magnetopause, so the bulk flow on the magnetospheric side of the magnetopause is small. However, the magnetosheath plasma flows around the magnetopause. This sets up a flow shear (a velocity gradient) across the magnetopause. Flow shear in a fluid or unmagnetized plasma can lead to the Kelvin-Helmholtz instability, but a magnetic field parallel or anti-parallel to the flow slows the instability or can stop it. Similarly, flow parallel or anti-parallel to reconnecting magnetic fields makes the reconnection slower, and can even stop it if fast enough, which is discussed further in Sect. 6.3.3.

From the perspective of the gas dynamic flow of the solar wind around the magnetosphere, high flow velocities tangent to the magnetopause occur at high latitudes near the poles and on the flanks of the magnetosphere. One might suspect that flow shear could be important for all clock angles, but this is not likely to be the case. For example, for due southward IMF with no dipole tilt, the flow around the magnetosphere towards the flanks is out of the reconnection plane (Komar et al. 2015). However, as discussed in Sect. 6.2.4, reconnection sites may occur at high latitudes when the IMF is strongly northward and may occur at low latitudes on the flanks when the IMF is southward, so it is important to consider the effect of flow shear for these conditions.

The structural effect of flow shear on (2D) reconnection is to twist the dissipation region and to cause the opening angle of the separatrix in the outflow region to increase (La Belle-Hamer et al. 1994; Cassak 2011). These effects have been seen in simulations, as exemplified in Fig. 6.9 which show the out-of-plane current density and magnetic field lines for two-fluid simulations with increasing flow shear from (a) to (d). (The axis labels are again different than the current convention.) The extent of the twist and opening angle were predicted in terms of upstream parameters (Cassak 2011). However, they would be difficult to verify observationally using single- or multi-spacecraft missions.

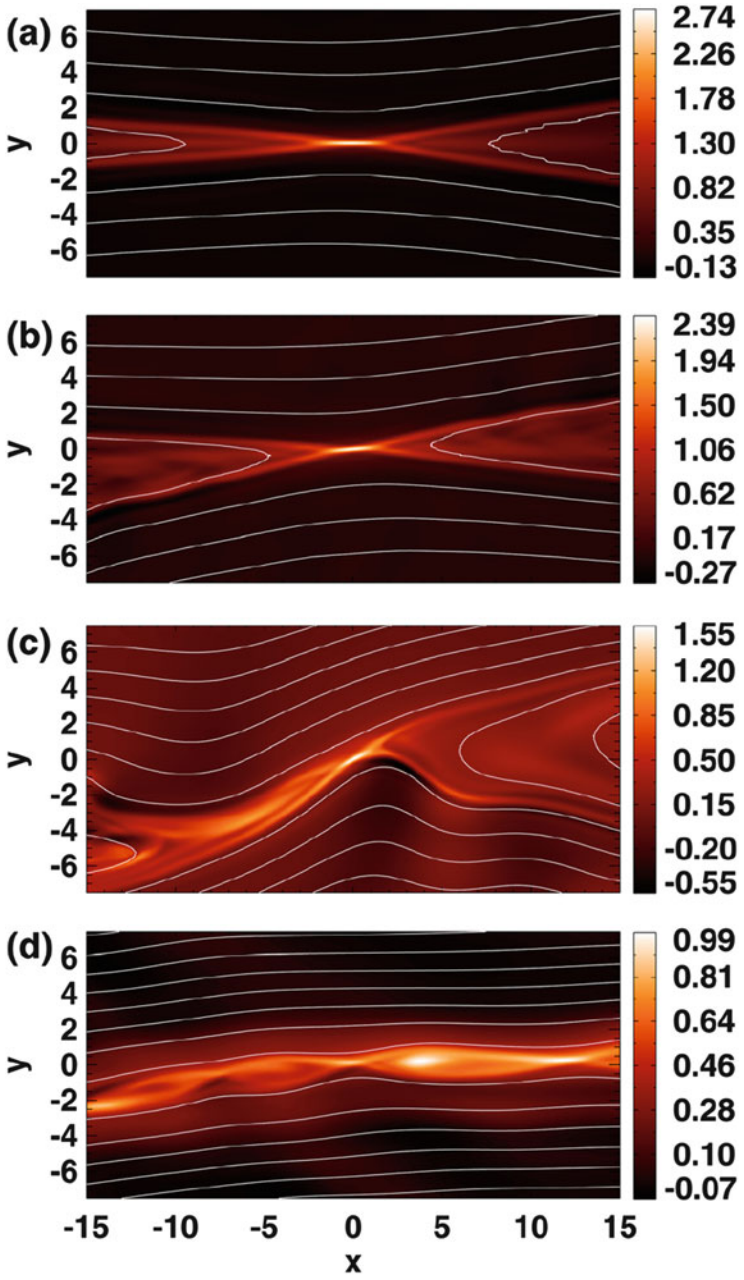

Fig. 6.9 Fluid simulation of (symmetric) reconnection with a flow shear. The top has no background flow, and it increases for subsequent figures. Reprinted with permission from Cassak (2011). Copyright 2011, AIP Publishing LLC

Another important effect on the dissipation region caused by flow shear is that the X-line can move. For symmetric reconnection with equal and opposite upstream flows, the X-line is stationary, but this is not the case for asymmetric reconnection (Tanaka et al. 2010; Doss et al. 2015). This will be quantified in Sect. 6.3.3.

6.2.3.4 Other Features of Dayside Reconnection

The picture of reconnection as a single X-line is typically an oversimplification, even within the 2D description. The reason is that long, thin sheets of current undergoing reconnection are more likely to splinter into multiple pieces than to splinter only at a single X-line. This can occur due to inhomogeneities in the upstream plasma (Matthaeus and Lamkin 1985), but can also occur even in completely laminar 2D reconnection (Biskamp 1986; Daughton et al. 2006). The magnetosheath is highly turbulent (Retinó et al. 2006; Karimabadi et al. 2014), so it is reasonable to expect a reconnection region with multiple X-lines. It has also been suggested that flow shear at the dayside can produce multiple X-lines (Fermo et al. 2012). The region in-between X-lines contains reconnected flux and is called a **magnetic island** or a **plasmoid**; if there is a guide field as is common at the dayside, it is called a **flux rope** (Eastwood and Kiehas 2015).

Such behavior was discovered observationally and were dubbed **flux transfer events (FTEs)** (Russell and Elphic 1978, 1979). An idealized FTE is sketched in Fig. 6.10a. The observational signature of an FTE depends on the path of the satellite's traversal; for the path in panel (a), the signatures of the reconnecting B_L and normal B_N magnetic fields are sketched in panel (b); there is a reversal B_L accompanied by a reversal in the reconnected magnetic field B_N. They tend to be associated with enhanced "core" magnetic fields B_M (Karimabadi et al. 1999) and contain a mixture of magnetospheric and magnetosheath plasma.

There is a long history of debate into the cause of FTEs, but this topic is not emphasized in this chapter; instead the reader is referred to review articles (Elphic 1995; Dorelli and Bhattacharjee 2009). One reason they are potentially interesting is they have long been thought of as a significant mechanism for magnetic flux transport from the dayside. In addition, with oppositely directed plasma jets from outflows of adjacent X-lines, there is strong potential for plasma heating (Øieroset et al. 2011, 2014). Interestingly, a recent observation of FTE remnants near the

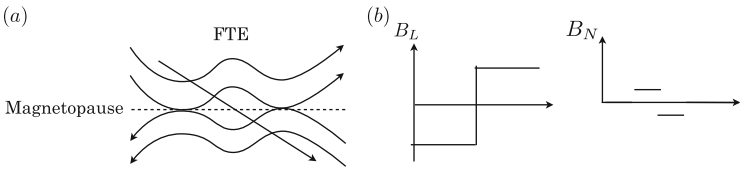

Fig. 6.10 (**a**) Sketch of a flux transfer event (FTE) at the magnetopause, with a sample spacecraft trajectory. (**b**) Reconnecting B_L and normal B_N signatures along the trajectory

moon's orbit with the ARTEMIS satellites suggest that they are fossils that do not continue to reconnect all the way around the magnetopause (Eastwood et al. 2012). Recent work has predicted the statistics of FTEs using a Vlasov-type equation for their size and magnetic flux (Fermo et al. 2010), which compared favorably with observations of FTEs (Fermo et al. 2011).

Much of the discussion thus far can be thought of in the simple 2D picture. There is an interesting property of the magnetopause that is manifestly 3D. It has been suggested that magnetic islands can grow in multiple locations, and they can interact to produce stochastic magnetic fields (Galeev et al. 1986). The magnetic field is said to undergo percolation, and closed field lines containing both magnetosheath and magnetospheric plasma would result. Stochastic fields can contribute to enhanced particle acceleration in at reconnection sites (Dahlin et al. 2015). Detecting this observationally may be very challenging.

6.2.4 Where Dayside Reconnection Occurs

The location on the dayside magnetopause where reconnection occurs was first addressed by Dungey. In the early sketches of magnetospheric reconnection (Dungey 1963), similar to those from simulations shown in Fig. 6.1, he correctly realized that when the IMF is due southward and there is no dipole tilt, the field is oppositely directed to the northward-pointing terrestrial magnetic field at the subsolar point, as shown in by the blue oval at the dayside in panel (a). When the IMF points due northward, reconnection does not occur at the subsolar point because the magnetic fields are parallel; instead the IMF drapes over the magnetosphere. However, the IMF as anti-parallel to the magnetospheric field near the cusp, so reconnection can occur there, as shown as the blue ovals in panel (b).

This sketches were groundbreaking, but it is worth noting their limitations. The illustrations do not incorporate Earth's dipole tilt and do not address when the IMF is tilted toward or away from Earth ($B_x \neq 0$) or when the IMF is not due northward or due southward ($B_y \neq 0$). These can have a sizable effect. Indeed, one might expect that for oblique IMF directions, the location where reconnection happens continuously migrates from the equatorial plane to the cusps.

Another critical issue is that Fig. 6.1 contains 2D representations of the 3D magnetosphere. As the dayside magnetopause is roughly ellipsoidal, one must consider what happens out of the $y = 0$ plane. Consider the ideal case of perfectly southward IMF and ignore the dipole tilt, as in Fig. 6.1a. At non-zero y, the picture should look similar, but a key difference is that there is a flow around the magnetopause due to the solar wind. However, the magnetic field lines still can undergo reconnection. This implies that reconnection does not happen only at a single point; rather, it takes place along a one-dimensional curve. This curve has been called the **reconnection line** or the **magnetic separator** or just the **separator** because being a location where reconnection takes place it separates regions of differing magnetic topology (Cowley 1973; Lau and Finn 1990; Siscoe et al. 2001).

This generalizes the concept of the X-line in standard 2D sketches of reconnection. For southward IMF with no dipole tilt, the separator lies in the equatorial plane at its intersection with the magnetopause. It goes all the way around to the nightside (where reconnection in the magnetotail occurs), forming a closed loop around the entire magnetopause. Thus, finding where reconnection occurs is not as simple as finding a single point; one must find the whole separator.

It should be noted that there is some debate about the utility of the separator concept. It has been suggested that for reconnection to occur, the existence of a separator is neither necessary nor sufficient. Indeed, one can envision reconnection in a twisted magnetic field where it would be difficult or impossible to identify a field line that separates the fields into regions of different topology. Also, one could have a separator without reconnection; for example, a magnetic field with separatrices making an angle of 90° would have a separator where the separatrices meet, but would not spontaneously undergo reconnection because there is no free magnetic energy. These objections are valid. However, due to the geometry of the magnetospheric field, there are magnetic separators in the system, and reconnection does tend to happen there. Consequently, using separators to help study dayside reconnection is beneficial.

There is a long history of thought on where dayside reconnection occurs for arbitrary direction of the IMF. Motivated by Dungey's original sketches, it was originally suggested that reconnection always happens at the subsolar point (Petschek 1966). If the IMF is not due southward, then the magnetic fields in this model are not anti-parallel. Only a component of the magnetic field reconnects, so this model is often referred to as **component reconnection**, and there is a non-zero guide field. It was later suggested that for an arbitrary direction of the IMF, reconnection occurs in the plane that enforces the guide field is uniform (Sonnerup 1974; Gonzalez and Mozer 1974), though this is no longer a favored model (Teh and Sonnerup 2008).

A second approach suggested that reconnection is not always at the subsolar point; instead reconnection happens at the locations on the dayside where the magnetic fields are anti-parallel (Crooker 1979). This more appropriately describes the migration of the dominant reconnection site from the subsolar point to the cusps as the IMF goes from southward to northward.

What do observations reveal? Remote observations in the cusp and in situ observations at reconnection sites at the magnetopause indicate the **magnetic shear angle** θ, the angle between the magnetosheath and magnetospheric magnetic fields, tends to be close to 180° (e.g., Petrinec and Fuselier 2003; Phan et al. 2003; Bobra et al. 2004; Trattner et al. 2004; Fuselier et al. 2010). Observationally, measurements of θ are uncertain by 5–10° (Haaland et al. 2004); fluctuations in the magnetic field on both sides of the magnetopause preclude reduction of this uncertainty. Thus, what is defined observationally as anti-parallel reconnection at the magnetopause may include magnetic shear angles that range from 170° to 180° and there is no way to determine if exactly anti-parallel reconnection occurs at the magnetopause for any solar wind conditions.

However, remote observations in the cusps and in situ observations at the magnetopause also infer sizable guide fields. The guide field B_g is often parametrized in terms of θ and the reconnecting (anti-parallel) component of the magnetic field B_L from geometry using $\tan(\theta/2) = B_L/B_g$. A wide range of magnetic shear angles (typically between 45° and 150°) have been observed (e.g., Gosling et al. 1990b; Paschmann et al. 1986; Phan and Paschmann 1996; Petrinec and Fuselier 2003; Fuselier et al. 2005; Trattner et al. 2007c; Trenchi et al. 2008).

In summary, both anti-parallel and component reconnection have been observed at the dayside magnetopause. Consequently, the classical debate of "anti-parallel vs. component" is not actually the right question to debate. The real answer must lie beyond these two options, and must do so in a way that describes the locus of points where reconnection occurs (the separator) rather than a single point. Recent observational, theoretical, and numerical attempts to predict where reconnection occurs are summarized next.

6.2.4.1 Observations and an Empirical Model for Reconnection Location

In general, the statistical location of the reconnection line is difficult to establish using data from spacecraft magnetopause crossings (see, e.g., Fuselier and Lewis 2011) because it is difficult to determine the exact location of the reconnection line except when a spacecraft encounters it, and these encounters are rare (e.g., Phan et al. 2003; Trattner et al. 2012). That said, remote observations clearly reveal that the location and type of reconnection is a strong function of the IMF orientation.

For northward IMF ($B_z > 0$), there are many examples of magnetic reconnection poleward of the magnetospheric cusps in regions where magnetic shear angles are near 180° (e.g., Gosling et al. 1991; Fuselier et al. 2000b; Bobra et al. 2004; Lavraud et al. 2005b). To gain perspective on what controls the location of reconnection when the IMF has a northward component, observations have been compared to model magnetospheric and magnetosheath magnetic fields. A model for the 3D magnetospheric magnetic field is the Tsyganenko model (Tsyganenko 1995); a model for the magnetosheath magnetic field including the deflection of the IMF across the bow shock and its draping over the magnetosphere is the Cooling model (Cooling et al. 2001) based on a calculation by Kobel and Flückiger (1994). The input to use these models is conditions in the solar wind; these are obtained from ACE and WIND data for each observed event. As a first comparison to the data, the magnetic shear angle θ at all points on the magnetopause is calculated from the modeled magnetic fields.

Figure 6.11 shows the modeled location of anti-parallel reconnection sites poleward of the magnetospheric cusps when (top plot) IMF $|B_y| > |B_z|$ and (bottom plot) IMF $|B_z| > |B_y|$. In each panel, the magnetic shear angle θ at the model magnetopause boundary is projected into the $y - z$ plane and color coded with red showing high θ (>150°) and purple showing low θ (<50°). Anti-parallel reconnection lines occur where the magnetosheath and magnetospheric fields are exactly opposed (i.e., anti-parallel with $\theta = 180°$). The circle is the projected

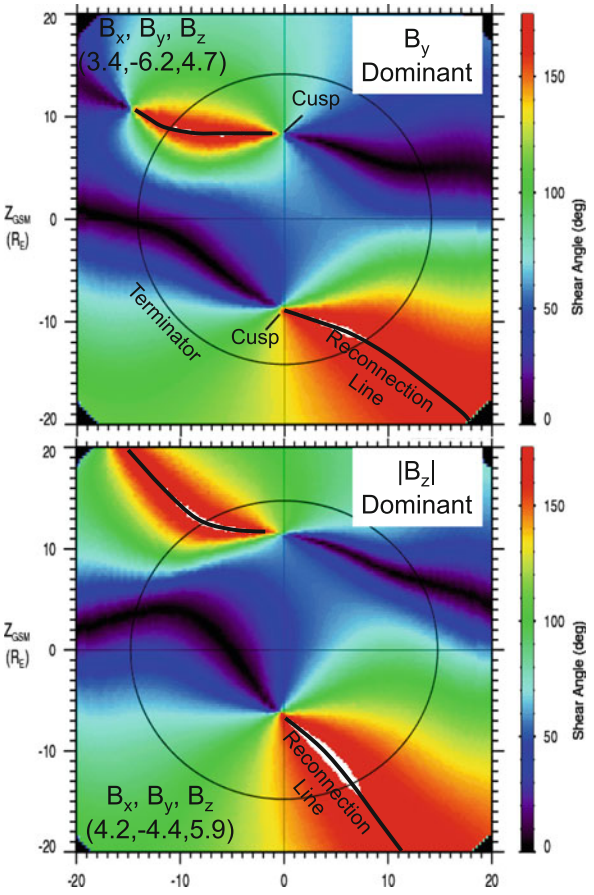

Fig. 6.11 Empirical model for the location of the reconnection line for two different solar wind IMF conditions for northward IMF assuming reconnection happens where the magnetic field is anti-parallel. *Each panel* shows a view from the sun of the color-coded magnetic shear angle θ between modeled magnetosheath and magnetospheric magnetic fields. *Red regions* are where θ is the highest (up to 180°). During B_y dominant conditions (top panel), the reconnection lines go from the cusps poleward. For $|B_z|$ dominant conditions (*bottom panel*), the reconnection lines extend further poleward of the cusps. Figure courtesy of K. J. Trattner

location of the **terminator**, the location of the magnetopause in the $x = 0$ plane. In the top panel, the locations of the magnetospheric cusps in the northern and southern hemispheres are indicated. In this plot, the anti-parallel regions start at the cusp location in the noon meridian ($y = 0$) and project poleward and dawnward in the northern hemisphere and poleward and duskward in the southern hemisphere. If the IMF B_y component were positive instead of negative, then the anti-parallel reconnection lines would mirror about $y = 0$. The different behavior of the northern and southern hemisphere is due to the finite IMF B_x component for this event. If the IMF B_x component was negative (and the IMF B_y component remained negative), then the reconnection lines in the northern and southern hemisphere would mirror about both the $y = 0$ meridian and the equator $z = 0$.

Some observations suggest that reconnection occurs at other high-latitude regions poleward of the cusp and at low-latitude regions equatorward of the cusp where magnetic shear angles are much smaller (e.g., Onsager and Fuselier 1994; Fuselier et al. 1997; Trattner et al. 2004). Thus, for northward IMF, both anti-parallel

and component reconnection have been reported. It is not known at present which type of reconnection dominates, though there are indications from MHD simulations that low-latitude reconnection sites can dominate for northward IMF (Glocer et al. 2015). Observations of reconnection equatorward of the cusp remain controversial (Fuselier et al. 2014a) and the character of the reconnection line for northward IMF, especially for times when the IMF B_y component dominates, is the subject of current research.

For southward IMF ($B_z < 0$), both anti-parallel and component reconnection have been reported (e.g., Gosling et al. 1990b; Onsager and Fuselier 1994; Fuselier et al. 2002, 2005; Petrinec and Fuselier 2003; Trattner et al. 2007a; Pu et al. 2007). However, unlike for northward IMF, the location of the reconnection line is determined using observations in Earth's magnetospheric cusps (Fuselier et al. 2000a). From a large number of cusp observations, an empirical model of the reconnection line location for southward IMF was developed (Trattner et al. 2007c,a). As in Fig. 6.11, this empirical model uses a 3D model magnetopause and draping of the IMF (including deflection of the field across the shock) to compute the magnetic shear angle θ at all points on the magnetopause. The location of reconnection has been empirically related to regions where θ varies from high to low. The model, called the maximum magnetic shear model, has been validated through several independent tests (Petrinec et al. 2011; Fuselier et al. 2011; Dunlop et al. 2011; Trattner et al. 2012; Fuselier et al. 2014b).

In the empirical model, the only quantities that determine the type and location of reconnection are distance from the subsolar point and IMF orientation. Figure 6.12 shows the predicted location of the reconnection line for three IMF orientations (top to bottom, these orientations are B_y dominant, $|B_z|$ dominant, and B_x dominant, with $B_z < 0$ for all three orientations). The format is the same as that in Fig. 6.11.

The top panel of Fig. 6.12 shows the reconnection line location when the IMF is southward ($B_z < 0$) and B_y is negative and dominant. The reconnection line is qualitatively similar when the IMF clock angle is between 90° and 155° (or between 205° and 270°). Under these conditions, the reconnection line stretches across the entire dayside magnetopause from dawn (left) to dusk (right). From the dawnside, it follows where the magnetic fields are anti-parallel but, at some point approaching the northern cusp, it deviates from the anti-parallel location and cuts across the dayside magnetopause somewhat south of the subsolar point (where $y = z = 0$). It eventually joins the other anti-parallel location in the southern hemisphere and follows this location out past the terminator on the dusk side. The angle the reconnection line makes with respect to the $y = 0$ axis depends on the relative magnitudes of B_y and B_z. If $B_y > 0$, then the reconnection line mirrors about the noon meridian $y = 0$, as in the northward IMF case.

The location of the reconnection line relative to the subsolar point is controlled by season (i.e., by dipole tilt). For summer in the northern hemisphere, the reconnection line passes south of the subsolar point as illustrated in the top panel of Fig. 6.12. For the equinoxes, the reconnection line passes through the subsolar point. For winter in the northern hemisphere, it passes north of the subsolar point.

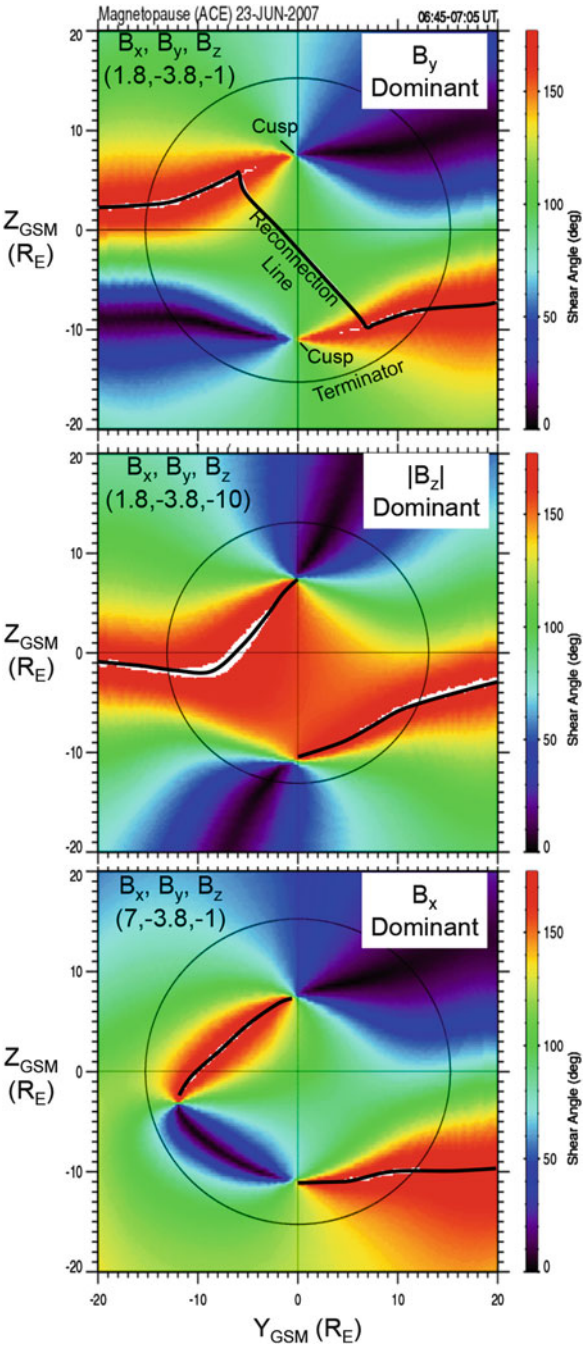

Fig. 6.12 Empirical model for the location of the reconnection line for three different solar wind IMF conditions for southward IMF. The format is the same as Fig. 6.11. During B_y dominant conditions (*top panel*), the reconnection line follows the anti-parallel reconnection region the dawn flank, but then cuts across the dayside magnetopause to connect with the anti-parallel reconnection region on the duskside. For $|B_z|$ dominant conditions (*middle panel*), the reconnection lines follow the anti-parallel regions up to the northern and southern cusps. At the noon meridian, there is a split in the reconnection line. When B_x is dominant (*bottom panel*), the reconnection lines also follow the anti-parallel regions up to the cusp. There is considerable asymmetry between the north and south because of the large B_x. Figure courtesy of K. J. Trattner

The middle panel of Fig. 6.12 shows the reconnection line location when the IMF is southward ($B_z < 0$) and $|B_z|$ is dominant. This reconnection line is qualitatively similar to those that occur when the IMF clock angle is between 155° and about 205°. Under these conditions, the reconnection line follows the anti-parallel location from the dawn terminator up to the cusp. There is a break in the line at the noon meridian $y = 0$, and the reconnection line follows the anti-parallel location from the southern cusp to the dusk terminator. As the clock angle approaches 180° (exactly southward IMF), the anti-parallel region shifts closer to the subsolar point. At 180°, the reconnection line is nearly parallel to the geomagnetic equator $z = 0$ right up to the noon-midnight meridian. At that point, the reconnection line becomes nearly vertical as it connects to the northern and southern cusps. Similar to the reconnection line for B_y dominant conditions, the location of the reconnection line relative to the geomagnetic equator for $|B_z|$ dominant conditions depends on season. For summer in the northern hemisphere, the reconnection line parallels the geomagnetic equator in the southern hemisphere ($z < 0$) as shown in the middle panel of Fig. 6.12. For the equinoxes, the reconnection line is at the geomagnetic equator, and for winter in the northern hemisphere, the line parallels the geomagnetic equator in the northern hemisphere $z > 0$.

The bottom panel of Fig. 6.12 shows the reconnection line when the IMF is southward ($B_z < 0$) and B_x is dominant. Specifically, this panel shows the reconnection line when $|B_x|/|B| > 0.9$ and is representative of cases with $|B_x|/|B| > 0.7$. Under these conditions, the reconnection line is similar to that for $|B_z|$ dominant conditions in that it follows the anti-parallel location from the dawn and dusk terminators up to the northern and southern hemisphere cusps, respectively. There is a break in the reconnection line at the noon meridian and the reconnection line follows the anti-parallel location from the southern cusp. Figures 6.11 and 6.12 empirically define the location of reconnection on the dayside magnetopause for all orientations of the IMF (excepting that there may be reconnection equatorward of the cusps for northward IMF).

6.2.4.2 Theoretical and Numerical Studies of Reconnection Location

There has been a recent flurry of activity in developing a first principles prediction of the location of reconnection on the dayside. The leading example is the maximum magnetic shear model (Trattner et al. 2007c), the semi-empirical generalization of the anti-parallel model discussed in Sect. 6.2.4.1.

There have been a number of other suggestions for what determines the dayside reconnection location. One prediction is that it is where the outflow speed of the reconnection is maximized (Swisdak and Drake 2007). A related suggestion is where the local reconnection electric field is maximized (Shay, 2009, private communication; Borovsky 2013). A recent suggestion was the maximum in the product of the magnetic energy density on the two sides of the current sheet (Hesse et al. 2013). Others are simply where the current is a maximum (Alexeev et al. 1998) or along the line that bisects the magnetospheric and magnetosheath fields (Moore et al. 2002).

Which of these models—if any—is correct? There are two complementary numerical approaches to test them. One is using local simulations in an idealized rectangular geometry with varying upstream conditions and let the system choose its preferred orientation of reconnection. In one such test using 3D Hall-magnetohydrodynamic (Hall-MHD) simulations, it was shown that the maximum in outflow speed and reconnection rate were consistent with simulations (Schreier et al. 2010). In another, a series of 2D simulations in planes rotated around in a fixed magnetic geometry suggested the magnetic energy density maximization was consistent with the simulations (Hesse et al. 2013), which turns out to be equivalent to the reconnection line bisecting the upstream magnetic fields. Recent 3D PIC simulations were also consistent with this conclusion (Liu et al. 2015).

An alternate approach is to use global magnetospheric simulations, which retain an appropriate 3D structure of the magnetospheric geometry, but contain less small-scale physics that may be relevant to the reconnection process. This, until recently, has proven challenging. The reason is because if one does not know where reconnection happens, how can one test the models?

This has been addressed systematically only in the last decade. Finding the reconnection line (the magnetic separators) can be done purely from information about the magnetic fields. There have been numerous approaches. One, which works only for cases with high levels of symmetry, is finding the "last closed field line" (Dorelli et al. 2007). With no dipole tilt or IMF B_x, the separator goes through the Earth-Sun line, so one starts at Earth and takes steps toward the sun, tracing the magnetic field in both directions at each point. When the field line goes from being a terrestrial field line to an interplanetary field line, the separator has been crossed. This technique works reasonably well for northward IMF ($B_z > 0$), but is less reliable for southward IMF ($B_z < 0$) (Komar et al. 2013).

Another approach is to simply plot a large number of magnetic field lines and map their topology to find the separator. Since magnetic field tracing is relatively expensive, this brute force technique is undesirable. However, if one knows approximately where the magnetopause is, one can use this approach over a smaller region of space (Laitinen et al. 2006, 2007). This research group has also used the divergence of the Poynting flux to approximately find where reconnection occurs.

A recent set of approaches builds off of knowing the separator goes through magnetic nulls, where the magnetic field goes to zero. Magnetic nulls in a 3D geometry can be found using a Newton-Raphson technique that identifies simulation grid cells over which all three components of the magnetic field change direction (Haynes and Parnell 2010). One approach to finding the separator is to place a small ring around a null, and follow points on the ring parallel to the field lines to form a new ring approach (Haynes and Parnell 2010). The point with the weakest field on the new ring is used as the center for a new ring. This procedure is repeated until another null is reached, tracing out the separator in the process.

A related but conceptually simpler and more precise technique (Komar et al. 2013) is to start at a null and center a sphere on it. One finds the topology of fields piercing the sphere; where the topologies intersect is where the separator pierces

that sphere. Center a new sphere around that point and iterate. This approach works for any solar wind conditions and can be made arbitrarily precise.

More recently, other techniques were developed (Glocer et al. 2015). One can use a bisection method to find the locations on radial cuts from the center of Earth where the topology changes. This results in entire "separator surfaces" which are 2D surfaces separating two different topologies of magnetic fields. The intersection of two separator surfaces is the separator. Another technique is simply taking a number of non-intersecting planes of arbitrary closeness, and finding the separator using a bisection method (Glocer et al. 2015). This is more efficient than the approach in Komar et al. (2013), is easily parallelizable, and can easily be generalized to find multiple branches of separators if more than one exist. The newfound ability to locate reconnection sites in 3D geometry using these separator finding techniques now affords the ability to find the reconnection sites and study them.

One example of this is studying the location of reconnection. In global simulations in which the IMF was slowly rotated, it was found that the separator was close to the angle of bisection (Pulkkinen et al. 2010). In distinct simulations with different IMF clock angles, it was shown that the angle of bisection was a reasonable approximation though not exact (Komar et al. 2013).

Recently a systematic test of the models discussed at the beginning of this section was carried out using a similar approach to that described in the previous section for the observations (Komar et al. 2015). Since the simulations give self-consistently determined magnetic fields, no models were needed to find the magnetospheric and magnetosheath fields; it was sufficient to find the magnetopause and find the upstream parameters. Then, as in the previous section, the quantity in question, whether magnetic shear angle or a property of the local reconnection process, was calculated everywhere on the magnetopause and projected onto the yz plane. Sample data is plotted for various clock angles for the maximum magnetic shear model in Fig. 6.13, though each model described here was tested. The background color is the magnetic shear angle. Image processing techniques were used to find the predicted reconnection location from each model, corresponding to the maximum of the quantity in question. This is plotted as the gray dotes in the figure. The results were compared to the measured location of the separators, shown as the white line. If the agreement between theory and simulations were perfect, the two lines would overlap. It was found that all the models discussed above did reasonably well for southward IMF ($B_z < 0$), but none did particularly well for northward IMF ($B_z > 0$). The only model of the ones tested to accurately predict the reconnection location poleward of the cusp for northward IMF was the maximum magnetic shear model. In summary, there is yet to be a definitive first-principles resolution of what controls the location of dayside reconnection. The maximum magnetic shear model has some measure of success over other models in addition to observational support as discussed in Sect. 6.2.4.1, though none of the models tested were perfect.

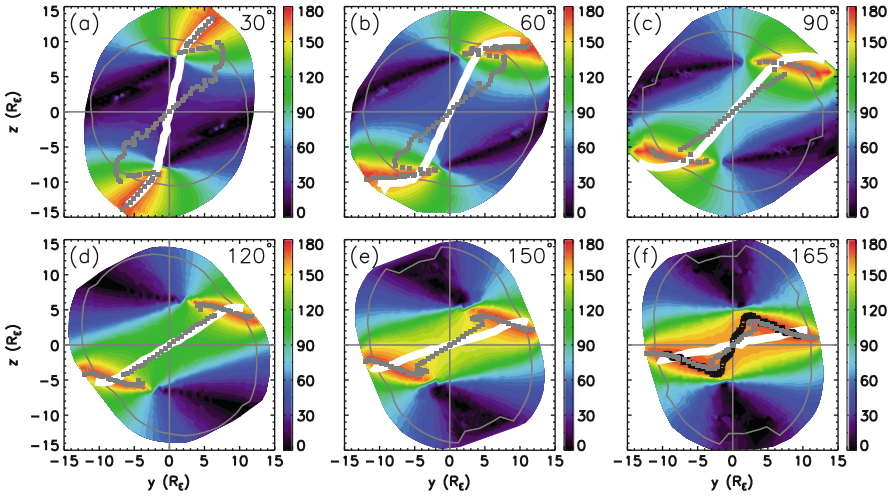

Fig. 6.13 Numerical test of the location of dayside reconnection. The color is the prediction of the maximum magnetic shear model projected into the *yz* plane. The *gray dots* denote the "ridge" of the prediction. The *white line* is the projection of the separator. Panels (**a**)–(**f**) are for θ_{IMF} values as given in the upper right of each panel. Reprinted with permission from Komar et al. (2015)

6.3 Dependence of Dayside Reconnection on Ambient Conditions

In Sect. 6.2, the fundamentals of dayside reconnection were discussed largely at a phenomenological level. The questions of "when" and "where" dayside reconnection occurs leave the impression that this plasma transfer process is ubiquitous and its location on the dayside magnetopause depends only on the orientation of the IMF. Section 6.2 was careful to segregate the occurrence of reconnection from more quantitative properties like the rate of reconnection, which is a measure of how rapidly magnetic field lines get reconnected. For dayside reconnection, the reconnection rate is intimately related to the efficiency of solar wind-magnetospheric coupling. It is important to distinguish the rate of occurrence of reconnection from the reconnection rate because much more information is known about the rate of occurrence from observations. In contrast, the reconnection rate is very difficult to measure and there are few reports of its value at the magnetopause.

There are both global and local definitions of the reconnection rate. The **global reconnection rate** is quantified using the integral form of Faraday's law,

$$\frac{d\Phi_B}{dt} = \frac{d}{dt}\int_S \mathbf{B}\cdot d\mathbf{S} = -\int_C \mathbf{E}\cdot d\mathbf{l}, \tag{6.6}$$

where Φ_B is the magnetic flux through an (open) surface S and $d\mathbf{l}$ is a differential line element along a path C confined to the surface S that is not moving in time. The right hand side is merely the potential drop along the path C, often called the **reconnection potential**. Suppose one identifies the surface with a portion of the magnetopause. In the absence of reconnection, the magnetosheath and magnetosphere are not magnetically connected, so the magnetic flux through the magnetopause is zero. If reconnection at the magnetopause occurs, then the magnetic flux through the surface is non-zero, and the terms in Eq. (6.6) are non-zero.

The most meaningful path C for evaluating the reconnection potential is the magnetic separator. Integrating around the entire separator corresponds to the closed surface of the whole magnetopause, which would give a result of zero since the magnetic flux through any closed surface is zero. Thus, one must take only a portion of the separator to get a meaningful result. This can be done from northern magnetic null to southern magnetic null, but other approaches are also used including integrating from null to null and down to where the magnetic field pierces the ionosphere, but care is needed in interpreting the results for a given convention. Note also that Eq. (6.6) shows that there needs to be an electric field parallel to the separator to have reconnection; this is related to the general condition for reconnection (Hesse and Schindler 1988).

The **local reconnection rate** is defined as the global reconnection rate per unit length in the direction of the separator. From Eq. (6.6), this is simply equivalent to the *local* electric field parallel to the separator, which was previously referred to as the reconnection electric field E. In a perfectly 2D system, this is the out-of-plane electric field at the X-line. For 2D reconnection in a steady-state (where plasma parameters are not changing in time), from the differential form of Faraday's law, $\nabla \times \mathbf{E} = 0$, so the out-of-plane electric field cannot be a function of in-plane coordinates. This implies that the out-of-plane convective electric field $-(\mathbf{v} \times \mathbf{B})_M$ upstream of the dissipation region must equal the reconnection electric field E at the X-line. Both the global and local reconnection rates are important for dayside reconnection. In what follows, the local reconnection rate is emphasized here since it is more accessible to measurement by satellites; global considerations are discussed further in Sect. 6.4.1.

For symmetric reconnection, the reconnection rate is commonly presented in a normalized fashion, dividing it by $B_L c_A$, where B_L is the reconnecting field and $c_A = B_L/(\mu_0 \rho)^{1/2}$ is the Alfvén speed based on B_L and the upstream mass density ρ (all of which are the same on both sides of the where the magnetic field reverses for symmetric reconnection). Note, the magnetic field of import is the reconnecting field B_L, so if there is a guide field B_g it is not included in the normalization; this is because the guide field does not drive the reconnection process. Since the upstream convective electric field comes from flow v_N in the normal direction toward the X-line, $E = v_N B_L$. Therefore, the normalized reconnection rate E' is

$$E' = \frac{v_N}{c_A}. \tag{6.7}$$

Since the magnetic flux into and out of the dissipation region is the same, $B_N c_A = v_N B_L$, where B_N is the normal component of the magnetic field, so an equivalent form of E' is

$$E' = \frac{B_N}{B_L}. \tag{6.8}$$

A third equivalent way this is often written is to note that the magnetic field is constrained by geometry. To ensure $\nabla \cdot \mathbf{B} = 0$, one expects $B_L \delta \sim B_N L$, where δ is the thickness of the dissipation region and L is its length. Using this result gives

$$E' \sim \frac{\delta}{L}. \tag{6.9}$$

Thus, the aspect ratio of the dissipation region is related to the normalized reconnection rate.

A host of 2D numerical simulations with fluid, hybrid, and kinetic PIC numerical techniques have investigated the parametric dependence of E'. The prevailing understanding is that E' for symmetric reconnection tends to be approximately 0.1 (see e.g., Birn et al. 2001). In addition to the 0.1 value being of interest, it is crucial to note that this seems to be a characteristic value that is independent of any system parameter (Shay et al. 1999, 2004). It had previously been determined that reconnection rates of this order would be sufficient to explain solar and magnetospheric applications of reconnection (Parker 1973). There is no widely accepted first principles theoretical prediction for what determines why $E' \simeq 0.1$ for collisionless reconnection.

Direct measurements of the reconnection rate during dayside reconnection are quite challenging. One complication is it requires an accurate measure of the direction normal to the magnetopause current layer. It is the measurement of this normal that generates the largest uncertainty in the determination of the reconnection rate. Since the theory suggests the normal magnetic field B_N is on the order of 0.1 of the reconnecting magnetic field B_L, observations to require knowledge of the normal direction to within a few degrees. This accuracy is typically not obtainable from single or even from multiple spacecraft observations (e.g., Haaland et al. 2004). In addition to this accuracy issue, the measurement of the normal and other plasma parameters must be done at the reconnection site. Most of the time a spacecraft crosses some distance from this site and that distance is poorly known.

Another complication, as discussed in Sect. 6.2.3, is that reconnection at the magnetopause is most often far from the simple symmetric case discussed here. Until recently, it was not even clear which magnetic field and density to normalize to in order to get the most meaningful result. Modifications of the theory for asymmetric systems and systems with flow shear are discussed in the remainder of this section.

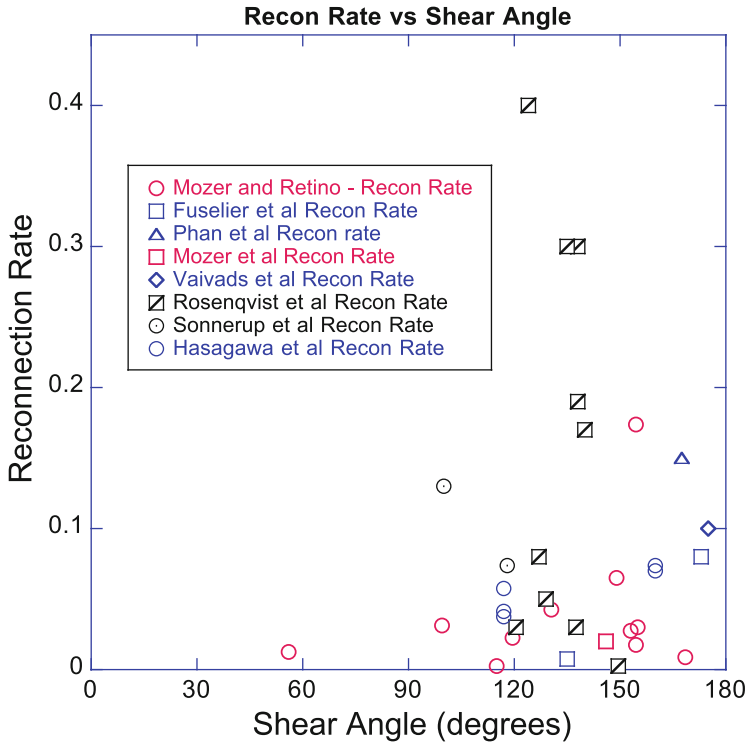

Fig. 6.14 Normalized reconnection rates E' at the magnetopause versus magnetic shear angle θ. The rates, from a variety of sources and methods, show large scatter and no clear pattern with magnetic shear angle. While the scatter may be an indication of large variability in the rate, it may also indicate the uncertainties in the measurement

Despite these issues, there have been several attempts to measure the normalized reconnection rate at the magnetopause. Figure 6.14 shows a compilation of a large subset of these attempts. Shown are reconnection rates normalized to magnetosheath parameters as a function of magnetic shear angle at the magnetopause (Sonnerup 1981; Phan et al. 2001; Mozer et al. 2002; Vaivads et al. 2004; Fuselier et al. 2005, 2010; Hasegawa et al. 2006; Mozer and Retinó 2007; Rosenqvist et al. 2008). Fuselier and Lewis (2011) discusses a similar compilation. The emphasis in Fig. 6.14 is on the large range of reconnection rates from a variety of measurement techniques. The rates vary by large amounts even from measurements taken within a few minutes of one another under essentially the same external conditions (Rosenqvist et al. 2008). While this variation is interpreted as true variation in the reconnection rate at the magnetopause, the uncertainties in the determination of the normal suggest that it is equally valid to interpret the variation as indicative of the uncertainty in the reconnection rate measurement.

Because the reconnection rate is difficult to measure with satellites, it is equally difficult to determine if this rate depends on external conditions at the

magnetopause. For example, some simulations show the reconnection rate decreases by about 30 % over the range of magnetic shear angles from 180° to 90° (Pritchett 2001; Hesse et al. 2004), though others suggest no significant decrease when a guide field is present (Hesse et al. 1999). No decrease is evident in the data in Fig. 6.14. Thus, it is not clear how the reconnection rate depends on magnetic shear angle. Further, the magnetic shear angles in Fig. 6.14 are mostly measured at the spacecraft crossing and not at the reconnection site, and the uncertainties in the reconnection rate are much larger than 30 %.

Although the reconnection rate at the magnetopause is poorly determined observationally, it is still important to consider the theoretical limitations on this rate. In particular, it is important to understand if there are ambient conditions at the magnetopause that locally inhibit reconnection. In the remainder of this section, ambient conditions that are expected to influence dayside reconnection rates and occurrence are discussed. Specifically, the efficiency of asymmetric reconnection and the suppression of reconnection by diamagnetic effects (i.e., the dependence on plasma beta), flow shear, and plasmaspheric plasma are discussed.

6.3.1 *Efficiency of Asymmetric Reconnection*

As discussed in Sect. 6.2.3, reconnection is most commonly asymmetric at the magnetopause. This was known going back to early discussions of dayside reconnection (Levy et al. 1964). That study influenced many future studies on asymmetric reconnection, often focusing on the shock structure of the exhaust (far downstream from the X-line) (see references within Cassak and Shay 2007). More recently, an analysis of asymmetric reconnection giving the reconnection rate E, outflow speed $v_{\rm out}$, and outflowing mass density $\rho_{\rm out}$ for 2D anti-parallel reconnection was given (Cassak and Shay 2007).

The results follow from a steady-state control-volume analysis of the dissipation region in the reference frame in which the X-line is stationary; one puts a box around the dissipation region (the thin black box in Fig. 6.15) and balances the flux of mass and energy and the magnetic flux into and out of the box in terms of the upstream reconnecting magnetic fields and densities (denoted with subscripts "1" and "2" for the two upstream sides of the dissipation region). The result of this analysis is (Cassak and Shay 2007)

$$E \sim \frac{B_1 B_2}{B_1 + B_2} \frac{2\delta}{L} v_{\rm out} \tag{6.10}$$

$$v_{\rm out}^2 \sim c_{A,\rm asym}^2 = \frac{B_1 B_2}{\mu_0} \frac{B_1 + B_2}{\rho_1 B_2 + \rho_2 B_1} \tag{6.11}$$

$$\rho_{\rm out} \sim \frac{\rho_1 B_2 + \rho_2 B_1}{B_1 + B_2}, \tag{6.12}$$

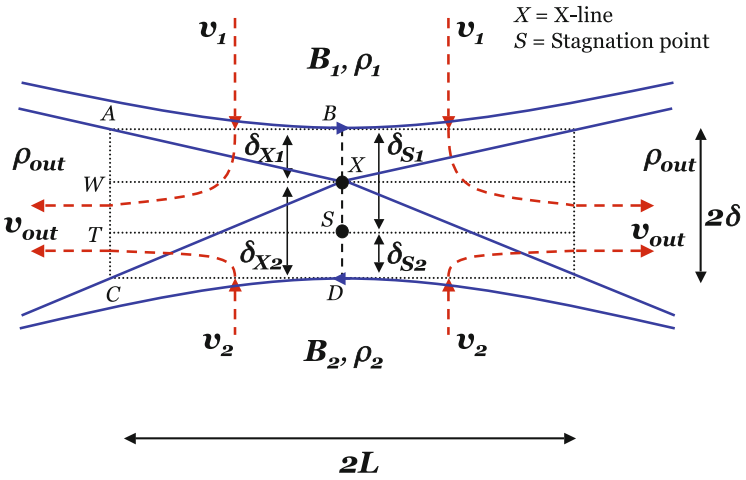

Fig. 6.15 Reconnection geometry for asymmetric reconnection. The *black box* denotes the dissipation region, *blue curves* are magnetic field lines and *red curves* are bulk flow lines. Reprinted with permission from Cassak and Shay (2007). Copyright 2011, AIP Publishing LLC

where δ/L is the aspect ratio of the reconnection dissipation region. These relations apply regardless of the dissipation mechanism (collisional or collisionless). In the symmetric limit for which $B_1 = B_2 = B_L$ and $\rho_1 = \rho_2 = \rho$, each of the predictions reduces to the symmetric (Sweet-Parker) results (Parker 1957), namely $v_{\rm out} \sim c_A$ and $E' \sim \delta/L$. An alternate derivation of Eq. (6.11) was given in Swisdak and Drake (2007). It should be noted that the analysis assumed incompressibility; an analysis with compressible MHD theory revealed that the reconnection rate is slightly smaller than the above prediction, while the outflow speed is unchanged (Birn et al. 2010).

It is crucial to point out the assumptions and limitations of this theory. For one, it is purely a 2D analysis. In addition, there is no upstream flow parallel to the reconnecting magnetic field (a limitation that is addressed in Sect. 6.3.3) and it is assumed that either there is no guide field or out-of-plane bulk flow, or that they are not dynamically significant.

Another way to interpret the above results is noting that while the reconnection rate is 0.1 for symmetric reconnection when normalized to $B_L c_A$, it is not even clear what magnetic field and Alfvén speed to normalize to in asymmetric reconnection. The predictions answer this question; if the electric field is normalized to $v_{\rm out} 2B_1B_2/(B_1 + B_2)$, then $E' = \delta/L$ as in symmetric reconnection.

The theory has been tested in a number of studies using various geometries and approaches. In 2D simulations, it was verified with resistive MHD (Borovsky and Hesse 2007; Cassak and Shay 2007; Birn et al. 2008), two-fluid (Cassak and Shay 2008, 2009), and PIC (Malakit et al. 2010) codes. The results from the PIC simulations are shown in Fig. 6.16; note that E and $v_{\rm out}$ show good agreement in the scaling sense, but are approximately two times smaller than the absolute

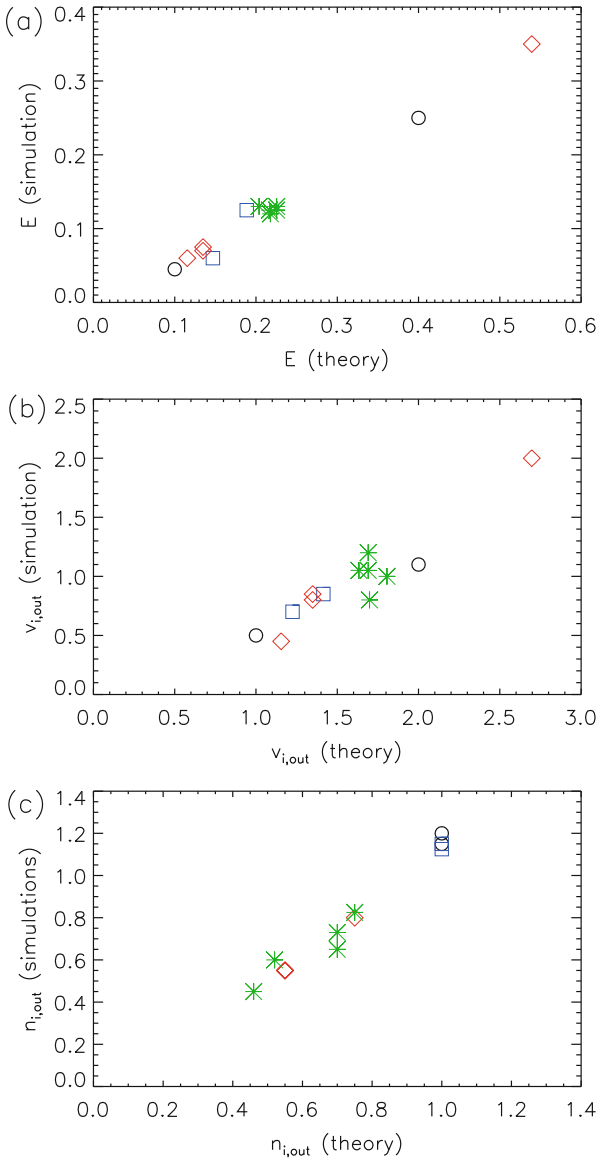

Fig. 6.16 Numerical verification of the asymmetric theory predictions for (**a**) reconnection rate E, (**b**) outflow speed v_{out}, and (**c**) outflow density n_{out} (or equivalently, ρ_{out}) with 2D particle-in-cell simulations. Reprinted with permission from Malakit et al. (2010)

predictions of the theory, which will be discussed later. These results essentially reveal that $E' \sim \delta/L$, which is approximately 0.1 for symmetric reconnection, remains a constant near 0.1 for asymmetric reconnection. The theory also performed

well in tests using laboratory experiments (Yoo et al. 2014; Rosenberg et al. 2015) and simulations of decaying turbulence (Servidio et al. 2009, 2010; Zhdankin et al. 2013).

In global magnetospheric simulations, the theory has been tested mostly for due southward IMF for systems with no dipole tilt because it is relatively easy to find the reconnection location. It bears noting that the theory assumed 2D reconnection while the magnetopause is 3D, so it is not obvious that the theory should apply to the magnetosphere. However, it was shown to work well with resistive MHD with a localized resistivity (Borovsky et al. 2008). Using an MHD code with reconnection that takes place at the grid, it was shown that the agreement was reasonable with a given resolution, and improved for higher resolution (Ouellette et al. 2014). A further study using well resolved resistive-MHD simulations found excellent agreement for due southward IMF (Komar 2015). This study also went further by testing the theory for simulations with other IMF clock angles. It was found that the prediction qualitatively tracked the simulation results for oblique IMF, but there was an absolute multiplicative offset that appeared to be a function of the clock angle (Komar 2015). As of the writing of this chapter, this topic needs further work to be fully understood.

To see whether this theory is consistent with observations, we interpret the "1" side as the magnetosheath side (for which a "sh" subscript is used) and the "2" side as the magnetospheric side (with a "ms" subscript). Since $\rho_{\rm sh} \gg \rho_{\rm ms}$ for typical magnetopause conditions, this limit of the general result is used. Let the ratio of the magnetic fields be a, so that $B_{\rm sh} = aB_{\rm ms}$; this is done with the goal of writing Eqs. (6.10) and (6.11) in terms of the magnetosheath magnetic field $B_{\rm sh}$ and magnetosheath Alfvén speed $c_{A,\rm sh} = B_{\rm sh}/(\mu_0\rho_{\rm sh})^{1/2}$ (since the observations in Fig. 6.14 were normalized to the magnetosheath parameters). The results are

$$E \sim \frac{2}{[a(1+a)]^{1/2}} B_{\rm sh} c_{A,\rm sh} \frac{\delta}{L} \tag{6.13}$$

$$v_{\rm out} \sim \left(\frac{1+a}{a}\right)^{1/2} c_{A,\rm sh}. \tag{6.14}$$

From Table 6.2, the most probable value of the magnetosheath magnetic field $B_{\rm sh}$ is 22 nT with a 5–95 % range of 8.8–39.6 nT, and Table 6.1 gives a typical magnetospheric magnetic field of $B_{\rm ms} = 56$ nT. Using these values, the most probable value of a is 0.39, with a range of 0.16–0.71. Also, it is known from numerical simulations, as shown in Fig. 6.16a, b, that the theory overpredicts the reconnection rate and outflow speed by a factor of two (Malakit et al. 2010). This could be due to compression effects (Birn et al. 2010) or a kinetic effect in which the reconnected magnetic field preferentially heats the downstream plasma parallel to the field (Drake et al. 2006; Schoeffler et al. 2011) which inhibits the reconnected field line from straightening in the same way an Alfvén wave is slowed down by a pressure anisotropy when the parallel pressure exceeds the perpendicular pressure (Parker 1958). This is included by dividing the predictions in Eqs. (6.13) and (6.14) by two.

Using these results and assuming $\delta/L \simeq 0.1$ in Eqs. (6.13) and (6.14) give typical values of

$$E \sim 0.14\, B_{\rm sh} c_{A,\rm sh} \tag{6.15}$$

$$v_{\rm out} \sim 0.94\, c_{A,\rm sh} \tag{6.16}$$

with a range of E given by 0.091–0.23 $B_{\rm sh} c_{A,\rm sh}$ and $v_{\rm out}$ given by 0.78–1.35 $c_{A,\rm sh}$. This prediction can be compared with the data in Fig. 6.14. It is found that a good portion of the data is in that range, though there are a large number of data points with lower values. Interestingly, the prediction does a little better for magnetic shear angles near 180°, where the system is anti-parallel (consistent with the assumptions of the theory). New physics not included in the theory comes in when the magnetic shear angle is sufficiently less than 180°, and this effect lowers the reconnection rate; this will be discussed in Sect. 6.3.2.

It should be pointed out that this comparison is done purely for illustrative purposes to determine whether the theory might apply to the magnetosphere. A more careful test using individual measurements of a instead of a range would be preferable. Such a study was undertaken, and the results of observations with the Polar satellite were consistent with the predictions (for nearly due southward IMF) (Mozer and Hull 2010). Another important limitation is that many of the reported values for E are measured as $B_N/B_{\rm sh}$ or $v_N/c_{A,\rm sh}$. However, it is known from simulations that B_N is highly structured in the exhaust for asymmetric reconnection, so this is not a great measure to use, and v_N is difficult to assess because the magnetopause could be breathing and one needs to go into the reference frame of the X-line to test the theory. Despite these limitations, the theory is in the right ballpark.

Testing the theory for $v_{\rm out}$ is potentially more straightforward, although is still complicated by asymmetries in the outflow direction except for due southward IMF. MHD simulations employing a due southward IMF revealed good agreement for the outflow speed (Ouellette et al. 2014). (The authors noted that the predicted $\rho_{\rm out}$ did not agree with simulations, but this is known from local simulations Cassak and Shay 2009; Birn et al. 2010 as a limitation of the MHD model in describing plasma mixing.) Observationally, the Walén relation is commonly used to determine if one is at a reconnection exhaust; it states that if one has a rotational discontinuity, which one expects at the boundary of a reconnection exhaust, that the jump in tangential velocity across the discontinuity is equal to the change in the Alfvén speed across the discontinuity. In observational studies, the measured outflow velocity was compared with the local Alfvén speed in the magnetosheath (i.e., assuming symmetric reconnection). The results show outflow speeds between 0.7 and 0.8 of the magnetosheath Alfvén speed (Sonnerup et al. 1981; Paschmann et al. 1986; Gosling et al. 1990b). Magnetic shear angles were not considered in these studies and the magnetic shear angle at the reconnection site was generally not determined; therefore, results from these early studies are not necessarily reflective of anti-parallel reconnection. This important issue notwithstanding, it is interesting to note that a simple analysis of the average plasma properties at the magnetopause yields

a mean value of that is reduced relative to $c_{A,\mathrm{sh}}$ when asymmetric reconnection is accounted for that is at least similar to what is observed. Future work on this would be interesting.

6.3.2 *Suppression of Reconnection by Diamagnetic Effects*

While the previous section treated asymmetric reconnection without a guide field, the dayside magnetopause often has one, as seen in Fig. 6.14. A guide field gives rise to qualitatively different physics which is very important. Consider the reconnection geometry sketched in Fig. 6.17, with guide field B_g directed out-of-the plane and an in-plane electron pressure gradient in the inflow (horizontal) direction. Any system with a pressure gradient normal to a magnetic field experiences the diamagnetic drift.

The **diamagnetic drift velocity** $\mathbf{v}_{*j}$ of species j is

$$\mathbf{v}_{*j} = -\frac{\nabla p_j \times \mathbf{B}}{q_j n_j B^2}, \tag{6.17}$$

where p_j is the pressure (written as a scalar for simplicity), n_j is the density, q_j is the charge, and $\mathbf{B}$ is the total magnetic field. In a uniform system, as particles undergo gyro-motion around the magnetic field, there are equal numbers of particles moving up as down, leading to zero bulk flow velocity. However, if there is a gradient in either particle number density or thermal speed, an imbalance in particle flux arises that results in a net bulk flow, which is the physical cause of the diamagnetic drift. Interestingly, the drift arises even though the gyro-orbits of the particles creating it are stationary. This fact has caused some to believe that it is impossible for the diamagnetic drift to generate real, physical transport. However, this is not the case.

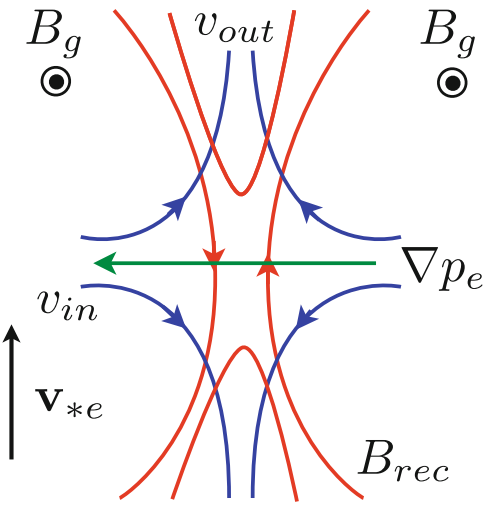

Fig. 6.17 Reconnection geometry in the presence of a guide field B_g and an electron pressure gradient ∇p_e in the inflow (*horizontal*) direction. These give rise to an electron diamagnetic drift $\mathbf{v}_{*e}$ in the outflow (*vertical*) direction

There is a long history on this going back to fusion research in the 1960s (Coppi 1965; Scott and Hassam 1987). Here, it is shown that the diamagnetic drift produces real physical transport. Start with the generalized Ohm's law from Eq. (6.2), but ignore electron inertia and resistivity for simplicity and combine the convection and Hall terms using $\mathbf{v}_e \simeq \mathbf{v} - \mathbf{J}/ne$, where $\mathbf{v}_e$ is the bulk velocity of the electrons. The result is

$$\mathbf{E} = -\mathbf{v}_e \times \mathbf{B} - \frac{\nabla p_e}{ne} = -(\mathbf{v}_e + \mathbf{v}_{*e}) \times \mathbf{B}. \tag{6.18}$$

In the second equality, the electron pressure gradient term is written in terms of the diamagnetic drift using Eq. (6.17). In 2D, one can define a flux function ψ such that $\mathbf{B} = \hat{\mathbf{y}} \times \nabla\psi$, where y is the invariant direction. From Faraday's law, $E_y = \partial\psi/\partial t$, so eliminating the electric and magnetic fields in the y component of Eq. (6.18) in favor of ψ gives

$$\frac{\partial \psi}{\partial t} + (\mathbf{v}_e + \mathbf{v}_{*e}) \cdot \nabla\psi = 0. \tag{6.19}$$

This shows that the diamagnetic drift, in addition to standard convection, does indeed generate a real transport of magnetic flux.

How does the diamagnetic drift affect reconnection? The inclusion of diamagnetic effects suppresses the tearing instability (Coppi et al. 1979; Galeev 1984; Zakharov et al. 1993; Rogers and Zakharov 1995), the linear phase of magnetic reconnection. Diamagnetic effects also suppress nonlinear reconnection, and there is a simple physical interpretation of why (Swisdak et al. 2003). Figure 6.17 has a diamagnetic drift in the outflow direction. This implies that the X-line convects in the outflow direction. If this convection is faster than the reconnected magnetic field lines release their tension, then magnetic energy is not released via the change in magnetic topology, and magnetic reconnection is throttled. To quantify this, the X-line convects at the electron diamagnetic drift speed v_{*e} from Eq. (6.19). Reconnection is *locally* suppressed if this speed exceeds the nominally Alfvénic outflow speed v_{out} (Swisdak et al. 2010)

$$v_{*e} > v_{\text{out}}. \tag{6.20}$$

Convection of the X-line has been seen in independent simulations of asymmetric reconnection with a guide field (Pritchett and Mozer 2009; Tanaka et al. 2010; Beidler and Cassak 2011).

Equation (6.20) can be reformulated, subject to some simplifying assumptions, as a condition relating the jump in the plasma beta $\Delta\beta$ across the current layer and the magnetic shear angle θ between the fields as

$$\Delta\beta > \frac{2L_p}{d_i} \tan\left(\frac{\theta}{2}\right) \tag{6.21}$$

to suppress reconnection, where $L_p = p/|\nabla p|$ represents a typical pressure scale length. Magnetopause observations reveal that the thickness of the dayside current sheet for local times from 0800 to 1700 range from 400–1000 km (Berchem and Russell 1982), and there are pressure gradients on the scale on the order of a few d_i (Eastman et al. 1996), so we might expect L_p/d_i to be close to one. Consequently, if $\Delta\beta$ is small across the magnetopause, then reconnection is allowed for almost any magnetic shear angle. However, if $\Delta\beta$ is sufficiently large, then reconnection can be inhibited, as least locally.

The assumptions made in going from Eq. (6.20) to (6.21) are briefly pointed out. First, it is assumed that the system is low β on both sides of the dissipation region or, equivalently, that the magnetic pressure on either side is approximately the same. This is only true when the guide field is large. This is because if there is a gas pressure gradient across the dissipation region, there will also be an opposing magnetic pressure gradient to keep total (gas plus magnetic) pressure approximately the same. If the magnetic pressure is large relative to the change in pressure, this variation is negligible. An expression that does not make the low β assumption is

$$\frac{2\mu_0 \Delta p}{B_{\rm mp}^2} > \frac{2L_p}{d_i} \tan\left(\frac{\theta}{2}\right), \tag{6.22}$$

where $B_{\rm mp}$ is the *total* magnetic field strength at the magnetopause. A second technical point is that the $L_p \sim d_i$ assumption is really only expected to be true for magnetic shear angles near 180°, i.e., low guide fields. With strong guide fields, as discussed in Sect. 6.2.3, the characteristic ion scale of the dissipation region is ρ_s instead of d_i, so L_p/d_i might have an additional factor of $\beta^{1/2}$. There are also important questions that require further investigation—is the gradient of import on the ion scale or electron scale, and does v_{*e} need to exceed the ion Alfvén speed or the electron Alfvén speed? A third assumption in saying v_{*e} needs to exceed $v_{\rm out}$ is that Eq. (6.21) is written assuming symmetric reconnection. Systematic studies of diamagnetic suppression have not been carried out in systems with asymmetric reconnecting magnetic fields.

Figure 6.18 shows the magnetic shear angle − delta beta ($\theta - \Delta\beta$) parameter space. The s-shaped curve labeled "$L = 1d_i$" denotes the boundary between the θ and $\Delta\beta$ values where reconnection is possible and where it is suppressed from Eq. (6.21). The boundary is also plotted if it is assumed that $L = 2d_i$ and $L = 0.5d_i$ as the dashed curves. The light shaded vertical bar shows the most probable value of $\Delta\beta$ at the magnetopause from Table 6.2 and the darker shaded region shows the 5–95 % $\Delta\beta$ range for Earth's magnetopause. From these shaded regions, it is evident that for the majority of ambient conditions, reconnection is possible at essentially all observed magnetic shear angles.

There is also significant observational support for diamagnetic suppression of reconnection. Evidence for reconnection for magnetic shear angles as small as 40° have been identified. Observational tests to confirm the predictions in Eq. (6.21) have been largely successful, showing that reconnection signatures at the point of observation occur for $\theta - \Delta\beta$ values in the "reconnection possible" region

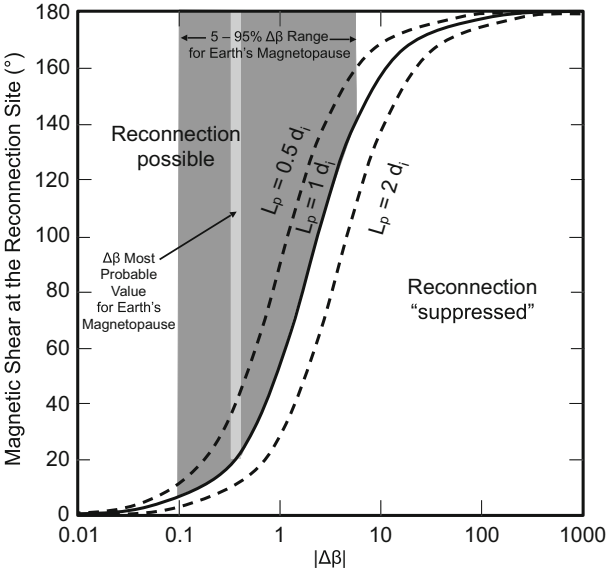

Fig. 6.18 Regimes where reconnection is possible and suppressed in the magnetic shear angle − delta beta ($\theta - \Delta\beta$) plane. For typical $\Delta\beta$ at the magnetopause and for the full range of $\Delta\beta$, reconnection is possible at almost any θ. Verification of the suppression of reconnection is difficult because it may be that reconnection migrates to regions where θ is high in response to large $\Delta\beta$ at the magnetopause

in Fig. 6.18 (Trenchi et al. 2008; Phan et al. 2013). However, demonstrating that reconnection is suppressed at the dayside magnetopause for $\theta - \Delta\beta$ values in the "reconnection suppressed" region in Fig. 6.18 is more difficult. First, studies identified reconnection using the Walén test or the presence of reconnection jets (Trenchi et al. 2008; Phan et al. 2013). These techniques are limited to local reconnection that is one-dimensional and time-independent. If reconnection is occurring remote from the spacecraft location or there are multiple reconnection sites, then the Walén test is not valid or there may not be reconnection jets present. Second, these techniques only identify local reconnection and not remote reconnection that may be occurring in regions where the magnetic shear angle is larger than that observed at the spacecraft. Accepting these limitations, the local $\theta - \Delta\beta$ values fall within the "reconnection suppressed" region in Fig. 6.18 when there is no evidence of local reconnection.

In summary, theory and observations suggest that reconnection can proceed for almost any typically observed magnetic shear angle at Earth's subsolar magnetopause. Magnetic shear angles as low as about 40° have been observed at the magnetopause during reconnection. Furthermore, there is evidence that local reconnection is confined to $\theta - \Delta\beta$ values in the "reconnection possible" region in Fig. 6.18. For higher $\Delta\beta$, i.e., for values of one or greater as is expected at the magnetopause from Table 6.2, the theory predicts that reconnection should be

limited to higher magnetic shear angles. Observations of continuous reconnection at high latitudes for northward IMF may be consistent with this prediction. For northward IMF, the magnetic shear angle at the subsolar point is low ($<50°$ as seen in Fig. 6.11), so it is possible that diamagnetic suppression could hinder reconnection at the subsolar point. A Walén test would fail locally, yet reconnection is still occurring elsewhere at the dayside magnetopause (at the high latitudes). Although this association between high-latitude reconnection and northward IMF is consistent with observations to date, there is no observational verification of true suppression of reconnection at Earth. Surprisingly, there may be evidence of this restricted range of magnetic shear angles for high $\Delta\beta$ at Saturn (Fuselier et al. 2014b).

It may be tempting to suggest that the local suppression of reconnection could stop reconnection globally. However, this is not clear; magnetic fields that do not reconnect could simply convect with the magnetosheath flow and reconnect at a different location that is favorable for it to occur. This is not well understood at present; one complication is that most global simulations use the MHD model, and diamagnetic drifts are not present in MHD. It will require global Hall-MHD or kinetic simulations to address these questions. It is also worth noting that if there is a sub-Alfvénic diamagnetic drift, reconnection continues to proceed, though it is at a slower rate (Swisdak et al. 2003). There is no quantitative prediction for this at the present time, though results in the next section are likely relevant.

6.3.3 Quantitative Effect on Reconnection by Flow Shear

As discussed in Sect. 6.2.3.3, flow shear across a reconnection site parallel or anti-parallel to the reconnecting magnetic field can be important at the polar cusps and at the flanks. There is an interesting analogy between the effect of flow shear and the diamagnetic drift effect discussed in Sect. 6.3.2. In each case, there is an upstream flow in the reference frame in which the X-line is stationary. Thus, the diminishing of the magnetic tension force of the reconnected field by the bulk flow which causes the outflow speed and reconnection rate to decrease is equally the case when the flow is caused by diamagnetic effects or flow shear (Cassak and Otto 2011).

Conventional wisdom suggests that the flow velocity in the magnetosheath must be less than the local Alfvén speed for stable reconnection to occur. That is, the flow must be sub-Alfvénic or, equivalently, the Alfvén Mach number of the flow must be >1. It was suggested that reconnection still proceeds under super-Alfvénic flow, but the reconnection site must propagate poleward or tailward such that, in the frame of reference of the reconnection site, the flow is sub-Alfvénic (Gosling et al. 1991). In this model, when the Alfvénic Mach number of the flow exceeds 2, the reconnection site cannot propagate tailward fast enough for the condition of sub-Alfvénic flow in the frame of reference of the (moving) reconnection site, so reconnection would not be possible.

Observationally, stable reconnection occurs at high latitudes for northward IMF even in regions where the gas-dynamic flow is predicted to be super-Alfvénic (Fuselier et al. 2000b). Stable reconnection at these locations appears to contradict the statements in the previous paragraph. However, Fuselier et al. (2000b) also showed that the formation of a plasma depletion layer adjacent to the magnetopause for northward IMF resolves this apparent contradiction. In a plasma depletion layer, the magnetic field strength increases and the plasma density decreases, increasing the local Alfvén speed. For a field strength increase of a factor of 2 and a similar decrease in the plasma density, the Alfvén speed increases by almost a factor of 3. Petrinec et al. (2003) analyzed a large number of reconnection events for northward IMF, studying the effects of the plasma depletion layer. Using remote sensing of the reconnection site, they were able to demonstrate that stable reconnection at high latitudes required a depletion factor of between 2.3 (for 66 % of the events) and 3.6 (to account for 95 % of the events). Observations at the high-latitude magnetopause show sub-Alfvénic flow and this flow has been attributed to the presence of a depletion layer (e.g., Lavraud et al. 2005a; Panov et al. 2008)

In addition to the decrease in the Alfvén Mach number in the depletion layer, the bulk flow in the magnetosheath at high latitudes is typically slower than predicted by gas dynamic models. The magnetopause shape is indented due to the presence of the cusps (e.g., Petrinec and Russell 1995). This indentation may act to slow the magnetosheath flow poleward of the cusps (where the reconnection is occurring) (Petrinec et al. 2003). Indeed, in situ observations show that plasma flow in the magnetosheath at the high-latitude magnetopause is considerably slower than predicted by gas dynamics (Avanov et al. 2001; Onsager et al. 2001) and a statistical analysis suggests that the bulk flow slows down poleward of the magnetospheric cusps (Panov et al. 2008).

For southward IMF, a depletion layer forms only for high solar wind dynamic pressures (Anderson et al. 1997). Furthermore, there is no indentation of the magnetopause at low latitudes on the flanks and the $\mathbf{J}\times\mathbf{B}$ force in the magnetosheath accelerates the plasma (by as much as the local Alfvén speed) on the flanks when the field is strongly northward or southward (Petrinec et al. 2003). Thus, for typical solar wind conditions, the magnetosheath flow is super-Alfvénic only very near the subsolar region, and the boundary where the flow exceeds twice the Alfvén speed is well inside the terminator. The high bulk flows in the magnetosheath would have the effect of limiting the dawn-dusk extent of the reconnection X-line in Fig. 6.12, especially when the $|B_z|$ component of the IMF is dominant, although it is important to note that the magnetosheath flow is not necessary aligned or anti-aligned with the magnetic field (Komar et al. 2015), which would be necessary to suppress reconnection. Stable reconnection has been observed close to the terminator (e.g., Trattner et al. 2007c,a). However, there has not been a detailed study of the flow Mach number on the flanks near the magnetopause nor has there been a statistical study of the bulk flow properties of the magnetosheath during reconnection on the flanks. Thus, these predictions for suppression of reconnection by flow shear remain untested.

From the theoretical perspective, the effect of upstream flow shear on the reconnection rate for asymmetric systems such as the dayside magnetosphere was recently addressed, though still within the confines of 2D anti-parallel reconnection (Doss et al. 2015). Before discussing the effect of flow shear on asymmetric reconnection, results for symmetric reconnection are presented first. Analytic theory using linear theory for symmetric reconnection with equal and opposite upstream flow speeds reveal that the tearing mode is suppressed by super-Alfvénic upstream flow (Mitchell and Kan 1978; Chen and Morrison 1990). This was confirmed by numerical simulations (La Belle-Hamer et al. 1994). For sub-Alfvénic flow speeds, reconnection still occurs but it is slower. This was quantified for flow shear as (Cassak and Otto 2011)

$$E \sim E_0 \left(1 - \frac{v_{\text{shear}}^2}{c_A^2}\right), \tag{6.23}$$

where E_0 is the reconnection rate in the absence of flow shear ($= 0.1 B_L c_A$ for collisionless reconnection) and v_{shear} is the equal and opposite parallel flow in the upstream regions. The outflow speed decreases like (Cassak 2011)

$$v_{\text{out}}^2 \sim c_A^2 - v_{\text{shear}}^2. \tag{6.24}$$

This comes about because the straightening of the magnetic field line opposes the flow (as with the diamagnetic drift Swisdak et al. 2010), where the tension must overcome the plasma convection.

For asymmetric reconnection with flow shear, there are important qualitative and quantitative differences (Doss et al. 2015). A sketch of the region near the dissipation region is shown in Fig. 6.19. One difference is that if the upstream flow speeds are equal and opposite, the X-line is not stationary, as it would be

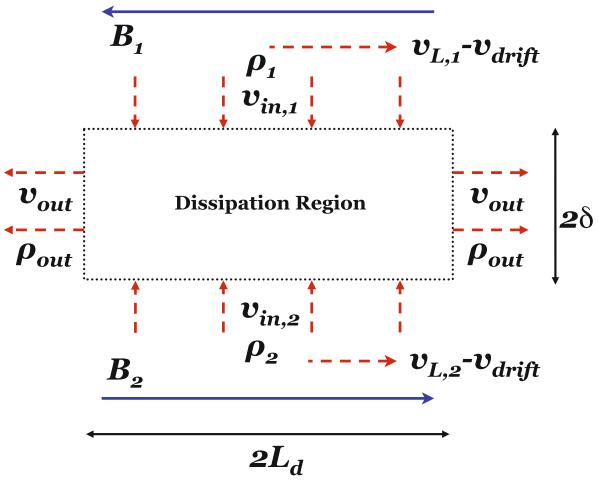

Fig. 6.19 Reconnection geometry for asymmetric reconnection with a flow shear (Doss et al. 2015). *Blue lines* are magnetic field and *red lines* are flow. C. E. Doss provided assistance with this figure

for symmetric reconnection. This is because the X-line and stagnation point are not colocated at the center of the dissipation region for asymmetric reconnection (Cassak and Shay 2007), as discussed in Sect. 6.2.3.2 and shown in Fig. 6.15. The offset of the stagnation point implies that one of the upstream plasmas contributes more by volume to the dissipation region makeup than the other, so the upstream plasmas contribute their momentum in the outflow directions in different proportions. This can be quantified (Doss et al. 2015); the convection speed of the X-line is

$$v_{\rm drift} \sim \frac{\rho_1 B_2 v_{L,1} + \rho_2 B_1 v_{L,2}}{\rho_1 B_2 + \rho_2 B_1}, \tag{6.25}$$

where $v_{L,1}$ and $v_{L,2}$ are the (arbitrary) upstream parallel flow speeds on the two sides of the dissipation region.

The offset of the stagnation point impacts the outflow speed as well. The reason is that the retracting reconnected magnetic field line opposes the flow of the side which contributes more of the plasma by volume. A calculation gives an outflow speed $v_{\rm out}$ of Doss et al. (2015)

$$v_{\rm out}^2 \sim c_{A,\rm asym}^2 - v_{\rm shear}^2 \frac{4\rho_1 B_2 \rho_2 B_1}{(\rho_1 B_2 + \rho_2 B_1)^2}, \tag{6.26}$$

where

$$v_{\rm shear} = \frac{v_{L,1} - v_{L,2}}{2} \tag{6.27}$$

is the average bulk flow velocity across the dissipation region and $c_{A,\rm asym}$ is defined in Eq. (6.11). The corresponding reconnection rate E generalizing Eq. (6.23) is

$$E \sim E_0 \left(1 - \frac{v_{\rm shear}^2}{c_{A,\rm asym}^2} \frac{4\rho_1 B_2 \rho_2 B_1}{(\rho_1 B_2 + \rho_2 B_1)^2} \right), \tag{6.28}$$

where E_0 is the asymmetric reconnection rate given by Eq. (6.10). Note that these predictions were tested in 2D two-fluid simulations in a rectangular domain (Doss et al. 2015), but they have not yet been carefully tested in global magnetospheric simulations or by observations.

Equation (6.28) leads to a surprising prediction. Above a critical speed, the reconnection rate vanishes, so reconnection can be suppressed by flow shear. While this critical speed $v_{\rm crit}$ is the Alfvén speed for symmetric reconnection, for asymmetric reconnection it is

$$v_{\rm crit} \sim c_{A,\rm asym} \frac{\rho_1 B_2 + \rho_2 B_1}{2(\rho_1 B_2 \rho_2 B_1)^{1/2}}. \tag{6.29}$$

Since the fraction multiplying $c_{A,\mathrm{asym}}$ is always greater than one, this result shows that the critical speed exceeds the asymmetric Alfvén speed. Thus, reconnection can occur even for super-Alfvénic flow. For the representative values at the magnetopause (although this is more relevant at the polar cusps than the subsolar point where the data is estimated), the critical speed is $v_{\mathrm{crit}} = 13.4\, c_{A,\mathrm{asym}} = 2370\,\mathrm{km/s}$, which from Eq. (6.27) implies a critical magnetosheath flow speed of 4740 km/s (since the magnetosphere is essentially stationary). Since the typical solar wind speed is 468 km/s (Gosling 2007), and it becomes slower when it crosses the bow shock, this suggests that reconnection is not typically suppressed by flow shear, and the change of the reconnection rate due to flow shear is typically not significant. An exception is when the asymmetry is less significant than typical conditions; examples of this are events when cold, high density material from the plasmasphere come out to the magnetopause, as discussed in the next section.

This section has outlined two independent interpretations for why reconnection at the cusps can occur even when the flow shear is super-Alfvénic. The extent to which either, both, or neither, explains the observations is currently not well understood and will be the subject of future research.

6.3.4 *Effect on Dayside Reconnection by Plasmaspheric Plasma*

The conditions at the magnetospheric side of the magnetopause reconnection site are typically quite steady, with densities, temperatures, and magnetic field strengths changing only little in response to more significant variations in solar wind conditions. An interesting counter example is so-called plasmaspheric drainage plumes (see, e.g., Sandel et al. 2003 for a review).

When the IMF follows a prolonged northward period (with relatively little reconnection at the subsolar point) by a sudden change to a southward period, there is a relatively abrupt increase in the inflow toward the subsolar reconnection site that occurs. This inflow brings in plasma from the magnetosphere, which can pull material out from the plasmasphere. This plume of material, an example of which is shown in Fig. 6.20, can extend all the way to the magnetopause, where it can interact with the dayside reconnection site. It was observed that geomagnetic indices used to quantify the efficiency of solar wind-magnetospheric coupling became less strong when the high density plume material was present (Borovsky and Denton 2006).

It was suggested that this decrease in the magnitude of geomagnetic indices was related to the increased mass present locally at the reconnection site (Borovsky and Denton 2006). This can be seen quantitatively from Eqs. (6.10) and (6.11); the outflow velocity is reduced if the magnetospheric plasma mass density becomes significant, which also lowers the reconnection rate. This reduction was investigated using 3D global MHD simulations (Borovsky et al. 2008). A narrow plume of plasmaspheric plasma arose in the simulations, and the reconnection rate was found

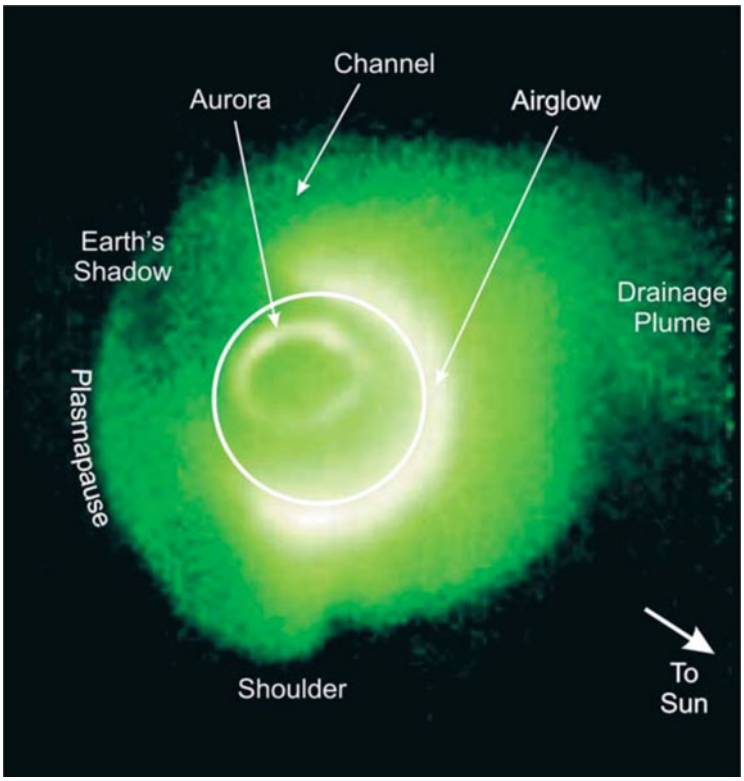

Fig. 6.20 Data from IMAGE satellite of a plasmaspheric drainage plume from Sandel et al. (2003). With kind permission from Springer Science and Business Media. Original caption—Extreme Ultraviolet Imager data at 07:34 UT on 24 May 2000, during a magnetic storm. A drainage plume extends sunward past the right edge of the image. Earth's shadow is visible in the direction away from the Sun, because only He+ illuminated by the Sun scatters the target wavelength. The *white circle* shows the approximate size and position of Earth

to agree with Eq. (6.10), which demonstrated that there could be a reduction in the *local* reconnection rate.

Searching for concrete evidence of a reduction in the reconnection rate in the observations is difficult because of the wide variability in the reconnection rate measurements, but there has been progress. It is difficult to correlate a reduction in the reconnection rate with plasmaspheric density because it is difficult to determine the mass density of the plasmaspheric plume near the magnetopause. In the boundary layer, the cold plasmaspheric plasma gains the $\mathbf{E} \times \mathbf{B}$ velocity of the reconnected plasma and is readily observable (Gosling et al. 1990a; Fuselier et al. 1991; Fuselier 1995). Thus, it is clear that cold plasma is entrained in the reconnection flow. However, it is rare to find events when the cold plasma mass density is greater than the magnetosheath mass density (Fuselier 1995). Most of the time, protons dominate the plasmaspheric plasma. Times when the plume

extends to the magnetopause are usually disturbed times and often occur when the magnetosphere is compressed. Thus, the solar wind density is also high and the relative contribution from the magnetosphere is low. On rare occasions, there is significant O+ in the magnetosphere and plasmasphere and this ion may dominate the mass density at the magnetopause.

Recently, direct observations were able to overcome these limitations. Using THEMIS, there was an event where one satellite passed through a reconnection site with a plume while another passed through an associated reconnection site where the plume was not present (Walsh et al. 2014a). It was shown that the portion with the plume had a much slower outflow speed. Also, it was shown that in the event with the plume, the magnetospheric density was larger than the magnetosheath density. An interesting aspect of the observation is that the reconnection outflow jet is primarily on the magnetosheath side when the plume is present, while the outflow jet for the event without the plume is primarily on the magnetospheric side. Recall the discussion in Sect. 6.2.3.2, which said the stagnation point is typically on the magnetospheric side because of its lower density, but is on whichever side has the lower value of ρ/B (Cassak and Shay 2007). The observations were consistent with the theory, as the side with smaller ρ/B became the magnetosheath side when the plume was present. In another event, there was a simultaneous measurement of a signature of a plume both with THEMIS at the magnetopause and with total electron current maps in the ionosphere (Walsh et al. 2014b), giving evidence that the plume stretched the whole way to the magnetopause.

The conclusion of these results is that the magnetospheric side of the magnetopause can impact the efficiency of the dayside reconnection process, at least locally at the reconnection site. This has led to an interesting debate about what controls dayside reconnection, which will be discussed in Sect. 6.4.1.

6.4 Open Questions and the Future of Dayside Reconnection

This chapter contains a few examples of topics in dayside reconnection that remain unsolved and how they will be addressed in the future. This list is certainly not exhaustive, but is intended only as a sampling.

6.4.1 Local vs. Global Control of Dayside Reconnection

As discussed in Sect. 6.3.4, recent work on the effect of plasmaspheric plumes on dayside reconnection have reopened important questions about long held notions of what controls dayside reconnection. As discussed in Chap. 1, the prevailing view for an extended time has been that dayside reconnection is controlled by the input by the solar wind. This is embodied by the Axford conjecture, stating that small scale

dissipation is necessary for reconnection but the large scale properties are governed by global input and boundary conditions.

In practice, for Earth's magnetopause, this effectively means that the total (global) amount of reconnected flux and/or the global reconnection rate is controlled by interplanetary conditions. Recall from Sect. 6.3 that the rate that the total flux is reconnected is given by the integrated reconnection rate E along the reconnection line (the separator). Thus, the Axford conjecture effectively means that this integrated electric field, the potential difference across the separator, is controlled by conditions in the solar wind. In other words, changing the solar wind speed or magnetic field strength would change the total rate of reconnection, but changing the dissipation mechanism (collisional vs. collisionless) or the magnetospheric density or magnetic field would not. See Newell et al. (2007) for an historical review of attempts to parametrize the efficiency of solar wind-magnetospheric coupling in terms of solar wind parameters.

This was called into question (Borovsky and Denton 2006; Borovsky et al. 2008) with the observation and subsequent numerical investigation of the effect of plasmaspheric plumes on dayside reconnection and on geomagnetic indices. The local change in magnetospheric density changed the (local) rate of reconnection, which seemingly contradicts the Axford conjecture by suggesting local physics can play a role. A parametrization of the coupling function using Eq. (6.10) as a starting point was presented (Borovsky 2008) and it performed as well as the best previous coupling functions.

Interestingly, it was shown that the simulations in Borovsky et al. (2008) that revealed the *local* change in reconnection rate due to plumes reveal that the *global* reconnection rate was relatively steady (Lopez, 2014, private communication). The situation at the time of writing remains fluid. It should be pointed out that the two scenarios are not necessarily contradictory. The Axford conjecture is that the large scale (global) properties are set by global conditions, so a local change that alters the local properties without changing the global properties does not contradict it. However, there has been no definitive evidence observationally or numerically that the Axford conjecture is correct. Also, it is clear from the research on plumes that the local changes to the reconnection process can alter geomagnetic indices, so it would be incorrect to say that the global conditions alone control the geoeffectiveness of a particular event, as one might have surmised from the Axford conjecture.

Answers to the questions posed on this topic are bound to be solved in the near future. It is unfortunately unlikely that observations will be able to answer this question because it is not possible to gain global information from a handful of satellites. Thus, it falls to using numerical simulations to address these questions. With the enhanced ability to locate reconnection sites (the separators) as discussed in Sect. 6.2.4, these questions will be able to be definitively answered in the near future.

6.4.2 Saturation of Reconnection

The reconnection rate is determined by the inflow rate into the reconnection site. Since the input conditions at the magnetopause are variable, an obvious question is whether or not reconnection can keep up with an increasing forcing from the external solar wind. One indication that the reconnection cannot keep up, i.e., there is **saturation** of the reconnection, is the pile-up of magnetic field against the dayside magnetopause. This occurs because the IMF and magnetosheath plasma can either flow around or through the magnetopause. Considering southward IMF, if the reconnection is fast enough, then particles and magnetic flux convect over the poles and there is no pile-up of magnetosheath field at the dayside magnetopause. However, if reconnection saturates, then increases in the dynamic pressure results in pile-up of magnetic field at the magnetopause.

The development of a plasma depletion layer for southward IMF is evidence of this pile-up. Observations revealed that a plasma depletion layer forms at the dayside magnetopause only when the solar wind dynamic pressure is high (approximately 10 nPa, or of the order of 10 times higher than nominal dynamic pressures) (Anderson et al. 1997). The existence of this depletion layer may be the strongest case for saturation of the reconnection rate at the magnetopause.

What causes saturation has also been discussed using theory and simulations. For example, it was suggested that saturation occurs when the magnetosheath $\mathbf{J} \times \mathbf{B}$ force exceeds the pressure gradient force (Lopez et al. 2010). The enhanced ability to locate separators will allow for continued progress from simulations on what causes saturation and linking the results with the observations.

6.4.3 MMS and What It Will Learn About Dayside Reconnection

The focus in this chapter has been macroscopic properties of reconnection. This is because the macroscopic properties have been studied observationally the most since dissipation region crossings are rare. This is expected to change soon due to the Magnetospheric Multiscale (MMS) Mission. This NASA mission was launched in 2015 to use Earth's magnetosphere as a laboratory to study the micro-processes of magnetic reconnection at the scale of the electron dissipation region (Burch et al. 2015). It builds on the successes of the ESA Cluster mission, which consists of four identical spacecraft with variable separations down to ion scale lengths at the magnetopause. MMS also consists of four identical spacecraft, but their separation is down to 10 km, and the time resolution of the particle instruments is 100 times faster than previous missions, allowing the spacecraft to resolve electron scale physics. With its high time resolution plasma and 3D electric and magnetic field measurements, MMS targets the electron dissipation region of reconnection at the

magnetopause and in the near-Earth magnetotail by using a trajectory near the equatorial plane.

The focus of the mission is contained in Eq. (6.2), the generalized Ohm's law. MMS will determine which terms in the generalized Ohm's law dominate the breaking of the frozen-in condition for electrons in the very tiny electron dissipation region. This determination requires 3D electric and magnetic field measurements (to determine the magnetic field and current density) as well as 3D electron distribution functions (to determine the electron pressure tensor). By targeting the electron dissipation region, the processes that initiate, sustain, and ultimately extinguish reconnection will be determined.

Acknowledgements The authors dedicate this chapter to Gene Parker, whose insight into the field of reconnection cannot be overestimated. Special thanks go out to Walter Gonzalez, who organized the Parker Reconnection Workshop in Saõ Jose dos Campos and was the driving force behind the production of this book. The authors thank Christopher Doss, Colin Komar and Karlheinz Trattner for the use of figures they made and/or assisted with. Helpful conversations with James Drake, Stefan Eriksson, Ramon Lopez, Kittipat Malakit, Michael Shay, and Marc Swisdak are acknowledged.

References

I.I. Alexeev, D.G. Sibeck, S.Y. Bobrovnikov, J. Geophys. Res. **103**, 6675 (1998)
B.J. Anderson, T.D. Phan, S.A. Fuselier, J. Geophys. Res. **102**, 9531 (1997)
L.A. Avanov, V.N. Smirnov, J.H. Waite Jr., S.A. Fuselier, O.L.Vaisberg, J. Geophys. Res. **106**, 29491 (2001)
M.P. Aubry, C.T. Russell, M.G. Kivelson, J. Geophys. Res. **75**, 7018 (1970)
M.T. Beidler, P.A. Cassak, Phys. Rev. Lett. **107**, 255002 (2011)
J. Berchem, C.T. Russell, J. Geophys. Res. **87**, 2108 (1982)
J. Birn, J.F. Drake, M.A. Shay, B.N. Rogers, R.E. Denton, M. Hesse, M. Kuznetsova, Z.W. Ma, A. Bhattacharjee, A. Otto, P.L. Pritchett, J. Geophys. Res. **106**, 3715 (2001)
J. Birn, J.E. Borovsky, M. Hesse, Phys. Plasmas **15**, 032101 (2008)
J. Birn, J.E. Borovsky, M. Hesse, K. Schindler, Phys. Plasmas **17**, 052108 (2010)
D. Biskamp, Phys. Fluids **29**, 1520 (1986)
M.G. Bobra, S.M. Petrinec, S.A. Fuselier, E.S. Chaflin, H.E. Spence, Geophys. Res. Lett. **31**, L04805 (2004)
J.E. Borovsky, J. Geophys. Res. **113**, A08228 (2008)
J.E. Borovsky, J. Geophys. Res. **118**, 2113 (2013)
J.E. Borovsky, M.H. Denton, Geophys. Res. Lett. **33**, L20101 (2006)
J.E. Borovsky, M. Hesse, Phys. Plasmas **14**, 102309 (2007)
J.E. Borovsky, M. Hesse, J. Birn, M.M. Kuznetsova, J. Geophys. Res. **113**, A07210 (2008)
J.L. Burch, T.E. Moore, R.B. Torbert, B.L. Giles, Space Sci. Rev. (2015). doi:10.1007/s1124-015-0164-9
P.A. Cassak, Phys. Plasmas **18**, 072106 (2011)
P.A. Cassak, J.F. Drake, Astrophys. J. Lett. **707**, L158 (2009)
P.A. Cassak, J.F. Drake, Phys. Plasmas **20**, 061207 (2013)
P.A. Cassak, A. Otto, Phys. Plasmas **18**, 074501 (2011)
P.A. Cassak, M.A. Shay, Phys. Plasmas **14**, 102114 (2007)
P.A. Cassak, M.A. Shay, Geophys. Res. Lett. **35**, L19102 (2008)

P.A. Cassak, M.A. Shay, Phys. Plasmas **16**, 055704 (2009)
P.A. Cassak, M.A. Shay, J.F. Drake, Phys. Rev. Lett. **95**, 235002 (2005)
P.A. Cassak, M.A. Shay, J.F. Drake, Phys. Plasmas **16**, 102702 (2009)
X.L. Chen, P.J. Morrison, Phys. Fluids B **2**, 495 (1990)
G. Chisham, M.P. Freeman, G.A. Abel, M.M. Lam, M. Pinnock, I.J. Coleman, S.E. Milan, M. Lester, W.A. Bristow, R.A. Greenwald, G.J. Sofko, J.P. Villain, Rev. Geophys. **46**, RG1004 (2008)
B.M.A. Cooling, C.J. Owen, S.J. Schwartz, J. Geophys. Res. **106**, 18763 (2001)
B. Coppi, Phys. Fluids **8**, 2273 (1965)
B. Coppi, J.W.K. Mark, L. Sugiyama, G. Bertin, Phys. Rev. Lett. **42**, 1058 (1979)
S.W.H. Cowley, Radio Sci. **8**, 903 (1973)
N.U. Crooker, J. Geophys. Res. **84**, 951 (1979)
J.T. Dahlin, J.F. Drake, M. Swisdak (2015). arXiv:1503.02218
W. Daughton, V. Roytershteyn, Space Sci. Rev. **172**, 271 (2012)
W. Daughton, J. Scudder, H. Karimabadi, Phys. Plasmas **13**, 072101 (2006)
W. Daughton, V. Roytershteyn, B.J. Albright, H. Karimabadi, L. Yin, K.J. Bowers, Phys. Plasmas **16**, 072117 (2009a)
W. Daughton, V. Roytershteyn, B.J. Albright, H. Karimabadi, L. Yin, K.J. Bowers, Phys. Rev. Lett. **103**, 065004 (2009b)
X.H. Deng, H. Matsumoto, Nature **410**, 557 (2001)
J.C. Dorelli, A. Bhattacharjee, *Reconnection of Magnetic Fields: Magnetohydrodynamics and Collisionless Theory and Observations*, chap. 4.1 (Cambridge University Press, Cambridge, 2007)
J.C. Dorelli, A. Bhattacharjee, Phys. Plasmas **15**, 056504 (2008)
J.C. Dorelli, A. Bhattacharjee, J. Geophys. Res. **114**, A06213 (2009)
J.C. Dorelli, M. Hesse, M.M. Kuznetsova, L. Rastaetter, J. Raeder, J. Geophys. Res. **109**, A12216 (2004)
J.C. Dorelli, A. Bhattacharjee, J. Raeder, J. Geophys. Res. **112**, A02202 (2007)
C.E. Doss, C.M. Komar, P.A. Cassak, F.D. Wilder, S. Eriksson, J.F. Drake, J. Geophys. Res. **120**, 7748 (2015)
J.F. Drake, M. Swisdak, H. Che, M.A. Shay, Nature **443**, 553 (2006)
J.W. Dungey, Philos. Mag. **44**, 725 (1953)
J.W. Dungey, Phys. Rev. Lett. **6**, 47 (1961)
J.W. Dungey, in *Geophysics The Earth's Environment*, ed. by C.D. Witt, J. Hieblot, A. Lebeau (Gordon Breach, New York, 1963)
J.W. Dungey, CC/Phys. Chem. Earth **49**, 20 (1983)
M.W. Dunlop, Q.H. Zhang, Y.V. Bogdanova, K. Trattner, Z. Pu, H. Hasegawa, J. Berchem, M. Taylor, M. Volwerk, J. Eastwood, B. Lavraud, C. Shen, J.K. Shi, J. Wang, D. Constantinescu, A. Fazakerley, H. Frey, D. Sibeck, P. Escoubet, J. Wild, Z. Liu, C. Carr, Ann. Geophys. **29**, 1683 (2011)
T.E. Eastman, S.A. Fuselier, J.T. Gosling, J. Geophys. Res. **101**, 49 (1996)
J.P. Eastwood, Phil. Trans. R. Soc. A **366**, 4489 (2008)
J. Eastwood, S.A. Kiehas, in *Magnetotails in the Solar System*, ed. by A. Keiling, C.M. Jackman, P.A. Delamere (Wiley, Hoboken, 2015)
J.P. Eastwood, T.D. Phan, M. Øieroset, M.A. Shay, J. Geophys. Res. **115**, A08215 (2010)
J.P. Eastwood, T.D. Phan, R.C. Fear, D.G. Sibeck, V. Angelopoulos, M. Øieroset, M.A. Shay, J. Geophys. Res. **117**, A08222 (2012)
J. Egedal, A. Le, P.L. Pritchett, W. Daughton, Phys. Plasmas **18**, 102901 (2011)
R.C. Elphic, in *Physics of the Magnetopause*, ed. by P. Song, B.U.O. Sonnerup, M.F. Thomsen (American Geophysical Union, Washington, DC, 1995)
D.H. Fairfield, L.J. Cahill Jr., J. Geophys. Res. **71**, 155 (1966)
J.F. Fennell, J. Geophys. Res. **78**, 1036 (1973)
R.L. Fermo, J.F. Drake, M. Swisdak, Phys. Plasmas **17**, 010702 (2010)
R.L. Fermo, J.F. Drake, M. Swisdak, K.J. Hwang, J. Geophys. Res. **116**, A09226 (2011)

R.L. Fermo, J.F. Drake, M. Swisdak, Phys. Rev. Lett. **108**, 255005 (2012)
H.P. Furth, J. Killeen, M.N. Rosenbluth, Phys. Fluids **6**, 459 (1963)
S.A. Fuselier, in *Physics of the Magnetopause*, ed. by P. Song. Geophysical Monograph 90 (American Geophysical Union, Washington, DC, 1995), p. 181
S.A. Fuselier, W. Lewis, Space Sci. Rev. **160**, 95 (2011)
S.A. Fuselier, D.M. Klumpar, E.G. Shelley, Geophys. Res. Lett. **18**, 139 (1991)
S.A. Fuselier, B.J. Anderson, T.G. Onsager, J. Geophys. Res. **102**, 4847 (1997)
S.A. Fuselier, K.J. Trattner, S.M. Petrinec, J. Geophys. Res. **105**, 255 (2000a)
S.A. Fuselier, S.M. Petrinec, K.J. Trattner, Geophys. Res. Lett. **27**, 473 (2000b)
S.A. Fuselier, H.U. Frey, K.J. Trattner, S.B. Mende, J.L. Burch, J. Geophys. Res. **107**, 1111 (2002)
S.A. Fuselier, K.J. Trattner, S.M. Petrinec, C.J. Owen, H. R'eme, J. Geophys. Res. **110**, A06212 (2005)
S.A. Fuselier, S.M. Petrinec, K.J. Trattner, J. Geophys. Res. **115**, A10207 (2010)
S.A. Fuselier, K.J. Trattner, S.M. Petrinec, J. Geophys. Res. **116**, A10227 (2011)
S.A. Fuselier, S.M. Petrinec, K.J. Trattner, B. Lavraud, J. Geophys. Res. **119**, 9051 (2014a)
S.A. Fuselier, R. Frahm, W.S. Lewis, A. Masters, J. Mukherjee, S.M. Petrinec, I.J. Sillanpaa, J. Geophys. Res. **119**, 2563 (2014b)
A. Galeev, in *Basic Plasma Physics: Selected Chapters, Handbook of Plasma Physics*, Amsterdam, vol. 1 (1984), p. 305
A.A. Galeev, M.M. Kuznetsova, L.M. Zeleny, Space Sci. Rev. **44**, 1 (1986)
R.G. Giovanelli, Astrophys. J. **89**, 555 (1939)
R.G. Giovanelli, Mon. Not. R. Astron. Soc. **107**(4), 338 (1947)
A. Glocer, J. Dorelli, G. Toth, C.M. Komar, P.A. Cassak, J. Geophys. Res. **120**, (2015). doi:10.1002/2015JA021417
M.V. Goldman, G. Lapenta, D.L. Newman, S. Markidis, H. Che, Phys. Rev. Lett. **107**, 135001 (2011)
W.D. Gonzalez, F.S. Mozer, J. Geophys. Res. **79**, 4186 (1974)
J.T. Gosling, in *Encyclopedia of the Solar System*, ed. by T. Spohn, D. Breuer, and T. Johnson. (Elsevier, Amsterdam, 2007), p. 99
J.T. Gosling, M.F. Thomsen, S.J. Bame, R.C. Elphic, C.T. Russell, Geophys. Res. Lett. **17**, 2244 (1990a)
J.T. Gosling, M.F. Thomsen, S.J. Bame, R.C. Elphic, C.T. Russell, J. Geophys. Res. **95**, 8073 (1990b)
J.T. Gosling, M.F. Thomsen, S.J. Bame, R.C. Elphic, J. Geophys. Res. **96**, 14097 (1991)
S.E. Haaland, B.U.O. Sonnerup, M.W. Dunlop, A. Balogh, E. Georgescu, H. Hasegawa, B. Klecker, G. Paschmann, P. Puhl-Quinn, H. R'eme, H. Vaith, A. Vaivads, Ann. Geophys. **22**, 1347 (2004)
H. Hasegawa, B.U.Ö. Sonnerup, C.J. Owen, B. Klecker, G. Paschmann, A. Balogh, H. Rème, Ann. Geophys. **24**, 603 (2006)
A.L. Haynes, C.E. Parnell, Phys. Plasmas **17**, 092903 (2010)
M. Hesse, K. Schindler, J. Geophys. Res. **93**, 5559 (1988)
M. Hesse, K. Schindler, J. Birn, M. Kuznetsova, Phys. Plasmas **6**, 1781 (1999)
M. Hesse, M. Kuznetsova, J. Birn, Phys. Plasmas **11**, 5387 (2004)
M. Hesse, S. Zenitani, A. Klimas, Phys. Plasmas **15**, 112102 (2008)
M. Hesse, N. Aunai, S. Zenitani, M. Kuznetsova, J. Birn, Phys. Plasmas **20**, 061210 (2013)
M. Hesse, N. Aunai, D. Sibeck, J. Birn, Geophys. Res. Lett. **41**, 8673 (2014)
F. Hoyle, *Some Recent Researches in Solar Physics* (Cambridge University Press, Cambridge, 1949)
Y.M. Huang, A. Bhattacharjee, Phys. Plasmas **17**, 062104 (2010)
J. Huang, Z.W. Ma, Chin. J. Geophys. **51**, 960 (2008)
Y.M. Huang, A. Bhattacharjee, B.P. Sullivan, Phys. Plasmas **18**, 072109 (2011)
W.J. Hughes, *Introduction to Space Physics*, chap. 9 (Cambridge University Press, Cambridge, 1995)
H. Ji, W. Daughton, Phys. Plasmas **18**, 111207 (2011)

H. Karimabadi, D. Krauss-Varban, N. Omidi, H.X. Vu, J. Geophys. Res. **104**, 12313 (1999)
H. Karimabadi, W. Daughton, J. Scudder, Geophys. Res. Lett. **34**, L13104 (2007)
H. Karimabadi, V. Roytershteyn, H.X. Vu, Y.A. Omelchenko, J. Scudder, W. Daughton, A. Dimmock, K. Nykyri, M. Wan, D. Sibeck, M. Tatineni, A. Majumdar, B. Loring, B. Geveci, Phys. Plasmas **21**, 062308 (2014)
R. Kleva, J. Drake, F. Waelbroeck, Phys. Plasmas **2**, 23 (1995)
E. Kobel, E.O. Fl"uckiger, J. Geophys. Res. **99**, 23617 (1994)
D. Koga, W.D. Gonzalez, F.S. Mozer, M.V.D. Silveira, F.R. Cardoso, Phys. Plasmas **21**, 100701 (2014)
C.M. Komar, The nature of magnetic reconnection at the dayside magnetopause. Ph.D. thesis, West Virginia University (2015)
C.M. Komar, P.A. Cassak, J.C. Dorelli, A. Glocer, M.M. Kuznetsova, J. Geophys. Res. **118**, 4998 (2013)
C.M. Komar, R.L. Fermo, P.A. Cassak, J. Geophys. Res. **120**, 276 (2015)
T.V. Laitinen, P. Janhunen, T.I. Pulkkinen, M. Palmroth, H.E.J. Koskinen, Ann. Geophys. **24**, 3059 (2006)
T.V. Laitinen, M. Palmroth, T.I. Pulkkinen, P. Janjunen, H.E.J. Koskinen, J. Geophys. Res. **112**, A11201 (2007)
A.L. La Belle-Hamer, A. Otto, L.C. Lee, Phys. Plasmas **1**, 706 (1994)
Y.T. Lau, J.M. Finn, Astrophys. J. **350**, 672 (1990)
B. Lavraud, A. Fedorov, E. Budnik, M.F. Thomsen, A.Grigoriev, P.J. Cargill, M.W. Dunlop, H. Rème, I. Dandouras, A. Balogh, J. Geophys. Res. **110**, A02209 (2005a)
B. Lavraud, M.F. Thomsen, M.G.G.T. Taylor, Y.L. Wang, T.D. Phan, S.J. Schwartz, R.C. Elphic, A. Fazakerley, H. Rème, A. Balogh, J. Geophys. Res. **110**, A06209 (2005b)
B. Lavraud, C. Foullon, C.J. Farrugia, J.P. Eastwood, in *Dynamic Magnetosphere*, ed. by W. Lui, M. Fujimoto. IAGA Special Sopron Book Series, Heidelberg, vol. 3 (2011), p. 3
R.H. Levy, H.E. Petschek, G.L. Siscoe, Am. Inst. Aeronaut. Astronaut. J. **2**, 2065 (1964)
R.E. Lopez, R. Bruntz, E.J. Mitchell, M. Wiltberger, J.G. Lyon, V.G. Merkin, J. Geophys. Res. **115**, A12216 (2010)
Y.H. Liu, J.F. Drake, M. Swisdak, Phys. Plasmas **18**, 062110 (2011a)
Y.H. Liu, J.F. Drake, M. Swisdak, Phys. Plasmas **18**, 092102 (2011b)
Y.H. Liu, J.F. Drake, M. Swisdak, Phys. Plasmas **19**, 022110 (2012)
Y.H. Liu, M. Hesse, M. Kuznetsova, J. Geophys. Res. **120**, 7331 (2015)
A.T.Y. Lui, C. Jacquey, G.S. Lakhina, R. Lundin, T. Nagai, T.D. Phan, Z.Y. Pu, M. Roth, Y. Song, R.A. Treumann, M. Yamauchiq, L.M. Zelenyi, Space Sci. Rev. **116**, 497 (2005)
K. Malakit, Asymmetric magnetic reconnection: a particle-in-cell study. Ph.D. thesis, University of Delaware (2012)
K. Malakit, M.A. Shay, P.A. Cassak, C. Bard, J. Geophys. Res. **115**, A10223 (2010)
K. Malakit, M.A. Shay, P.A. Cassak, D. Ruffolo, Phys. Rev. Lett. **111**, 135001 (2013)
M.E. Mandt, R.E. Denton, J.F. Drake, Geophys. Res. Lett. **21**, 73 (1994)
W.H. Matthaeus, S.L. Lamkin, Phys. Fluids **26**, 303 (1985)
H.G. Mitchell Jr., J.R. Kan, J. Plasma Phys. **20**, 31 (1978)
T.E. Moore, M.C. Fok, M.O. Chandler, J. Geophys. Res. **107**, 1332 (2002)
T.E. Moore, J.L. Burch, W.S. Daughton, S.A. Fuselier, H. Hasegawa, S.M. Petrinec, Z.Y. Pu, J. Atmos. Terr. Phys. **99**, 32 (2013)
F.S. Mozer, A. Hull, Phys. Plasmas **17**, 102906 (2010)
F.S. Mozer, P.L. Pritchett, Phys. Today **63**, 34 (2010)
F.S. Mozer, P.L. Pritchett, Space Sci. Rev. **158**, 119 (2011)
F. Mozer, A. Retinó, J. Geophys. Res. **112**, A10206 (2007)
F. Mozer, S.D. Bale, T.D. Phan, Phys. Rev. Lett. **89**, 015002 (2002)
F.S. Mozer, V. Angelopoulos, J. Bonnell, K.H. Glassmeier, J.P. McFadden, Geophys. Res. Lett. **35**, L17S04 (2008a)
F.S. Mozer, P. Pritchett, J. Bonnell, D. Sundqvist, M. Chang, J. Geophys. Res. **113**, A00C03 (2008b)

N.A. Murphy, C.R. Sovinec, P.A. Cassak, J. Geophys. Res. **115**, A09206 (2010)
F.M. Muzamil, C.J. Farrugia, R.B. Torbert, P.R. Pritchett, F.S. Mozer, J.D. Scudder, C.T. Russell, P.E. Sandholt, W.F. Denig, L. Wilson III, J. Geophys. Res. **119**, 7343 (2014)
T. Nagai, I. Shinohara, M. Fujimoto, M. Hoshino, Y. Saito, S. Machida, T. Mukai, J. Geophys. Res. **106**, 25929 (2001)
M. Nakamura, M. Scholer, J. Geophys. Res. **105**, 23179 (2000)
P.T. Newell, T. Sotirelis, K. Liou, C.I. Meng, F.J. Rich, J. Geophys. Res. **112**, A01206 (2007)
M. Øieroset, T.D. Phan, M. Fujimoto, R.P. Lin, R.P. Lepping, Nature **412**, 417 (2001)
M. Øieroset, T.D. Phan, M. Fujimoto, Geophys. Res. Lett. **31**, L12801 (2004)
M. Øieroset, T.D. Phan, J.P. Eastwood, M. Fujimoto, W. Daughton, M.A. Shay, V. Angelopoulos, F.S. Mozer, J.P. McFadden, D.E. Larson, K.H. Glassmeier, Phys. Rev. Lett. **107**, 165007 (2011)
M. Øieroset, D. Sundkvist, C.C. Chaston, T.D. Phan, F.S. Mozer, J.P. McFadden, V. Angelopoulos, L. Andersson, J.P. Eastwood, J. Geophys. Res. **119**, 6256 (2014)
T.G. Onsager, S.A. Fuselier, in *Solar System Plasmas in Space and Time*, ed. by J.L. Burch, J.H. Waite Jr. Geophysical Monograph 84 (American Geophysical Union, 1994), p. 183
T.G. Onsager, J.D. Scudder, M. Lockwood, C.T. Russell, J. Geophys. Res. **106**, 25467 (2001)
J.E. Ouellette, J.G. Lyon, B.N. Rogers, J. Geophys. Res. **119**, 1673 (2014)
E.V. Panov, J. Büchner, M. Fränz, A. Korth, S.P. Savin, H. Rème, K.H. Fornaçon, J. Geophys. Res. **113**, A01220 (2008)
E.N. Parker, J. Geophys. Res. **62**, 509 (1957)
E.N. Parker, Phys. Rev. **109**, 1874 (1958)
E.N. Parker, Astrophys. J. **8**, 177 (1963)
E.N. Parker, Astrophys. J. **180**, 247 (1973)
G. Paschmann, Geophys. Res. Lett. **35**, L19109 (2008)
G. Paschmann, B.U.Ö. Sonnerup, I. Papamastorakis, N. Sckopke, G. Haerendel, S.J. Bame, J.R. Asbridge, J.T. Gosling, C.T. Russell, R.C. Elphie, Nature **282**, 243 (1979)
G. Paschmann, I. Papamastorakis, W. Baumjohann, N. Sckopke, C.W. Carlson, B.U.Ø. Sonnerup, H. Lühr, J. Geophys. Res. **91**, 11099 (1986)
G. Paschmann, M. Øieroset, T. Phan, Space Sci. Rev. **178**, 385 (2013)
S.M. Petrinec, S.A. Fuselier, Geophys. Res. Lett. **30**, 1519 (2003)
S.M. Petrinec, C.T. Russell, J. Geophys. Res. **100**, 9559 (1995)
S.M. Petrinec, K.J. Trattner, S.A. Fuselier, J. Geophys. Res. **108**, 1458 (2003)
S.M. Petrinec, M. Dayeh, H. Funsten, S. Fuselier, D. Heirtzler, P. Janzen, H. Kucharek, D. McComas, E. M"obius, T. Moore, D. Reisenfeld, N. Schwadron, K.J. Trattner, P. Wurz, J. Geophys. Res. **116**, A07203 (2011)
H.E. Petschek, in *AAS/NASA Symposium on the Physics of Solar Flares*, ed. by W.N. Ness (NASA, Washington, DC, 1964), p. 425
H.E. Petschek, in *The Solar Wind*, ed. by J.R.J. Mackin, M. Neugebauer (Pergamon, New York, 1966), p. 257
H.E. Petschek, R.M. Thorne, Astrophys. J. **147**, 1157 (1967)
T.D. Phan, G. Paschmann, J. Geophys. Res. **101**, 7801 (1996)
T.D. Phan, G. Paschmann, W. Baumjohann, N. Sckopke, H. Lühr, J. Geophys. Res. **99**, 121 (1994)
T.D. Phan, B.U.O. Sonnerup, R.P. Lin, J. Geophys. Res. **106**, 25489 (2001)
T. Phan, H.U. Frey, S. Frey, L. Peticolas, S. Fuselier, C. Carlson, H. Rème, J.M. Bosqued, A. Balogh, M. Dunlop, L. Kistler, C. Mouikis, I. Dandouras, J.A. Sauvard, S. Mende, J. McFadden, G. Parks, E. Moebius, B. Klecker, G. Paschmann, M. Fujimoto, S. Petrinec, M.F. Marcucci, A. Korth, R. Lundin, Geophys. Res. Lett. **30**, 1509 (2003)
T.D. Phan, C.P. Escoubet, L. Rezeau, R.A. Treumann, A. Vaivads, G. Paschmann, S.A. Fuselier, D.A.B. Rogers, B. Sonnerup, Space Sci. Rev. **118**, 367 (2005)
T.D. Phan, J.F. Drake, M.A. Shay, F.S. Mozer, J.P. Eastwood, Phys. Rev. Lett. **99**, 255002 (2007)
T.D. Phan, G. Paschmann, J.T. Gosling, M. Øieroset, M. Fujimoto, J.F. Drake, V. Angelopoulos, Geophys. Res. Lett. **40**, 1 (2013)
J.H. Piddington, Hist. Rec. Aust. Sci. **6**, 223 (1985)
E. Priest, T. Forbes, *Magnetic Reconnection* (Cambridge University Press, Cambridge, 2000)

E.R. Priest, V.S. Titov, R.E. Grundy, A.W. Hood, Proc. R. Soc. Lond. A **456**, 1821 (2000)
P.L. Pritchett, J. Geophys. Res. **106**, 3783 (2001)
P.L. Pritchett, J. Geophys. Res. **113**, A06210 (2008)
P.L. Pritchett, F.S. Mozer, J. Geophys. Res. **114**, A11210 (2009)
Z.Y. Pu, X.G. Zhang, X.G. Wang, J. Wang, X.Z. Zhou, M.W. Dunlop, L. Xie, C.J. Xiao, Q.G. Zong, S.Y. Fu, Z.X. Liu, C. Carr, Z.W. Ma, C. Shen, E. Lucek, H. Réme, P. Escoubet, Geophys. Res. Lett. **34**, L20101 (2007)
T. Pulkkinen, Living Rev. Solar Phys. **4**, 1 (2007)
T.I. Pulkkinen, M. Palmroth, H.E.J. Koskinen, T.V. Laitinen, C.C. Goodrich, V.G. Merkin, J.G. Lyon, J. Geophys. Res. **115**, A03207 (2010)
A. Retinó, A. Vaivads, M. André, F. Sahraoui, Y. Khotyaintsev, J.S. Pickett, M.B.B. Cattaneo, M.F. Marcucci, M. Morooka, C.J. Owen, S.C. Buchert, N. Comilleau-Wehrlin, Geophys. Res. Lett. **33**, L06101 (2006)
B. Rogers, L. Zakharov, Phys. Plasmas **2**, 3420 (1995)
B.N. Rogers, R.E. Denton, J.F. Drake, M.A. Shay, Phys. Rev. Lett. **87**, 195004 (2001)
M.J. Rosenberg, C.K. Li, W. Fox, I. Igumenshchev, F.H. Séguin, R.P.J. Town, J.A. Frenje, C. Stoeckl, V. Glebov, R.D. Petrasso, Nat. Commun. **6**, 6190 (2015)
L. Rosenqvist, A. Vaivads, A. Retin'o, T. Phan, H.J. Opgenoorth, I. Dandouras, S. Buchert, Geophys. Res. Lett. **35**, L08104 (2008)
C.T. Russell, R.C. Elphic, Space Science Rev. **22**, 681 (1978)
C.T. Russell, R.C. Elphic, Geophys. Res. Lett. **6**, 33 (1979)
B.R. Sandel, J. Goldstein, D.L. Gallagher, M. Spasojevic, Space Sci. Rev. **109**, 25 (2003)
K.M. Schoeffler, J.F. Drake, M. Swisdak, Astrophys. J. **743** (2011)
R. Schreier, M. Swisdak, J.F. Drake, P.A. Cassak, Phys. Plasmas **17**, 110704 (2010)
B.D. Scott, A.B. Hassam, Phys. Fluids **30**, 90 (1987)
V.S. Semenov, Adv. Space Res. **21**, 583 (1998)
S. Servidio, W.H. Matthaeus, M.A. Shay, P.A. Cassak, P. Dmitruk, Phys. Rev. Lett. **102**, 115003 (2009)
S. Servidio, W.H. Matthaeus, M.A. Shay, P. Dmitruk, P.A. Cassak, M. Wan, Phys. Plasmas **17**, 032315 (2010)
M.A. Shay, J.F. Drake, B.N. Rogers, R.E. Denton, Geophys. Res. Lett. **26**, 2163 (1999)
M.A. Shay, J.F. Drake, M. Swisdak, B.N. Rogers, Phys. Plasmas **11**, 2199 (2004)
M.A. Shay, J.F. Drake, M. Swisdak, Phys. Rev. Lett. **99**, 155002 (2007)
K. Shibata, S. Tanuma, Earth Planets Space **53**, 473 (2001)
G.L. Siscoe, G.M. Erickson, B.U.Ö. Sonnerup, N.C. Maynard, K.D. Siebert, D.R. Weimer, W.W. White, J. Geophys. Res. **106**, 13015 (2001)
G.L. Siscoe, G.M. Erickson, B.U.Ö. Sonnerup, N.C. Maynard, J.A. Schoendorf, K.D. Siebert, D.R. Weimer, W.W. White, G.R. Wilson, Geophys. Res. Lett. **29**, 1626 (2002)
B.U.Ö. Sonnerup, J. Geophys. Res. **79**, 1546 (1974)
B.U.Ö. Sonnerup, in *Solar System Plasma Physics*, vol. 3, ed. by L.J. Lanzerotti, C.F. Kennel, E.N. Parker (North Halland Publications, Amsterdam, 1979), p. 46
B.U.Ö. Sonnerup, J. Geophys. Res. **86**, 10049 (1981)
B.U.Ö. Sonnerup, J.L.J. Cahill, J. Geophys. Res. **72**, 171 (1967)
B.U.Ö. Sonnerup, G. Paschmann, I. Papamastorakis, N. Sckopke, G. Haerendel, S.J. Bame, J.R. Asbridge, J.T. Gosling, C.T. Russell, J. Geophys. Res. **86**, 10049 (1981)
T.W. Speiser, J. Geophys. Res. **70**, 4219 (1965)
L. Spitzer, R. Härm, Phys. Rev. **89**, 977 (1953)
P.A. Sweet, in *Electromagnetic Phenomena in Cosmical Physics*, ed. by B. Lehnert (Cambridge University Press, New York, 1958), p. 123
M. Swisdak, J.F. Drake, Geophys. Res. Lett. **34**, L11106 (2007)
M. Swisdak, J.F. Drake, M.A. Shay, B.N. Rogers, J. Geophys. Res. **108**, 1218 (2003)
M. Swisdak, M. Opher, J.F. Drake, F. Alouani Bibi, Astrophys. J. **710**, 1769 (2010)
K.G. Tanaka, A. Retino, Y. Asano, M. Fujimoto, I. Shinohara, A. Vaivads, Y. Khotyaintsev, M. Andre, M.B. Bavassano-Cattaneo, S.C. Buchert, C.J. Owen, Ann. Geophys. **26**, 2471 (2008)

K.G. Tanaka, M. Fujimoto, I. Shinohara, Int. J. Geophys. **2010**, 202583 (2010)
W.L. Teh, B.U.Ö. Sonnerup, Ann. Geophys. **26**, 2673 (2008)
K.J. Trattner, S.A. Fuselier, S.M. Fuselier, J. Geophys. Res. **109**, A03219 (2004)
K.J. Trattner, J.S. Mulcock, S.M. Petrinec, S.A. Fuselier, Geophys. Res. Lett. **34**, L03108 (2007a)
K.J. Trattner, S.A. Fuselier, S.M. Petrinec, *Reconnection of Magnetic Fields: Magnetohydrodynamics and Collisionless Theory and Observations*, chap. 4.2 (Cambridge University Press, Cambridge, 2007b)
K.J. Trattner, J.S. Mulcock, S.M. Petrinec, S.A. Fuselier, J. Geophys. Res. **112**, A08210 (2007c)
K.J. Trattner, S.M. Petrinec, S.A. Fuselier, T.D. Phan, J. Geophys. Res. **117**, A01201 (2012)
L. Trenchi, M.F. Marcucci, G. Pallocchia, G. Consolini, M.B.B. Cattaneo, A.M.D. Lellis, H. Rème, L. Kistler, C.M. Carr, J.B. Cao, J. Geophys. Res. **113**, A07S10 (2008)
N.A. Tsyganenko, J. Geophys. Res. **100**, 5599 (1995)
D.A. Uzdensky, Astrophys. J. **671**, 2139 (2007)
A. Vaivads, Y. Khotyaintsev, M. André, A. Retin‘o, S.C. Buchert, B.N. Rogers, P. Décréau, G. Paschmann, T.D. Phan, Phys. Rev. Lett. **93**, 105001 (2004)
V.M. Vasyliunas, Rev. Geophys. **13**(1), 303 (1975)
R.J. Walker, C.T. Russell, *Introduction to Space Physics*, chap. 6 (Cambridge University Press, Cambridge, 1995)
B.M. Walsh, T.D. Phan, D.G. Sibeck, V.M. Souza, Geophys. Res. Lett. **41**, 223 (2014a)
B.M. Walsh, J.C. Foster, P.J. Erickson, D.G. Sibeck, Science **343**, 1122 (2014b)
C.P. Wang, M. Gkioulidou, L.R. Lyons, V. Angelopoulos, J. Geophys. Res. **117**, A08215 (2012)
A.C. Williams, T.W. Moorehead (eds.). *Hannes Alfvén Keynote Address*, NASA Conference Publication 2469 (1987)
J. Yoo, M. Yamada, H. Ji, J. Jara-Almonte, C.E. Myers, L.J. Chen, Phys. Rev. Lett. **113**, 095002 (2014)
L. Zakharov, B. Rogers, Phys. Fluids B **4**, 3285 (1992)
L. Zakharov, B. Rogers, S. Migliuolo, Phys. Fluids B **5**, 2498 (1993)
S. Zenitani, M. Hesse, A. Klimas, M. Kuznetsova, Phys. Rev. Lett. **106**, 195003 (2011)
V. Zhdankin, D.A. Uzdensky, J.C. Perez, S. Boldyrev, Astrophys. J. **771**, 124 (2013)

Chapter 7
Magnetotail Reconnection

A. Petrukovich, A. Artemyev, and R. Nakamura

Abstract Reconnection is the key process responsible for the magnetotail dynamics. Driven reconnection in the distant tail is not sufficient to support global magnetospheric convection and the near Earth neutral line spontaneously forms to restore the balance. Mechanisms of initiation of such near-Earth magnetotail reconnection still represent one of major unresolved issues in space physics. We review the progress in this topic during the last decade. Recent theoretical advances suggest several variants of overcoming the famous tearing stability problem. Multipoint spacecraft observations reveal detailed structure of pre-onset current sheet of and reconnection zone down to ion larmor scale, supporting the importance of unstable state development through internal magnetotail reconfiguration.

Keywords Current sheet • Magnetospheric reconnection • Magnetotail • Plasma sheet • Reconnection onset • Substorms

7.1 Introduction

In the Solar system, the Earth's magnetosphere is a unique example of a fair balance between external driving and inherent dynamics. Mercury, Venus, and Mars magnetospheres are almost entirely driven by solar wind, while that of the giant planets are dominated by rotation effects. Solar wind flow shapes the Earth's magnetosphere, however global convection inside the magnetosphere is largely determined by the interplanetary magnetic field (IMF). This convection is substantially mediated by the relatively strong Earth's magnetic field, in particular through cycles of solar wind energy accumulation and release, known as substorms. Substorms, producing auroras and geomagnetic variations at polar latitudes, are the

A. Petrukovich (✉) • A. Artemyev
Space Research Institute, Russian Academy of Science, Moscow, Russia
e-mail: apetruko@iki.rssi.ru; ante0226@gmail.com

R. Nakamura
Space Research Institute, Austrian Academy of Science, Graz, Austria
e-mail: rumi.nakamura@oeaw.ac.at

W. Gonzalez, E. Parker (eds.), *Magnetic Reconnection*, Astrophysics and Space Science Library 427, DOI 10.1007/978-3-319-26432-5_7

most spectacular everyday manifestation of magnetospheric dynamics and space weather in general.

The magnetotail plays the central role in substorm dynamics. The magnetotail includes the plasma sheet, filled with the hot plasmas on the closed magnetic field lines with both their ends in the ionosphere, and the tail lobes with empty open field lines, having one end in the Earth's polar cap ionosphere and another connected to interplanetary magnetic field (IMF). The current sheet (CS) here is introduced qualitatively as a zone in the plasma sheet, in which the major part of magnetic field reversal occurs.

Already, early spacecraft observations revealed that substorms are associated with southward IMF ($B_z < 0$, GSM frame is used hereafter). Substorms start with gradual accumulation of open magnetic flux in the lobes, thinning and stretching of plasma sheet (growth phase). At a substorm onset, the expansion phase starts with a rapid decrease of magnetic flux and dipolarization (a return to a more dipolar configuration of the magnetic field) of plasma sheet, coincident with auroral brightening and geomagnetic variations on the ground (McPherron et al. 1973; Baker et al. 1996, and references therein).

Historically, two scenarios of solar wind effect on the magnetosphere were proposed: viscous interaction supported by various diffusive-like processes at the magnetospheric boundary (Axford and Hines 1961) and reconnection of IMF lines and geomagnetic field lines at the dayside magnetopause and in the magnetotail (Dungey 1961). Though spacecraft observations demonstrate elements of both scenarios (Wing et al. 2014), magnetic reconnection is of primary importance for substorms and for magnetospheric dynamics in general (Paschmann et al. 2013).

When the IMF is directed southward, it reconnects with field lines of the Earth magnetic field at the day-side magnetopause (see Chap. 3 in this book). This process can be considered as a forced reconnection, as interplanetary magnetic field frozen into the solar wind plasma flow collides with the Earth dipole field and has no chance to avoid reconnection in case when two field lines are directed approximately opposite to each other. Thus, the basic dynamics of the magnetopause reconnection may be essentially controlled by external (i.e. boundary) conditions.

The situation is different for the reconnection in the tail (Fig. 7.1). First of all, simple estimates show that the global convection forms the night-side reconnection region around 100–200 R_E downtail (distant neutral line, DNL). Motion of solar wind plasma $\mathbf{V}_{sw}$ with frozen-in IMF $\mathbf{B}_{IMF}$ corresponds to the electric field $\mathbf{E} = -[\mathbf{V}_{sw} \times \mathbf{B}_{IMF}]$. For southward IMF $\mathbf{E}$ is predominantly directed from dusk to dawn, $E_y^i \sim 2$ mV/m (for moderate conditions with $B_z = -5$ nT and $V_{sw} = 400$ km/s). At the field lines in the lobe with dominating B_x it corresponds to convection electric field $E_y^m = 0.2$–0.4 mV/m (reconnection efficiency 10–20 %) and equatorward drift equal to 10–20 % of solar wind velocity. With a magnetotail radius about 20 R_E an open field line reaches equator and meets an oppositely directed line from the reciprocal lobe at 100–200 R_E downtail. The DNL reconnection is also forced by plasma flows in external electric field (Dungey 1963). This zone was well studied with ISEE-3 and Geotail spacecraft (Baker et al. 1984; Tsurutani and von Rosenvinge 1984; Nishida et al. 1998; Ho et al. 1994).

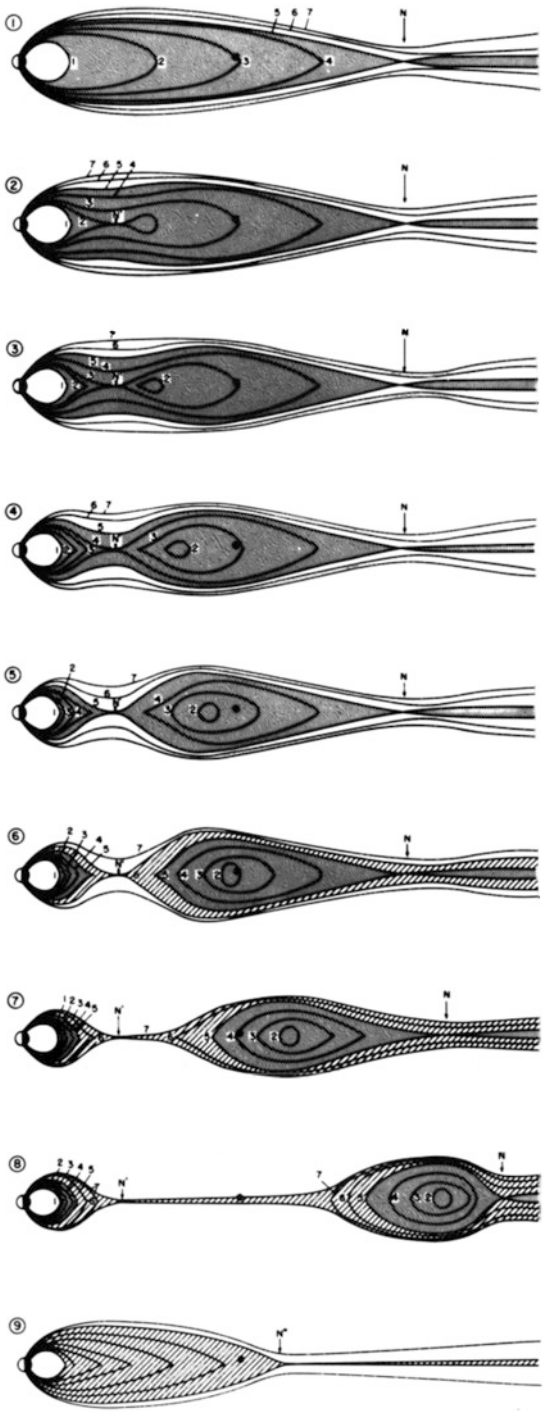

Fig. 7.1 Dynamics of distant and near-earth neutral lines in the magnetotail. Reprinted figure with permission from [E.W. Hones Jr, Journal of Geophysical Research, 82, 5633–5640, 1977]. Copyright (1977) by John Wiley and Sons

DNL operates almost continuously, although not necessarily as a single large-scale object. However the reconnection rate at the DNL is less than the convection field E_y^m, since incoming field lines are already loaded with magnetosheath (solar wind) plasma and the resulting Alfven velocity is rather low. Thus DNL reconnection can not be in balance with the dayside reconnection and it is also of minor importance for substorms, since it is too far to produce ground magnetic variations and auroras. Moreover, the 'return" plasma convection from the distant tail to Earth cannot be a steady (quasi-stationary) process, because it results in an unrealistic growth of the plasma pressure in the near-Earth region (so called pressure catastrophe see Erickson and Wolf 1980).

The Near-Earth neutral line concept (NENL) is a natural solution to all these problems, see Fig. 7.1 (Hones 1979). NENL reconnection starts at a substorm onset in a bursty manner at distances $\sim$15–25R_E downtail and propels open magnetic flux and plasma sheet material back to solar wind, as well as increases efficiency of Earthward convection with fast plasma flows (Baker et al. 1996; Baumjohann 2002). The reconnection rate at a NENL is at least order of magnitude higher (several mV/m) when empty lobe field lines are involved and it is capable of unloading the magnetotail in a matter of minutes. The near-Earth reconnection also occurs close enough to Earth to have a role in observed ground substorm signatures. Thus, the NENL model of substorms is commonly used to explain the overall ground-based magnetic disturbances as well as large-scale evolution of the magnetotail, from near-Earth to distant tail region (e.g., Baker et al. 1996).

The NENL reconnection is not driven by any directly impinging plasma flows (though, of course, it is a consequence of solar wind driving) and develops due to some internal reconfiguration (instability) of the current sheet. Thus NENL reconnection has spontaneous nature, unlike dayside and DNL reconnection.

Reconnection in the rarefied magnetospheric plasmas is unobservable from Earth and spacecraft measurements are the only means to study it in situ. Magnetospheric plasma scales (ion scale of the order of 1000 km and electron scale of the order of 10 km) allow in principle to study reconnection in detail by a (much smaller) spacecraft. However such measurements inside a reconnection zone are very rare and mostly observations of reconnection exhausts (plasma flows) are analyzed.

The first generation of magnetospheric spacecraft (OGO, IMP) helped to fix general tail structure and the substorm sequence (McPherron et al. 1973). The first observational evidence that the reconnection may take place in the near Earth-tail (Earthward of 30 R_E) comes from a statistical study of changes in the magnetic field configuration during substorms (Nishida and Nagayama 1973). A more comprehensive observation of the magnetotail reconnection, detection of fast plasma flow, energetic particles associated with changes in the magnetic field component normal to the current sheet was then shown by Hones (1979).

The later spacecraft, especially ISEE and AMPTE, helped to identify the reconnection zone (active current sheet) on some occasions (e.g., McPherron and Manka 1985, and references therein) as well as provided the first evidence of its bursty and localized nature (Baumjohann et al. 1990). In the 1990s, a fleet of spacecraft in the magnetotail, solar wind, inner magnetosphere (Geotail, Polar,

Interball, IMP8, LANL, GOES, Wind) collected significant statistics of substorm and reconnection observations and established the causal links from solar wind to magnetotail, and further to inner magnetosphere and auroral zone.

Detailed characteristics of magnetotail reconnection site were first reported by Nagai et al. (1998) basing on high-temporal resolution of plasma and magnetic field observations from Geotail. These observations resolved the different distributions of inflowing and outflowing electrons and ions and the field-aligned currents closing the Hall current system (e.g., Nagai et al. 2013b). A quadrupole magnetic field disturbance was found by Øieroset et al. (2001) due to the Hall current system in the ion diffusion region, where decoupling of ion and electron motion occurs. A comprehensive review of recent magnetospheric observations of magnetic reconnection is provided by Paschmann et al. (2013).

In the twenty-first century, new multi-point Cluster project permitted direct observations of the spatial configuration of the reconnection on ion and sub-ion scales (thousands and hundreds km). The spatial gradients of magnetic field components (and hence, current density) can be obtained from the four-point magnetic field measurements based on linear gradient estimation (Chanteur and Harvey 1998). The detailed profile of the current density in the current sheet can be best obtained when the spacecraft is vertically crossing the current sheet rapid enough to assume that the current sheet is simply translated without any change of its structure. Integration of the translation velocity projected onto the local current sheet normal during the crossing gives an estimate for the vertical scale of the current sheet (Runov et al. 2005).

While there are no big doubts about a role of reconnection in the global dynamics, still there is a lot of controversy with understanding it's geophysical context (causal scheme of substorm onset) as well as with initiation mechanisms in terms of plasma instabilities (Petrukovich 2008; Angelopoulos et al. 2008; Lui et al. 2008). We review in this chapter several issues, which were significantly advanced during the last 10 years: development of reconnection instability models, magnetotail current sheet structure before reconnection, multi-point reconnection zone observations at ion scales.

7.2 Theoretical Models of Magnetotail Reconnection

Instabilities of the magnetotail current sheet, resulting in reconnection and NENL formation have been investigated theoretically for over last 50 years. Starting from the paper by Furth (1962) (see also Furth et al. 1963), it became clear that an instability of current filament attraction (tearing instability) should result in magnetic field merging and the following formation of the X-line (see schematic picture in Fig. 7.2). The survey of earlier models of magnetic field dissipation and charged particle acceleration in (and around) the X-line region can be found in the paper by Vasyliunas (1975). In this section we concentrate on the progress in one of the most intriguing problems of the magnetospheric physics—the problem of the

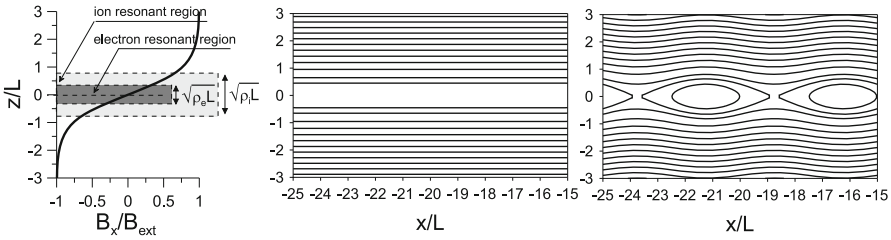

Fig. 7.2 Schematic view of the reconnection of magnetic field lines: transformation from straight magnetic field lines to X-lines and islands. *Left panel* shows resonance regions of ions and electrons

initialization of the magnetotail reconnection. Discussion of theoretical descriptions of charged particle acceleration and plasma heating can be found in the recent reviews by Birn et al. (2012), Egedal et al. (2013), and Treumann and Baumjohann (2013).

The tearing instability is the most natural candidate for triggering reconnection in the magnetotail geometry. Investigation of the tearing instability was started by Laval et al. (1966), Coppi et al. (1966), Schindler (1966); and Hoh (1966) for a simplified configuration of two regions with oppositely directed magnetic field B_x (Harris 1962) (Harris sheet).

In the center of such a 1D current sheet (CS), particles can freely drift along dawn-dusk direction contributing to the growth of the unstable tearing mode which (in the simplest form) is an increasing perturbation $\sim\exp(ikx - i\omega t)$ without oscillations, i.e. $\Re\omega = 0$, and a growth rate $\gamma = -i\omega$. A spatial scale of the region of resonant particle interaction with the unstable mode is defined as a scale of particle demagnetization, i.e. a local particle gyroradius $\rho(z)$ should be larger than the magnetic field inhomogeneity scale L (sheet thickness). For linear approximation $B_x = B_{ext}(z/L)$ the resonant region is $|z| < \sqrt{L\rho_\alpha}$ (Dobrowolny 1968) where $\rho_\alpha = v_{T\alpha}m_\alpha c/|q_\alpha|B_{ext}$ is a particle gyroradius at the boundary, while $v_{T\alpha}$, m_α, and q_α are thermal velocity (the corresponding temperature is T_α), mass, and charge of particles α ($\alpha = e$ for electrons, $\alpha = i$ for ions). Thus, in the Harris (1962) sheet there are two resonance regions: a small-scale electron region is embedded into the ion region (see Fig. 7.2). For the unstable mode, the electron resonant current $j_{res,e} = (\gamma/kv_{Te})\sqrt{\pi}(1 + T_i/T_e)^{-1}A_{1y}/\rho_e^2$ dominates (where $A_{1y} \sim \exp(ikx + \gamma t)$ is a perturbation of the vector potential, e.g., Galeev and Sudan 1985). The corresponding growth rate of the electron tearing mode can be found matching solutions of perturbations within the resonance region and in the outer region: $\gamma \sim (v_{Te}/L)(\rho_e/L)^{3/2}$.

The growth of tearing mode results in generation of B_z magnetic field $\delta B_z \sim \partial A_{1y}/\partial x \sim kA_{1y}$. Thus, electrons become magnetized and cannot contribute to the resonant current anymore when $\gamma \sim |q_e|\delta B_z/m_e c$. The corresponding amplitude of δB_z is about $\sim B_{ext}(\rho_e/L)^{5/2}(1 + T_i/T_e) \sim (\rho_i/L)^{5/2}(m_i/m_e)^{5/4}(T_e/T_i)^{1/4}$. For realistic magnetotail conditions $L \leq \rho_i$, $T_e/T_i \sim 3$–5 we have $\delta B_z/B_{ext} < 10^{-4}$. Thus, resonant electrons can trigger the unstable mode, but ion resonant currents

are necessary for following growth of magnetic field perturbations up to realistic level $\delta B_z/B_{ext} \sim 1$.

Schindler (1974) admitted that in the realistic magnetotail a finite $B_z \sim 0.1B_{ext}$ should magnetize electrons and, thus, the initial CS is stable to the electron tearing mode. As a result, the ion resonant current should trigger the tearing, while the corresponding growth rate is about the ion gyrofrequency $\omega_i = |q_i|B_{ext}/m_i c$. Starting with the Schindler (1974) paper, the long story of investigation of the ion tearing mode in the Earth magnetotail began. Already after 2 years Galeev and Zelenyi (1976) showed that the magnetization of electrons by B_z field not only destroys the electron tearing mode, but also significantly influences the ion mode. The tearing instability assumes the perturbation of B_z magnetic field component δB_z, and should result in the perturbation of the density of magnetized electrons $\delta n_e \sim n_0 \delta B_z/B_z$ (where n_0 is an unperturbed plasma density). The quasineutrality condition requires the same perturbation of the ion density $\delta n_i \approx \delta n_e$, while unmagnetized ions are distributed in the resonant ion region according to the Boltzmann distribution with $\delta n_i \sim n_0(q_i\varphi/T_i)$. Here φ is a perturbation of a scalar potential due to decoupling of electron and ion motions in the perturbed magnetic fields. Thus, the development of the ion tearing mode requires the generation of $\varphi \sim q_i T_i(\delta B_z/B_z)$. This is rather strong electrostatic potential and, the initial system (equilibrium CS) may not have enough free energy (energy of current filament attraction) to generate this potential. In this case, the magnetotail CS is stable to the ion tearing mode. Of course, these estimates are rough and more details can be found elsewhere (Galeev and Sudan 1985; Schindler 2006; Treumann and Baumjohann 2013).

Besides the effect of electron magnetization, the inclusion of B_z component results in additional problems for the tearing mode. The B_z component is responsible for the magnetic tension force $\sim B_z j_y$ acting on plasma at the neutral plane (where $(4\pi/c)j_y \approx \partial B_x/\partial z$). To balance this force one can introduce a plasma pressure gradient $\partial p/\partial x$ for isotropic plasma or a curvature force $4\pi(p_\parallel - p_\perp)B_z j_y/B^2$ for anisotropic plasma (Rich et al. 1972; Hill 1975). For kinetic models with the full pressure tensor the curvature force takes a form $\sim \partial p_{xz}/\partial z$ (Ashour-Abdalla et al. 1994). Thus, the simplified modification of the isotropic (Harris 1962) model with B_z represents a 2D plasma equilibrium (Schindler 1972; Kan 1973; Lembege and Pellat 1982). Investigation of the tearing mode in such 2D CS requires taking into account additional constraints (Schindler et al. 1973). The first constraint comes from the requirement that the average value of the first order perturbation of the particle distribution function should be equal to zero $\langle f_{1j} \rangle = 0$ where the averaging is performed over (x, z) space. For 1D models with f_{0j} depending only on z, the first order perturbation depends on x periodically $f_{1j} \sim \exp(ikx)$ and the requirement $\langle f_{1j} \rangle = 0$ is satisfied automatically. However, for 2D models $f_{1j} = \tilde{f}_{1j}(x)\exp(ikx)$ this condition can be satisfied only for some particular perturbations. The second constraint comes from the quasineutrality condition in 2D system (Schindler et al. 1973). The combination of these two constraints gives the following criterion for

the total energy of the tearing mode in CS (Schindler 2006):

$$W \geq \frac{1}{2}\int\left(\frac{|\nabla A_{1y}|^2}{4\pi}+\frac{1}{c}\frac{dj_y}{dA_y}|A_{1y}|^2+p|Q_1|^2\right)dxdz \tag{7.1}$$

where A_y is the unperturbed component of the vector potential. If integral in Eq. (7.1) is positive, then the total energy of perturbation is positive and the development of tearing mode is not energy effective. The necessary condition for the tearing instability is a negative value of this integral. The first term in (7.1) corresponds to the magnetic energy of the tearing mode (i.e. this energy is required to generate the magnetic field perturbations). The second term is a free energy of the current filament attraction (this negative term is responsible for CS instability). The last positive term includes all constraints and depends on spatial distribution of the perturbation

$$Q_1 = \frac{1}{\int ds/B}\frac{d}{dA_y}\int A_{1y}\frac{ds}{B} \tag{7.2}$$

where the integrals are taken along the unperturbed magnetic field lines.

For 2D modification of Harris (1962) model, Lembege and Pellat (1982) estimated (7.2) and rewrote condition (7.1) as: $kL < (4/\pi)(B_z/B_{ext})$. Thus, for 2D models only rather large wavelength modes with $\lambda = 2\pi/k > L(B_{ext}/B_z)(\pi^2/2)$ could be unstable. However, such a large wavelength already cannot be considered in WKB regime ($\lambda \ll L_x$ where $L_x \approx 2L(B_{ext}/B_z)$ is a spatial scale of CS inhomogeneity along x-axis). Thus, only a full description of the CS stability relative to the tearing mode should be used and Goldstein and Schindler (1982) showed that 2D CS becomes unstable relative to the tearing for $\lambda > L_x$. However, such modes are not of interest in the magnetotail, because spatial scales $L_x \sim 5$–$10R_E$ (Artemyev et al. 2011; Artemyev and Zelenyi 2013) significantly exceed reasonable estimates of scales of the X-line region (e.g., Alexandrova et al. 2012). Thus, the applicability of the theory of the tearing instability as a key factor for triggering the magnetosphere substorms was questioned (Pellat et al. 1991; Quest et al. 1996; Brittnacher et al. 1998).

The essential element of the CS stabilization relative to the tearing mode is a perturbation of the electrostatic potential due to electron magnetization by B_z field (in many papers this effect is called *electron compressibility*). Pitch-angle diffusion (Coroniti 1980) and stochastization of electron motion due to scattering in the CS neutral plane (Büchner and Zelenyi 1987; Kuznetsova and Zelenyi 1991) cannot decrease this effect due to the conservation of a number of the electrons in the flux tube (Brittnacher et al. 1994, 1998).

Thus, alternative ways for CS destabilization should be considered. The first way corresponds to the magnetic energy dissipation due to particle heating by turbulence. This approach introduces a so-called effective resistivity via wave-particle interaction. Besides the effective resistivity, there are two ways to make energy W from Eq. (7.1) negative: one can try to increase the absolute value of the free energy

dj_y/dA_y or decrease the stabilizing effect of $\sim Q_1^2$ term. Below we present a short review of such ways: in Sect. 7.2.1 we discuss the effect of wave-particle interaction (this effect does not directly modify terms in Eq. (7.1), but increases the effective currents of resonant particles Zelenyi and Artemyev 2013), Sect. 7.2.2 is devoted to the increase of the free energy due to peculiarities of the current generation, in Sect. 7.2.3 we describe effects related to the modification of $\sim Q_1^2$ term.

7.2.1 *Effective Resistivity Produced by Strong Wave Activity*

Observations of various waves near the reconnection region (review of Fujimoto et al. 2011) suggest that charged particle scattering in the momentum space by these waves can be responsible for generation of an effective resistivity (Yoon and Lui 2006; Büchner 2007, and references therein) supporting the reconnection process. Including the effective resistivity due to wave-particle interactions into the reconnection models is rather popular idea in the magnetospheric physics due to the absence of a collisional dissipation. The corresponding effective resistivity can be defined as $\eta_{eff} = m_e \nu_{eff}/ne^2$ where n is plasma concentration and ν_{eff} is the effective collisional frequency depending on the integral of the energy density of waves $\Upsilon(k)$ (Galeev and Sagdeev 1979). The main problem with direct implementation of the equations for ν_{eff} is a lack of information about the spectrum of wave energies $\Upsilon(k)$. Such information can be obtained from theoretical models or spacecraft observations if a time variations of electromagnetic fields can be transformed into spatial variations (e.g., Narita et al. 2014).

For a long time, lower-hybrid drift (LHD) waves were considered as one of the most promising wave modes significantly contributing to the effective resistivity (Huba et al. 1977). The lower-hybrid drift mode is driven by gradients of plasma density and magnetic fields and differences in electron and ion drifts . The simplified expression of the corresponding resistivity was proposed by Davidson and Gladd (1975)

$$\eta_{eff} \approx 2^{1/2}\pi^{3/2}\sqrt{\frac{m_i}{m_e}}\frac{\omega_e}{\omega_{pe}^2}\frac{\Upsilon}{nT_i} \tag{7.3}$$

where ω_e, ω_{pe} are electron gyrofrequency and plasma frequency, and Υ is a density of wave electric field energy. However, initial estimates of a realistic η_{eff} value showed that the observed level of LHD waves in the magnetotail is insufficient to trigger the magnetic reconnection (Coroniti 1985). This estimate was confirmed recently by Eastwood et al. (2009).

Moreover, the LHD instability is significantly suppressed in the central region of CS where the magnetic field is weak (Huba et al. 1980). Thus, additional factors should be taken into account, e.g. the long-wavelength electromagnetic mode of LHD (Daughton 2003), the strong electric field (Malkov and Sotnikov 1985), the

finite normal magnetic field component (e.g., Lui 2004, and references therein), or the effect of the finite electron gyroradius in the vicinity of the CS neutral plane (so called Pitaevskii effect which transforms ν_{eff} to $\nu_{eff}(k\rho_e B_{ext}/B_z)^2$ for $k\rho_e > B_z/B_{ext}$ see Zelenyi and Artemyev 2013, and references therein). All these effects can contribute to the effective resistivity supporting magnetic reconnection process (Daughton et al. 2004; Ricci et al. 2004a; Silin et al. 2005) or can be included into the theory of the tearing mode (Zelenyi and Artemyev 2013). Besides LHD waves, other wave types (Hasegawa 1971; Mikhailovskii 1974) can contribute to effective resistivity, e.g. Chaston et al. (2009) and Huang and et al. (2012) suggested that kinetic Alfven waves can provide rather high level of particle scattering in the reconnection region.

7.2.2 Peculiarity of Ion Kinetics: Transient Particles

To increase the free energy $\sim dj_y/dA_y$ in the energy functional W [see Eq. (7.1)] one can reconsider the internal CS structure. The Harris (1962) CS model (and many modifications of this model, see Schindler and Birn 2002; Camporeale and Lapenta 2005; Liu et al. 2010) considers the current density j_y generated by the diamagnetic drift due to inhomogeneity of the plasma distribution across CS (Baumjohann and Treumann 1996). Thus, dj_y/dA_y is determined by a spatial scale L (i.e. the CS thickness). For example, in Harris (1962) CS model we have

$$\frac{1}{c}\frac{dj_y}{dA_y}\bigg|_{z=0} = \frac{j_0}{B_x(z)}\left(\frac{d}{dz}\frac{1}{\cosh^2(z/L)}\right)_{z=0} \sim -\frac{2j_0}{B_{ext}L} = -\frac{1}{2\pi L^2} \tag{7.4}$$

where current density amplitude is $j_0 = (c/4\pi)B_{ext}/L$. Thus, the decrease of L results in the increase of the current density as $1/L^2$ [Eq. (7.4) shows that L is a single free parameter influencing the free energy], but simultaneously the term $\sim Q_1^2$ increases as $k/L \sim kL/L^2$ (see Lembege and Pellat 1982). The Q_1^2 increase is the effect of the simplified (Harris 1962) model, for which the current density amplitude is regulated by CS thickness L alone. Therefore, the problem of the increase of the free energy can be formulated as: is there a possibility to increase j_0 with fixed L? Because the integral of $j_y(z)$ along $0 < z < L$ should give $(c/4\pi)B_{ext}$, we need to redistribute the current density within the spatial scale $\sim L$.

Such current density redistribution can be achieved, for example, with the presence of so-called transient particles. Speiser (1965) showed that in the magnetic field reversal with $B_z \neq 0$, unmagnetized charged particles (particles with gyroradii comparable with a spatial scale of the B_x inhomogeneity) can move along open orbits (see the example in Fig. 7.3a). The analytical theory of the transient particle motion (Büchner and Zelenyi 1986, 1989) suggests that these particles are moving along open orbits without significant scattering in the CS, when the adiabatic parameter $\kappa = (B_z/B_{ext})\sqrt{L/\rho_i}$ is small enough. This parameter determines the chaotization rate of particle motion (e.g. diffusion of particle pitch angles) and for

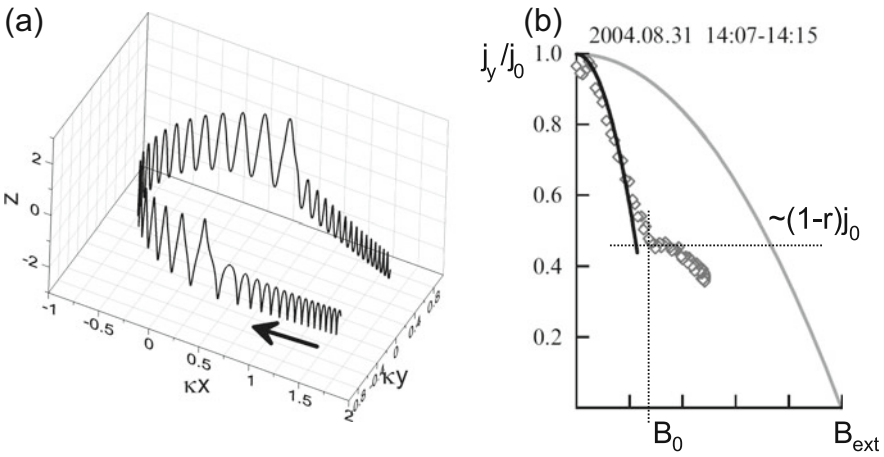

Fig. 7.3 Trajectory of Speiser proton (**a**) and profile current density measured in the magnetotail CS (**b**). *Black curve* shows approximation $j_y \sim 1 - r(B_x/B_{ext})^2$, while *grey curve* shows the Harris (1962) model with $j_y \sim 1 - (B_x/B_{ext})^2$. The *diamonds* denote the observed profile (see details in Zelenyi et al. 2010)

$\kappa \sim 1$ even initially transient particles likely will be trapped within CS (see review by Zelenyi et al. 2013). Thus, transient particles can be present in thin CSs with small L or in CSs with very stretched field lines (small B_z/B_{ext}).

As Fig. 7.3a shows, a transient particle makes a half of gyrorotation in the CS neutral plane $z = 0$ and escapes from the CS. Thus, these particles carry a very strong current in the CS center $j_{sp} \sim en_{sp}v_{Tsp}$ (Eastwood 1972, 1974) where n_{sp} is a concentration of transient (Speiser) particles and v_{Tsp} is the corresponding thermal velocity. There are several numerical (Burkhart et al. 1992a; Pritchett and Coroniti 1992; Mingalev et al. 2007) and analytical (Sitnov et al. 2000, 2006; Zelenyi et al. 2000, 2011) CS models including a population of transient ions. These models show the formation of strong maximum of the current density with a spatial scale $\sim\rho_i$. Spacecraft observations in the Earth magnetotail demonstrate that similar thin CSs really exist (e.g., Petrukovich et al. 2015, and references therein).

Intense thin CS generated by transient protons (sometimes with a significant contribution of oxygen ions,e.g., Kistler et al. 2005; Artemyev et al. 2009) should be embedded into thick background CS where diamagnetic currents dominate. Thus, in the diagram (j_y, B_x) we observe double profile of the current density with the clear maximum at the CS center and weaker flanks (see Fig. 7.3b). The effect of CS embedding can significantly influence the tearing mode due to the effective increase of the CS free energy (Burkhart et al. 1992b; Krallmann et al. 1994; Schindler 2006). To demonstrate this effect we use a simplified model of embedded CS with the current density profile

$$j_y = j_0 \begin{cases} 1 - r(B_x/B_0)^2, & |B_x| < B_0 \\ (1-r)\frac{\left(1-(B_x/B_{ext})^2\right)}{1-(B_0/B_{ext})^2}, & B_{ext} < |B_x| < B_0 \end{cases} \tag{7.5}$$

where B_0 is the magnetic field amplitude at the thin CS boundary (see Fig. 7.3b) and $j_0(1-r)$ is the current density at the thin CS boundary. Substituting Eq. (7.5) to the free energy term from Eq. (7.1), we get

$$W_{free} = \frac{1}{c}\int \frac{dj_y}{dB_x^2}|A_{1y}|^2 dB_x dx \approx -\frac{j_0 r}{cB_0}\int |A_{1y}|^2 dx \tag{7.6}$$

where we use $d/dA_y = (d/dB_x)/B_x$, $dz = dB_x/(dB_x/dz)$ and integrate over the central CS region $|B_x| < B_0$, where $|A_{1y}|$ is significant (Schindler 2006). For comparison, for the same region of integration $|B_x| < B_0$ the Harris (1962) CS model with $j_y = j_0(1-(B_x/B_{ext})^2)$ gives

$$W_{free,H} \approx -\frac{j_0 B_0}{cB_{ext}^2}\int |A_{1y}|^2 dx \tag{7.7}$$

Thus, the comparison of the free energy in thin embedded CS (7.5) and in Harris (1962) CS (7.7) gives the factor $l = W_{free}/W_{free,H} = (B_{ext}/B_0)^2 r$. Zelenyi et al. (2010) showed that for embedded CSs observed in the Earth magnetotail this factor l reaches 3. Therefore, realistic multiscale CS (thin CS embedded into thick background CS) can have more free energy necessary for the tearing mode than the original (Harris 1962) CS model and its modifications (Schindler 1972; Lembege and Pellat 1982; Kan 1973).

One additional advantage of the thin CS with transient particles is establishment of a horizontal pressure balance along x-axis even in 1D case with finite B_z. The transient ions move along field lines and generate significant pressure anisotropy with $p_\parallel > p_\perp$. If the population of transient particles is large enough, the pressure anisotropy can reach the critical level $p_\parallel - p_\perp \approx B^2/4\pi$. Moreover, the contribution of anisotropic electrons also can be substantial in the Earth magnetotail, where $p_{\parallel,e}/p_{\perp,e}$ is often larger than 1.2 (Artemyev et al. 2014). Observation of the ion anisotropy is complicated due to effect of CS embedding when ~80 % of particles belong to the isotropic background population which does not contribute to the pressure balance at a scale of the thin inner CS (Artemyev et al. 2010; Artemyev and Zelenyi 2013). However, at active regions spacecraft observe a finite p_{xz} component of the ion pressure tensor (Aunai et al. 2011) indicating the presence of the transient population.

The balance of thin CS with anisotropic pressure tensor $p_\parallel - p_\perp \approx B^2/4\pi$ excludes the necessity of gradients along it (i.e. $\partial p/\partial x = 0$) (Burkhart and Chen 1993). Thus, the system can be described by a 1D equilibrium with $B_z \neq 0$. Such CS models with transient ions (Sitnov et al. 2000; Zelenyi et al. 2000) are developed as the asymptotic solutions of Vlasov equation for $B_z/B_0 \ll 1$. In this case, $\kappa \ll 1$ and ion dynamics can be described with an additional adiabatic invariant corresponding to the averaging over fast particle oscillations in B_x field (see review Zelenyi et al. 2013). As a result, the condition for tearing perturbation $\langle f_{1j}\rangle = 0$ is satisfied automatically (Zelenyi et al. 2008) and the system becomes more unstable relative to the tearing mode.

The linear theory of the tearing instability in a thin CS with transient particles predicts that increased free energy can overcome stabilizing effect of magnetized electrons within a finite region in the parametric space $(L/\rho_i, B_z/B_0)$: the tearing mode can potentially develop in $L/\rho_i \leq 1$ and $B_z/B_0 \in [0.05, 0.25]$ (Zelenyi et al. 2010). For $B_z/B_0 < 0.05$ (but $B_z/B_0 > 10^{-4}$, so electrons are magnetized) perturbations of electron density become so strong that Q_1 term dominates and CS is stable relative to the tearing mode. It is interesting to note that CS observed by Cluster spacecraft in the course of thinning (i.e. formation of thin CS) move in the plane $(L/\rho_i, B_z/B_0)$ toward the region of instability, while the thin CS observed under quiet conditions are located out of instability region (Artemyev et al. 2008; Zelenyi et al. 2010).

7.2.3 A Local Maximum of B_z

The absence of regular and reliable spacecraft observations of the ion pressure anisotropy in the magnetotail (Stiles et al. 1978; Walsh et al. 2011) encourages to search for a mechanism of 2D CS destabilization without introduction of a significant transient particle population. Equation (7.1) shows that a possible way is to decrease the stabilization term $\sim Q_1^2$. Thus, we come to the problem of development of a CS model with small enough term (7.2). This term essentially depends on the configuration of magnetic field lines, e.g. the necessary condition of the tearing instability can be written as $kL < \pi(B_z/B_{ext})H^2$ with $H = VB_z/\pi L$ and $V = \int ds/B$ is the flux-tube volume (Schindler 2006). The wide variety of weakly 2D CSs (with $B_z/B_0 \ll 1$) is described by the following magnetic field components (Schindler 1972; Lembege and Pellat 1982; Zwingmann 1983)

$$\begin{aligned} B_x &= B_{ext} \tanh\left(z/Lg(x)\right) \\ B_z &= -\frac{B_{ext}L}{g(x)}\frac{dg(x)}{dx}\left(1 - \frac{z}{Lg(x)}\tanh\left(z/Lg(x)\right)\right) \end{aligned} \tag{7.8}$$

where the function $g(x)$ determines the B_z amplitude: $B_z/B_{ext} \sim L(d\ln g(x)/dx)$. The condition $B_z/B_{ext} \ll 1$ means that $g(x)$ depends weakly on x. Several examples of CSs for different $g(x)$ are shown in Fig. 7.4. For $g = 1$ we obtain the Harris (1962) CS model, while for $g = \exp(\varepsilon x/L)$ with $\varepsilon \ll 1$ we get the Lembege and Pellat (1982) CS model.

For the Lembege and Pellat (1982) CS model, the flux-tube volume is $V \approx L\pi/B_z$ (Lembege and Pellat 1982). Thus, $H = 1$ and the necessary condition for the tearing mode $kL < \pi(B_z/B_0)$ could be satisfied only for large wavelengths. However, Sitnov and Schindler (2010) showed that this condition can be changed for a modified $g(x)$ function $g = \exp(\varepsilon h(x))$ with

$$h = \frac{x}{L} + \frac{\alpha}{\tilde{\varepsilon}}\left(1 + \tanh\left(\tilde{\varepsilon}(x - x_0)/L\right)\right) \tag{7.9}$$

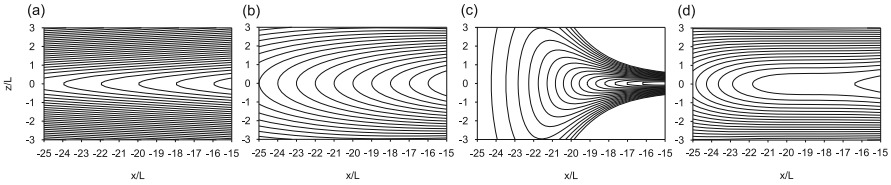

Fig. 7.4 Field lines of CS models: (**a**) Sitnov et al. (2000), Zelenyi et al. (2000) with $B_z = const$, (**b**) Lembege and Pellat (1982) with $B_z \sim 1/x$, (**c**) Sitnov and Schindler (2010) with (7.9), (**d**) Pritchett and Coroniti (2010) with a local B_z minimum

where $1 \gg \tilde{\varepsilon} \gg \varepsilon$ and α is a constant parameter, while x_0 determines the position of a local B_z maximum (see Fig. 7.4). The amplitude of the B_z maximum in the neutral plane $z = 0$ is $\sim 1 + \alpha$. For this model the flux tube volume can be estimated as $V \approx L\pi/(B_z(1+\alpha))$ (Sitnov and Schindler 2010). Thus, $H = 1/(1+\alpha)$ and the necessary condition for the tearing mode is $kL < \pi(B_z/B_0)(1+\alpha)$. Sitnov and Schindler (2010) showed that 2D CS with the local maximum of B_z could be potentially unstable relative to the tearing mode for a wider wavelength range than the (Lembege and Pellat 1982) CS model. A numerical modeling (Sitnov and Swisdak 2011) demonstrated the development of some analog of the ion tearing mode in 2D CSs with the B_z maximum. However, further investigations showed that dynamics of 2D CS with the B_z maximum is even more complicated and cannot be directly attributed to the classical tearing mode (Sitnov et al. 2013; Bessho and Bhattacharjee 2014).

7.2.4 Local Minimum of B_z and 3D Stability of CS

An alternative 2D CS configuration was proposed by Pritchett and Büchner (1995) to describe CS dynamics in the near-Earth magnetotail (10–15 R_E downtail). In this region the local minimum of the B_z magnetic field can be created by strong currents of hot ions convected toward the Earth by a quasi-stationary electric field (Coroniti and Pritchett 2014). Such 2D CS with the B_z minimum can be described by the same model (7.8) with the specifically chosen $g(x)$ function. The corresponding magnetic field lines are shown in Fig. 7.4.

The local minimum of B_z cannot destabilize CS relative to the tearing mode (as shown in Sect. 7.2.3, the B_z maximum is necessary for this). However, such a CS configuration becomes unstable relative to the ballooning mode propagating as a wave along the dawn-dusk direction (Pritchett and Coroniti 1997). To investigate CS stability to both tearing and ballooning modes, a full 3D simulation is necessary. The development of the ballooning mode in the near-Earth CS with minimum B_z results in strong perturbation of the B_z component: in the region with the inverse B_z gradient, *fingers* of strong/weak B_z are generated and these structures propagate along the dawn-dusk direction (Pritchett and Coroniti 2010). This instability

resembles the interchange instability developing at the boundary of strong magnetic field and plasma, thus, in literature it is called the ballooning/interchange instability. Recent spacecraft observations in the magnetotail (Panov et al. 2012a,b) and the all-sky images (Pritchett et al. 2014) suggest that such instability really can develop in the near-Earth CS.

The nonlinear stage of the ballooning/interchange instability results in very strong perturbations of B_z magnetic field component. Thus, the local decrease of the B_z can be so substantial that localized X-lines occur (Pritchett and Coroniti 2011). This is the alternative scenario relative to that with only the tearing instability. It suggests that CS that are stable relative to the tearing mode can be destabilized by dawn-dusk modes, while these modes in the system with inverse B_z (or, even, with a specific plasma pressure distribution along the magnetotail Pritchett and Coroniti 2013) disturb B_z component eventually resulting in the magnetic reconnection (Pritchett 2013). Such a scenario seems to be unrealistic at the more distant magnetotail ($x < -15R_E$) where the initial B_z is weak, while its gradients are even weaker. However, in the near-Earth tail the scenario of such 3D destabilization of CS looks promising.

7.3 Plasma Sheet Before Reconnection Onset

7.3.1 Onset Location

The location of NENL in the magnetotail, especially the place of its initial formation at substorm onset, is one of the most debated issues in substorm studies (Angelopoulos et al. 2008; Petrukovich 2008; Lui et al. 2008). Besides the importance to the substorm initiation models, the location at a specific downtail distance defines expected initial conditions (see the previous section) for the reconnection-causing instability.

Since direct observations of the reconnection zone are very improbable (e.g., only 30 events during 10 years of Geotail observations, selected by Nagai et al. 2013a), indirect signatures in high-β plasma sheet are used to locate the NENL: (1) Simultaneous observations of oppositely directed plasma flows by two spacecraft separated along the tail axis, allowing to place the origin point between the spacecraft or even to perform back tracing of flows to fix exact location (e.g., Petrukovich et al. 1998). Such an occasion is also rather improbable. (2) The reversal of plasma flow V_x and magnetic field B_z in high-β plasma sheet is interpreted as a moving (usually downtail) active reconnection zone. (3) The tailward flow with negative B_z is interpreted as reconnection Earthward from spacecraft. (4) The Earthward flow interpreted as reconnection tailward from spacecraft. Variants #2–3 are the most useful, since the proximity of the NENL to Earth is of the main interest. Outside of high-β plasma sheet a judgement on the NENL location in the case studies can be based on energetic plasma flows (Angelopoulos et al. 2008) or

specific magnetic signatures (travelling compression regions Sharma et al. 2008). Finally it is also important to note, that an observation of a tailward plasma flow as such (without supporting evidence) is not the ultimate signature, since other causes of such flows exist, like rebound of the Earthward flow (e.g., Panov et al. 2010).

Early observations suggested a downtail distance about 10–15 R_E as the NENL initial location (McPherron et al. 1973; Hones et al. 1986; Sergeev et al. 1995). Later extensive statistics of Geotail data have shown that the most probable observations of reconnection are beyond 20–25 R_E (Miyashita et al. 2003; Machida et al. 2009). Miyashita et al. (2004) specified that for stronger substorms, tailward flows are first observed as close as 17 R_E. Baumjohann et al. (1999) with a superposed epoch study, pointed to a tailward flow formation at 20 R_E at a substorm onset with the later downtail shift.

Double spacecraft techniques as well as specific case studies suggest however typical downtail locations 12–16 R_E even for small substorms and pseudo-breakups (Petrukovich et al. 1998, 1999; Petrukovich and Yahnin 2006, and references therein). Cluster project statistics for 2001–2007 also revealed frequent observations of tailward flows with reconnection signatures at 16 R_E and even closer in the premidnight sector; however, often with the lower tailward flow speed down to 100–200 km/s (as compared with the more typical threshold 400 km/s) (Petrukovich et al. 2009) (Fig. 7.5).

The Geotail statistics are not necessarily in contradiction with other results. One needs to take into account temporal evolution of reconnection. In the near-Earth tail

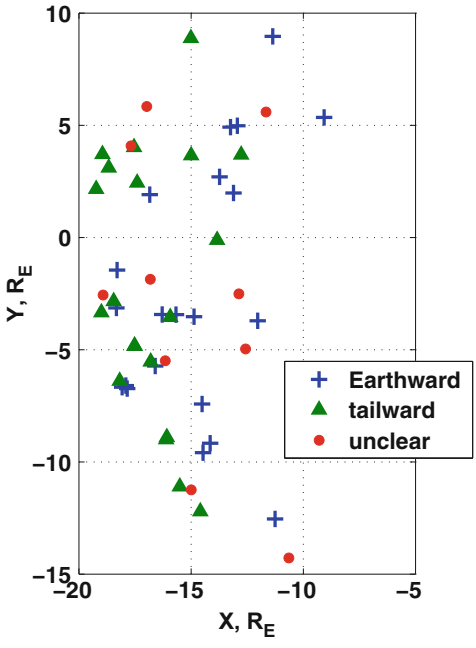

Fig. 7.5 Locations of flow registration and flow directions (Earthward, tailward and unclear, see details in Petrukovich et al. 2009). Figure adapted with permission from Petrukovich et al. (2009). Copyrighted by John Wiley and Sons

($\sim$15 R_E) reconnection starts deep inside plasma sheet on the closed field lines with dense plasmas and should promptly cease or shift downtail due to pile-up of the reconnected magnetic flux on the Earthward side (Baumjohann et al. 1999). Since the reconnection speed is proportional to Alfven velocity in the inflow zone, such an initial reconnection pulse has rather low outflow velocity and is rather ineffective in unloading. For example a 200 km/s outflow velocity for a typical plasma sheet corresponds to B_x $\sim$5–10 nT in the inflow zone (Petrukovich et al. 2009).

On the other hand, in the middle tail (beyond 20 R_E) the plasma sheet is thinner, the tailward retreat is slowed down (tailward flows are observed within 45 min after onsets Baumjohann et al. 1999). Here the reconnection pulse is able to promptly involve open (lobe) magnetic field lines, resulting in more efficient energy conversion. Lobe field reconnection with the order of 1000 km/s outflow speed starts faster. Substorms indeed often have several activations, initial low-latitude onsets, likely corresponding to the near-Earth reconnection, and subsequent higher latitude stronger intensifications, corresponding to middle tail reconnection pulse (Mishin et al. 2001).

Therefore it is more probable to observe reconnection in the middle tail in agreement with the general Geotail statistics. However, studies targeted at the initial pulse localisation and weaker flows may point to more near-Earth locations. The recently launched NASA MMS mission, aimed at reconnection electron diffusion zone has the 25 R_E apogee (for the second stage) to maximize the probability of reconnection observations.

7.3.2 Current Sheet Structure

Parameters of current sheet before reconnection onset are of primary interest to theory, since they help to determine instability criteria. Relevant characteristics of current sheet are normal magnetic field B_z, intensity of current sheet and/or its thickness as well as gradients of these parameters along the tail axis.

With a single spacecraft only B_z is well measured. During a growth phase B_z decreases down to 1–2 nT in a wide range of downtail distances (up to geostationary orbit for very strong solar wind driving), what is interpreted as stretching of the magnetic configuration due to general intensification of cross-tail current. It is accompanied by plasma sheet thinning due to pressure build-up in the magnetotail (McPherron et al. 1973; Caan et al. 1978; Baker et al. 1996). It was possible to determine thickness only indirectly, by analyzing the probability of a high-β plasma sheet observation (e.g., Baumjohann et al. 1992).

Only with the two-spacecraft mission ISEE have the current sheet thickness and current density been determined directly for several events (Sergeev et al. 1990, 1993; Sanny et al. 1994; McComas et al. 1986). It was shown, that during the late growth phase a very thin current sheet (with a scale of proton larmor radius) was formed inside a much wider background plasma sheet (so called embedded configuration).

Cluster data were used to measure quantitatively and on a regular basis the local current density, and during the later Cluster mission (after 2005) it was also possible to estimate gradients along tail axis (see Petrukovich et al. 2015, for review and method description). First of all, it was demonstrated that embedding is a regular feature. The profile of current density is substantially narrower than that of plasma density (these profiles are identical for Harris model) (Asano et al. 2005; Runov et al. 2006; Petrukovich et al. 2011). The new parameter of such embedded configuration was introduced empirically—magnetic field B_0 at a boundary of thin sheet (Artemyev et al. 2010). Determination of the boundary field is critical to calculate correctly the current sheet thickness. Typical thickness of an embedded sheet was found to be several proton larmor radii. Further approaches to quantification of embedded configuration were discussed by Petrukovich et al. (2011).

The introduction of such an embedded rather than Harris profile as a typical one has several important consequences. The embedded configuration has larger free energy (see Sect. 7.2.2) and thus a problem with tearing instability initiation can be solved. The high-β zone of plasma sheet is then narrower, and reconnection reaches faster the outer plasma sheet field lines, where reconnection effectiveness is much larger. Finally, formation of an intense current sheet is then not identical to thinning of plasma sheet as a whole. This current sheet can arise due to internal reasons (appearance of more efficient current carriers—transient ions, see Sect. 7.2.2) not necessarily directly related with external pressure changes.

On several occasions it was possible to trace current sheet evolution during the growth phase (Thompson et al. 2005; Petrukovich et al. 2007; Snekvik et al. 2012). It should be noted, that the observational task of tracing sheet evolution (that is, being inside a sheet for a long time) is contradictory to the main approach to determination of current sheet parameters (using a fast crossing). Thus for a resolved growth phase observation it is not always possible to determine thickness and B_0 reliably enough. It was found that current density was increasing gradually up to onset but remained moderate within 10 nA/m^2. B_z was stable or decreasing. The variety of conditions before onsets were rather broad: B_z = 1–5 nT, current density—1–10 nA/m^2. (Fig. 7.6). Though quantitative comparison with theory predictions on current sheet stability is not always possible (for the growth phase cases the thickness is not always reliably determined), the current sheet is definitely drifting towards the instability zone in the course of growth phase (Zelenyi et al. 2010).

The highest current density was registered after onsets (e.g., Petrukovich et al. 2009) in agreement with earlier indirect studies (Baumjohann et al. 1992). Typical B_0/B_{ext} ratio before onset was 0.3–0.5, after onsets it increased to 0.5–0.8 (Petrukovich et al. 2011).

With new reconnection initiation models, involving profile of B_z with a local maximum or minimum (see Sects. 7.2.3 and 7.2.4), extensive search of such configuration was done with Cluster and THEMIS multi-point observations. It should be noted however, that modern models require relatively strong B_z gradients before onset (at least 1–2 nT/R_E). Indeed there were couple of times detected with THEMIS mission (Saito et al. 2010). A review of Cluster data did not revealed similar

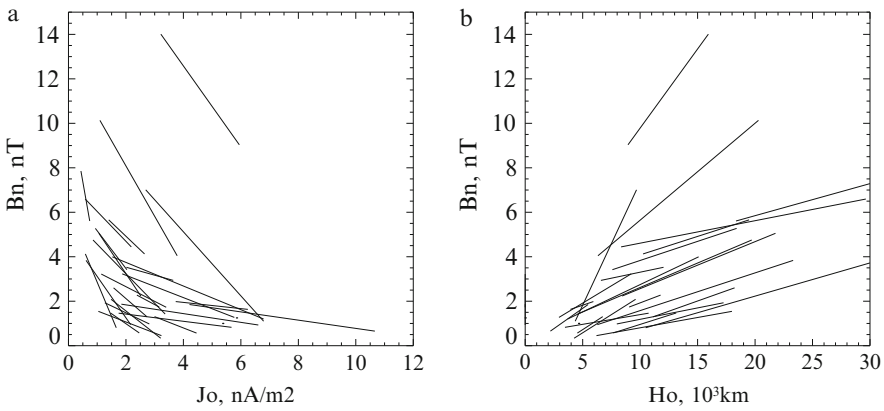

Fig. 7.6 Scenarios of current sheet thinning and stretching in coordinates: current density—normal magnetic field (**a**) and thickness—normal magnetic field (**b**). Only first and last points of growth phase are shown. Thickness is computed using lobe magnetic field and is expected to be overestimated by a factor of 2. Figure adapted with permission from Petrukovich et al. (2007). Copyrighted by John Wiley and Sons

configuration in the near-Earth quiet sheet (with no plasma flows) (Petrukovich et al. 2013). The situation with intense transient local maxima of B_z forming due to incoming dipolarization fronts is much more common. Beyond 15 R_E in stretched current sheet, meso-scale breathing with varying gradient within 0.5 nT/R_E (overall difference in B_z is 1–2 nT) is rather frequently observed.

A relatively weak first pulse of reconnection (not extended enough to cause full-scale substorm expansion phase), similar to that detected by Cluster (Petrukovich et al. 2007), can thus facilitate secondary reconnection both Earthward, by generating extremum of B_z due to magnetic flux pile-up, and tailward, by removing significant part of plasma and magnetic flux from the plasma sheet. Plasma sheet then becomes thinner and susceptible to a stronger subsequent reconnection pulse (Nakamura et al. 2011).

Earlier studies revealed a very wide variety of substorm magnitudes, measured as pressure increases in the magnetotail, as input solar wind energy (coupling function), or ground magnetic disturbance (e.g., Petrukovich 2000, 2003). On one hand, contracted-oval (small) substorms, have often negligible pressure build-up in the magnetotail and close to zero solar wind input (Petrukovich et al. 2000, and references therein). On the other hand, very strong storm-time substorms accumulate energy with orders of magnitude larger than nominal event. Strong increase of pressure and lobe magnetic field creates a very intense current sheet (e.g. Sergeev et al. 1993), which remains stable (throughout a growth phase) with much larger current density, as compared with that during weak events. A notion of the embedded thin current sheet helps to solve the problem with the small substorms. An intense current sheet can form with no increase of external pressure if other conditions are favourable (existence of transient particles). Still the stability of intense current sheets emerging under strong driving remains unclear.

7.3.3 Role of Guide Magnetic Field

The magnetotail configuration in general and reconnection geometry in particular are often considered as 2D with only B_x and B_z magnetic field and X, Z spatial dependence. However in the Earth's magnetotail B_y magnetic field, along the nominal electric current direction (guide or shear component), is also present due to IMF influence (Fairfield 1979; Petrukovich 2011, and references therein).

The guide magnetic field can effectively influence the properties of the magnetotail current sheet and reconnection rate. Even a small guide field changes significantly dynamics of resonant electrons resulting in modification of CS stability criteria (Galeev et al. 1986; Daughton and Karimabadi 2005). Particle dynamics changes from quasi-adiabatic (in a thin sheet) to stochastic, the differences between north-bound and south-bound particle trajectories appear, causing substantial asymmetry in the current sheet structure and particle drifts (Petrukovich 2011, and references therein). More detailed analysis of reconnection with substantial guide field configuration is usually performed for magnetopause geometry.

Although linear stability of current sheets is influenced by the guide field, the numerical simulations demonstrate that the nonlinear reconnection rate is not substantially modified in presence of moderate guide field (Ricci et al. 2004b; Pritchett and Coroniti 2004). However, the configuration of the reconnected current sheet differs for guided field and anti-parallel configurations. In a case of initial nonzero guide field, the familiar quadrupolar magnetic structure of the reconnection region is substantially skewed (Pritchett and Coroniti 2004) (see also the next section). This effect is especially important because the quadrupole magnetic configuration is often considered as a marker of reconnection region in observational data (Eastwood et al. 2010).

Generally a configuration with a significant guide field in the initial quiet magnetotail was considered as relatively rare and thus unimportant. B_y in the plasma sheet is usually related to the IMF B_y. For a typical penetration efficiency in the mid-tail of 0.3 and an average IMF $|B_y| \sim 5$ nT, the expected B_y is 1–2 nT, smaller than the usual B_z. A detailed investigation of Geotail data showed however a more complicated scheme (Petrukovich 2011). First of all, besides IMF penetration, an additional regular contribution to B_y is provided by increased interhemispheric currents during solstices. In the premidnight sector within 20 R_E it is comparable to the IMF contribution. The second aspect is a substantial amount of observations of an "amplified" B_y (much larger than the model-expected, defined somewhat arbitrarily as $|B_y| > 5$ nT, $|B_y| > |B_y^{IMF}|$ for 15-min averages). The share of such data points grows with geomagnetic activity and during solar maximum years reaches 20 % in the premidnight tail within 20 R_E. The duration of large B_y intervals can last for several hours.

Cluster observations of growth phase current sheets during 2001–2004, the years of very strong geomagnetic activity, revealed a 30 % share of large B_y events (Fig. 7.7, note a cloud of points above the bisector, along with a more standard distribution with regression coefficient ~0.4) (Petrukovich et al. 2007). Cao et al.

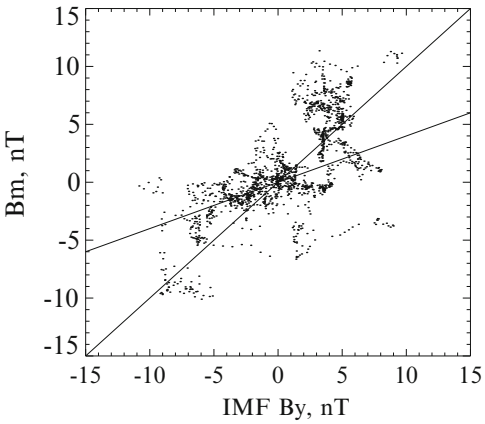

Fig. 7.7 Magnetic component B_m (B_y) relative to IMF B_y. Line $B_m = 0.4 \cdot B_y^{IMF}$ and bisector are shown. Cluster growth phase observations. Figure adapted with permission from Petrukovich et al. (2007). Copyrighted by John Wiley and Sons

(2014) confirmed unusually large IMF B_y penetration efficiency for Cluster data (about 0.6–0.8, ~50 % greater than expected) for a more general data selection.

Any regular differences between properties of guide and anti-parallel current sheets (thickness, intensity, B_z, electric current distribution, etc.) have not been reported up to now. The only difference is domination of the parallel (to magnetic field) component of the cross-tail current in the guide field configuration. However the field-aligned currents in the current sheets are poorly understood by theory at present.

The guide field configuration is more frequent in the near-Earth tail, and is therefore more important to initial reconnection pulses. The mid-tail sheet configuration and reconnection are expected to be mostly with small B_y. Nevertheless a strong guide field is frequently found in reconnection exhausts (plasmoids), which are then called flux ropes (Sibeck et al. 1984; Borg et al. 2012, and references therein). The axial (guide) magnetic field in the ropes is found to have the same sign a that expected in the initial quiet sheet (IMF related). For some cases the guide field may be amplified in the course of plasmoid propagation.

7.4 Observations of Reconnection

An encounter of an X-line in the magnetotail is usually evidenced by the reversal(s) of the tailward-Earthward flow and B_z (normal component of the magnetic field to the current sheet). For a single spacecraft observation, the structure of the reconnection region needs to be inferred by assuming the X-line motion as well as orientation of the current sheet itself. Multi-point observations by Cluster, on the other hand, have an advantage to obtain the spatial gradient (structure) or estimate the motion of the magnetic structures (such as X-line or current sheet). Properties of ion diffusion expected in a 2D magnetic reconnection geometry have been well recovered based on statistical studies (Eastwood et al. 2010, 2013). Individual event

studies, on the other hand, obtained that the current sheet during reconnection can be also significantly tilted from the nominal equatorial plane (e.g., Wygant et al. 2005; Nakamura et al. 2006) or overlaid with a kink-like structure (Laitinen et al. 2007). Furthermore, localized/transient features during magnetic reconnection were found, complicating the standard picture. These include islands/flux ropes inside the thin current sheet (Eastwood et al. 2007; Nakamura et al. 2006, 2008; Retinò et al. 2008; Chen et al. 2008; Teh et al. 2014), or the signatures of the variable reconnection rate (Sergeev et al. 2007; Runov et al. 2008). The complicated dynamics may be partly because of the variable properties of the background current sheet. Note that in contrast to the magnetopause, which is a permanent plasma boundary driven directly by the solar wind, the magnetotail current sheet is affected by internal processes as well as external drivers.

In the following we highlight examples of Cluster multi-point observations of the thin ion-scale current sheets near the reconnection region showing (1) overall structure of the ion-scale current sheet, (2) small-scale/transient magnetic structures, (3) electron dynamics within the ion-scale current sheet. We discuss the observed signatures of reconnection including peculiar/new features, which may not be explained by a simple X-line encounter, detected from multi-point observations.

7.4.1 Overall Structure of the Reconnecting Ion-Scale Current Sheet

Identification of the spatial structure of the current sheet, i.e. the distribution of the current density across the current sheet, together with the reconnection geometry, is essential to investigate the dynamics of particles in the reconnection site. Rapid vertical crossings of the current sheet were occasionally observed by Cluster during the encounter of the near-Earth magnetotail reconnection region. Cluster data from 2003, with the smallest tetrahedron with about 250 km scale are most suitable to examine the detailed current sheet structure.

Figure 7.8 a, b, d, and e show the current density profiles during rapid crossings (<10 s) of the current sheet plotted against the distance from the neutral sheet determined from the translation velocity. These crossings took place during high-speed flow intervals associated with B_z signatures indicating that the spacecraft were tailward of an X-line at 18:43 UT (Fig. 7.8a, b) and Earthward of an X-line at 1903 UT (Fig. 7.8d, e) on August 24, 2003. The coordinate systems used are denoted in Fig. 7.8c, f. The full thickness of the current sheet for the two crossings was 1.0 and 1.2 c/ω_{pi} (the ion inertia length). The enhanced j_Y of the current sheet of 18:43 UT crossing (Fig. 7.8a), is accompanied by the positive j_X flow perpendicular to the field at the center of the j_Y current sheet, while negative j_X flows along the magnetic field (Fig. 7.8b) at the both outer edges of the j_Y current sheet. This pattern is expected from the Hall current in the ion diffusion region and its closure current, as illustrated in Fig. 7.8c (taken from Teh et al. 2011). The possible orbit of the Cluster spacecraft

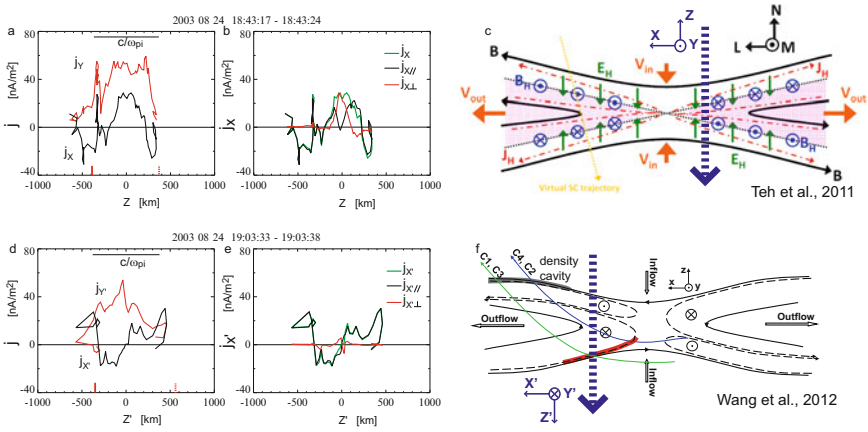

Fig. 7.8 Observation of rapid current sheet crossings near the X-line around 18:43 UT (**a**, **b**) and 1903 UT (**d**, **e**) on August 24, 2003 (from Nakamura et al. 2006). Reconstructed profiles of the cross-tail component (*red line*) and X (Earthward) component of the current density (*solid line*) are shown in panels **a** and **d**, while X component of the current density (*green*) together with components parallel (*black*) and perpendicular (*red*) to the ambient magnetic field are shown in panels **b** and **e**. Schematic view of ion diffusion region (**c**) for a 2D X-line case (from Teh et al. 2011) and (**f**) for a X-line with guide field case (from Wang et al. 2012). The *thick dashed lines* in panel **c** (**f**) illustrates the Cluster orbit with respect to the X-line where the current density profile in panels **a** and **b** (**d** and **e**) can be expected. The coordinates used in **a**, **b** and **d**, **e** are explicitly given in the drawings of **c** and **f**, respectively. Figure adapted with permission from Nakamura et al. (2006), Teh et al. (2011), and Wang et al. (2012). Copyrighted by Springer and John Wiley and Sons

is illustrated by a thick dotted arrow. It should be also noted that the observed profile of j_Y shows further fine structures, which suggest electron scale processes that need to be taken into account.

The current density profile in j'_Y for the 19:03 UT crossing (Fig. 7.8d, coordinate system is defined in Fig. 7.8f) also shows multiple peaks around the center of the current sheet similar to the previous example, but the direction of j'_X is asymmetric with respect to the neutral sheet ($Z' = 0$). That is, positive j'_X in the northern hemisphere ($Z' > 0$), turns negative at equator and then returns earthward at the southern edge. Unlike the previous example at 18:43 UT, this j'_X current almost exclusively flows along the magnetic field projected in the $X'Z'$ plane (Fig. 7.8e). This current sheet is nearly vertical and as a result, an effective guide field $B'_Y > 0$ is present. Accordingly, the pattern of currents j'_X and j'_Y is typical for a guide-field reconnection distorted quadrupole structure (Fig. 7.8f). The guide field was detected also during a number of the observations of magnetotail reconnection (Øieroset et al. 2001; Nakamura et al. 2008; Eastwood et al. 2010; Aunai et al. 2011; Wang et al. 2012). The presence of the guide field component in the reconnection zone may be related to the structure of the pre-onset current sheet (see Sect. 7.3.3).

While the overall spatial distribution of the ion-scale current sheet determined from the magnetic field observations was that expected from the X-line geometry

with or without guide field, the corresponding plasma observations, particularly for the guide-field case, did not necessarily follow the results expected from theory or simulation. Numerical simulations for the guide field case (e.g., Pritchett and Coroniti 2004) showed that the outward electron flow region was expected to be an intense current layer centered at one hemisphere, while a density cavity dominates the other side hemisphere, depending on the guide field direction. In a geometry such as shown in Fig. 7.8f, the intense current layer corresponds to the upper part ($Z > 0$ or $Z' < 0$) and the density cavity at the lower part for the Earthward flow side (left part).

It is interesting to note, however, that for the asymmetric case in the study by Wang et al. (2012), a strong thin intense current sheet region was found near the separatrix at the southern hemisphere (red region in Fig. 7.8i). Further more a density cavity region was found near the separatrix at the northern hemisphere (black region), which is an opposite sense from those reported in the simulation works with the stronger guide fields. It is suggested that in the observed case with the relatively weak guide field, an electron current loop is produced as a consequence of the Hall-current pattern as in a 2D reconnection case, but the current loop is only distorted due to the existence of a weak guide field (Wang et al. 2012, 2014).

In a case of weaker guide field, such different current structures were also predicted in the simulation (Lapenta et al. 2011; Le et al. 2013), particularly showing prolonged asymmetric electron current layer in the outflow region due to the electron pressure anisotropy (Egedal et al. 2013). The profile in Fig. 7.8d indeed shows a three peak current sheet of j'_Y concentrated at one hemisphere, supporting the sense of the asymmetry seen in the simulation by Egedal et al. (2010). The corresponding particle anisotropic signatures in these embedded current layers inside the ion-scale current sheet have the time scale less than 8 s (Fig. 7.8a, b or c, d) and are expected to be resolved in the MMS mission.

7.4.2 Small-Scale/Transient Magnetic Structures

Observation of an X-line usually reveals a mixture of localized/short-time scale disturbances in B_z component, which can be interpreted as multiple flux rope type signatures within the thin current sheets. Having multiple spacecraft within the thin current sheet enables characterization of these structures.

Cluster data for the flow reversal and B_z reversals during the current sheet crossing are shown in Fig. 7.9 (adapted from Wang et al. 2014). In this interval, spacecraft crossing of an ion diffusion region from tailward to Earthward was identified basing on the highly correlated reversals of B_z and V_{px}, the clear quadrupolar Hall magnetic structure (Wang et al. 2014). The speed of this current sheet crossing was rather slow ($>$ 6 times slower than the rapid crossing event discussed in the previous section) so that the reversals of Earthward-tailward flow and B_z sign were well observed in this ion diffusion region. Furthermore, the spacecraft were distributed up to about 4000 km across the current sheet so that

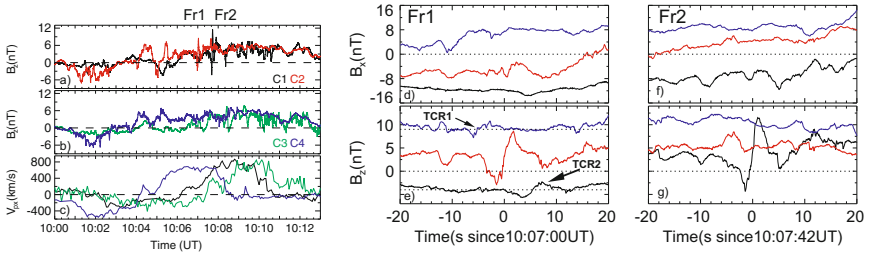

Fig. 7.9 Cluster observation of the reconnection event between 10:00 to 10:13 UT on 28 August 2002: B_z component of the magnetic field from (**a**) C1 (*black line*) and C2 (*red line*) and from (**b**) C3 (*green line*) and C4 (*blue line*), (**c**) x component of proton bulk flows V_{px} from C1, C3, and C4. *Fr*1 and *Fr*2 denote the two flux-ropes/islands. B_x and B_z around *Fr*1 and *Fr*2 are displayed in (**d**) (**e**) and (**f**) (**g**), respectively, from C1 (*black*), C2 (*red*), and C4 (*blue*). Figure adapted with permission from Wang et al. (2014)

the evolution of the embedded magnetic structures within the thin current sheet could be monitored. Clear bipolar magnetic signatures with the sign change were observed by C2 (red) and C1 (black) in the central plasma sheet (10:07 and 10:09 UT, Fig. 7.9a), marked as *Fr*1 and *Fr*2, respectively. They can be interpreted as two small flux ropes, originating after two reconnection pulses. An expanded view of the magnetic field disturbance around *Fr*1 and *Fr*2 are shown in Fig. 7.9d, e and f, g, respectively. Perturbations in the B_z component observed at C2 for *Fr*1 and at C1 for *Fr*2 exhibit asymmetric features with the negative amplitude smaller than the positive amplitude. Although it is tempting to interpret *Fr*1 and *Fr*2 as the same structure propagating Earthward (Note that C1 was located about 2300 km Earthward of C2), these two B_z signatures are likely of different origin. From the minimum variance and timing analysis, it was obtained that the average velocity of these *Fr*1 signatures between C4 and C2 was 416 km/s and between C2 and C1—457 km/s. The scale size was inferred to be comparable to the spacecraft distance, which was 4126 km in X and 1737 km in Z direction. For *Fr*2 C2 observed only a positive B_z peak, while C1 observed a bipolar B_z profile. These different profiles among the spacecraft for Fr2 suggest that the magnetic structure *Fr*2 was possibly created between C2 and C1 and then moved earthward. Consequently, only C1 in the earthward side of C2 detected the flux rope with bipolar perturbation, while C2 observed only an enhancement in B_z. Taking into account the possible X-line motion of -56.5 km/s in X-direction, *Fr*2 was interpreted to be formed due to a secondary reconnection at about 38 c/ω_{pi} Earthward of the primary reconnection site, in its earthward outflow jet region (Wang et al. 2014). The duration of this secondary reconnection pulse can then be estimated as approximately one ion gyration period (5 s).

Signatures of variable reconnection rates were also reported in other Cluster observations of reconnection events based on electric field observations (Sergeev et al. 2007; Runov et al. 2008) as well as based on the signatures of dipolarization fronts in the ion diffusion region (Fu et al. 2013). Secondary reconnection, that takes

place spontaneously and transiently in the outflow jet, has been found in numerical simulations (Divin et al. 2007; Sitnov et al. 2009). Note that the plasma sheet fast flows, called bursty bulk flows (BBF), show 10-min timescale flow enhancements, with embedded 1-min duration velocity peaks called flow bursts (Baumjohann et al. 1989; Angelopoulos et al. 1992). Whether these individual flow bursts correspond to the transient magnetic structures discussed above need further investigation of their propagation in a more realistic background condition of the current sheet, for example taking into account the change in the normal component of the magnetic field.

7.4.3 Electron Dynamics in the Ion-Scale Current Sheet

Different acceleration mechanisms have been proposed to operate for electrons within and in the vicinity of the ion diffusion region in addition to the direct acceleration by the reconnection electric field. These include: surfing acceleration at the boundary of the current sheet (Hoshino 2005); acceleration due to a positive potential along the field line (Egedal et al. 2010); wave-particle interaction in the reconnecting current sheet (Shinohara et al. 1998) or near the pileup region (Hoshino et al. 2001; Imada et al. 2007); acceleration due to contracting magnetic islands (Drake et al. 2006; Chen et al. 2008) or due to merging/coalescence of island/flux-rope (Retinò et al. 2008; Oka et al. 2010). The structure and dynamics of the current sheet near the reconnection region is expected to reflect these different processes acting on the electrons, since the electrons are the main carrier of the current. It is therefore, essential, to determine both the current sheet configuration and the dynamics of electrons simultaneously.

Two-dimensional (2-D) field and plasma configuration has been successfully reconstructed using the Grad-Shafranov (GS) method (e.g., Sonnerup and Guo 1996) when the observed signatures can be assumed to be a static structure within the time-scale of the crossing. This method has been further developed for thin current sheets by Teh et al. (2011) using Hall-MHD equations. For this analysis, sufficient numbers of plasma moment data are required during the current sheet crossing by a single spacecraft. An example Cluster observation of a north-south crossing of a current sheet in the ion diffusion region, Earthward of an X-line is illustrated in Fig. 7.10, in the upper right panel. The reconstruction map of the magnetic field lines (black lines in Fig. 7.10g) and the streamlines of ion flow (gray lines in Fig. 7.10h) with the out-of-plane magnetic field B_z in color are shown for C1. The coordinate system used in Fig. 7.10g, h is explained in the caption. The maps demonstrate that the Hall magnetic field, coded by the red, is surrounded by the loops of the electron flows (white arrows in Fig. 7.10h), which are the Hall current loops as predicted by the theory. The reconstructed electron current loops are confirmed by another Cluster satellite (C2) observations of electron velocity, in which the sign of the parallel electron velocity is reversed within the Hall magnetic field region (Fig. 7.10b). Hence, Cluster data provided observational evidence for

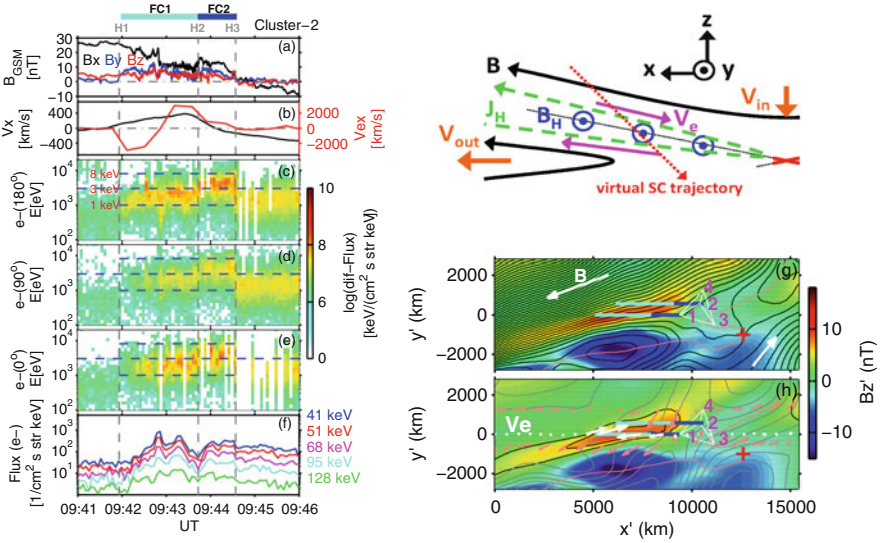

Fig. 7.10 Cluster observation of a north-south crossing of a current sheet: (**a**) magnetic field, (**b**) x component of the ion and electron velocity, (**c**)–(**e**) electron energy spectrograms for pitch angles 0, 90, and 180 °, and (**f**) high energy electron fluxes from C2. The crossing took place in the ion diffusion region as shown in the schematics. Results of Hall-MHD reconstruction of the current sheet using data from C1: (**g**) Map of the magnetic field lines with the out-of-plane magnetic field B_z' in color, (**h**) map of the streamlines of ion flow (*grey*) and selected velocity vector of electron (*white*) with the B_z' in *color*. The reconstruction axes (x', y', z') are: $x' = (0.896, 0.016, 0.445)$; $y' = (0.444, 0.014, 0.896)$; $z' = (0.021, 1.000, 0.006)$ in GSM. The *red plus symbol* denotes the magnetic X-point and the *pink curve* is the contour of $B_z' = 0$ representing the current sheet center. The *white arrows* in (**g**) denote the magnetic field directions on both sides of the current sheet. The *white arrows* in (**h**) at $y' = 0$ are the reconstructed electron velocities along the C1 spacecraft trajectory, crossing the current sheet from *left* to *right*. The *pink arrows* represent the reconstructed ion flow velocities along the C3 and C4 spacecraft trajectory. The *white tetrahedron configuration* denotes the spacecraft locations at the time when the reconnection jet reversal was seen. The *cyan* and *blue bars* denote the *FC*1 and *FC*2 regions at C1 and C2. Figure adapted with permission from Teh et al. (2012). Copyrighted by John Wiley and Sons

the electron current loops responsible for generating the out-of-plane Hall magnetic field (Teh et al. 2011).

Once the current sheet configuration is determined from the reconstruction map, the changes in the electron distribution with respect to the current sheet (X-line) can be examined to identify the possible acceleration processes. Figure 7.10a–f shows the electron observations from Cluster-2 in the ion diffusion region enclosed by the $H1$ and $H3$ grey dashed lines (from Teh et al. 2012). Two distinct regions of the field-aligned counter-streaming electrons with the flat-top distribution were found. $FC1$ region is associated with V_{ex} reversal (Hall current loop) and with enhanced flux in the energy between 1 and 3 keV. $FC2$ region is closer to the neutral sheet near the edge of the Hall current loop, with the energy between 3 and 8 keV. The energetic electrons (>40 keV) enhancements were seen in both, but with a dip at

the transition between *FC*1 and *FC*2 (Fig. 7.10f). These observations indicate that the ion diffusion region has fine substructures in which the electrons are energized differently. The location of *FC*1 and *FC*2 relative to X-line is shown in Fig. 7.10h. Teh et al. (2012) concluded that this event seems to favor wave-particle interaction with the obliquely propagating lower-hybrid waves (Shinohara et al. 1998) as a responsible mechanism for the observed electron acceleration, although the specific mechanism to create *FC*1 and *FC*2 is unknown.

Structured profile of electrons with parallel anisotropy in the outflow region, can be also produced due to temporal evolution of reconnection, as has been shown by Shuster et al. (2014) based on 2D PIC simulation and relevant Cluster observation. Reconstruction of ion-scale current sheet by applying Hall-MHD to a single-spacecraft data can be a powerful additional tool for detailed analysis of electron-scale physics by MMS four spacecraft.

7.5 Summary

Reconnection is one of the fundamental energy conversion processes in rarefied, high-β space plasma. Such conditions are frequent in space but are poorly modeled in a lab. The Earth's magnetotail is the only accessible location of spontaneous reconnection, not immediately forced by external driving. Recent developments promise significant advance in understanding this fundamental process. The theory appeared to overcome the multi-year stagnation related with the stabilizing B_z effect, suggesting a variety of new unstable configurations. Observations also show rich variety of initial configurations and of subsequent structures in the reconnection region. Despite the large natural scale of the magnetotail, the system self-consistently develops ion-scale objects such as current sheet, ensuring efficient energy conversion due to dominance of kinetic processes. Future studies will concentrate on electron kinetics, down to smaller electron scales with NASA, MMS mission and the currently acquired knowledge will help to understand the background ion-scale physics. Another still unresolved problem is the role of global structure and convection in magnetotail reconnection dynamics. Though small-scale reconnection happens almost permanently, the development of this process to a larger scale and subsequent magnetotail unloading occurs at rather differing conditions.

Acknowledgements The authors thank Waileong Teh and Rongsheng Wang for the use of figures they made and/or assisted with. Authors would like to acknowledge Cluster Science Archive and Cluster instrument teams, in particular FGM, CIS, PEACE, EFW for excellent data.

References

A. Alexandrova, R. Nakamura, V.S. Semenov, I.V. Kubyshkin, S. Apatenkov, E.V. Panov, D. Korovinskiy, H. Biernat, W. Baumjohann, K.-H. Glassmeier, J.P. McFadden, Remote estimation of reconnection parameters in the Earth's magnetotail: model and observations. Ann. Geophys. **30**, 1727–1741 (2012)

V. Angelopoulos, W. Baumjohann, C.F. Kennel, F.V. Coronti, M.G. Kivelson, R. Pellat, R.J. Walker, H. Luehr, G. Paschmann, Bursty bulk flows in the inner central plasma sheet. J. Geophys. Res. **97**, 4027–4039 (1992)

V. Angelopoulos, J.P. McFadden, D. Larson, C.W. Carlson, S.B. Mende, H. Frey, T. Phan, D.G. Sibeck, K. Glassmeier, U. Auster, E. Donovan, I.R. Mann, I.J. Rae, C.T. Russell, A. Runov, X. Zhou, L. Kepko, Tail reconnection triggering substorm onset. Science **321**, 931–935 (2008)

A.V. Artemyev, L.M. Zelenyi, Kinetic structure of current sheets in the Earth magnetotail. Space Sci. Rev. **178**, 419–440 (2013).

A.V. Artemyev, A.A. Petrukovich, L.M. Zelenyi, H.V. Malova, V.Y. Popov, R. Nakamura, A. Runov, S. Apatenkov, Comparison of multi-point measurements of current sheet structure and analytical models. Ann. Geophys. **26**, 2749–2758 (2008)

A.V. Artemyev, A.A. Petrukovich, L.M. Zelenyi, R. Nakamura, H.V. Malova, V.Y. Popov, Thin embedded current sheets: cluster observations of ion kinetic structure and analytical models. Ann. Geophys. **27**, 4075–4087 (2009)

A.V. Artemyev, A.A. Petrukovich, R. Nakamura, L.M. Zelenyi, Proton velocity distribution in thin current sheets: cluster observations and theory of transient trajectories. J. Geophys. Res. **115**, A12255 (2010)

A.V. Artemyev, L.M. Zelenyi, A.A. Petrukovich, R. Nakamura, Hot electrons as tracers of large-scale structure of magnetotail current sheets. Geophys. Res. Lett. **38**, L14102 (2011)

A. V. Artemyev, A.P. Walsh, A.A. Petrukovich, W. Baumjohann, R. Nakamura, A.N. Fazakerley, Electron pitch angle/energy distribution in the magnetotail. J. Geophys. Res. **119**, 7214–7227 (2014)

Y. Asano, R. Nakamura, W. Baumjohann, A. Runov, Z. Vörös, M. Volwerk, T.L. Zhang, A. Balogh, B. Klecker, H. Rème, How typical are atypical current sheets? Geophys. Res. Lett., **32**, 3108 (2005)

M. Ashour-Abdalla, L.M. Zelenyi, V. Peroomian, R.L. Richard, Consequences of magnetotail ion dynamics. J. Geophys. Res. **99**, 14891–14916 (1994)

N. Aunai, A. Retinò, G. Belmont, R. Smets, B. Lavraud, A. Vaivads, The proton pressure tensor as a new proxy of the proton decoupling region in collisionless magnetic reconnection. Ann. Geophys. **29**, 1571–1579 (2011)

W.I. Axford, C.O. Hines, A unifying theory of high-latitude geophysical phenomena and geomagnetic storms. Can. J. Phys. **39**, 1433 (1961)

D.N. Baker, S.J. Bame, J. Birn, W.C. Feldman, J.T. Gosling, E.W. Hones Jr., R.D. Zwickl, J.A. Slavin, E.J. Smith, B.T. Tsurutani, Direct observations of passages of the distant neutral line (80–140 RE) following substorm onsets - ISEE-3. Geophys. Res. Lett. **11**, 1042–1045 (1984)

D.N. Baker, T.I. Pulkkinen, V. Angelopoulos, W. Baumjohann, R.L. McPherron, Neutral line model of substorms: past results and present view. J. Geophys. Res. **101**, 12975–13010 (1996)

W. Baumjohann, Modes of convection in the magnetotail. Phys. Plasmas **9**, 3665–3667 (2002)

W. Baumjohann, R.A. Treumann, *Basic Space Plasma Physics* (Imperial College Press, London, 1996)

W. Baumjohann, G. Paschmann, C.A. Cattell, Average plasma properties in the central plasma sheet. J. Geophys. Res. **94**, 6597–6606 (1989)

W. Baumjohann, G. Paschmann, H. Luehr, Characteristics of high-speed ion flows in the plasma sheet. J. Geophys. Res. **95**, 3801–3809 (1990)

W. Baumjohann, G. Paschmann, T. Nagai, Thinning and expansion of the substorm plasma sheet. J. Geophys. Res. **97**, 17173 (1992)

W. Baumjohann, M. Hesse, S. Kokubun, T. Mukai, T. Nagai, A.A. Petrukovich, Substorm dipolarization and recovery. J. Geophys. Res. **104**, 24995–25000 (1999)
N. Bessho, A. Bhattacharjee, Instability of the current sheet in the Earth's magnetotail with normal magnetic field. Phys. Plasmas **21**(10), 102905 (2014)
J. Birn, A.V. Artemyev, D.N. Baker, M. Echim, M. Hoshino, L.M. Zelenyi, Particle acceleration in the magnetotail and aurora. Space Sci. Rev. **173**, 49–102 (2012)
A.L. Borg, M.G.G.T. Taylor, J.P. Eastwood, Observations of magnetic flux ropes during magnetic reconnection in the Earth's magnetotail. Ann. Geophys. **30**, 761–773 (2012)
M. Brittnacher, K.B. Quest, H. Karimabadi, On the energy principle and ion tearing in the magnetotail. Geophys. Res. Lett. **21**, 1591–1594 (1994)
M. Brittnacher, K.B. Quest, H. Karimabadi, A study of the effect of pitch angle and spatial diffusion on tearing instability using a new finite element based linear code. J. Geophys. Res. **103**, 4587–4596 (1998)
J. Büchner, Astrophysical reconnection and collisionless dissipation. Plasma Phys. Controlled Fusion **49**, 325–339 (2007)
J. Büchner, L.M. Zelenyi, Deterministic chaos in the dynamics of charged particles near a magnetic field reversal. Phys. Lett. A **118**, 395–399 (1986)
J. Büchner, L.M. Zelenyi, Chaotization of the electron motion as the cause of an internal magnetotail instability and substorm onset. J. Geophys. Res. **92**, 13456–13466 (1987)
J. Büchner, L.M. Zelenyi, Regular and chaotic charged particle motion in magnetotail like field reversals. I - basic theory of trapped motion. J. Geophys. Res. **94**, 11821–11842 (1989)
G.R. Burkhart, J. Chen, Particle motion in x-dependent Harris-like magnetotail models. J. Geophys. Res. **98**, 89–97 (1993)
G.R. Burkhart, J.F. Drake, P.B. Dusenbery, T.W. Speiser, A particle model for magnetotail neutral sheet equilibria. J. Geophys. Res. **97**, 13799–13815 (1992a)
G.R. Burkhart, J.F. Drake, P.B. Dusenbery, T.W. Speiser, Ion tearing in a magnetotail configuration with an embedded thin current sheet. J. Geophys. Res. **97**, 16749–16756 (1992b)
M.N. Caan, R.L. McPherron, C.T. Russell, The statistical magnetic signature of magnetospheric substorms. Planet. Space Sci. **26**, 269–279 (1978)
E. Camporeale, G. Lapenta, Model of bifurcated current sheets in the Earth's magnetotail: Equilibrium and stability. J. Geophys. Res. **110**, 7206 (2005)
J. Cao, A. Duan, M. Dunlop, X. Wei, C. Cai, Dependence of IMF B_y penetration into the neutral sheet on IMF B_z and geomagnetic activity. J. Geophys. Res. Space Phys. **119**, 5279–5285 (2014)
G. Chanteur, C.C. Harvey, Spatial interpolation for four spacecraft: application to magnetic gradients. ISSI Sci. Rep. Ser. **1**, 371–394 (1998)
C.C. Chaston, J.R. Johnson, M. Wilber, M. Acuna, M.L. Goldstein, H. Reme, Kinetic Alfvén wave turbulence and transport through a reconnection diffusion region. Phys. Rev. Lett. **102**(1), 015001 (2009)
L.-J. Chen, A. Bhattacharjee, P.A. Puhl-Quinn, H. Yang, N. Bessho, S. Imada, S. Mühlbachler, P.W. Daly, B. Lefebvre, Y. Khotyaintsev, A. Vaivads, A. Fazakerley, E. Georgescu, Observation of energetic electrons within magnetic islands. Nat. Phys. **4**, 19–23 (2008)
B. Coppi, G. Laval, R. Pellat, Dynamics of the geomagnetic tail. Phys. Rev. Lett. **16**, 1207–1210 (1966)
F.V. Coroniti, On the tearing mode in quasi-neutral sheets. J. Geophys. Res. **85**, 6719–6728 (1980)
F.V. Coroniti, Space plasma turbulent dissipation - reality or myth? Space Sci. Rev. **42**, 399–410 (1985)
F.V. Coroniti, P.L. Pritchett, The quiet evening auroral arc and the structure of the growth phase near-Earth plasma sheet. J. Geophys. Res. Space Phys. **119**, 1827–1836 (2014)
W. Daughton, Electromagnetic properties of the lower-hybrid drift instability in a thin current sheet. Phys. Plasmas **10**, 3103–3119 (2003)
W. Daughton, H. Karimabadi, Kinetic theory of collisionless tearing at the magnetopause. J. Geophys. Res. **110**, 3217 (2005)

W. Daughton, G. Lapenta, P. Ricci, Nonlinear evolution of the lower-hybrid drift instability in a current sheet. Phys. Rev. Lett. **93**(10), 105004 (2004)
R.C. Davidson, N.T. Gladd, Anomalous transport properties associated with the lower-hybrid-drift instability. Phys. Fluids **18**, 1327–1335 (1975)
A.V. Divin, M.I. Sitnov, M. Swisdak, J.F. Drake, Reconnection onset in the magnetotail: particle simulations with open boundary conditions. Geophys. Res. Lett. **34**, 9109 (2007)
M. Dobrowolny, Instability of a neutral sheet. Nuovo Cimento B Ser. **55**, 427–442 (1968)
J.F. Drake, M. Swisdak, H. Che, M.A. Shay, Electron acceleration from contracting magnetic islands during reconnection. Nature **443**, 553–556 (2006)
J.W. Dungey, Interplanetary magnetic field and the auroral zones. Phys. Rev. Lett. **6**, 47–48 (1961)
J.W. Dungey, Interactions of solar plasma with the geomagnetic field. Planet. Space Sci. **10**, 233–237 (1963)
J.W. Eastwood, Consistency of fields and particle motion in the 'Speiser' model of the current sheet. Planet. Space Sci. **20**, 1555–1568 (1972)
J.W. Eastwood, The warm current sheet model, and its implications on the temporal behaviour of the geomagnetic tail. Planet. Space Sci. **22**, 1641–1668 (1974)
J.P. Eastwood, T.-D. Phan, F.S. Mozer, M.A. Shay, M. Fujimoto, A. Retinò, M. Hesse, A. Balogh, E.A. Lucek, I. Dandouras, Multi-point observations of the Hall electromagnetic field and secondary island formation during magnetic reconnection. J. Geophys. Res. Space Phys. **112**, 6235 (2007)
J.P. Eastwood, T.D. Phan, S.D. Bale, A. Tjulin, Observations of turbulence generated by magnetic reconnection. Phys. Rev. Lett. **102**(3), 035001 (2009)
J.P. Eastwood, T.D. Phan, M. Øieroset, M.A. Shay, Average properties of the magnetic reconnection ion diffusion region in the Earth's magnetotail: the 2001–2005 Cluster observations and comparison with simulations. J. Geophys. Res. **115**, 8215 (2010)
J.P. Eastwood, T.D. Phan, J.F. Drake, M.A. Shay, A.L. Borg, B. Lavraud, M.G.G.T. Taylor, Energy partition in magnetic reconnection in Earth's magnetotail. Phys. Rev. Lett. **110**, 225001 (2013)
J. Egedal, A. Lê, N. Katz, L.-J. Chen, B. Lefebvre, W. Daughton, A. Fazakerley, Cluster observations of bidirectional beams caused by electron trapping during antiparallel reconnection. J. Geophys. Res. **115**, 3214 (2010)
J. Egedal, A. Le, W. Daughton, A review of pressure anisotropy caused by electron trapping in collisionless plasma, and its implications for magnetic reconnection. Phys. Plasmas **20**(6), 061201 (2013)
G.M. Erickson, R.A. Wolf, Is steady convection possible in the Earth's magnetotail. Geophys. Res. Lett. **7**, 897–900 (1980)
D.H. Fairfield, On the average configuration of the geomagnetic tail. J. Geophys. Res. **84**, 1950–1958 (1979)
H.S. Fu, J.B. Cao, Y.V. Khotyaintsev, M.I. Sitnov, A. Runov, S.Y. Fu, M. Hamrin, M. André, A. Retinò, Y.D. Ma, H.Y. Lu, X.H. Wei, S.Y. Huang, Dipolarization fronts as a consequence of transient reconnection: in situ evidence. Geophys. Res. Lett. **40**, 6023–6027 (2013)
M. Fujimoto, I. Shinohara, H. Kojima, Reconnection and waves: a review with a perspective. Space Sci. Rev. **160**, 123–143 (2011)
H.P. Furth, The 'mirror instability' for finite particle gyro-radius. Nucl. Fusion **1**, 169–174 (1962)
H.P. Furth, J. Killeen, M.N. Rosenbluth, Finite-resistivity instabilities of a sheet pinch. Phys. Fluids **6**, 459–485 (1963)
A.A. Galeev, R.Z. Sagdeev, Nonlinear plasma theory, in *Reviews of Plasma Physics*, ed. by A.M.A. Leontovich, vol. 7, p. 1 (1979)
A.A. Galeev, R.N. Sudan, *Handbook of Plasma Physics. Vol. 2: Basic Plasma Physics II* (Elsevier, Amsterdam, 1985)
A.A. Galeev, L.M. Zelenyi, Tearing instability in plasma configurations. Sov. J. Exp. Theor. Phys. **43**, 1113 (1976)
A.A. Galeev, M.M. Kuznetsova, L.M. Zelenyi, Magnetopause stability threshold for patchy reconnection. Space Sci. Rev. **44**, 1–41 (1986)

H. Goldstein, K. Schindler, Large-scale collision-free instability of two-dimensional plasma sheets. Phys. Rev. Lett. **48**, 1468–1471 (1982)
E. Harris, On a plasma sheet separating regions of oppositely directed magnetic field. Nuovo Cimento **23**, 115–123 (1962)
A. Hasegawa, Plasma instabilities in the magnetosphere. Rev. Geophys. Space Phys. **9**, 703–772 (1971)
T.W. Hill, Magnetic merging in a collisionless plasma. J. Geophys. Res. **80**, 4689–4699 (1975)
C.M. Ho, B.T. Tsurutani, E.J. Smith, W.C. Feldman, A detailed examination of a X-line region in the distant tail: ISEE-3 observations of jet flow and B(sub z) reversals and a pair of slow shocks. Geophys. Res. Lett. **21**, 3031–3034 (1994)
F.C. Hoh, Stability of sheet pinch. Phys. Fluids **9**, 277–284 (1966)
E.W. Hones Jr., Transient phenomena in the magnetotail and their relation to substorms. Space Sci. Rev. **23**, 393–410 (1979)
E.W. Hones Jr., T.A. Fritz, J. Birn, J. Cooney, S.J. Bame, Detailed observations of the plasma sheet during a substorm on April 24, 1979. J. Geophys. Res. **91**, 6845–6859 (1986)
M. Hoshino, Electron surfing acceleration in magnetic reconnection. J. Geophys. Res. **110**, A10215 (2005)
M. Hoshino, K. Hiraide, T. Mukai, Strong electron heating and non-Maxwellian behavior in magnetic reconnection. Earth Planets Space **53**, 627–634 (2001)
S.Y. Huang, et al., Observations of turbulence within reconnection jet in the presence of guide field. Geophys. Res. Lett. **39**, 11104 (2012)
J.D. Huba, N.T. Gladd, K. Papadopoulos, The lower-hybrid-drift instability as a source of anomalous resistivity for magnetic field line reconnection. Geophys. Res. Lett. **4**, 125–126 (1977)
J.D. Huba, J.F. Drake, N.T. Gladd, Lower-hybrid-drift instability in field reversed plasmas. Phys. Fluids **23**, 552–561 (1980)
S. Imada, R. Nakamura, P.W. Daly, M. Hoshino, W. Baumjohann, S. Mühlbachler, A. Balogh, H. Rème, Energetic electron acceleration in the downstream reconnection outflow region. J. Geophys. Res. **112**, 3202 (2007)
J.R. Kan, On the structure of the magnetotail current sheet. J. Geophys. Res. **78**, 3773–3781 (1973)
L.M. Kistler, C. Mouikis, E. MöBius, B. Klecker, J.A. Sauvaud, H. RéMe, A. Korth, M.F. Marcucci, R. Lundin, G.K. Parks, A. Balogh, Contribution of nonadiabatic ions to the cross-tail current in an O^+ dominated thin current sheet. J. Geophys. Res. **110**, 6213 (2005)
T. Krallmann, J. Dreher, K. Schindler, On the stability of the ion-tearing mode in equilibria with embedded thin current sheets, in *International Conference on Substorms*, pp. 499–503 (1994)
M.M. Kuznetsova, L.M. Zelenyi, Magnetic reconnection in collisionless field reversals - the universality of the ion tearing mode. Geophys. Res. Lett. **18**, 1825–1828 (1991)
T.V. Laitinen, R. Nakamura, A. Runov, H. Rème, E.A. Lucek, Global and local disturbances in the magnetotail during reconnection. Ann. Geophys. **25**, 1025–1035 (2007)
G. Lapenta, S. Markidis, A. Divin, M.V. Goldman, D.L. Newman, Bipolar electric field signatures of reconnection separatrices for a hydrogen plasma at realistic guide fields. Geophys. Res. Lett. **38**, 17104 (2011)
G. Laval, R. Pellat, M. Vuillemin, Instabilités électromagnétiques des plasmas sans collisions (CN-21/71), in *Plasma Physics and Controlled Nuclear Fusion Research*, vol. II, pp. 259–277 (1966)
A. Le, J. Egedal, O. Ohia, W. Daughton, H. Karimabadi, V.S. Lukin, Regimes of the electron diffusion region in magnetic reconnection. Phys. Rev. Lett. **110**(13), 135004 (2013)
B. Lembege, R. Pellat, Stability of a thick two-dimensional quasineutral sheet. Phys. Fluids **25**, 1995–2004 (1982)
W.W. Liu, J. Liang, E.F. Donovan, Electrostatic field and ion temperature drop in thin current sheets: a theory. J. Geophys. Res. **115**, 3211 (2010)
A.T.Y. Lui, Potential plasma instabilities for substorm expansion onsets. Space Sci. Rev. **113**, 127–206 (2004)

A.T.Y. Lui, M. Volwerk, M.W. Dunlop, I.V. Alexeev, A.N. Fazakerley, A.P. Walsh, M. Lester, A. Grocott, C. Mouikis, M.G. Henderson, L.M. Kistler, C. Shen, J.K. Shi, T.L. Zhang, H. Rème, Near-Earth substorm features from multiple satellite observations. J. Geophys. Res. **113**, 7 (2008)

S. Machida, Y. Miyashita, A. Ieda, M. Nosé, D. Nagata, K. Liou, T. Obara, A. Nishida, Y. Saito, T. Mukai, Statistical visualization of the Earth's magnetotail based on geotail data and the implied substorm model. Ann. Geophys. **27**(3), 1035–1046 (2009). http://www.ann-geophys.net/27/1035/2009/.

M.A. Malkov, V.I. Sotnikov, Lower hybrid drift instability and reconnection of magnetic lines of force. Soviet J. Plasma Phys. **11**, 626–631 (1985)

D.J. McComas, S.J. Bame, C.T. Russell, R.C. Elphic, The near-Earth cross-tail current sheet - detailed ISEE 1 and 2 case studies. J. Geophys. Res. **91**, 4287–4301 (1986)

R.L. McPherron, R.H. Manka, Dynamics of the 1054 UT March 22, 1979, substorm event - CDAW 6. J. Geophys. Res. **90**, 1175–1190 (1985)

R.L. McPherron, C.T. Russell, M.P. Aubry, Satellite studies of magnetospheric substorms on August 15, 1968: 9. Phenomenological model for substorms. J. Geophys. Res. **78**, 3131 (1973)

A.B. Mikhailovskii, *Theory of Plasma Instabilities: Instabilities of an Inhomogeneous Plasma*, vol. 2 (Springer, New York, 1974)

O.V. Mingalev, I.V. Mingalev, K.V. Malova, L.M. Zelenyi, Numerical simulations of plasma equilibrium in a one-dimensional current sheet with a nonzero normal magnetic field component. Plasma Phys. Rep. **33**, 942–955 (2007)

V.M. Mishin, T. Saifudinova, A. Bazarzhapov, C.T. Russell, W. Baumjohann, R. Nakamura, M. Kubyshkina, Two distinct substorm onsets. J. Geophys. Res. **106**, 13105–13118 (2001)

Y. Miyashita, S. Machida, K. Liou, T. Mukai, Y. Saito, C.-I. Meng, G.K. Parks, Relationship between magnetotail variations and auroral activities during substorms. J. Geophys. Res. Space Phys. **108**, 1022 (2003)

Y. Miyashita, Y. Kamide, S. Machida, K. Liou, T. Mukai, Y. Saito, A. Ieda, C.-I. Meng, G.K. Parks, Difference in magnetotail variations between intense and weak substorms. J. Geophys. Res. Space Phys. **109**, 11205 (2004)

T. Nagai, M. Fujimoto, Y. Saito, S. Machida, T. Terasawa, R. Nakamura, T. Yamamoto, T. Mukai, A. Nishida, S. Kokubun, Structure and dynamics of magnetic reconnection for substorm onsets with Geotail observations. J. Geophys. Res. **103**, 4419–4440 (1998)

T. Nagai, I. Shinohara, S. Zenitani, R. Nakamura, T.K.M. Nakamura, M. Fujimoto, Y. Saito, T. Mukai, Three-dimensional structure of magnetic reconnection in the magnetotail from Geotail observations. J. Geophys. Res. Space Phys. **118**, 1667–1678 (2013a)

T. Nagai, S. Zenitani, I. Shinohara, R. Nakamura, M. Fujimoto, Y. Saito, T. Mukai, Ion and electron dynamics in the ion-electron decoupling region of magnetic reconnection with Geotail observations. J. Geophys. Res. Space Phys. **118**, 7703–7713 (2013b)

R. Nakamura, W. Baumjohann, A. Runov, Y. Asano, Thin current sheets in the magnetotail observed by Cluster. Space Sci. Rev. **122**, 29–38 (2006)

R. Nakamura, W. Baumjohann, M. Fujimoto, Y. Asano, A. Runov, C.J. Owen, A.N. Fazakerley, B. Klecker, H. Rème, E.A. Lucek, M. Andre, Y. Khotyaintsev, Cluster observations of an ion-scale current sheet in the magnetotail under the presence of a guide field. J. Geophys. Res. **113**, 7 (2008)

R. Nakamura, W. Baumjohann, E. Panov, A.A. Petrukovich, V. Angelopoulos, M. Volwerk, W. Magnes, Y. Nishimura, A. Runov, C.T. Russell, J.M. Weygand, O. Amm, H.-U. Auster, J. Bonnell, H. Frey, D. Larson, J. McFadden, Flux transport, dipolarization, and current sheet evolution during a double-onset substorm. *J. Geophys. Res.* **116**, 0 (2011)

Y. Narita, H. Comisel, U. Motschmann, Spatial structure of ion-scale plasma turbulence. Front. Phys. **2**, 13 (2014)

A. Nishida, N. Nagayama, Synoptic survey for the neutral line in the magnetotail during the substorm expansion phase. J. Geophys. Res. **78**, 3782 (1973)

A. Nishida, T. Mukai, T. Yamamoto, S. Kokubun, K. Maezawa, A unified model of the magnetotail convection in geomagnetically quiet and active times. J. Geophys. Res. **103**, 4409–4418 (1998)

M. Øieroset, T.D. Phan, M. Fujimoto, R.P. Lin, R.P. Lepping, In situ detection of collisionless reconnection in the Earth's magnetotail. Nature **412**, 414–417 (2001)
M. Oka, M. Fujimoto, I. Shinohara, T.D. Phan, Island surfing mechanism of electron acceleration during magnetic reconnection. J. Geophys. Res. **115**, A08223 (2010)
E.V. Panov, R. Nakamura, W. Baumjohann, V. Angelopoulos, A.A. Petrukovich, A. Retinò, M. Volwerk, T. Takada, K.-H. Glassmeier, J.P. McFadden, D. Larson, Multiple overshoot and rebound of a bursty bulk flow. Geophys. Res. Lett. **37**, 8103 (2010)
E.V. Panov, R. Nakamura, W. Baumjohann, M.G. Kubyshkina, A.V. Artemyev, V.A. Sergeev, A.A. Petrukovich, V. Angelopoulos, K.-H. Glassmeier, J.P. McFadden, D. Larson, Kinetic ballooning/interchange instability in a bent plasma sheet. J. Geophys. Res. **117**, 6228 (2012a)
E.V. Panov, V.A. Sergeev, P.L. Pritchett, F.V. Coroniti, R. Nakamura, W. Baumjohann, V. Angelopoulos, H.U. Auster, J.P. McFadden, Observations of kinetic ballooning/interchange instability signatures in the magnetotail. Geophys. Res. Lett. **39**, 8110 (2012b)
G. Paschmann, M. Øieroset, T. Phan, In-situ observations of reconnection in space. Space Sci. Rev. **178**, 385–417 (2013)
R. Pellat, F.V. Coroniti, P.L. Pritchett, Does ion tearing exist? Geophys. Res. Lett. **18**, 143–146 (1991)
A.A. Petrukovich, The growth phase: comparison of small and large substorms, in *Fifth International Conference on Substorms*, volume 443 of ESA Special Publication, ed. by A. Wilson, p. 9 (2000)
A.A. Petrukovich, Storm-time and quiet-time substorms in the magnetotail, in *Disturbances in Geospace: The Storm-substorm Relationship*, volume 142 of Washington DC American Geophysical Union Geophysical Monograph Series, ed. by A. Surjalal Sharma, Y. Kamide, G.S. Lakhina, p. 37 (2003)
A.A. Petrukovich, The elusive onset of geomagnetic substorms. Science **321**(5891), 920–921 (2008). http://www.sciencemag.org/content/321/5891/920.short.
A.A. Petrukovich, Origins of plasma sheet B_y. J. Geophys. Res. **116**, 7217 (2011)
A.A. Petrukovich, A.G. Yahnin, The substorm onset location controversy. Space Sci. Rev. **122**, 81–87 (2006)
A.A. Petrukovich, V.A. Sergeev, L.M. Zelenyi, T. Mukai, T. Yamamoto, S. Kokubun, K. Shiokawa, C.S. Deehr, E.Y. Budnick, J. Büchner, A.O. Fedorov, V.P. Grigorieva, T.J. Hughes, N.F. Pissarenko, S.A. Romanov, I. Sandahl, Two spacecraft observations of a reconnection pulse during an auroral breakup. J. Geophys. Res. **103**, 47–60 (1998)
A.A. Petrukovich, J. Wanliss, T. Mukai, S. Kokubun, T. Yamamoto, Small-amplitude bipolar flows in the near-Earth tail. Geophys. Res. Lett. **26**, 2909–2912 (1999)
A.A. Petrukovich, W. Baumjohann, R. Nakamura, T. Mukai, O.A. Troshichev, Small substorms: solar wind input and magnetotail dynamics. J. Geophys. Res. **105**, 21109–21118 (2000)
A.A. Petrukovich, W. Baumjohann, R. Nakamura, A. Runov, A. Balogh, H. Rème, Thinning and stretching of the plasma sheet. J. Geophys. Res. **112**, 10213 (2007)
A.A. Petrukovich, W. Baumjohann, R. Nakamura, H. Rème, Tailward and earthward flow onsets observed by Cluster in a thin current sheet. J. Geophys. Res. **114**, 9203 (2009)
A.A. Petrukovich, A.V. Artemyev, H.V. Malova, V.Y. Popov, R. Nakamura, L.M. Zelenyi, Embedded current sheets in the Earth magnetotail. J. Geophys. Res. **116**, A00I25 (2011)
A.A. Petrukovich, A.V. Artemyev, R. Nakamura, E.V. Panov, W. Baumjohann, Cluster observations of dBz/dx during growth phase magnetotail stretching intervals. J. Geophys. Res. **118**, 5720–5730 (2013)
A.A. Petrukovich, A.V. Artemyev, I.Y. Vasko, R. Nakamura, L.M. Zelenyi, Current sheets in the Earth magnetotail: plasma and magnetic field structure with Cluster project observations. Space Sci. Rev. **188**, 311–337 (2015)
P.L. Pritchett, The onset of magnetic reconnection in three dimensions. Phys. Plasmas **20**(8), 080703 (2013)
P.L. Pritchett, J. Büchner, Collisionless reconnection in configurations with a minimum in the equatorial magnetic field and with magnetic shear. J. Geophys. Res. **100**, 3601–3611 (1995)

P.L. Pritchett, F.V. Coroniti, Formation and stability of the self-consistent one-dimensional tail current sheet. J. Geophys. Res. **97**, 16773–16787 (1992)
P.L. Pritchett, F.V. Coroniti, Interchange and kink modes in the near-Earth plasma sheet and their associated plasma flows. Geophys. Res. Lett. **24**, 2925–2928 (1997)
P.L. Pritchett, F.V. Coroniti, Three-dimensional collisionless magnetic reconnection in the presence of a guide field. J. Geophys. Res. **109**, 1220 (2004)
P.L. Pritchett, F.V. Coroniti, A kinetic ballooning/interchange instability in the magnetotail. J. Geophys. Res. **115**, A06301 (2010)
P.L. Pritchett, F.V. Coroniti, Plasma sheet disruption by interchange-generated flow intrusions. Geophys. Res. Lett. **381**, 10102 (2011)
P.L. Pritchett, F.V. Coroniti, Structure and consequences of the kinetic ballooning/interchange instability in the magnetotail. J. Geophys. Res. **118**, 146–159 (2013)
P.L. Pritchett, F.V. Coroniti, Y. Nishimura, The kinetic ballooning/interchange instability as a source of dipolarization fronts and auroral streamers. J. Geophys. Res. **119**, 4723–4739 (2014)
K.B. Quest, H. Karimabadi, M. Brittnacher, Consequences of particle conservation along a flux surface for magnetotail tearing. J. Geophys. Res. **101**, 179–184 (1996)
A. Retinò, R. Nakamura, A. Vaivads, Y. Khotyaintsev, T. Hayakawa, K. Tanaka, S. Kasahara, M. Fujimoto, I. Shinohara, J.P. Eastwood, M. André, W. Baumjohann, P.W. Daly, E.A. Kronberg, N. Cornilleau-Wehrlin, Cluster observations of energetic electrons and electromagnetic fields within a reconnecting thin current sheet in the Earth's magnetotail. J. Geophys. Res. **113**, 12215 (2008)
P. Ricci, J.U. Brackbill, W. Daughton, G. Lapenta, Influence of the lower hybrid drift instability on the onset of magnetic reconnection. Phys. Plasmas **11**, 4489–4500 (2004a)
P. Ricci, J.U. Brackbill, W. Daughton, G. Lapenta, Collisionless magnetic reconnection in the presence of a guide field. Phys. Plasmas **11**, 4102–4114 (2004b)
F.J. Rich, V.M. Vasyliunas, R.A. Wolf, On the balance of stresses in the plasma sheet. J. Geophys. Res. **77**, 4670–4676 (1972)
A. Runov, V.A. Sergeev, R. Nakamura, W. Baumjohann, T.L. Zhang, Y. Asano, M. Volwerk, Z. Vörös, A. Balogh, H. Rème, Reconstruction of the magnetotail current sheet structure using multi-point Cluster measurements. Planet. Space Sci. **53**, 237–243 (2005)
A. Runov, V.A. Sergeev, R. Nakamura, W. Baumjohann, S. Apatenkov, Y. Asano, T. Takada, M. Volwerk, Z. Vörös, T.L. Zhang, J. Sauvaud, H. Rème, A. Balogh, Local structure of the magnetotail current sheet: 2001 Cluster observations. Ann. Geophys. **24**, 247–262 (2006)
A. Runov, W. Baumjohann, R. Nakamura, V.A. Sergeev, O. Amm, H. Frey, I. Alexeev, A.N. Fazakerley, C.J. Owen, E. Lucek, M. André, A. Vaivads, I. Dandouras, B. Klecker, Observations of an active thin current sheet. J. Geophys. Res. **113**, 7 (2008)
M.H. Saito, L.-N. Hau, C.-C. Hung, Y.-T. Lai, Y.-C. Chou, Spatial profile of magnetic field in the near-Earth plasma sheet prior to dipolarization by THEMIS: feature of minimum B. Geophys. Res. Lett. **37**, L08106 (2010)
J. Sanny, R.L. McPherron, C.T. Russell, D.N. Baker, T.I. Pulkkinen, A. Nishida, Growth-phase thinning of the near-Earth current sheet during the CDAW 6 substorm. J. Geophys. Res. **99**, 5805–5816 (1994)
K. Schindler, A variational principle for one-dimensional plasmas, in *VII International Conference on Phenomena in Ionized Gases*, ed. by B. Perović, D. Tošić, vol. II, pp. 736–740 (1966)
K. Schindler, A self-consistent theory of the tail of the magnetosphere, in *Earth's Magnetospheric Processes*, volume 32 of Astrophysics and Space Science Library, ed. by B.M. McCormac, pp. 200–+ (1972)
K. Schindler, A theory of the substorm mechanism. J. Geophys. Res. **79**, 2803–2810 (1974)
K. Schindler, *Physics of Space Plasma Activity*. (Cambridge University Press, Cambridge, 2006)
K. Schindler, J. Birn, Models of two-dimensional embedded thin current sheets from Vlasov theory. J. Geophys. Res. **107**, 1193 (2002)
K. Schindler, D. Pfirsch, H. Wobig, Stability of two-dimensional collision-free plasmas. Plasma Phys. **15**, 1165–1184 (1973)

V.A. Sergeev, P. Tanskanen, K. Mursula, A. Korth, R.C. Elphic, Current sheet thickness in the near-Earth plasma sheet during substorm growth phase. J. Geophys. Res. **95**, 3819–3828 (1990)

V.A. Sergeev, D.G. Mitchell, C.T. Russell, D.J. Williams, Structure of the tail plasma/current sheet at $\sim 11R_E$ and its changes in the course of a substorm. J. Geophys. Res. **98**, 17345–17366 (1993)

V.A. Sergeev, V. Angelopoulos, D.G. Mitchell, C.T. Russell, In situ observations of magnetotail reconnection prior to the onset of a small substorm. J. Geophys. Res. **100**, 19121–19134 (1995)

V. Sergeev, V. Semenov, M. Kubyshkina, V. Ivanova, W. Baumjohann, R. Nakamura, T. Penz, A. Runov, T.L. Zhang, K.-H. Glassmeier, V. Angelopoulos, H. Frey, J.-A. Sauvaud, P., Daly J.B. Cao, H. Singer, E. Lucek, Observation of repeated intense near-Earth reconnection on closed field lines with Cluster, double star, and other spacecraft. Geophys. Res. Lett. **34**, 2103 (2007)

A.S. Sharma, R. Nakamura, A. Runov et al., Transient and localized processes in the magnetotail: a review. Ann. Geophys. **26**, 955–1006 (2008)

I. Shinohara, T. Nagai, M. Fujimoto, T. Terasawa, T. Mukai, K. Tsuruda, T. Yamamoto, Low-frequency electromagnetic turbulence observed near the substorm onset site. J. Geophys. Res. **103**, 20365–20388 (1998)

J.R. Shuster, L.-J. Chen, W.S. Daughton, L.C. Lee, K.H. Lee, N. Bessho, R.B. Torbert, G. Li, M.R. Argall, Highly structured electron anisotropy in collisionless reconnection exhausts. Geophys. Res. Lett. **41**, 5389–5395 (2014)

D.G. Sibeck, G.L. Siscoe, J.A. Slavin, E.J. Smith, S.J. Bame, F.L. Scarf, Magnetotail flux ropes. Geophys. Res. Lett. **11**, 1090–1093 (1984)

I. Silin, J. Büchner, A. Vaivads, Anomalous resistivity due to nonlinear lower-hybrid drift waves. Phys. Plasmas **12**(6), 062902 (2005)

M.I. Sitnov, K. Schindler, Tearing stability of a multiscale magnetotail current sheet. Geophys. Res. Lett. **37**, 8102 (2010)

M.I. Sitnov, M. Swisdak, Onset of collisionless magnetic reconnection in two-dimensional current sheets and formation of dipolarization fronts. J. Geophys. Res. **116**, 12216 (2011)

M.I. Sitnov, L.M. Zelenyi, H.V. Malova, A.S. Sharma, Thin current sheet embedded within a thicker plasma sheet: self-consistent kinetic theory. J. Geophys. Res. **105**, 13029–13044 (2000)

M.I. Sitnov, M. Swisdak, P.N. Guzdar, A. Runov, Structure and dynamics of a new class of thin current sheets. J. Geophys. Res. **111**, 8204 (2006)

M.I. Sitnov, M. Swisdak, A.V. Divin, Dipolarization fronts as a signature of transient reconnection in the magnetotail. J. Geophys. Res. **114**, A04202 (2009)

M.I. Sitnov, N. Buzulukova, M. Swisdak, V.G. Merkin, T.E. Moore, Spontaneous formation of dipolarization fronts and reconnection onset in the magnetotail. Geophys. Res. Lett. **40**, 22–27 (2013)

K. Snekvik, E. Tanskanen, N. Østgaard, L. Juusola, K. Laundal, E.I. Gordeev, A.L. Borg, Changes in the magnetotail configuration before near-Earth reconnection. J. Geophys. Res. **117**, 2219 (2012)

B.U.Ö. Sonnerup, M. Guo, Magnetopause transects. Geophys. Res. Lett. **23**, 3679–3682 (1996)

T.W. Speiser, Particle trajectories in model current sheets, 1, analytical solutions. J. Geophys. Res. **70**, 4219–4226 (1965)

G.S. Stiles, E.W. Hones Jr., S.J. Bame, J.R. Asbridge, Plasma sheet pressure anisotropies. J. Geophys. Res. **83**, 3166–3172 (1978)

W.-L. Teh, R. Nakamura, B.U.Ö. Sonnerup, J.P. Eastwood, M. Volwerk, A.N. Fazakerley, W. Baumjohann, Evidence of the origin of the Hall magnetic field for reconnection: Hall MHD reconstruction results from Cluster observations. J. Geophys. Res. **116**, 11218 (2011)

W.-L. Teh, R. Nakamura, M. Fujimoto, E.A. Kronberg, A.N. Fazakerley, P.W. Daly, W. Baumjohann, Electron dynamics in the reconnection ion diffusion region. J. Geophys. Res. **117**, 12225 (2012)

W.-L. Teh, R. Nakamura, H. Karimabadi, W. Baumjohann, T.L. Zhang, Correlation of core field polarity of magnetotail flux ropes with the IMF B_y: reconnection guide field dependency. J. Geophys. Res. **119**, 2933–2944 (2014)

S.M. Thompson, M.G. Kivelson, K.K. Khurana, R.L. McPherron, J.M. Weygand, A. Balogh, H. RéMe, L.M. Kistler, Dynamic Harris current sheet thickness from Cluster current density and plasma measurements. J. Geophys. Res. Space Phys. **110**, 2212 (2005)

R.A. Treumann, W. Baumjohann, Collisionless magnetic reconnection in space plasmas. Front. Physics **1**, 31 (2013)

B.T. Tsurutani, T.T. von Rosenvinge, ISEE-3 distant geotail results. Geophys. Res. Lett. **11**, 1027–1029 (1984)

V.M. Vasyliunas, Theoretical models of magnetic field line merging. I. Rev. Geophys. Space Phys. **13**, 303–336 (1975)

A.P. Walsh, C.J. Owen, A.N. Fazakerley, C. Forsyth, I. Dandouras, Average magnetotail electron and proton pitch angle distributions from Cluster PEACE and CIS observations. Geophys. Res. Lett. **38**, 6103 (2011)

R. Wang, R. Nakamura, Q. Lu, A. Du, T. Zhang, W. Baumjohann, Y.V. Khotyaintsev, M. Volwerk, M. André, M. Fujimoto, T.K.M. Nakamura, A.N. Fazakerley, J. Du, W. Teh, E.V. Panov, B. Zieger, Y. Pan, S. Lu, Asymmetry in the current sheet and secondary magnetic flux ropes during guide field magnetic reconnection. J. Geophys. Res. Space Phys. **117**, 7223 (2012)

R. Wang, R. Nakamura, T. Zhang, A. Du, W. Baumjohann, Q. Lu, A.N. Fazakerley, Evidence of transient reconnection in the outflow jet of primary reconnection site. Ann. Geophys. **32**, 239–248 (2014)

S. Wing, J.R. Johnson, C.C. Chaston, M. Echim, C.P. Escoubet, B. Lavraud, C. Lemon, K. Nykyri, A. Otto, J. Raeder, C.-P. Wang, Review of solar wind entry into and transport within the plasma sheet. Space Sci. Rev. **184**, 33–86 (2014)

J.R. Wygant, C.A. Cattell, R. Lysak, Y. Song, J. Dombeck, J. McFadden, F.S. Mozer, C.W. Carlson, G. Parks, E.A. Lucek, A. Balogh, M. Andre, H. Reme, M. Hesse, C. Mouikis, Cluster observations of an intense normal component of the electric field at a thin reconnecting current sheet in the tail and its role in the shock-like acceleration of the ion fluid into the separatrix region. J. Geophys. Res. **110**, 9206 (2005)

P.H. Yoon, A.T.Y. Lui, Quasi-linear theory of anomalous resistivity. J. Geophys. Res. **111**, 2203 (2006)

L. Zelenyi, A. Artemyev, Mechanisms of spontaneous reconnection: from magnetospheric to fusion plasma. Space Sci. Rev. **178**, 441–457 (2013)

L.M. Zelenyi, M.I. Sitnov, H.V. Malova, A.S. Sharma, Thin and superthin ion current sheets. Quasi-adiabatic and nonadiabatic models. Nonlinear Processes Geophys. **7**, 127–139 (2000)

L.M. Zelenyi, A.V. Artemyev, H.V. Malova, V.Y. Popov, Marginal stability of thin current sheets in the Earth's magnetotail. J. Atmos. Sol. Terr. Phys. **70**, 325–333 (2008)

L.M. Zelenyi, A.V. Artemyev, K.V. Malova, A.A. Petrukovich, R. Nakamura, Metastability of current sheets. Physics Uspekhi **53**, 933–941 (2010)

L.M. Zelenyi, H.V. Malova, A.V. Artemyev, V.Y. Popov, A.A. Petrukovich, Thin current sheets in collisionless plasma: equilibrium structure, plasma instabilities, and particle acceleration. Plasma Phys. Rep. **37**, 118–160 (2011)

L.M. Zelenyi, A.I. Neishtadt, A.V. Artemyev, D.L. Vainchtein, H.V. Malova, Quasiadiabatic dynamics of charged particles in a space plasma. Physics Uspekhi **56**, 347–394 (2013)

W. Zwingmann, Self-consistent magnetotail theory - equilibrium structures including arbitrary variation along the tail axis. J. Geophys. Res. **88**, 9101–9108 (1983)

Chapter 8
Reconnection Separatrix: Simulations and Spacecraft Measurements

G. Lapenta, R. Wang, and E. Cazzola

Abstract In this chapter, we review the progress in understanding the processes near the separatrices during magnetic reconnection. The results are obtained from numerical simulation and spacecraft measurement. The reconnection separatrices represent the surface (cross curve in two-dimensional regime) separating the reconnected magnetic field lines from the reconnecting lines, and thereby connect to the reconnection X-line. The average properties of the particle distribution and physical processes in the separatrix region are summarized. Recent studies confirm that various instabilities occur in the separatrix region and lead to a complex interplay and affecting the plasma in this region. The microphysics in the separatrix region should play an important role in reconnection dynamics. Furthermore, electrons are accelerated up to 100 keV before they enter into the electron diffusion region: a significant part of energy conversion takes place in the separatrix region during reconnection.

Keywords Double layer • Electron energization • Electron holes • Electron pitch angle • Hall reconnection • Kinetic reconnection • Particle in cell (PIC) simulation • Separatrix • Streaming instabilities

8.1 Definition of Separatrix

Magnetic reconnection is a fundamental process in magnetized plasmas, by which magnetic energy is released and converted into kinetic energy of charged particles. The importance of the separatrix was noticed (Petschek 1964) shortly after magnetic reconnection was originally proposed to explain explosive solar flares (Dungey

G. Lapenta (✉) • E. Cazzola
Afdeling Plasma-Astrofysica, Departement Wiskunde, KU Leuven, Celestijnenlaan 200b – bus 2400, Heverlee 3001, Belgium
e-mail: Giovanni.Lapenta@wis.kuleuven.be; Emanuele.Cazzola@wis.kuleuven.be

R. Wang
CAS Key Laboratory of Geospace Environment, Department of Geophysics and Planetary Science, University of Science and Technology of China, Hefei 230026, China
e-mail: rswan@ustc.edu.cn

W. Gonzalez, E. Parker (eds.), *Magnetic Reconnection*, Astrophysics and Space Science Library 427, DOI 10.1007/978-3-319-26432-5_8

1961). At that time, slow-mode shocks were supposed to be located along the separatrices and energy conversion could happen there. From then on, many theoretical and experimental efforts have been devoted to study the physics in the separatrix (Sonnerup 1970; Priest and Forbes 1986; Labellehamer et al. 1994; Shay et al. 2001; Pritchett and Coroniti 2004; Drake et al. 2005; Fu et al. 2006; Lu et al. 2010; Lapenta et al. 2010; Lapenta et al. 2011; Divin et al. 2012; Markidis et al. 2012a, b; Andre et al. 2004; Vaivads et al. 2004; Retinò et al. 2006; Khotyaintsev et al. 2006; Wang et al. 2012; Wang et al. 2013). The slow-mode shocks are frequently observed in the plasma sheet boundary layer in the magnetotail and are associated with magnetic reconnection (Feldman et al. 1984; Smith et al. 1984; Eriksson et al. 2004). However, conclusive evidence of the slow shock in the separatrix is still absent so far (Vaivads et al. 2006). On the other hand, more and more evidence shows that different kinds of microphysical processes (ion, electron scales or less) occur in the separatrix region (Andre et al. 2004; Retinò et al. 2006; Khotyaintsev et al. 2006; Vaivads et al. 2006; Divin et al. 2012; Markidis et al. 2012a, b; Wang et al. 2012; Wang et al. 2013; Wang et al. 2014; Lapenta et al. 2015). These microphysical processes play an important role in energy dissipation and transfer during magnetic reconnection.

The separatrix is the surface separating the plasma not yet entered into the reconnection process from the plasma already processed by reconnection. The separatrix is a surface in 3D but becomes a line in 2D. The present description is based on a quasi 2D point of view. In many situations, the region of reconnection is extended in one (ignorable) direction, allowing a 2D point of view where reconnection develops around a central null point. In MHD, the separatrix assumes a very different nature in the Sweet-Parker (SP) and in the Petschek reconnection scenario. For SP, a separatrix is merely the field line connected to the central null point, for that reason referred to as X-point. Dissipation is entirely localized in the central SP layer, with no dissipation of energy in the separatrix. For Petschek instead, a separatrix becomes a slow shock that produces a great portion of the dissipation of the reconnection process. Full kinetic models reconcile these two points of view confirming that energy is converted and transported not only near the central X-point but also along the separatrices.

Numerical simulation and observation researches have illuminated some key features of the separatrix region: the special flow pattern, the strong parallel current, the density cavity, various waves, and so on. Ions and electrons display different distribution near the separatrices. The electrons are mainly streaming towards the X-line along the separatrix while ions cross the separatrix (Lapenta et al. 2015). The distribution can naturally excite instability and results in various waves. The electron density cavity and thin current layer are frequently observed near the separatrices (Mozer et al. 2002; Andre et al. 2004; Vaivads et al. 2004; Retinò et al. 2006; Khotyaintsev et al. 2006; Wang et al. 2012), and sometimes concurrently observed (Wang et al. 2013). Electrostatic solitary waves, including electron holes (Farrell et al. 2002; Matsumoto et al. 2003; Cattell et al. 2005; Wang et al. 2013; Li et al. 2014; Wang et al. 2014) and electric double layers (Wang et al. 2014), lower hybrid waves (Retinò et al. 2006; Wang et al. 2012), whistler waves (Wei et al. 2007;

Deng and Matsumoto 2001; Zhou et al. 2011), and other electromagnetic waves (Fujimoto et al. 2011) exist near the separatrices also. These researches indicate that the separatrix is not only a low-energy electron flow channel but also an accelerator. Here, we will review the physics near the separatrices on the basis of numerical simulation and spacecraft measurement in the magnetosphere.

8.2 Electron Distribution in the Separatrix Region: Spacecraft Measurement

Over the last decades, magnetic reconnection has been frequently captured by spacecraft in the magnetotail and at the magnetopause. Occasionally, the ion diffusion region was encountered directly by spacecraft also, providing a good opportunity to investigate the electron distribution around the ion diffusion region (Fuselier and Lewis 2011; Paschmann et al. 2013). Based on previous measurements, a few special types of electron distributions were measured around the reconnection X-line, e.g. the field-aligned bidirectional distribution, the beam distribution, the flat-top distribution. These specific electron distributions are related to the electrostatic and magnetic geometry of the ion diffusion region (Egedal et al. 2005; Chen et al. 2008). Therefore, some of the observed distributions were even used to identify the ion diffusion region. Here, we will review the electron distributions observed around the reconnection site and discuss potential mechanisms.

The electron field-aligned bidirectional distribution is commonly observed during reconnection (Øieroset et al. 2002; Chen et al. 2008; Wang et al. 2010). In general, this type of distribution is clear in the ion diffusion region while disappears outside of the region (Øieroset et al. 2002). The distribution displays peaks in the directions parallel and antiparallel to magnetic field and minima in the perpendicular direction in the energy range from tens of eV to a few keV. The peaks in the parallel and antiparallel directions are gradually flattened out as the energy increases whereas the minima at the perpendicular direction are still evident. The distribution becomes isotropic at higher energy ($\geq$8 keV). If this type of electron distribution were purely due to the magnetic field geometry, a closed field structure would be required. However, the ion diffusion region is localized and the magnetic field geometry therein is open. Considering the typical magnetic field structure of ion diffusion region commonly used in the literature and shown in Fig. 8.1, an electrostatic potential is inferred near the X-line to account for the electron distribution (Egedal et al. 2005). The electrostatic potential was subsequently found in numerical simulations (e.g. Egedal et al. 2008) and can be distributed in a large area around the X-line (Egedal et al. 2012). In Egedal's model, the electrons can reach the X-line via two distinct types of trajectories: passing and trapped. Passing electrons drift into the X-line region and then flow away from it. Instead, trapped electrons rapidly bounce back and forth along magnetic field lines due to the

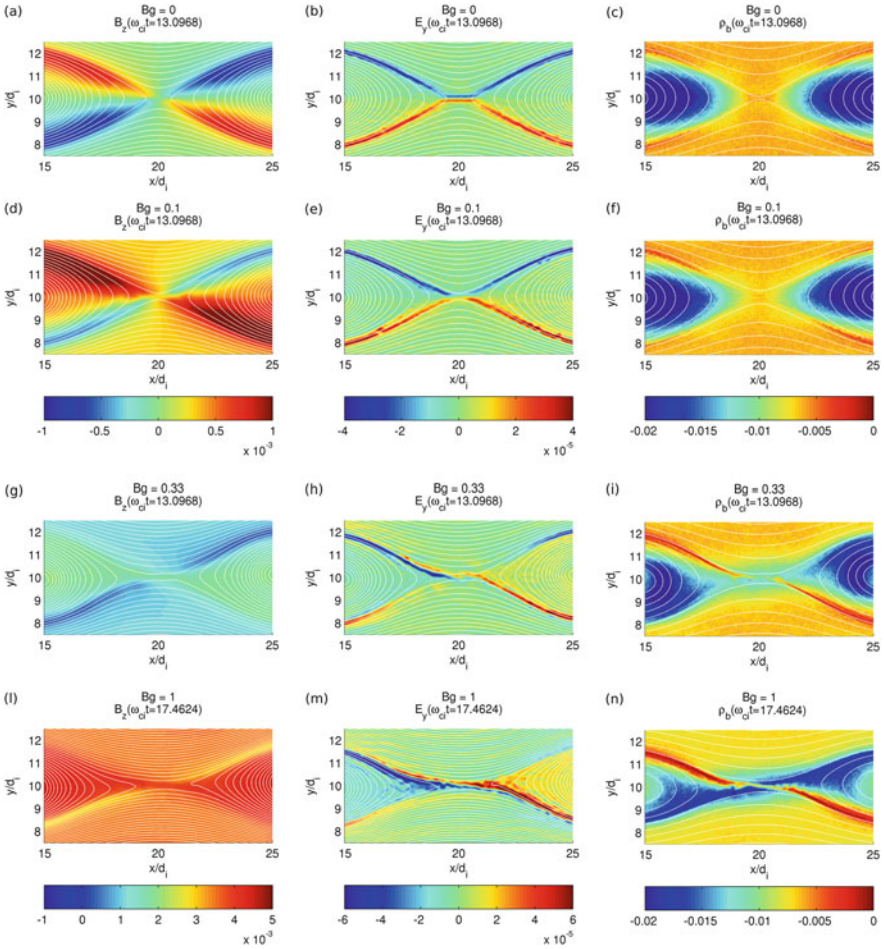

Fig. 8.1 Plot of the Hall magnetic field (i.e. Bz), Hall electric field (i.e. Ey) and the background density with the different values of the guide field considered in this work, namely Bg = 0 (panels **a**, **b** and **c**), Bg = 0.1 (panels **d**, **e**, **f**), Bg = 0.33 (panels **g**, **h**, **i**) and Bg = 1 (panels **l**, **m**, **n**). Ey has been preferred to E_perp1 for clarity. Time steps are chosen in order to capture the same reconnection outcome despite the differences driven by the presence of a guide field

particular electric and magnetic field geometry in the ion diffusion region, leading to the field-aligned bidirectional distribution.

More recently, the effects of the magnetic mirror have been considered to be one potential candidate for anisotropic distributions (Wang et al. 2010). Because collisionless reconnection in the magnetosphere is often bursty, reconnected magnetic field lines tend to pile up in the outflow region. The curved reconnected field lines lead to localized strong magnetic field regions also near the separatrices (Shay et al. 2001; Wang et al. 2010; Lu et al. 2010). Therefore, the electrons will bounce up

and down along the field lines and field-aligned anisotropic distributions are formed naturally.

In addition to the field-aligned bidirectional distribution, electrons frequently display a beam distribution in the vicinity of the X-line. The beam is primarily confined near the separatrices and regarded as part of the Hall current system (Fujimoto et al. 1997; Nagai et al. 2001; Nagai et al. 2003; Øieroset et al. 2001; Retinò et al. 2006; Wang et al. 2010). This beam streams towards the X-line along magnetic field and its energy is less than 5 keV during magnetic reconnection. Recent observations by Cluster demonstrated that the energy of the inflowing electron beam can extend up to 127 keV before electrons get into the electron diffusion region (Wang et al. 2012; Wang et al. 2013; Wang et al. 2014). This finding indicates that electrons have been accelerated near the separatrices. More details can be found in Sect. 8.5 below.

The flat-top distribution is commonly measured also at reconnection sites (Shinohara et al. 1998; Asano et al. 2008). A flat-top distribution shows a near constant phase space density in a certain energy range but a sharp decrease at relatively higher energies. In magnetotail reconnection, the shoulder energy range of the flat-top distribution is a few keV. Using multiple events of magnetic reconnection encountered by Cluster in the magnetotail, this type of distribution is found to be accompanied by large reconnection outflows and a finite magnetic field in the direction normal to the neutral sheet. The conclusion is than that flat-top distributions are mainly located near the outer boundary of the ion diffusion region. The analysis further points out that flat-top distributions are not correlated with the generation of suprathermal electrons (Asano et al. 2008).

8.3 Processes Developing at the Separatrices

Since the first full kinetic simulations of reconnection have started to uncover the physics of the separatrices, several processes have emerged to the limelight. Below we will discuss in order:

- The Hall physics that produces a strong electron current, associated with perhaps the most charismatic aspect of kinetic reconnection, the quadrupolar magnetic field, and linked also to a very strong Hall electrostatic field.
- These two Hall fields have strong energetic consequences, producing a strong electron energization and producing a strong Poynting flux signal propagating along the separatrix and carrying energy away from the reconnection site
- A strong electron, but also ion, flow pattern develops, producing a characteristic cavity with a reduced electron density.

These processes are generally developing in any configuration, but their detailed qualitative and quantitative features depend strongly on the configuration, and especially on the presence of out of plane guide fields and on asymmetries between the two reconnecting plasmas. To describe the physics of separatrices, we use the

simulation approach described in Appendix and based on an initial Harris current sheet. The reference frame adopted is based on the so-called simulation coordinate, i.e. with the plasma flowing in from the upper and lower side with the predominant velocity component along the vertical axis y. The reconnected plasma outflow is instead considered as macroscopically parallel to the abscissa coordinate x. The z component completes the reference frame and refers to the initial current direction.

8.3.1 Hall Physics at the Separatrices

The electromagnetic pattern in magnetic reconnection is mainly governed by the presence of an electric field along z around the reconnection point. This field is the reconnection electric field and is responsible for the process of reconnection: its strength defines the reconnection rate.

The main characteristic features of kinetic reconnection are

- the strong z-component (out-of-plane) of the magnetic field (i.e. B_z), also referred as Hall magnetic field,
- the in-plane perpendicular electric field (i.e. $E_{\perp 1}$).

The former is the natural consequence of the out-of-plane acceleration caused by E_z on magnetized electrons. Due to the progressively weakening of the magnetic field in approaching the reconnection region, electrons are in fact able to highly affect the magnetic field lines motion, by dragging them along and generating the out-of-plane component B_z. Electrons in this region are in fact fully magnetized, unlike the ions which result completely unmagnetized.

The resulting B_z will show different structures according to the initial field configuration. This dependence is visible in Fig. 8.1, where the same simulation with different initial guide fields B_g is shown. Panel (a) represents the case with no initial guide field. We observe the B_z structure to be quadrupolar with a specular symmetry across the current sheet. When the top-left magnetic field shows a positive polarity pattern, the corresponding low-right region show it as well. The same pattern results for the other two quadrants but with an inversed polarity.

This well-defined anti-symmetric pattern no longer holds when a progressively stronger guide field is initially set, which will significantly distort the Hall magnetic field, as shown in panels (d), (g), (l) in the same figure. The distortion is caused by the uniform polarity that B_z acquires when a guide field is initially set. The accelerated out-of-plane electrons will then have a significant parallel motion, affecting the field lines bending. A theoretical model of the Hall field polarity and symmetry can be found in Rogers et al. (2003).

The area occupied by the Hall B_z extends far beyond from the reconnection region, expanding mostly along the separatrices. This expansion is accompanied by a strong Poynting flux. The process has been recently studied in depth (Sonnerup 1979; Terasawa 1983), showing that the expansion of the Hall region along the separatrix develops at a speed far exceeding the Alfven speed (Shay et al.

2011). This super-Alfvenic expansion is carried by the wave characteristics of the dispersive kinetic Alfven wave (Lapenta et al. 2013). The strength of the energy flow carried by the Poynting flux is significant and capable of affecting the auroral region of the Earth (Shay et al. 2011; Lapenta et al. 2013).

The second peculiar feature of kinetic reconnection is the in-plane Hall electric field. This field is electrostatic (Lapenta et al. 2015) and is caused by the density imbalance caused by the differential motion of electrons and ions (Ma and Feng 2008).

The Hall electric field gives a good indication of the separatrices location, as noticeable in panels (b), (e), (h) and (m) in Fig. 8.1, where the quantity E_y is plotted as signature of the in-plane perpendicular component. Comparing the different panels the effect of the guide field can be determined. While the case with no guide field (panel b) shows a clear anti-symmetric structure with a well defined inverse polarity between the upper and lower side, as the guide field magnitude increases the pattern becomes more distorted with two dominant separatrices more in evidence. This is the first indication of a differentiation of the four separatrices. The physics developing on the upper-left and lower-right is similar but rather different from the other two.

Finally, the rightmost panels in Fig. 8.1 show the electron density. The case with no guide field shows the typical features of magnetic reconnection, namely the downstream regions where the outflowing jets interact with the ambient plasma to form density pile ups. The separatrices also form a characteristic pattern. At higher values of the guide field, a quadrupolar pattern forms with low densities regions at the top-left and bottom-right separatrices and higher density at the other two (e.g. panels i and n). This effect is an indication of the mechanisms at work in fast kinetic reconnection and their origin has been explained by Kleva et al. (1995) and a simple cartoon interpretation is given in Lapenta et al. (2014).

8.3.2 Energetics at the Separatrices

We can analyze the energetics at the separatrices by considering the two terms of the electromagnetic energy equation governing the rate of energy variation

$$-\frac{\partial e}{\partial t} = \nabla \cdot S + J \cdot E$$

Where e energy density and $S = \frac{\mathbf{E} \times \mathbf{B}}{\mu_0}$ is the Poynting flux.

Figure 8.2 plots the scalar term $J \cdot E$, which describes the work done by the fields on the, respectively, electrons (left column) and ions (right column). We clearly notice this work to be mainly done on the ions at the dipolarization fronts, with a much lower contribution on the electrons when the guide field is low or null. Dipolarization fronts are those plasma and magnetic field pile-up seen, for instance, at the lateral edges of the panels in Fig. 8.2 (blue in the left column and red in the

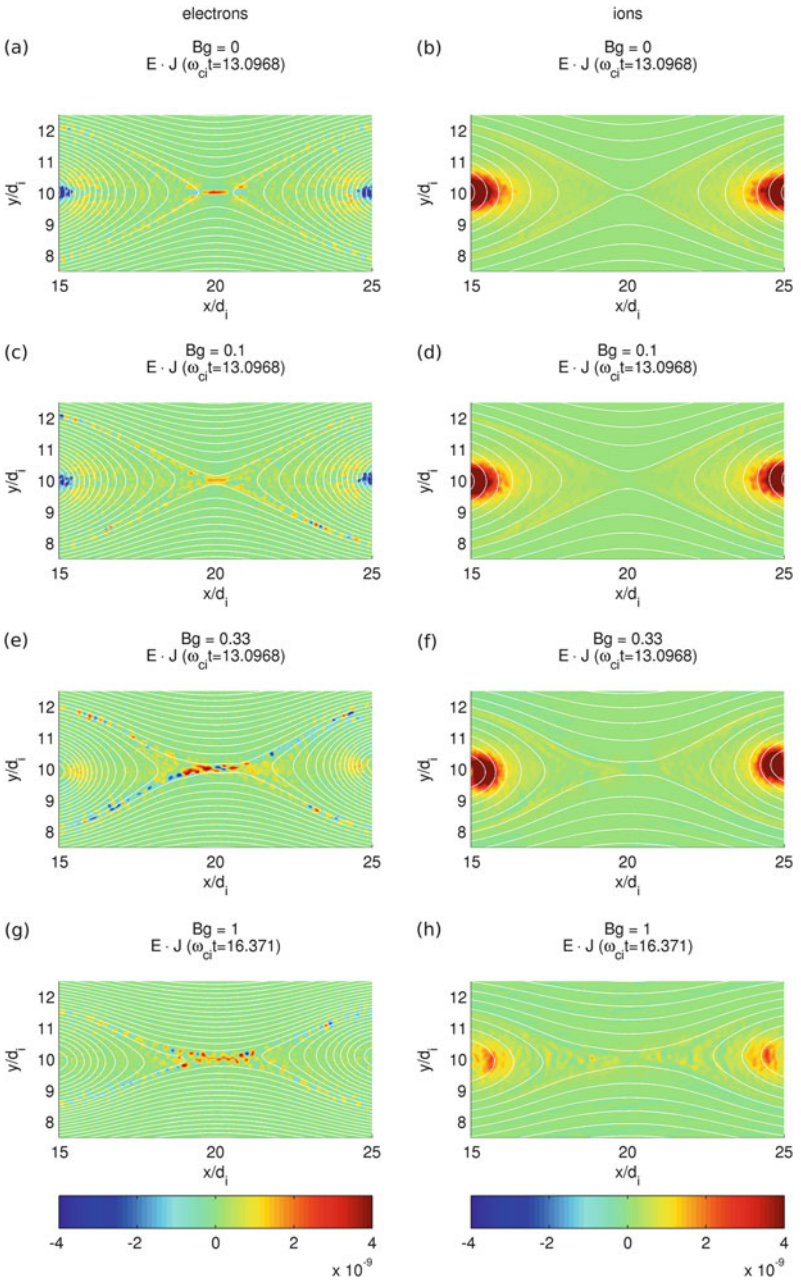

Fig. 8.2 Plot of the quantity E.J for the two species (electrons are shown in the *left panels* and ions are shown in the *right panels*) with the different initial guide fields used in this work. This quantity represents the work done by the electric field on charged particles. Two different regions are predominantly underlined, namely the electric bipolar structures at the separatrices for the electrons and the dipolarization fronts for the ions

right column). They represent the interaction between the reconnected outflow with the unperturbed background plasma, whose ultimate effect is a strong accumulation together associated with an increase in the plasma energy (Sitnov et al. 2009). The name comes from the natural tendency of the field lines to restore the initial dipolar configuration typical of the terrestrial field.

Conversely, at the separatrices the latter is observed to be predominantly electrons oriented. While an increase of the guide field does not show any global influence on the ions pattern, except only for the inhibition seen in the panel (h) with $B_g = B_{0x}$, the work done by the electric field on the electrons turns out particularly sensitive to the guide field. The electron work at the separatrices becomes much stronger in presence of strong B_g. In particular, the bipolar structures associated to the strong localized bipolar parallel electric field (see next section) are particularly evident. Furthermore, in all cases concerning the electrons, but especially with low guide fields, a relevant energy exchange very close to the reconnection region is present in consequence of the work done on electrons by the Hall fields.

Likewise, the Poynting flux $S = \frac{\mathbf{E}\times\mathbf{B}}{\mu_0}$ describes the energy and momentum flux carried by electromagnetic fields. This term, is considered in the energy equation with its divergence to represent the magnitude of the energy flow. Plots of the Scomponents are shown in Figs. 8.3 and 8.4, together with $\nabla \cdot S$ (right column in Fig. 8.4), as a function of the initial guide field.

This quantity is particularly useful at better understanding the evolution of the Hall fields (Lapenta et al. 2013), as noted above. Bearing in mind the frame of reference chosen, the component S_x describes the energetic evolution of the Hall magnetic field B_z, whereas the component S_z describes the evolution of the Hall electric field E_y. We notice the Poynting component along x starting from an ordered pattern with no guide field, which is expected given the strict symmetry typical of fast reconnection in absence of guide field, and increasing its bipolarity along the top-left and bottom-right separatrices, as well as being fully predominant within the outflow regions when $B_g = B_{0x}$. This pattern directly follows the positive regions of B_z displayed in Fig. 8.1.

On the other hand, the dominant component is S_z (left panels in Fig. 8.4), which is directly linked to the Hall electric field. Peculiar of this component is the positive value held when the guide field is null or very low, e.g. panel (a) and (c). A negative component only shows up when a strong guide field is initially set (panel g).

8.3.3 Flow Pattern and Density Structures

Ions and electrons move very differently at the separatrices. Given the large extension of the separatrices, only very few particles will pass through the central reconnection region, whereas the majority of them will be involved in the reconnection only crossing the separatrices far from the X-point. In particular, while ions are directly deflected outwards following the reconnected outflow, electrons are instead observed to preferentially follow the separatrices shape inward by flowing towards

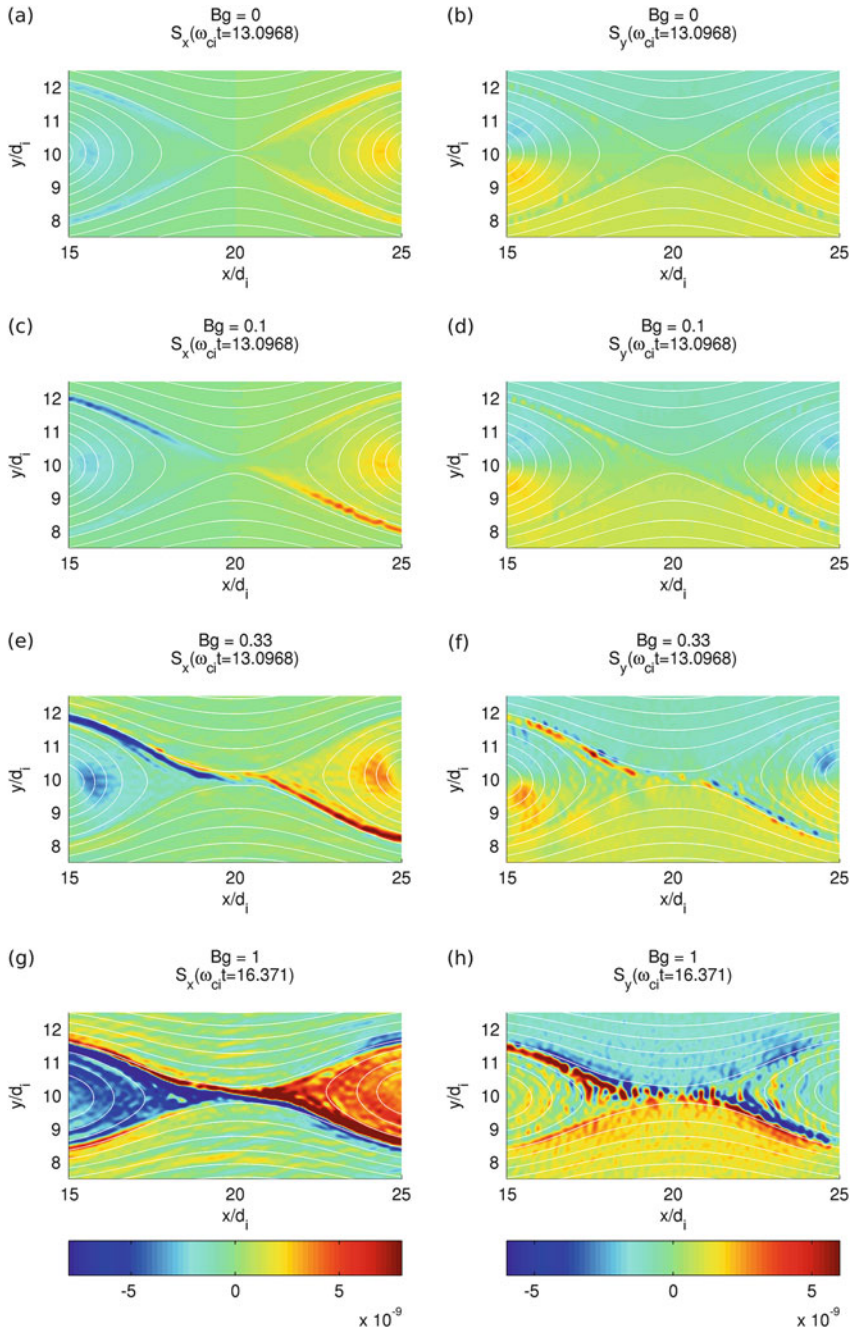

Fig. 8.3 X- (*left panels*) and Y-component (*right panels*) of the Poynting flux with different the initial guide fields considered in this work. In particular, Sx represents the energetics of the Hall field Bz, which shows the typical distortion at the separatrices for strong guide fields

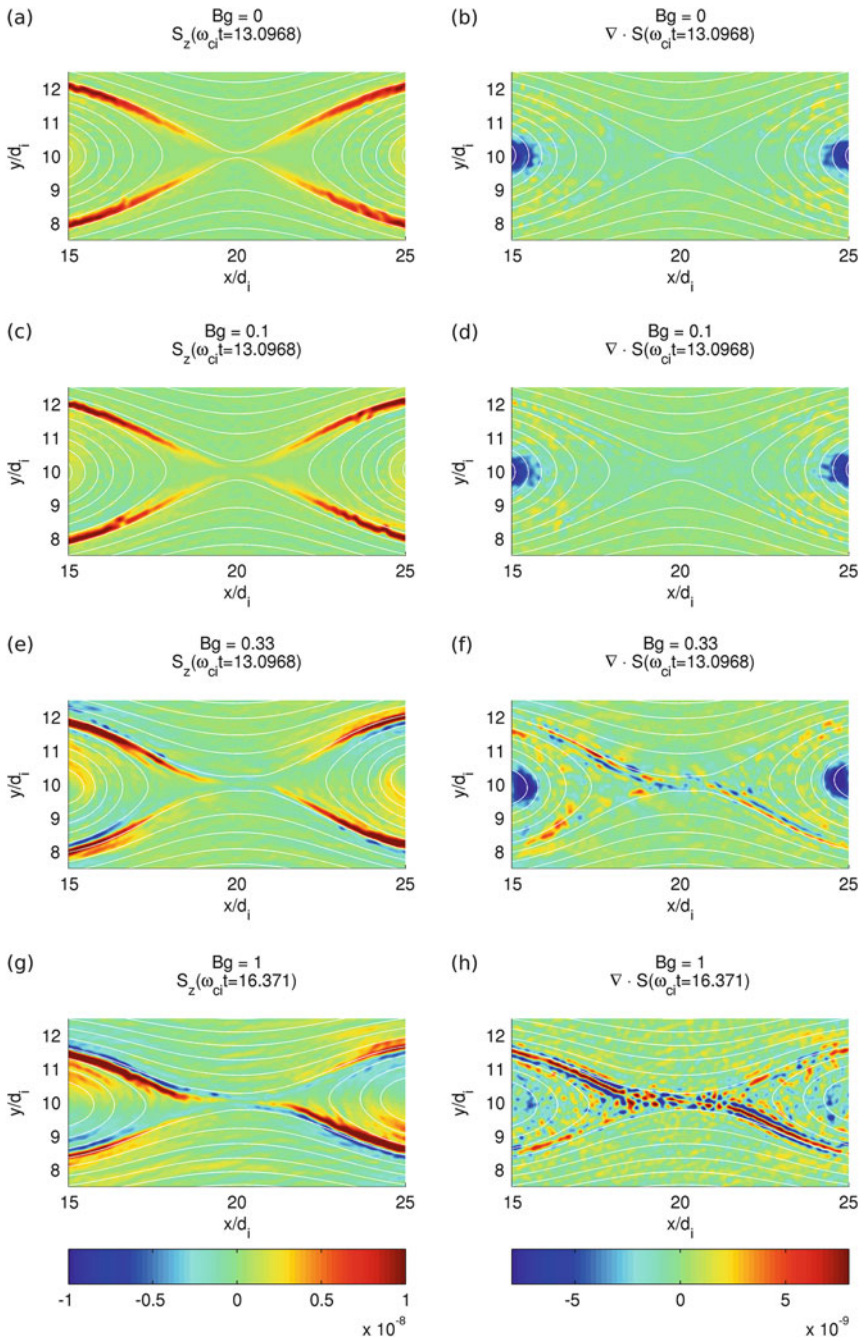

Fig. 8.4 Z-component (*left column*) and the divergence (*right column*) of the Poynting flux with the considered guide fields. Sz represents the energetics of the Hall field Ey, which peculiarly shows negative values only when relatively strong guide fields are present

the central X-point, and being later expelled outwards catching up with the ions in the outflow region. A dominant parallel electron motion then is formed along the separatrices. Particles in fact encounter less resistance at flowing parallel to the magnetic field than following the $E \times B$ drift. The dominant electron parallel motion is clearly visible in the panels (b), (d), (f) and (h) in Fig. 8.5, where this component normalized to the initial thermal velocity is shown for the different guide fields considered in this work. Given the structure of the Hall physics, in the case with $B_g = 0$ the electron flow is seen to always be toward the X-point (panel b). However, situation changes significantly when the guide field is set with relatively high values, such as in panel (f) and (h). Here we observe the electron motion to head toward the X-line in the top-left and bottom-right separatrix, and flowing away from it at the top-right and bottom-left. This effect is connected to the quadrupolar density pattern mentioned in the previous section (Kleva et al. 1995; Ricci et al. 2004; Lapenta et al. 2014).

The parallel motion gives origin to different instabilities. First, given the different species behavior observed at the separatrices, local density unbalance are generated in very narrow regions around them, which in turn leads to a charge imbalance and the formation of strong localized parallel and perpendicular electric fields. The latter represents the Hall electric field mentioned earlier and responsible for the further lines bending near the separatrices. The former is instead the main source of some important streaming instabilities described in the next section.

8.4 Instabilities Developing at the Separatrices

The flow, density and current pattern described above around the separatrices makes them highly susceptible to important instabilities. We focus here especially on three: beam instabilities leading to electron holes, drift instabilities leading to rippling of the separatrix layer and current driven tearing instabilities causing secondary reconnection sites.

8.4.1 Streaming Instabilities and Electron Holes

The main obvious source of free energy is the presence of populations of highly accelerated electrons that produces electrostatic parallel propagating instabilities. Figure 8.5 shows the electron parallel flow and the parallel electric field. Well defined bipolar signatures are evident, in some cases appearing in the form of isolated structures and in others as a train of oscillations. The presence, size and strength of the streaming instabilities and of the electron holes depends strongly on the plasma conditions. When, starting from antiparallel reconnection, increasingly larger guide fields are considered, the strength of the plasma flow at the separatrices intensifies. As a consequence, the streaming instability increases and the number of

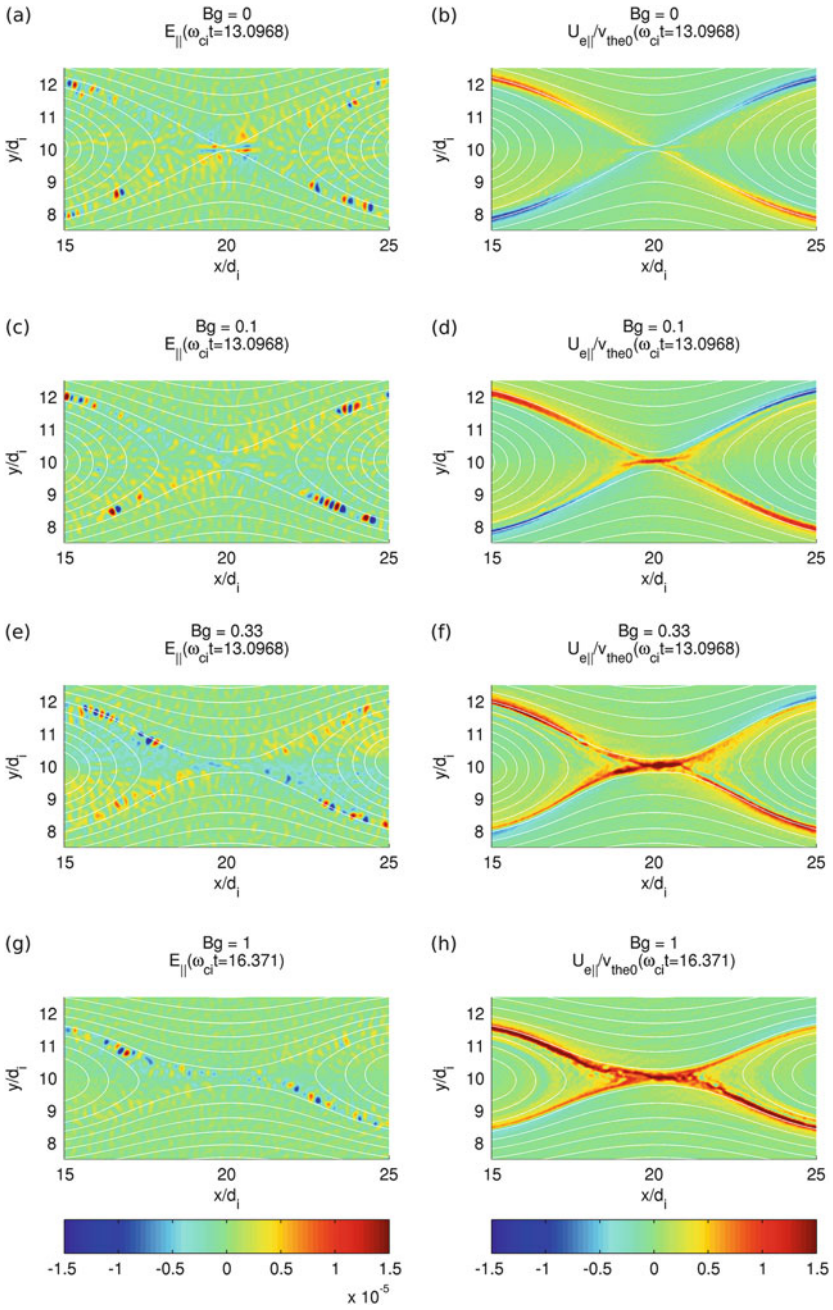

Fig. 8.5 Parallel component of the electric field (*left panels*) and the parallel electron velocity (*right panels*) with different initial guide fields. In the *left panels*, presence of strong bipolar structures are clearly visible along the separatrices with an evident incrementing distortion for stronger guide fields. Similarly, the *right panels* show the flow asymmetry attained by the electron parallel velocity when stronger guide field is incrementally increased

electron holes generated becomes larger (Lapenta et al. 2011). An additional effect of the guide field is to create a distinct asymmetry between the four separatrices, with stronger electron flows and consequently more EH forming on the two opposite low density separatrices. Figure 8.5 in the bottom panels shows how at the largest guide field considered (Bg = 1) the flow channel on the upper-left and lower-right separatrix is stronger and wider. Correspondingly, EH are predominantly present there.

The results in Fig. 8.5 are for realistic parameters (Lapenta et al. 2011). The mass ratio is that of hydrogen and the thermal speed of the species is typical of the Earth magnetotail. In space, of course, the plasma in the separatrices is made primarily of hydrogen. However, sometimes simulations must resort to smaller mass ratios for numerical expediency. Especially explicit PIC methods need to use the largest computing possible (Bowers et al. 2009) to use physical mass ratios. Implicit PIC, as is the case of iPic3D (Markidis et al. 2010) used here, remove this difficulty and the physical mass ratio becomes readily manageable (Lapenta et al. 2006; Lapenta 2012). The use of reduced mass ratios forced by the numerical limitations of explicit codes requires to carefully evaluate the scales of the streaming instabilities. When observed in real terms, the size of the electron holes decrease as the mass ratio is increased, being as large as an ion inertial length (di) at mass ratio 64, decreasing to a fifth of that at physical mass ratio of 1836. But when measured in terms of the electron skin depth, (de), the size is always the same: 8de (Lapenta et al. 2010).

The exact nature of the instability can be debated. The Buneman instability and the two electron stream instability are clean modes from neatly arranged well-defined plasma conditions (Melrose 1986). In the separatrix, instead, there are very complex conditions with different ion and electron populations drifting with respect to each other. Additionally, the standard instabilities mentioned above are relative to a uniform plasma, but the conditions at the separatrix are highly non uniform.

At relatively high guide fields, comparable in size with the in plane reconnecting magnetic field, the instability is reported to have primarily the nature of a Buneman instability (Pritchett 2005; Goldman et al. 2008; Divin et al. 2012). At lower guide fields, the relative drift of different electron populations causes two-stream type instabilities (Goldman et al. 2014). In either case, the end result is the formation of electron phase space holes.

Figure 8.6 shows an example of the phase space along a separatrix showing strong bipolar structures in the parallel electric field (Divin et al. 2012). The electron phase space shows the presence of two characteristic phase space vortices: the signatures of electron holes (EH).

Even in presence of multiple reconnection sites, the streaming instabilities develop in the electron flow along the separatrices leading to each X-point with the same mechanism outlined above causing the onset of EH (Markidis et al. 2012a). 3D kinetic simulations confirm that along the separatrix surfaces parallel electric fields and EH still form even when the full 3D evolution is considered (Markidis et al. 2012b).

The presence of electron holes (EH) along the separatrices is of great importance.

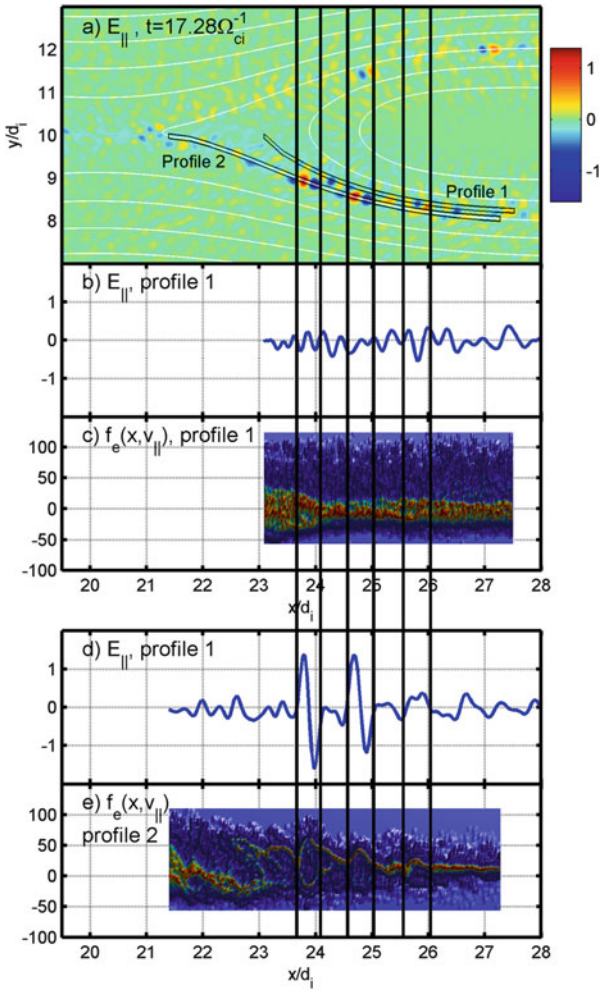

Fig. 8.6 The phase space is shown along two different magnetic flux tubes indicated in the *top panel*. Electron holes are shown forming in phase space. This figure is taken from Divin et al. (2012)

First, the EH are present in a region where electrons are flowing towards the reconnection region and their presence affects the plasma and fluctuation properties of the inflowing plasma. Recently, this effect has been identified in the presence of a whistler fluctuations emitted by the EH via the Cerenkov mechanism and irradiated from the separatrices in the inflow plasma region (Goldman et al. 2014).

Second, the EH can be used as observational markers of separatrices and indirectly of being in the vicinity of a reconnection site.

Finally, the EH tend to heat the electrons leading to substantial conversion of directed electron energy caused by the electric field into electron thermal energy

(Lapenta et al. 2015). The electrons participating in reconnection are therefore heated even before reaching the reconnection site itself.

8.4.2 *Low Density Separatrices: Drift Instabilities and Separatrix Rippling*

The presence of strong gradients in all quantities and especially in the velocity and density cause another classic class of modes: the drift instabilities. These instabilities propagate in the plane normal to the reconnection plane and therefore cannot be seen in 2D simulations. Their presence was uncovered first in 3D simulations (Markidis et al. 2012b).

Their appearance ripples the separatrix surface forming spines that propagate along the magnetic field lines. Figure 8.7 shows the ion density in two different views in a iPic3D simulation. The top panel shows in false colours the perturbation of the ion density. An instability develops deforming the edge of the density cavity to form a highly rippled surface. The instability affects the whole cavity but it is much more developed on the inner ridge facing the neutral line, being less pronounced in the outer edge. The 3D volume rendering of the ion density in the bottom panel shows the ribs of a spine-like structure forming on the surface of the separatrix. Higher densities are in yellow and lower in blue. The transfer function of the volume rendering makes the intense yellow transparent and invisible, to highlight and make visible the pale yellow and especially the blue. A few selected field lines (coloured based on the Bx local component) are shown to identify the central X-point. The ribs of the spine are bent by the magnetic field and follow it. The wave causing it, therefore has wavefronts parallel to B and direction of propagation perpendicular to B, as expected for drift modes.

The exact kinetic nature of the free energy driving the instability is a combination of different gradients in density and velocity, but simple electron-fluid theories provide a good approximation to the observed growth rate (Divin et al. 2012). The drift mode at work here is sinuous (kink-like) in nature, making the initially smooth surface of the density cavities become rippled. The paradigmatic sinuous mode is the Kelvin–Helmholtz instability. In the present case we are in fact in presence of several effects: density gradients, velocity shear and curvature of the field lines so many free energy drives are present to determine the exact growth rate. Considering just the simple mode based on electron KHI leads to a correct order of magnitude estimation but not to an accurate representation of the mode growth rate (Divin et al. 2012) observed in the simulations. A more accurate estimation requires to consider also the other effects mentioned above.

In full 3D models as well as in Nature, the two modes described above, the streaming modes propagating along the magnetic field and the drift modes propagating across it both develop concurrently and their non-linear evolution leads to an interaction between the spines and the EH (Markidis et al. 2012b). The electron

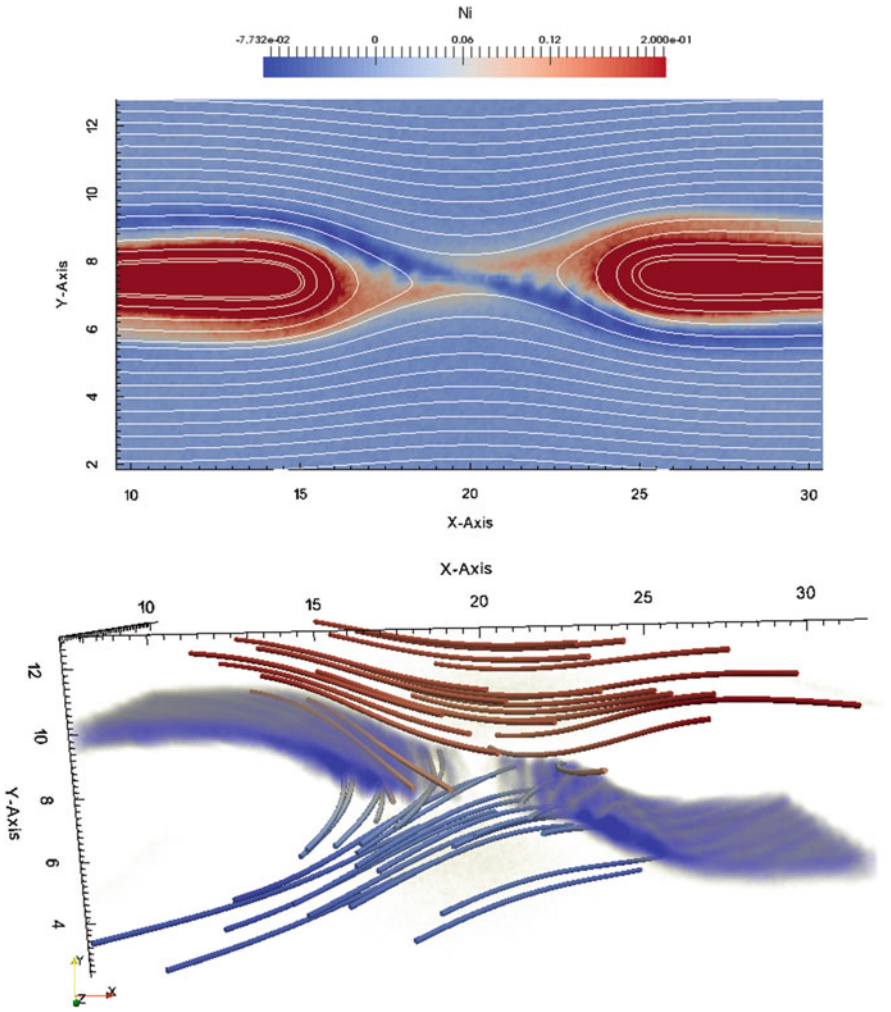

Fig. 8.7 Run Tred47 at $t \sim 18\ \omega_{ci}^{-1}$. *Top panel*: density perturbation N_i-n_b in false colour. *Bottom panel*: Volume rendering of the ion density N_i. The volume rendering uses a transfer function that makes values above 0.2 invisible allowing to focus only on the density cavity. A few selected field lines are shown to guide the eye. The color of the field lines is given by the local value of B_x

holes tend to move along the magnetic fields and therefore move along the spines. EH tend to appear between consecutive low density ribs in relatively higher density regions of the cavities. The positive hemisphere of the bipolar electric field precedes the negative part in the direction pointing toward the X-point along the separatrix (Markidis et al. 2012b).

8.4.3 *High Density Separatrices: Tearing of the Separatrix Currents*

The narrow current present at the separatrix is the source of a third class of instabilities: tearing causing the formation of secondary reconnection sites. The effect is especially strong in presence of large guide fields when the four separatrices are highly asymmetric. Two opposite separatrices form the density cavities with the strong electron inflow towards the reconnection site that causes the streaming and drift instabilities described above.

However, the other two separatrices form a density enhancement and a strong thin current. This current can become unstable to a different mode. Figure 8.8 shows the isosurfaces of the intensity of the electron current. The current layer along the two high density and high current separatrices becomes fragmented into different current filaments. These are magnetic flux ropes representing secondary reconnection sites (Daughton et al. 2011).

The exact nature of the instability in the two high density and high current separatrix is also a branch of drift modes but in this case its parity is opposite to that observed in the low density separatrices. The mode here is varicose (sausage-like) and transforms the initially smooth current channel forming filaments of intensified currents. These filaments are the seed of flux ropes forming along the separatrices. The mode is the classic drift tearing mode and the observed growth rate can be accurately described in its terms (Daughton et al. 2011).

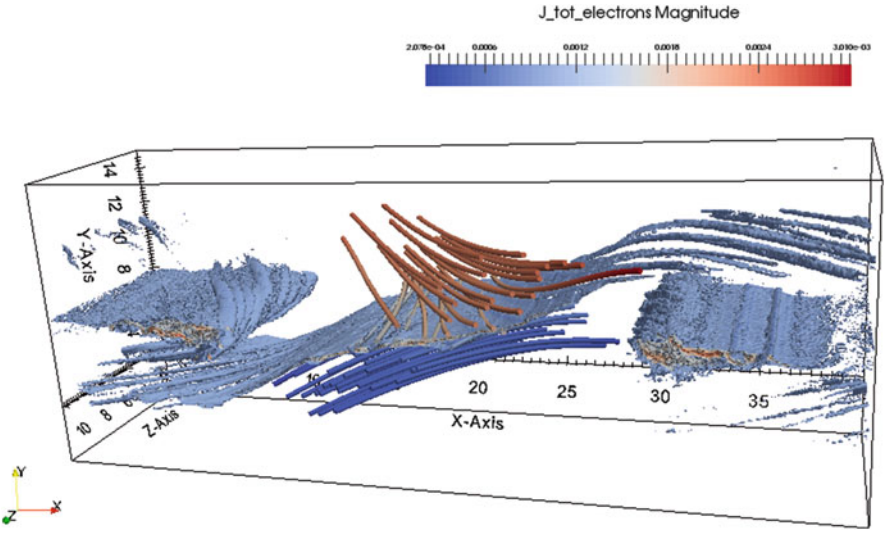

Fig. 8.8 Run Tred47 at $t \sim 24\ \omega_{ci}^{-1}$. Isosurfaces of the electron current. A few selected field lines are shown to guide the eye. The color of the field lines is given by the local value of B_x

8.5 Electron Acceleration Near the Separatrices

One long outstanding issue in the study of magnetic reconnection is where and how electrons are accelerated. According to Hall magnetic reconnection (Sonnerup 1979; Terasawa 1983), electrons can only be accelerated in the so-called electron diffusion region where electrons are decoupled from the magnetic field ($\mathbf{E} + \mathbf{V}_e \times \mathbf{B} \neq 0$) and accelerated by the reconnection electric field. In the plasma sheet of the magnetotail, the scale of the electron diffusion region in the Sun-Earth direction is only about tens of km. It is so localized a region that it cannot be utilized to reasonably explain the abundance and pervasive presence of energetic electrons in the magnetotail. Using Wind data over three and a half hours, Øieroset et al. reported a reconnection event in the magnetotail at $-60\ R_E$ and found that the suprathermal electron fluxes peaked in the ion diffusion region and gradually decreased as the spacecraft got away from the region (Øieroset et al. 2002). Within a rough X-line point of view, this observation indicates that electrons were accelerated near the X-line point. However, at closer inspection, using a much shorter time interval (30 min) around the X-line, the peak of the suprathermal electron fluxes did not exactly correspond to the reversal point of the high speed flow. Afterwards, on the basis of tens of reconnection events observed by Geotail in the near-earth ($-30\ RE < X_{GSM} < -15\ RE$) and in the distant magnetotail ($X_{GSM} < -50\ RE$), Imada et al. (2005) showed that the suprathermal electrons piled up in the outflow region and not at the X-point in the vicinity of the reconnection diffusion region. Using Cluster measurements in the near-Earth tail, Wang et al. also found that the fluxes of energetic electrons peaked near the pile up region of the reconnected magnetic field rather than at the X-point (Wang et al. 2008). These measurements confirm that the electrons are accelerated in reconnection but the mechanisms are still unclear.

According to the Hall reconnection model, the low energy electrons stream towards the electron diffusion region along magnetic field lines near the separatrices. The low-energy inflowing electrons have been often observed by spacecraft and generally display a beam distribution (Øieroset et al. 2001; Nagai et al. 2001; Nagai et al. 2003). The typical energy of the inflowing electrons is several hundred eV and the highest energy is less than 5 keV (Nagai et al. 2003). Recent observation by Cluster in the magnetotail pointed out that the energy of the inflowing electrons extends up to 20 keV in the separatrix region during reconnection with moderate guide fields (Wang et al. 2012). This finding implies that the electrons might have been accelerated near the separatrices. In general, the inflowing electrons are confined to a narrow region in the direction normal to the separatrices (Andre et al. 2004; Vaivads et al. 2004; Retinò et al. 2006; Wang et al. 2012). Consequently, the time resolution of the electron data obtained by the spacecraft on-orbit is too low to accurately resolve the distribution of the higher energy electrons in the narrow region. By using the Cluster spacecraft in Burst mode when data in the higher time resolution is available, the electron data in the narrow region can be analyzed in detail. The results show that the electrons have already been accelerated in the separatrix region before they enter into the electron diffusion region.

The mechanisms for generation of the suprathermal electrons in the separatrix region are still controversial (Pritchett and Coroniti 2004; Drake et al. 2005; Pritchett 2006; Divin et al. 2012; Wang et al. 2014; Lapenta et al. 2015). In two-dimensional particle-in-cell simulations of magnetic reconnection with a guide field, the electron acceleration processes were found to consist of two steps: a cold electron beam is created by the parallel electric field in the separatrix and is further accelerated in the X-line to relativistic energy (Pritchett and Coroniti 2004; Pritchett 2006). Drake et al. (2005) suggested that electrons could be directly accelerated to relativistic energy in the separatrix, acting as plasma accelerator because of the strong parallel electric field therein (Drake et al. 2005). Moreover, the electron surfing acceleration in the separatrix was proposed also during externally driven reconnection (Hoshino 2005). The electrons were trapped due to the electrostatic potential well of the polarization electric field and accelerated by the convection/inductive reconnection electric field. More details on the simulation results are presented in Sect. 8.3. By using Cluster measurements in the magnetotail, electron acceleration up to 100 keV in the separatrix is confirmed (Wang et al. 2013) and the roles of the electrostatic isolated waves (Double layers and Electron hole) in the separatrix are addressed (Wang et al. 2014).

An overview of the reconnection event encountered by Cluster in Burst mode can be found in Wang et al. (2013) and Nakamura et al. (2008). Here, we focus on the data in the separatrix crossing. The spacecraft crossed the separatrices in the northern hemisphere of the tailward outflow (the first crossing) and in the southern hemisphere of the earthward outflow (the second crossing) and the trajectories of the two crossing can be found in Fig. 8.9. The measurements during the two crossings correspond to the Figs. 8.10 and 8.11, respectively. In the first crossing inside the tailward outflow (Fig. 8.10a), the spacecraft passed through the ion diffusion region from south to north (Fig. 8.10d) and measured a reversal of the out-of-plane magnetic field from positive to negative (Fig. 8.10e); while it partly travelled the separatrix region within the earthward flow in the second crossing (Figs. 8.11d, e). During both crossings, a thin electric current layer was observed in outer boundary of the Hall magnetic field region (Figs. 8.10f and 8.11f), the time scale being about 10 s, and the current was primarily along the magnetic field. In both current layers, low energy inflowing electrons were measured and could be the main carrier of the current. It is surprising that a high-energy electron beam was observed to stream towards the X-line in both layers as well. The energy of the beam reached 127 keV (Figs. 8.10g and 8.11g). So, it is undoubted that electrons are accelerated while they are streaming toward the X-line. The separatrices can extend as far as tens of ion inertial lengths in the outflow direction, as previously reported (Retinò et al. 2006; Khotyaintsev et al. 2006; Wang et al. 2012). If electrons can be accelerated in the entire separatrix region, most of the electrons would be accelerated there and the released energy in this region would be noteworthy during reconnection. In both observed separatrix regions, the electric field oscillation was enhanced dramatically and the variation could be as large as 150 mV/m (Figs. 8.10c and 8.11c). However, the electric field was only measured by Cluster in the spin plane. Thus, we cannot calculate the parallel electric field unless the magnetic field lay in the spin plane.

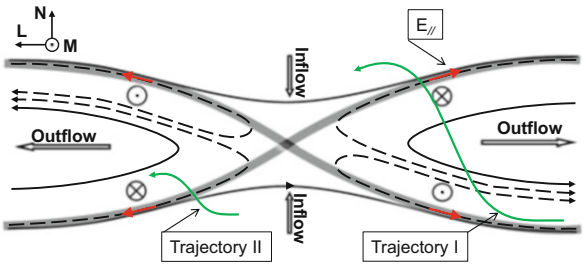

Fig. 8.9 A schematic illustrator for ion diffusion region of magnetic reconnection. The *green curves* represent trajectories I and II which correspond to the first and second crossing of the separatrices, respectively. The *shadow area* denotes the region near the separatrices

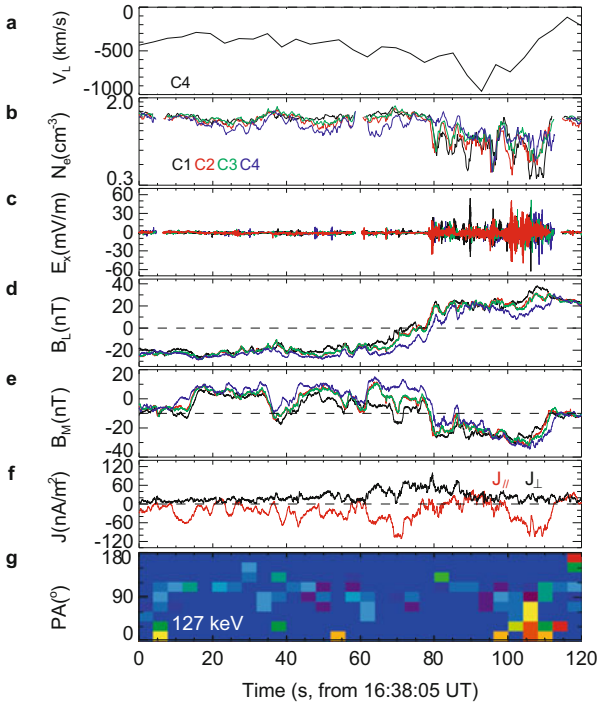

Fig. 8.10 The measurement in the first separatrix crossing. (**a**) Ion bulk flow at the spacecraft C4, (**b**) electron number density, (**c**) electric field in the x component of the spacecraft spin system, (**d**–**e**) magnetic field in the L and M components, (**f**) current density in the parallel (*red line*) and perpendicular (*black line*) directions. The current density is estimated by the Curlometer technique, (**g**) electron pitch angle distribution at 127 keV are shown from top to bottom

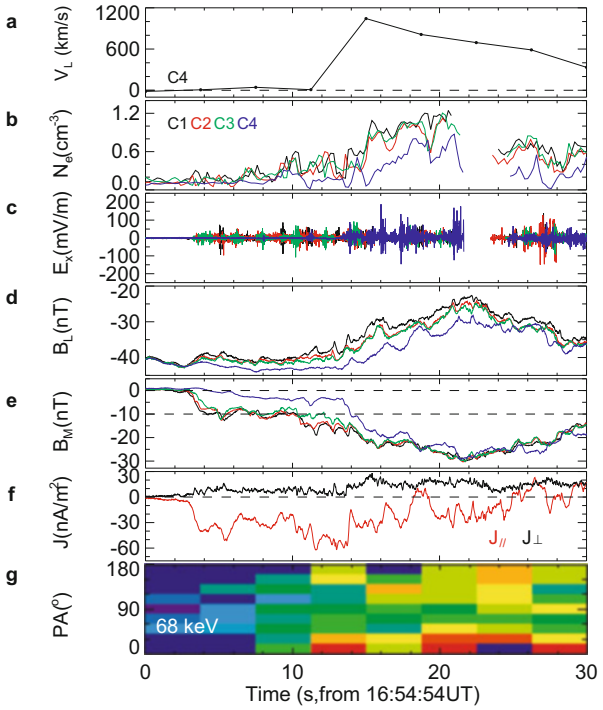

Fig. 8.11 The measurement in the second separatrix crossing in the same format as Fig. 8.2. The *bottom panel* represent electron pitch angle distribution at 67 keV

Fortunately, there was a short span when the magnetic field was mainly in the spin plane in both current layers. The estimated parallel electric field and one component of perpendicular electric field during the first and second separatrix crossings are shown in the left and right columns of Fig. 8.12, respectively.

In the first crossing, the parallel electric field was negative and displayed a series of pulses. The parallel electric field directs away from the X-line and the amplitude could reach −10 mV/m, so the inflowing electron beam was created and accelerated. Assuming the parallel electric field was everywhere near the separatrices and its value was about −10 mV/m, an electron would get kinetic energy of 100 keV by experiencing a displacement of about ten ion inertial lengths which is shorter than the estimated length of the separatrices. In addition, the perpendicular electric field was much stronger than the parallel component.

In the second crossing, a few electric double layers were measured. The double layer was accompanied by a series of electron holes in its high potential side. One of the double layers is presented in the right column of Fig. 8.12. The parallel electric field carried by the double layer was as strong as −20 mV/m and directed away from the X-line. These double layers were propagating along magnetic field lines away from the X-line, with a velocity comparable to the ion acoustic speed.

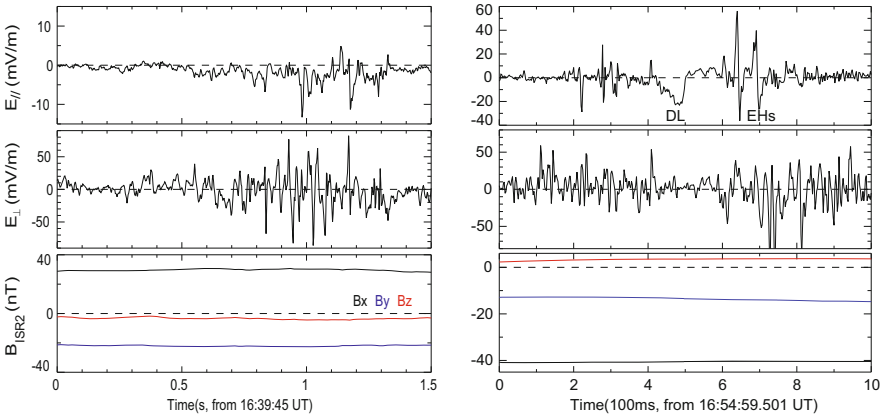

Fig. 8.12 The *left column* shows the parallel and perpendicular electric field, and three components of magnetic field in the spacecraft spin system in a short interval in the first separatrix crossing. The *right column* shows the similar data in the second separatrix crossing

Therefore, electrons near the separatrices were accelerated and injected toward the X-line as a beam. Double layers were persistently created during reconnection, and propagated away from the X-line, leading to a large number of electrons near the separatrices being accelerated. The series of electron holes at the high potential side of the double layer could be created by the instability of the electron beam resulted from the double layer. The electron holes were gathering towards the electron diffusion region. These finding can be compared with the role of the electron holes in simulation discussed in Sect. 8.4.1.

Localized parallel electric fields were also found at the reconnecting magnetopause. They are associated with plasma density depletion (cavity) and primarily observed on the magnetospheric side of the magnetopause current sheet (Mozer et al. 2002; Mozer and Pritchett 2010). The direction was such as to accelerate electrons streaming towards the electron diffusion region (Mozer and Pritchett 2010). Similar characteristics of parallel electric field associated with magnetic reconnection are measured both at the magnetopause and in the magnetotail, indicating that the formation of parallel electric fields can be created both in symmetric and asymmetric reconnections. These findings shed new light on the microphysics near the separatrices but at the same time raise a new issue: e.g. where and how double layers are created, how long they can survive, what roles the electron holes play in reconnection (Wang et al. 2014). To resolve these issues, data in milliseconds is needed. The new mission MMS will provide such data in the vicinity of magnetic reconnection and give us a fantastic chance to uncover the mystery.

8.6 Conclusions and Future Directions

We have reviewed several results relative to the recent understanding gained in the study of the role of the separatrices in reconnection processes. Many new discoveries have been reported:

- the presence of the Hall physics caused by fast moving electrons
- the presence of a powerful and rapidly propagating Poyting flux that carries substantial energy to the Earth inner space environment
- the role of the separatrices in particle energization
- the presence of characteristic particle distribution function
- the development of electrostatic and electromagnetic instabilities at the separatrices

These processes reviewed above have a profound impact on our understanding of reconnection. But most importantly they have a profound impact on the evolution of reconnecting plasmas. In a 2D vision, most plasma goes from the inflow to the reconnection outflow via the separatrices without coming in the vicinity of the X-point. This fundamental concept first outlined by the Petschek model is also a critical feature of kinetic reconnection. Several points remain open, despite the great progress.

The role of the separatrices in kinetic reconnection is so similar to that of the Petschek model that a question emerges with powerful: as the scales of the systems undergoing reconnection become larger and larger are the separatrices acquiring the role of slow shocks? Are they becoming shocks? A first answer to the negative has been given by Liu et al. (2012). But this conclusion reached at zero guide field is reversed at higher guide fields (Innocenti et al. 2015) where the evidence in numerical simulations is compelling to the presence of shocks and rotational discontinuities.

When moving to a fully 3D point of view, separatrices become surfaces and separatrix layers are formed playing an important role in reconnection. The studies reported above still assume a mostly 2D-like vision of reconnection where 3D effects are studied in a system with an extended so-called X-line, where the classic 2D configuration is repeated in every plane in the third dimension. This is an acceptable assumption in many situations in the tail and in the magnetopause of the Earth (and other planets) where a certain amount of symmetry can be assumed over a span of the GSM y coordinate.

But in space there are many examples also of truly 3D configurations with isolated null points. The study of the structure around such null points is just beginning within a full kinetic approach (Olshevsky et al. 2013, 2015a, b), already uncovering a very different evolution with the formation of channels of intense dissipation reminding Z-pinches.

The upcoming years will be of intense revision of the results reviewed above thanks to the new discoveries that will be made by the MMS mission. We have focused above on many electron-scale phenomena at the separatrices. MMS will have the temporal and spatial resolution needed for the first time to measure the features so far only guessed in simulations. The review above presents some key diagnostics that MMS will be able to try to detect. But surely MMS will also present us with challenges that will require new thinking and new modeling that will push forward our understanding of the role of separatrices.

Acknowledgements All Cluster data are available at ESA Cluster Active Archive. We thank the FGM, CIS, EFW, PEACE, and RAPID instrument teams. This work is supported by the National Science Foundation of China (NSFC) grants (41474126, 41104092, 41174122, and 41274144) and by the National Basic Research Program of China (2014CB845903).

A.1 Appendix: List of the Simulations Shown

The present review reproduces a few very selected results in the literature and uses for the largest part new results from the suite of simulations developed by the University of Colorado and the KU Leuven for the MMS mission. These runs are available at the NAS supercomputing server of NASA. The full list of runs is described in the accompanying wiki and are summarised in Lapenta et al. (2014). Here we identify the properties of the specific runs shown.

We reported four 2D runs of increasing guide field:

- Run98: Bg/B0 = 0
- Run99: Bg/B0 = 1/10
- Run97: Bg/B0 = 1/3
- Run100: Bg/B0 = 1

with several more guide fields available on the server. All these runs use a initial Harris equilibrium with background with nb = 0.1 n0, mi/me = 1836, Ti/Te = 5, vthe/c = 0.045 and thickness L/di = 0.5. The box has Lx/di = 40 and Ly/di = 20. All details of the simulations are described in Lapenta et al. (2011).

We report also one 3D run called conventionally tred47 based on an initial Harris equilibrium with background with nb = 0.1 n0, mi/me = 256, Ti/Te = 5, vthe/c = 0.045 and thickness L/di = 0.5. The guide field is Bg/b0 = 1. Many other values are available on the server. The box has Lx/di = 40 and Ly/di = 15 and Lz/di = 10. All details of the simulations are provided in Vapirev et al. (2013).

In all runs, we consider the classic case of a 2D Harris sheet, which considers an initial balanced current sheet between magnetic and plasma pressure, such that

$$n_0 (T_e + T_i) = \frac{B_0^2}{8\pi}$$

In order to satisfy this equilibrium, we consider the initial hyperbolic profiles for the density and magnetic field made very famous by the GEM challenge (Birn et al. 2001), which read

$$B_x(y) = B_0 tanh\left(\frac{y}{L}\right)$$

$$n(y) = n_0 sech^2\left(\frac{y}{L}\right) + n_b$$

where $L = 0.5$ the current sheet half-thickness and n_b the background density. All the spatial quantities are normalized to the ions skin depth $d_i = \frac{c}{\omega_{pi}}$, with ω_{pi} the ion plasma frequency, computed with the reference asymptotic values B_0 and n_0. Temporal frames are instead normalized to the ion gyrofrequency ω_{ci}^{-1}. In the figures, electric fields are normalized as $\frac{eE}{m_i c \omega_{pi}}$, magnetic fields as $\frac{eB}{m_i \omega_{pi}}$ and currents as $\frac{e\mu_0 d_i J}{\omega_{pi}}$, where e and μ_0 are, respectively, the electric and magnetic permeability in vacuum, m_i the ions mass and c the speed of light.

All simulations use the implicit fully electromagnetic and fully kinetic code iPic3D (Markidis et al. 2010). The code makes use of the CGS unit system.

References

M. Andre, A. Vaivads, S.C. Buchert, A.N. Fazakerley, A. Lahiff, Thin electron-scale layers at the magnetopause. Geophys. Res. Lett. **31**(3), L03803 (2004)

Y. Asano, R. Nakamura, I. Shinohara, M. Fujimoto, T. Takada, W. Baumjohann, C.J. Owen, A.N. Fazakerley, A. Runov, T. Nagai, E.A. Lucek, H. Reme, Electron flat-top distributions around the magnetic reconnection region. J. Geophys. Res. **113**(A1), A01207 (2008)

J. Birn, J.F. Drake, M.A. Shay, B.N. Rogers, R.E. Denton, M. Hesse, M. Kuznetsova, Z.W. Ma, A. Bhattacharjee, A. Otto, P.L. Pritchett, Geospace Environmental Modeling (GEM) magnetic reconnection challenge. J. Geophys. Res. **106**(A3), 3715–3719 (2001)

K.J. Bowers, B.J. Albright, L. Yin, W. Daughton, V. Roytershteyn, B. Bergen, T.J.T. Kwan, Advances in petascale kinetic plasma simulation with VPIC and Roadrunner. J. Phys. Conf. Ser. **180**, 012055 (2009)

C. Cattell, J. Dombeck, J. Wygant, J.F. Drake, M. Swisdak, M.L. Goldstein, W. Keith, A. Fazakerley, M. Andre, E. Lucek, A. Balogh, Cluster observations of electron holes in association with magnetotail reconnection and comparison to simulations. J. Geophys. Res. **110**(A1), 1211 (2005)

L.J. Chen, N. Bessho, B. Lefebvre, H. Vaith, A. Fazakerley, A. Bhattacharjee, P.A. Puhl-Quinn, A. Runov, Y. Khotyaintsev, A. Vaivads, E. Georgescu, R. Torbert, Evidence of an extended electron current sheet and its neighboring magnetic island during magnetotail reconnection. J. Geophys. Res. **113**(A12), 12213 (2008)

W. Daughton, V. Roytershteyn, H. Karimabadi, L. Yin, B.J. Albright, B. Bergen, K.J. Bowers, Role of electron physics in the development of turbulent magnetic reconnection in collisionless plasmas. Nat. Phys. **7**(7), 539–542 (2011)

X.H. Deng, H. Matsumoto, Rapid magnetic reconnection in the Earth's magnetosphere mediated by whistler waves. Nature **410**(6828), 557–560 (2001)

A. Divin, G. Lapenta, S. Markidis, D.L. Newman, M.V. Goldman, Numerical simulations of separatrix instabilities in collisionless magnetic reconnection. Phys. Plasmas **19**(4), 042110 (2012)

J.F. Drake, M.A. Shay, W. Thongthai, M. Swisdak, Production of energetic electrons during magnetic reconnection. Phys. Rev. Lett. **94**(9), 09500 (2005)

J.W. Dungey, Interplanetary magnetic field and auroral zones. Phys. Rev. Lett. **6**(2), 47 (1961)

J. Egedal, M. Oieroset, W. Fox, R.P. Lin, In situ discovery of an electrostatic potential, trapping electrons and mediating fast reconnection in the earth's magnetotail. Phys. Rev. Lett. **94**(2), 025006 (2005)

J. Egedal, W. Fox, N. Katz, M. Porkolab, M. Oieroset, R.P. Lin, W. Daughton, J.F. Drake, Evidence and theory for trapped electrons in guide field magnetotail reconnection. J. Geophys. Res. **113**(A12), A12207 (2008)

J. Egedal, W. Daughton, A. Le, Large-scale electron acceleration by parallel electric fields during magnetic reconnection. Nat. Phys. **8**, 321–324 (2012)

S. Eriksson, M. Oieroset, D.N. Baker, C. Mouikis, A. Vaivads, M.W. Dunlop, H. Reme, R.E. Ergun, A. Balogh, Walen and slow-mode shock analyses in the near-Earth magnetotail in connection with a substorm onset on 27 August 2001. J. Geophys. Res. **109**(A10), A10212 (2004)

W.M. Farrell, M.D. Desch, M.L. Kaiser, K. Goetz, The dominance of electron plasma waves near a reconnection X-line region. Geophys. Res. Lett. **29**(19), 1902 (2002)

W.C. Feldman, S.J. Schwartz, S.J. Bame, D.N. Baker, J. Birn, J.T. Gosling, E.W. Hones, D.J. Mccomas, J.A. Slavin, E.J. Smith, R.D. Zwickl, Evidence for slow-mode shocks in the deep geomagnetic tail. Geophys. Res. Lett. **11**(6), 599–602 (1984)

X.R. Fu, Q.M. Lu, S. Wang, The process of electron acceleration during collisionless magnetic reconnection. Phys. Plasmas **13**(1), 012309 (2006)

M. Fujimoto, M.S. Nakamura, I. Shinohara, T. Nagai, T. Mukai, Y. Saito, T. Yamamoto, S. Kokubun, Observations of earthward streaming electrons at the trailing boundary of a plasmoid. Geophys. Res. Lett. **24**(22), 2893–2896 (1997)

M. Fujimoto, I. Shinohara, H. Kojima, Reconnection and waves: a review with a perspective. Space Sci. Rev. **160**(1–4), 123–143 (2011)

S.A. Fuselier, W.S. Lewis, Properties of near-earth magnetic reconnection from in-situ observations. Space Sci. Rev. **160**(1–4), 95–121 (2011)

M.V. Goldman, D.L. Newman, P. Pritchett, Vlasov simulations of electron holes driven by particle distributions from PIC reconnection simulations with a guide field. Geophys. Res. Lett. **35**(22), 22109 (2008)

M.V. Goldman, D.L. Newman, G. Lapenta, L. Andersson, J.T. Gosling, S. Eriksson, S. Markidis, J.P. Eastwood, R. Ergun, Cerenkov emission of quasiparallel whistlers by fast electron phase-space holes during magnetic reconnection. Phys. Rev. Lett. **112**(14), 145002 (2014)

M. Hoshino, Electron surfing acceleration in magnetic reconnection. J. Geophys. Res. **110**, A10215 (2005). doi:10.1029/2005JA011229

S. Imada, M. Hoshino, T. Mukai, Average profiles of energetic and thermal electrons in the magnetotail reconnection regions. Geophys. Res. Lett. **32**(9), L09101 (2005)

M.E. Innocenti, M. Goldman, D. Newman, S. Markidis, G. Lapenta, Evidence of magnetic field switch-off in PIC simulations of collisionless magnetic reconnection with guide field. Astrophys. J. Lett. in press, (2015)

Y.V. Khotyaintsev, A. Vaivads, A. Retino, M. Andre, Formation of inner structure of a reconnection separatrix region. Phys. Rev. Lett. **97**(20), 205003 (2006)

R.G. Kleva, J.F. Drake, F.L. Waelbroeck, Fast reconnection in high-temperature plasmas. Phys. Plasmas **2**(1), 23–34 (1995). doi:10.1063/1.871095

A.L. Labellehamer, A. Otto, L.C. Lee, Magnetic reconnection in the presence of sheared plasma-flow - intermediate shock formation. Phys. Plasmas **1**(3), 706–713 (1994)

G. Lapenta, Particle simulations of space weather. J. Comput. Phys. **231**(3), 795–821 (2012)

G. Lapenta, J.U. Brackbill, P. Ricci, Kinetic approach to microscopic-macroscopic coupling in space and laboratory plasmas. Phys. Plasmas **13**(5), 055904 (2006)

G. Lapenta, S. Markidis, A. Divin, M. Goldman, D. Newman, Scales of guide field reconnection at the hydrogen mass ratio. Phys. Plasmas **17**(8), 082106 (2010)
G. Lapenta, S. Markidis, A. Divin, M.V. Goldman, D.L. Newman, Bipolar electric field signatures of reconnection separatrices for a hydrogen plasma at realistic guide fields. Geophys. Res. Lett. **38**, L17104 (2011)
G. Lapenta, M. Goldman, D. Newman, S. Markidis, Propagation speed of rotation signals for field lines undergoing magnetic reconnection. Phys. Plasmas **20**(10), 102113 (2013)
G. Lapenta, M. Goldman, D. Newman, S. Markidis, A. Divin, Electromagnetic energy conversion in downstream fronts from three dimensional kinetic reconnection. Phys. Plasmas **21**(5), 055702 (2014)
G. Lapenta, S. Markidis, A. Divin, D. Newman, M. Goldman, Separatrices: the crux of reconnection. J. Plasma Phys. **81**, 325810109 (2015)
S.Y. Li, Y. Omura, B. Lembege, X.H. Deng, H. Kojima, Y. Saito, S.F. Zhang, Geotail observation of counter directed ESWs associated with the separatrix of magnetic reconnection in the near-Earth magnetotail. J. Geophys. Res. **119**(1), 202–210 (2014)
Y.H. Liu, J.F. Drake, M. Swisdak, The structure of the magnetic reconnection exhaust boundary. Phys. Plasmas **19**(2), 022110 (2012)
Q.M. Lu, C. Huang, J.L. Xie, R.S. Wang, M.Y. Wu, A. Vaivads, S. Wang, Features of separatrix regions in magnetic reconnection: comparison of 2-D particle-in-cell simulations and cluster observations. J. Geophys. Res. **115**, A11208 (2010)
Z.W. Ma, S.L. Feng, Generation of electric field and net charge in Hall reconnection. Chin. Phys. Lett. **25**(8), 2934–2937 (2008)
S. Markidis, G. Lapenta, Rizwan-uddin, Multi-scale simulations of plasma with iPIC3D. Math. Comput. Simul. **80**(7), 1509–1519 (2010)
S. Markidis, P. Henri, G. Lapenta, A. Divin, M.V. Goldman, D. Newman, S. Eriksson, Collisionless magnetic reconnection in a plasmoid chain. Nonlinear Process. Geophys. **19**(1), 145–153 (2012a)
S. Markidis, G. Lapenta, A. Divin, M. Goldman, D. Newman, L. Andersson, Three dimensional density cavities in guide field collisionless magnetic reconnection. Phys. Plasmas **19**(3), 032119 (2012b)
H. Matsumoto, X.H. Deng, H. Kojima, R.R. Anderson, Observation of electrostatic solitary waves associated with reconnection on the dayside magnetopause boundary. Geophys. Res. Lett. **30**(6), 1326 (2003)
D.B. Melrose, *Instabilities in Space and Laboratory Plasmas* (Cambridge University Press, Cambridge, 1986)
F.S. Mozer, P.L. Pritchett, Spatial, temporal, and amplitude characteristics of parallel electric fields associated with subsolar magnetic field reconnection. J. Geophys. Res. **115**, A04220 (2010)
F.S. Mozer, S.D. Bale, T.D. Phan, Evidence of diffusion regions at a subsolar magnetopause crossing. Phys. Rev. Lett. **89**(1), 015002 (2002)
T. Nagai, I. Shinohara, M. Fujimoto, M. Hoshino, Y. Saito, S. Machida, T. Mukai, Geotail observations of the Hall current system: evidence of magnetic reconnection in the magnetotail. J. Geophys. Res. **106**(A11), 25929–25949 (2001)
T. Nagai, I. Shinohara, M. Fujimoto, S. Machida, R. Nakamura, Y. Saito, T. Mukai, Structure of the Hall current system in the vicinity of the magnetic reconnection site. J. Geophys. Res. **108**(A10), 1357 (2003)
R. Nakamura, W. Baumjohann, M. Fujimoto, Y. Asano, A. Runov, C.J. Owen, A.N. Fazakerley, B. Klecker, H. Reme, E.A. Lucek, M. Andre, Y. Khotyaintsev, Cluster observations of an ion-scale current sheet in the magnetotail under the presence of a guide field. J. Geophys. Res. **113**(A7), A07S16 (2008)
M. Øieroset, T.D. Phan, M. Fujimoto, R.P. Lin, R.P. Lepping, In situ detection of collisionless reconnection in the Earth's magnetotail. Nature **412**(6845), 414–417 (2001)
M. Øieroset, R.P. Lin, T.D. Phan, D.E. Larson, S.D. Bale, Evidence for electron acceleration up to similar to 300 keV in the magnetic reconnection diffusion region of Earth's magnetotail. Phys. Rev. Lett. **89**(19), 195001 (2002)

V. Olshevsky, G. Lapenta, S. Markidis, Energetics of kinetic reconnection in a three-dimensional null-point cluster. Phys. Rev. Lett. **111**(4), 045002 (2013)
V. Olshevsky, G. Lapenta, S. Markidis, A. Divin, Role of Z-pinches in magnetic reconnection in space plasmas. J. Plasma Phys. **81**(01), 325810105 (2015a)
V. Olshevsky, S. Markidis, A. Divin, E. Eriksson, G. Lapenta, Energy dissipation in magnetic null points at kinetic scales. APJ **807**, 155 (2015b)
G. Paschmann, M. Oieroset, T. Phan, In-situ observations of reconnection in space. Space Sci. Rev. **178**(2–4), 385–417 (2013)
H.E. Petschek, Magnetic field annihilation, in *The Physics of Solar Flares*, ed. by W.N. Hess, vol. 50 (NASA SP, Washington, 1964), pp. 425–439
E.R. Priest, T.G. Forbes, New models for fast steady-state magnetic reconnection. J. Geophys. Res. **91**(A5), 5579–5588 (1986)
P.L. Pritchett, Onset and saturation of guide-field magnetic reconnection. Phys. Plasmas **12**(6), 062301 (2005)
P.L. Pritchett, Relativistic electron production during guide field magnetic reconnection. J. Geophys. Res. **111**, A10212 (2006)
P.L. Pritchett, F.V. Coroniti, Three-dimensional collisionless magnetic reconnection in the presence of a guide field. J. Geophys. Res. **109**(A1), 1220 (2004)
A. Retinò, A. Vaivads, M. Andre, F. Sahraoui, Y. Khotyaintsev, J.S. Pickett, M.B.B. Cattaneo, M.F. Marcucci, M. Morooka, C.J. Owen, S.C. Buchert, N. Cornilleau-Wehrlin, Structure of the separatrix region close to a magnetic reconnection X-line: cluster observations. Geophys. Res. Lett. **33**(6), L06101 (2006)
P. Ricci, J.U. Brackbill, W. Daughton, G. Lapenta, Collisionless magnetic reconnection in the presence of a guide field. Phys. Plasmas **11**(8), 4102–4114 (2004)
B.N. Rogers, R.E. Denton, J.F. Drake, Signatures of collisionless magnetic reconnection. J. Geophys. Res. **108**(A3), 1111 (2003)
M.A. Shay, J.F. Drake, B.N. Rogers, R.E. Denton, Alfvenic collisionless magnetic reconnection and the Hall term. J. Geophys. Res. **106**(A3), 3759–3772 (2001)
M.A. Shay, J.F. Drake, J.P. Eastwood, T.D. Phan, Super-Alfvenic propagation of substorm reconnection signatures and poynting flux. Phys. Rev. Lett. **107**(8), 089901 (2011)
I. Shinohara, T. Nagai, M. Fujimoto, T. Terasawa, T. Mukai, K. Tsuruda, T. Yamamoto, Low-frequency electromagnetic turbulence observed near the substorm onset site. J. Geophys. Res. **103**(A9), 20365–20388 (1998)
M. I. Sitnov, M. Swisdak, A.V. Divin. Dipolarization fronts as a signature of transient reconnection in the magnetotail. J. Geophys. Res. Space Phys. (1978–2012) **114**(A4), (2009)
E.J. Smith, J.A. Slavin, B.T. Tsurutani, W.C. Feldman, S.J. Bame, Slow mode shocks in the Earths magnetotail - Isee-3. Geophys. Res. Lett. **11**(10), 1054–1057 (1984)
B.U. Sonnerup, Magnetic-field Re-connexion in a highly conducting incompressible fluid. J. Plasma Phys. **4**, 161 (1970)
B.U.O. Sonnerup, Magnetic field reconnection, in *Solar System Plasma Physics*, ed. by L.T. Lanzerotti, C.F. Kennel, E.N. Parker, vol. III (North-Holland, New York, 1979), pp. 45–108
T. Terasawa, Hall current effect on tearing mode-instability. Geophys. Res. Lett. **10**(6), 475–478 (1983)
A. Vaivads, Y. Khotyaintsev, M. Andre, A. Retino, S.C. Buchert, B.N. Rogers, P. Decreau, G. Paschmann, T.D. Phan, Structure of the magnetic reconnection diffusion region from four-spacecraft observations. Phys. Rev. Lett. **93**(10), 105001 (2004)
A. Vaivads, A. Retino, M. Andre, Microphysics of magnetic reconnection. Space Sci. Rev. **122**(1–4), 19–27 (2006)
A.E. Vapirev, G. Lapenta, A. Divin, S. Markidis, P. Henri, M. Goldman, D. Newman, Formation of a transient front structure near reconnection point in 3-D PIC simulations. J. Geophys. Res. **118**(4), 1435–1449 (2013)
R.S. Wang, Q.M. Lu, J. Guo, S. Wang, Spatial distribution of energetic electrons during magnetic reconnection. Chin. Phys. Lett. **25**(8), 3083–3085 (2008)

R.S. Wang, Q.M. Lu, C. Huang, S. Wang, Multispacecraft observation of electron pitch angle distributions in magnetotail reconnection. J. Geophys. Res. **115**, A01209 (2010)

R.S. Wang, R. Nakamura, Q.M. Lu, A.M. Du, T.L. Zhang, W. Baumjohann, Y.V. Khotyaintsev, M. Volwerk, M. Andre, M. Fujimoto, T.K.M. Nakamura, A.N. Fazakerley, J. Du, W. Teh, E.V. Panov, B. Zieger, Y.X. Pan, S. Lu, Asymmetry in the current sheet and secondary magnetic flux ropes during guide field magnetic reconnection. J. Geophys. Res. **117**, 7223 (2012)

R.S. Wang, A.M. Du, R. Nakamura, Q.M. Lu, Y.V. Khotyaintsev, M. Volwerk, T.L. Zhang, E.A. Kronberg, P.W. Daly, A.N. Fazakerley, Observation of multiple sub-cavities adjacent to single separatrix. Geophys. Res. Lett. **40**(11), 2511–2517 (2013)

R.S. Wang, Q.M. Lu, Y.V. Khotyaintsev, M. Volwerk, A.M. Du, R. Nakamura, W.D. Gonzalez, X. Sun, W.G. Baumjohann, X. Li, T.L. Zhang, A.N. Fazakerley, C. Huang, M.Y. Wu, Observation of double layer in the separatrix region during magnetic reconnection. Geophys. Res. Lett. **41**(14), 4851–4858 (2014)

X.H. Wei, J.B. Cao, G.C. Zhou, O. Santolik, H. Reme, I. Dandouras, N. Cornilleau-Wehrlin, E. Lucek, C.M. Carr, A. Fazakerley, Cluster observations of waves in the whistler frequency range associated with magnetic reconnection in the Earth's magnetotail. J. Geophys. Res. **112**(A10), A10225 (2007)

M. Zhou, Y. Pang, X.H. Deng, Z.G. Yuan, S.Y. Huang, Density cavity in magnetic reconnection diffusion region in the presence of guide field. J. Geophys. Res. **116**, A06222 (2011)

Chapter 9
Simulation Studies of Plasma Transport at Earth, Jupiter and Saturn

R.J. Walker and X. Jia

Abstract In this chapter we present a review of plasma transport in the magnetospheres of the rapidly rotating outer planets Jupiter and Saturn with emphasis on the effects of magnetic reconnection. Unlike the Earth's magnetosphere where reconnection is the dominant transport mechanism, atmospherically driven corotation dominates at Jupiter and Saturn. However, there is both observational and theoretical basis for reconnection at the outer planets. Since observations at the outer planets are sparse we have used numerical simulations to give an overall view of transport. For northward IMF, reconnection can erode the dayside Jovian magnetopause position by as much as 10 % while the simulations at Saturn indicate very little erosion. In the magnetotail, reconnection at Jupiter can become quasi-periodic in both Jupiter and Saturn simulations. There is observational evidence for this at Jupiter but the observational evidence is not as clear at Saturn. Solar wind dynamic pressure controls whether or not periodic reconnection occurs at Saturn while both dynamic pressure and the IMF are important at Jupiter. Both outflow-driven reconnection in which flux tubes reconnect as they convect from the dayside to the tail and solar-wind-driven reconnection are found in the simulations. One simulation study indicates that a pulse of increased dynamic pressure can trigger reconnection at Saturn. Large scale plasmoids do not remove enough plasma from the magnetospheres of either outer planet to account for loss of plasma from the inner magnetosphere sources. There is evidence in the Saturn simulations of Kelvin–Helmholtz waves driving transport.

Keywords Jupiter magnetosphere • Kelvin–Helmholtz instability • Magnetospheric reconnection • MHD simulations • Plasma transport • Rotating magnetospheres • Saturn magnetosphere

R.J. Walker (✉)
Department of Earth, Planetary and Space Sciences, University of California Los Angeles, Los Angeles, CA, USA
e-mail: rwalker@igpp.ucla.edu

X. Jia
Department of Climate and Space Science and Engineering, University of Michigan, Ann Arbor, MI, USA
e-mail: xzjia@umich.edu

W. Gonzalez, E. Parker (eds.), *Magnetic Reconnection*, Astrophysics and Space Science Library 427, DOI 10.1007/978-3-319-26432-5_9

9.1 Introduction

Six planets have intrinsic magnetic fields. Plasma transport is very different in the relatively small and slowly rotating terrestrial planet magnetospheres (Mercury and Earth), the relatively large and rapidly rotating magnetospheres of Jupiter and Saturn, and in the highly tilted magnetospheres of Uranus and Neptune. In this paper we will use numerical simulations to model plasma transport in the magnetospheres of Earth, Jupiter and Saturn. In keeping with the spirit of this volume the emphasis will be on reconnection-driven transport, but we will compare and contrast the effects of reconnection with competing mechanisms. First we present a brief review of the basic properties of transport at each planet based primarily on observational investigations. There have been a number of recent general reviews of planetary magnetospheres (Kivelson 2007; Bagenal 2009; Jackman et al. 2014).

9.1.1 Transport in Earth's Magnetosphere

Earth's magnetosphere has been observed much more extensively than those of the other planets. These observations have led to the conclusion that magnetic reconnection (Dungey 1961) is the main coupling mechanism between the solar wind and Earth's magnetosphere. At the dayside magnetopause when the interplanetary magnetic field (IMF) B_Z component is southward, reconnection removes closed magnetic flux from the dayside magnetosphere and adds open magnetic flux to the magnetotail lobes. During this process the magnetopause position can be eroded by 10–20 % (see Volwerk et al. 2011 for a recent study). The reconnection process can be either relatively steady or unsteady. Frequently the reconnection is episodic in the form of flux transfer events (FTE) in which localized reconnection transfers about 10 MWb in a few minutes (Russell and Elphic 1978). Overall in the reconnection process at Earth, approximately 10 % of the solar wind electric potential difference across the width of the magnetosphere is imposed across the magnetosphere. This typically is 50–100 kV. Reconnection in the night-side plasma sheet allows the open reconnected flux in the tail lobes to close and the magnetic flux to return to the dayside. Like dayside reconnection, night-side reconnection can be steady or unsteady. Frequently, the reconnection in the plasma sheet is limited in temporal and spatial extent and may generate local channels of earthward flows which have been associated with the observed Bursty Bulk Flows (BBF) (Angelopoulos et al. 1992). Tailward of the reconnection site, structures variously referred to as magnetic flux rope, magnetic-flux rope-like, or plasmoids form and move away from Earth carrying some of the plasma from the magnetosphere into the solar wind (Hones 1976; Slavin et al. 1983). See Sharma et al. (2008) for a more detailed review of tail dynamics.

In addition to reconnection, a quasi-viscous interaction at the low latitude magnetopause leads to transport (Axford 1961; Axford and Hines 1964). This requires a mechanism to transfer momentum along the flanks of the magnetosphere. A leading candidate for this is the Kelvin–Helmholtz (KH) instability, which is driven by flow shear at the magnetopause (Dungey 1955). Typically the transport driven by the KH waves is much less than that from reconnection.

Closer to Earth in the plasmasphere, the transport is largely rotational and is driven by coupling between the ionosphere and the inner magnetosphere. Within a few Earth radii (R_E) the plasma is largely from the ionosphere. However, beyond a few R_E both the solar wind and the ionosphere contribute plasma. During magnetically quiet times and during weak magnetic activity, the solar wind source dominates in most of the magnetosphere, while during large magnetic storms the ionospheric source is dominant (see Walker et al. (1999) for a review of plasma sources in the magnetosphere).

9.1.2 Transport in Jupiter's Magnetosphere

Jupiter is a rapid rotator with a rotation period of slightly less than 10 h. A frictional torque in Jupiter's ionosphere tries to bring the plasma in Jupiter's magnetosphere into corotation with the atmosphere (Hill 1979). In the magnetosphere a $\boldsymbol{J} \times \boldsymbol{B}$ force, where $\boldsymbol{J}$ is the current density in the equatorial current sheet and $\boldsymbol{B}$ is the local magnetic field, accelerates the plasma toward corotation. The current in the magnetosphere connects along magnetic field lines to the ionosphere where another $\boldsymbol{J} \times \boldsymbol{B}$ force opposes corotation. However, the current in the magnetosphere is limited by ionospheric conductance so full corotation is not achieved. The dominant plasma source at Jupiter is within the magnetosphere. Volcanoes on the moon Io produce neutral particles which when ionized create sulfur and oxygen ions. The Io plasma source is estimated to be between 260 and 1400 kg/s (Jackman et al. 2014 Table 2).

Studies of dayside reconnection at the outer planets have been handicapped by the lack of simultaneous observations from a nearby solar wind monitor. Investigations either must use observations from a previous crossing of the magnetopause or propagate the solar wind observations from as far away as Earth orbit. However, when the Cassini spacecraft passed near Jupiter on its way to Saturn it was possible to investigate more directly the effects of an interplanetary shock at Jupiter. Following the shock passage, the Galileo satellite which had been orbiting within the Jovian magnetosphere in the late afternoon sector emerged into the solar wind plasma during an interval with northward IMF. (Northward IMF is the favored direction for dayside reconnection at Jupiter since Jupiter's magnetic field is directed opposite to that of Earth). This is consistent with the magnetopause erosion by reconnection during the northward IMF interval (Kivelson and Southwood 2003). Walker and Russell (1985) presented more direct evidence of dayside reconnection at Jupiter's magnetopause when they reported magnetic signatures similar to those of FTEs at Earth. They estimated the flux transfer in a Jovian FTE at about 0.5 MWb

over 30 s. Nichols et al. (2006) used a solar wind algorithm based on observations at Earth to estimate the flux opened by reconnection at a rate of 18 GWb/day.

Both magnetic and plasma signatures of reconnection have been reported in the tail. Russell et al. (1998) and Vogt et al. (2010) found signatures in the magnetic record consistent with plasma sheet reconnection while Kronberg et al. (2012) observed counter-streaming flows in a region similar to the plasma sheet boundary layer at Earth (Kasahara et al. 2011) that is consistent with plasma sheet reconnection. The X-line at Jupiter is typically tailward of 90 R_J (R_J is Jupiter's radius). The average distance is approximately 90 R_J near dawn, about 100 R_J at midnight and more than 120 R_J in the evening sector (Woch et al. 2002; Vogt et al. 2010). Kasahara et al. (2013) carried out a multi-instrument study of Galileo data and found large radial flows and density changes consistent with lobe reconnection in the dawn sector tail. They did not find corresponding density changes in the evening sector. The reconnection in Jupiter's tail may be quasi-periodic. A number of studies have reported periods of 2–4 days (Krupp et al. 1998; Woch et al. 1998; Kronberg et al. 2007, 2009). Although there is considerable evidence that reconnection occurs in Jupiter's magnetosphere, it is not necessarily important for driving flows in the Jovian system. Vogt et al. (2011) estimate the reconnection voltage at 100–300 kV across the tail, which is much less than the 2–4 MV due to corotation.

One of the outstanding questions at Jupiter is how the plasma from Io leaves the Jovian system. One suggestion is that it leaves via reconnection in tailward moving plasmoids. Vogt et al. (2014) estimated the mass loss by plasmoids at 0.7–120 kg/s. This is much less than the mass added by the Io interaction. Vogt et al. (2014) also estimated the flux closed on the nightside at between 7 and 70 GWb/day which is roughly in accord with the dayside reconnection estimate of Nichols et al. (2006) of 18 GWb/day.

In a series of papers Cowley et al. (2003, 2008) (see Jackman et al. 2014 for a list) proposed that Earth like transport with dayside reconnection followed by nightside reconnection in the dawn sector could be important at Jupiter. However, this Dungey cycle at Jupiter has been controversial. McComas and Bagenal (2007) argued that Jupiter does not complete the Dungey cycle. They question the return flow from tail reconnection and argue that high latitude reconnection with a southward IMF may occur before the tail reconnection. Vasyliunas (1983) pointed out that in a rapidly rotating magnetosphere the flux tubes in the evening quadrant will be stretched and can reconnect. (See Jackman et al. (2014) Fig. 4 for a drawing showing the relative locations of Dungey and Vasyliunas type reconnection in Jupiter's magnetosphere.)

9.1.3 Transport in Saturn's Magnetosphere

Saturn is the other rapid rotator with a rotational period of a little less than 11 h. Like Jupiter, it has a major plasma source within the magnetosphere. Water-group neutrals escaping from Enceladus geysers provide a plasma source to Saturn's

magnetosphere at rates between 12 and 250 kg/s (Jackman et al. 2014). Also like Jupiter the plasma in the inner magnetosphere is atmospherically driven toward corotation. There is debate on whether reconnection will be important due to the high Mach number solar wind at Saturn (Scurry and Russell 1991; Grocott et al. 2009). Masters et al. (2011a) found evidence for a low latitude boundary layer at Saturn but that it was independent of the IMF suggesting little flux transfer due to reconnection. Lai et al. (2012) examined observations during 71 Cassini magnetopause crossings and did not find any FTEs.

In Saturn's tail Simon et al. (2010) and Jackman and Arridge (2011) did not find evidence for a plasmasheet boundary layer like those at Earth and Jupiter. Only a handful of events similar to earthward moving bursty bulk flows at Earth have been reported at Saturn (Bunce et al. 2005; Russell et al. 2008; Jackman et al. 2013; Thomsen et al. 2015). However, Jackman et al. (2011) report tailward moving bipolar magnetic structures consistent with reconnection occurring more frequently. Flow signatures consistent with tail reconnection have been reported moving tailward by McAndrews et al. (2009) and while Masters et al. (2011b) found flow toward Saturn which they attribute to Vasyliunas cycle reconnection. Finally Mitchell et al. (2009) has used ENA images to show injections into the inner magnetosphere consistent with tail reconnection.

Like Jupiter the loss of mass from the system due to reconnection has a wide range. Thomsen et al. (2013) estimate the loss at 34 kg/s while Jackman et al. (2014) estimate it to be 2.59 kg/s. Again at Saturn like Jupiter there is a problem in accounting for all of the mass entering the system from the Enceladus interaction.

9.2 Simulation Studies

A unified overall picture based on observations of transport in the magnetospheres of Jupiter and Saturn is not available. In this section we will use magnetohydrodynamic (MHD) simulations to model transport in the magnetospheres of Jupiter and Saturn. The goal in this section is to place the observations in a global context. Since we know the most about reconnection at Earth, we compare the simulation results at the rapid rotators with Earth results. This helps us to separate out rotational effects, effects of viscous type processes, and internal processes. Also, we compare the simulation picture with insights gained from the large number of observational studies.

9.2.1 Simulated Transport at Earth

Simulations have proven useful at Earth to give the global picture of magnetospheric dynamics. Here we will briefly outline some of the results in order to establish a base line against which the outer planet simulations can be compared. As noted above,

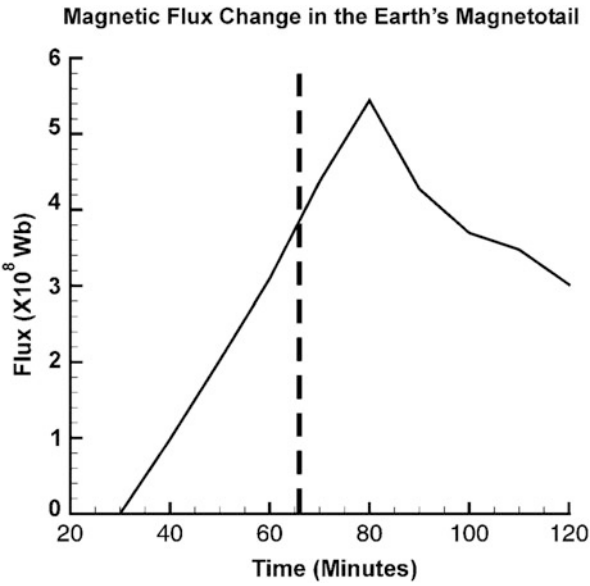

Fig. 9.1 The magnetic flux added to the tail lobes following a change in the IMF B_Z from northward to southward. The magnitude of the magnetic field was 5 nT, the solar wind speed was 400 km/s and the number density was 5×10^6 m^{-3}

dayside reconnection occurs at Earth for southward IMF. For a purely southward IMF, reconnection occurs at the subsolar point. Thirty to 60 m later reconnection occurs in the tail. An examination of the changes in the lobe magnetic flux can give a view into the overall transport. In Fig. 9.1 we show the change in lobe magnetic flux for southward IMF following an interval with northward IMF. This simulation was run with typical solar wind parameters ($Vx = -400$ km/s, B_z was changed from 5nT to -5nT and the solar wind density was 5×10^6 m^{-3}), using the code described in Ogino et al. (1992). About 30 m after the IMF turned southward, magnetic flux from dayside reconnection increased in the tail lobes. At about 65 m the tail reconnection started in the tail plasma sheet on closed magnetic field lines. Reconnection of lobe magnetic field began at about 80 m. Once lobe reconnection started, the flux in the lobes decreased. The reconnection site was at about $X = -18$ R_E. The cross-magnetosphere potential was about 150 kV in this run. After reconnection began on lobe field lines, there were earthward and tailward flows of about 500 km/s. A plasmoid-like structure moved tailward after lobe reconnection.

In addition to reconnection, viscous-like processes also can drive transport at Earth. In Fig. 9.2 we have plotted with color coding the electric field ($|-\boldsymbol{V} \times \boldsymbol{B}|$) where $\boldsymbol{V}$ is the velocity and $\boldsymbol{B}$ is the magnetic field in a plane 0.2 R_E above the equator. The solid white line labeled $B_z = 0$ is approximately the magnetopause position while the dashed line labeled $V_X = 0$ gives the location of the inner edge of the low latitude boundary layer in the simulation. The black arrows give the velocity vectors. Note the ripples on the boundary. This simulation is unstable to the Kelvin–Helmholtz instability driven by the flow shear across the magnetopause. The boundary waves start at about 0900LT where the linear KH instability criterion is met. If we take the distance between the white lines as a measure of the LLBL

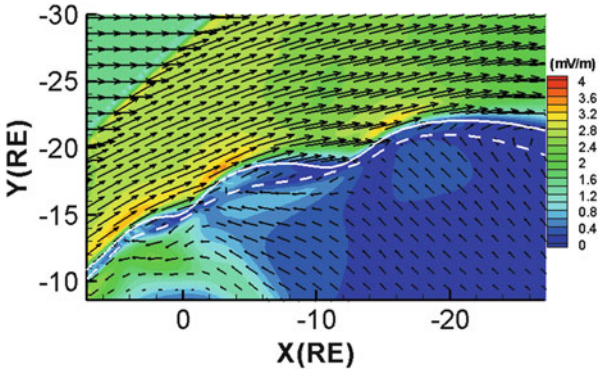

Fig. 9.2 The color coded electric field magnitude 0.2 R_E above the equatorial plane with superimposed flow vectors for the simulation in Fig. 9.1. The *solid white line* gives the location of $B_Z = 0$ and is used to approximate the magnetopause. The *dashed white line* gives $V_X = 0$ and is used to determine the thickness of the boundary layer *d*. The simulated velocity, magnetic field and mass density are consistent with the Kelvin–Helmholtz instability criterion at about 0900LT. The simulated wave number *k* times the thickness of the boundary layer $kd \sim 1$ as expected for Kelvin–Helmholtz waves

thickness, the wave number (k) times that distance (d) is about 1, consistent with KH theory (Walker 1981; Kivelson and Pu 1984). See Claudepierre et al. (2008) for a more detailed analysis of KH waves in a global MHD model during a period with southward IMF.

The example in Figs. 9.1 and 9.2 is the simplest example of the magnetosphere with dayside reconnection. Reality is much more complex even in simulations. In Fig. 9.3 we have extracted the configuration in the tail from a global MHD simulation of a substorm on February 15, 2008 (Ashour-Abdalla et al. 2011). Input to the simulation was the observed solar wind and the model ionospheric conductances including the contributions from particle precipitation and solar ultra violet radiation. During this substorm a series of three dipolarization fronts were observed by the THEMIS satellites in the near-Earth tail region. The color background in Fig. 9.3 gives the north–south component of the magnetic field (B_Z) on the surface of maximum thermal pressure in the plasma sheet. In a simulation for an actual event the plasma sheet is not a plane. The use of maximum pressure surface allows display of the configuration in a 2D plot. Superimposed on B_Z are flow vectors in white. In the top panel a narrow channel of earthward flow can be seen extending from a localized reconnection site tailward of the outer edge of the display at $X = -25$ R_E. This is very similar to busty bulk flows observed on spacecraft (Angelopoulos et al. 1992). As the flow moves earthward, B_Z at its leading edge steepens into a dipolarization front. In the top panel at 0356UT the first dipolarization indicated by orange and yellow has reached the three THEMIS satellites labeled P3, P4 and P5. Three minutes later in the bottom panel the second

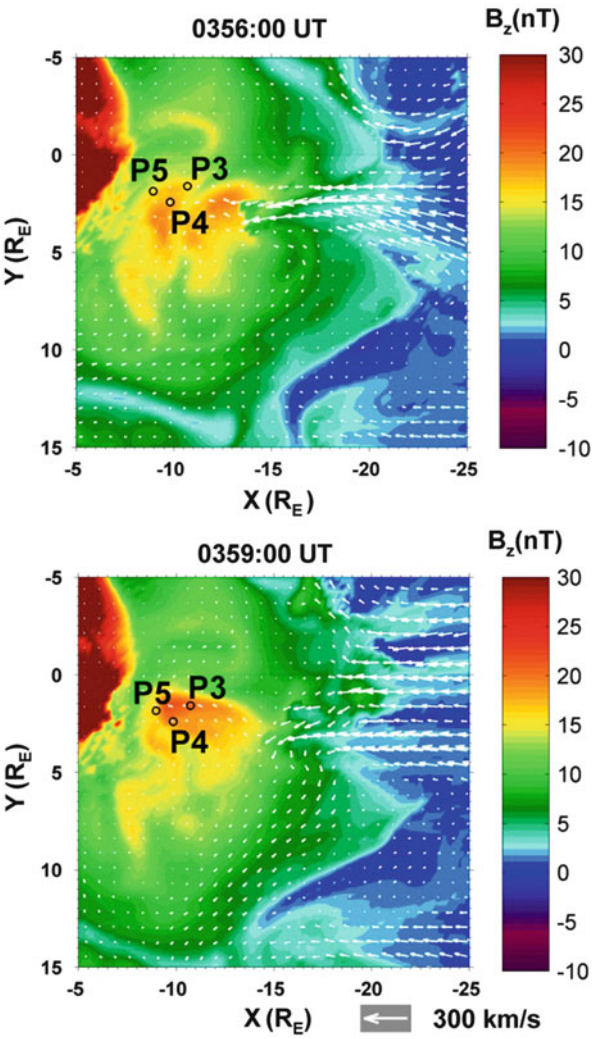

Fig. 9.3 Color coded B_Z on the maximum pressure surface from a simulation of a substorm of a substorm on February 15, 2008. *White* flow vectors have been superimposed. The earthward flow is confined to narrow channels which steepen into dipolarization fronts (*yellow* and *red* B_Z) as the flows approach the inner magnetosphere. From Ashour-Abdalla et al. (2011)

reconnection driven front has crossed the satellites. Narrow flow channels like the one shown here are characteristic of the transport found in global simulations of Earth's magnetosphere during actual magnetospheric substorms.

9.2.2 Simulated Transport at Jupiter

The simulations in this section were made with the Jovian simulation code described in Ogino et al. (1998) and Fukazawa et al. (2010). The simulation does not explicitly

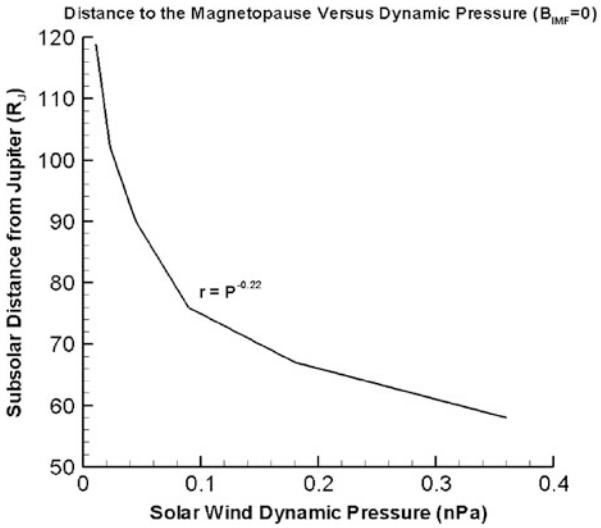

Fig. 9.4 The distance to the subsolar magnetopause from Jupiter as a function of solar wind dynamic pressure. The simulation was run without an IMF. The inner magnetosphere source was 1.2×10^{30} AMU/s. For reference the average solar wind dynamic pressure at Jupiter is about 0.09 nPa

include the Io torus. Instead there is a source of plasma from an equatorial plasma sheet model in the inner magnetosphere. The inner boundary is at 15 R_J (Jovian radii). Several source rates have been investigated. The values are discussed below.

At all of the planets, the position of the magnetopause at the subsolar point varies as the solar wind dynamic pressure (P_{SW}) changes. At Earth the location of the magnetopause varies as one would expect from simple pressure balance arguments with Earth's magnetic field taken as a dipole ($\sim P_{SW}^{-1/6}$). In Fig. 9.4 we have plotted the location of the subsolar magnetopause as a function of dynamic pressure from a series of Jovian simulations with the IMF set to zero. The excursions in position are much more sensitive to changes in the pressure at Jupiter than at Earth. In the simulation the boundary location varied as $P_{SW}^{-0.22}$. The actual location is more complex than is found in the simulations. Joy et al. (2002) used the MHD simulations and magnetic field observations at Jupiter to develop a probabilistic model of the location of the magnetopause. They found a bipolar distribution with most probable distances from Jupiter of 63 to 92 R_J. The reason for this is not understood. Joy et al. suggested a cause in the solar wind, but an internal source at Jupiter also is possible. As at Earth, the position also can change with the IMF. In Fig. 9.5 we have plotted the location of the subsolar magnetopause as a function of IMF B_Z for three dynamic pressures. For a given dynamic pressure, the location of the boundary decreases as the northward IMF increases. For the average solar wind dynamic pressure at Jupiter's orbit (0.09 nPa), the magnetopause is eroded by about 10 % when the northward IMF increased from 0.105 to 0.42 nT.

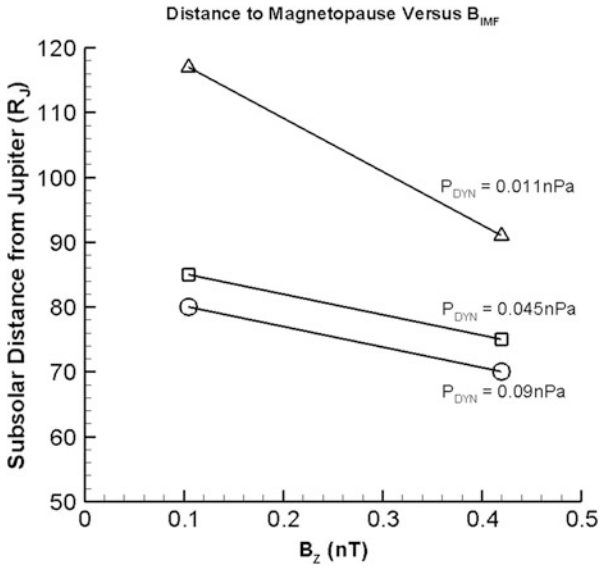

Fig. 9.5 The simulated location of Jupiter's subsolar magnetopause as a function of IMF B_Z for three values of the solar wind dynamic pressure. For a given solar wind pressure the subsolar magnetopause moves closer to Jupiter because of erosion due to magnetic reconnection

As noted in the introduction, both outflow-driven (Vasyliunas cycle) and solar-wind-driven (Dungey cycle) reconnection have been proposed for Jupiter's tail. In Fig. 9.6 we have plotted the B_Z component of the magnetic field just above the equator for a simulation with zero IMF. Flow vectors have been superimposed in white. The location of reconnection in a simulation without an IMF can give an indication of where reconnection will occur due to the stretching of field lines as they convect into the evening sector. The dynamic pressure was 0.09 nPa and the source rate of plasma from inner magnetosphere (Io source) was 1.2×10^{30} AMU/s.

Examination of the overall configuration indicates that tail reconnection occurred on closed plasma sheet field lines in a region extending from pre-midnight into the morning quadrant (the red regions in Fig. 9.6). This is consistent with our expectations for outflow reconnection as flux tubes with outflowing plasma are stretched tailward when they convect into the evening magnetosphere. In the top panel of Fig. 9.7 we have plotted the distance to the tail X-line at midnight as a function of solar wind dynamic pressure for a series of simulations with the IMF set to zero. The distance was calculated at midnight. The location of the reconnection site occurs closer to Jupiter with increasing dynamic pressure. The bottom panel of Fig. 9.7 gives the location of the subsolar magnetopause for the same simulations. The location of the outflow (Vasyliunas cycle) reconnection in the tail follows the position of the magnetopause.

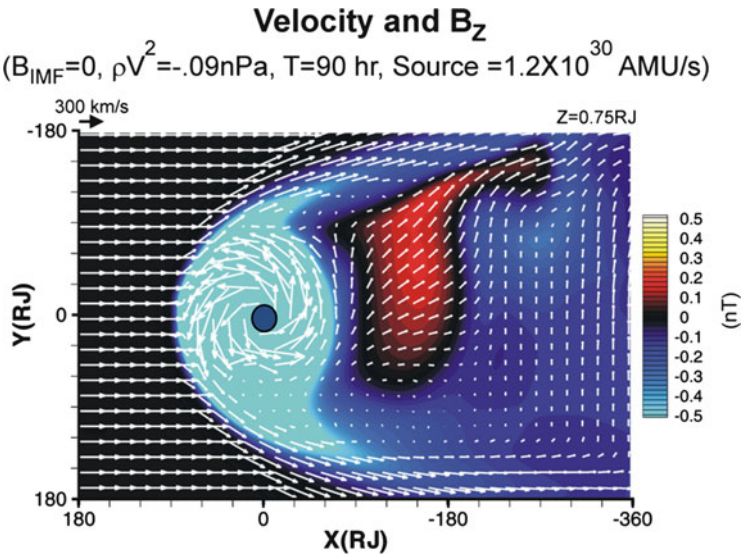

Fig. 9.6 The north–south component of the magnetic field in the equatorial plane for the simulation in Fig. 9.4. The *white arrows* give the flow vectors. The reconnection occurs at about −90 R_J. The reconnection extends from duskward of midnight to near the dawn magnetopause

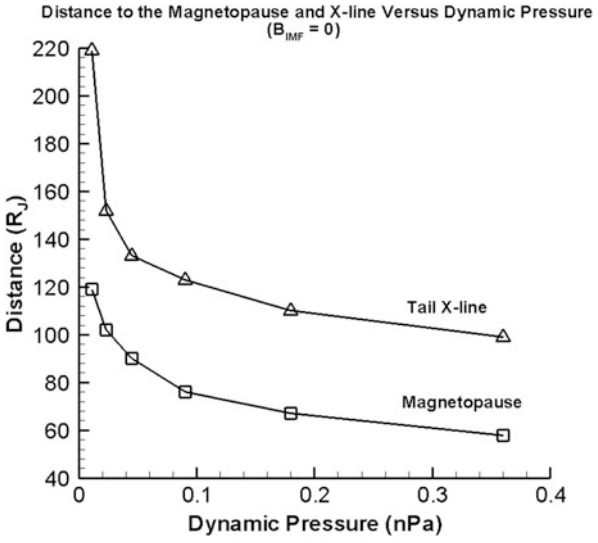

Fig. 9.7 The distance to the reconnection site at midnight from the Jupiter simulations as a function of solar wind dynamic pressure for simulations without an IMF (*top*). The *bottom panel* repeats the curve from Fig. 9.4. The tail reconnection is found closer to Jupiter for increasing dynamic pressure

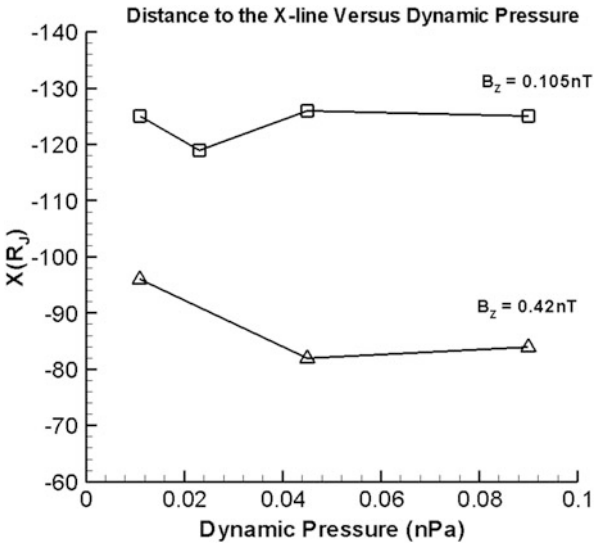

Fig. 9.8 The position of the tail reconnection site at Jupiter as a function of solar wind dynamic pressure for two values of the IMF B_Z component. The location is sensitive to IMF B_Z and for a given B_Z varies little as the dynamic pressure changes

For IMF-dependent reconnection, the location of the neutral line in the tail is sensitive to the magnitude of the IMF. In Fig. 9.8 we have plotted the distance to the reconnection site at midnight as a function of solar wind dynamic pressure for two IMF B_Z values. For 0.105 nT the reconnection occurs at about 125 R_J down the tail, while increasing the IMF by a factor of 4 to 0.42 nT moves the distance to the X-point into about 85 R_J. At a given dynamic pressure the IMF-dependent reconnection occurs further from Jupiter for weaker IMF. For instance for $Bz = 0.42$ nT the reconnection for 0.09 nPa is at 85 R_J compared with about 125 R_J for the outflow reconnection in Fig. 9.7.

In Figs. 9.5 and 9.8 we have plotted the location of the subsolar magnetopause and the reconnection site in the tail. In Fig. 9.9 we show an additional boundary: the location at midnight where the velocity of rotational flow decreases sharply. The exact location was determined by plotting the velocity components in the equatorial plane at midnight as a function of distance along the Sun-Jupiter line. An example of this can be seen in Fig. 1 of Fukazawa et al. (2006). The location of the sharp decrease in velocity has been circled and labeled 2 in that figure. In Fig. 9.9 we have plotted the location versus solar wind dynamic pressure for three northward IMF values. At all of the IMF values, the boundary location moves closer to Jupiter as the dynamic pressure increases. In addition, for a given dynamic pressure the location moves closer to Jupiter as the northward IMF increases. The one exception is for an IMF B_Z of 0.105 nT at 0.09 nPa pressure where the value is approximately constant. It was difficult to determine the exact value of the sharp decrease in rotational velocity for that case.

When the IMF is northward, the potential across the polar cap in the simulations typically is about 400 kV. This compares to about 4 MV in the solar wind across

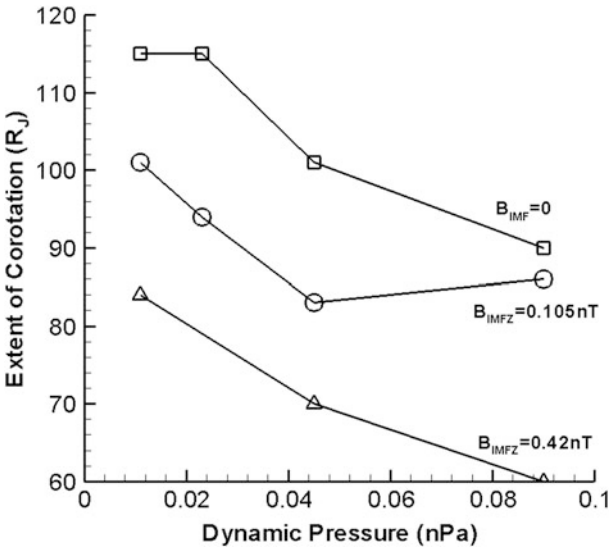

Fig. 9.9 The location at Jupiter of the sharp decrease in the rotational velocity at midnight versus dynamic pressure for two values of IMF Bz and no IMF. For a given IMF it moves toward Jupiter for increasing dynamic pressure. For a given dynamic pressure it moves toward Jupiter for increasing B_Z

the width of Jupiter's magnetosphere. As in Earth simulations, the reconnection efficiency is about 10 % in this simulation.

However, the response of the Jovian system to constant driving from the solar wind is not constant. Using the same approach we used at Earth (Fig. 9.1), we have plotted the lobe flux versus time following a northward turning of the IMF in the top panel of Fig. 9.10. The curve in the bottom panel is the change in the flux during a 3 h interval. The simulation was run with a solar wind dynamic pressure of 0.011 nPa, $B_Z = 0.105$ nT and an inner magnetosphere source of 2.41×10^{29} AMU/s. After reconnection begins in the low-latitude dayside magnetopause, the flux in the tail lobe begins to increase. The dashed lines show the times at which an X-line formed in the tail. For this simulation there were three distinct intervals of reconnection. The second interval of reconnection occurred 23 h after the first and the third occurred 35 h after the second. After the first interval the slope of the lobe flux curve decreases while after the second and third episode of reconnection the lobe flux decreased. Figure 9.11 from Fukazawa et al. (2010) shows results from a simulation with the same parameters as Fig. 9.10 but with a longer tail. The quantity plotted in color is the energy of the plasma in keV/AMU just above the equator and the white arrows give the velocity. At this time there are two plasmoid-like structures in the tail and a third is just forming. Note that the plasmoids move both tailward and across the tail toward the dawn magnetopause.

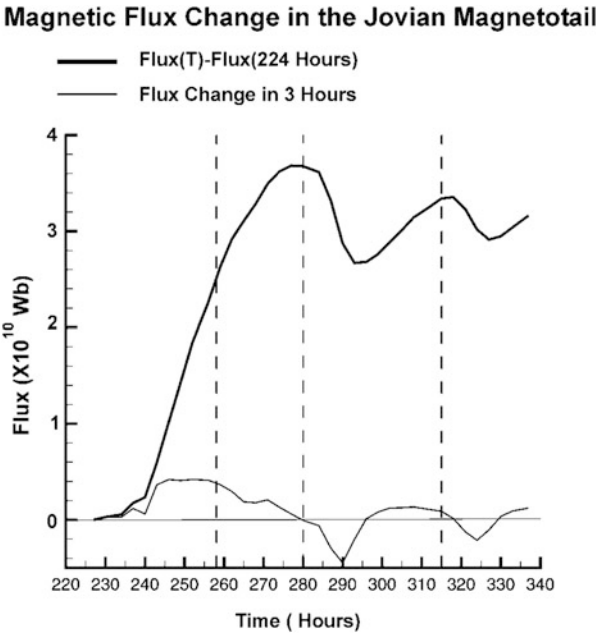

Fig. 9.10 The change in magnetic flux in the tail lobes following a southward to northward change in the IMF (*top*). This simulation was run with $P_{SW} = 0.011$ nPa, $B_Z = 0.105$ nT and an inner magnetosphere source of 2.41×10^{29} AMU/s. The *bottom panel* gives the change in magnetic flux in 3 h

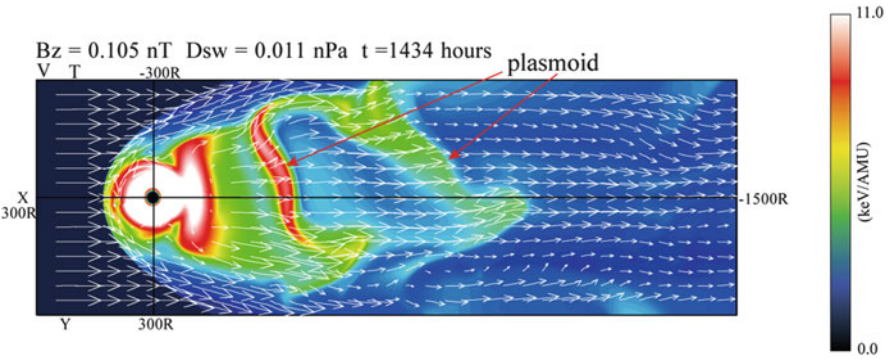

Fig. 9.11 The plasma temperature in keV/AMU from a simulation with the same parameters as Fig. 9.10 but with the simulation box extended in the tailward direction. Two plasmoids are moving tailward and toward the dawn magnetopause. A third is just forming the nearer Jupiter. (Adapted from Fukazawa et al. 2010)

Fukazawa et al. (2005, 2010) have carried out a number of simulations by varying the input parameters. The period of plasmoid release varied between 20 and 60 h. However, not all simulations with northward IMF produced multiple plasmoids.

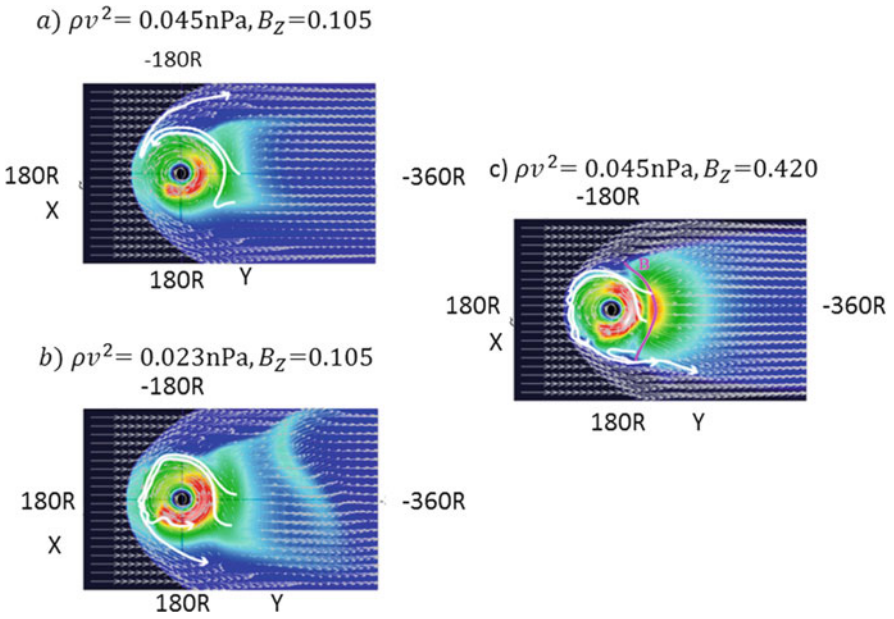

Fig. 9.12 A series of color coded plots of the plasma temperature with superimposed *gray* flow vectors and selected flow streamlines (*white*). This figure serves as a summary of our explanation of the solar wind dependence of the multiple plasmoids found in some of the simulations (see text). (Adapted from Fukazawa et al. 2006)

Whether or not multiple plasmoids occurred was dependent on the solar wind parameters (Fukazawa et al. 2006). The background in Fig. 9.12 gives a measure of the temperature of the plasma from three simulations that are representative of the results. Flow vectors and streamlines selected to show the range of trajectories from the reconnection site have been superimposed. The top panel (a) in Fig. 9.12 shows the results for a case with solar wind dynamic pressure of 0.045 nPa and $B_Z = 0.015$ nT. It is representative of cases with larger pressure and relatively small north–south component of the IMF. For these cases the outer edge of the plasma sheet is relatively far from the X-line (Figs. 9.8 and 9.9). The reconnection flow streamlines exit the dawn magnetopause and steady reconnection results. Multiple plasmoids form for relatively small dynamic pressure and IMF. The middle panel is from a simulation with dynamic pressure of 0.023 nPa and B_Z of 0.105 nT. For this case the reconnection occurs closer to the rotation boundary and the reconnected flux tubes can convect all of the way around Jupiter. When they return to the tail they again become stretched and reconnect again, leading to the periodic behavior. For relatively large dynamic pressure and IMF B_Z (0.045 nPa and 0.42 nT) in panel c the X-line forms close enough to the rotation boundary that the Jupiterward flow compresses the current sheet enough that flow can go around Jupiter. However, the flux tubes return along the dusk magnetopause and do not participate again in reconnection.

Fukazawa et al. (2010) carried out several numerical experiments to investigate other possible mechanisms for the observed periodic plasmoid signatures. For instance they set the IMF to zero and oscillated the dynamic pressure from 0.023 to 0.090 nPa with a period of 30 h. The dynamic pressure was changed by changing the solar wind density. The result was a series of enhancements in plasma density and thermal pressure moving down the tail. However, each enhancement was accompanied by an enhancement in B_Z and not by the bipolar signature of a plasmoid. The IMF is mostly in the Y direction at Jupiter's orbit; however, as the planet rotates, even an IMF pointing only in the Y direction will have an alternating north–south component. To investigate this possible source for the periodic plasmoids, B_Z was varied sinusoidally between plus and minus 0.105 nT with a 10 h period. The main effect of the B_Z oscillation was to increase the period of the plasmoid release by a factor of 2 (100 h in this case). In this case the total flux added to the tail from the dayside reconnection was decreased by a factor of two. In addition, when the IMF is southward the reconnection site moves to the tail lobe field tailward of the polar cusps, similarly to the mechanism suggested by McComas and Bagenal (2007) for convection at Jupiter.

We have used the simulation output to estimate the amount of plasma lost to the tail by the plasmoids. For the plasmoids in Fukazawa et al. (2005) we have estimated the amount of plasma lost to be about 40 kg/s. This value is in the range from observation based estimates (0.7 kg–120 kg/s) (Bagenal 2007; McComas and Bagenal 2007; Vogt et al. 2014). This is about 10 % of the source rate of 400 kg/s in this simulation (Fukazawa et al. 2005).

9.2.3 Simulated Transport at Saturn

Three simulation codes have been presented for Saturn's magnetosphere. One was developed at the University of Michigan (Hansen et al. 2005; Zieger et al. 2010; Jia et al. 2012). It is based on the BAT-R-US code developed for the Earth's magnetosphere (Powell et al. 1999; Gombosi et al. 2004). The version we will show results from in this paper uses a non-uniform spherical grid spacing that varies between 0.1 R_S (Saturn radii) near Enceladus orbit (5 R_S) and 0.3 R_S near Titan's orbit (20 R_S). This code includes the main plasma source at Enceladus and the rings as an axisymmetric disk centered at 5.35 R_S with a scale height to 0.5 R_S. In the simulations presented here the mass-loading rate was 3×10^{27} s^{-1} of water group ions (∼85 kg/s). In addition, a source of N^+ from Titan is included at 5×10^{25} s^{-1}. Although not affecting the source rate, charge exchange which can influence momentum and energy exchange, peaking at 4 R_S, is included in the model. In the ionosphere the current continuity equation is solved with an ionospheric Pedersen conductance of 0.5 S. The Hall conductance is set to zero.

The second code is based on the Ogino et al. (1998) Jupiter code (Fukazawa et al. 2007a; Walker et al. 2011). This code uses a Cartesian grid with uniform grid spacing of either 0.1 R_S or 0.3 R_S. The simulation does not include a model Enceladus torus but has inner magnetosphere source rates of either 2.75×10^{27} s^{-1} or 1.1×10^{28} s^{-1} water group ions. The source, which is placed at 5 Rs, comes from

an equilibrium current sheet at the equator Saturnward of 5 R_S, similar to the one used at Jupiter (Walker et al. 2011). The ionospheric Pedersen conductance is taken as 1 S and the Hall conductance is set to zero.

The final code is a multi-fluid simulation (Kidder et al. 2012) based on the Earth model of Winglee (2004). This code has a grid spacing of 0.25 R_S near Saturn and twice that in the outer parts of the magnetosphere. The Enceladus ion source is modeled by placing a torus of water group ions with a density of 2 cm^{-3} at the orbital distance of Enceladus. An extended torus develops in the simulation by ionization of neutrals away from Enceladus. Charge exchange is included near Enceladus. The ionospheric ions were assumed to be H^+. The density and temperature are held constant at the ionospheric boundary located 2.25 R_S from Saturn.

Two of the simulations were used to determine the dependence of the subsolar magnetopause position on the solar wind dynamic pressure. Fukazawa et al. (2007a) found $R_{MP} \propto P_{dyn}^{-0.20}$ while Jia et al. (2012) found that $R_{MP} \sim 10P_{dyn}^{-1/(5.0\mp0.8)}$. These are consistent with observations which also give an exponent of $\sim -1/5$ (Kanani et al. 2010). Saturn's magnetopause position is more sensitive to changes in the solar wind dynamic pressure than Earth's but less sensitive than Jupiter's. It is much less sensitive than either to changes in the IMF. In Fig. 9.13 the electric

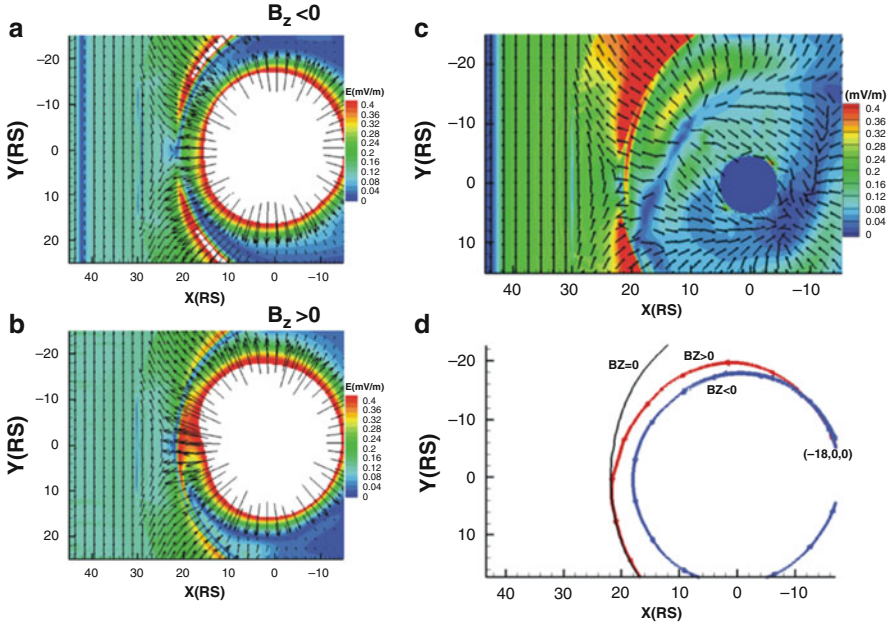

Fig. 9.13 The magnitude of the electric field in the equatorial plane for two simulations of Saturn's magnetosphere with superimposed electric field vectors. For these simulations the solar wind velocity was 300 km/s and the inner magnetosphere source was 2×10^{29} AMU/s. In panel (**a**) the IMF was $B_Z = -0.4$ nT while in panel (**b**) it was $B_Z = 0.4$ nT. Panel (**c**) contains the difference in the electric fields and panel (**d**) shows two flow streamlines demonstrating the change in transport in the two simulations. (Adapted from Walker et al. 2011)

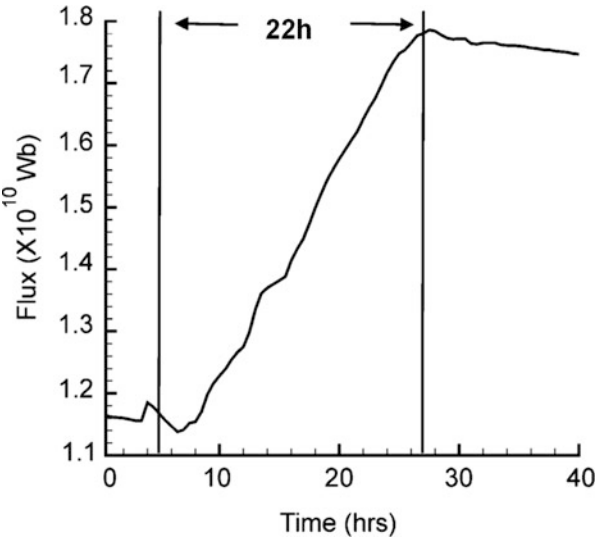

Fig. 9.14 The magnetic flux in the northern lobes following a change in the IMF from southward to northward. The simulation used the same parameters as Fig. 9.13. The tail reconnection starts about 22 h after the reconnection starts at the dayside magnetopause

field has been plotted in the equatorial plane for southward IMF (a) and northward IMF (b) (Walker et al. 2011). The solar wind parameters were held constant. The position of the magnetopause differs very little between the two simulations. Jia et al. (2012) compared the positions of the magnetopause for constant dynamic pressure and different IMF directions in a numerical experiment mimicking the passage of a corotating interaction region (CIR) past Saturn. They too found that the magnetopause was insensitive to the IMF orientation. These results suggest that reconnection is not as important at Saturn as it is at Earth or at Jupiter. In Fig. 9.14 we have plotted the magnetic flux in the northern tail lobe as a function of time following a southward to northward turning of the IMF. This plot was made by using the simulation in Fig. 9.13. The two vertical bars show the start of dayside reconnection and the start of tail reconnection. The difference in the two times is 22 h. It takes the solar wind a little more than 1 h to convect over the dayside magnetopause at Saturn. Thus tail reconnection at Saturn took about 20 dayside convection times. At Earth tail reconnection begins in about 3–6 convection times and at Jupiter it begins in 8–10 convection times. The reconnection process is much less effective at Saturn than at Earth or Jupiter. The electric potential difference across Saturn's magnetosphere is about 80 kV in this simulation while the potential difference in the solar wind across the magnetosphere was about 580 kV.

Jia et al. (2012) also looked at the change in polar cap (open) magnetic flux. They looked at the series of changes in the dynamic pressure and the IMF direction that are plotted in the top panel of Fig. 9.15. The bottom panel gives the resulting polar cap flux. When the IMF is southward there is relatively little open flux in the polar

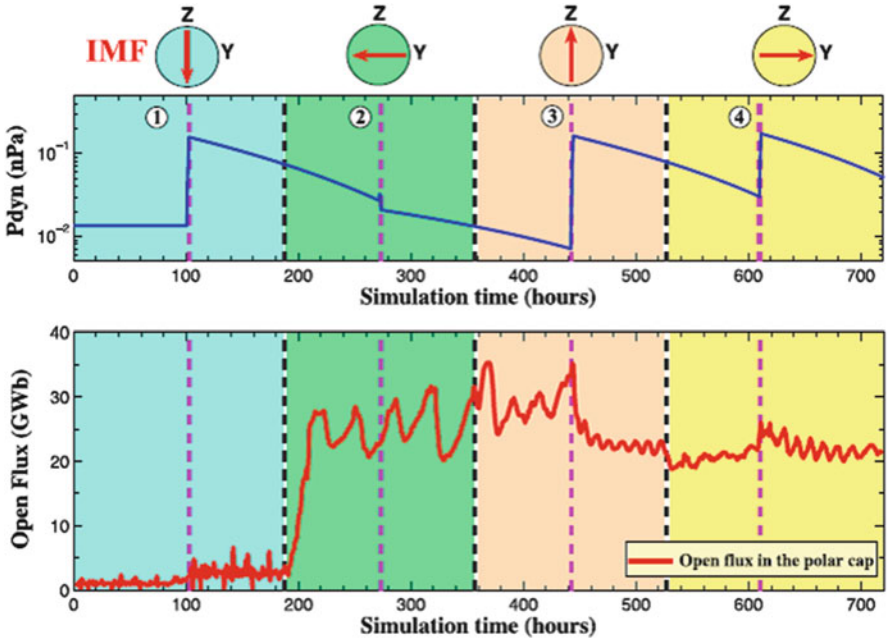

Fig. 9.15 The time history of the amount of open flux in the polar cap from a simulation of Saturn's magnetosphere (*bottom*). The *top panel* gives the IMF orientation and the *middle panel* gives the solar wind dynamic pressure used in the simulation. The *magenta dashed lines* indicate the times of shocks and *black dashed lines* indicate when the IMF direction was rotated. (From Jia et al. 2012)

cap. As the IMF was rotated from southward to dawnward, the amount of open flux increases as reconnection starts at the dayside magnetopause. The increase occurs because there is dayside reconnection without tail reconnection. During the rest of the simulation they found between 20 and 35 GWb in the polar cap. The decreases in polar cap flux were associated with reconnection in the tail. A few GWb (the average is 3.5 GWb) of flux is closed by the tail reconnection.

When the IMF is southward the reconnection site moves to the tail lobes. Any plasma sheet reconnection then will be caused by internal processes. Figure 9.16 is from the simulation sequence in Fig. 9.15 at 90 h. In this figure a plasmoid can be seen as a region of enhanced density extending toward dawn. Within the enhanced density region are green reconnected field lines with a flux-rope-like structure. The dawnward end of the green field lines maps to the northern hemisphere ionosphere while the other end maps to the southern hemisphere. Overlaying this structure are magenta closed field lines indicating that the reconnection occurred on closed field lines. This effectively keeps the plasmoid-like structure from moving tailward. Instead it moves azimuthally toward the dawn magnetopause.

IMF-driven reconnection occurs in all three simulations, leading to the formation of plasmoid-like structures. Figure 9.17 from Jia et al. (2012) shows the structure

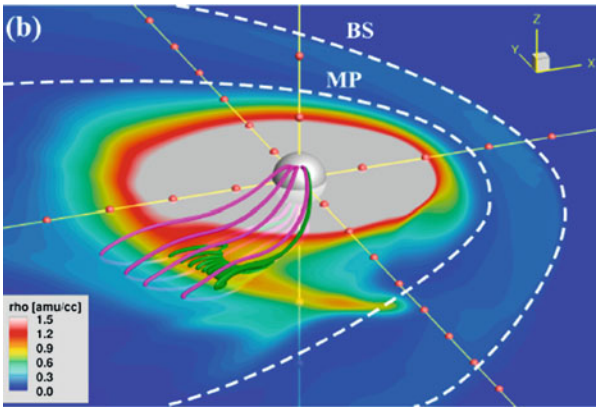

Fig. 9.16 Three dimensional rendering of a flux-rope-like structure at Saturn formed by reconnection while the IMF was purely southward. The background is the plasma density and with *magnetic field lines* superimposed. (Adapted from Jia et al. 2012)

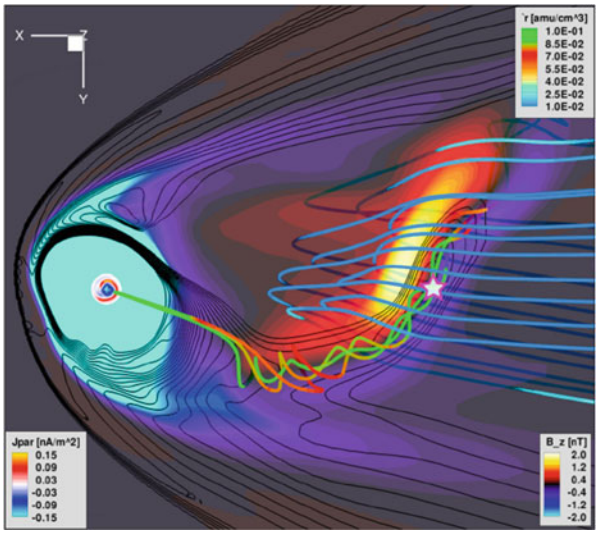

Fig. 9.17 Three dimensional rendering of a plasmoid formed at 225 h in the simulation of Fig. 9.15. The background is the B_Z component of the magnetic field, the *black lines* are contours of plasma density, the *flux rope field lines* are color coded with the plasma density and the *blue field lines* drape over the plasmoid. (From Jia et al. 2012)

of a plasmoid formed by reconnection in 3D at hour 225 in the simulation in Fig. 9.15. This is about 35 h after the IMF was turned from southward to duskward. The reconnection associated with this plasmoid caused the first decrease in open flux in Fig. 9.15. The background in this figure is B_z. The reconnection site is approximately along the transition from blue to red background and occurs from

pre-midnight to the dawn magnetopause with a rather irregular shape. The field lines at this time have been color coded with density. Although the plasmoid is draped with IMF (blue) field lines indicating lobe reconnection, the plasmoid has not detached from Saturn and still closes in the ionosphere. With time the entire structure becomes detached due to reconnection. The plasmoid is a region of enhanced density. Plasmoid-like structures also have been found in the other two simulations (Fukazawa et al. 2007a, 2012; Kidder et al. 2012). Figure 1 (16 h panel) in Fukazawa et al. (2012) shows the initiation of tail reconnection in the equatorial plane for a simulation with a purely northward IMF. The initial neutral line has a similar configuration to that in Fig. 9.17. Tail reconnection starts in the late evening sector (about 2200LT) and extends into the dawn quadrant.

Kidder et al. (2012) carried out two numerical experiments. In one they found that a rotation of the IMF from south to north could lead to the formation of tail reconnection and a plasmoid (their Fig. 5), and in the other they found that with constant northward IMF a pulse of solar wind dynamic pressure could trigger the formation of a plasmoid (their Fig. 6).

Saturn, like Jupiter, may generate periodic reconnection and tailward moving plasmoids even for constant solar wind. Jia et al. (2012) found large periodic plasmoids like that in Fig. 9.17 with a period that was inversely proportional to the solar wind dynamic pressure. The periods varied from less than 10 h to greater than 30 h (their Fig. 11). They evaluated the mass loss down the tail from the large plasmoids during a part of the simulation when the periodicity was about 30 h and found that about 10 kg/s were lost. This is much less than the source rate of 85 kg/s in this simulation. We have reexamined the frequency of plasmoid injection by using the simulation in Fukazawa et al. (2012). After the large scale plasmoid exits the tail through the tail boundary on the dawn side, a series of smaller plasmoids forms nearer the flanks of the magnetosphere and these too exit the magnetosphere. The smaller plasmoids have a period of about 1 h (Fukazawa et al. 2007a). Jia et al. (2012) suggested that such small plasmoids may account for a large fraction of the plasma lost. Note that based on the Fig. 9.11 of Jia et al. we would expect that the period of large plasmoid formation would be about 30 h in the Fukazawa et al. simulation. However, the simulation was run for only about 35 h and that is not sufficient time for a second large plasmoid to form. We can, however, calculate the amount of plasma in the one large plasmoid. About 8×10^5 kg was in the plasmoid. This is a little less than 10^6 kg reported in Jia et al. but Fukazawa et al. used a lower source rate. As at Jupiter, large plasmoids at Saturn do not remove all of the plasma from the source. The simulations conserve mass so it should be possible to determine how the mass moves through the magnetosphere from the source region. Walker and Fukazawa (2015) have analyzed one simulation for northward IMF and found that the most of the mass exited the dayside magnetopause.

In addition to solar wind driven reconnection Jia et al. (2012) have argued that outflow Vasyliunas-type reconnection also occurs in northward IMF simulations. The IMF-driven reconnection occurs primarily in the morning quadrant. They have reported reconnection in the dusk quadrant consistent with outflow reconnection (Fig. 13 in Jia et al. 2012).

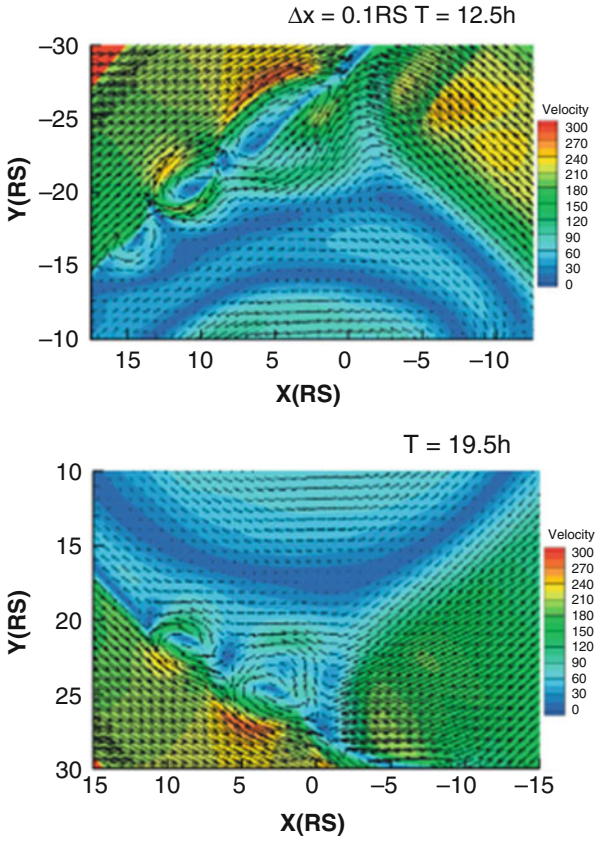

Fig. 9.18 The speed of the plasma in the equatorial plane, from a simulation of Saturn's magnetosphere when the IMF was northward with superimposed flow vectors. The solar wind dynamic pressure was 0.0083 nPa, the IMF B_Z was 0.4 nT and the inner magnetosphere source was 5.510^{28} AMU/s. The grid spacing was 0.1 R_S. Kelvin–Helmholtz waves developed first on morning magnetopause and then in the afternoon. (Adapted from Walker et al. 2011)

In addition to rotationally driven flows and reconnection-driven flows Fukazawa et al. (2007a, b) reported boundary oscillations and vorticity which they attributed to the Kelvin-Helmholtz (KH) instability. Figure 9.18 shows the speed of the plasma in the background with color coding and superimposed velocity vectors from the northward IMF simulation in Fukazawa et al. (2012). The top panel shows a section of the dawn magnetopause region 12.5 h into the simulation, while the bottom panel shows a section of the dusk magnetopause region at 19.5 h. Walker et al. (2011) found that the magnetopause became unstable to the KH instability first on the dawn side and then later on the dusk side. The boundary first became unstable in the morning magnetopause where the corotating Saturn flows are opposite to the magnetosheath flow. Later when there was return flow from the tail, increasing the flow shear at the boundary, the dusk side also became unstable. Reconnection may

also be important for the KH waves. Walker et al. (2011) argued that for northward IMF dayside reconnection can increase the flow shear at the magnetopause. An example of this is shown in panels (c) and (d) of Fig. 9.13. The effect of a rotation from southward to northward IMF increases the electric field near the morning magnetopause and thereby increases the flow velocity. In addition the twisted flux tubes created by the KH vortices can lead to reconnection. Fukazawa et al. calculated the field aligned currents from the KH vorticity and mapped them to the ionosphere where the away currents may create localized auroral emissions. There is some observational evidence for the KH waves both from Cassini observations in the magnetosphere (Masters et al. 2009; Walker et al. 2011) and auroral emissions (Grodent et al. 2011). The simulation shown in Fig. 9.18 along with the other simulations of KH waves used purely northward IMF. The KH instability is maximally unstable for northward and southward IMF. However, the IMF at Saturn has very large azimuthal component. Recently Fukazawa et al. (2014) ran a simulation by using Cassini observations of the solar wind and IMF at Saturn and found waves.

9.3 Discussion

In this review we have used the results from simulations of the magnetospheres of Jupiter and Saturn to model magnetospheric transport with emphasis on magnetic reconnection. Not surprisingly, magnetospheric transport at the rapidly rotating outer planets is dominated by motion in the direction of corotation. Unlike at Earth where reconnection is the dominant mechanism for transport, it is secondary at these rotating planets. However, there is both direct and indirect observational evidence for reconnection, and the simulations can help us put it in the perspective of its overall effect on the configuration and dynamics of these planets.

For northward IMF, reconnection at the dayside Jovian magnetopause causes erosion of the magnetopause position by about 10 % while magnetopause erosion is much less important at Saturn. If the IMF stays northward long enough, tail reconnection in the simulations becomes quasi-periodic with multiple plasmoid-like structures moving tailward at both magnetospheres. At Jupiter the periods are consistent with those inferred from observations. However, not all intervals with northward IMF lead to the generation of periodic reconnection in the tail. Fukazawa et al. (2010) have argued that both the solar wind dynamic pressure and the IMF determine whether or not periodic reconnection can occur. Only cases in which reconnected flux tubes can convect all of the way around Jupiter and return to the reconnection region will have periodic reconnection. At Saturn Jia et al. (2012) have shown that for fixed plasma source rate the period of the quasi-periodic plasmoids

should be controlled by the solar wind dynamic pressure with larger periods for lower dynamic pressures. The observational evidence for periodic plasmoids is not as clear at Saturn as at Jupiter.

There has been considerable debate about whether the reconnection at Jupiter and Saturn is outflow reconnection (Vasyliunas cycle) in which flux tubes that are stretched as they propagate into the evening magnetosphere, pinch off and reconnect, or whether the reconnection is Dungey-cycle reconnection driven by the solar wind and IMF. The simulations at both planets show evidence for both. In the simulations, however, the Vasyliunas cycle reconnection is on closed field lines while the Dungey cycle reconnection progresses to open field lines and creates plasmoids. McComas and Bagenal (2007) have argued that the conditions for solar-wind-driven reconnection cannot occur at Jupiter because the IMF does not stay northward long enough for the Dungey cycle to be set up. Before the Dungey cycle can be completed, the dayside reconnection site will move to the tail lobes. In simulations in which the IMF is southward the reconnection does move to the lobes. However, Walker et al. (2001) examined a large amount of solar wind data in the vicinity of Jupiter and found that at least part of the time the IMF kept the same direction long enough for a Dungey cycle to occur. Overall the reconnection pattern seen in the simulations is consistent with the predictions of the theoretical model of Cowley et al. (2003).

There is an on-going question as to where the plasmas whose ultimate sources are Io at Jupiter and Enceladus at Saturn leave the two magnetospheres. One mechanism that has been suggested is that the plasma leaves the magnetosphere with large scale plasmoids. However, this does not seem to be the case. In the simulations the rate of plasma lost in large plasmoids is much smaller than the plasma source rate. Jia et al. (2012) have suggested for Saturn that small scale plasmoids formed near the flanks may be an important way to remove the plasma. Since mass is conserved it should be possible to determine where the mass exits the magnetosphere. This is currently being studied in high resolution simulations.

Finally, simulations at Earth and Saturn suggest that Kelvin Helmholtz waves at the magnetopause may also contribute to transport. KH waves have not been found in the Jupiter simulations. The Kelvin Helmholtz instability is sensitive to the grid spacing used in the simulation. Very dense grids like that used for the calculation in Fig. 9.18 are not currently possible for Jupiter's very large magnetosphere but that too will come with time.

Acknowledgments RJW served as the NSF Program Director for Magnetospheric Physics during the period when much of this work was carried out. He gratefully acknowledges the NSF Individual Research and Development program. He also acknowledges NASA grant NASA NNG05GB82G under which this work was completed. The work of XJ is supported by the NASA Cassini Data Analysis Program through grant NNX12AK34G, and by the NASA Cassini mission under contract 1409449 with JPL.

References

V. Angelopoulos, W. Baumjohann, C.F. Kennel, F.V. Coroniti, M.G. Kivelson, R. Pellat et al., Bursty bulk flows in the inner central plasma sheet. J. Geophys. Res. **97**, 4027 (1992). doi:10.1029/91JA02701

M. Ashour-Abdalla, M. El-Alaoui, M.L. Goldstein, M. Zhou, D. Schriver, R. Richard et al., Observations and simulations of non-local acceleration of electrons in magnetotail magnetic reconnection events. Nat. Phys. **7**, 360 (2011). doi:10.1038/nphys1903

W.I. Axford, Viscous interaction between the solar wind and the Earth's magnetosphere. Planet. Space Sci. **12**, 45 (1961)

W.I. Axford, C.O. Hines, A unifying theory of high-latitude geophysical phenomena and geomagnetic storms. Can. J. Phys. **39**, 1433–1464 (1964)

F. Bagenal, The magnetosphere of Jupiter: coupling the equator to the poles. J. Atmos. Sol. Terr. Phys. **69**, 387 (2007). doi:10.1016/j.jastp.2006.08.012

F. Bagenal, Comparative planetary environments, in *Heliophysics: Plasma Physics of the Local Cosmos*, ed. by C.J. Schrijver, G.L. Siscoe (Cambridge University Press, Cambridge, 2009), p. 360

E.J. Bunce, S.W.H. Cowley, D.M. Wright, A.J. Coates, M.K. Dougherty, N. Krupp, W.S. Kurth, A.M. Rymer, In situ observations of a solar wind compression-induced hot plasma injection in Saturn's tail. Geophys. Res. Lett. **32**, L20S04 (2005). doi:10.1029/2005GL022888

S.G. Claudepierre, S.R. Elkington, M. Wiltberger, Solar wind driving of magnetospheric ULF waves: pulsations driven by velocity shear at the magnetopause. J. Geophys. Res. **113**, A05218 (2008). doi:10.1029/2007JA012890

S.W.H. Cowley, E.J. Bunce, T.S. Stallard, S. Miller, Jupiter's polar ionospheric flows: theoretical interpretation. Geophys. Res. Lett. **30**(5), 1220 (2003). doi:10.1029/2002GL016030

S.W.H. Cowley, S.V. Badman, S.M. Imber, S.E. Milan, Comment on "Jupiter: a fundamentally different magnetospheric interaction with the solar wind" by D.J. McComas and F. Bagenal. Geophys. Res. Lett. **35**, L10101 (2008). doi:10.1029/2007GL032645

J.W. Dungey, Interplanetary magnetic field and the auroral zones. Phys. Rev. Lett. **6**, 47 (1961). doi:10.1103/PhysRevLett.6.47

J.W. Dungey, Electrodynamics of the outer magnetosphere, paper presented at Ionosphere Conference. Paper presented at the Phys. Soc. of London, Cambridge, 1955

K. Fukazawa, T. Ogino, R.J. Walker, Dynamics of the Jovian magnetosphere for northward interplanetary magnetic field (IMF). Geophys. Res. Lett. **32**, L03202 (2005). doi:10.1029/2004GL021392

K. Fukazawa, K.T. Ogino, R.J. Walker, Configuration and dynamics of the Jovian magnetosphere. J. Geophys. Res. **111**, A10207 (2006). doi:10.1029/2006JA011874

K. Fukazawa, S. Ogi, T. Ogino, R.J. Walker, Magnetospheric convection at Saturn as a function of IMF BZ. Geophys. Res. Lett. **34**, L01105 (2007a). doi:10.1029/2006GL028373

K. Fukazawa, T. Ogino, R.J. Walker, Vortex-associated reconnection for northward IMF in the Kronian magnetosphere. Geophys. Res. Lett. **34**, L23201 (2007b). doi:10.1029/2007GL031784

K. Fukazawa, T. Ogino, R.J. Walker, A simulation study of dynamics in the distant Jovian magnetotail. J. Geophys. Res. **116**, A09219 (2010). doi:10.1029/2009JA01522

K. Fukazawa, T. Ogino, R.J. Walker, A magnetohydrodynamic simulation of Kronian field-aligned currents and auroras. J. Geophys. Res. **117**, A002214 (2012). doi:10.1029/2011JA016945

K. Fukazawa, R. J. Walker, S. Eriksson, Massively parallel MHD simulation of Kronian magnetosphere convection and auroral emission with solar wind. Paper presented at the fall AGU meeting, San Francisco, 7–12 Dec 2014

T.I. Gombosi et al., Solution-adaptive magnetohydrodynamics for space plasmas: Sun-to-Earth simulations. Comput. Sci. Eng. **6**(2), 14 (2004). doi:10.1109/MCISE.2004.1267603

A. Grocott, S.V. Badman, S.W.H. Cowley, S.E. Milan, J.D. Nichols, T.K. Yeoman, Magnetosonic Mach number dependence of the efficiency of reconnection between planetary and interplanetary magnetic fields. J. Geophys. Res. **114**, A07219 (2009). doi:10.1029/2009JA01433

D. Grodent, J. Gustin, J.-C. Gérard, A. Radioti, B. Bonfond, W.R. Pryor, Small-scale structures in Saturn's ultraviolet aurora. J. Geophys. Res. **116**, A09225 (2011). doi:10.1029/2011JA016818

K.C. Hansen, A.J. Ridley, G.B. Hospodarsky, N. Achilleos, M.K. Dougherty, T.I. Gombosi, G. Tóth, Global MHD simulations of Saturn's magnetosphere at the time of Cassini approach. Geophys. Res. Lett. **32**, L20S06 (2005). doi:10.1029/2005GL022835

T.W. Hill, Inertial limit on corotation. J. Geophys. Res. **84**, 6554–6558 (1979). doi:10.1029/JA084iA11p06554

E.W. Hones Jr., The magnetotail: its generation and dissipation, in *Physics of Solar Planetary Environments*, ed. by D.J. Williams (AGU, Washington, 1976), p. 559

C.M. Jackman, C.S. Arridge, Statistical properties of the magnetic field in the Kronian magnetotail lobes and current sheet. J. Geophys. Res. **116**, A05224 (2011). doi:10.1029/2010JA01597

C.M. Jackman, J.A. Slavin, S.W.H. Cowley, Cassini observations of plasmoid structure and dynamics: implications for the role of magnetic reconnection in magnetospheric circulation at Saturn. J. Geophys. Res. **116**, A10212 (2011). doi:10.1029/2011JA016682

C.M. Jackman, N. Achilleos, S.W.H. Cowley, E.J. Bunce, A. Radioti, D. Grodent, S.V. Badman, M.K. Dougherty, W. Pryor, Auroral counterpart of magnetic field dipolarizations in Saturn's tail. Planet. Space Sci. **82–83**, 34–42 (2013). doi:10.1016/j.pss.2013.03.01

C.M. Jackman, C.S. Arridge, N. André, F. Bagenal, J. Birn, M.P. Freeman et al., Large-scale structure and dynamics of the magnetotails of Mercury, Earth, Jupiter and Saturn. Space Sci. Rev. **182**, 85–154 (2014). doi:10.1007/s112140-014-0060-8

X. Jia, K.C. Hansen, T.I. Gombosi, M.G. Kivelson, G. Tóth, D.L. DeZeeuw, A.J. Ridley, Magnetospheric configuration and dynamics of Saturn's magnetosphere: a global MHD simulation. J. Geophys. Res. **117**, A05225 (2012). doi:10.1029/2012JA017575

S.P. Joy, M.G. Kivelson, R.J. Walker, K.K. Khurana, C.T. Russell, T. Ogino, Probalistic models of the Jovian magnetopause and bow shock locations. J. Geophys. Res. **107**, 1309 (2002). doi:10.1029/200IJA009146

S.J. Kanani, C.S. Arridge, G.H. Jones, A.N. Fazakerley, H.J. McAndrews, N. Sergis et al., A new form of Saturn's magnetopause using a dynamic pressure balance model, based on in-situ, multi-instrument Cassini measurements. J. Geophys. Res. **115**, A06207 (2010). doi:10.1029/2009JA014262

S. Kasahara, E.A. Kronberg, N. Krupp, T. Kimera, C. Tao, S.V. Badman, H. Retino, M. Fijimoto, Magnetic reconnection in the Jovian tail: X-line evolution and consequent plasma sheet structures. J. Geophys. Res. **116**, A11219 (2011). doi:10.1029/2011JA016892

S. Kasahara, E.A. Kronberg, T. Kimura, C. Tao, S.V. Badman, A. Masters, A. Retinò, N. Krupp, M. Fujimoto, Asymmetric distribution of reconnection jet fronts in the Jovian nightside magnetosphere. J. Geophys. Res. **118**, 375 (2013). doi:10.1029/2012JA018130

A. Kidder, C.S. Paty, R.M. Winglee, E.M. Harnett, External triggering of plasmoid development at Saturn. J. Geophys. Res. **117**, A07206 (2012). doi:10.1029/2012JA017625

M.G. Kivelson, Planetary magnetospheres, in *Solar Terrestrial Environment*, ed. by Y. Kamide, C.-L. Chian (Springer, New York, 2007), p. 470

M.G. Kivelson, Z.-Y. Pu, The Kelvin-Helmholtz instability on the magnetopause. Planet. Space Sci. **32**, 1341 (1984). doi:10.1016/0032-0633(84)90077-

M.G. Kivelson, D.J. Southwood, First evidence of IMF control of Jovian magnetospheric boundary locations: Cassini and Galileo magnetic field measurements compared. Planet. Space Sci. **51**, 891–898 (2003). doi:10.1016/S0032-0633(03)0075-8

E.A. Kronberg, K.-H. Glassmeier, J. Woch, N. Krupp, A. Lagg, M.K. Dougherty, A possible intrinsic mechanism for the quasi-periodic dynamics of the Jovian magnetosphere. J. Geophys. Res. **112**, A05203 (2007). doi:10.1029/2006JA011994

E.A. Kronberg, J. Woch, N. Krupp, A. Lagg, A summary of observational records on periodicities above the rotational period in the Jovian magnetosphere. Ann. Geophys. **27**, 2565 (2009). doi:10.5194/angeo-27-2565-2009

E.A. Kronberg, S. Kasahara, N. Krupp, J. Woch, Field-aligned beams and reconnection in the Jovian magnetotail. Icarus **217**, 55–65 (2012)

N. Krupp, J. Woch, A. Lagg, B. Wilken, S. Livi, D.J. Williams, Energetic particle bursts in the predawn Jovian magnetotail. Geophys. Res. Lett. **25**(8), 1249 (1998). doi:10.1029/98GL00863

H.R. Lai, H.Y. Wei, C.T. Russell, C.S. Arridge, M.K. Dougherty, Reconnection at the magnetopause of Saturn: perspective from FTE occurrence and magnetosphere size. J. Geophys. Res. **117**, A05222 (2012). doi:10.1029/2011JA017263

A. Masters, N. Achilleos, C. Bertucci, M.K. Dougherty, S.J. Kanani, C.S. Arridge et al., Surface waves on Saturn's dawn flank magnetopause driven by the Kelvin-Helmholtz instability. Planet. Space Sci. **57**, 1769 (2009). doi:10.1016/j.pss.2009.02.010

A. Masters, D.G. Mitchell, A.J. Coates, M.K. Dougherty, Saturn's low-latitude boundary layer: 1. Properties and variability. J. Geophys. Res. **116**, A06210 (2011a). doi:10.1029/2010JA016421

A. Masters, M.F. Thomsen, S.V. Badman, C.S. Arridge, D.T. Young, A.J. Coates, M.K. Dougherty, Supercorotating return flow from reconnection in Saturn's magnetotail. Geophys. Res. Lett. **38**, L03103 (2011b). doi:10.1029/2010GL046149

H.J. McAndrews, M.F. Thomsen, C.S. Arridge, C.M. Jackman, R.J. Wilson, M.G. Henderson, R.L. Tokar, K.K. Khurana, E.C. Sittler, A.J. Coates, M.K. Dougherty, Plasma in Saturn's nightside magnetosphere and the implications for global circulation. Planet. Space Sci. **57**(14–15), 1714–1722 (2009). doi:10.1016/j.pss.2009.03.003

D.J. McComas, F. Bagenal, Jupiter: a fundamentally different magnetospheric interaction with the solar wind. Geophys. Res. Lett. **34**, L20106 (2007). doi:10.1029/2007GL031078

D.G. Mitchell, S.M. Krimigis, C. Paranicas, P.C. Brandt, J.F. Carbary, E.C. Roelof, W.S. Kurth, D.A. Gurnett, J.T. Clarke, J.D. Nichols, J. Gerard, D.C. Grodent, M.K. Dougherty, W.R. Pryor, Recurrent energization of plasma in the midnight to-dawn quadrant of Saturn's magnetosphere and it relationship to auroral UV and radio emissions. Planet. Space Sci. **57**, 1732–1742 (2009). doi:10.1016/j.pss.2009.04.002

J.D. Nichols, S.W.H. Cowley, D.J. McComas, Magnetopause reconnection rate estimates for Jupiter's magnetosphere based on interplanetary measurements at ∼5 AU. Ann. Geophys. **24**, 393–406 (2006). doi:10.5194/angeo-24-393-2006

T. Ogino, R.J. Walker, M. Ashour-Abdalla, A global magnetohydrodynamic simulation of the magnetosheath and magnetosphere when the interplanetary magnetic field is northward. IEEE Trans. Plasma Sci. **20**, 817 (1992). doi:10.1109/27.19953

T. Ogino, R.J. Walker, M.G. Kivelson, A global magnetohydrodynamic simulation of the Jovian magnetosphere. J. Geophys. Res. **103**, 225 (1998). doi:10.1029/97JA02247

K.G. Powell, P.L. Roe, T.J. Linde, T.I. Gombosi, D.L.D. Zeeuw, A solution-adaptive upwind scheme for ideal magnetohydrodynamics. J. Comput. Phys. **154**, 284 (1999). doi:10.1006/jcph.1999.6299

C.T. Russell, R.C. Elphic, Initial ISEE magnetometer results - magnetopause observations. Space Sci. Rev. **22**, 681 (1978). doi:10.1007/BF0021619

C.T. Russell, K.K. Khurana, D.E. Huddleston, M.G. Kivelson, Localized reconnection in the near Jovian magnetotail. Science **280**, 1061–1064 (1998). doi:10.1126/science.280.5366.1961

C.T. Russell, C.M. Jackman, H.Y. Wei, C. Bertucci, M.K. Dougherty, Titan's influence on Saturnian substorm occurrence. Geophys. Res. Lett. **35**, L12105 (2008). doi:10.1029/2008GL034080

L. Scurry, C.T. Russell, Proxy studies of energy transfer to the magnetosphere. J. Geophys. Res. **96**, 9541 (1991). doi:10.1029/91JA00569

S. Sharma, R. Nakamura, A. Runov, E.E. Grigorenko, H. Hasegawa, M. Hoshino et al., Transient and localized processes in the magnetotail: a review. Ann. Geophys. **26**, 955 (2008). doi:10.5194/angeo-26-955-2008

S. Simon, A. Wennmacher, F.M. Neubauer, C.L. Bertucci, H. Kriegel, J. Saur, C.T. Russell, M.K. Dougherty, Titan's highly dynamic magnetic environment: a systematic survey of Cassini magnetometer observations from flybys TA-T62. Planet. Space Sci. **58**, 1230–1251 (2010). doi:10.1016/j.pss.2010.04.021

J.A. Slavin, B.T. Tsurutani, E.J. Smith, D.E. Jones, D.G. Sibeck, Average configuration of the distant (<220 *Re*) magnetotail: initial ISEE-3 magnetic field results. Geophys. Res. Lett. **10**, 973–976 (1983). doi:10.1029/GL010i010p00973

M.F. Thomsen, R.J. Wilson, R.L. Tokar, D.B. Reisenfeld, C.M. Jackman, Cassini/CAPS observations of duskside tail dynamics at Saturn. J. Geophys. Res. **118**, 5767–5781 (2013). doi:10.1002/jgra.50552

M.F. Thomsen, D. Mitchell, X. Jia, C.M. Jackman, G. Hospodarsky, A. Coates, Plasmapause formation at Saturn. J. Geophys. Res. **120**, 2571–2583 (2015). doi:10.1002/2015JA021008

V.M. Vasyliunas, Plasma distribution and flow, in *Physics of the Jovian Magnetosphere*, ed. by A.J. Dessler (Cambridge Univ. Press, Cambridge, 1983), pp. 395–453

M.F. Vogt, M.G. Kivelson, K.K. Khurana, S.P. Joy, R.J. Walker, Reconnection and flows in the Jovian magnetotail as inferred from magnetometer observations. J. Geophys. Res. **115**, A06219 (2010). doi:10.1029/2009JA015098

M.F. Vogt, M.G. Kivelson, K.K. Khurana, R.J. Walker, B. Bonfond, D. Grodent, A. Radioti, Improved mapping of Jupiter's auroral features to magnetospheric sources. J. Geophys. Res. **116**, A03220 (2011). doi:10.1029/2010JA016148

M.F. Vogt, C.M. Jackman, J.A. Slavin, E.J. Bunce, S.W.H. Cowley, M.G. Kivelson, K.K. Khurana, Structure and statistical properties of plasmoids in Jupiter's magnetotail. J. Geophys. Res. **119**, 821–843 (2014). doi:10.1002/2013JA019393

M. Volwerk, J. Berchem, Y.V. Bogdanova, O.D. Constantinescu, M.W. Dunlop, J.P. Eastwood et al., Interplanetaruy magnetic field rotations followed from L1 to the ground: the response of the Earth's magnetosphere as seen by multi-spacecraft events and ground-based observations. Ann. Geophys. **29**, 1549–1569 (2011). doi:10.5194/angeo-29-1549-2011

A.D.M. Walker, The Kelvin-Helmholtz instability in the low-latitude boundary layer. Planet. Space Sci. **29**, 1119 (1981). doi:10.1016/0032-0633(81)90011-8

R.J. Walker, C.T. Russell, Flux transfer events at the Jovian magnetopause. J. Geophys. Res. **90**(A8), 7397 (1985). doi:10.1029/JA090iA08p07397

R.J. Walker, T. Terasawa, S.P. Christon, V. Angelopoulos, M. Hoshino, W. Lennartsson et al., Source and loss processes in the magnetotail. Space Sci. Rev. **88**, 285 (1999). doi:10.1023/A:100520791863

R.J. Walker, T. Ogino, M.G. Kivelson, Magnetohydrodynamic simulation of the effect of the solar wind on the Jovian magnetosphere. Planet. Space. Sci. **49**, 237 (2001)

R.J. Walker, K. Fukazawa, T. Ogino, D. Morozoff, A simulation study of Kelvin-Helmholtz waves at Saturn's magnetopause. J. Geophys. Res. **116**, A03203 (2011). doi:10.1029/2010JA015905

R.J. Walker, K. Fukazawa, Simulation studies of plasma transport in outer planet magnetospheres, paper presented at the 12th International School of Space Simulations, Prague, July 2015

R.M. Winglee, Ion cyclotron and heavy ion effects on reconnection in a global magnetotail. J. Geophys. Res. **109**, A09206 (2004). doi:10.1029/2004JA010385

J. Woch, J.N. Krupp, A. Lagg, B. Wilken, S. Livi, D.J. Williams, Quasiperiodic modulations of the Jovian magnetotail. Geophys. Res. Lett. **25**, 1253–1256 (1998). doi:10.1029/98GL00861

J. Woch, N. Krupp, A. Lagg, Particle bursts in the Jovian magnetosphere: evidence for a near-Jupiter neutral line. Geophys. Res. Lett. **29**(7), 1138 (2002). doi:10.1029/2001GL014080

B. Zieger, K.C. Hansen, T.I. Gombosi, D.L. DeZeeuw, Periodic plasma escape from the mass-loaded Kronian magnetosphere. J. Geophys. Res. **115**, A08208 (2010). doi:10.1029/2009JA014951

Chapter 10
Fractal Reconnection in Solar and Stellar Environments

K. Shibata and S. Takasao

Abstract Recent space based observations of the Sun revealed that magnetic reconnection is ubiquitous in the solar atmosphere, ranging from small scale reconnection (observed as nanoflares) to large scale one (observed as long duration flares or giant arcades). Often the magnetic reconnection events are associated with mass ejections or jets, which seem to be closely related to multiple plasmoid ejections from fractal current sheet. The bursty radio and hard X-ray emissions from flares also suggest the fractal reconnection and associated particle acceleration. We shall discuss recent observations and theories related to the plasmoid-induced-reconnection and the fractal reconnection in solar flares, and their implication to reconnection physics and particle acceleration. Recent findings of many superflares on solar type stars that has extended the applicability of the fractal reconnection model of solar flares to much a wider parameter space suitable for stellar flares are also discussed.

Keywords Astrophysical jets • Fractal reconnection • Particle acceleration • Reconnection plasmoids • Solar flares • Solar reconnection • Superflares

10.1 Introduction

The recent progress of space based solar observations in last few decades such as Yohkoh (1991–2001), SOHO (1995-) , TRACE (1998–2010), RHESSI (2002-), Hinode (2006-), SDO (2010-) has revolutionized the field of solar physics significantly. With the help of space missions, it has been revealed that the solar corona is much more dynamic than had been thought, the quiet Sun is never quiet, the solar atmosphere is full of dynamic phenomena such as nanoflares, jets, waves, and shocks. An understanding that has emerged from the new observations is that *the magnetic reconnection is ubiquitous in the solar atmosphere*. So far, many pieces of evidence of magnetic reconnection have been found in solar flares and flare-like

K. Shibata (✉) • S. Takasao
Kwasan and Hida Observatories, Kyoto University, Yamashina, Kyoto 607-8471, Japan
e-mail: shibata@kwasan.kyoto-u.ac.jp; takasao@kwasan.kyoto-u.ac.jp

W. Gonzalez, E. Parker (eds.), *Magnetic Reconnection*, Astrophysics and Space Science Library 427, DOI 10.1007/978-3-319-26432-5_10

phenomena, and now we can say that the magnetic reconnection mechanism of solar flares is established, at least, phenomenologically (see review by Shibata and Magara 2011), although there are a number of unsolved problems that exist and these problems are highlighted in the present article. The long-standing puzzle of solar coronal heating mechanism has not yet been solved, although some of the new observations suggest that even quiet corona may be heated by small scale reconnection such as microflares, nanoflares, or picoflares (e.g., Parker 1988; Priest and Forbes 2000).

Virtually, almost all active phenomena occurring in the solar atmosphere seem to be related to magnetic reconnection, directly or indirectly. This is probably a consequence of universal properties of magnetized plasmas: the solar corona is in a low plasma-$\beta (= p_{gas}/p_{mag} \ll 1)$ state, where magnetic force and magnetic energy dominate over other force (e.g. gravitational forces) and energy, respectively. As a result, it is expected that the magnetic reconnection will have significant impact on heating as well as dynamics in the solar corona. In addition, there is evidence that even the dynamic phenomena in the chromosphere (average $\beta \sim 1$) and photosphere (average $\beta \sim 10^4$) may be related to reconnection. This is also a result of properties of magnetized plasma (e.g., Parker 1979, 1994; Priest 1982; Tajima and Shibata 1997): Magnetic fields tend to be concentrated to thin filaments in high β plasmas, so that the magnetic energy density in the filaments is much larger than the average value. Therefore, once reconnection occurs in the filaments, the influence of reconnection can be significant.

On the other hand, some of the recent stellar observations have reported many dynamic activities in various stars such as jets and flares from young stellar objects and binary stars. Even superflares have been discovered on many solar type stars. These dynamic events are much more energetic than solar flares, but the basic properties of these explosive events appear to be similar to the solar flares. Although evidence is still considered "indirect", both theories and observations suggest similarity between solar flares and stellar flares.

In this article, we provide a review on the recent observations of magnetic reconnection in solar flares and related phenomena in the solar atmosphere, with particular emphasis on a unified model of solar flares and flare-like phenomena based on the physics of magnetic reconnection. The recent observations of stellar flares will also be discussed briefly.

10.2 Fundamental Problems with Magnetic Reconnection in Solar Atmosphere

There are some fundamental puzzles that need to be solved in order to fully understand the physics of solar and stellar flares.

First, we have to deal with the most basic problem related with magnetic reconnection:

(1) What determines the Reconnection Rate?

Recent magnetospheric observations and collisionless plasma theory suggest that fast reconnection (defined as the reconnection with the rate nearly independent of the Lundquist number) occurs if the current sheet thickness becomes comparable to ion Larmor radius (r_{Li}) and ion inertial length (λ_i) (either with anomalous resistivity or collisionless conductivity, see review by e.g., Yamada et al. 2010):

$$r_{Li} = \frac{c}{eB}(m_i kT)^{1/2} \simeq 100\left(\frac{T}{10^6\ \mathrm{K}}\right)^{1/2}\left(\frac{B}{10\ \mathrm{G}}\right)^{-1}\ \mathrm{cm}, \tag{10.1}$$

$$\lambda_i = \frac{c}{\omega_{pi}} \simeq 300\left(\frac{n}{10^{10}\ \mathrm{cm}^{-3}}\right)^{-1/2}\ \mathrm{cm}, \tag{10.2}$$

where ω_{pi} is the ion plasma frequency.

However, the typical size of solar flares (L_{flare}) is

$$L_{flare} \simeq 10^9\text{–}10^{10}\ \mathrm{cm},$$

and is much larger than the micro-plasma scales.

Such enormous gap between micro- and macro-scales (ratio of both scales $\sim 10^7$) in solar flares is quite different from the situation of plasmas in magnetospheric and laboratory plasmas where both scales are not so different, only within a factor of 100 (Terasawa et al. 2000).

Hence for the solar (as well as stellar) reconnection problem, one has to solve the following additional fundamental problem:

(2) How can we reach such a small scale to switch on anomalous resistivity or collisionless reconnection in solar flares?

Finally, nonthermal emissions are one of the most important characteristics of the solar and stellar flares (and also of other astrophysical flares and bursts). The nonthermal emissions are a result of acceleration of electrons (10 keV–1 MeV) and ions (10 MeV–1 GeV). However, not only the acceleration mechanism but also the acceleration site have not yet been understood very well (see review by Miller et al. 1997; Aschwanden 2002).

(3) What is the acceleration mechanism of high energy particles in solar flares and what is the relation to reconnection?

In this article, we would argue that the aforementioned fundamental puzzles are closely related each other and that plasmoid-induced-reconnection process occurring in the current sheet and fractal reconnection are the key to the fundamental problems related with the magnetic reconnection in the solar and stellar atmosphere.

10.3 A Unified View of Solar Flares and Flare-Like Phenomena in the Solar Atmosphere

10.3.1 Solar Flares, Coronal Mass Ejections, and Plasmoid Ejections

Solar flares have been observed with Hα line from the ground based observatories, and are known to show two ribbon bright patterns in Hα images. Motivated by the observations, a standard magnetic reconnection model called *CSHKP model* (after Carmichael 1964; Sturrock 1966; Hirayama 1974; Kopp and Pneuman 1976) has been proposed. The CSHKP model predicts the formation of hot, cusp-shaped flare loops or arcades. The predicted cusp-shaped flare loops were indeed discovered by Yohkoh soft X-ray observations (Tsuneta et al. 1992; Tsuneta 1996). Now, the standard reconnection model (CSHKP) of solar flares and flare-like phenomenon is considered well established.

However, cusp-shaped flares are rather rare, and many flares do not show clear cusps. Observations show that the shape of cusp in Soft X-rays is clear mainly during the *long duration event (LDE) flares*, that are long lived (more than 1 h) flares, large in size, but have small frequency of occurrence. On the other hand, many flares (often called *impulsive flares*) are short lived, small in size, with large occurrence frequency, but show only a simple loop structure. Therefore people sometimes argued that the observed "simple loop" structure of many flares is anti-evidence of magnetic reconnection.

It was Masuda et al. (1994) who changed the entire scenario. He discovered the *loop top hard X-ray source* well above the simple soft X-ray loop. Since hard X-ray source is produced by high energy electrons, it provided an important evidence that a high energy process related to the central engine of flares is occurring *not* in the soft X-ray loop but above the loop. Hence even non-cusped loop flares may be energized by the magnetic reconnection high above the loop in a similar way as the reconnection in the cusp-shaped flares (Masuda et al. 1994). Since then, a unified model has been proposed in which the plasmoid ejection well above the loop top hard X-ray source is considered (Shibata et al. 1995) (Fig. 10.1).

Indeed, many plasmoid ejections have been discovered above the Masuda-type flare loop (Shibata et al. 1995; Tsuneta 1997; Ohyama and Shibata 1997, 1998, 2000; Shimizu et al. 2008). It is important to note that the strong acceleration of plasmoid occurs during the impulsive phase of the flares. This may provide a hint to understand why and how a fast reconnection occurs in actual flares (Shibata and Tanuma 2001).

About the half of the observed coronal mass ejections (CMEs) occur in association with flares, but the other half are not associated with flares. This also led to a lot of confusion in the community because CMEs were thought to be fundamentally different from flares. However, Yohkoh/SXT revealed the formation of *giant arcade* at the feet of CMEs. These giant arcades are very similar to cusp-shaped flares in morphology, but very faint in soft X-rays and Hα, and cannot

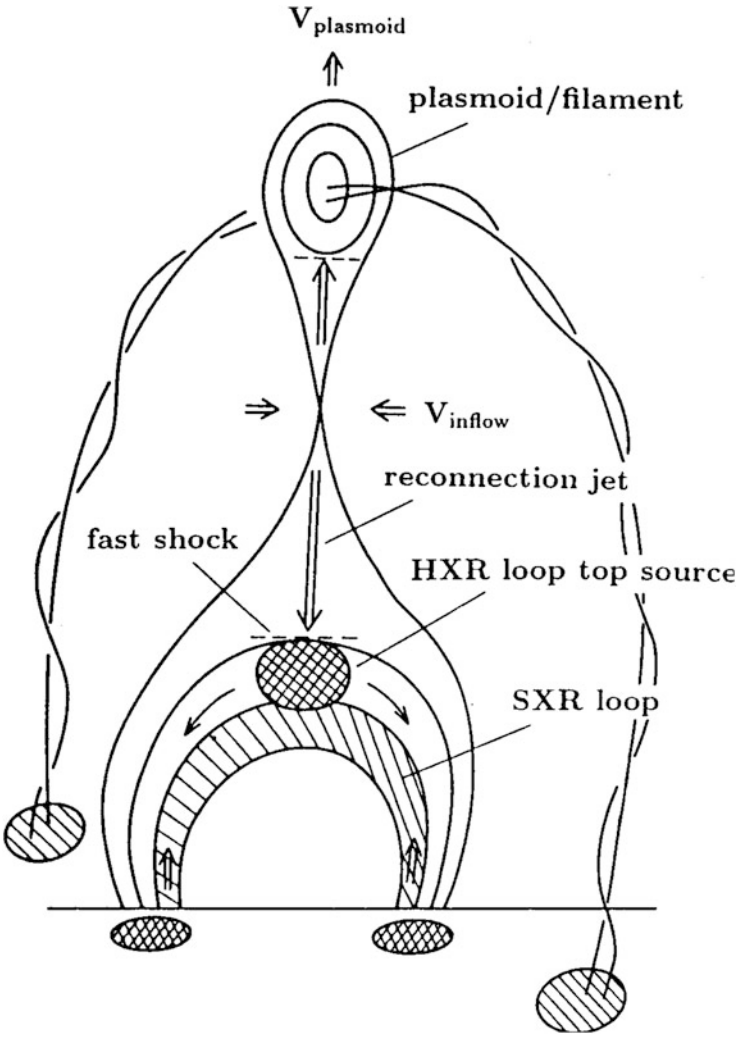

Fig. 10.1 A unified model (*plasmoid-induced-reconnection model*) of solar flares and flare-like phenomena (Shibata et al. 1995), where LDE flares (Tsuneta et al. 1992) and impulsive flares are unified (Masuda et al. 1994)

be seen in non-imaging observations of soft X-rays (such as GOES) or hard X-rays. Only high-sensitive soft X-ray imaging observations were able to reveal the existence of giant arcade and the association of most of the non-flare CMEs with giant arcades.

10.3.2 Microflares, Nanoflares, and Jets

Space based solar observations revealed that the solar atmosphere is full of small scale flares, called microflares, nanoflares, and even picoflares, and that these small scale flares are often associated with jets. One of the nice example of a jet is X-ray jets discovered by Yohkoh/SXT (Shibata et al. 1992; Shimojo et al. 1996). There are many pieces of observational evidence that shows that the jets are produced by magnetic reconnection (Shibata 1999). Yokoyama and Shibata (1995, 1996) performed MHD simulation of reconnection between an emerging flux and an overlying coronal field and successfully explained the observational characteristics of X-ray jets on the basis of their simulation results. A direct extension of the 2D model to 3D MHD simulation has been carried out by Isobe et al. (2005, 2006), where it was pointed out that the onset of the Rayleigh-Taylor instability at the top of the rising emerging flux leads to intermittent jets during reconnection. As a result, filamentary structures are formed naturally and are associated with patchy reconnection, that is in agreement with observations. As for the more recent development of 3D models, see e.g., Moreno-Insertis et al. (2008), Pariat et al. (2010), and Archontis and Hood (2013).

From the high resolution images taken with Hinode/SOT, Shibata et al. (2007) discovered numerous, tiny *chromospheric anemone jets* (whose apparent foot-point structures are similar to "sea anemone" in a three dimensional space) in the active region chromosphere. The morphology of the chromospheric anemone jets is quite similar to that of the coronal X-ray jets (Shibata et al. 1992; Shimojo et al. 1996; Cirtain 2007), suggesting that magnetic reconnection is occurring at the feet of these jets (Takasao et al. 2013), although the length and velocity of these jets are much smaller than those of the coronal jets (Table 10.1 and Fig. 10.2).

10.3.3 Unified Model: Plasmoid-Induced-Reconnection Model

Table 10.1 summarizes solar "flare" observations from microflares to giant arcades. The size and time scales range in wide values, from 200 km and 10 s for nanoflares to 10^6 km and 2 days for giant arcades. However, it is interesting to note that if we normalize the time scale by the Alfven time, then the normalized time scale becomes similar, 100–300t_A (Alfven time). So the "flares" mentioned in Table 10.1 can be unified by a common physical process i.e. magnetic reconnection. It is quite evident that although mass ejections are common in these "flares", the morphology is quite different between the large scale and small scale flares. In large scale flares (e.g., giant arcades, LDE flares, impulsive flares), mass ejections (CMEs, filament eruptions) are bubble like or flux rope type, while in small scale flares (e.g., microflares, nanoflares), mass ejections are jets or jet-like. So what causes such morphological differences between "flares"?

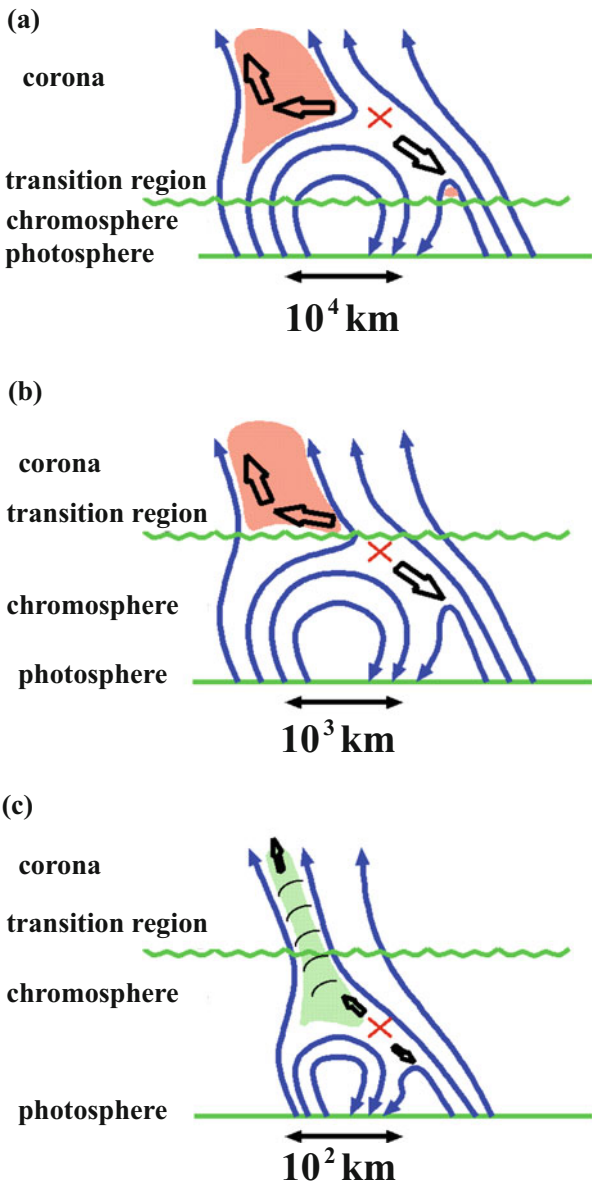

Fig. 10.2 A schematic illustration of magnetic reconnection that occurs at various altitudes in the solar atmosphere (Shibata et al. 2007). (**a**) X-ray jets/SXR microflares. (**b**) EUV jets/EUV microflares. (**c**) Chromospheric anemone jets/nanoflares

Our answer to the question on morphology is as follows. According to our view (Fig. 10.3), the plasmoid ejection is a key process that leads to a fast reconnection (so we call "plasmoid-induced-reconnection"), since plasmoids (magnetic islands or helical flux ropes in 3D) are created naturally in the current sheets as a result of the tearing instability. In the case of large scale flares, plasmoids (flux ropes) can

Table 10.1 Summary of observations of various "flares"

"Flare"	Length scale (L) (10^4 km)	Time scale (t) (s)	Alfven time (t_A) (s)	t/t_A	Type of mass ejection
Nanoflares	0.02–0.1	20–100	1–10	10–50	Chromospheric anemone jet
Microflares	0.1–1	100–1000	1–10	∼100	Coronal jet/surge
Impulsive flares	1–3	$60–3 \times 10^3$	10–30	60–100	Plasmoid/filament eruption
LDE flares	10–40	$3 \times 10^3 - 10^5$	30–100	100–300	CME/plasmoid/filament eruption
Giant arcades	30–100	$10^4 - 2 \times 10^5$	100–1000	100–300	CME/plasmoid/filament eruption

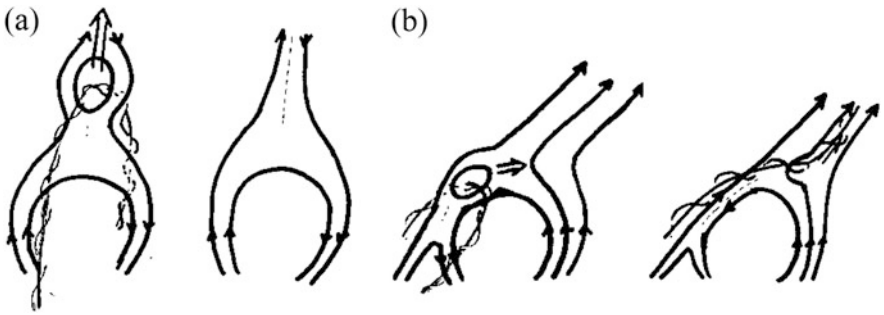

Fig. 10.3 A unified model (*plasmoid-induced-reconnection model*) of solar flares and flare-like phenomena (Shibata 1999): (**a**) large scale flares (giant arcades, LDE flares, impulsive flares), (**b**) small scale flares (microflares, nanoflares)

retain their coherent structures during the ejection even during the interaction with the ambient magnetic field. Therefore many CMEs look like the flux rope ejection. However, in the case of small scale flares, plasmoids will lose their coherent shape soon after reconnection with the ambient field, and are likely to disappear (or lose their structure) eventually after the interaction (collision) with the ambient field. As the remnant (eventually), one would expect a spinning helical jet along the reconnected field lines along with generation of Alfvén waves. We conjecture that it will explain why jets are usually observed in association with small scale flares, although this idea should be tested through future observations. It is interesting to mention that some of the observations (Kurokawa et al. 1987; Pike and Mason 1998; Alexander and Fletcher 1999) have revealed the formation of spinning (helical) jets (Shibata and Uchida 1985) after flare-like phenomena. Further, from the Hinode/XRT observations, Shimojo et al. (2007) found that an X-ray loop ejection (possibly helical loop ejection) finally led to an X-ray jet. These observations support the unified model shown in Fig. 10.3.

10.4 Plasmoid-Induced-Reconnection and Fractal Reconnection

10.4.1 Plasmoid-Induced Reconnection

As we have discussed in the previous section, it has become clear that the plasmoid ejections are observed quite often in solar flares and flare-like events. As the spatial and temporal resolutions of the observations have become better, more and more, smaller plasmoids have been discovered in association with flares. So, how does plasmoid ejections in flares are related with the fast reconnection?

From the Soft and Hard X-ray observations of impulsive flares, Ohyama and Shibata (1997) found that (1) a plasmoid was ejected long before the impulsive phase, (2) the plasmoid acceleration occurred during the impulsive phase (see Fig. 10.4a). As a result of the magnetic reconnection, plasmoid formation takes place (usually about 10 min) before the impulsive phase. When the fast reconnection ensues (i.e., in the impulsive phase), particle acceleration and huge amount of energy release occurs for $\sim 10t_A$. During this process the plasmoid acceleration is closely coupled to the reconnection inflow.

A similar relation between the energy release (and fast reconnection) and plasmoid acceleration has also been found in the case of CMEs (e.g., Zhang et al. 2001; Qiu et al. 2004; see Fig. 10.4d) as well as in laboratory experiment (Ono et al. 2011). What is the physical understanding that can be drawn from the relation between the plasmoid ejection and the fast reconnection?

It was Shibata and Tanuma (2001) who suggested that plasmoid ejection induces a strong inflow into the reconnection region as a result of mass conservation, and drive fast reconnection. Since the inflow (that determines the reconnection rate) is induced by the plasmoid motion, the reconnection process was termed as *plasmoid-induced reconnection* (Shibata et al. 1995; Shibata 1999).

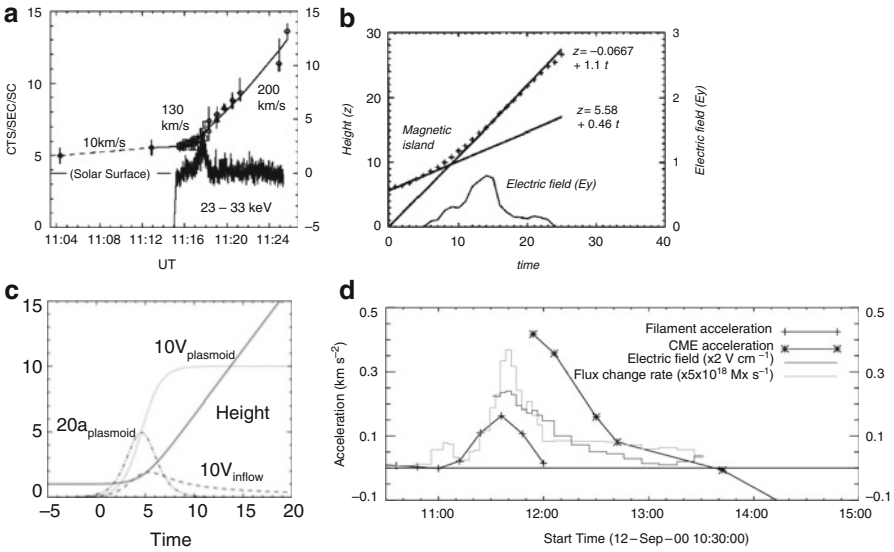

Fig. 10.4 (**a**) Time variations of the height of an observed plasmoid as well as hard X-ray intensity. From Ohyama and Shibata (1997). (**b**) Height-time relation of a magnetic island in a two-dimensional numerical simulation, which is supposed to be the two-dimensional counterpart of a plasmoid. Time variation of the electric field (i.e., the reconnection rate $\propto V_{inflow}$ is also plotted. From Magara et al. (1997). (**c**) Analytical model of plasmoid acceleration in the plasmoid-induced-reconnection model. From Shibata and Tanuma (2001). (**d**) Observations of a CME and associated filament eruption (Qiu et al. 2004). It is seen that the filament acceleration (+) show the time variation similar to that of electric field (reconnection rate; *thick solid curve*)

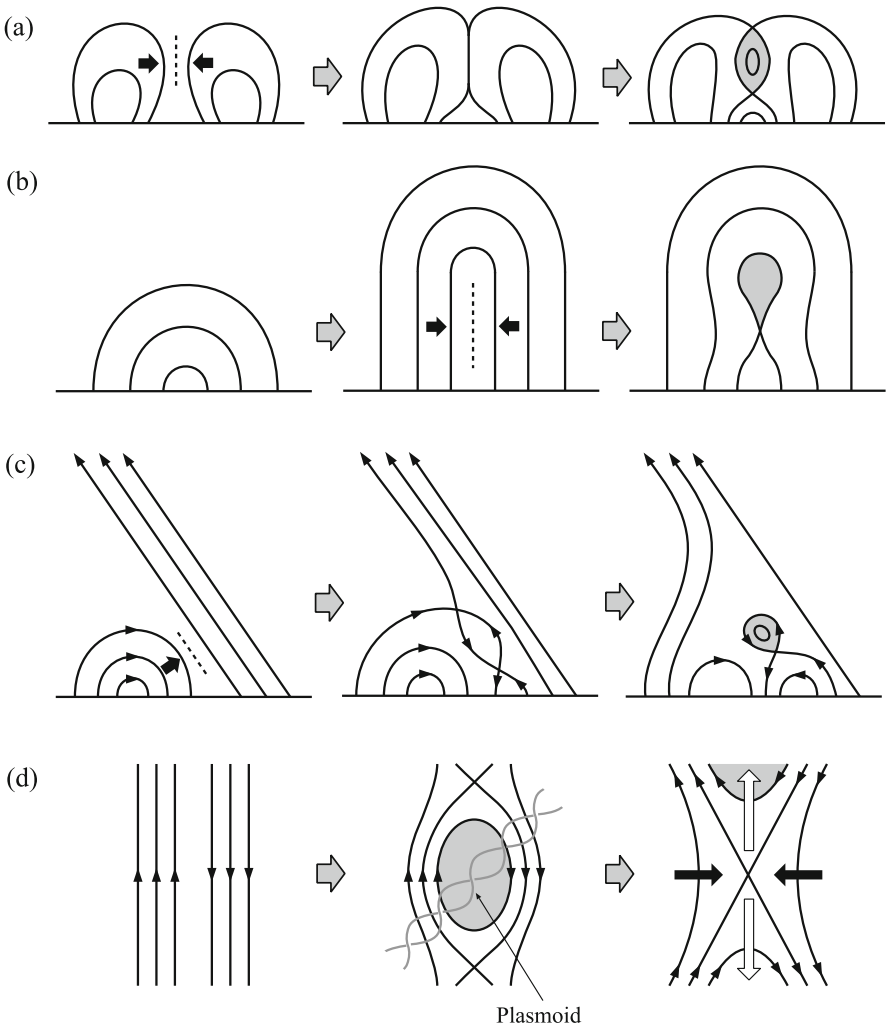

Fig. 10.5 Schematic diagram of the plasmoid-induced reconnection model. The *solid lines* indicate magnetic field lines. Panels (**a**)–(**c**) show the process creating the plasmoid in the antiparallel magnetic field by the magnetic reconnection in some typical magnetic field configurations. Panel (**d**) shows how the plasmoid in the current sheet inhibits the reconnection, and how reconnection can occur, after the ejection of the plasmoid (Nishida et al. 2009)

It should be noted that a plasmoid can be formed in any current sheet (Fig. 10.5) if the current sheet length is longer than the certain critical length scale. The critical length scale of the plasmoid instability comes from the physics of tearing mode instability (Furth et al. 1963).

During the initial stages of plasmoid formation, the plasmoid stays in the current sheet and during this stage, the plasmoid reduces the speed of reconnection

significantly by inhibiting the reconnection inflow towards the reconnection region. Only when the plasmoid ejects out from the current sheet, a substantial amount of magnetic flux can come towards the reconnection region and trigger a magnetic reconnection. This facilitates the ejection of the plasmoid via strong reconnection outflow (reconnection jet), further that in turn enables new magnetic flux to continuously enter the current sheet. The positive feedback between plasmoid ejection and reconnection inflow is established and fast reconnection continues, and eventually a plasmoid continues to eject from the current sheet with the Alfvén speed.

The 2D MHD numerical simulations (Magara et al. 1997; Choe and Cheng 2000; Tanuma et al. 2001) showed such dynamics very well. Figure 10.4b shows a height-time plot from a two-dimensional MHD simulation (Magara et al. 1997), in which magnetic reconnection produces an ejecting magnetic island (two-dimensional counterpart of a plasmoid). The time variation of the electric field is also plotted in the height-time plot. It is found that the electric field, that is also a measure of reconnection inflow and reconnection rate, becomes large when the magnetic island (plasmoid) is accelerated.

When comparing the MHD simulation and observations, it is assumed that the time variation of electric field in the reconnection region is closely related to the time variation of hard X-ray emissions because the electric field can accelerate particles which contribute to producing hard X-ray emissions. The comparison suggests that the plasmoid ejection drives a fast magnetic reconnection. More detailed investigations of plasmoid ejection are given in Choe and Cheng (2000), where multiple ejection of plasmoids and associated HXR bursts are discussed.

Shibata and Tanuma (2001) (Fig. 10.4c) developed a simple analytical model for the velocity of an ejecting plasmoid by assuming (1) mass conservation between inflow and outflow $V_p W_p = V_{inflow} L_p$, and (2) the plasmoid is accelerated by the momentum added by the reconnection outflow $\rho_p L_p W_p dV_p/dt = \rho_0 V_{inflow} L_p V_A$, where V_p is the plasmoid velocity, W_p the plasmoid width, L_p the plasmoid length, V_{inflow} the inflow velocity, V_A the Alfven velocity, ρ_p the plasmoid density, ρ_0 the density of ambient plasma. From these simple assumptions, they obtained the plasmoid velocity.

$$V_p = \frac{V_A \exp(\omega t)}{\exp(\omega t) - 1 + V_A/V_0}. \tag{10.3}$$

In Eq. (10.3), ω represents the velocity growth rate of a plasmoid, defined as

$$\omega = \frac{\rho_0 V_A}{\rho_p L}. \tag{10.4}$$

The plasmoid velocity V_p, its acceleration ($a_p = dV_p/dt$), inflow velocity V_{inflow}, and the height of the plasmoid obtained from the analytical model (Shibata and Tanuma 2001) are plotted in Fig. 10.4c. It is interesting to note that the acceleration and the inflow velocity (or reconnection rate) derived from this simple analytical

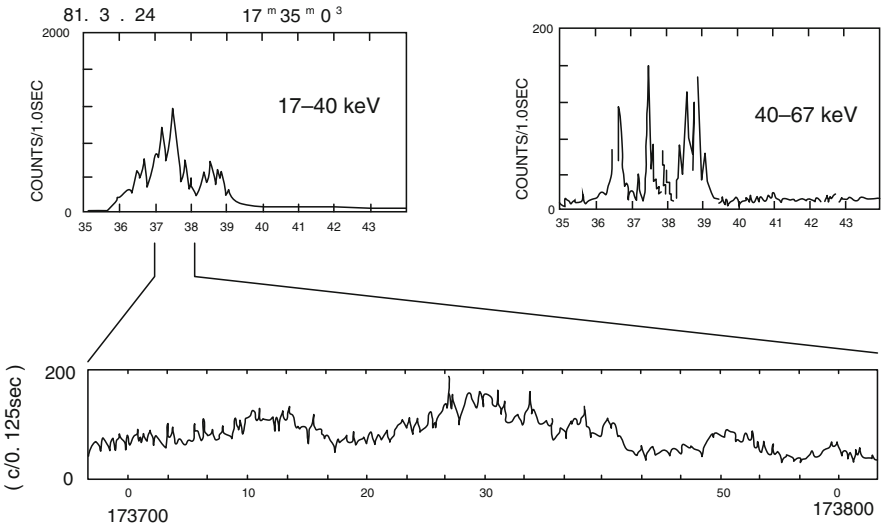

Fig. 10.6 Fractal-like time variability of hard X-ray emission from a flare (from Ohki et al. 1991)

model agree well with the observations (Qiu et al. 2004, see Fig. 10.4d) as well as the numerical simulation results (Cheng et al. 2003).

A detailed relation between the plasmoid velocity and the reconnection rate has been investigated by performing a series of numerical experiments (Nishida et al. 2009). An extension to 3D has also been developed by Nishida et al. (2013), and it was eventually revealed that the formation of multiple flux ropes (helically twisted field lines) in a reconnecting current sheet plays an important role in enhancing the reconnection rate. These experiments show that the reconnection rate (inflow velocity) becomes larger when the plasmoid is accelerated further by 3D effect (e.g., the kink instability) compared with 2D, whereas if the plasmoid velocity is decelerated, the reconnection rate becomes smaller. When the reconnection is inhibited, the plasmoid motion (or acceleration) is stopped (Fig. 10.5d).

10.4.2 Plasmoid Instability and Fractal Reconnection

By performing 2D MHD simulation of the magnetic reconnection on the current sheet triggered by a shock wave, Tanuma et al. (2001) found that (1) The reconnection does not start immediately after the passage of the shock wave across the current sheet. Instead, the current sheet slowly change the shape as a result of the tearing instability and becomes very thin in a fully nonlinear stage. (2) The current-sheet thinning is saturated when the sheet thickness becomes comparable to that of the Sweet-Parker sheet. Then, Sweet-Parker reconnection starts, and the

current-sheet length increases. (3) A secondary tearing instability occurs in the thin Sweet-Parker current sheet. (4) As a result of the secondary tearing instability, further current-sheet thinning occurs. (5) If the sheet becomes sufficiently thin to produce anomalous resistivity, a Petschek reconnection starts.

On the basis of the nonlinear MHD simulations, Shibata and Tanuma (2001) proposed that the current sheet eventually has a *fractal structure* consisting of many magnetic islands (plasmoids) with different sizes.

Once the current sheet has a fractal structure, it becomes possible to connect macro scale dynamics (with flare size of 10^9 cm) and micro plasma scale dynamics (with ion Larmor radius or ion skin depth of 10^2 cm). Then collisionless reconnection or anomalous resistivity can be applied to flare reconnection problems (see e.g., Cassak et al. 2005; Daughton et al. 2009, for the role of collisionless effects in reconnection).

The secondary instability of the Sweet-Parker sheet has been discussed by Biskamp (1993) and Biskamp (2000). According to Biskamp (2000), the condition of the secondary instability is that the tearing time scale ($t_{tearing} \sim 2(t_A t_d)^{1/2} \sim 2t_A {S_*}^{1/2}$, where $S_* = t_d/t_A = \delta V_A/\eta$ is the Lundquist number with respect to the sheet thickness δ) is shorter than the flow time scale ($t_{flow} \sim 0.5L/V_A \sim 0.5t_d$),[1] where $t_A = \delta/V_A$ is the Alfven time (across the sheet), $t_d = \delta^2/\eta$ is the diffusion time, δ is the thickness of the Sweet-Parker sheet, L is the length of the sheet, η is the magnetic diffusivity. From these relations, we find that the condition of the secondary instability is

$$t_d^{-1} < 0.25(t_d t_A)^{-1/2} \tag{10.5}$$

or $(t_d/t_A) > 16$. Using the global Lundquist number $S = LV_A/\eta$, we find $t_d/t_A = (\delta/L)(LV_A/\eta) = (\delta/L)S = S^{1/2}$ for the Sweet Parker sheet ($\delta/L = S^{-1/2}$). Then the above condition can be written $L/\delta > 16$. For more accurate calculation for large Lundquist number, this condition becomes $L/\delta > 10^2$ (or $S > 10^4$) (Biskamp 2000). This condition roughly explains the result of Tanuma et al. (2001).

Shibata and Tanuma (2001) calculated how the current sheet becomes thinner as a result of the secondary tearing instability (see Fig. 10.7a) whose condition is given by

$$\frac{\delta_n}{L} \leq A\left(\frac{\delta_{n-1}}{L}\right)^{5/6} \tag{10.6}$$

where $A = 6^{2/3}S^{-1/6}$ and $S = LV_A/\eta$.[2]

[1] In the Sweet-Parker sheet, we find $L/V_A = \delta/V_{inflow} = \delta^2/\eta = t_d$.

[2] Here Shibata and Tanuma (2001) assumed that the condition of the secondary instability was $(t_A t_d)^{1/2} < L/V_A$. If we use more rigorous condition $(t_A t_d)^{1/2} < aL/V_A$, where $a \simeq 4$ (see above), we find $A = (ab)^{2/3}S^{-1/6}$. Note that Shibata and Tanuma (2001) assumed $a = 1$ and $b = 6$. If we use $a = 4, b = 2\pi = 6.28$, then $A \simeq 0.05$ for $R_m = 10^{13}$. In this case, we find $n = 12$ for

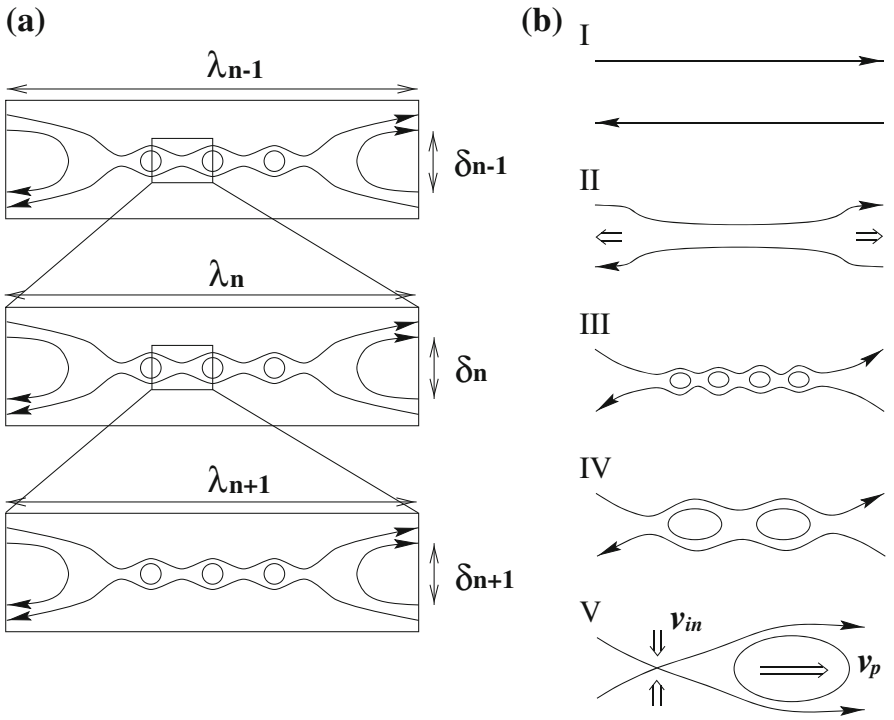

Fig. 10.7 (**a**) Schematic view of the fractal reconnection. (**b**) A scenario for fast reconnection. I: the initial current sheet. II: the current sheet thinning in the nonlinear stage of the tearing instability or global resistive MHD instability. The current sheet thinning stops when the sheet evolves to the Sweet-Parker sheet. III: the secondary tearing in the Sweet-Parker sheet. The current sheet becomes fractal because of further secondary tearing as shown in (**a**). IV: the magnetic islands coalesce with each other to form bigger magnetic islands. The coalescence itself proceeds in a fractal manner. During the III and IV phases, a microscopic plasma scale (ion Larmor radius or ion inertial length) is reached, so that the fast reconnection becomes possible at small scales, V: the greatest energy release occurs when the largest plasmoid (magnetic island or flux rope) is ejected. The maximum inflow speed (V_{inflow} = reconnection rate) is determined by the velocity of the plasmoid (V_p). Hence this reconnection is termed as *plasmoid-induced-reconnection* (from Shibata and Tanuma 2001)

From this, they obtain the solution

$$\frac{\delta_n}{L} \leq A^{6(1-x)} \left(\frac{\delta_0}{L}\right)^x \tag{10.7}$$

where $x = (5/6)^n$.

the condition that the sheet thickness becomes less than the ion Larmor radius ($\sim$ 100 cm), i.e., $\delta_n/L < 10^{-7}$ and the initial sheet thickness and length are 10^8 and 10^9 cm.

Note that Shibata and Tanuma (2001) did not assume that the sheet is exactly the same as the Sweet-Parker sheet, since in actual solar condition the Lundquist number is so large that we cannot have the Sweet Parker sheet as the initial condition. Instead they assumed that the sheet become unstable once the instability condition

$$\text{tearing time } (t_d t_A)^{1/2} = (\delta_n{}^3/(\eta V_A))^{1/2} < \text{flow traveling time } \lambda_n/V_A$$

is satisfied, where λ_n is the most unstable wavelength and is given by $\lambda_n \simeq 6\delta_n S_{*,n}{}^{1/4}$ where $S_* = \delta_n V_A/\eta$.

For actual solar coronal condition, it is found $n \geq 6$ to reach microscopic scale such as ion Larmor radius or ion skin depth $\delta_6/L < L_{ion-Larmor}/L \simeq 10^{-7}$.

Shibata and Tanuma (2001) presented a scenario for fast reconnection in the solar corona as shown in Fig. 10.7b. That is, the current sheet becomes a fractal sheet consisting of many plasmoids with different sizes. The plasmoids tend to coalesce with each other (Tajima et al. 1987) to form bigger plasmoids. When the biggest island (i.e., monster plasmoid) is ejected out of the sheet, we have the most violent energy release which may correspond to the impulsive phase of flares.

Solar observations show the fractal-like time variability of solar flare emission, especially in microwaves (Karlicky et al. 1996; Aschwanden 2002), and hard X-rays (Ohki et al. 1991; see Fig. 10.6). The above idea of the fractal reconnection seems to explain the observations very well, since the observations suggest fragmented energy release processes in the fractal (turbulent) current sheet. For example, Karlicky et al. (1996) showed that the temporal power spectrum analysis of the narrow band of dm-spikes of a flare show power-law spectrum, suggesting Kolmogorov spectra after transformation of the frequency scales to the distance scales.

More recently, Singh et al. (2015) extended the fractal reconnection theory of Shibata and Tanuma to that in a partially ionized plasma in the solar chromosphere, and basically obtained the similar result.

It is interesting to note that Tajima and Shibata (1997) found the growth rate of the secondary tearing instability of the Sweet-Parker sheet has positive dependence on the Lundquist number $\omega \propto S^{1/4}$ and the most unstable wavelength decreases with increasing with S with the scaling $\lambda \propto S^{-3/8}$.

The tearing mode instability in Sweet-Parker current sheet is studied by Loureiro et al. (2007), and the tearing instability of the Sweet-Parker sheet is now addressed as *plasmoid instability*. Numerical simulations of the nonlinear evolution of the plasmoid instability has been developed significantly in recent 10 years, and will be discussed in detail in Sect. 10.4.3.

10.4.3 Recent Development of Numerical Simulations of Plasmoid-Dominated Reconnection

The nonlinear evolution of the plasmoid-dominated reconnection has been extensively investigated in recent years using MHD simulations. Samtaney et al. (2009) performed 2D MHD simulations of the formation of plasmoid chains in a very high-Lundquist number ($10^4 < S < 10^8$), and confirmed the scaling of the plasmoid number (or plasmoid distribution) in the linear regime ($\sim S^{3/8}$) predicted by Tajima and Shibata (1997) and Loureiro et al. (2007). Cassak et al. (2009), Bhattacharjee et al. (2009) and Huang and Bhattacharjee (2010) found that once the plasmoid instability sets in, the reconnection rate becomes nearly independent of the Lundquist number (Figs. 10.8 and 10.9). An energy cascade to smaller scales during a tearing process is clearly presented by Bárta et al. (2011). Since other studies have also confirmed this result (e.g. Loureiro et al. 2012), it now seems to be a robust result. However, all the studies are restricted to 2D and to S of $\sim 10^8$. It is not obvious that the 2D results will remain unchanged for 3D astrophysical situations with a high-Lundquist number (e.g. $S \sim 10^{13}$ for solar applications).

The plasmoid distribution in the non-linear regime, which is essential for the understanding the current sheet thinning process, has been discussed by several authors. By considering a stochastic generation, growth, coalescence, and ejections of plasmoids, Uzdensky et al. (2010) predicted the dependence of the plasmoid distribution function f on flux Φ and plasmoid width w_x: $f(\Phi) \propto \Phi^{-2}$ and $f(w_x) \propto w_x^{-2}$ (a similar approach was independently done by Fermo et al. 2010). Loureiro et al. (2012) performed 2D MHD simulations to investigate the plasmoid distribution, and obtained double-power-law-like distributions (Fig. 10.10). It was argued that the distribution with steeper power law at larger flux and width (large plasmoids) seems to scale as the relations by Uzdensky et al. (2010). Huang and Bhattacharjee (2012) also studied the distribution, and found that the relative speed of plasmoids should be considered to understand the evolution of plasmoids. Considering this, a simple governing equation was constructed for the distribution function that gives the scaling $f(\Phi) \sim \Phi^{-1}$. The power law distribution has been confirmed by the following study by Huang and Bhattacharjee (2013). We note that the scaling $f(\Phi) \sim \Phi^{-1}$ can also be seen in the case of Loureiro et al. (2012). Observational tests for the scaling have just started (Guo et al. 2014).

Considering the plasmoid-induced-reconnection scenario, emergence and ejections of large plasmoids from the current sheet play an important role in enhancing the reconnection rate and carrying a large amount of magnetic flux towards the reconnection regions. Emergence of abnormally large (with the size of ~0.1 times the system size) "monster" plasmoids during a stochastic plasmoid-dominated reconnection was predicted by Uzdensky et al. (2010). Loureiro et al. (2012) studied the distributions of the magnetic flux of plasmoids and of the half-width of plasmoids, and found that monster plasmoids occasionally occur.

Thanks to the modern computational resources, it has become possible to investigate the plasmoid-dominated reconnection in 3D. The first 3D simulation

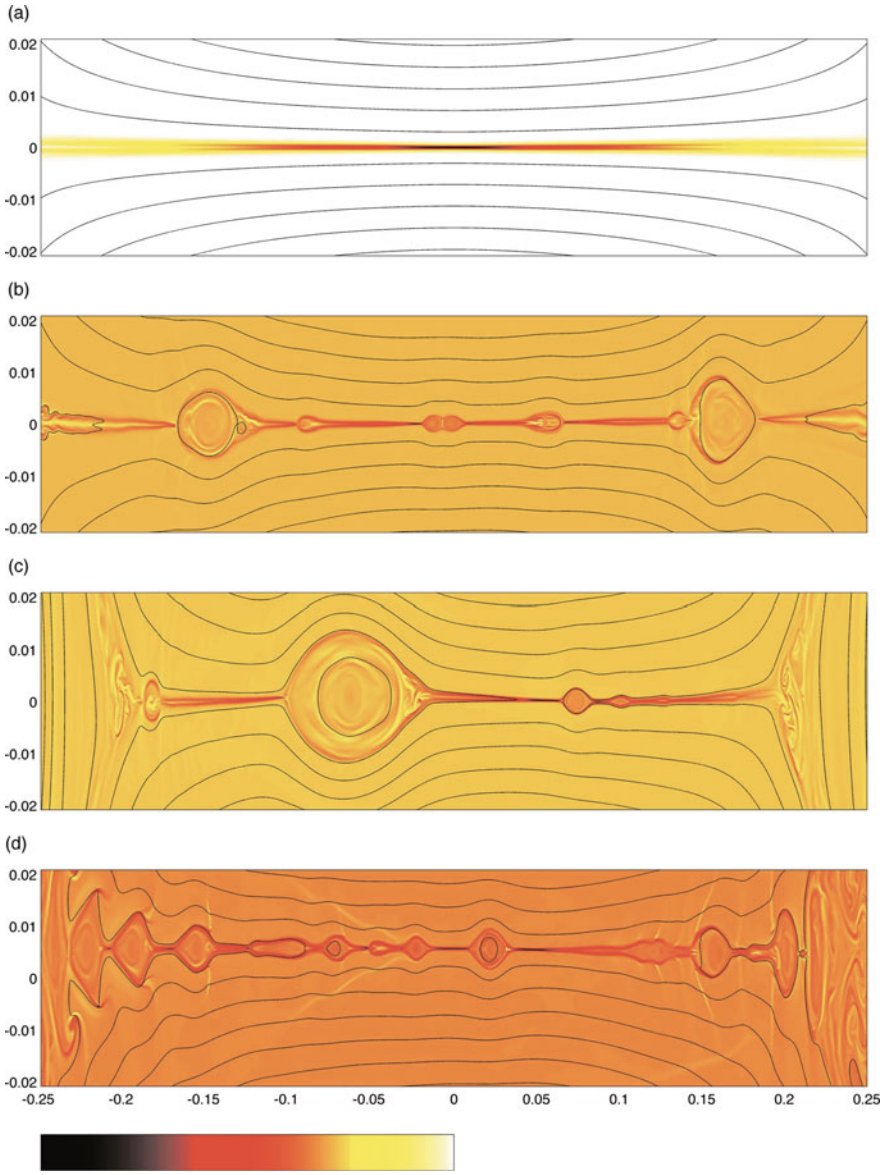

Fig. 10.8 Time-sequence of the nonlinear evolution of the current density J_y of a Sweet-Parker current sheet in a large system of Lundquist number $S = 6.28 \times 10^5$. The *black lines* represent surfaces of constant ψ (Bhattacharjee et al. 2009). (**a**) $S_L = 6.28e5$, $t = 3.00$, $J_y[-4.54e + 03, 8.06e + 00]$. (**b**) $S_L = 6.28e5$, $t = 6.00$, $J_y[-1.20e + 04, 4.94e + 03]$. (**c**) $S_L = 6.28e5$, $t = 9.10$, $J_y[-9.59e + 03, 3.71e + 03]$. (**d**) $S_L = 6.28e5$, $t = 12.00$, $J_y[-9.11e + 03, 4.70e + 03]$

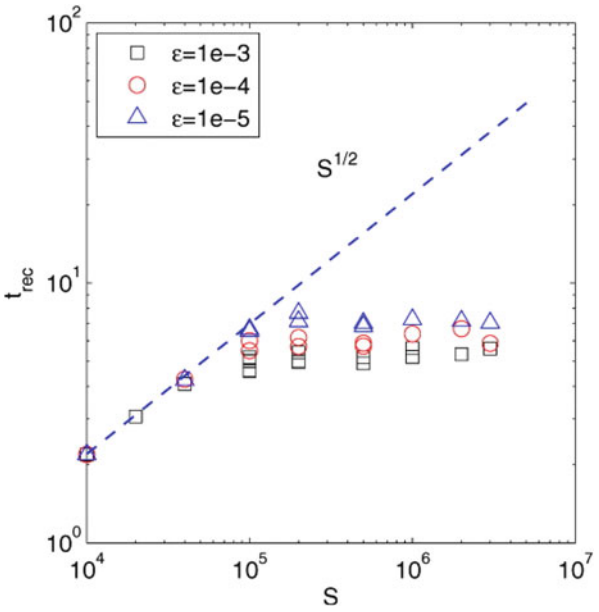

Fig. 10.9 The reconnection time $t_{\rm rec}$ for various S and ϵ. The *dashed line* is the Sweet-Parker scaling (Huang and Bhattacharjee 2010)

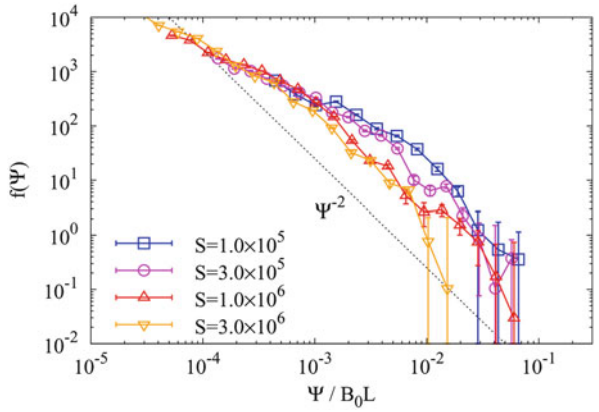

Fig. 10.10 Plasmoid distribution functions from direct numerical simulations (Loureiro et al. 2012)

was presented by Linton and Priest (2002), in which a pair of perpendicular, untwisted magnetic flux tubes collide to form a current sheet. Although the spatial resolution was not enough to discuss the evolution of the reconnection rate, they found the formation and coalescence of flux ropes (corresponding to plasmoids in 3D). Wyper and Pontin (2014) for the first time studied non-linear plasmoid instability of 3D null point current sheets. Comparing a 2D plasmoid-dominated reconnection scenario, they found that (1) 3D current sheets are subject to an instability analogous to the plasmoid instability, but are marginally more stable than equivalent 2D neutral sheets, (2) an efficient 3D flux mixing leads to a substantial

increase in the reconnection rate, and (3) the interaction of flux ropes appear to be driven primarily by kink instability which is a 3D instability.

The evolution of plasmoid chains in a relativistic Poynting-dominated plasma ($S = 10^3 - 10^5$) was investigated by Takamoto (2013), where the reconnection rate becomes nearly independent of the Lundquist number after the generation of plasmoids, similar to non-relativistic cases. This study indicates that the plasmoid formation plays an important role in fast reconnection even in relativistic plasma.

The formation of plasmoids could be a key to understand the origin of energetic nonthermal particles. Drake et al. (2006) have pointed out that the contracting plasmoids (magnetic islands) can accelerate electrons during reconnection because of Fermi-type processes that occur for electrons trapped in the contracting magnetic islands. Nishizuka and Shibata (2013) proposed when plasmoids pass through the fast mode termination shock in the reconnection region, particles trapped in plasmoids can be accelerated via Fermi-type process. Namely, particles in a plasmoid are reflected upstream the shock front by magnetic mirror effect. As the plasmoid passes through the shock front, the reflection distance becomes shorter and shorter driving Fermi acceleration, until it becomes particle's Larmor radius (Fig. 10.11). The fractal distribution of plasmoids may also have a role in naturally explaining the power-law spectrum in nonthermal emissions.

Recently, much attention has been paid to plasmoid-dominated reconnection in a partially ionized plasma. Since the electron-ion collisional timescale is much shorter than most of the timescales of interest, neutral-ion two fluid effects have been extensively concerned. Ni et al. (2015) performed 2D MHD simulations with

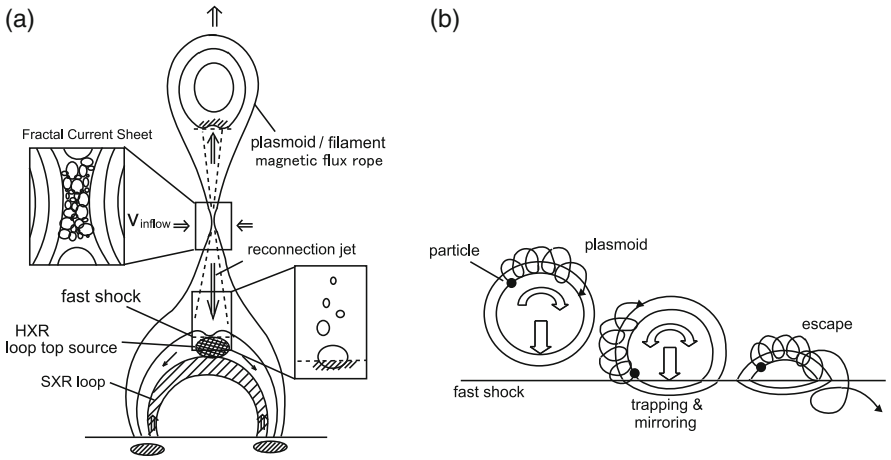

Fig. 10.11 Overall picture of a new particle acceleration mechanism in plasmoid-shock interaction. **(a)** Multiple plasmoids of various scales are intermittently ejected upward and downward out of a turbulent current sheet and collide with the termination shocks of reconnection outflows, i.e., fast shocks above and below a reconnection X point, where particles are effectively accelerated via shock acceleration process trapped in a plasmoid. **(b)** Scenario of shock acceleration at the fast shock trapped in a plasmoid

the effects of the ambipolar diffusion and radiative cooling to study the nature of reconnection in the solar chromosphere, where the ambipolar diffusion is a resistivity diffusion introduced by ion-neutral collisions (equivalently, a Pedersen resistivity). They investigated the role of both effects on the plasmoid instability changes in the presence of a guide field. They found that a fast reconnection takes place as a result of the plasmoid formation for zero as well as for strong guide field. When the current sheet becomes thin, the ion-neutral collisional timescale can be comparable to or shorter than a dynamical timescale, resulting in the decoupling of the neutral and ion fluids. In addition, ionization, recombination, and charge exchange processes will change the ionization degree depending on the local temperature and density, which will affect the removal processes of the neutrals and ions from the current sheet. Some multi-fluid treatments with the effects of ionization, recombination, and charge exchange are required to study the two fluid and non-equilibria partial ionization effects on the reconnection structure. Leake et al. (2013) performed two-fluid MHD simulations with the non-equilibrium partial ionization effects, and found a fast reconnection rate independent of the Lundquist number. In addition, it was found that the non-equilibrium partial ionization effects lead to the onset of the nonlinear secondary tearing instability at comparatively lower values of the Lundquist number than that has been reported in the case of fully ionized plasmas.

Because shocks are crucial for the energy conversion process during the reconnection, the shock structure in and around plasmoids has been studied by many authors. It has been argued for a long time that slow shocks emanating from reconnection points (so-called Petschek-type slow shocks) cannot be established with a uniform resistivity. Tanuma et al. (2001) pointed out for the first time that Petschek-like slow shocks can emanate from an X-point in a tearing current sheet. However, due to the formulation of their resistivity model, it was not clear what is the origin of the formation of slow shocks: due to the plasmoid nature, or due to the onset of the anomalous resistivity in their simulations. Recently, Mei et al. (2012) studied the evolution of the current sheet formed below the erupting CME using a uniform resistivity. They found that plasmoids are actually accompanied by Petschek-like slow shocks. Although it was not explicitly mentioned, the structure of the simulated current sheet seems to be a combination of plasmoid-dominated reconnection and global Petschek-like slow shocks. This motivates us to present a new view of flare reconnection shown in Fig. 10.12. For the understanding of the shock structure of flaring regions, further studies are necessary. As for a variety of shock and discontinuity structure in and around a plasmoid, the reader is also referred to Zenitani and Miyoshi (2011) and Zenitani (2015).

It would be worth noting that a fast reconnection can be obtained even in the MHD regimes if the Lundquist number is high enough to trigger the plasmoid instability. But it is the microphysics that may become important during the reconnection process. The recurrent plasmoid formation and ejection from the current sheet at multi-scales can lead to the formation of thin current sheets with the width of a microscopic scale like the ion skin depth or ion Larmor radius, and therefore some microphysics (e.g. anomalous resistivity) can set in at some

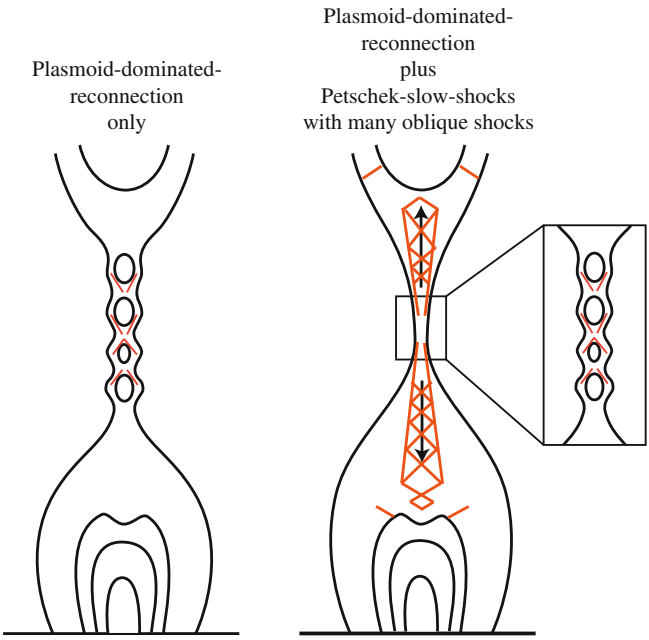

Fig. 10.12 Plasmoid-dominated current sheet vs plasmoid+Petschek slow shock

time. At this stage, one would expect that microphysics will play a crucial role in determining the reconnection process: from *collisional* physics to *collisionless* physics. For more information on the various regimes that lie between collisional and collisionless processes, readers are referred to the discussion of Ji and Daughton (2011) (Fig. 10.13). The link between micro- and macro-scales should be explored in more detail.

10.4.4 Observational Evidence of Plasmoid-Dominated Reconnection and Fractal Reconnection

Asai et al. (2004) reported that there are multiple downflow (supra arcade downflow; McKenzie and Hudson 1999; McKenzie 2013) which are associated with hard X-ray impulsive emissions. Although the origin of supra arcade downflow is still not yet understood well, the physical relation between downflow and hard X-ray emission may be similar to the relation between plasmoid ejections and hard X-ray emissions (see Fig. 10.4a).

Using the data on post-CME current sheets observed by SOHO/UVCS, Bemporad (2008) examined the evolution of turbulence by interpreting the nonthermal broadening of the [Fe xviii] line profiles, and found that the turbulent speeds decay from 60 to 30 km/s during 2 days after CME ejection.

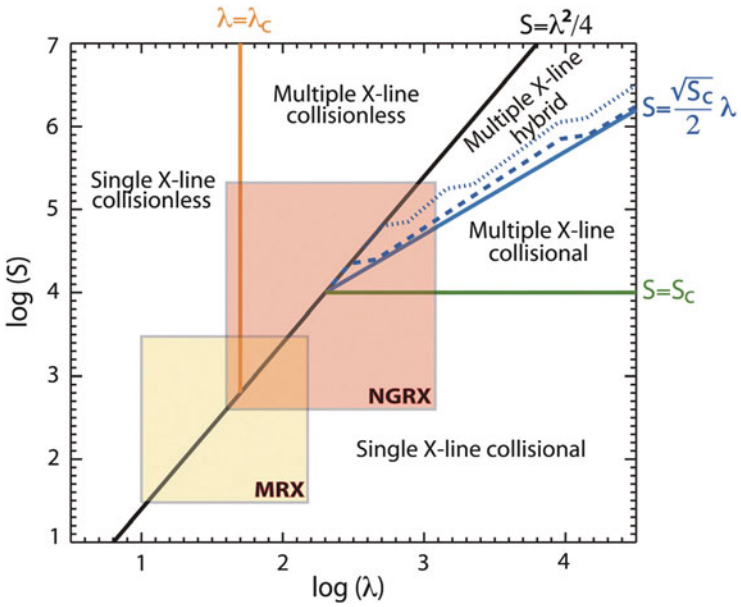

Fig. 10.13 A phase diagram for magnetic reconnection in two dimensions. λ and S are the effective plasma size normalized by the ion skin depth and the Lundquist number of the system (from Ji and Daughton 2011)

Nishizuka et al. (2009) examined the time variation of the intensity of the flare kernels and found that intermittent radio/HXR bursts, whose peak intensity, duration, and time interval were well described by power-law distribution functions. This result may be evidence either of "self-organized criticality" in avalanching behavior in a single flare event, or fractal current sheets in the impulsive reconnection region.

By analyzing the soft X-ray images and hard X-ray emission of a flare taken with Yohkoh satellite, Nishizuka et al. (2010) found multiple plasmoid ejections with velocities of 250–1500 km/s. They also found that each plasmoid ejection is associated with an impulsive burst of hard X-ray emissions which are a result of high energy electron acceleration and are signature of main energy release due to the fast reconnection.

Singh et al. (2012) analyzed chromospheric anemone jets (Shibata et al. 2007) observed by Hinode/SOT, and found that all the jets they analyzed show intermittent and recurrent ejections of the jet and the corresponding brightening of the loop. Such behavior is quite similar to plasmoid ejections from large flares (e.g., Nishizuka et al. 2010). Note that chromospheric jets are considered to be a result of *collisional* magnetic reconnection in a weakly ionized plasma (Singh et al. 2011). Nevertheless, the time-dependent behavior of chromospheric jets is quite similar to that of coronal reconnection (*collisionless* reconnection), suggesting the common macroscale dynamics, i.e., plasmoid-induced reconnection in a fractal current sheet.

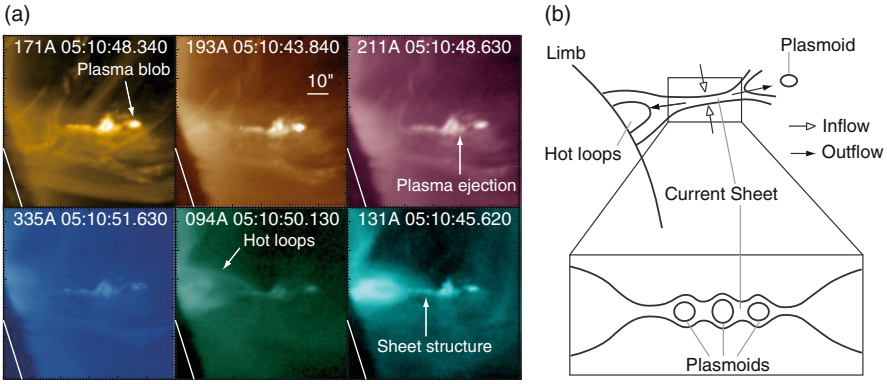

Fig. 10.14 (**a**) Close-up images of the reconnection site of a solar flare in six different wavelengths (171, 193, 211, 335, 94, and 131 A) of AIA at the time when the current sheet, the plasma blob, and the hot post flare loops are observed. *White solid lines* indicate the solar limb. (**b**) Schematic diagram of the flaring region. *Black solid lines* indicate the magnetic field. *Top*: the global configuration of the magnetic field. *Bottom*: a close-up image of the current sheet region (from Takasao et al. 2012)

Takasao et al. (2012) observed both reconnection inflow and outflow simultaneously using SDO/AIA EUV images of a flare and derived the nondimensional reconnection rate 0.055–0.2. They also found that during the rise phase of the flare, some plasma blobs appeared in the sheet structure above the hot flare loops, and they were ejected bidirectionally along the sheet (see Fig. 10.14). This is the first imaging observations of the plasmoid-dominated current sheet in a solar flare.

More recently, Nishizuka et al. (2015) examined observational data of slowly drifting pulsating structures (DPSs) in the 0.8–4.5 GHz frequency range taken with the radio spectrographs at Ondrejov Observatory. It is interesting to see that the DPSs are signatures of plasmoids, and from the observations of DPSs the plasmoid velocity and the reconnection rate were derived. The reconnection rate shows a good, positive correlation with the plasmoid velocity. Nishizuka et al. (2015) also confirmed that some of the DPS events show plasmoid counterparts in SDO/AIA images.

10.5 Stellar Flares

10.5.1 Unified Model of Solar and Stellar Flares: Emission Measure—Temperature Diagram

The stellar flares show X-ray light curves similar to those of solar flares. The time scale and typical properties derived from soft X-rays also show some similarities to solar flares, though dynamic range of stellar flare parameters are much wider than

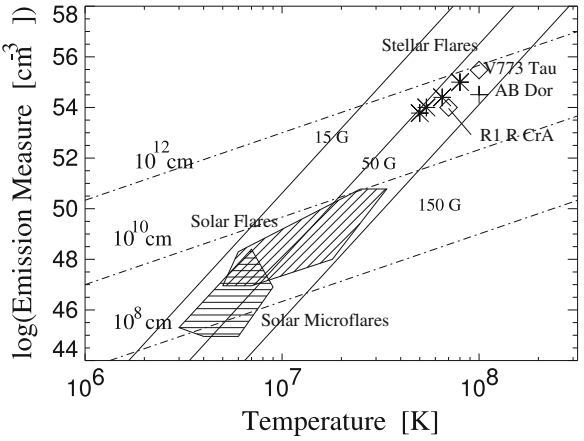

Fig. 10.15 The EM (emission measure)—T (temperature) diagram for solar and stellar flares and corona (Shibata and Yokoyama 2002). *Hatched area* shows solar flares (*oblique hatch*) and solar microflares (*horizontal hatch*), whereas other *symbols* denote stellar/protostellar flares. *Solid lines* correspond to magnetic field strength = constant, and *dash-dotted lines* correspond to flare size = constant

those of solar flares. Recent X-ray astronomy satellites, such as ASCA, revealed that flares are frequently occurring in young stars, even in class I protostars (Koyama et al. 1996). One remarkable characteristics of these protostellar flares is that the temperature is generally high, 50–100 MK, much hotter than the temperature of solar flares, 10–20 MK. The total energy estimated is also huge, and amounts to 10^{36-37} erg, much greater than that of solar flares, 10^{29-32} erg.

Can we explain the protostellar flares by magnetic reconnection models? The answer is, of course, yes. A part of the reason of this answer comes from our finding of empirical correlation between emission measure and temperature of solar, stellar, and protostellar flares. Figure 10.15 shows the observed relation between emission measure and temperature of solar flares, microflares, stellar flares (Feldman et al. 1995), and young stellar objects (YSO) flares (Shibata and Yokoyama 1999). It is remarkable that these data show the same tendency in a very wide dynamic range. What does this relation mean?

Our answer is as follows (Shibata and Yokoyama 1999, 2002). Yokoyama and Shibata (1998); Yokoyama et al. (2001) performed the self-consistent MHD simulation of reconnection with heat conduction and evaporation for the first time. From this simulation, they discovered a simple scaling relation for the flare temperature:

$$T \simeq 10^7 \left(\frac{B}{50\mathrm{G}}\right)^{6/7} \left(\frac{L}{10^9\mathrm{cm}}\right)^{2/7} \left(\frac{n_0}{10^9\mathrm{cm}^{-3}}\right)^{-1/7} \mathrm{K}. \tag{10.8}$$

This is simply a result of energy balance between reconnection heating ($B^2 V_A/4\pi$) and conduction cooling ($\kappa T^{7/2}/L$) (since the radiative cooling time is much longer than the conduction time) . With this equation and definition of emission measure ($EM = n^2 L^3$), and pressure equilibrium ($p = 2nkT = B^2/8\pi$), we finally obtain the following relation:

$$\mathrm{EM} \simeq 10^{48} \left(\frac{B}{50\mathrm{G}}\right)^{-5} \left(\frac{T}{10^7\mathrm{K}}\right)^{17/2} \left(\frac{n_0}{10^9\mathrm{cm}^{-3}}\right)^{3/2} \mathrm{cm}^{-3}. \tag{10.9}$$

We plotted this relation for constant field strength (B = 15, 50, 150 G) in Fig. 10.15. It is remarkable that these B = constant lines are consistent with the empirical correlation. In other words, the comparison between observation and our theory tells that the magnetic field strength of solar and stellar flares are not so different, of order of 50–150 G. In the solar case, this value agrees well with the observations (average field strength of active region). In the case of stars, we have only limited set of observations, but these observations show a kG field in the photosphere, suggesting a 100 G average field strength in the stellar corona, consistent with our theoretical prediction.

We can also plot constant loop length lines in the diagram in Fig. 10.15.

$$\mathrm{EM} \simeq 10^{48}\left(\frac{L}{10^9\mathrm{cm}}\right)^{5/3}\left(\frac{T}{10^7\mathrm{K}}\right)^{8/3}\left(\frac{n_0}{10^9\mathrm{cm}^{-3}}\right)^{2/3}\mathrm{cm}^{-3}. \tag{10.10}$$

The loop length for microflares and flares is 10^8–10^{10} cm, consistent with the observed sizes of microflares and flares, whereas the size of stellar flare loop is huge, even larger than 10^{11} cm, comparable to or even larger than stellar radius. Because of this large size, the total energy of protostellar flares become huge and their temperature becomes hotter than those of solar flares [see Eq. (10.1)]. Since it is not possible to resolve the stellar flares, the large sizes of stellar flares are simply theoretical prediction at present.

Shibata and Yokoyama (2002) noted that the EM-T diagram is similar to the Hertzsprung-Russell (HR) diagram, and examined basic properties of the EM-T diagram. They found the existence of coronal branch, forbidden regions, and also showed that flare evolution track can be plotted on the EM-T diagram, similarly to stellar evolution track in HR diagram.

10.5.2 Superflares on Solar Type Stars

It is well known that the first solar flare observed and recorded by human beings (Carrington 1859) was the largest solar flare ever observed and its released energy was estimated to be of order of 10^{32} erg (Tsurutani et al. 2003). This "Carrington flare" generated the largest geomagnetic storm in recent 200 years, and caused some damage to the telegraph system (Loomis 1861) even in such a beginning phase of modern civilization based on electricity. Is it possible for the Sun to produce "superflares" that are much more energetic than the "Carrington flare"?

By analyzing existing previous astronomical data, Schaefer et al. (2000) discovered nine superflares with energy $10^{33} \sim 10^{38}$ erg in ordinary solar type stars (G type main sequence stars with slow rotation with velocity less than 10 km/s). It was argued that the cause of the superflares is the hot Jupiter orbiting near to these stars (Rubenstein and Schaefer 2000), and thus concluded that the Sun has never produced superflares, because the Sun does not have a hot Jupiter (Schaefer et al. 2000).

Maehara et al. (2012) analyzed the photometric data obtained by the Kepler space telescope (which was intended for detecting exoplanets using transit method), and found 365 superflares on 148 solar type stars. Figure 10.16 shows a typical example of a superflare observed by Kepler, which shows the spike-like increase (1.5 %) in stellar brightness for a short time (a few hours). It should be remembered that even one of the largest solar flares in recent 20 years (X18 class solar flare in 2003) showed only 0.03 % solar brightness increase for 5 to 10 min. The total energy of this superflare was estimated to be around 10^{35} erg, 1000 times larger than the largest solar flare (10^{32} erg).

It is also interesting to see in Fig. 10.16 that the stellar brightness itself shows significant time variation with amplitude of a few percent with characteristic time of 10–15 days. It is remarkable that almost all superflare stars show such a time variation of the stellar brightness. Maehara et al. (2012) interpreted that the stellar brightness variation may be caused by the rotation of a star with big starspots. Notsu et al. (2013b) developed this idea in detail using the model calculation of the brightness change of the rotating star with big starspots. If this interpretation is correct, we can indirectly measure the rotation period of stars and the size of star spot (or total magnetic flux assuming the magnetic flux density is the same as that of the sunspot, 1000–3000 G). Since a big spot can store huge amount of magnetic energy around it, it is reasonable that almost all superflare stars show stellar brightness change of the order of a few percent or more.

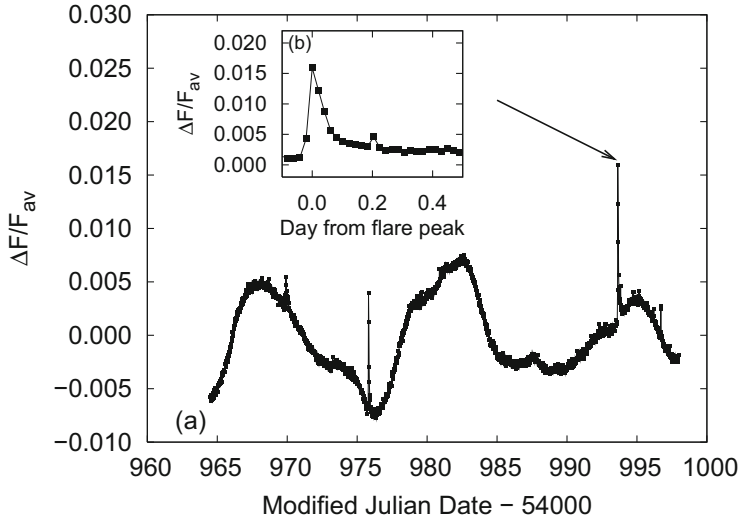

Fig. 10.16 A typical example of a superflare on a solar type star. **(a)** Light curve of superflares on the G-type main-sequence star KIC 9459362. **(b)** Enlarged light curve of a superflare observed at BJD2,454,993.63 (Maehara et al. 2012)

According to Shibata et al. (2013), the maximum energy of solar flares in a spot with magnetic flux density B and an area A has an upper limit determined by the total magnetic energy stored in a volume $A^{3/2}$ near the spot, i.e.,

$$E_{flare} \simeq fE_{mag} \simeq f\frac{B^2}{8\pi}A^{3/2} \simeq 7\times 10^{32}[\mathrm{erg}]\Big(\frac{f}{0.1}\Big)\Big(\frac{B}{10^3\mathrm{G}}\Big)^2\Big(\frac{A}{3\times 10^{19}\mathrm{cm}^2}\Big)^{3/2}$$
$$\simeq 7\times 10^{32}[\mathrm{erg}]\Big(\frac{f}{0.1}\Big)\Big(\frac{B}{10^3\mathrm{G}}\Big)^2\Big(\frac{A/2\pi {R_{sun}}^2}{0.001}\Big)^{3/2} \qquad (10.11)$$

where f is the fraction of magnetic energy that can be released as flare energy.

Figure 10.17 shows the empirical correlation between the solar flare energy (assuming that GOES X-ray flux is in proportion to flare energy) versus sunspot area. We see that the theoretical relation [upper limit is used in Eq. (10.11)] nicely explains observed upper limit of flare energy as a function of sunspot area. We also plotted the superflare data on Fig. 10.17. It is interesting to see that there exist many superflares above the theoretical upper limit. One possible solution of this

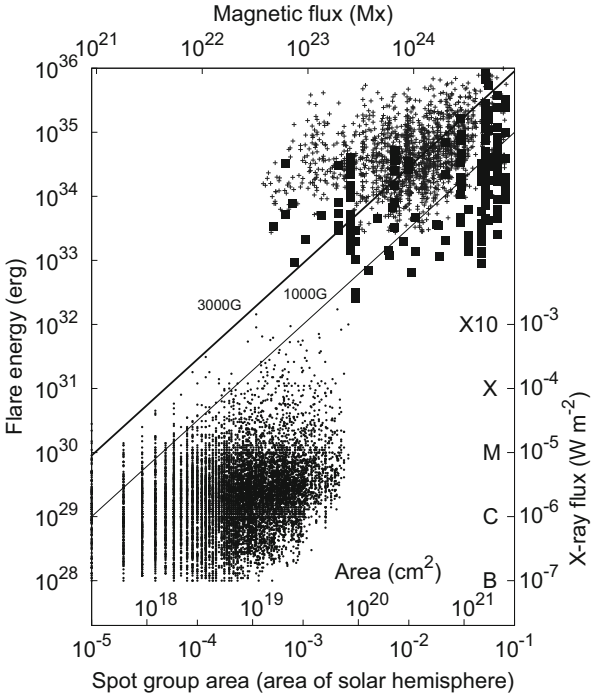

Fig. 10.17 Flare energy vs sunspot area (Maehara et al. 2015). *Thick* and *thin solid lines* in this figure represent Eq. (10.11) for f = 0.1, B = 3000 and 1000 G, respectively. *Filled squares* and *small crosses* show data of superflares on solar type stars, while *small dots* are solar flare data (Maehara et al. 2015)

apparent discrepancy is that these stars (above an upper limit) may be pole-on stars. Namely, if we observe stars from the pole, we tend to estimate smaller size of starspot, because the brightness change of stars (due to rotation) becomes small when viewing from rotating poles.

Later, Notsu et al. (2015), using spectroscopic observations of 34 superflare stars, confirmed the interpretation, in addition to the confirmation of the real rotation velocity of these 34 stars (see also Notsu et al. 2013a; Nogami et al. 2014).

Figure 10.17 shows that both solar and stellar flares are caused by the release of magnetic energy stored near spots. Figure 10.15 (EM-T diagram) along with Fig. 10.17 (energy vs magnetic flux diagram) makes us sure that in a statistical sense the stellar flares are actually caused by the magnetic reconnection.

Maehara et al. (2015) analyzed the short time cadence data (1 min) taken by the Kepler mission, and found that the duration of superflares scales with flare energy (E) as $t_{flare} \propto E^{0.39}$, which is similar to the correlation between the duration of solar flares and X-ray fluence E observed with the GOES ($t_{flare} \propto E^{1/3}$) (Veronig et al. 2002). This correlation is interesting because the reconnection model of flares predicts that the flare energy and duration scales with the length $E \propto L^3$ and $t_{flare} \propto L$, since the flare duration is basically determined by the inverse of the reconnection rate, of order of $100\, t_A = 100\, L/V_A$. From these relations, we find $t_{flare} \propto E^{1/3}$. This explains both solar and stellar flare observations. It provides another evidence of the magnetic reconnection model for *spatially unresolved* stellar flares.

What is the frequency of solar flares and stellar superflares? Figure 10.18 shows the occurrence frequency of flares as a function of flare energy, for solar flares, microflares, nanoflares and also superflares on Sun-like stars. It is remarkable to

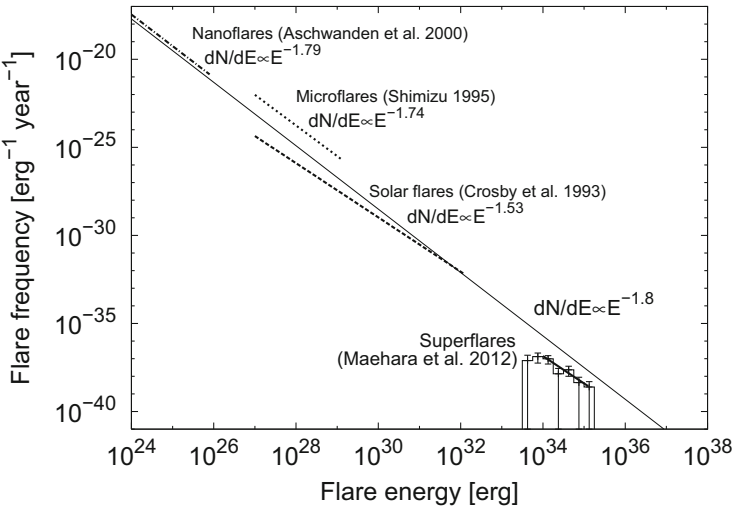

Fig. 10.18 Occurrence frequencies of solar flares, microflares, and nanoflares. Occurrence frequency of superflares on solar type stars are also shown in this figure (Shibata et al. 2013)

see that superflare frequency is roughly on the same line as that for solar flares, microflares, and nanoflares,

$$dN/dE \propto E^{-1.8} \tag{10.12}$$

suggesting the same physical mechanism for both solar and stellar flares. It was found that the occurrence frequency of superflares of 10^{34} erg is once in 800 years, and that of 10^{35} erg is once in 5000 years on Sun-like stars whose surface temperature and rotation are similar to those of the Sun.

It should be noted here that there is no evidence of hot Jupiters around the superflare stars, suggesting the possibility that superflares may occur on the Sun (Nogami et al. 2014).

Shibayama et al. (2013) extended and confirmed the work by Maehara et al. and found 1547 superflares on 279 solar type stars from 500 days Kepler data. Shibayama et al. found that in some Sun-like stars the occurrence rate of superflares was very high, four superflares in 500 days (i.e., once in 100 days).

It is interesting to note that large cosmic ray events in seventh and ninth century were found from tree ring (Miyake et al. 2012, 2013). Although the source of this cosmic ray is a matter of further investigation, the possibility that such events are caused by a solar super flare cannot be ignored. The frequency of the large cosmic ray events is pretty much consistent with the superflare frequency.

If a superflare with energy $10^{34} - 10^{35}$ erg (i.e., 100–1000 times larger than the largest solar flares ever observed, Carrington flare) occurs on the present Sun, the damage that such a superflare can cause to our civilization would be extremely large; Hence it is very important to study the basic properties of superflare on Sun-like stars to know the condition of occurrence of superflares and to understand how the superflares-producing stars are similar to our Sun. This is, of course, closely connected to the fundamental physics of reconnection: why and how fast reconnection occurs in magnetized plasma.

Finally, we should note that stellar flares sometimes show very bursty light curves in X-rays and visible light, which is similar to bursty radio or HXR light curves of solar flares during impulsive phase. This may be indirect evidence of turbulent (fractal) current sheet, since the fourier analysis of the time variability of the bursty light curve shows a power-law distribution (e.g., Inglis et al. 2015, , Maehara 2015 private communication).

Acknowledgements At first, we would like to thank Professor Eugene N. Parker for introducing us to the fascinating field of magnetic reconnection for many years. One of the authors (KS) remember that Prof. Parker said to KS "What an interesting talk !" just after KS gave a talk on "Plasmoid-induced-reconnection and fractal reconnection" in MR2000 conference held in Tokyo in 2000. This comment encouraged KS very much, and it became the primary motivation why this article was written. We also would like to thank Amitava Bhattacharjee, Hantao Ji, K. Daughton, N.F. Loureiro, Hiroyuki Maehara, Naoto Nishizuka, Yuta Notsu, Takuya Shibayama, Takuya Takahashi for allowing us to use figures of their papers and for their help for preparing the manuscript, Paul Cassak for giving us various useful comments as the referee, and Alkendra Singh for improving our English. This work is supported by the Grant-in-Aids from the Ministry of

Education, Culture, Sports, Science and Technology of Japan (Nos. 25287039). ST acknowledges support by the Research Fellowship of the Japan Society for the Promotion of Science (JSPS).

References

D.M. Alexander, L. Fletcher, High-resolution observations of plasma jets in the solar corona. Sol. Phys. **190**, 167–184 (1999)

V. Archontis, A.W. Hood, A numerical model of standard to blowout jets. Astrophys. J. **769**, L21 (2013)

A. Asai, T. Yokoyama, M. Shimojo, K. Shibata, Downflow motions associated with impulsive nonthermal emissions observed in the 2002 July 23 solar flare. Astrophys. J. **605**, L77–L80 (2004)

M. Aschwanden, Particle acceleration and kinematics in solar flares - a synthesis of recent observations and theoretical concepts. Space Sci. Rev. **101**, 1–227 (2002)

M. Bárta, J. Büchner, M. Karlický, J. Skála, Spontaneous current-layer fragmentation and cascading reconnection in solar flares. I. Model and analysis. Astrophys. J. **737**, 24–34 (2011)

A. Bemporad, Spectroscopic detection of turbulence in post-CME current sheets. Astrophys. J. **689**, 572–584 (2008)

A. Bhattacharjee, Y.-M. Huang, H. Yang, B. Rogers, Fast reconnection in high-Lundquist-number plasmas due to the plasmoid instability. Phys. Plasmas **16**, 112102 (2009)

D. Biskamp, *Nonlinear Magnetohydrodynamics* (Cambridge University Press, Cambridge, 1993), 392 pp.

D. Biskamp, *Magnetic Reconnection in Plasmas* (Cambridge University Press, Cambridge, 2000), 387 pp.

H. Carmichael, A process for flares, in *Proceedings of AAS-NASA Symposium on the Physics of Solar Flares*, ed. by W.N. Hess. NASA-SP 50 (1964), pp. 451–456

R.C. Carrington, Description of a singular appearance seen in the sun. Mon. Not. R. Astron. Soc. **20**, 13–15 (1859)

P.A. Cassak, M.A. Shay, J.F. Drake, Catastrophe model for fast magnetic reconnection onset. Phys. Rev. Lett. **95**, 235002 (2005)

P.A. Cassak, M.A. Shay, J.F. Drake, Scaling of Sweet-Parker reconnection with secondary islands. Phys. Plasmas **16**, 120702 (2009)

C.Z. Cheng, Y. Ren, G.S. Choe, Y.-J. Moon, Flux rope acceleration and enhanced magnetic reconnection rate. Astrophys. J. **596**, 1341–1346 (2003)

G.S. Choe, C.Z. Cheng, A model of solar flares and their homologous behavior. Astrophys. J. **541**, 449–467 (2000)

J.W. Cirtain et al., Evidence for Alfven waves in solar X-ray jets. Science **318**, 1580–1582 (2007)

W. Daughton, V. Roytershteyn, B.J. Albright, H. Karimabadi, L. Yin, K.J. Bowers, Transition from collisional to kinetic regimes in large-scale reconnection layers. Phys. Rev. Lett. **103**, 065004 (2009)

J.F. Drake, M. Swisdak, H. Che, M.A. Shay, Electron acceleration from contracting magnetic islands during reconnection. Nature **443**, 553–556 (2006)

U. Feldman, J.M. Laming, G.A. Doschek, The correlation of solar flare temperature and emission measure extrapolated to the case of stellar flares. Astrophys. J. **451**, L79–L81 (1995)

R.L. Fermo, J.F. Drake, M. Swisdak, A statistical model of magnetic islands in a current layer. Phys. Plasmas **17**, 010702 (2010)

H.P. Furth, J. Killeen, M. Rosenbluth, Finite-resistivity instabilities of a sheet pinch. Phys. Fluids **6**, 459–484 (1963)

L.-J. Guo, Y.-M. Huang, A. Bhattacharjee, D.E. Innes, Rayleigh-Taylor type instabilities in the reconnection exhaust jet as a mechanism for supra-arcade downflows in the sun. Astrophys. J. Lett. **796**, L29–L34 (2014)

T. Hirayama, Theoretical model of flares and prominences. I: evaporating flare model. Sol. Phys. **34**, 323–338 (1974)
Y.-M. Huang, A. Bhattacharjee, Scaling laws of resistive magnetohydrodynamic reconnection in the high-Lundquist-number, plasmoid-unstable regime. Phys. Plasmas **17**, 062104 (2010)
Y.-M. Huang, A. Bhattacharjee, Distribution of plasmoids in high-Lundquist-number magnetic reconnection. Phys. Rev. Lett. **109**, 265002 (2012)
Y.-M. Huang, A. Bhattacharjee, Plasmoid instability in high-Lundquist-number magnetic reconnection. Phys. Plasmas **20**, 055702 (2013)
A.R. Inglis, J. Ireland, M. Dominique, Quasi-periodic pulsations in solar and stellar flares: re-evaluating their nature in the context of power-law flare Fourier spectra. Astrophys. J. **798**, 108 (2015)
H. Isobe, T. Miyagoshi, K. Shibata, T. Yokoyama, Filamentary structure on the Sun from the magnetic Rayleigh-Taylor instability. Nature **434**, 478–481 (2005)
H. Isobe, T. Miyagoshi, K. Shibata, T. Yokoyama, Three-dimensional simulation of solar emerging flux using the earth simulator I. Magnetic Rayleigh-Taylor instability at the top of the emerging flux as the origin of filamentary structure. Publ. Astron. Soc. Jpn. **58**, 423–438 (2006)
H. Ji, K. Daughton, Phase diagram for magnetic reconnection in heliophysical, astrophysical, and laboratory plasmas. Phys. Plasmas **18**, 111207 (2011)
M. Karlicky, M. Sobotka, K. Jiricka, Narrowband dm-spikes in the 2 GHz frequency range and MHD cascading waves in reconnection outflows. Sol. Phys. **168**, 375–383 (1996)
R.A. Kopp, G.W. Pneuman, Magnetic reconnection in the corona and the loop prominence phenomenon. Sol. Phys. **50**, 85–98 (1976)
K. Koyama, K. Hamaguchi, S. Ueno, N. Kobayashi, E. Feigelson, Publ. Astron. Soc. Jpn. **48**, L87–L92 (1996)
H. Kurokawa, Y. Hanaoka, K. Shibata, Y. Uchida, Rotating eruption of an untwisting filament triggered by the 3B flare of 25 April, 1984. Sol. Phys. **79**, 77–84 (1987)
J.E. Leake, V.S. Lukin, M.G. Linton, Magnetic reconnection in a weakly ionized plasma. Phys. Plasmas **20**, 1251–1264 (2013)
M.G. Linton, E.R. Priest, Three-dimensional reconnection of untwisted magnetic flux tubes. Astrophys. J. **595**, 1259–1276 (2002)
E. Loomis, On the great auroral exhibition of Aug. 28th to Sept. 4, 1859, and on auroras generally. Am. J. Sci. **82**, 318–335 (1861)
N.F. Loureiro, A.A. Schekochihin, S.C. Cowley, Instability of current sheets and formation of plasmoid chains. Phys. Plasma **14**, 100703 (2007)
N.F. Loureiro, R. Samtaney, A.A. Schekochihin, D.A. Uzdensky, Magnetic reconnection and stochastic plasmoid chains in high-Lundquist-number plasmas. Phys. Plasmas **19**, 042303 (2012)
H. Maehara, T. Shibayama, S. Notsu et al., Superflares on solar type stars. Nature **485**, 478–481 (2012)
H. Maehara, T. Shibayama, Y. Notsu et al., Statistical properties of superflares on solar-type stars based on 1-min cadence data. Earth Planets Space **67**, 59 (2015)
T. Magara, K. Shibata, T. Yokoyama, Evolution of eruptive flares. I. Plasmoid dynamics in eruptive flares. Astrophys. J. **487**, 437–446 (1997)
S. Masuda, T. Kosugi, T. Hara, S. Tsuneta, Y. Ogawara, A loop-top hard X-ray source in a compact solar flare as evidence for magnetic reconnection. Nature **371**, 495–497 (1994)
D.E. McKenzie, Turbulent dynamics in solar flare sheet structures measured with local correlation tracking. Astrophys. J. **766**, 39–45 (2013)
D.E. McKenzie, H.S. Hudson, X-ray observations of motions and structure above a solar flare arcade. Astrophys. J. **519**, L93–L96 (1999)
Z. Mei, C. Shen, N. Wu et al., Numerical experiments on magnetic reconnection in solar flare and coronal mass ejection current sheets. Mon. Not. R. Astron. Soc. **425**, 2824–2839 (2012)
J.A. Miller, P.J. Cargill, A.G. Emslie et al., Critical issues for understanding particle acceleration in impulsive solar flares. J. Geophys. Res. **102**, 14631–14660 (1997)

F. Moreno-Insertis, K. Galsgaard, I. Ugarte-Urra, Jets in coronal holes: hinode observations and three-dimensional computer modeling. Astrophys. J. **673**, L211–L214 (2008)
F. Miyake, K. Nagaya, K. Masuda, T. Nakamura, A signature of cosmic-ray increase in AD 774-775 from tree rings in Japan. Nature **486**, 240–242 (2012)
F. Miyake, K. Masuda, T. Nakamura, Another rapid event in the carbon-14 content of tree rings. Nat. Commun. **4**, 1748 (2013)
L. Ni, B. Kliem, J. Lin, N. Wu, Fast magnetic reconnection in the solar chromosphere mediated by the plasmoid instability. Astrophys. J. **799**, 79 (2015)
K. Nishida, M. Shimizu, D. Shiota, H. Takasaki, T. Magara, K. Shibata, Astrophys. J. **690**, 748–757 (2009)
K. Nishida, N. Nishizuka, K. Shibata, The role of a flux rope ejection in a three-dimensional magnetohydrodynamic simulation of a solar flare. Astrophys. J. **775**, L39 (2013)
N. Nishizuka, K. Shibata, Fermi acceleration in plasmoids interacting with fast shocks of reconnection via fractal reconnection. Phys. Rev. Lett. **110**, 051101 (2013)
N. Nishizuka, A. Asai, H. Takasaki, H. Kurokawa, K. Shibata, The power-law distribution of flare Kernels and fractal current sheets in a solar flare. Astrophys. J. **694**, L74–L78 (2009)
N. Nishizuka, H. Takasaki, A. Asai, K. Shibata, Multiple plasmoid ejections and associated hard X-ray bursts in the 2000 November 24 flare. Astrophys. J. **711**, 1062–1072 (2010)
N. Nishizuka, M. Karlický, M. Janvier, M. Bárta, Particle acceleration in plasmoid ejections derived from radio drifting pulsating structures. Astrophys. J. **799**, 126–141 (2015)
D. Nogami, Y. Notsu, S. Honda et al., Two sun-like superflare stars rotating as slow as the Sun. Publ. Astron. Soc. Jpn. **66**, L4 (2014)
S. Notsu, S. Honda, Y. Notsu et al., High-dispersion spectroscopy of the superflare star KIC 6934317. Publ. Astron. Soc. Jpn. **65**, 112 (2013a)
Y. Notsu, T. Shibayama, H. Maehara et al., Superflares on solar-type stars observed with kepler II. Photometric variability of superflare-generating stars: a signature of stellar rotation and starspots. Astrophys. J. **771**, 127 (2013b)
Y. Notsu, S. Honda, H. Maehara, S. Notsu, T. Shibayama, D. Nogami, K. Shibata, High dispersion spectroscopy of solar-type superflare stars. II. Stellar rotation, starspots, and chromospheric activities. Publ. Astron. Soc. Jpn. **67**, 33 (2015)
K. Ohki, Physical implications of X-ray imaging observations. Lect. Notes Phys. **387**, 106 (1991)
M. Ohyama, K. Shibata, Preflare heating and mass motion in a solar flare associated with hot plasma ejection: 1993 November 11 C9.7 flare. Publ. Astron. Soc. Jpn. **49**, 249–261 (1997)
M. Ohyama, K. Shibata, X-ray plasma ejection associated with an impulsive flare on 1992 October 5: physical conditions of X-ray plasma ejection. Astrophys. J. **499**, 934–944 (1998)
M. Ohyama, K. Shibata, J. Atmos. Sol. Terr. Phys. **62**, 1509 (2000)
Y. Ono et al., Intermittent magnetic reconnection in TS-3 merging experiment. Phys. Plasma **18**, 11213 (2011)
E. Pariat, S. K. Antiochos, and C. R. DeVore, Three-dimensional modeling of quasi-homologous solar jets. Astrophys. J. **714**, 1762–1778 (2010)
E.N. Parker, *Cosmical Magnetic Fields: Their Origin and their Activity*. International Series of Monographs on Physics (Clarendon Press/Oxford University Press, Oxford/New York, 1979)
E.N. Parker, Nanoflares and the solar X-ray corona. Astrophys. J. **330**, 474–479 (1988)
E.N. Parker, *Spontaneous Current Sheets in Magnetic Fields: With Applications to Stellar X-Rays*. International Series on Astronomy and Astrophysics, vol. 2 (Oxford University Press, Oxford; New York, 1994)
C.D. Pike, H.E. Mason, Rotating transition region features observed with the SOHO coronal diagnostic spectrometer. Sol. Phys. **182**, 333–348 (1998)
E.R. Priest, *Solar Magnetohydrodynamics*. Geophysics and Astrophysics Monographs, vol. 21 (Reidel, Dordrecht, Boston, 1982)
E.R. Priest, T. Forbes, *Magnetic Reconnection: MHD Theory and Applications* (Cambridge University Press, Cambridge, New York, 2000)
J. Qiu, H. Wang, C.Z. Cheng, D.E. Gary, Magnetic reconnection and mass acceleration in flare-coronal mass ejection events. Astrophys. J. **604**, 900–905 (2004)

E.P. Rubenstein, B.E. Schaefer, Are superflares on solar analogues caused by extrasolar planets? Astrophys. J. **529**, 1031–1033 (2000)
R. Samtaney, N.F. Loureiro, D.A. Uzdensky, A.A. Schekochihin, S.C. Cowley, Formation of plasmoid chains in magnetic reconnection. Phys. Rev. Lett. **103**, 105004 (2009)
B.E. Schaefer, J.R. King, C.P. Deliyannis, Astrophys. J. **529**, 1026–1030 (2000)
K. Shibata, Evidence of magnetic reconnection in solar flares and a unified model of flares. Astrophys. Space Sci. **264**, 129–144 (1999)
K. Shibata, T. Magara, Solar flares: magnetohydrodynamic processes. Living Rev. Sol. Phys. **8**(6) 1–99 (2011)
K. Shibata, S. Tanuma, Plasmoid-induced-reconnection and fractal reconnection. Earth Planets Space **53**, 473–482 (2001)
K. Shibata, Y. Uchida, A magnetodynamic mechanism for the formation of astrophysical jets. I - Dynamical effects of the relaxation of nonlinear magnetic twists. Publ. Astron. Soc. Jpn. **37**, 31–46 (1985)
K. Shibata, T. Yokoyama, Origin of the universal correlation between the flare temperature and the emission measure for solar and stellar flares. Astrophys. J. Lett. **526** , L49– L52 (1999)
K. Shibata, T. Yokoyama, A Hertzsprung-Russell-like diagram for solar/stellar flares and corona: emission measure versus temperature diagram. Astrophys. J. **577**, 422–432 (2002)
K. Shibata, S. Nozawa, R. Matsumoto, Magnetic reconnection associated with emerging magnetic flux. Publ. Astron. Soc. Jpn. **44**, 265–272 (1992)
K. Shibata, S. Masuda, M. Shimojo, H. Hara, T. Yokoyama, S. Tsuneta, T. Kosugi, Hot-plasma ejections associated with compact-loop solar flares. Astrophys. J. **451**, L83–L85 (1995)
K. Shibata, T. Nakamura, T. Matsumoto et al., Chromospheric anemone jets as evidence of ubiquitous reconnection. Science **318**, 1591–1594 (2007)
K. Shibata, H. Isobe, A. Hillier, et al., Can superflares occur on our sun? Publ. Astron. Soc. Jpn. **65**, 49 (2013)
T. Shibayama, H. Maehara, S. Notsu et al., Superflares on solar-type stars observed with Kepler. I. Statistical properties of superflares. Astrophys. J. Suppl. Ser. **209**, 5 (2013)
M. Shimizu, K. Nishida, H. Takasaki, D. Shiota, T. Magara, K. Shibata, The correlation among the rise velocity of a soft X-ray loop, the ejection velocity of a plasmoid, and the height above the loop top of the hard X-ray source in Masuda-type flares, and its interpretation based on the reconnection model of flares. Astrophys. J. **683**, L203–L206 (2008)
M. Shimojo, S. Hashimoto, K. Shibata et al., Statistical study of solar X-ray jets observed with the Yohkoh soft X-ray telescope. Publ. Astron. Soc. Jpn. **48**, 123–136 (1996)
M. Shimojo, N. Narukage, R. Kano, T. Sakao, S. Tsuneta, K. Shibasaki, J.W. Cirtain, L.L. Lundquist, K.K. Reeves, A. Savcheva, Fine structures of solar X-ray jets observed with the X-ray telescope aboard Hinode. Publ. Astron. Soc. Jpn. **59**, S745–S750 (2007)
K.A.P. Singh, K. Shibata, N. Nishizuka, H. Isobe, Chromospheric anemone jets and magnetic reconnection in partially ionized solar atmosphere. Phys. Plasmas **18**, 111210 (2011)
K.A.P. Singh, H. Isobe, N. Nishizuka, K. Nishida, K. Shibata, Multiple plasma ejections and intermittent nature of magnetic reconnection in solar chromospheric anemone jets. Astrophys. J. **759**, 33–46 (2012)
K.A.P. Singh, A. Hillier, H. Isobe, K. Shibata, Nonlinear instability and intermittent nature of magnetic reconnection in solar chromosphere. Publ. Astron. Soc. Jpn. **67**, 96(1–11) (2015)
P.A. Sturrock, Model of the high-energy phase of solar flares. Nature **211**, 695–697 (1966)
T. Tajima, K. Shibata, *Plasma Astrophysics*. Frontiers in Physics, vol. 98 (Addison-Wesley, Reading, 1997)
T. Tajima, J. Sakai, H. Nakajima, T. Kosugi, F. Brunel, M.R. Kundu, Current loop coalescence model of solar flares. Astrophys. J. **321**, 1031–1048 (1987)
M. Takamoto, Evolution of relativistic plasmoid chains in a poynting-dominated plasma. Astrophys. J. **775**, 50–59 (2013)
S. Takasao, A. Asai, H. Isobe, K. Shibata, Simultaneous observation of reconnection inflow and outflow associated with the 2010 August 18 solar flare. Astrophys. J. Lett. **745**, L6–L12 (2012)

S. Takasao, H. Isobe, K. Shibata, Numerical simulations of solar chromospheric jets associated with emerging flux. Publ. Astron. Soc. Jpn. **65**, 62–81 (2013)
S. Tanuma, T. Yokoyama, T. Kudoh, K. Shibata, Two-dimensional magnetohydrodynamic numerical simulations of magnetic reconnection triggered by a supernova shock in the interstellar medium: generation of X-ray gas in the galaxy. Astrophys. J. **551**, 312–332 (2001)
T. Terasawa, K. Shibata, M. Scholer, Comparative studies of flares and substorms. Adv. Space Res. **26**, 573–583 (2000)
S. Tsuneta, Structure and dynamics of magnetic reconnection in a solar flare. Astrophys. J. **456**, 840–849 (1996)
S. Tsuneta, Moving plasmoid and formation of the neutral sheet in a solar flare. Astrophys. J. **483**, 507–514 (1997)
S. Tsuneta et al., Observation of a solar flare at the limb with the YOHKOH soft X-ray telescope. Publ. Astron. Soc. Jpn. **44**, L63–L69 (1992)
B.T. Tsurutani, W.D. Gonzalez, G.S. Lakhina, S. Alex, The extreme magnetic storm of 1–2 September 1859. J. Geophys. Res. A **108**, 1268–1275 (2003)
D.A. Uzdensky, N.F. Loureiro, A.A. Schekochihin, Fast magnetic reconnection in the plasmoid-dominated regime. Phys. Rev. Lett. **105**, 235002 (2010)
A. Veronig, M. Temmer, A. Hanslmeier, W. Otruba, M. Messerotti, Temporal aspects and frequency distributions of solar soft X-ray flares. Astron. Astrophys. **382**, 1070–1080 (2002)
P.F. Wyper, D.I. Pontin, Dynamic topology and flux rope evolution during non-linear tearing of 3D null point current sheets. Phys. Plasmas **21**, 102102 (2014)
M. Yamada, R.M. Kulsrud, H. Ji, Magnetic reconnection. Rev. Mod. Phys. **82**, 603–664 (2010)
T. Yokoyama, K. Shibata, Magnetic reconnection as the origin of X-ray jets , Halpha surges on the Sun. Nature **375**, 42–44 (1995)
T. Yokoyama, K. Shibata, Numerical simulation of solar coronal X-ray jets based on the magnetic reconnection model. Publ. Astron. Soc. Jpn. **48**, 353–376 (1996)
T. Yokoyama, K. Shibata, A two-dimensional magnetohydrodynamic simulation of chromospheric evaporation in a solar flare based on a magnetic reconnection model. Astrophys. J. **494**, L113–L116 (1998)
T. Yokoyama, K. Akita, T. Morimoto, K. Inoue, J. Newmark, Clear evidence of reconnection inflow of a solar flare. Astrophys. J. **546**, L69–L72 (2001)
S. Zenitani, Magnetohydrodynamic structure of a plasmoid in fast reconnection in low-beta plasmas: shock-shock interactions. Phys. Plasma **22**, 032114 (2015)
S. Zenitani, T. Miyoshi, Magnetohydrodynamic structure of a plasmoid in fast reconnection in low-beta plasmas. Phys. Plasma **18**, 022105 (2011)
J. Zhang, K.P. Dere, R.A. Howard, M.R. Kundu, S.M. White, On the temporal relationship between coronal mass ejections and flares. Astrophys. J. **559**, 452–462 (2001)

Chapter 11
Theory and Applications of Non-relativistic and Relativistic Turbulent Reconnection

A. Lazarian, G. Kowal, M. Takamoto, E.M. de Gouveia Dal Pino, and J. Cho

Abstract Realistic astrophysical environments are turbulent due to the extremely high Reynolds numbers of the flows. Therefore, the theories intended for describing astrophysical reconnection should not ignore the effects of turbulence. Turbulence is known to change the nature of many physical processes dramatically and in this review we claim that magnetic reconnection is not an exception. We stress that not only astrophysical turbulence is ubiquitous, but also the outflows from magnetic reconnection induce turbulence affecting the rate of turbulent reconnection. Thus turbulence must be accounted for any realistic astrophysical reconnection set up. We argue that due to the similarities of MHD turbulence in relativistic and non-relativistic cases the theory of magnetic reconnection developed for the non-relativistic case can be extended to the relativistic case and we provide numerical simulations that support this conjecture. We also provide quantitative comparisons of the theoretical predictions and results of numerical experiments, including the situations when turbulent reconnection is self-driven, i.e. the turbulence in the system is generated by the reconnection process itself. In addition, we consider

A. Lazarian (✉)
Department of Astronomy, University of Wisconsin, Madison, WI, USA
e-mail: lazarian@astro.wisc.edu

G. Kowal
Escola de Artes, Ciências e Humanidades, Universidade de São Paulo, São Paulo, SP, Brazil
e-mail: grzegorz.kowal@usp.br

M. Takamoto
Department of Earth and Planetary Science, The University of Tokyo, Tokyo, Japan
e-mail: mtakamoto@eps.s.u-tokyo.ac.jp

E.M. de Gouveia Dal Pino
Instituto de Astronomia, Geofísica e Ciencias Atmosfericas, Universidade de Sao Paulo, São Paulo, SP, Brazil
e-mail: dalpino@astro.iag.usp.br

J. Cho
Department of Astronomy and Space Science, Chungnam National University, Daejeon, Korea
e-mail: jcho@cnu.ac.kr

W. Gonzalez, E. Parker (eds.), *Magnetic Reconnection*, Astrophysics and Space Science Library 427, DOI 10.1007/978-3-319-26432-5_11

observational testing of turbulent reconnection as well as numerous implications of the theory. The former includes the Sun and solar wind reconnection, while the latter include the process of reconnection diffusion induced by turbulent reconnection, the acceleration of energetic particles, bursts of turbulent reconnection related to black hole sources and gamma ray bursts. Finally, we explain why turbulent reconnection cannot be explained by turbulent resistivity or derived through the mean field approach. We also argue that the tearing reconnection transfers to fully turbulent reconnection in 3D astrophysically relevant settings with realistically high Reynolds numbers.

Keywords Reconnection • Reconnection rate • turbulent reconnection • turbulence • plasma turbulence • particle acceleration • gamma ray bursts • stellar activity • black holes

11.1 Problem of Reconnection as We See It

This is a chapter that deals with magnetic reconnection in astrophysical environments that are generically turbulent. We discuss how turbulence makes reconnection fast and what this means for many astrophysical systems.

This is a contribution to the book on magnetic reconnection and therefore it is not particularly productive to repeat that magnetic reconnection is important for variety of processes from solar flares to gamma ray bursts. What we would like to stress here is that magnetic reconnection is not some exotic process that may be taking place occasionally in astrophysical environments, but it is bread and butter of most processes taking place in magnetized plasmas. The key to understanding of omnipresence of magnetic reconnection is the ubiquity of turbulence in astrophysical environments.

Turbulence is a feature of high Reynolds number (Re) flows and most of magnetized flows have extremely high Reynolds numbers. We show that even if the initial astrophysical setup is not turbulent or "not sufficiently turbulent", the development of reconnection, e.g. outflow, is bound to transfer the process of reconnection to fully turbulent regime. Therefore we view the laminar models with plasma instabilities, e.g. tearing instability. As transient states to the fully turbulent reconnection.

What is the speed of reconnection? It is important to stress that turbulent reconnection can address the apparent dichotomy suggested by observations, e.g. reconnection is sometimes fast and sometimes slow. The theory of turbulent reconnection relates this to the dependence of magnetic reconnection rate on the level of turbulence in the system. As the intensity of turbulence changes, the reconnection rate also changes.

As we will discuss in the review, the theory of turbulent reconnection predicts reconnection rates that do not depend on the details of plasma microphysics, but only on the level of MHD turbulence. The plasma physics related to the local reconnection events may still be important at small scales for the acceleration of particles from the thermal pool. At the same time, for understanding of particle acceleration at large energies the MHD description of turbulent reconnection is sufficient. We note, however, that the turbulent reconnection theory that we describe in the review is based on MHD and therefore it is not applicable to the Earth magnetosphere where the current sheets are comparable to the ion inertial scale.

The theory of turbulent reconnection has been covered in a number of reviews that include Lazarian et al. (2015a,?); Browning and Lazarian (2013). In a review by Karimabadi and Lazarian (2013) there was also an attempt to present side by side the theories of turbulent reconnection based on plasma turbulence and on MHD approach, that we discuss here. We warn our reader, however, that the statement in the latter review that the MHD approach cannot describe reconnection events in Solar wind was shown to be incorrect in a more recent work (Lalescu et al. 2015).

Within the present review we also discuss the implications of turbulent reconnection, the study becoming more important as the interconnection between turbulence and astrophysical reconnection is appearing more evident to the community. Indeed, in terms of implications, we are just scratching the surface of a very rich subject. For instance, it is generally believed that magnetic fields embedded in a highly conductive fluid retain their topology for all time due to the magnetic fields being frozen-in (Alfvén 1943; Parker 1979). This concept of frozen-in magnetic fields is at the foundation of many theories, e.g. of the theory of star formation in magnetized interstellar medium. At the same time, below we discuss that this concept is not correct in the presence of turbulence, i.e. serious revisions are necessary for the theoretical description of a large number of astrophysical systems.

In what follows we briefly discuss modern ideas on non-relativistic and relativistic MHD turbulence in Sects. 11.2 and 11.3 respectively, introduce the basic concepts of turbulent non-relativistic reconnection theory in Sect. 11.4, provide numerical testing of turbulent reconnection in Sect. 11.5. In Sect. 11.6 we discuss how non-relativistic turbulent reconnection theory can be generalized for the case of relativistic reconnection and provide numerical testing of the idea, while Sect. 11.7 deals with the case of turbulent reconnection where turbulence is injected by the reconnection process itself. The observational testing of turbulent reconnection is discussed in Sect. 11.8 and the implications of the theory of turbulent reconnection are summarized in Sect. 11.9. A comparison of turbulent reconnection to other popular ideas can be found in Sect. 11.10 and the final remarks are given in Sect. 11.11. There we also discuss the relation of this chapter to other chapters of the book.

11.2 Non-relativistic MHD Turbulence

Non-relativistic MHD turbulence is the best explored case with a lot of observational and numerical data available to test the theory.

11.2.1 Astrophysical Turbulence: Expectations and Evidence

Magnetized astrophysical fluids have huge Reynolds numbers $Re \equiv LV/\nu$ as magnetic field limits the diffusion of charged particles perpendicular to its local direction making viscosity ν small[1] while the scales of the flow L are astrophysically huge. High Re number flows are prey to numerous linear and finite-amplitude instabilities, from which turbulent motions readily develop. The plasma turbulence is sometimes driven by external energy sources, such as supernovae in the ISM (Norman and Ferrara 1996; Ferrière 2001), merger events and active galactic nuclei outflows in the intracluster medium (ICM) (Subramanian et al. 2006; Enßlin and Vogt 2006; Chandran 2005), and baroclinic forcing behind shock waves in interstellar clouds. In other cases, the turbulence is spontaneous, with available energy released by a rich array of instabilities, such as magneto-rotational instability (MRI) in accretion disks (Balbus and Hawley 1998), kink instability of twisted flux tubes in the solar corona (Galsgaard and Nordlund 1997; Gerrard and Hood 2003), etc. Finally, as we discuss in the review, magnetic reconnection can also be a source of turbulence.

Observations confirm that astrophysical environments are indeed turbulent. The spectrum of electron density fluctuations in the Milky Way is presented in Fig. 11.1, but similar examples are discussed in Leamon et al. (1998), Bale et al. (2005) for solar wind, and Vogt and Enßlin (2005) for the intracluster medium. As new techniques for studying turbulence are being applied to observational data, the evidence of the turbulent nature of astrophysical media becomes really undeniable. For instance, the Velocity Channel Analysis (VCA) and Velocity Coordinate Spectrum (VCS) techniques (Lazarian and Pogosyan 2000, 2004, 2006) provided unique insight into the velocity spectra of turbulence in molecular clouds (see Padoan et al. 2006, 2010), galactic and extragalactic atomic hydrogen (Stanimirović and Lazarian 2001; Chepurnov et al. 2010, 2015, see also the review by Lazarian 2009), where a compilation of velocity and density spectra obtained with contemporary HI and CO data is presented). We expect new flow of information on magnetic field spectra

[1] In addition, the mean free path of particles can also be constrained by the instabilities developed on the collisionless scales of plasma (see Schekochihin et al. 2009; Lazarian and Beresnyak 2006; Brunetti and Lazarian 2011), while ensures that compressible motions can also survive collisionless damping.

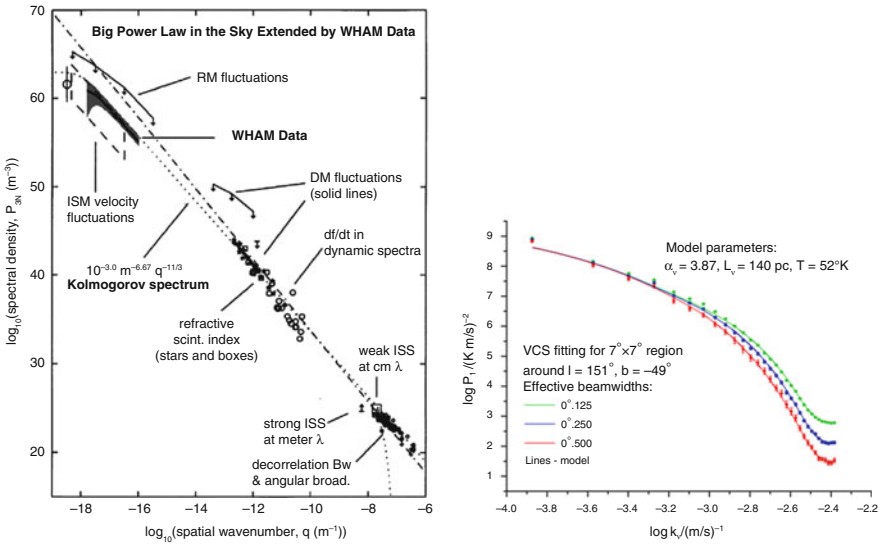

Fig. 11.1 *Left panel*: big power law in the sky from Armstrong et al. (1995) extended to scale of parsecs using the Wisconsin H-Alpha Mapper (WHAM) data. Reproduced from Chepurnov and Lazarian (2010) by permission of the AAS. *Right panel*: properties of turbulence in HI obtained with VCS techniques. Reproduced from Chepurnov et al. (2010) by permission of the AAS

to come from the new techniques that treat synchrotron fluctuations (Lazarian and Pogosyan 2012).

11.2.2 Theory of Weak and Strong MHD Turbulence

MHD theory is applicable to astrophysical plasmas at sufficiently large scales and for many astrophysical situations the Alfvénic turbulence, which is the most important for turbulent reconnection is applicable at the scales substantially larger than the ion gyroradius ρ_i (see a discussion in Eyink et al. 2011; Lazarian et al. 2015a).

The history of the theory of MHD turbulence can be traced back to the pioneering studies by Iroshnikov (1964) and Kraichnan (1965). A good account for the state of the field could be found in Biskamp (2003). Usually turbulence is subdivided into weak and strong regimes, depending on the strength of nonlinear interaction. While weak MHD turbulence allows for analytical perturbative treatment (Ng and Bhattacharjee 1996; Galtier et al. 2002; Chandran 2005), the progress in understanding strong turbulence came primarily from phenomenological and closure models that were tested by comparison with results of numerical simulations. Important theoretical works on strong MHD turbulence include Montgomery and Turner (1981), Matthaeus et al. (1983), Shebalin et al. (1983), and Higdon (1984). Those

clarified the anisotropic nature of the energy cascade and paved the way for further advancement in the field. The study by Goldreich and Sridhar (1995) identified the balance between perturbations parallel and perpendicular to the local direction of magnetic field, i.e., "critical balance", as the key component of dynamics in strong magnetic turbulence. For detailed recent reviews on MHD turbulence, see Brandenburg and Lazarian (2013) and Beresnyak and Lazarian (2015). Below we provide a simplified derivation of the Alfvénic turbulence scaling that we employ later to understand turbulent reconnection (see also Cho et al. 2003). Other ways of obtaining the same relations may be found in e.g. Goldreich and Sridhar (1995), Lazarian and Vishniac (1999), and Galtier et al. (2000). Other fundamental modes, i.e. slow and fast modes are of relatively marginal importance for the theory of turbulent reconnection and we do not discuss them in the review.

If all the Alfvénic wave packets are moving in one direction, then they are stable to nonlinear order. Therefore, in order to initiate turbulence, there must be opposite-traveling wave packets of similar dimensions and the energy cascade occurs only when they collide. It is also natural to assume that the wave packets are anisotropic and therefore to distinguish between the parallel $l_\parallel$ and the perpendicular $l_\perp$ scales of the wave-packets. The change of energy per collision is

$$\Delta E \sim (du^2/dt)\Delta t \sim \mathbf{u}_l \cdot \dot{\mathbf{u}}_l \Delta t \sim (u_l^3/l_\perp)(l_\parallel/V_A), \tag{11.1}$$

where we take into account that Alfvénic motions perpendicular to magnetic field providing $\dot{\mathbf{u}}_l \sim u_l^2/l_\perp$, while the time of interactions is determined by the time of wave packets interacting with each other, i.e. $\Delta t \sim l_\parallel/V_A$, where V_A is the Alfvén velocity.

The fractional energy change per collision is the ratio of ΔE to E,

$$\zeta_l \equiv \frac{\Delta E}{u_l^2} \sim \frac{u_l l_\parallel}{V_A l_\perp}, \tag{11.2}$$

which characterizes the strength of the nonlinear interaction. The cascading is a random walk process in such a description with

$$t_{cas} \sim \zeta_l^{-2} \Delta t. \tag{11.3}$$

The Alfvénic 3 wave resonant interactions are characterized by

$$\mathbf{k}_1 + \mathbf{k}_2 = \mathbf{k}_3, \tag{11.4}$$

$$\omega_1 + \omega_2 = \omega_3, \tag{11.5}$$

where $\mathbf{k}$'s are wavevectors and ω's are wave frequencies. The first condition is a statement of wave momentum conservation and the second is a statement of energy conservation. Alfvén waves satisfy the dispersion relation: $\omega = V_A|k_\parallel|$, where $k_\parallel$ is the component of wavevector parallel to the background magnetic field. Since only

opposite-traveling wave packets interact, $\mathbf{k}_1$ and $\mathbf{k}_2$ must have opposite signs, which formally means that the cascade is possible only in the perpendicular direction.

In fact, the energy relation is subject to the wave uncertainty principle, which means that the ambiguity of the order $\delta\omega \sim 1/t_{cas}$ is acceptable. When ζ_l is small, $\delta\omega \ll \omega$ and the energy transfer is happening mostly perpendicular to the *local* direction of magnetic field. As a result of such a cascade the parallel scale $l_\parallel$ is preserved, while the perpendicular scale $l_\perp$ decreases. This is the case of *weak Alfvénic turbulence*. In incompressible turbulence the energy flux is

$$\epsilon = u_l^2/t_{cas} \approx \frac{u_l^4}{V_A^2 \Delta t (l_\perp/l_\parallel)^2} = const \tag{11.6}$$

where Eqs. (11.3) and (11.2) are used. Taking into account that $l_\parallel$ is constant, it is easy to see that Eq. (11.6) provides $u_l \sim l_{perp}^{1/2}$ which in terms of energy spectrum of weak turbulence provides the relation

$$E_{k,weak} \sim k_\perp^{-2}, \tag{11.7}$$

where the relation $kE(k) \sim u_k^2$ is used. Equation (11.7) was obtained on the basis of similar arguments in Lazarian and Vishniac (1999, henceforth LV99) and later on the basis of a rigorous treatment of weak turbulence in Galtier et al. (2000). Note that $k_\parallel$ stays constant in the weak cascade.

Note, that the weak turbulence regime should have a limited inertial range. Indeed, as $k_\perp \sim l_\perp^{-1}$ increases, the energy change per collision ζ_l increases, the cascading time t_{cas} decreases. This makes the uncertainty in the wave frequency $\delta\omega \sim 1/t_{cas}$ comparable to wave frequency ω when ζ_l approaches unity. Naturally, one expects the nature of the cascade to change. Indeed, the cascading cannot happen in less than one wave period and therefore the cascading rate cannot increase further. Similarly with $\delta\omega \sim \omega$ the constraints given by Eq. (11.5) cannot prevent the decrease of the parallel length of wave packets $l_\parallel$. This signifies the advent of a regime of *strong Alfvénic turbulence*. The corresponding theory was formulated for the turbulent injection velocity $u_L = V_A$ by Goldreich and Sridhar (1995, henceforth GS95) and was generalized for subAlfvénic and superAlfvénic injection velocities in LV99 and Lazarian (2006), respectively. Below we follow LV99 in order to obtain the relations for strong MHD turbulence with subAlfvénic energy injection. This type of turbulence is the most important in the context of turbulent reconnection.

As we explained above the change of the turbulence regime happens when $\zeta_l \sim 1$, which in terms of the parameters of the interacting wave packets means that

$$u_l/l_\perp \sim V_A/l_\parallel, \tag{11.8}$$

which manifests the famous GS95 *critical balance*. This expression was originally formulated using not scales of the eddies, but wavevectors $k_\perp$ and $k_\parallel$ as the GS95 discussion did not include the fundamental concept of *local* magnetic field direction.

Indeed, the weak turbulence theory can be formulated in terms of mean magnetic field, as the distortions introduced by turbulence in terms of direction are marginal due to the marginal change of $l_\parallel$. In the strong turbulence the distinction between the mean direction of magnetic field and the local direction of the field that a wave packet is moving along may be significant. This is especially obvious in the case of transAlfvénic and superAlfvénic turbulence when the local direction of magnetic field may poorly correlate with the direction of the mean magnetic field in the volume. As a result no universal relations exist in the frame of the mean magnetic field and therefore in the global frame given by wavevectors k. The understanding of the importance of the local magnetic frame for the GS95 theory was introduced and elaborated in the later publications (LV99; Cho and Vishniac 2000; Maron and Goldreich 2001; Cho et al. 2002).

The turbulence is injected isotropically at scale L_i with the velocity $u_L < V_A$ and the cascading of energy follows the weak turbulence cascade u_L^2/t_{cas}, which for the weak cascading rate gives $u_L^4/(L_i V_A)$. Starting with the scale corresponding to $\zeta_l = 1$, i.e. at the perpendicular scale

$$l_{trans} \sim L_i (u_L/V_A)^2 \equiv L_i M_A^2, \quad M_A < 1 \tag{11.9}$$

where $M_A = u_L/V_A < 1$ is the Alfvénic Mach number.[2] The turbulence becomes strong and cascades over one wave period, namely, $l_\parallel/V_A$. The cascading of turbulent energy is $u_l^3/l_\perp$, which is similar to Kolmogorov cascade in the direction perpendicular to the local direction of magnetic field. Due to the conservation of energy in the cascade the weak and strong turbulence energy flows should be the same which gives the scaling relations in LV99

$$\ell_\parallel \approx L_i \left(\frac{\ell_\perp}{L_i}\right)^{2/3} M_A^{-4/3}, \tag{11.10}$$

$$\delta u_\ell \approx u_L \left(\frac{\ell_\perp}{L_i}\right)^{1/3} M_A^{1/3}. \tag{11.11}$$

Those relations give the GS95 scaling for $M_A \equiv 1$. These are equations that we will use further to derive the magnetic reconnection rate.

When the measurements are done in the global system of reference, the turbulence scaling is dominated by perpendicular fluctuations containing most of energy, and therefore using Eq. (11.11) with $kE(k) \sim u_k^2$ one can get $E(k) \sim k^{-5/3}$, which coincides with the Kolmogorov scaling. One can intuitively understand this result assuming that eddies freely evolve in the direction perpendicular to magnetic field.

[2]Thus, weak turbulence has a limited, i.e. $[L_i, L_i M_A^2]$ inertial range and at small scales it transits into the regime of strong turbulence. We should stress that weak and strong are not the characteristics of the amplitude of turbulent perturbations, but the strength of non-linear interactions (see more discussion in Cho et al. 2003) and small scale Alfvénic perturbations can correspond to a strong Alfvénic cascade.

Finally, we want to point out that the isotropic driving of MHD turbulence is somewhat idealized. For instance, when turbulence is driven by magnetic reconnection, magnetic field lines are not straight on the injection scale and therefore the weak cascade ideas are not applicable. This is an important point for understanding Solar flares and similar reconnection phenomena.

11.2.3 Controversy Related to GS95 Model

Testing of GS95 turbulence numerically presented a challenging task. The measurements of the spectral slope in MHD simulations (see Maron and Goldreich 2001) were better fitted by the spectrum $\sim k^{-3/2}$ rather than GS95 prediction of $k^{-5/3}$. This resulted in theoretical attempts to explain the measured slope by Boldyrev (2005, 2006). Another explanation of the slope difference was suggested in Beresnyak and Lazarian (2010). It was based on the conjecture that the MHD turbulence is less local compared to hydrodynamic turbulence and therefore low resolution numerical simulations were not measuring the actual slope of the turbulence, but the slope distorted by the bottleneck effect. The latter is generally accepted to be a genuine feature of turbulence and is attributed to the partial suppression of non-linear turbulent interactions under the influence of viscous dissipation. Studied extensively for hydrodynamics the bottleneck effect reveals itself as a pile-up of kinetic energy near the wave number of maximum dissipation (see Sytine et al. 2000; Dobler et al. 2003). With the limited inertial range of existing numerical simulations, the bottleneck effect may strongly interfere with the attempts to measure the actual turbulence spectrum. The locality of turbulence determines whether the bottleneck produces a localized or more extended bump of the turbulence spectrum. In the latter case the low resolution numerical simulations may be affected by the bottleneck effect for the whole range of wave numbers in the simulation and the distorted spectrum can be mistaken for an inertial range. A smooth extended bottleneck is expected for MHD turbulence being less local compared to its hydrodynamic counterpart. This feature of MHD turbulence was termed by Beresnyak and Lazarian "diffuse locality" (see Beresnyak and Lazarian 2010). This effect is illustrated by Fig. 11.2.

All in all, the bottleneck is a physical effect and the failure to detect it in the low resolution MHD simulations is suggestive that the measured spectral slope is not the actual slope of the turbulent energy. In fact, the bottleneck effect has tricked researchers earlier. For instance, the initial compressible simulations suggested the spectral index of high Mach number hydrodynamic turbulence to be $-5/3$, which prompted theoretical attempts to explain this (e.g. Boldyrev 2002). However, further high resolution research (Kritsuk et al. 2007) revealed that the flattering of the spectrum observed was the result of a bottleneck effect, which is more extended in compressible than in incompressible fluids. Similarly, we believe that the simulations that reported the spectral slope of $-3/2$ for the MHD turbulence (Maron and Goldreich 2001; Müller and Grappin 2005; Mason et al. 2006, 2008;

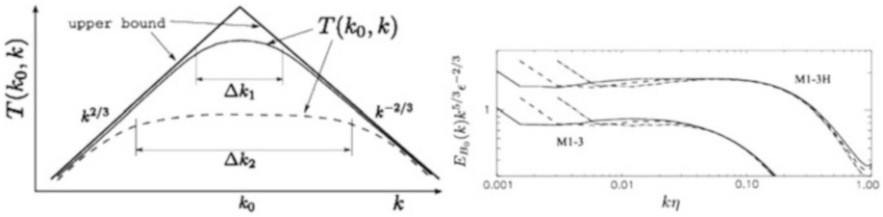

Fig. 11.2 *Left panel*: illustration of "diffuse locality" of MHD turbulence. The upper bounds for the energy transfer window could be consistent with both rather "local" transfer (*upper solid curve*) or "non-local" and "diffuse-local" transfer (*lower dashed curve*). Reproduced from Beresnyak and Lazarian (2010) by permission of the AAS. *Right panel*: spectrum of MHD turbulence in high resolution simulations is consistent with GS95 predictions. Reproduced from Beresnyak (2015) by permission of the AAS

Perez et al. 2012) are affected by the bottleneck effect. This conclusion is supported by the study of scaling properties of turbulence with numerical resolution in Beresnyak (2014). This study shows that the Reynolds number dependence of the dissipation scale is not fulfilled with the $-3/2$ spectral slope.

We believe that the new higher resolution simulations (see Beresnyak 2013, 2014) resolve the controversy and, indeed, the putative $k^{-3/2}$ spectrum is the result of the bottleneck. However, whether the slope is $-3/2$ or $-5/3$ has only marginal impact on the theory of turbulent reconnection. A discussion of turbulent reconnection for an arbitrary spectral index and arbitrary anisotropy can be found in LV99.

11.2.4 Compressible MHD Turbulence

As we discuss later, the Alfvénic mode is the most important mode for turbulent reconnection. Therefore we do not dwell upon compressible MHD turbulence. In fact, it is important for us to be able to consider Alfvénic perturbations in compressible turbulence.

Original ideas of how Alfvénic modes can interact with other fundamental modes, i.e. slow and fast modes, can be traced back to GS95. They were elaborated further in Lithwick and Goldreich (2001). A numerical and theoretical study of the modes was then performed in Cho and Lazarian (2002, 2003) and Kowal and Lazarian (2010).

For our further discussion of magnetic reconnection it is important to know that the Alfvénic mode preserves its identity and forms an independent Alfvénic cascade even in compressible fluid. The numerical evidence for this can be found in Cho and Lazarian (2002, 2003). The effects of compressibility have been extensively studied in Kowal et al. (2007) and scaling relations has been tested in Kowal and Lazarian (2007). A detailed discussion of the effects of compressibility on MHD turbulence can be found in a review by Beresnyak and Lazarian (2015).

11.3 Relativistic MHD Turbulence

Some astrophysical fluids involve relativistic motions. In recent years, interest on MHD turbulence in relativistic fluids has been growing. Can the ideas of GS95 turbulence be transferred to relativistic fluids? This is the issue that has been addressed by recent research. Due to advances in numerical techniques, it is now possible to numerically investigate fully relativistic MHD turbulence (e.g. Zrake and MacFadyen 2012).

11.3.1 Relativistic Force-Free MHD Turbulence

Due to its numerical and theoretical simplicity, MHD turbulence in relativistic force-free regime has been studied first. Relativistic force-free formalism can be used for a system, such as the magnetosphere of a pulsar or a black hole, in which the magnetic energy density is much larger than that of matter. In this case, the Alfvén speed approaches the speed of light, and we need relativity to describe the physics of the system. If we take the flat geometry, the relativistic MHD equations

$$\partial_\mu(\rho u^\mu) = 0, \tag{11.12}$$

$$\partial_\mu T^{\mu\nu} = 0, \tag{11.13}$$

$$\partial_t \mathbf{B} = \nabla \times (\mathbf{v} \times \mathbf{B}), \tag{11.14}$$

$$\nabla \cdot \mathbf{B} = 0, \tag{11.15}$$

where u^μ is the fluid four velocity and $T^{\mu\nu}$ is the stress-energy tensor of the fluid and the electromagnetic field, reduce to

$$\frac{\partial \mathbf{Q}}{\partial t} + \frac{\partial \mathbf{F}}{\partial x^1} = 0, \tag{11.16}$$

where

$$\mathbf{Q} = (S_1, S_2, S_3, B_2, B_3), \tag{11.17}$$

$$\mathbf{F} = (T_{11}, T_{12}, T_{13}, -E_3, E_2), \tag{11.18}$$

$$T_{ij} = -(E_i E_j + B_i B_j) + \frac{\delta_{ij}}{2}(E^2 + B^2), \tag{11.19}$$

$$\mathbf{S} = \mathbf{E} \times \mathbf{B}, \tag{11.20}$$

$$\mathbf{E} = -\frac{1}{B^2}\mathbf{S} \times \mathbf{B}. \tag{11.21}$$

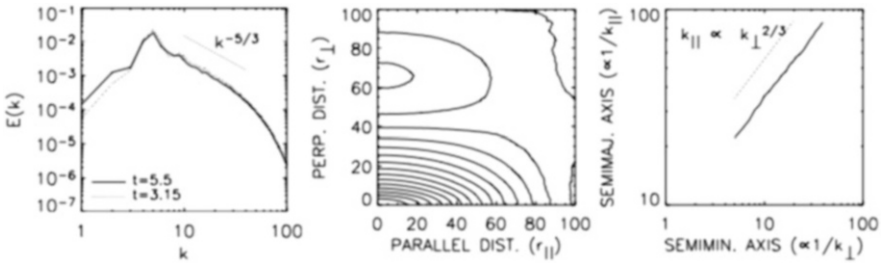

Fig. 11.3 Simulation of decaying relativistic force-free MHD turbulence. (*Left*) Energy spectrum is compatible with a Kolmogorov one. (*Middle*) Eddy shapes, represented by contours, show scale-dependent anisotropy: smaller eddies are more elongated. (*Right*) The anisotropy of eddy shape follows a Goldreich-Sridhar type anisotropy. Reproduced from Cho (2005) by permission of the AAS

Here, **E** is the electric field, **S** is the Poynting flux vector, and we use units such that the speed of light and π do not appear in the equations (see Komissarov 2002). After solving equations along x^1 direction, we repeat similar procedures for x^2 and x^3 directions with appropriate rotation of indexes.

Scaling relations for relativistic Alfvénic MHD turbulence were first derived by Thompson and Blaes (1998) and were numerically tested by Cho (2005). Cho (2005) performed a numerical simulation of a decaying relativistic force-free[3] MHD turbulence with numerical resolution of 512^3 and calculated energy spectrum and anisotropy of eddy structures. At the beginning of the simulation, only Alfvén modes are present and the condition for critical balance, $\chi \equiv (bk_\perp)/(B_0 k_\parallel) \sim 1$, is satisfied (see Cho 2005, 2014 for heuristic discussions on the critical balance in relativistic force-free MHD turbulence). The left panel of Fig. 11.3 shows energy spectrum of magnetic field at two different times. Although only large-scale (i.e. small k) Fourier modes are excited at t=0 (not shown), cascade of energy produces small scale (i.e. large k) modes at later times. After $t \sim 3$, the energy spectrum decreases without changing its slope. The spectrum at this stage is very close to a Kolmogorov spectrum:

$$E(k) \propto k^{-5/3}. \tag{11.22}$$

Contours in the middle panel of Fig. 11.3 shows shapes of eddies revealed by the second-order structure function of magnetic field. Note that the shape of eddies is measured in a local frame, which is aligned with the local mean magnetic field (see Cho et al. 2002; Cho and Vishniac 2000; Kowal and Lazarian 2010, for details). The contour plot clearly shows existence of scale-dependent anisotropy: smaller eddies are more elongated. The relation between the semi-major axis ($\sim l_\parallel \sim 1/k_\parallel$) and the

[3]One can obtain the force-free condition from Maxwell's equations and the energy-momentum equation: $\partial_\mu T^{\nu\mu}_{(f)} = -F_{\nu\mu} J^\mu = 0$. Here, $F^{\nu\mu}$ is the electromagnetic field tensor.

semi-minor axis ($\sim l_\perp \sim 1/k_\perp$) of the contours fits very well the Goldreich-Sridhar type anisotropy:

$$k_\parallel \propto k_\perp^{2/3} \tag{11.23}$$

(see the right panel of Fig. 11.3). All these results are consistent with the theoretical predictions in Thompson and Blaes (1998). A driven turbulence simulation in Cho (2014) also confirms the scaling relations.

Although the similarity between relativistic and non-relativistic Alfvénic turbulences may not be so surprising because the conditions for critical balance are identical, it has many astrophysical implications. So far, we do not fully understand turbulent processes in extremely relativistic environments, such as black hole/pulsar magnetospheres or gamma-ray bursts. The close similarities between extremely relativistic and non-relativistic Alfvénic turbulences enable us to understand the physical processes, e.g., reconnection, particle acceleration, etc., in such media better.

Due to the similarity, it is also possible that we can test non-relativistic theories using relativistic turbulence simulations. For example, Cho and Lazarian (2014) performed numerical simulations of imbalanced relativistic force-free MHD turbulence. The results of a simulation for 512^3 resolution is presented in Fig. 11.4, in which the energy injection rate for Alfvén waves moving in one direction (dominant waves) is 4 times larger than that for waves moving in the other direction (sub-dominant waves). The left panel of Fig. 11.4 shows that, even though the ratio of the energy injection rates is about $\sim$4, the ratio of the energy densities is about $\sim$100. The middle panel of the figure shows that the spectrum for the dominant waves is a bit steeper than a Kolmogorov spectrum, while that for the sub-dominant waves is a bit shallower. The right panel of the figure shows that the anisotropy of the dominant waves is a bit weaker than the Goldreich-Sridhar type anisotropy, while that of the

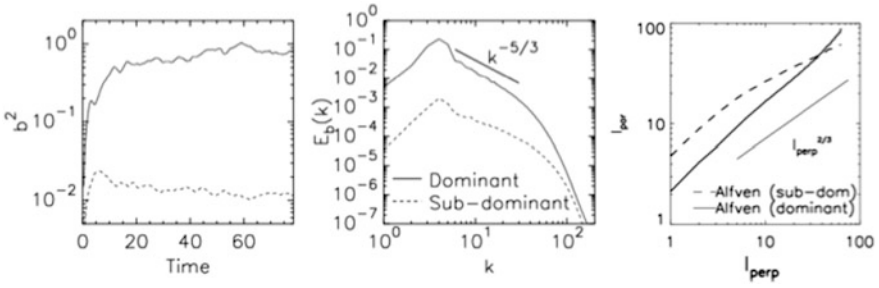

Fig. 11.4 Simulation of imbalanced relativistic force-free MHD turbulence. (*Left*) About a factor of four difference in energy injection rates results in a huge imbalance in energy densities. (*Middle*) The spectra for the dominant and the sub-dominant waves have different slopes: the dominant waves have a steeper spectrum. (*Right*) The degrees of anisotropy for the dominant and the sub-dominant waves are different: the dominant waves have a weaker anisotropy. Reproduced from Cho and Lazarian (2014) by permission of the AAS

sub-dominant waves is a bit stronger. All these results are consistent with the model of Beresnyak and Lazarian (2008) for non-relativistic Alfvénic MHD turbulence.

11.3.2 Fully Relativistic MHD Turbulence

Fully relativistic MHD turbulence has been studied since 2009 (Zhang et al. 2009; Inoue et al. 2011; Beckwith and Stone 2011; Zrake and MacFadyen 2012, 2013; Garrison and Nguyen 2015, see also Radice and Rezzolla 2013, for non-magnetized turbulence). The results in Zrake and MacFadyen (2012, 2013) for the mean lab-frame Lorentz factor of $\sim$1.67 and numerical resolutions of up to 2048^3 confirm that there exists an inertial sub-range of relativistic velocity fluctuations with a $-5/3$ spectral index. They also found that intermittency based on the scaling exponents of the longitudinal velocity structure functions follows the She and Leveque (1994) model fairly well. On the other hand, simulations for unmagnetized relativistic turbulence with average Lorentz factors up to $\sim$1.7 revealed that relativistic effects enhance intermittency, so that the scaling exponents for high-order structure functions deviate from the prediction of the She-Leveque model significantly (Radice and Rezzolla 2013).

We note that the decomposition of the relativistic MHD cascade into fundamental MHD modes has not been performed yet. The corresponding study in Cho and Lazarian (2002, 2003) and Kowal and Lazarian (2010) provided the framework for considering the separate Alfvénic, slow and fast mode cascades. We, however, expect that in analogy with what we already learned about the MHD turbulence, the results for relativistic and non-relativistic cases will not be much different.

11.4 Turbulent MHD Reconnection

11.4.1 Sweet-Parker Model and Its Generalization to Turbulent Media

The model of turbulent reconnection in LV99 generalizes the classical Sweet-Parker one (Parker 1957; Sweet 1958).[4] In the latter, two regions with uniform *laminar* magnetic fields are separated by a thin current sheet. The speed of reconnection is given roughly by the resistivity divided by the sheet thickness, i.e.

$$V_{rec1} \approx \eta/\Delta. \tag{11.24}$$

[4]The basic idea of the model was first discussed by Sweet and the corresponding paper by Parker refers to the model as "Sweet model".

For *steady state reconnection* the plasma in the current sheet must be ejected from the edge of the current sheet at the Alfvén speed, V_A. Thus the reconnection speed is

$$V_{rec2} \approx V_A \Delta / L_x, \tag{11.25}$$

where L_x is the length of the current sheet, which requires Δ to be large for a large reconnection speed. As a result, the overall reconnection speed is reduced from the Alfvén speed by the square root of the Lundquist number, $S \equiv L_x V_A / \eta$, i.e.

$$V_{rec,SP} = V_A S^{-1/2}. \tag{11.26}$$

The corresponding Sweet-Parker reconnection speed is negligible in astrophysical conditions as S may be 10^{16} or larger.

It is evident that the Sweet-Parker reconnection should be modified in the presence of turbulence. Figure 11.5 illustrates the modification that takes place. It is evident that the outflow in the turbulent flow is not limited by the microscopic region determined by resistivity, but is determined by magnetic field wandering. Therefore there is no disparity between L_x and Δ, e.g. for transAlfvénic turbulence they can be comparable. Actually, Fig. 11.5 provides the concise illustration of the LV99 model of reconnection.

Adopting that the field wondering is the cause of the reconnection zone opening up, it is easy to calculate Δ in the regime when the turbulence injection scale L_i is less than L_x. Substituting $l_\parallel = L_i$ in Eq. (11.10) one finds that the perpendicular extend of the eddy at the injection scale is $L_i M_A^2$. The transverse contributions from different eddies at the injection scale are not correlated and therefore Δ is a result of random walk with a step of $L_i M_A^2$. The number of the steps along L_x is L_x / L_i and thus

$$\Delta \approx \left(\frac{L_x}{L_i} \right)^{1/2} L_i M_A^2, \quad L_i < L_x, \tag{11.27}$$

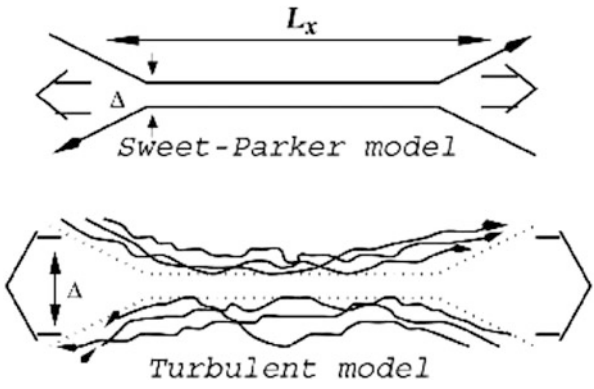

Fig. 11.5 *Upper plot*: Sweet-Parker model of reconnection. The outflow is limited to a thin width δ, which is determined by Ohmic diffusivity. The other scale is an astrophysical scale $L_x \gg \delta$. Magnetic field lines are laminar. Modified from Lazarian et al. (2004). Reproduced by permission of the AAS

and therefore

$$v_{rec,LV99} \approx V_A \left(\frac{L_i}{L_x}\right)^{1/2} M_A^2, \quad L_i < L_x, \tag{11.28}$$

which coincides with the LV99 result in this limit.

The result for $L_i > L_x$ can be obtained using the concept of Richardson dispersion following the approach in Eyink et al. (2011). Richardson diffusion/dispersion can be illustrated with a simple hydrodynamic model. Consider the growth of the separation between two particles $dl(t)/dt \sim v(l)$, which for Kolmogorov turbulence is $\sim \alpha_t l^{1/3}$, where α_t is proportional to the energy cascading rate, i.e. $\alpha_t \approx V_L^3/L$ for turbulence injected with superAlfvénic velocity V_L at the scale L. The solution of this equation is

$$l(t) = [l_0^{2/3} + \alpha_t (t - t_0)]^{3/2}, \tag{11.29}$$

which at late times leads to Richardson dispersion or $l^2 \sim t^3$ compared with $l^2 \sim t$ for ordinary diffusion. This superdiffusive and even superballistic behavior, i.e. l^2 increases faster than t^2, can be easily understood if one takes into account that for points separated by the distance less than turbulence injection scale, the larger the separation of the points the larger the eddies that induce the point separation.

Both terms "diffusion and dispersion" can be used interchangeably, but keeping in mind that the Richardson process results in superdiffusion (see Lazarian and Yan 2014, and references therein) we feel that it is advantageous to use the term "dispersion".

We again start with the Sweet-Parker reconnection. There magnetic field lines are subject to Ohmic diffusion. The latter induces the mean-square distance across the reconnection layer that a magnetic field-line can diffuse by resistivity in a time t given by

$$\langle y^2(t) \rangle \sim \lambda t. \tag{11.30}$$

where $\lambda = c^2/(4\pi\sigma)$ is the magnetic diffusivity. The field lines are advected out of the sides of the reconnection layer of length L_x at a velocity of order V_A. Therefore, the time that the lines can spend in the resistive layer is the Alfvén crossing time $t_A = L_x/V_A$. Thus, field lines that can reconnect are separated by a distance

$$\Delta = \sqrt{\langle y^2(t_A) \rangle} \sim \sqrt{\lambda t_A} = L_x/\sqrt{S}, \tag{11.31}$$

where S is Lundquist number. Combining Eqs. (11.25) and (11.31) one gets again the well-known Sweet-Parker result, $v_{rec} = V_A/\sqrt{S}$.

The difference with the turbulent case is that instead of Ohmic diffusion one should use the Richardson one (Eyink et al. 2011). In this case the mean squared separation of particles is $\langle |x_1(t) - x_2(t)|^2 \rangle \approx \epsilon t^3$, where t is time, ϵ is the energy

cascading rate and $\langle \ldots \rangle$ denote an ensemble averaging (see Kupiainen 2003). For subAlfvénic turbulence $\epsilon \approx u_L^4/(V_A L_i)$ (see LV99) and therefore analogously to Eq. (11.31) one can write

$$\Delta \approx \sqrt{\epsilon t_A^3} \approx L_x (L_x/L_i)^{1/2} M_A^2, \tag{11.32}$$

where it is assumed that $L_x < L_i$. Combining Eqs. (11.25) and (11.32) one obtains

$$v_{rec,LV99} \approx V_A (L/L_i)^{1/2} M_A^2, \quad L_i > L_x, \tag{11.33}$$

that together with Eq. (11.28) provides the description of the reconnection for turbulent reconnection in the presence of sub-Alfvénic turbulence. Naturally, LV99 can be easily generalized for the case of superAlfvénic turbulence.

11.4.2 Temporal and Spatial Richardson Diffusion

We would like to stress that two formally different ways of obtaining LV99 reconnection rates have clear physical connection. In both cases we are dealing with magnetic field lines stochasticity, but the case of Richardson dispersion considers the evolution of magnetic fields lines in turbulent fluids, while magnetic field wandering presents the spatial distribution of magnetic field lines for a given moment of time. In a sense the dispersion of magnetic field lines that was quantified in LV99[5] presents the Richardson dispersion in space.

While we employed the Alfvénic incompressible motions to describe the physics of Richardson dispersion, the process also takes place in compressible MHD turbulence. This is due to the fact, that Alfvénic cascade is a part and parcel of compressible MHD turbulence (Cho and Lazarian 2003). We can, however, note parenthetically that even for turbulence of shocks, i.e. Burgers' turbulence, the phenomenon of Richardson diffusion is present (Eyink et al. 2013).

11.4.3 Turbulent Reconnection and Violation of Magnetic Flux Freezing

Magnetic flux freezing is a concept that is widely used in astrophysics. It is based on the Alfvén theorem, the proof of which is rather trivial for perfectly

[5]The magnetic field wandering was discussed for an extended period to explain the diffusion of cosmic rays perpendicular to the mean magnetic field, but, as was shown in Lazarian and Yan (2014), those attempts employed scalings that were erroneous even for the hypothetical Kolmogorov turbulence of magnetic fields, for which they were developed.

conductive laminar fluids. For laminar fluids of finite conductivity, the violation of Alfvén theorem becomes negligible as fluid conductivity increases. This, however, is not true for turbulent fluids. Turbulent reconnection as we discussed above induces reconnection diffusion. Mathematically the failure of the flux freezing is discussed in Lazarian et al. (2015a). The numerical proof based on demonstrating of Richardson dispersion of magnetic field lines is in Eyink et al. (2013).

11.4.4 Turbulent Reconnection in Compressible Media

Two new effects become important in compressible media as compared to its incompressible counterpart that we discussed above. First of all, the density of plasmas changes in the reconnection region and therefore the mass conservation takes the form

$$\rho_i v_{rec,comp} L_x = \rho_s V_A \Delta. \tag{11.34}$$

where ρ_i is the density of the incoming plasma far from the reconnection layer and ρ_s is the density of plasma in the reconnection layer.

In addition, the derivation of the magnetic field wandering rate that we discussed above was performed appealing to the Alfvénic component of MHD turbulence. Numerical simulations in Cho and Lazarian (2002, 2003) demonstrated that the Alfvénic component develops independently from the compressible MHD components in agreement with theoretical considerations in GS95. Therefore one can estimate the amplitude in incompressible Alfvénic perturbations by subtracting the contribution of the slow and fast modes from the total energy of the turbulent motions

$$u_L^2 \approx V_{total}^2 - V_{comp}^2. \tag{11.35}$$

Using Eq. (11.34) and Eqs. (11.27) and (11.32) one can generalize the expression for the reconnection rate [compare to Eqs. (11.33), (11.28)]:

$$v_{rec,comp} \approx V_A \frac{\rho_i}{\rho_s} \min\left[\left(\frac{L_i}{L_x}\right)^{1/2}, \left(\frac{L_x}{L_i}\right)^{1/2}\right] \frac{V_{total}^2 - V_{comp}^2}{V_A^2}. \tag{11.36}$$

If our turbulence driving is incompressible, another form of presenting the reconnection rate is useful if one takes into account the relation between the Alfvénic modes and the generated compressible modes obtained in Cho and Lazarian (2002)

$$\frac{V_{comp}^2}{V_{Alf}^2} \approx C_1 \frac{v_{inj}}{V_{Alf}}, \tag{11.37}$$

where C_1 is a coefficient which depends on the media equation of state. Taking into account the relation between the injection velocity and the resulting velocity in weak turbulence given by Eq. (11.37), one can rewrite Eq. (11.36) as

$$v_{rec,comp} \sim V_A \frac{\rho_i}{\rho_s} \min\left[\left(\frac{L_i}{L_x}\right)^{1/2}, \left(\frac{L_x}{L_i}\right)^{1/2}\right] \frac{v_{inj}(1 - C_1(v_{inj}/V_A))}{V_A}. \quad (11.38)$$

11.4.5 Turbulent Reconnection in Partially Ionized Gas

Partially ionized gas is presents in a complex medium where the ions co-exist with neutrals. Complex processes of ionization and recombination are taking place in turbulent partially ionized gas. However, in view of turbulent reconnection, the major feature of the partially ionized gas is that the turbulent motions in partially ionized gas are subject to damping which arises from both neutral-ion collisions and the viscosity associated with neutrals (see Lazarian et al. 2004; Xu et al. 2015, for a detailed discussion of the latter process). Figure 11.6 illustrates the damping of Alfvén modes in a typical environment of molecular cloud. The corresponding damping scales are substantially larger than in the fully ionized gas, which poses the question of how turbulent reconnection is modified.

The reconnection in partially ionized gas was discussed on the basis of the Richardson dispersion in Lazarian et al. (2015). The essence of the approach is that on the scales at which Richardson dispersion is applicable, the magnetic fields are not frozen in and therefore magnetic reconnection is fast. Therefore the issue at

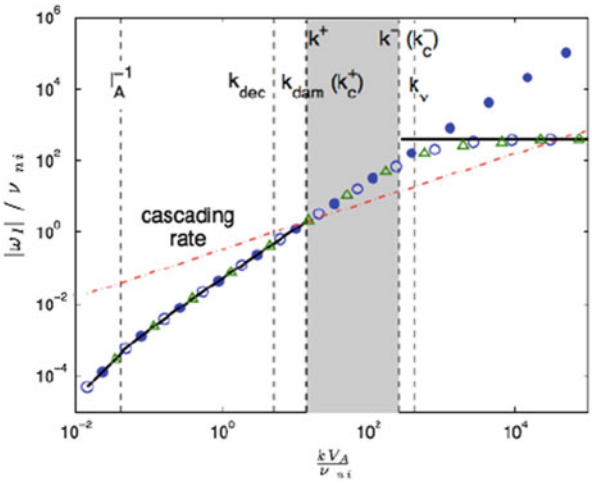

Fig. 11.6 Damping of Alfvénic turbulence in low beta partially ionized gas. The damping of turbulence happens when the rate of damping (*solid line*) intersects the *dashed line* corresponding to the cascading rate. From Xu et al. (2015)

which scale the reconnection is fast boils down to what is the scale of the onset of the Richardson dispersion description for the magnetic field lines.

It is natural to identify the magnetic field lines as subject to the Richardson dispersion as soon as the separation of the lines exceeds the size of the smallest turbulence eddy, i.e. the size of the critically damped eddy. In partially ionized gas the ion-neutral damping or viscosity determines this size. As the eddies are anisotropic, we would associate the damping scale with the parallel scale of the eddies $l_{\parallel,crit}$. Due to the shear induced by perpendicular motions associated with these eddies the magnetic field lines which are initially separated by r_{init} are spreading further and further from each other. The rate of line dr/dl is proportional to the $r/l_{\perp,crit}$ and this provides an exponential rate of separation. It is easy to show that separation becomes equal to $l_{\perp,crit}$ after the field lines are traced over a distance of

$$L_{RR} \approx l_{\parallel,crit} \ln(l_{\perp,crit}/r_{init}), \tag{11.39}$$

which was introduced by Rechester and Rosenbluth (1978) in the framework of "turbulence" with a single scale of driving. We follow Narayan and Medvedev (2003) and Lazarian (2006) associating this scale with the smallest turbulent eddies (cf. Chandran et al. 2000), as the smallest scales induce the largest shear. For r_{init} it is natural to associate this length with the separation of the field lines arising from the action of Ohmic resistivity on the scale of the critically damped eddies

$$r_{init}^2 = \eta l_{\parallel,crit}/V_A, \tag{11.40}$$

where η is the Ohmic resistivity coefficient. Taking into account Eq. (11.40) and that

$$l_{\perp,crit}^2 = \nu l_{\parallel,crit}/V_A, \tag{11.41}$$

where ν is the viscosity coefficient, one can rewrite Eq. (11.39) as:

$$L_{RR} \approx l_{\parallel,crit} \ln Pt, \tag{11.42}$$

where $Pt = \nu/\eta$ is the Prandtl number. This means that when the current sheets are much longer than L_{RR}, magnetic field lines undergo Richardson dispersion and according to Eyink et al. (2011) the reconnection follows the laws established in LV99. At the same time on scales less than L_{RR} magnetic reconnection may be slow.[6]

[6]Incidentally, this can explain the formation of density fluctuations on scales of thousands of AU, that are observed in the ISM.

Additional effects, e.g. diffusion of neutrals perpendicular to magnetic field may influence the reconnection rate (see Vishniac and Lazarian 1999). Indeed, ions can recombine in the reconnection zone and this can allow the matter to outflow as a flow of neutrals. This outflow is not directly constrained by magnetic field and therefore Vishniac and Lazarian (1999) obtained large reconnection rates even for laminar magnetic fields provided that magnetic fields are perfectly anti-parallel and astrophysical medium is pure ionized hydrogen (see also a numerical study by Heitsch and Zweibel 2003). The reconnection rates plummet in the presence of the guide field and heavy ions ("metals") which are subject to ionization by the ambient field. Therefore the effect of "ambipolar reconnection" is of marginal importance for most of the settings involving realistically turbulent media (see Lazarian et al. 2004)

11.5 Testing Turbulent Reconnection

Figure 11.7 illustrates results of numerical simulations of turbulent reconnection with turbulence driven using wavelets in Kowal et al. (2009) and in real space in Kowal et al. (2012).

As we show below, simulations in Kowal et al. (2009, 2012) confirmed LV99 prediction that turbulent reconnection is fast, i.e. it does not depend on resistivity, and provided a good correspondence with the LV99 prediction on the injection power.

In the simulations subAlfvénic turbulence was induced, i.e. with the energy of kinetic motions less than the energy of magnetic field. Indeed, according to

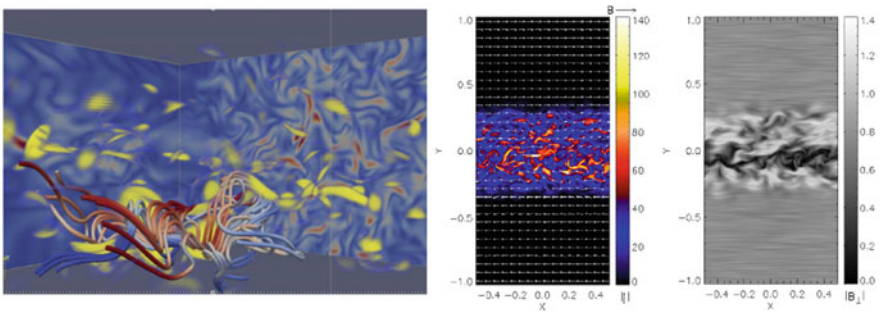

Fig. 11.7 Visualization of reconnection simulations in Kowal et al. (2009, 2012). *Left panel*: magnetic field in the reconnection region. *Central panel*: current intensity and magnetic field configuration during stochastic reconnection. The guide field is perpendicular to the page. The intensity and direction of the magnetic field is represented by the length and direction of the *arrows*. The *color bar* gives the intensity of the current. *Right panel*: representation of the magnetic field in the reconnection zone with textures. Reproduced from Kowal et al. (2009) by permission of the AAS

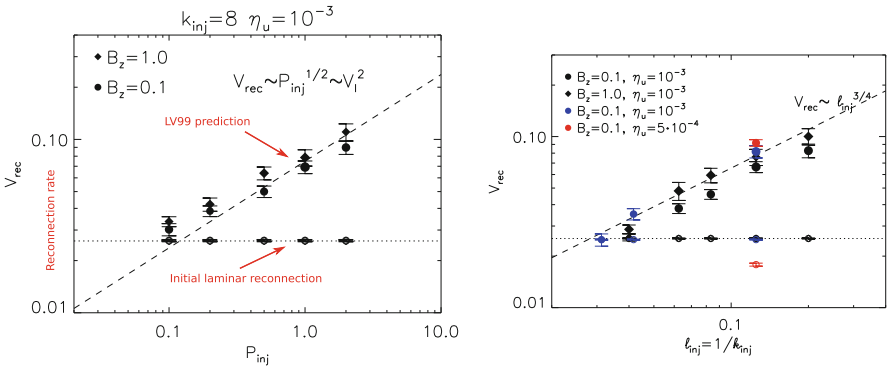

Fig. 11.8 *Left panel*: the dependence of the reconnection velocity on the injection power for different simulations with different drivings. The predicted LV99 dependence is also shown. P_{inj} and k_{inj} are the injection power and scale, respectively, B_z is the guide field strength, and η_u is the value of uniform resistivity coefficient. *Right panel*: the dependence of the reconnection velocity on the injection scale. Reproduced from Kowal et al. (2012)

Eq. (11.28) $v_{rec,LV99} \sim u_l^2$. At the same time for the weak turbulence the injected power

$$P_{inj} \sim v_{inj}^2 / \Delta t_{inj} \tag{11.43}$$

is equal to the cascading power given by Eq. (11.6). This provides a relation

$$v_{rec,LV99} \sim u_l^2 \sim v_{inj} \sim P_{inj}^{1/2}. \tag{11.44}$$

The corresponding dependence is shown in Fig. 11.8, left panel.

We also see some differences from the idealized theoretical predictions. For instance, the injection of energy in LV99 is assumed to happen at a given scale and the inverse cascade is not considered in the theory. Therefore, it is not unexpected that the measured dependence on the turbulence scale differs from the predictions. In fact, it is a bit more shallow compared to the LV99 predictions (see Fig. 11.8, right panel).

The left panel of Fig. 11.9 shows the dependence of the reconnection rate on explicit uniform viscosity obtained from the isothermal simulations of the magnetic reconnection in the presence of turbulence (Kowal et al. 2012). The open symbols show the reconnection rate for the laminar case when there was no turbulence driving, while closed symbols correspond to the mean values of reconnection rate in the presence of saturated turbulence. All parameters in those models were kept the same, except the uniform viscosity which varied from 10^{-4} to 10^{-2} in the code units. We believe, that this dependence can be explained as the effect of the finite inertial range of turbulence, of the effect of energy balance affected by viscosity or boundary conditions. For an extended range of motions, LV99 does not predict any

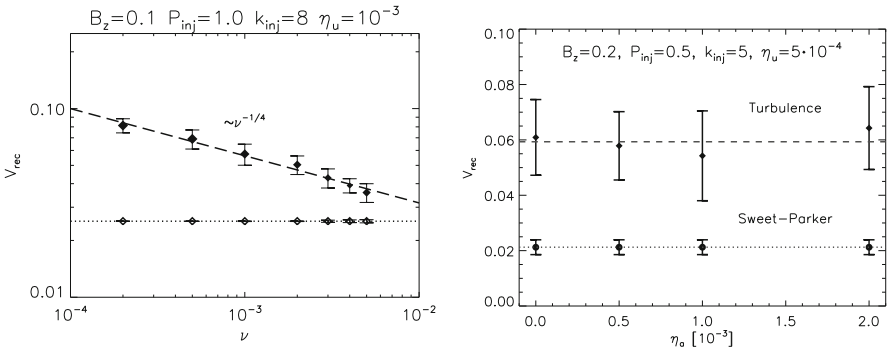

Fig. 11.9 *Left panel*: the dependence of the reconnection velocity on uniform viscosity in the 3D isothermal models of Sweet-Parker reconnection (*open symbols*) and reconnection enhanced by the presence of turbulence (*closed symbols*) from Kowal et al. (2012). *Right panel*: the reconnection rate in models with anomalous resistivity for Sweet-Parker case (*filled circles*) and in the presence of turbulence (*filled diamonds*). We observe no dependence of the reconnection rate on the strength of anomalous effects. Reproduced from Kowal et al. (2009)

viscosity dependence, if the dissipation scale lies much below the scale of current sheet. However, for numerical simulations the range of turbulent motions is very limited and any additional viscosity decreases the resulting velocity dispersion and the field wandering thus affecting the reconnection rate.

LV99 predicted that in the presence of sufficiently strong turbulence, plasma effects should not play a role. The accepted way to simulate plasma effects within MHD code is to use anomalous resistivity. The results of the corresponding simulations are shown in the right panel of Fig. 11.9 and they confirm that the change of the anomalous resistivity does not change the reconnection rate.

As we discussed in Sect. 11.3, the LV99 expressions can be obtained by applying the concept of Richardson dispersion to a magnetized layer. Thus by testing the Richardson diffusion of magnetic field, one also provides tests for the theory of turbulent reconnection. A successful direct testing of the temporal Richardson dispersion of magnetic field lines was performed in Eyink et al. (2013). The study confirmed that magnetic fields are not frozen in highly conducting fluids, as this follows from the LV99 theory.

Within the derivation adopted in LV99 current sheet is broad with individual currents distributed widely within a three dimensional volume and the turbulence within the reconnection region is similar to the turbulence within a statistically homogeneous volume. Numerically, the structure of the reconnection region was analyzed by Vishniac et al. (2012) based on the numerical work by Kowal et al. (2009). The results support LV99 assumptions about reconnection region being broad, the magnetic shear is more or less coincident with the outflow zone, and the turbulence within it is broadly similar to turbulence in a homogeneous system.

Another prediction that follows from LV99 theory is that the turbulence required for the process of turbulent reconnection can be generated by the process of

turbulent reconnection. In particular, a theory of reconnection flares in low β (highly magnetized) plasmas was discussed in Lazarian and Vishniac (2009), while the expressions presenting reconnection rates in high β plasmas are presented in Lazarian et al. (2015).

11.6 Towards Theory of Turbulent Relativistic Reconnection

Recently, it has been recognized that the relativistically magnetized plasma, so-called Poynting-dominated plasma, plays an important role for many high energy astrophysical phenomena with relativistic outflows, such as pulsar wind nebulae, relativistic jets, and gamma-ray bursts. Those phenomena are believed to have a strongly magnetized compact object with rapid spin which naturally explains collimated jets or magnetized winds. The energy stored in the magnetic field initially needs to be converted into kinetic and radiation energy to explain the observations. However, the usual collisional magnetic field dissipation fails to explain the necessary dissipation rate. Relativistic turbulent magnetic reconnection is considered to be one of the most probable mechanism for the magnetic dissipation, and we review our recent development of the relativistic version of turbulent reconnection theory reported in Takamoto et al. (2015).

We have seen that the relativistic balanced MHD turbulence in terms of theory is a clone of the GS95 model. We noticed that the imbalanced Alfvénic turbulence simulations provide very similar results in relativistic and non-relativistic cases.[7] As properties of Alfvénic turbulence dominate the LV99 reconnection, one can expect that the LV99 theory can be reformulated in terms of relativistic physics. However, instead of reformulating LV99 in terms of relativistic variables, for the time being, we shall use the theory in its non-relativistic formulation and seek its correspondence with the simulations of the relativistic turbulent reconnection.

For instance, it is obvious that effects of compressibility are likely to be more important in relativistic reconnection compared to its non-relativistic counterpart. This is because in Poynting-flux-dominated plasmas the magnetic field can induce a relativistic velocity in current sheets but the Alfvén velocity is limited by the light velocity, which allows the induced turbulence to be trans-Alfvénic one. Therefore, we use our results from Sect. 11.5, in particular Eq. (11.36).

The comparison between the theoretical expectations and numerical simulations was performed in Takamoto et al. (2015). The simulation is calculated using the relativistic resistive MHD code developed in Takamoto and Inoue (2011). The initial current sheet is assumed to be the relativistic Harris current sheet with uniform temperature $k_B T/mc^2 = 1$ where k_B, T, m, c are the Boltzmann constant, temperature, rest mass, and light velocity, respectively. The relativistic ideal gas is

[7] Thus we can expect that the theory of imbalanced relativistic MHD can be also very similar to Beresnyak and Lazarian (2008) model.

assumed, $h = 1 + p/\rho c^2 \Gamma/(\Gamma - 1)$ with $\Gamma = 4/3$ where h, p, ρ are the specific enthalpy, gas pressure, rest mass density. Following Kowal et al. (2009), we used the open boundary in the direction perpendicular to the current sheet and parallel to the magnetic field, which corresponds to x and z direction. The periodic boundary is used along the third direction. The guide field is basically omitted other than the runs used for obtaining Fig. 11.13. Turbulence is driven by injecting a randomly determined turbulent flow every fixed time steps. The turbulent flow has a flat kinetic energy spectrum and a characteristic wavelength is distributed around sheet width scale. More detailed setup is provided in Takamoto et al. (2015). To quantify the reconnection rate the approach based on measurements of the change of the absolute value of magnetic flux in Kowal et al. (2009) was used. In the calculations, we investigated turbulent reconnection in plasmas with the magnetization parameter from 0.04 (matter dominated) to 5 (Poynting dominated). Note that we assume a relativistic temperature, so that the plasma is always relativistic.

Figure 11.10 illustrates the magnetic field structure and gas pressure profile obtained by the simulations in Takamoto et al. (2015). The magnetization parameter is $\sigma = 5$ and there is no guide field. The lines describe the magnetic field, and the background plane shows the gas pressure profile in units of the upstream magnetic pressure. It indicates the turbulence induces reconnecting points around the central sheet region. It also shows the magnetic field is wandering similarly to the non-relativistic case, which is responsible for determining the size of exhaust region and reconnection rate in LV99 theory. Note that the injected turbulence is sub-Alfvénic velocity but it can cause the stochastic magnetic field lines even in the case of Poynting-dominated plasma whose Alfvén velocity is relativistic.

Figure 11.11 (left panel) illustrates that in the process of relativistic magnetic reconnection the density inside the sheet changes substantially as the injected

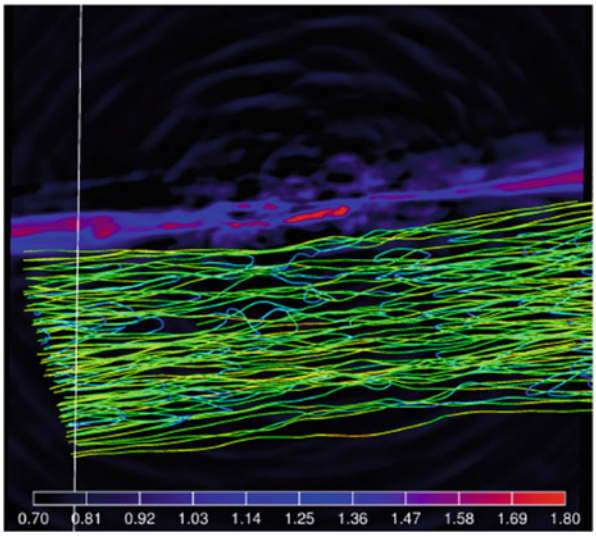

Fig. 11.10 Visualization of relativistic reconnection simulations in the case of the magnetization parameter $\sigma = 5$ from Takamoto et al. (2015). The *lines* describe the magnetic field line relating magnetic reconnection. The *background plane* shows the gas pressure profile in the unit of the upstream magnetic pressure. Similarly to the non-relativistic case, the magnetic field lines are wandering due to the injected turbulence, even in a Poynting-dominated plasma, which results in a wider reconnection exhaust region and large reconnection rate

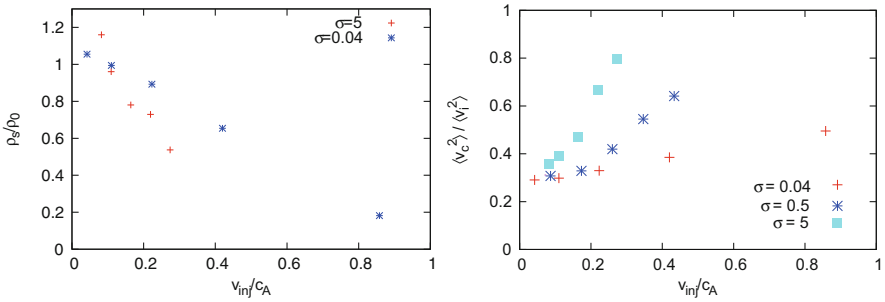

Fig. 11.11 *Left panel*: variations of plasma density in relativistic reconnection. *Right panel*: generation of compressible modes in relativistic reconnection. From Takamoto et al. (2015)

turbulent energy increases comparing with the energy flux of the reconnection outflow. This is expected and is explained by simple arguments in Takamoto et al. (2015). Indeed, the conservation of energy flux can be written as:

$$\rho_{\rm i} h_{\rm i} c^2 \gamma_{\rm i}^2 \left(1+\sigma_{\rm i}\right) v_{\rm i} L \;= \rho_{\rm s} h_{\rm s} c^2 \gamma_{\rm s}^2 \left(1+\sigma_{\rm s}\right) v_{\rm s} \delta, \tag{11.45}$$

where ρ, h, γ are the mass density, specific enthalpy, and Lorentz factor, respectively. c is the light velocity, and $\sigma \equiv B^2/4\pi\rho h c^2 \gamma^2$ is the magnetization parameter. The subscript i, s means the variables defined in the inflow and outflow region, respectively. If we inject turbulence externally, this can be written as an input of turbulent energy into sheet, so that Eq. (11.45) becomes

$$\begin{aligned}\rho_{\rm i} h_{\rm i} c^2 \gamma_{\rm i}^2 \left(1+\sigma_{\rm i}\right) v_{\rm i} L + (\rho_{\rm in} + B_0^2)\epsilon_{\rm inj} l_x l_z &= \rho_{\rm s} h_{\rm s} c^2 \gamma_{\rm s}^2 \left(1+\sigma_{\rm s}\right) v_{\rm s} \delta \\ &= \rho_{\rm s} h_{\rm s} c^2 \gamma_{\rm s}^2 \left(1+\sigma_{\rm s}\right) v_{\rm s} \sqrt{\epsilon t_A^3}, \end{aligned} \tag{11.46}$$

where ϵ is the energy injection rate of the turbulence, and we used $\mathbf{E}_{\rm turb}^2 = (\mathbf{v}_{\rm turb} \times \mathbf{B}_0)^2 \sim B_0^2 v_{\rm turb}^2/2$. l_x, l_z are the injection size along x and z axis and Eq. (11.32) is used in the second line. Note that the outflow energy flux is measured at the boundary of the reconnection outflow, and we assumed all the injected energy into the sheet is ejected as the outflow flux along the sheet, that is, the escaping components as compressible modes is assumed at least less than the Alfvénic component. Equation (11.46) shows that when the injected turbulence, ϵ, is small, the second term in the left-hand side of the equation can be neglected, and the inflow velocity $v_{\rm i}$ increases as $\delta \propto \sqrt{\epsilon}$. However, if the injected turbulence is sufficiently strong, the neglected term increases as ϵ, and becomes comparable to the outflow flux which increases more slowly as $\epsilon^{1/2}$. In this case, combining with the conservation of mass,

$$\rho_{\rm i} \gamma_{\rm i} v_{\rm i} L = \rho_{\rm s} \gamma_{\rm s} v_{\rm s} \delta, \tag{11.47}$$

equation (11.46) gives

$$\frac{\rho_{\rm s}}{\rho_{\rm i}} = \frac{1}{(1+\sigma-\gamma_{\rm s})\gamma_{\rm s}} \left[2\sigma\gamma_{\rm s}^2 - (1+\sigma)\frac{\epsilon_{\rm inj}}{\sqrt{\epsilon t_A^3}}\frac{l_x l_z}{v_{\rm s} c^2} \right]. \tag{11.48}$$

This shows that the density ratio decreases as $\epsilon^{1/2} \propto v_{\rm inj}$, indicated as Fig. 11.11 (left panel). The change of the matter density is an important factor in expression for the turbulent reconnection rate given by Eq. (11.36).

The other factor that we have to account is the decrease of the energy in Alfvénic turbulence as more energy is getting transferred to compressible modes for highly magnetized plasmas as illustrated by Fig. 11.11 (right panel). Note, that the compressible component is obtained through the Helmholtz decomposition into solenoidal and compressible part rather than through the mode decomposition as in Cho and Lazarian (2002, 2003) or Kowal and Lazarian (2010). The latter procedure has not been adopted for the relativistic turbulence so far. Interestingly, the compressible component increases with the increase of the σ-parameter.[8] All in all, we conjecture that the compressible generalization of LV99 theory, see Eq. (11.38), can provide the description of relativistic reconnection.

Accounting for both effects Takamoto et al. (2015) obtained a good correspondence between the theoretical predictions and numerical results. Figure 11.12 illustrates the dependence of reconnection rate on the strength of the injected turbulence with different magnetization cases. It shows that the maximal reconnection rate increases with the driving intensity [cf. Fig. 11.8 (left panel)] in the sub-Alfvénic Mach number region. This can be basically explained by the law of turbulent reconnection given by LV99. However, as the injected Alfvén Mach number approaches to trans-Alfvénic region, the reconnection rate reaches a maximum value and even decreases with injected power. This is because the injected turbulence becomes compressible and the effect of compressibility should be accounted for (see Sect. 11.4.4). The detailed discussion including the compressibility effects for relativistic reconnection is given in Takamoto et al. (2015).

The guiding field effect is plotted in the left panel of Fig. 11.13. Following Kowal et al. (2009, 2012), we increased the guiding field while fixing the strength of reconnecting magnetic field component, that is, the total σ-parameter increases as increasing the guide field. The figure shows the reconnection rate that marginally depends of the guide field, which is very similar to the non-relativistic results obtained in Kowal et al. (2009, 2012) presented in Fig. 11.8. Thus we conclude that turbulent reconnection in relativistic and non-relativist cases is similar and a compressible generalization of the LV99 theory does reflect the main features of relativistic reconnection.

[8] This may indicates a relation similar to one predicted by Galtier and Banerjee (2011), i.e. that the compressible component is proportional to B_0^2, exists even in relativistic MHD turbulence.

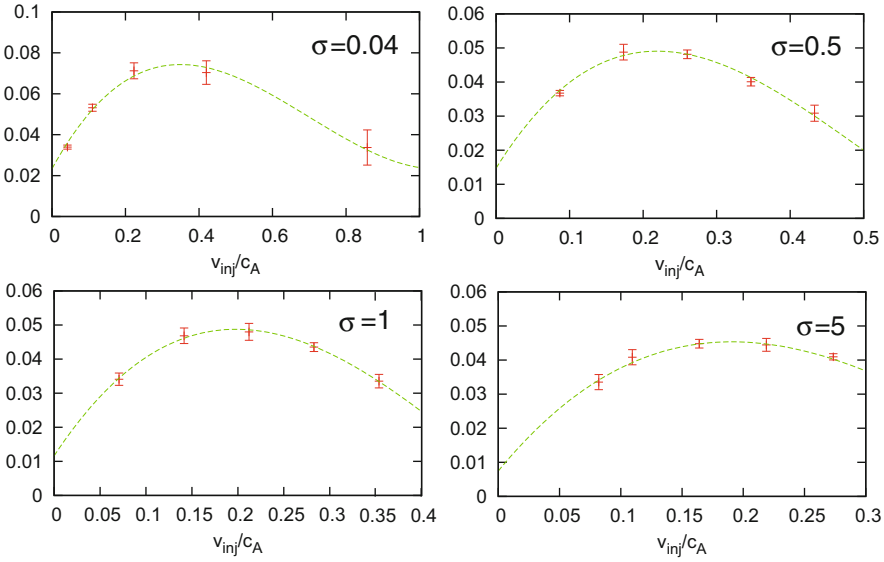

Fig. 11.12 Reconnection rate in terms of various magnetization parameters: $\sigma = 0.04, 0.5, 1, 5$. The *green dashed curves* are the modified turbulent reconnection law taking into account the effect of density decrease and compressible turbulence effects

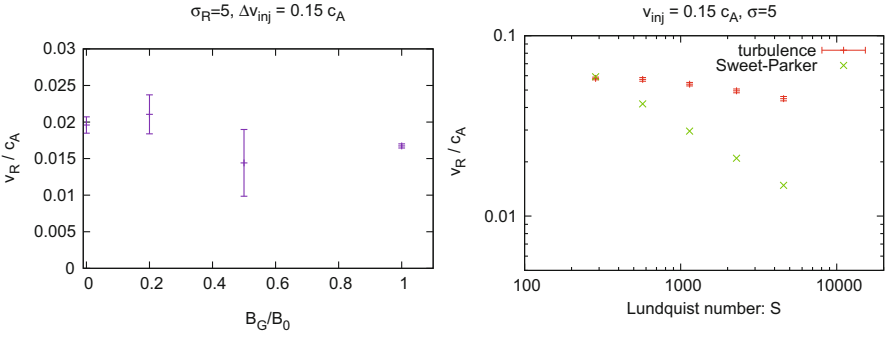

Fig. 11.13 *Left panel*: dependence of the reconnection rate on the guide field. *Right panel*: dependence of the reconnection rates on resistivity. From Takamoto et al. (2015)

The right panel of Fig. 11.13 shows that the reconnection rate does not show dependence on the resistivity. This supports the idea that the turbulent relativistic reconnection is fast.

The obtained results indicate that the reconnection rate can approach $0.3c$ if we assume a sufficient injection scale l, and this is enough to explain most cases of relativistic reconnection (see Lyutikov and Lazarian 2013, for review). Note that obtaining such a rate may be problematic at the MHD scale other than the Petschek

reconnection which is known to exist only when assuming an artificially localized resistivity.[9]

Naturally, there are many important issues that must be studied in relation to turbulent relativistic reconnection and related processes. For instance, it is interesting and important to relate this reconnection with the relativistic analog of Richardson dispersion.

11.7 Reconnection with Self-Generated Turbulence

Turbulence that drives turbulent reconnection is not necessarily pre-existent but can be generated as a result of reconnection. This was discussed in various publications starting with LV99 (see also Lazarian and Vishniac 2009), but it is only with high resolution simulations that it became possible to observe this effect. Simulations by Lapenta (2008) that showed a transfer to fast reconnection in the MHD regime can be interpreted as spontaneous turbulent reconnection. The turbulence generation is seen in PIC simulations (see Karimabadi et al. 2014), incompressible simulations (Beresnyak 2013) and compressible simulations (Oishi et al. 2015). The latter two papers identified the process of reconnection with fast turbulent reconnection.

Below we present results from our calculations in Kowal et al. (2015) where the both open and periodic boundary conditions are adopted. With the open boundary conditions the calculations are performed over several crossing times.

In the reconnection with a laminar configuration, the presence of initial noise in the velocity or magnetic fields results in the development of instabilities of the current sheet layer inducing its deformation and fragmentation. In such situations, we would expect that any deformation of the current sheet layer would grow, fed by the continuous plasma ejection from the local reconnection events pumping more kinetic energy into the surrounding medium. In such a picture the injection scale would be related to the spatial separation of the randomly oriented small "jets" of the outflows from the local reconnection events. Those local outflows are estimated to have speeds comparable to the local Alfvénic speeds, i.e., capable of deforming local field. The corresponding bending of magnetic field lines is presented in Fig. 11.14 in one of the models presented in Kowal et al. (2015). The view from the bottom is shown, with the current sheet being perpendicular to the line of sight. In the initial configuration the magnetic field lines in the upper and bottom half of the domain are antiparallel with a small inclination due to the presence of the guide field. After some time, a turbulent region is developed around the midplane of the box due to the stochastic reconnection taking place there. This turbulent region is characterized by the magnetic line topology change. The lines are bent and twisted in this region, as seen in Fig. 11.14. The color corresponds to the degree of line alignment with

[9] Although collisionless reconnection can also provide fast reconnection rate around $0.3c$, it is still unclear if the collisionless reconnection rate can be applied to the MHD scale.

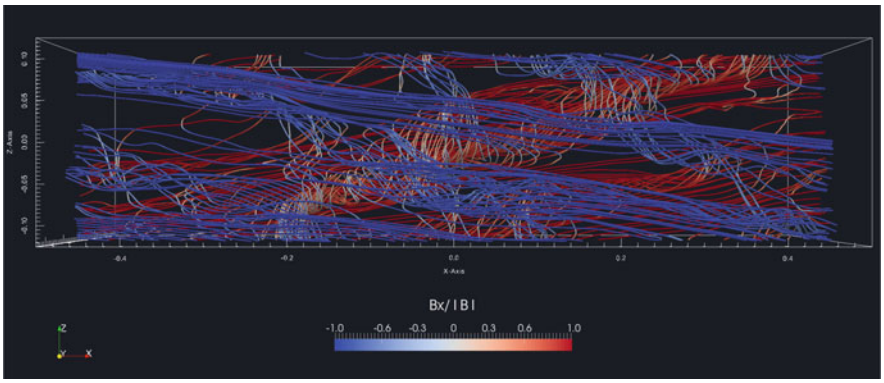

Fig. 11.14 Visualization of the magnetic field lines in the reconnection with self-generated turbulence as seen from the below of the current sheet plane. The *colors* correspond to the line orientation with respect to the X direction with *red* and *blue* being parallel and antiparallel to the X axis, respectively. We can recognize the organized field above and below the reconnection region and strongly turbulent flux tubes within the reconnection region. From Kowal et al. (2015)

−1 (blue) being perfectly antiparallel and 1 (red) being perfectly parallel to the X direction.

In the next figure, Fig. 11.15, we show the velocity power spectra calculated in two different ways for the snapshot shown in Fig. 11.14. The blue line shows the classical power spectrum using the Fourier transform. However, since our domain is not periodic (periodicity is enforced only along the Z direction, otherwise the boundaries are open), the Fourier transform may not be a proper way to obtain the power spectra. Therefore, in the same figure we plot the velocity power spectrum obtained using the second-order structure function (SF) which is calculated in the real space and is insensitive to the type of the boundaries. Figure 11.15 shows that the power spectrum obtained from the structure function is more regular and approaches the Kolmogorov (dashed lines) slope better. This is a clear indication of the turbulence developed in such simulation. For comparison, we also show the Fourier power spectrum of the Z-component of the velocity (red line in Fig. 11.15) for which should be less sensitive to the open boundaries since along this component we impose the periodicity. The power spectrum of this component is significantly weaker in amplitudes, especially in the large scale regime (small wave numbers k). This component is perpendicular both to the Y component, along which the new magnetic flux is brought, and to the X component, along which the reconnected flux is removed. In fast reconnection, both these components are comparable to the Alfvén speed. The weak amplitudes of the Z-component of velocity may indicate strong anisotropies of the velocity eddies in the generated turbulence.

Some other features of the self-generated turbulence like the growth of the turbulence region were presented in Lazarian et al. (2015). For more detailed description of these models and analysis of the Kelvin-Helmholtz instability as the suspected mechanism of the injection, we refer to Kowal et al. (2015).

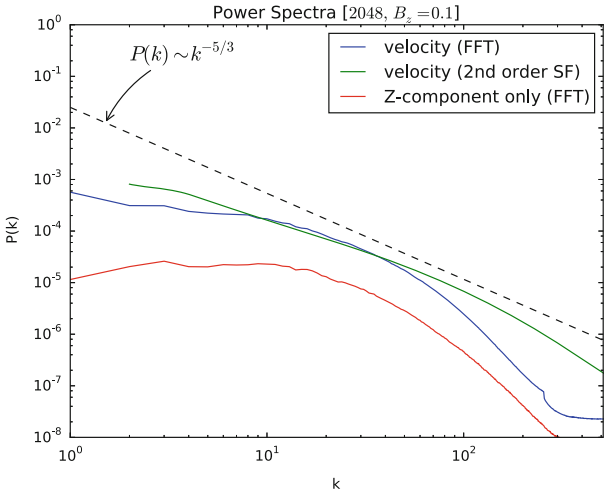

Fig. 11.15 Velocity power spectra obtained in a few different ways corresponding to the simulation snapshot shown in the previous figure. We show the power spectrum of the velocity obtained using the fast Fourier transform and the second order structure function (*blue* and *green lines*, respectively). The spectrum from the structure function approaches the Kolmogorov slope (*dashed line*) better, most probably because it is not sensitive to the type of boundary conditions. For comparison we show the power spectrum of Z-component (*red line*). From Kowal et al. (2015)

11.8 Observational Testing

The criterion for the application of LV99 theory is that the outflow region is much larger than the ion Larmor radius $\Delta \gg \rho_i$. This is definitely applicable for solar atmosphere, solar wind, but not for the magnetosphere. In the latter case the corresponding scales are comparable and plasma effects are important for reconnection.

11.8.1 Solar Reconnection

Solar reconnection was studied by Ciaravella and Raymond (2008) in order to test LV99 prediction of thick outflows. As we discussed earlier, the driving by magnetic reconnection is not isotropic and therefore the turbulence is strong from the injection scale. In this case

$$V_{rec} \approx U_{obs,turb}(L_{inj}/L_x)^{1/2}, \tag{11.49}$$

where $U_{obs,turb}$ is the spectroscopically measured turbulent velocity dispersion. Similarly, the thickness of the reconnection layer should be defined as

$$\Delta \approx L_x (U_{obs,turb}/V_A)(L_{inj}/L_x)^{1/2}. \tag{11.50}$$

The expressions given by Eqs. (11.49) and (11.50) can be compared with observations in Ciaravella and Raymond (2008). There, the widths of the reconnection regions were reported in the range from $0.08L_x$ up to $0.16L_x$ while the observed Doppler velocities in the units of V_A were of the order of 0.1. It is easy to see that these values are in a good agreement with the predictions given by Eq. (11.50). The agreement obtained in the original comparison by Ciaravella and Raymond (2008) was based on the original expressions in LV99 that assume isotropic driving and weak turbulent cascading. Therefore the correspondence that the authors got was not so impressive and the authors concluded that both LV99 and Petschek X-point reconnection are potentially acceptable solutions.

At the same time, triggering of magnetic reconnection by turbulence generated in adjacent sites is a unique prediction of LV99 theory. This prediction was successfully tested in Sych et al. (2009), where authors explained quasi-periodic pulsations in observed flaring energy releases at an active region above the sunspots as being triggered by the wave packets arising from the sunspots.

11.8.2 Solar Wind, Parker Spiral, Heliospheric Current Sheet

Solar wind reconnection was considered in Karimabadi and Lazarian (2013) review from the point of view of tearing plasma reconnection. The possibility of turbulent MHD reconnection was not considered in spite of the fact that $\Delta \gg \rho_i$, the deficiency of this review that was compensated in more recent review by Lazarian et al. (2015). There on the basis of studies of Solar wind in Lalescu et al. (2015) it was concluded that the Solar wind reconnection is well compatible with LV99 theory (see Fig. 11.16). The general features of the turbulent reconnection in MHD simulations correspond to the features of solar wind reconnection searched to identify reconnection events in the Solar wind (Gosling 2007).

Similarly Eyink (2014) discussed some implications of turbulent reconnection for heliospheric reconnection, in particular for deviations from the Parker spiral model of interplanetary magnetic field. The latter model assumed frozen-in condition for magnetic field, which according to turbulent reconnection should be violated. Indeed, Burlaga et al. (1982) studied the magnetic geometry and found "notable deviations" from the spiral model using Voyager 1 and 2 data at solar distances $R = 1 - 5$ AU. The deviations from the theoretical expectations based on the frozen-in condition were substantiated by Khabarova and Obridko (2012), who presented evidence on the breakdown of the Parker spiral model for time- and space-averaged values of the magnetic field from several spacecraft (Helios 2, Pioneer Venus Orbiter, IMP8, Voyager 1) in the inner heliosphere at solar distances 0.3–5

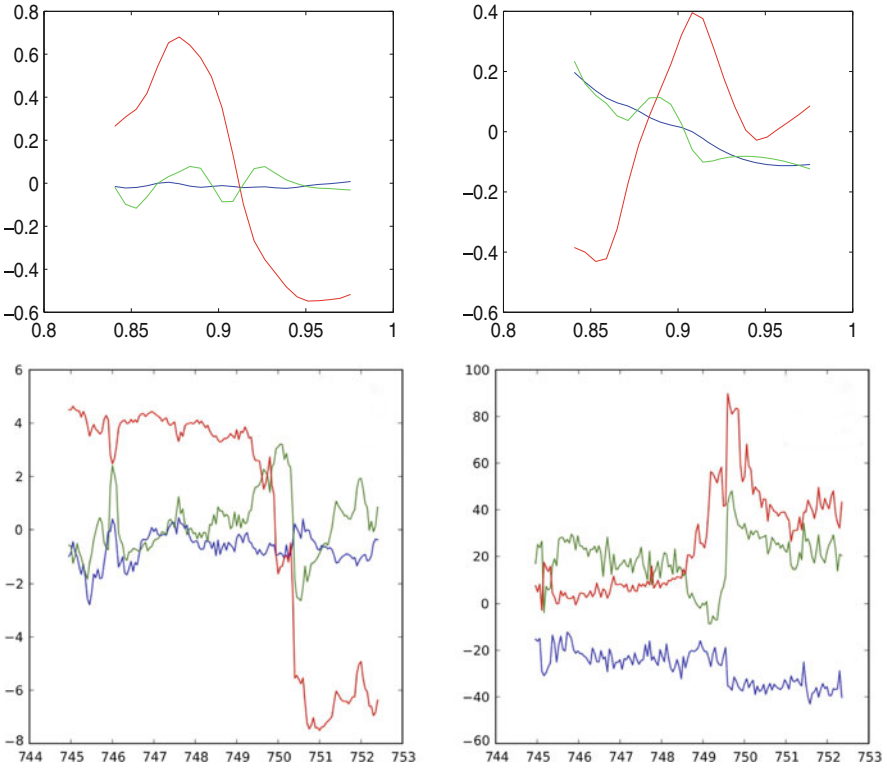

Fig. 11.16 Candidate events for turbulent reconnection. *MHD turbulence simulation (top panels) and high-speed solar wind (bottom panels)*. The *left panels* show magnetic field components and the *right panels* velocity components, both rotated into a local minimum-variance frame of the magnetic field. The component of maximum variance in *red* is the apparent reconnecting component, the component of medium variance in *green* is the nominal guide-field direction, and the minimum-variance direction in *blue* is perpendicular to the reconnection layer. Reprinted figure with permission from Lalescu et al. (2015). Copyright (2015) by the American Physical Society

AU. The latter authors interpret their observations as due to "a quasi-continuous magnetic reconnection, occurring both at the heliospheric current sheet and at local current sheets". Eyink (2014) estimated the magnetic field slippage velocities and related the deviation from Parker original predictions to LV99 reconnection. In addition, Eyink (2014) analyzed the data relevant to the region associated with the broadened heliospheric current sheet (HCS), noticed its turbulent nature and provided arguments on the applicability of LV99 magnetic reconnection model to HCS.

11.8.3 Indirect Observational Testing

Magnetic reconnection is extremely difficult to observe directly in generic astrophysical situations. Observations of the Sun, direct measurements of the Solar wind are notable exeptions. However, turbulent reconnection is happening everywhere in astrophysical turbulent magnetized environments and one can test the properties of reconnection by comparing the predictions that follow from the turbulent reconnection theory for particular astrophysical phenomena. This is an indirect way of testing turbulent reconnection and testing of different applications of the turbulent reconnection theory, including those that we cover in our review, also puts turbulent reconnection at test.

We believe that the spectrum of turbulent fluctuations observed in astrophysical settings, e.g. in molecular clouds, galactic atomic hydrogen (see Lazarian 2009, for review) testifies in favor of turbulent reconnection. Indeed, the measurements are consistent with numerical simulations (see Kowal and Lazarian 2010), which are performed in situations when turbulence induces fast reconnection. As it is discussed in Lazarian et al. (2015) it is the turbulent reconnection that makes the GS95 theory of strong turbulence self-consistent.

Similarly, we can say that testing of the processes of rapid diffusion of magnetic field in turbulent fluids that are mediated by turbulent reconnection, i.e. processes of reconnection diffusion that we discuss ahead in the review, is also a testing of the underlying turbulent reconnection predictions. The same can be said about testing of the theories of gamma ray bursts, accretion disks, black hole sources that are based on the theory of turbulent reconnection (see below). We are sure that further detailed modeling of these phenomena based on the predictions of turbulent reconnection theory is an exciting avenue of research.

11.9 Implications of the Theory

11.9.1 Reconnection Diffusion: Star Formation and Accretion Disk Evolution

Within the textbook theory of star formation, magnetic fields can influence and even control star formation at different stages, from the formation of the molecular cloud to the evolution of an accretion disk around a newly formed star (see Shu 1983). The basic pillar of the corresponding theoretical constructions is that magnetic field is well frozen in highly conducting ionized component of the media so that the characteristic displacement of the magnetic field lines arising from Ohmic effects $\sqrt{\eta t}$ is much less than the scale of the system for any characteristic times of the system existence. This, however, assumes slow reconnection. Because the media is typically only partially ionized, the segregation of matter and magnetic field can

still happen at higher rate which is controlled by the differential drift of ions and neutrals, i.e. by the process that is termed *ambipolar diffusion*.

On the basis of LV99 theory, Lazarian (2005) suggested that the diffusion of magnetic fields in turbulent systems will be fast and independent of resistivity (see also Lazarian and Vishniac 2009). This resulted in the concept that was termed "reconnection diffusion" in analogy to the earlier concept of ambipolar diffusion. A detailed discussion of the reconnection diffusion concept and its relation to star formation is presented in Lazarian (2014).

A formal theoretical proof that magnetic fields are not frozen in turbulent fluids is presented in Lazarian et al. (2015), while the numerical proof of the violation of flux freezing in turbulent media is provided through confirming the Richardson dispersion in Eyink et al. (2013). This also follows directly from LV99 and this is what motivated the reconnection diffusion concept. The corresponding review dealing with the reconnection diffusion is in Lazarian (2014) and we refer the interested reader to this extended work. In what follows, we just briefly discuss some of the implication of the reconnection diffusion concept as well as its implications.

The process of reconnection diffusion can be illustrated by Fig. 11.17 (upper), where the reconnection of flux tubes belonging to the two adjacent eddies is shown. It is evident that as a result of magnetic reconnection the matter is being exchanged between the flux tubes and that in the presence of the cascade of turbulent motion at different scales the concept of the flux tube has a transient character, as the flux tubes evolve constantly being reformed by the motion of eddies at different scales.

Naturally, the concept of reconnection diffusion is applicable beyond the star formation range of problems. Quantitatively it boils down to understanding that on the scales larger than the turbulent injection scale the transfer of matter and magnetic field in superAlfvénic turbulence is happening through the turbulent advection by the eddies at the injection scale and the corresponding diffusion coefficient coincides with that in hydrodynamics, i.e. $k_{rec.diff,super} \approx 1/3 u_L L$. At the same time, for subAlfvénic turbulence the transfer is enabled by the strong turbulence eddies of the l_{trans} size and therefore the diffusion is reduced by the third power of Alfvén Mach number, i.e. $k_{rec.diff,sub} \approx 1/3 u_L L (u_L/V_A)^3$ (Lazarian 2006). Note that weak turbulence is subdominant in mixing the matter. On the scales smaller than the injection scale the transport of magnetic field and matter follows the Richardson dispersion and accelerates as the scale under study increases. A discussion of the reconnection process from the point of view of plasma slippage (see Eyink 2014) is presented in Lazarian et al. (2015).

We would like to clarify that when we are talking about the suppression of reconnection diffusion in subAlfvénic turbulence, this is the suppression at the *large scales*, comparable with and larger than the injection scale. The local mixing of magnetic field lines at the scales l less than the scales at which turbulence is transferred to the strong regime, i.e. at scales smaller than $l_{trans} = LM_A^2$ [see Eq. (11.9)], is still given by the product lv_l and the corresponding small scale reconnection diffusion is governed by the Richardson dispersion and exhibits superdiffusive behavior. It is inability of scales larger than l_{trans} that are in the regime

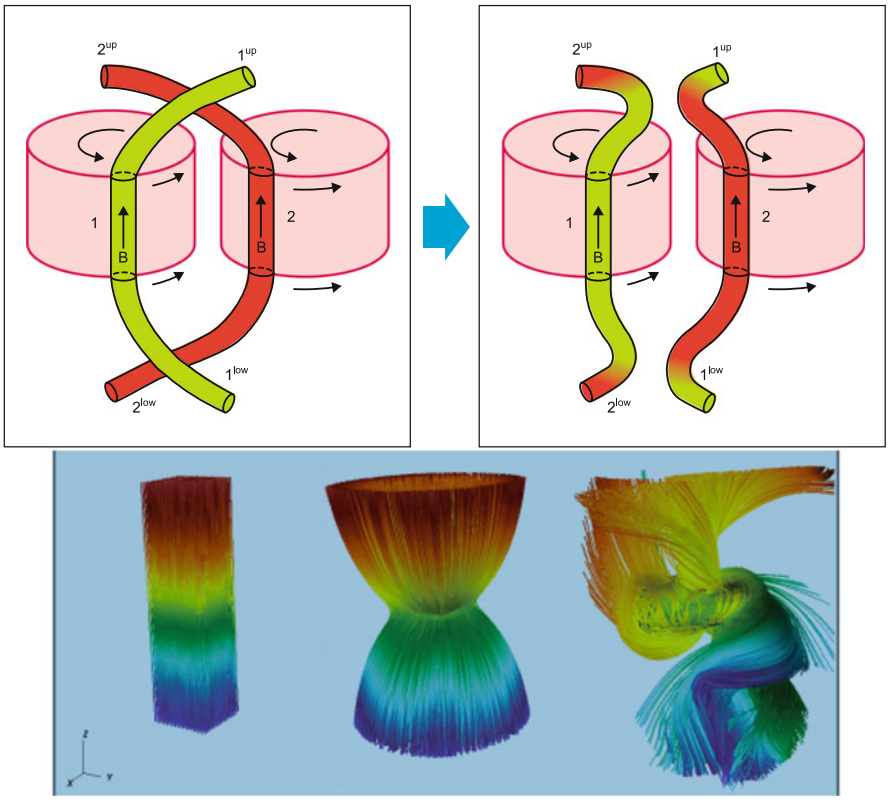

Fig. 11.17 *Upper panel*: reconnection diffusion: exchange of flux with entrained matter. Illustration of the mixing of matter and magnetic fields due to reconnection as two flux tubes of different eddies interact. Only one scale of turbulent motions is shown. In real turbulent cascade such interactions proceed at every scale of turbulent motions. From Lazarian (2011). *Lower panel*: visualization of magnetic field lines in a turbulent accretion disk. Illustration of the process using *smoothed lines*. From Casanova et al. (2015)

of weak MHD turbulence to provide efficient mixing that impedes reconnection diffusion for scales $\gg l_{trans}$.

The first numerical work that explored the consequences of reconnection diffusion for star formation was performed by Santos-Lima et al. (2010), where the reconnection diffusion was applied to idealized setting motivated by magnetized diffuse interstellar medium and molecular clouds. A later paper by Leão et al. (2013) provided a numerical treatment of the reconnection diffusion for 3D collapse of self-gravitating clouds. In addition, the problem of the transport of angular momentum in protostellar accretion disks was considered in Santos-Lima et al. (2012, 2013), where it was numerically demonstrated that the long-standing problem of magnetic breaking in the formation of protostellar accretion disks can be solved if disks are formed from turbulent media and therefore, reconnection diffusion takes place. A

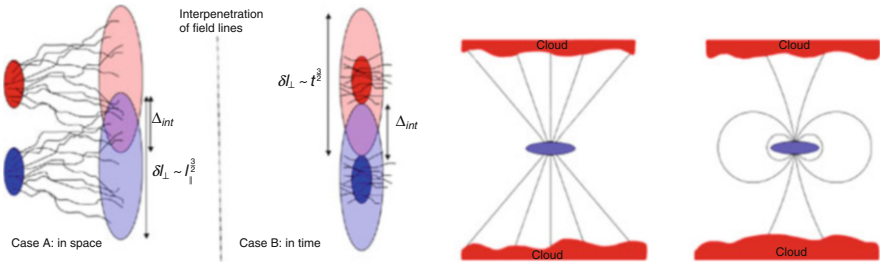

Fig. 11.18 *Left panel*: Case A: microscopic physical picture of reconnection diffusion. Magnetized plasma from two regions is spread by turbulence and mixed up over the region Δ. Case B: description of the process in terms of field wandering in space. Case B: description of the magnetic field line spread with time. *Right panel*: change of the magnetic field configuration from the split monopole on the *left* to the dipole configuration on the *right* decreases the degree of coupling of the disk with the surrounding ISM without removing magnetic field from the disk. From Casanova et al. (2015)

more recent study by Casanova et al. (2015) (see Fig. 11.17, lower) provides more evidence on how potent the concept of reconnection diffusion can be.

It is important to understand that reconnection diffusion does not require magnetic fields changing their direction in space to the opposite one. On the contrary, in subAlfvénic turbulence, reconnection diffusion proceeds with magnetic field lines roughly directed along the mean magnetic field as shown in Fig. 11.18, (left panel). When reconnection diffusion happens on the scales smaller than the turbulence injection scale, the spread of magnetic field lines obeys superdiffusion and superballistic Richardson dispersion law. In addition, the process of reconnection diffusion that does not change the topology of magnetic flux in the statistical sense and the process of reconnection that radically changes the magnetic field topology can happen simultaneously, as it is illustrated in Fig. 11.18 (right panel). There an additional process that facilitates the accretion disk formation is shown, namely, the change of magnetic field topology from the so-called "split monopole" to the dipole configuration. This change in turbulent interstellar plasmas is induced by turbulent reconnection and, similar to the reducing of the flux through the accretion disk that the reconnection diffusion entails, this topology change decreases the coupling of the accretion disk to the surrounding gas. Thus in reality both incarnations of turbulent reconnection process work together to solve the so-called "magnetic breaking catastrophe" problem.

A number of important implications of reconnection diffusion is discussed in Lazarian et al. (2012). Those include the independence of the star formation rate on the metallicity in galaxies, star formation in galaxies with high ionization of matter, e.g. star formation in ultra-luminous infrared galaxies or ULIRGs (Papadopoulos et al. 2011), the absence of correlation between the magnetic field strength and gaseous density, etc.

These observational facts contradicting to the paradigm based on ambipolar diffusion naturally follow from the reconnection diffusion theory. Potential impli-

cations of reconnection diffusion in dynamos are also addressed in de Gouveia Dal Pino et al. (2012).

Finally, we would like to compare the concept of reconnection diffusion with that of "turbulent ambipolar diffusion" (Fatuzzo and Adams 2002; Zweibel 2002). The latter concept is based on the idea that turbulence can create gradients of neutrals and those can accelerate the overall pace of ambipolar diffusion. The questions that naturally arise are (1) whether this process can proceed without magnetic reconnection and (2) what is the role of ambipolar diffusion in the process. Heitsch et al. (2004) performed numerical simulations with 2D turbulent mixing of a layer with magnetic field perpendicular to the layer and reported fast diffusion that was of the order of turbulent diffusivity number $V_L L$, *independent of ambipolar diffusion coefficient*. This is because this sort of mixing can happen without reconnection only in a *degenerate case of 2D mixing* with exactly parallel magnetic field lines. Any realistic 3D cases do involve reconnection and must be treated from the point of view of reconnection theory. If reconnection is slow, the turbulent ambipolar diffusion cannot proceed in any 3D turbulent settings, as inability of magnetic field lines to cross each other should arrest the mixing that is observed in 2D with magnetic lines exactly perpendicular to the mixing plane. If, however, reconnection is fast as predicted in LV99, then the diffusion is independent of ambipolar diffusion processes and proceeds in partially ionized gas with the same rate as in fully ionize gas. Thus we believe that it does not make sense to talk about turbulent ambipolar diffusion in any astrophysical 3D setting. The actual diffusion is controlled by magnetic reconnection turbulent media and is independent of ambipolar diffusion process!

11.9.2 Acceleration of Energetic Particles

Magnetic reconnection results in shrinking of magnetic loops and the charged particles entrained over magnetic loops get accelerated. This process was proposed by de Gouveia Dal Pino and Lazarian (2005, henceforth GL05).

The acceleration process is illustrated by Fig. 11.19. Particles bounce back and forth between converging magnetic fluxes and undergo a first-order Fermi acceleration. An easy way to understand the process is by making an analogy with shock acceleration. As in shocks particles trapped within two converging magnetic flux tubes (moving to each other with the reconnection velocity V_R), will bounce back and forth undergoing head-on interactions with magnetic fluctuations and their energy after a round trip will increase by $< \Delta E/E > \sim V_R/c$, which implies a first-order Fermi process with an exponential energy growth after several round trips. Disregarding the particles backreaction one can get the spectrum of accelerated cosmic rays (GL05):

$$N(E)dE = const_1 E^{-5/2} dE. \tag{11.51}$$

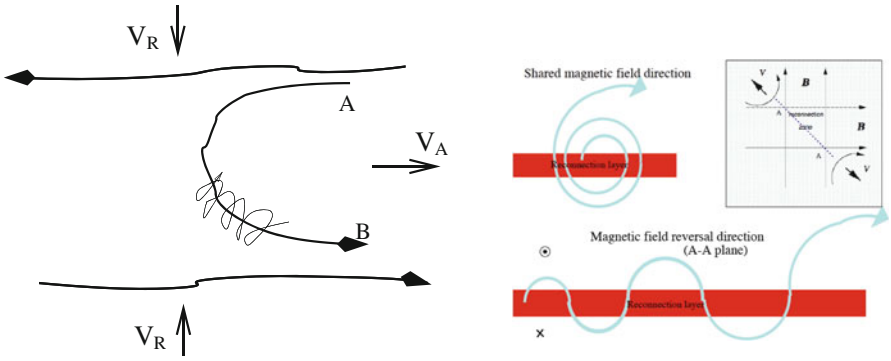

Fig. 11.19 *Left panel*: cosmic rays spiral about a reconnected magnetic field line and bounce back and forth at points A and B. The reconnected regions move towards each other with the reconnection velocity V_R. Reprinted figure with permission from Lazarian (2005). Copyright (2005), AIP Publishing LLC. *Right panel*: particles with a large Larmor radius gyrate about the guide/shared magnetic field. As the particle interacts with converging magnetized flow the particle gets energy gain during every gyration. Reprinted from Lazarian et al. (2012)

This result of GL05 is valid for particle acceleration in the absence of compression (see Drury 2012, for a study of the effects of compression which may result a flatter power-law spectrum).

Before GL05, reconnection was discussed in the context of particle acceleration (e.g., Litvinenko 1996; Shibata and Tanuma 2001; Zenitani and Hoshino 2001), but the first-order Fermi of the acceleration process was not discovered in these studies. A process similar to that in GL05 was later suggested as a driver of particle acceleration within collisionless reconnection in Drake et al. (2006). The physics of the acceleration is the same, although GL05 appealed to 3D magnetic bundles (see, e.g., Fig. 11.19), while Drake et al. (2006) considered 2D shrinking islands. The latter is actually an artifact of the constrained 2D geometry. The difference in dimensions, however, affects the acceleration efficiency according to Kowal et al. (2011).

Several other studies explored particle acceleration in magnetic reconnection discontinuities considering collisionless pair plasmas (e.g. Drake et al. 2010; Jaroschek et al. 2004; Zenitani and Hoshino 2008; Zenitani et al. 2009; Cerutti et al. 2013, 2014; Sironi and Spitkovsky 2014; Werner et al. 2014; Guo et al. 2015), where magnetic islands or Petschek-like X-point configurations of fast reconnection can be driven by kinetic instabilities (Shay et al. 2004; Yamada et al. 2010), or anomalous resistivity (e.g., Parker 1979), see also Hoshino and Lyubarsky (2012) for a review. But in collisional plasmas, embedded turbulence in the current sheets arises as a natural process to make reconnection fast (LV99) and thus particle acceleration efficient. In this scenario, first-order Fermi acceleration of particles entrained on the contracting helical magnetic loops in the embedded turbulence can be understood

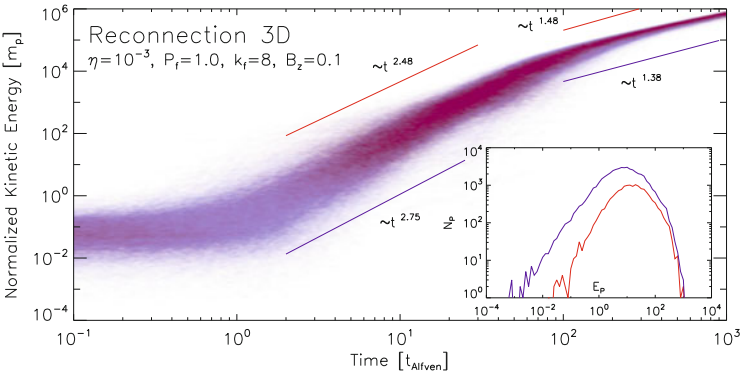

Fig. 11.20 Particle kinetic energy distributions for 10,000 protons injected in the fast magnetic reconnection domain. The *colors* indicate which velocity component is accelerated (*red* or *blue* for parallel or perpendicular, respectively). The energy is normalized by the rest proton mass. *Subplot* shows the particle energy distributions at $t = 5.0$. Models with $B_{0z} = 0.1$, $\eta = 10^{-3}$, and the resolution $256 \times 512 \times 256$ is shown. Reprinted figure with permission from Kowal et al. (2012). Copyright (2012) by the American Physical Society

from the Liouville's theorem. In the process of loop contraction a regular increase of the particles energies takes place.[10]

Testing of particle acceleration in a large scale current sheet with embedded turbulence to make reconnection fast was performed in Kowal et al. (2012) and its results are presented in Fig. 11.20. The simulations were performed considering 3D MHD domains of reconnection with the injection of 10,000 test particles. This study showed that the process of acceleration by large-scale turbulent reconnection can be adequately described by magnetohydrodynamics. Figure 11.20 depicts the evolution of the kinetic energy of the particles. After injection, a large fraction of test particles accelerates and the particle energy grows exponentially (see also the energy spectrum at $t = 5$ in the detail at the bottom right). This is explained by a combination of two effects: the presence of a large number of converging small scale current sheets and the broadening of the acceleration region due to the turbulence. The acceleration process is clearly a first-order Fermi process and involves large number of particles since the size of the acceleration zone and the number of scatterers naturally increases by the presence of turbulence. Moreover, the reconnection speed, which in this case is independent of resistivity (LV99, Kowal et al. 2009), determines the velocity at which the current sheets scatter particles ($V_{rec} \sim V_A$). During this stage the acceleration rate is $\propto E^{-0.4}$ (Khiali

[10]We note that this process will also occur in pure turbulent environments, i.e., without the presence of large scale magnetic discontinuities formed by coherent flux tubes of opposite polarity, but in such cases, the absence of the large scale converging flux tubes will also allow for catch-up collisions, where particles lose energy to the magnetic fluctuations rather than gaining. In such a case, the process is more like a second-order Fermi acceleration (Kowal et al. 2012).

et al. 2015a) and the particle power law index in the large energy tail is very flat (of the order of $1-2$).

The process of fast magnetic reconnection acceleration is expected to be widespread. In particular, it has been discussed in Lazarian and Opher (2009) as a cause of the anomalous cosmic rays observed by Voyagers and in Lazarian and Desiati (2010) as a source of the observed cosmic ray anisotropies.

Magnetic reconnection was also discussed in the context of acceleration of energetic particles in relativistic environments, like pulsars (e.g. Cerutti et al. 2013, 2014; Sironi and Spitkovsky 2014; Uzdensky and Spitkovsky 2014, see also Uzdensky this volume), in particular, turbulent reconnection in the surrounds of black hole sources (GL05, de Gouveia Dal Pino et al. 2010b; Kadowaki et al. 2015; Singh et al. 2015; Khiali et al. 2015a; Khiali and de Gouveia Dal Pino 2015); and relativistic jets of active galactic nuclei (AGNs) (e.g. Giannios 2010) and gamma ray bursts (GRBs) (e.g. Lazarian et al. 2003; Zhang and Yan 2011). The aforementioned simulations employ non-relativistic turbulent reconnection. However, the evidence that we provided above indicates on the similarity between the relativistic and non-relativistic turbulent reconnection. Thus we also expect similarities between the particle acceleration processes. A more detailed discussion of the acceleration of energetic particles by magnetic reconnection can be found in de Gouveia Dal Pino et al. (2014) and de Gouveia Dal Pino and Kowal (2015).

11.9.3 Flares of Magnetic Reconnection and Associated Processes

It is obvious that in magnetically dominated media the release of energy must result in the outflow that induces turbulence in astrophysical high Reynolds number plasmas. This inevitably increases the reconnection rate and therefore the energy release. As a result we get a *reconnection instability*. The details of such energy release and the transfer to turbulence have not been sufficiently studied yet. Nevertheless, on the basis of LV99 theory a simple quantitative model of flares was presented in Lazarian and Vishniac (2009), where it is assumed that since stochastic reconnection is expected to proceed unevenly, with large variations in the thickness of the current sheet, one can expect that some fraction of this energy will be deposited inhomogeneously, generating waves and adding energy to the local turbulent cascade. A more detailed discussion of the model is provided in Lazarian et al. (2015).

The applications of the theory include from solar flares to gamma ray bursts (GRBs). In particular, a model for GRBs based on LV99 reconnection was suggested in Lazarian et al. (2003). It was elaborated and compared with observations in Zhang and Yan (2011), where collisions of magnetic turbulent fluxes were considered. A different version of gamma ray bursts powered by turbulent reconnection proposed by Lazarian and Medvedev (2015) is based on kink instability. It is illustrated in Fig. 11.21, left panel. Naturally, the model appeals to the relativistic turbulent

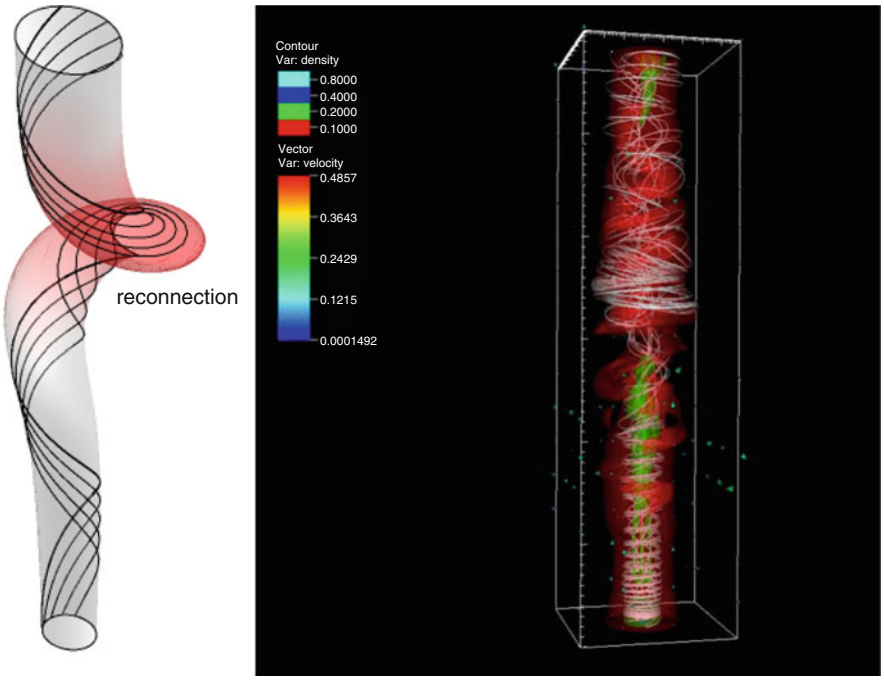

Fig. 11.21 *Left panel*: in the model by Lazarian and Medvedev (2015) magnetized jet with spiral magnetic field is being ejected. The spiral undergoes kink instability which results in turbulent reconnection. *Right panel*: numerical simulations of 3D relativistic jet that is subject to the kink instability and turbulent reconnection. From Mizuno et al. (2015)

reconnection that we described above. The difference of this model from other kink-driven models of GRBs (e.g. Drenkhahn and Spruit 2002; Giannios and Spruit 2006; Giannios 2008; McKinney and Uzdensky 2012) is that the kink instability also induces turbulence which drives magnetic reconnection.

In a similar line of research, Mizuno et al. (2015), have performed 3D relativistic MHD simulations of rotating jets subject to the kink instability, considering several models with different initial conditions (i.e., different density ratios between the jet and the environment, different angular velocities, etc.) in order to explore fast magnetic reconnection, magnetic energy dissipation and a potential transition from magnetic to a matter dominated regime as predicted for GRBs and AGN jets (see also Rocha da Silva et al. 2015; McKinney and Uzdensky 2012). The results indicate that a complex structure develops in the helical magnetic field due to the kink instability, developing several regions with large current densities, suggestive of intense turbulent reconnection (see Fig. 11.21, right panel). Further numerical investigation of the process is in progress. Within the GRB models in Zhang and Yan (2011) and Lazarian and Medvedev (2015) turbulent reconnection explains the dynamics of GRBs.

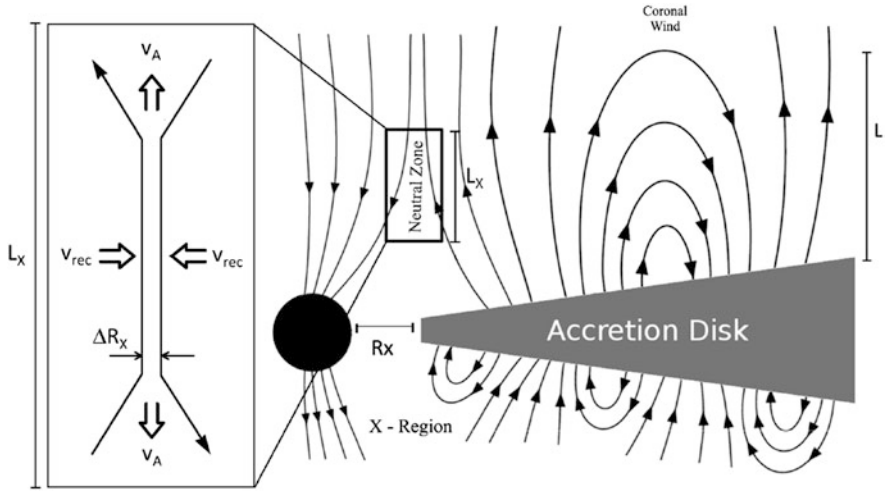

Fig. 11.22 Scheme of magnetic reconnection between the lines arising from the accretion disk and the lines of the BH magnetosphere. Reconnection is made fast by the presence of embedded turbulence in the reconnection zone (see text for more details). Particle acceleration occurs in the magnetic reconnection zone by a first-order Fermi process. Reprinted from Kadowaki et al. (2015) by permission of the AAS

Turbulent reconnection is, unlike the Sweet Parker one, is a volume-filling reconnection. The magnetic energy is being released in the volume and is being transferred into the kinetic energy of fluid and energetic particles. Combined with fast rates of magnetic reconnection this makes the first-order Fermi process of particle acceleration efficient, which makes it plausible that a substantial part of the energy in magnetic field should be transferred to the accelerated particles. Therefore we believe that magnetic reconnection in the case of AGN jets (see Giannios 2010) can be a copious source of high energy particles. Numerical simulations of in situ particle acceleration by magnetic reconnection in the turbulent regions of relativistic jets (see de Gouveia Dal Pino and Kowal 2015) demonstrate that the process can be competitive with the acceleration in shocks.

Particle acceleration arising from magnetic reconnection in the surrounds of black hole sources like active galactic nuclei (AGNs) and galactic black hole binaries (GHBs) has been also extensively studied. In particular, GL05 (see also de Gouveia Dal Pino et al. 2010b,a) proposed that fast turbulent reconnection events occurring between the magnetic field lines arising from the inner accretion disk and the magnetosphere of the BH (see Fig. 11.22) could be efficient enough to accelerate the particles and produce the observed core radio outbursts in GBHs and AGNs.

More recently, Kadowaki et al. (2015) revisited the aforementioned model and extended the study to explore also the gamma-ray flare emission of these sources. The current detectors of high energy gamma-ray emission, particularly at TeVs

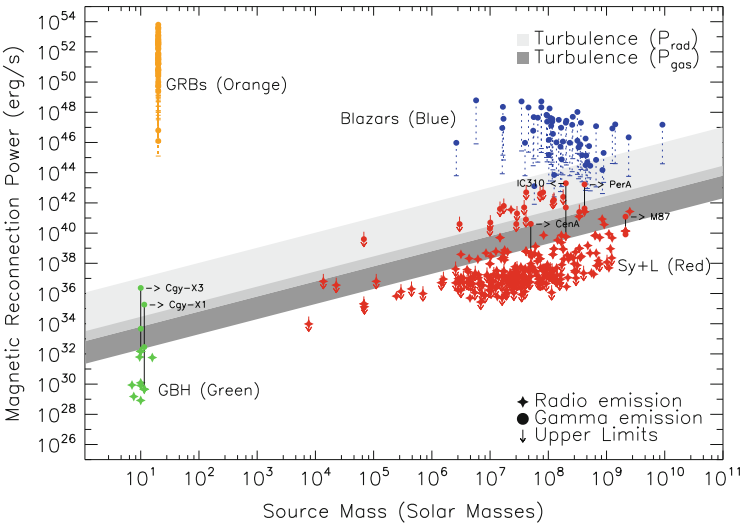

Fig. 11.23 Turbulent driven magnetic reconnection power against BH source mass (*gray region*) compared to the observed emission of low luminous AGNs (LLAGNs: LINERS and Seyferts), galactic black hole binaries (GBHs), high luminous AGNs (blazars) and gamma ray burst (GRBs). The core radio emission of the GBHs and LLAGNs is represented by *red* and *green diamonds*, the gamma-ray emission of these two classes is represented by *red* and *green circles*, respectively. In the few cases for which there is observed gamma-ray luminosity it is plotted the maximum and minimum values linking both circles with a *vertical black line* that extends down to the radio emission of each of these sources. The *inverted arrows* associated to some sources indicate upper limits in gamma-ray emission. For blazars and GRBs only the gamma-ray emission is depicted, represented in *blue* and *orange circles*, respectively. The *vertical dashed lines* correct the observed emission by Doppler boosting effects. The calculated reconnection power clearly matches the observed radio and gamma-ray emissions from LLAGNs and GBHs, but not that from blazars and GRBs. This result confirms early expectations that the emission in blazars and GRBs is produced along the jet and not in the core of the sources. Reprinted from Kadowaki et al. (2015) by permission of the AAS

(e.g., the FERMI-LAT satellite and the ground observatories HESS, VERITAS and MAGIC) have too poor resolution to determine whether this emission is produced in the core or along the jets of these sources. This study confirmed the earlier trend found in GL05 and de Gouveia Dal Pino et al. (2010b) and verified that if fast reconnection is driven by turbulence, there is a correlation between the calculated fast magnetic reconnection power and the BH mass spanning 10^{10} orders of magnitude that can explain not only the observed radio, but also the gamma-ray emission from GBHs and low luminous AGNs (LLAGNs). This match has been found for more than 230 sources which include those of the so called *fundamental plane of black hole activity* (Merloni et al. 2003) as shown in Fig. 11.23. This figure also shows that the observed emission from blazars (i.e., high luminous AGNs whose jet points to the line of sight) and GRBs does not follow the same trend as that of the low luminous AGNs and GBHs, suggesting that the observed

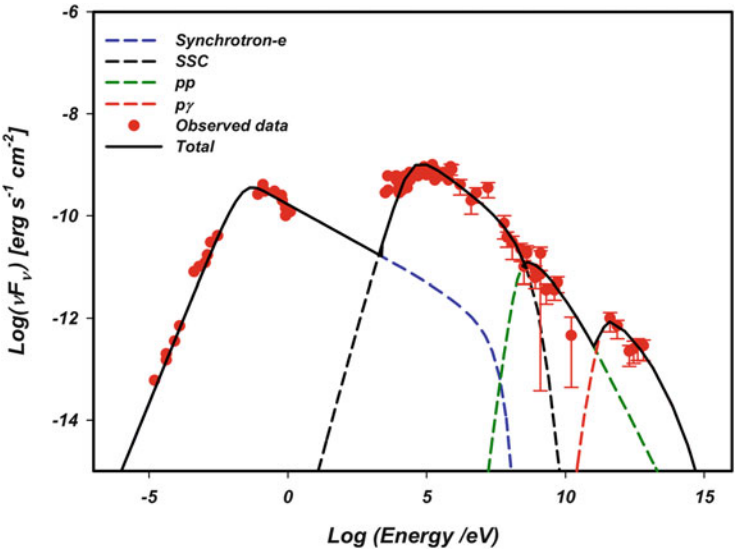

Fig. 11.24 Calculated spectral energy distribution (SED) for the AGN Cen A employing the turbulent magnetic reconnection acceleration model in the core region. The data depicted in the radio to optical energy range (10^{-5} eV−1 eV) are from ISO and SCUBA and in the hard x-rays range from *Swift-BAT*, *OSSE* and *COMPTEL*. The data observed in the energies 10^8-10^{10} eV are taken by *EGRET* and in the energies 10^8-10^{10} eV by *Fermi-LAT*. The TeV data are taken by *HESS*. Reprinted from Khiali et al. (2015b)

radio and gamma-ray emission in these cases is *not* produced in the core of these sources. This result is actually exactly what one should expect because the jet in these systems points to the line of sight thus screening the nuclear emission, so that in these sources the emission is expected to be produced by another population of particles accelerated along the jet.

In another concomitant work, Singh et al. (2015) explored the same mechanism, but instead of considering a standard thin, optically thick accretion disk as in the works above, adopted a magnetically-dominated advective accretion flow (M-ADAF; Narayan and Yi 1995; Meier 2012) around the BH, which is suitable for sub-Eddington sources. The results obtained are very similar to those of Kadowaki et al. (2015) depicted in Fig. 11.23 ensuring that the details of the accretion physics are not relevant for the turbulent magnetic reconnection process which actually occurs in the corona around the BH and the disk.

The correlations found in Fig. 11.23 (Kadowaki et al. 2015; Singh et al. 2015) have motivated further investigation. Employing the particle acceleration induced by turbulent reconnection and considering the relevant non-thermal loss processes of the accelerated particles (namely, Synchrotron, inverse Compton, proton-proton and proton-photon processes), Khiali et al. (2015a) and Khiali et al. (2015b) have computed the spectral energy distribution (SED) of several GBHs and LLAGNs and found that these match very well with the observations (see for instance Fig. 11.24,

which depicts the SED of the radio galaxy Cen A), especially at the gamma-ray tail, thus strengthening the conclusions above in favor of a core emission origin for the very high energy emission of these sources. The model also naturally explains the observed very fast variability of the emission. The same model has been also recently applied to explain the high energy neutrinos observed by the IceCube as due to LLAGNs (Khiali and de Gouveia Dal Pino 2015).

11.10 Comparison of Approaches to Magnetic Reconnection

11.10.1 Turbulent Reconnection and Numerical Simulations

Whether MHD numerical simulations reflect the astrophysical reality depends on how correctly magnetic reconnection is presented within these simulations. The problem is far from trivial. With the Lundquist number being sometimes more than 10^{15} orders different, direct numerical simulation may potentially be very misleading. To deal with the issue Large Eddy Simulations (LES) approach may look promising (see Miesch et al. 2015). The catch here is that LES requires the explicit parametrization of reconnection rates. For instance, assume that following the ideas of tearing research we adopt a particular maximal value of reconnection speed, e.g. $0.01V_A$. This means that the motions where the fluids are moving with velocities larger than this chosen reconnection speed will be constrained. In MHD transAlfvénic turbulence, this would predict constraining the motions of eddies on the scales $[10^{-6}L, L]$ if we adopt the usual Kolmogorov $v \sim l^{1/3}$ scaling. This means that for this range of scales our results obtained with MHD turbulence theory are not applicable and the physics of many related processes is radically different. We believe that wiring this into LES provide erroneous unphysical results.

From the point of view of the turbulent reconnection theory a normal MHD code reproduces magnetic reconnection correctly for turbulent regions, as for turbulent volumes the reconnection rate does not depend on resistivity and varies with the level of turbulence. As turbulence is the generic state of astrophysical fluids, the regions that are turbulent within numerical studies are correctly represented in terms of magnetic reconnection. On the contrary, the regions where the turbulence is damped in simulations due to numerical diffusivity do not represent magnetic reconnection correctly. Situations where the initial set up is laminar requires following the development of turbulent reconnection and the prescriptions based on the corresponding simulation may be useful for parameterizing the process.

11.10.2 Turbulent Reconnection Versus Tearing Reconnection

It has been known for quite a while that Sweet-Parker current sheet is unstable to tearing and this can affect the reconnection rate (see Syrovatskii 1981, LV99). What was a more recent development is that the 2D current sheet starting with a particular Lundquist number larger than 10^4 develops fast reconnection (see Loureiro et al. 2007; Uzdensky et al. 2010), i.e. reconnection that does not depend on the fluid resistivity. The study of tearing momentarily eclipsed the earlier mainstream research of the reconnection community, which attempted to explain fast reconnection appealing to the collisionless plasma effects that were invoked to stabilize the Petschek-type X point configuration for reconnection (Shay et al. 1998; Drake 2001; Drake et al. 2006). We view this as a right step in abandoning the artificial extended X point configurations the stability of which in the situation of realistic astrophysical forcing was very doubtful (see discussion in LV99). However, we believe that tearing by itself does not provide a generic solution for the astrophysical reconnection.

To what extend tearing is important for the onset of 3D turbulent reconnection should be clarified by the future research. Here we can provide arguments suggesting that tearing inevitably transfers to turbulent reconnection for sufficiently large Lundquist numbers S. Indeed, from the mass conservation constraint requirement in order to have fast reconnection one has to increase the outflow region thickness in proportion to L_x, which means the proportionality to the Lundquist number S. The Reynolds number Re of the outflow is $V_A \Delta / \nu$, where ν is viscosity, grows also as S. The outflow gets turbulent for sufficiently large Re. It is natural to assume that once the shearing rate introduced by eddies is larger than the rate of the tearing instability growth, the instability should get suppressed.

If one assumes that tearing is the necessary requirement for fast reconnection this entails the conclusion that tearing should proceed at the critically damped rate, which implies that the Re number and therefore Δ should not increase. This entails, however, the decrease of reconnection rate driven by tearing in proportion $L_x \sim S$ as a result of mass conservation. As a result, the reconnection should stop being fast. Fortunately, we know that turbulence itself provides fast reconnection irrespectively whether tearing is involved or not.

We also note that tearing reconnection in numerical simulations provides the reconnection rate around $0.01 V_A$ for collisional and somewhat larger rates for collisionless reconnection. These limitations are incompatible with the requirements of astrophysical reconnection, which, for instance, requires reconnection of the order of V_A for large scale eddies in transAlfvénic turbulence. In addition, fixed reconnection rates do not explain why observed reconnection may sometimes be slow and sometimes fast.

11.10.3 Turbulent Reconnection Versus Turbulent Resistivity and Mean Field Approach

Attempts to describe turbulent reconnection introducing some sort of turbulent resistivity are futile and misleading. It is possible to show that "turbulent/eddy resistivity" description has fatal problems of inaccuracy and unreliability, due to its poor physical foundations for turbulent flow. It is true that coarse-graining the MHD equations by eliminating modes at scales smaller than some length l will introduce a "turbulent electric field", i.e. an effective field acting on the large scales induced by motions of magnetized eddies at smaller scales. However, it is well-known in the fluid dynamics community that the resulting turbulent transport is not "down-gradient" and not well-represented by an enhanced diffusivity. Indeed, turbulence lacks the separation in scales to justify a simple "eddy-resistivity" description. As a consequence, energy is often not absorbed by the smaller eddies, but supplied by them, a phenomenon called "backscatter". The turbulent electric field often creates magnetic flux rather than destroys it.

If we know the reconnection rate, e.g. from LV99, then an eddy-resistivity can always be tuned by hand to achieve that rate. But this is not science. While the tuned reconnection rate will be correct by construction, other predictions will be wrong. The required large eddy-resistivity will smooth out all turbulence magnetic structure below the coarse-graining scale l. In reality, the turbulence will produce strong small-scale inhomogeneities, such as current sheets, from the scale l down to the micro-scale. In addition, field-lines in the flow smoothed by eddy-resistivity will not show the explosive, super-diffusive Richardson-type separation at scales below l. These are just examples of effects that will be lost if the wrong concept of "eddy resistivity" is adopted. Note, that the aforementioned are important for understanding particle transport/scattering/acceleration in the turbulent reconnection zone. We can also point out that in the case of relativistic reconnection that we also deal with in this review, turbulent resistivities will introduce non-causal, faster than light propagation effects. Nevertheless, the worst feature of the crude "eddy-resistivity" parametrization is its unreliability: because it has no scientific justification whatsoever, it cannot be applied with any confidence to astrophysical problems.

We would like to stress that the fast turbulent reconnection concept is definitely not equivalent to the dissipation of magnetic field by resistivity. While the parametrization of some particular effects of turbulent fluid may be achieved in models with different physics, e.g. of fluids with enormously enhanced resistivity, the difference in physics will inevitably result in other effects being wrongly represented by this effect. For instance, turbulence with fluid having resistivity corresponding to the value of "turbulent resistivity" must have magnetic field and fluid decoupled on most of its inertia range turbulent scale, i.e. the turbulence should not be affected by magnetic field in gross contradiction with theory, observations and numerical simulations. Magnetic helicity conservation which is essential for astrophysical dynamo should also be grossly violated.

The approach is quite different. It is not based on coarse-graining. The stochasticity of magnetic field-lines is a real, verified physical phenomenon in turbulent fluids. Whereas "eddy-resistivity" ideas predict that magnetic flux is destroyed by turbulence, our work shows that turbulent motions constantly changes connectivity of magnetic field lines without dissipating magnetic fields. Being moved by fluid motions the stochastic world-lines in relativistic turbulence do remain within the light-cone and no non-causal effects such as produced by "eddy-resistivity" being entailed.

Understanding that "resistivity arising from turbulence" is not a real plasma non-ideality "created" by the turbulence is essential for understanding why mean field approach fails in dealing with reconnection in turbulent fluids. Indeed, turbulence induced apparent non-ideality is dependent on the length and timescales of the averaging and it emerges only as a consequence of observing the plasma dynamics at a low resolution, so that the observed coarse-grained velocity and magnetic field do not satisfy the true microscopic equations of motion. It is obvious, that coarse-graining or averaging is a purely passive operation which doesn't change the actual plasma dynamics. The non-ideality in a turbulent plasma observed at length-scales in the inertial-range or larger is a valid representation of the effects of turbulent eddies at smaller scales. However, such apparent non-ideality cannot be represented by an effective "resistivity", a representation which in the fluid turbulence literature has been labeled the "gradient-transport fallacy" (Tennekes and Lumley 1972).

A recent paper that attempts to address turbulent reconnection using mean field approach is Guo et al. (2012), where ideas originally proposed in Kim and Diamond (2001) were modified and extended. Thus while the study in Kim and Diamond (2001) concluded that turbulence cannot accelerate reconnection, the more recent study came to the opposite conclusions. The expressions for reconnection rates in Guo et al. (2012) are different from those in LV99 and grossly contradict the results of numerical testing of turbulent reconnection in Kowal et al. (2009). Another model of turbulent reconnection based on the mean field approach is presented in Higashimori and Hoshino (2012).

The mean field approach invoked in the aforementioned studies is plagued by poor foundations and conceptual inconsistencies (Eyink, Lazarian & Vishniac 2011, henceforth ELV11). In such an approach effects of turbulence are described using parameters such as anisotropic turbulent magnetic diffusivity experienced by the fields once averaged over ensembles. The problem is that it is the lines of the full magnetic field that must be rapidly reconnected, not just the lines of the mean field. ELV11 stress that the former implies the latter, but not conversely. No mean-field approach can claim to have explained the observed rapid pace of magnetic reconnection unless it is shown that the reconnection rates obtained in the theory are strictly independent of the length and timescales of the averaging.

Other attempts to get fast magnetic reconnection from turbulence are related to the so-called hyper-resistivity concept (Strauss 1986; Bhattacharjee and Hameiri 1986; Hameiri and Bhattacharjee 1987; Diamond and Malkov 2003), which is another attempt to derive fast reconnection from turbulence within the context of mean-field resistive MHD. Apart from the generic problems of using the mean field

approach, the derivation of the hyper-resistivity is questionable from yet another point of view. The form of the parallel electric field is derived from magnetic helicity conservation. Integrating by parts one obtains a term which looks like an effective resistivity proportional to the magnetic helicity current. There are several assumptions implicit in this derivation, however. Fundamental to the hyper-resistive approach is the assumption that the magnetic helicity of mean fields and of small scale, statistically stationary turbulent fields are separately conserved, up to tiny resistivity effects. However, this ignores magnetic helicity fluxes through open boundaries, essential for stationary reconnection, that vitiate the conservation constraint (see more discussion in LV99, ELV11 and Lazarian et al. 2015).

11.10.4 Turbulent Reconnection: 3D Versus 2D

A lot of physical phenomena are different in 3D and 2D with hydrodynamic turbulence being a striking example. However, due to numerical constraints many numerical studies of the physical phenomena are sometimes initially attempted in the systems of reduced dimensions. Whether the physics in the system of reduced dimensions is representative of the physics of the 3D system in such situations must be theoretically justified and is eventually tested when the simulations of realistic set ups are available. The crucial differences between 2D and 3D magnetic reconnection are stressed in Priest (this volume) and also in publications by Boozer (2012, 2013), where it is shown that an extrapolation from reconnection physics obtained in 2D to 3D is poorly justified. In what follows, we add additional points why we do not believe that 2D turbulent reconnection can be a guide for our understanding of the 3D astrophysical reconnection.

Matthaeus and Lamkin (1985, 1986) explored numerically turbulent reconnection in 2D. As a theoretical motivation the authors emphasized analogies between the magnetic reconnection layer at high Lundquist numbers and homogeneous MHD turbulence. They also pointed out various turbulence mechanisms that would enhance reconnection rates, including multiple X-points as reconnection sites, compressibility effects, motional electromotive force (EMF) of magnetic bubbles advecting out of the reconnection zone. However, the authors did not realize the importance of stochastic magnetic field wondering and they did not arrive at an analytical prediction for the reconnection speed. Although an enhancement of the reconnection rate was reported in their numerical study, but the setup precluded the calculation of a long-term average reconnection rate.

We would like to stress the importance of this study in terms of attracting the attention of the community to the influence of turbulence on reconnection. However, the relation of this study with LV99 is not clear, as the nature of turbulence in 2D is different. In particular, shear-Alfvén waves that play the dominant role in 3D MHD turbulence according to GS95 are entirely lacking in 2D, where only pseudo-Alfvén wave modes exist.

We believe that the question whether turbulent reconnection is fast in 2D has not been resolved yet if we judge from the available publications. For instance, in a more recent study along the lines of the approach in Matthaeus and Lamkin (1985), i.e. in Watson et al. (2007), the effects of small-scale turbulence on 2D reconnection were studied and no significant effects of turbulence on reconnection was reported. Servidio et al. (2010) have more recently made a study of Ohmic electric fields at X-points in homogeneous, decaying 2D MHD turbulence. However, they studied a case of small-scale magnetic reconnection and their results are not directly relevant to the issue of reconnection of large-scale flux tubes that we deal with in this review. The study by Loureiro et al. (2009) and that by Kulpa-Dybeł et al. (2010) came to different conclusions on whether 2D turbulent reconnection is fast in 2D. If it is fast, the physics of 2D turbulent reconnection is nevertheless different from that in 3D, as both the nature of MHD turbulence that drives the reconnection and the nature of 2D and 3D reconnection processes are very different (see our discussions above).

We also stress that the small scale plasma turbulence that can change the local resistivity and local reconnection rates (see Karimabadi and Lazarian 2014 for a review) does not affect the global rate of turbulent reconnection. The latter is a MHD phenomenon that depends on the properties of turbulence only.

11.11 Final Remarks

11.11.1 Suggestive Evidence

There are pieces of evidence that are consistent with turbulent reconnection and can be interpreted as indirect suggestive evidence. For instance, Mininni and Pouquet (2009) showed that *fast dissipation* takes place in 3D MHD turbulence. This phenomenon is consistent with the idea of fast reconnection, but naturally cannot be treated as any proof. Obviously, fast dissipation and fast magnetic reconnection are rather different physical processes, dealing with decrease of energy on the one hand and decrease of magnetic flux on the other.

Similarly, works by Galsgaard and Nordlund (1997) could also be considered as being in agreement with fast reconnection idea. The authors showed that in their simulations they could not produce highly twisted magnetic fields. These configurations are subject to kink instability and the instability can produce turbulence and induce reconnection. However, in view of many uncertainties of the numerical studies, this relation is unclear. In fact, with low resolution involved in the simulations the Reynolds numbers could not allow a turbulent inertial-range. It is more likely that numerical finding in Lapenta and Bettarini (2011) which showed that reconnecting magnetic configurations spontaneously get chaotic and dissipate are related to LV99 reconnection. This connection is discussed in Lapenta and Lazarian (2012).

11.11.2 Interrelation of Different Concepts

The concept of turbulent magnetic field wandering is a well known concept of that was long adopted and widely used in the cosmic ray literature to explain observational evidence for the fast diffusion of cosmic rays perpendicular to the mean galactic magnetic field.[11] Although this concept existed in cosmic ray literature decades before the theory of turbulent reconnection was formulated, it is easy to understand that it is impossible to account for the magnetic field wandering if magnetic field lines do not reconnect.

The concept transport of heat by turbulent eddies in magnetized plasmas (Cho et al. 2002; Maron et al. 2004; Lazarian 2006) can only be understood within the paradigm of fast turbulent reconnection that allows mixing motions perpendicular to the local magnetic field. The same is applicable to the turbulent transport of metals in interstellar gas. Both phenomena are related to the reconnection diffusion. At scales smaller than the scale of injection scale, reconnection diffusion follows the superdiffusive law dictated by the Richardson dispersion, which on the scales larger than the injection scale, the diffusive behavior is restored.

At scales smaller than the injection scale the magnetic field wandering quantified in LV99 represents the Richardson dispersion in space. Last, but not the least, fast turbulent reconnection makes the GS95 theory of MHD turbulence self-consistent (LV99, see also Lazarian et al. 2015). All in all, magnetic turbulence and turbulent reconnection are intrinsically related.

11.11.3 Relation to Other Chapters of the Volume

This review deals with turbulent reconnection in MHD regime. MHD reconnection in laminar regime is addressed in the contribution by Priest (this volume). An interesting overlap in terms of conclusions is that the 3D and 2D reconnection processes are very different. Plasma effects related to reconnection and their laboratory studies are covered by Yamada et al. (this volume). The corresponding Reynolds numbers of reconnecting plasma outflows is insufficient for observing the regime of turbulent reconnection, but corresponds well to the present day two fluid simulations. The fact that thickness of the reconnection layers in the experiments is comparable with the ion inertial length makes this experiments very relevant to magnetospheric reconnection (see Cassak and Fuselier; Petrukovich et al., Raymond et al. this volume). We hope that in future experiments the reconnection will be

[11] It was shown in Lazarian and Yan (2014) that the mathematical formulation of the field wandering is an error in the classical papers, but this does not diminish the importance of the idea. In fact, the diffusion perpendicular to magnetic field by charged particles that follow magnetic field lines was an important impetus for one of the authors towards the idea of turbulent reconnection.

studied in the conditions closer to those that we discuss in the review and turbulent driving will be employed to test our predictions.

A case of interlaced, but not turbulent fields is considered by Parker and Rappazzo (this volume). In terms of turbulent reconnection, such configurations generating flares of reconnection may be important for inducing turbulence in the system.

Within turbulent reconnection the microphysics of individual local small scale reconnection events is not relevant for determining the global reconnection rate. However, many processes that accompany turbulent reconnection events, e.g. energization/acceleration of particles from the thermal pool do depend on the detailed microphysics, e.g. collisionless plasma physics (see Yamada et al.; Scudder et al., this volume), electric field at the separatrix of local reconnection events (Lapenta et al., this volume).

Turbulent reconnection theory that we described does not deal with complex radiative processes that are frequently manifest the reconnection events observationally. Their effect is described in detail by Uzdensky (this volume).

The closest in spirit review is that by Shibata and Takasao (this volume). Fractal structure is the accepted feature of turbulence and transition from laminar to fractal reconnection that the authors describe has the important overlap with the physical processes that we describe in this review. The authors, however, more focused on reconnection mediated by plasmoid generation, which may also be viewed as a complementary approach. As we discuss above we view tearing as a transient process that for systems of sufficiently high Reynolds numbers leads to turbulent reconnection.

We feel that the beauty of astrophysical turbulent reconnection is that it makes magnetic reconnection fast independently of detailed properties of plasmas, making magnetic reconnection really universal. This corresponds to observations as well as to the principal of parsimony. The plasma physics is, however, important for reconnection layers of the order of Larmor radius as is the case of the Earth magnetosphere and laboratory plasma experiments. It also may be important for the initiation of turbulent reconnection. We feel that magnetic reconnection presents a multi-facet problem where different approaches can be complementary.

Acknowledgements AL acknowledges the NSF grant AST 1212096, a distinguished visitor PVE/CAPES appointment at the Physics Graduate Program of the Federal University of Rio Grande do Norte and thanks the INCT INEspao and Physics Graduate Program/UFRN for hospitality. Final work on the review were done in a stimulating atmosphere of Bochum University during the visit supported by the Humboldt Foundation. GK acknowledges support from FAPESP (grants no. 2013/04073-2 and 2013/18815-0). EMGDP: Brazilian agencies FAPESP (2013/10559-5) and CNPq (306598/2009-4). JC acknowledges support from the National Research Foundation of Korea (NRF-2013R1A1A2064475).

References

H. Alfvén, On the existence of electromagnetic-hydrodynamic waves. Ark. Astron. **29**, 1–7 (1943)

J.W. Armstrong, B.J. Rickett, S.R. Spangler, Electron density power spectrum in the local interstellar medium. Astrophys. J. **443**, 209–221 (1995). doi:10.1086/175515

S.A. Balbus, J.F. Hawley, Instability, turbulence, and enhanced transport in accretion disks. Rev. Mod. Phys. **70**, 1–53 (1998). doi:10.1103/RevModPhys.70.1

S.D. Bale, P.J. Kellogg, F.S. Mozer, T.S. Horbury, H. Reme, Measurement of the electric fluctuation spectrum of magnetohydrodynamic turbulence. Phys. Rev. Lett. **94**(21), 215002 (2005). doi:10.1103/PhysRevLett.94.215002, physics/0503103

K. Beckwith, J.M. Stone, A second-order Godunov method for multi-dimensional relativistic magnetohydrodynamics. Astrophys. J. Suppl. Ser. **193**, 6 (2011). doi:10.1088/0067-0049/193/1/6, 1101.3573

A. Beresnyak, Comment on Perez et al. [PRX 2, 041005 (2012), arXiv:1209.2011] (2013) [ArXiv e-prints], 1301.7425

A. Beresnyak, Reply to comment on "spectra of strong magnetohydrodynamic turbulence from high-resolution simulations" (2014) [ArXiv e-prints], 1410.0957

A. Beresnyak, On the parallel spectrum in magnetohydrodynamic turbulence. Astrophys. J. Lett. **801**, L9 (2015). doi:10.1088/2041-8205/801/1/L9, 1407.2613

A. Beresnyak, A. Lazarian, Strong imbalanced turbulence. Astrophys. J. **682**, 1070–1075 (2008). doi:10.1086/589428, 0709.0554

A. Beresnyak, A. Lazarian, Scaling laws and diffuse locality of balanced and imbalanced magnetohydrodynamic turbulence. Astrophys. J. Lett. **722**, L110–L113 (2010). doi:10.1088/2041-8205/722/1/L110, 1002.2428

A. Beresnyak, A. Lazarian, MHD turbulence, turbulent dynamo and applications, in *Magnetic Fields in Diffuse Media*, ed. by A. Lazarian, E.M. de Gouveia Dal Pino, C. Melioli. Astrophysics and Space Science Library, vol. 407 (Springer, Heidelberg, 2015), p. 163. doi:10.1007/978-3-662-44625-6_8, 1406.1185

A. Bhattacharjee, E. Hameiri, Self-consistent dynamolike activity in turbulent plasmas. Phys. Rev. Lett. **57**, 206–209 (1986). doi:10.1103/PhysRevLett.57.206

D. Biskamp, *Magnetohydrodynamic Turbulence* (Cambridge University Press, Cambridge, 2003)

S. Boldyrev, Kolmogorov-Burgers model for star-forming turbulence. Astrophys. J. **569**, 841–845 (2002). doi:10.1086/339403, astro-ph/0108300

S. Boldyrev, On the spectrum of magnetohydrodynamic turbulence. Astrophys. J. Lett. **626**, L37–L40 (2005). doi:10.1086/431649, astro-ph/0503053

S. Boldyrev, Spectrum of magnetohydrodynamic turbulence. Phys. Rev. Lett. **96**(11), 115002 (2006). doi:10.1103/PhysRevLett.96.115002, astro-ph/0511290

A.H. Boozer, Separation of magnetic field lines. Phys. Plasmas **19**(11), 112901 (2012). doi:10.1063/1.4765352

A.H. Boozer, Tokamak halo currents. Phys. Plasmas **20**(8), 082510 (2013). doi:10.1063/1.4817742

A. Brandenburg, A. Lazarian, Astrophysical hydromagnetic turbulence. Space Sci. Rev. **178**, 163–200 (2013). doi:10.1007/s11214-013-0009-3, 1307.5496

P. Browning, A. Lazarian, Notes on magnetohydrodynamics of magnetic reconnection in turbulent media. Space Sci. Rev. **178**, 325–355 (2013). doi:10.1007/s11214-013-0022-6

G. Brunetti, A. Lazarian, Acceleration of primary and secondary particles in galaxy clusters by compressible MHD turbulence: from radio haloes to gamma-rays. Mon. Not. R. Astron. Soc. **410**, 127–142 (2011). doi:10.1111/j.1365-2966.2010.17457.x, 1008.0184

L.F. Burlaga, R.P. Lepping, K.W. Behannon, L.W. Klein, F.M. Neubauer, Large-scale variations of the interplanetary magnetic field - Voyager 1 and 2 observations between 1–5 AU. J. Geophys. Res. **87**, 4345–4353 (1982). doi:10.1029/JA087iA06p04345

D. Casanova, A. Lazarian, R. Santos-Lima, Magnetic fields in early protostellar disk formation. Astrophys. J. (2016, in press)

B. Cerutti, G.R. Werner, D.A. Uzdensky, M.C. Begelman, Simulations of particle acceleration beyond the classical synchrotron burnoff limit in magnetic reconnection: an explanation of the crab flares. Astrophys. J. **770**, 147 (2013). doi:10.1088/0004-637X/770/2/147, 1302.6247

B. Cerutti, G.R. Werner, D.A. Uzdensky, M.C. Begelman, Three-dimensional relativistic pair plasma reconnection with radiative feedback in the crab nebula. Astrophys. J. **782**, 104 (2014). doi:10.1088/0004-637X/782/2/104, 1311.2605

B.D.G. Chandran, AGN-driven convection in galaxy-cluster plasmas. Astrophys. J. **632**, 809–820 (2005). doi:10.1086/432596, astro-ph/0506096

B.D.G. Chandran, S.C. Cowley, M. Morris, Magnetic flux accumulation at the galactic center and its implications for the strength of the pregalactic magnetic field. Astrophys. J. **528**, 723–733 (2000). doi:10.1086/308184

A. Chepurnov, A. Lazarian, Extending the big power law in the sky with turbulence spectra from Wisconsin Hα mapper data. Astrophys. J. **710**, 853–858 (2010). doi:10.1088/0004-637X/710/1/853, 0905.4413

A. Chepurnov, A. Lazarian, S. Stanimirović, C. Heiles, J.E.G. Peek, Velocity spectrum for H I at high latitudes. Astrophys. J. **714**, 1398–1406 (2010). doi:10.1088/0004-637X/714/2/1398, astro-ph/0611462

A. Chepurnov, B. Burkhart, A. Lazarian, S. Stanimirovic, The turbulence velocity power spectrum of neutral hydrogen in the small magellanic cloud (2015) [ArXiv e-prints], 1506.03448

J. Cho, Simulations of relativistic force-free magnetohydrodynamic turbulence. Astrophys. J. **621**, 324–327 (2005). doi:10.1086/427493, astro-ph/0408318

J. Cho, Properties of balanced and imbalanced relativistic Alfvénic magnetohydrodynamic turbulence. J. Korean Phys. Soc. **65**, 871–875 (2014). doi:10.3938/jkps.65.871

J. Cho, A. Lazarian, Compressible sub-Alfvénic MHD turbulence in low- β plasmas. Phys. Rev. Lett. **88**(24), 245001 (2002). doi:10.1103/PhysRevLett.88.245001, astro-ph/0205282

J. Cho, A. Lazarian, Compressible magnetohydrodynamic turbulence: mode coupling, scaling relations, anisotropy, viscosity-damped regime and astrophysical implications. Mon. Not. R. Astron. Soc. **345**, 325–339 (2003). doi:10.1046/j.1365-8711.2003.06941.x, astro-ph/0301062

J. Cho, A. Lazarian, Imbalanced relativistic force-free magnetohydrodynamic turbulence. Astrophys. J. **780**, 30 (2014). doi:10.1088/0004-637X/780/1/30, 1312.6128

J. Cho, E.T. Vishniac, The anisotropy of magnetohydrodynamic Alfvénic turbulence. Astrophys. J. **539**, 273–282 (2000). doi:10.1086/309213, astro-ph/0003403

J. Cho, A. Lazarian, E.T. Vishniac, Simulations of magnetohydrodynamic turbulence in a strongly magnetized medium. Astrophys. J. **564**, 291–301 (2002). doi:10.1086/324186, astro-ph/0105235

J. Cho, A. Lazarian, E.T. Vishniac, MHD turbulence: scaling laws and astrophysical implications, in *Turbulence and Magnetic Fields in Astrophysics*, ed. by E. Falgarone, T. Passot. Lecture Notes in Physics, vol. 614 (Springer, Berlin, 2003), pp. 56–98, astro-ph/0205286

A. Ciaravella, J.C. Raymond The current sheet associated with the 2003 November 4 coronal mass ejection: density, temperature, thickness, and line width. Astrophys. J. **686**, 1372–1382 (2008). doi:10.1086/590655

E.M. de Gouveia Dal Pino, G. Kowal, Particle acceleration by magnetic reconnection, in *Magnetic Fields in Diffuse Media*, ed. by A. Lazarian, E.M. de Gouveia Dal Pino, C. Melioli. Astrophysics and Space Science Library, vol. 407 (Springer, Heidelberg, 2008), p. 373. doi:10.1007/978-3-662-44625-6_13, 1302.4374

E.M. de Gouveia Dal Pino, A. Lazarian, Production of the large scale superluminal ejections of the microquasar GRS 1915+105 by violent magnetic reconnection. Astron. Astrophys. **441**, 845–853 (2005). doi:10.1051/0004-6361:20042590

E.M. de Gouveia Dal Pino, G. Kowal, L.H.S. Kadowaki, P. Piovezan, A. Lazarian, Magnetic field effects near the launching region of astrophysical jets. Int. J. Mod. Phys. D **19**, 729–739 (2010a). doi:10.1142/S0218271810016920, 1002.4434

E.M. de Gouveia Dal Pino, P.P. Piovezan, L.H.S. Kadowaki, The role of magnetic reconnection on jet/accretion disk systems. Astron. Astrophys. **518**, A5 (2010b). doi:10.1051/0004-6361/200913462, 1005.3067

E.M. de Gouveia Dal Pino, M.R.M. Leão, R. Santos-Lima, G. Guerrero, G. Kowal, A. Lazarian, Magnetic flux transport by turbulent reconnection in astrophysical flows. Phys. Scr. **86**(1), 018401 (2012). doi:10.1088/0031-8949/86/01/018401, 1112.4871

E.M. de Gouveia Dal Pino, G. Kowal, A. Lazarian, Fermi acceleration in magnetic reconnection sites, in *8th International Conference of Numerical Modeling of Space Plasma Flows (ASTRONUM 2013)*, ed. by N.V. Pogorelov, E. Audit, G.P. Zank. Astronomical Society of the Pacific Conference Series, vol. 488 (2014), p. 8, 1401.4941

P.H. Diamond, M. Malkov, Dynamics of helicity transport and Taylor relaxation. Phys. Plasmas **10**, 2322–2329 (2003). doi:10.1063/1.1576390

W. Dobler, N.E. Haugen, T.A. Yousef, A. Brandenburg, Bottleneck effect in three-dimensional turbulence simulations. Phys. Rev. E **68**(2), 026304 (2003). doi:10.1103/PhysRevE.68.026304, astro-ph/0303324

J.F. Drake, Magnetic explosions in space. Nature **410**, 525–526 (2001)

J.F. Drake, M. Swisdak, H. Che, M.A. Shay, Electron acceleration from contracting magnetic islands during reconnection. Nature **443**, 553–556 (2006). doi:10.1038/nature05116

J.F. Drake, M. Opher, M. Swisdak, J.N. Chamoun, A magnetic reconnection mechanism for the generation of anomalous cosmic rays. Astrophys. J. **709**, 963–974 (2010). doi:10.1088/0004-637X/709/2/963, 0911.3098

G. Drenkhahn, H.C. Spruit, Efficient acceleration and radiation in Poynting flux powered GRB outflows. Astron. Astrophys. **391**, 1141–1153 (2002). doi:10.1051/0004-6361:20020839, astro-ph/0202387

L.O. Drury, First-order Fermi acceleration driven by magnetic reconnection. Mon. Not. R. Astron. Soc. **422**, 2474–2476 (2002). doi:10.1111/j.1365-2966.2012.20804.x, 1201.6612

T.A. Enßlin, C. Vogt, Magnetic turbulence in cool cores of galaxy clusters. Astron. Astrophys. **453**, 447–458 (2006). doi:10.1051/0004-6361:20053518, astro-ph/0505517

G.L. Eyink, Turbulent general magnetic reconnection (2014) [ArXiv e-prints], 1412.2254

G.L. Eyink, A. Lazarian, E.T. Vishniac, Fast magnetic reconnection and spontaneous stochasticity. Astrophys. J. **743**, 51 (2011). doi:10.1088/0004-637X/743/1/51, 1103.1882

G. Eyink, E. Vishniac, C. Lalescu, H. Aluie, K. Kanov, K. Bürger, R. Burns, C. Meneveau, A. Szalay, Flux-freezing breakdown in high-conductivity magnetohydrodynamic turbulence. Nature **497**, 466–469 (2013). doi:10.1038/nature12128

M. Fatuzzo, F.C. Adams, Enhancement of ambipolar diffusion rates through field fluctuations. Astrophys. J. **570**, 210–221 (2002). doi:10.1086/339502, astro-ph/0201131

K.M. Ferrière, The interstellar environment of our galaxy. Rev. Mod. Phys. **73**, 1031–1066 (2001). doi:10.1103/RevModPhys.73.1031, astro-ph/0106359

K. Galsgaard, Å Nordlund, Heating and activity of the solar corona. 3. Dynamics of a low beta plasma with three-dimensional null points. J. Geophys. Res. **102**, 231–248 (1997). doi:10.1029/96JA02680

S. Galtier, S. Banerjee, Exact relation for correlation functions in compressible isothermal turbulence. Phys. Rev. Lett. **107**(13), 134501 (2011). doi:10.1103/PhysRevLett.107.134501, 1108.4529

S. Galtier, S.V. Nazarenko, A.C. Newell, A. Pouquet, A weak turbulence theory for incompressible magnetohydrodynamics. J. Plasma Phys. **63**, 447–488 (2000). doi:10.1017/S0022377899008284, astro-ph/0008148

S. Galtier, S.V. Nazarenko, A.C. Newell, A. Pouquet, Anisotropic turbulence of shear-Alfvén waves. Astrophys. J. Lett. **564**, L49–L52 (2002). doi:10.1086/338791

D. Garrison, P. Nguyen, Characterization of relativistic MHD turbulence (2015) [ArXiv e-prints], 1501.06068

C.L. Gerrard, A.W. Hood, Kink unstable coronal loops: current sheets, current saturation and magnetic reconnection. Sol. Phys. **214**, 151–169 (2003). doi:10.1023/A:1024053501326

D. Giannios, Prompt GRB emission from gradual energy dissipation. Astron. Astrophys. **480**, 305–312 (2008). doi:10.1051/0004-6361:20079085, 0711.2632

D. Giannios, UHECRs from magnetic reconnection in relativistic jets. Mon. Not. R. Astron. Soc. **408**, L46–L50 (2010). doi:10.1111/j.1745-3933.2010.00925.x, 1007.1522

D. Giannios, H.C. Spruit, The role of kink instability in Poynting-flux dominated jets. Astron. Astrophys. **450**, 887–898 (2006). doi:10.1051/0004-6361:20054107, astro-ph/0601172

P. Goldreich, S. Sridhar, Toward a theory of interstellar turbulence. 2: strong Alfvenic turbulence. Astrophys. J. **438**, 763–775 (1995). doi:10.1086/175121

J.T. Gosling, Observations of magnetic reconnection in the turbulent high-speed solar wind. Astrophys. J. Lett. **671**, L73–L76 (2007). doi:10.1086/524842

Z.B. Guo, P.H. Diamond, X.G. Wang, Magnetic reconnection, helicity dynamics, and hyper-diffusion. Astrophys. J. **757**, 173 (2012). doi:10.1088/0004-637X/757/2/173

F. Guo, Y.H. Liu, W. Daughton, H. Li, Particle acceleration and plasma dynamics during magnetic reconnection in the magnetically dominated regime. Astrophys. J. **806**, 167 (2015). doi:10.1088/0004-637X/806/2/167, 1504.02193

E. Hameiri, A. Bhattacharjee, Turbulent magnetic diffusion and magnetic field reversal. Phys. Fluids **30**, 1743–1755 (1987). doi:10.1063/1.866241

F. Heitsch, E.G. Zweibel, Suppression of fast reconnection by magnetic shear. Astrophys. J. **590**, 291–295 (2003). doi:10.1086/375009

F. Heitsch, E.G. Zweibel, A.D. Slyz, J.E.G. Devriendt, Magnetic flux transport in the ISM through turbulent ambipolar diffusion. Astrophys. Space Sci. **292**, 45–51 (2004). doi:10.1023/B:ASTR.0000044999.25908.a5

K. Higashimori, M. Hoshino, The relation between ion temperature anisotropy and formation of slow shocks in collisionless magnetic reconnection. J. Geophys. Res. Space Phys. **117**, A01220 (2012). doi:10.1029/2011JA016817, 1201.4213

J.C. Higdon, Density fluctuations in the interstellar medium: evidence for anisotropic magneto-gasdynamic turbulence. I - model and astrophysical sites. Astrophys. J. **285**, 109–123 (1984). doi:10.1086/162481

M. Hoshino, Y. Lyubarsky, Relativistic reconnection and particle acceleration. Space Sci. Rev. **173**, 521–533 (2012). doi:10.1007/s11214-012-9931-z

T. Inoue, K. Asano, K. Ioka, Three-dimensional simulations of magnetohydrodynamic turbulence behind relativistic shock waves and their implications for gamma-ray bursts. Astrophys. J. **734**, 77 (2011). doi:10.1088/0004-637X/734/2/77, 1011.6350

P.S. Iroshnikov, Turbulence of a conducting fluid in a strong magnetic field. Sov. Astron. **7**, 566 (1964)

C.H. Jaroschek, H. Lesch, R.A. Treumann, Relativistic kinetic reconnection as the possible source mechanism for high variability and flat spectra in extragalactic radio sources. Astrophys. J. Lett. **605**, L9–L12 (2004). doi:10.1086/420767

L.H.S. Kadowaki, E.M. de Gouveia Dal Pino, C.B. Singh, The role of fast magnetic reconnection on the radio and gamma-ray emission from the nuclear regions of microquasars and low luminosity AGNs. Astrophys. J. **802**, 113 (2015). doi:10.1088/0004-637X/802/2/113, 1410.3454

H. Karimabadi, A. Lazarian, Magnetic reconnection in the presence of externally driven and self-generated turbulence. Phys. Plasmas **20**(11), 112102 (2013). doi:10.1063/1.4828395

H. Karimabadi, V. Roytershteyn, H.X. Vu, Y.A. Omelchenko, J. Scudder, W. Daughton, A. Dimmock, K. Nykyri, M. Wan, D. Sibeck, M. Tatineni, A. Majumdar, B. Loring, B. Geveci, The link between shocks, turbulence, and magnetic reconnection in collisionless plasmas. Phys. Plasmas **21**(6), 062308 (2014). doi:10.1063/1.4882875

O. Khabarova, V. Obridko, Puzzles of the interplanetary magnetic field in the inner heliosphere. Astrophys. J. **761**, 82 (2012). doi:10.1088/0004-637X/761/2/82, 1204.6672

B. Khiali, E.M. de Gouveia Dal Pino, Very high energy neutrino emission from the core of low luminosity AGNs triggered by magnetic reconnection acceleration (2015) [ArXiv e-prints], 1506.01063

B. Khiali, E.M. de Gouveia Dal Pino, M.V. del Valle, A magnetic reconnection model for explaining the multiwavelength emission of the microquasars Cyg X-1 and Cyg X-3. Mon. Not. R. Astron. Soc. **449**, 34–48 (2015a). doi:10.1093/mnras/stv248, 1406.5664

B. Khiali, E.M. de Gouveia Dal Pino, H. Sol, Particle acceleration and gamma-ray emission due to magnetic reconnection in the core region of radio galaxies (2015b) [ArXiv e-prints], 1504.07592

E.J. Kim, P.H. Diamond, On turbulent reconnection. Astrophys. J. **556**, 1052–1065 (2001). doi:10.1086/321628, astro-ph/0101161
S.S. Komissarov, Time-dependent, force-free, degenerate electrodynamics. Mon. Not. R. Astron. Soc. **336**, 759–766 (2002). doi:10.1046/j.1365-8711.2002.05313.x, astro-ph/0202447
G. Kowal, A. Lazarian, Astrophys. J. **666**, L69 (2007)
G. Kowal, A. Lazarian, Velocity field of compressible magnetohydrodynamic turbulence: wavelet decomposition and mode scalings. Astrophys. J. **720**, 742–756 (2010). doi:10.1088/0004-637X/720/1/742, 1003.3697
G. Kowal, A. Lazarian, A. Beresnyak, Astrophys. J. **658**, 423 (2007)
G. Kowal, A. Lazarian, E.T. Vishniac, K. Otmianowska-Mazur, Numerical tests of fast reconnection in weakly stochastic magnetic fields. Astrophys. J. **700**, 63–85 (2009). doi:10.1088/0004-637X/700/1/63, 0903.2052
G. Kowal, E.M. de Gouveia Dal Pino, A. Lazarian, Magnetohydrodynamic simulations of reconnection and particle acceleration: three-dimensional effects. Astrophys. J. **735**, 102 (2011). doi:10.1088/0004-637X/735/2/102, 1103.2984
G. Kowal, A. Lazarian, E.T. Vishniac, K. Otmianowska-Mazur, Reconnection studies under different types of turbulence driving. Nonlinear Process. Geophys. **19**, 297–314 (2012). doi:10.5194/npg-19-297-2012, 1203.2971
G. Kowal, D.A. Falceta-Gon, calves, A. Lazarian, E.T. Vishniac, Turbulence generated by reconnection (2015, preprint)
R.H. Kraichnan, Inertial-range spectrum of hydromagnetic turbulence. Phys. Fluids **8**, 1385–1387 (1965). doi:10.1063/1.1761412
A.G. Kritsuk, M.L. Norman, P. Padoan, R. Wagner, The statistics of supersonic isothermal turbulence. Astrophys. J. **665**, 416–431 (2007). doi:10.1086/519443, 0704.3851
K. Kulpa-Dybeł, G. Kowal, K. Otmianowska-Mazur, A. Lazarian, E. Vishniac, Reconnection in weakly stochastic B-fields in 2D. Astron. Astrophys. **514**, A26 (2010). doi:10.1051/0004-6361/200913218, 0909.1265
A. Kupiainen, Nondeterministic dynamics and turbulent transport. Ann. Henri Poincaré **4**, 713–726 (2003). doi:10.1007/s00023-003-0957-3
C.C. Lalescu, K.K. Shi, G.L. Eyink, T.D. Drivas, E.T. Vishniac, A. Lazarian, Inertial-range reconnection in magnetohydrodynamic turbulence and in the solar wind. Phys. Rev. Lett. **115**(2), 025001 (2015). doi:10.1103/PhysRevLett.115.025001, 1503.00509
G. Lapenta, Self-feeding turbulent magnetic reconnection on macroscopic scales. Phys. Rev. Lett. **100**(23), 235001 (2008). doi:10.1103/PhysRevLett.100.235001, 0805.0426
G. Lapenta, L. Bettarini, Spontaneous transition to a fast 3D turbulent reconnection regime. Europhys. Lett. **93**, 65001 (2011). doi:10.1209/0295-5075/93/65001, 1102.4791
G. Lapenta, A. Lazarian, Achieving fast reconnection in resistive MHD models via turbulent means. Nonlinear Process. Geophys. **19**, 251–263 (2012). doi:10.5194/npg-19-251-2012, 1110.0089
A. Lazarian, Astrophysical implications of turbulent reconnection: from cosmic rays to star formation, in *Magnetic Fields in the Universe: From Laboratory and Stars to Primordial Structures*, ed. by E.M. de Gouveia dal Pino, G. Lugones, A. Lazarian. American Institute of Physics Conference Series, vol. 784 (American Institute of Physics, New York, 2005), pp. 42–53. doi:10.1063/1.2077170, astro-ph/0505574
A. Lazarian, Enhancement and suppression of heat transfer by MHD turbulence. Astrophys. J. Lett. **645**, L25–L28 (2006). doi:10.1086/505796, astro-ph/0608045
A. Lazarian, Obtaining spectra of turbulent velocity from observations. Space Sci. Rev. **143**, 357–385 (2009). doi:10.1007/s11214-008-9460-y, 0811.0839
A. Lazarian, Fast reconnection and reconnection diffusion: implications for star formation (2011) [ArXiv e-prints], 1111.0694
A. Lazarian, Reconnection diffusion in turbulent fluids and its implications for star formation. Space Sci. Rev. **181**, 1–59 (2014). doi:10.1007/s11214-013-0031-5
A. Lazarian, A. Beresnyak, Cosmic ray scattering in compressible turbulence. Mon. Not. R. Astron. Soc. **373**, 1195–1202 (2006). doi:10.1111/j.1365-2966.2006.11093.x, astro-ph/0606737

A. Lazarian, P. Desiati, Magnetic reconnection as the cause of cosmic ray excess from the heliospheric tail. Astrophys. J. **722**, 188–196 (2010). doi:10.1088/0004-637X/722/1/188, 1008.1981
A. Lazarian, M.V. Medvedev (2015, preprint)
A. Lazarian, M. Opher, A model of acceleration of anomalous cosmic rays by reconnection in the heliosheath. Astrophys. J. **703**, 8–21 (2009). doi:10.1088/0004-637X/703/1/8, 0905.1120
A. Lazarian, D. Pogosyan, Velocity modification of H I power spectrum. Astrophys. J. **537**, 720–748 (2000). doi:10.1086/309040, astro-ph/9901241
A. Lazarian, D. Pogosyan, Velocity modification of the power spectrum from an absorbing medium. Astrophys. J. **616**, 943–965 (2004). doi:10.1086/422462, astro-ph/0405461
A. Lazarian, D. Pogosyan, Studying turbulence using doppler-broadened lines: velocity coordinate spectrum. Astrophys. J. **652**, 1348–1365 (2006). doi:10.1086/508012, astro-ph/0511248
A. Lazarian, D. Pogosyan, Statistical description of synchrotron intensity fluctuations: studies of astrophysical magnetic turbulence. Astrophys. J. **747**, 5 (2012). doi:10.1088/0004-637X/747/1/5, 1105.4617
A. Lazarian, E.T. Vishniac, Reconnection in a weakly stochastic field. Astrophys. J. **517**, 700–718 (1999). doi:10.1086/307233, astro-ph/9811037
A. Lazarian, E.T. Vishniac, Model of reconnection of weakly stochastic magnetic field and its implications, in *Revista Mexicana de Astronomia y Astrofisica Conference Series*, vols. 27, 36 (2009), pp. 81–88, 0812.2019
A. Lazarian, H. Yan, Superdiffusion of cosmic rays: implications for cosmic ray acceleration. Astrophys. J. **784**, 38 (2014). doi:10.1088/0004-637X/784/1/38, 1308.3244
A. Lazarian, V. Petrosian, H. Yan, J. Cho, Physics of gamma-ray bursts: turbulence, energy transfer and reconnection (2003) [ArXiv Astrophysics e-prints] astro-ph/0301181
A. Lazarian, E.T. Vishniac, J. Cho, Magnetic field structure and stochastic reconnection in a partially ionized gas. Astrophys. J. **603**, 180–197 (2004). doi:10.1086/381383, physics/0311051
A. Lazarian, G. Kowal, B. de Gouveia dal Pino, Astrophysical reconnection and particle acceleration, in *Numerical Modeling of Space Plasma Slows (ASTRONUM 2011)*, ed. by N.V. Pogorelov, J.A. Font, E. Audit, G.P. Zank. Astronomical Society of the Pacific Conference Series, vol. 459 (2012), p. 21, 1202.1559
A. Lazarian, G.L. Eyink, E.T. Vishniac, G. Kowal, Magnetic reconnection in astrophysical environments, in *Magnetic Fields in Diffuse Media*, ed. by A. Lazarian, E.M. de Gouveia Dal Pino, C. Melioli. Astrophysics and Space Science Library, vol. 407 (Springer, Heidelberg, 2015a), p. 311. doi:10.1007/978-3-662-44625-6_12, 1407.6356
A. Lazarian, G.L. Eyink, E.T. Vishniac, G. Kowal, Turbulent reconnection and its implications. Philos. Trans. R. Soc. Lond. Ser. A **373**, 40144 (2015b)
M.R.M. Leão, E.M. de Gouveia Dal Pino, R. Santos-Lima, A. Lazarian, The collapse of turbulent cores and reconnection diffusion. Astrophys. J. **777**, 46 (2013). doi:10.1088/0004-637X/777/1/46, 1209.1846
R.J. Leamon, C.W. Smith, N.F. Ness, W.H. Matthaeus, H.K. Wong, Observational constraints on the dynamics of the interplanetary magnetic field dissipation range. J. Geophys. Res. **103**, 4775 (1998). doi:10.1029/97JA03394
Y. Lithwick, P. Goldreich, Compressible magnetohydrodynamic turbulence in interstellar plasmas. Astrophys. J. **562**, 279–296 (2001). doi:10.1086/323470, astro-ph/0106425
Y.E. Litvinenko, Particle acceleration in reconnecting current sheets with a nonzero magnetic field. Astrophys. J. **462**, 997 (1996). doi:10.1086/177213
N.F. Loureiro, A.A. Schekochihin, S.C. Cowley, Instability of current sheets and formation of plasmoid chains. Phys. Plasmas **14**(10), 100703 (2007). doi:10.1063/1.2783986, astro-ph/0703631
N.F. Loureiro, D.A. Uzdensky, A.A. Schekochihin, S.C. Cowley, T.A. Yousef, Turbulent magnetic reconnection in two dimensions. Mon. Not. R. Astron. Soc. **399**, L146–L150 (2009). doi:10.1111/j.1745-3933.2009.00742.x, 0904.0823
M. Lyutikov, A. Lazarian, Topics in microphysics of relativistic plasmas. Space Sci. Rev. **178**, 459–481 (2013). doi:10.1007/s11214-013-9989-2, 1305.3838

J. Maron, P. Goldreich, Simulations of incompressible magnetohydrodynamic turbulence. Astrophys. J. **554**, 1175–1196 (2001). doi:10.1086/321413, astro-ph/0012491

J. Maron, B.D. Chandran, E. Blackman, Divergence of neighboring magnetic-field lines and fast-particle diffusion in strong magnetohydrodynamic turbulence, with application to thermal conduction in galaxy clusters. Phys. Rev. Lett. **92**(4), 045001 (2004). doi:10.1103/PhysRevLett.92.045001, astro-ph/0303217

J. Mason, F. Cattaneo, S. Boldyrev, Dynamic alignment in driven magnetohydrodynamic turbulence. Phys. Rev. Lett. **97**(25), 255002 (2006). doi:10.1103/PhysRevLett.97.255002, astro-ph/0602382

J. Mason, F. Cattaneo, S. Boldyrev, Numerical measurements of the spectrum in magnetohydrodynamic turbulence. Phys. Rev. E **77**(3), 036403 (2008). doi:10.1103/PhysRevE.77.036403, 0706.2003

W.H. Matthaeus, S.L. Lamkin, Rapid magnetic reconnection caused by finite amplitude fluctuations. Phys. Fluids **28**, 303–307 (1985). doi:10.1063/1.865147

W.H. Matthaeus, S.L. Lamkin, Turbulent magnetic reconnection. Phys. Fluids **29**, 2513–2534 (1986). doi:10.1063/1.866004

W.H. Matthaeus, D.C. Montgomery, M.L. Goldstein, Turbulent generation of outward-traveling interplanetary Alfvenic fluctuations. Phys. Rev. Lett. **51**, 1484–1487 (1983). doi:10.1103/PhysRevLett.51.1484

J.C. McKinney, D.A. Uzdensky, A reconnection switch to trigger gamma-ray burst jet dissipation. Mon. Not. R. Astron. Soc. **419**, 573–607 (2012). doi:10.1111/j.1365-2966.2011.19721.x, 1011.1904

D.L. Meier, *Black Hole Astrophysics: The Engine Paradigm* (Springer, Berlin, 2012). ISBN: 978-3-642-01935-7

A. Merloni, S. Heinz, T. di Matteo, A fundamental plane of black hole activity. Mon. Not. R. Astron. Soc. **345**, 1057–1076 (2003). doi:10.1046/j.1365-2966.2003.07017.x, astro-ph/0305261

M.S. Miesch, W.H. Matthaeus, A. Brandenburg, A. Petrosyan, A. Pouquet, C. Cambon, F. Jenko, D. Uzdensky, J. Stone, S. Tobias, J. Toomre, M. Velli, Large-Eddy simulations of magnetohydrodynamic turbulence in astrophysics and space physics (2015) [ArXiv e-prints], 1505.01808

P.D. Mininni, A. Pouquet, Finite dissipation and intermittency in magnetohydrodynamics. Phys. Rev. E **80**(2), 025401 (2009). doi:10.1103/PhysRevE.80.025401, 0903.3265

Y. Mizuno, C. Singh, E.M. de Gouveia Dal Pino (2015, in preparation)

D. Montgomery, L. Turner, Anisotropic magnetohydrodynamic turbulence in a strong external magnetic field. Phys. Fluids **24**, 825–831 (1981). doi:10.1063/1.863455

W.C. Müller, R. Grappin, Spectral energy dynamics in magnetohydrodynamic turbulence. Phys. Rev. Lett. **95**(11), 114502 (2005). doi:10.1103/PhysRevLett.95.114502, physics/0509019

R. Narayan, M.V. Medvedev, Self-similar hot accretion on to a spinning neutron star: matching the outer boundary conditions. Mon. Not. R. Astron. Soc. **343**, 1007–1012 (2003). doi:10.1046/j.1365-8711.2003.06747.x, astro-ph/0305002

R. Narayan, I. Yi, Advection-dominated accretion: underfed black holes and neutron stars. Astrophys. J. **452**, 710 (1995). doi:10.1086/176343, astro-ph/9411059

C.S. Ng, A. Bhattacharjee, Interaction of shear-Alfven wave packets: implication for weak magnetohydrodynamic turbulence in astrophysical plasmas. Astrophys. J. **465**, 845 (1996). doi:10.1086/177468

C.A. Norman, A. Ferrara, The turbulent interstellar medium: generalizing to a scale-dependent phase continuum. Astrophys. J. **467**, 280 (1996). doi:10.1086/177603, astro-ph/9602146

J.S. Oishi, M.M. Mac Low, D.C. Collins, M. Tamura, Self-generated turbulence in magnetic reconnection (2015) [ArXiv e-prints], 1505.04653

P. Padoan, M. Juvela, A. Kritsuk, M.L. Norman, The power spectrum of supersonic turbulence in perseus. Astrophys. J. Lett. **653**, L125–L128 (2006). doi:10.1086/510620, astro-ph/0611248

P. Padoan, A.G. Kritsuk, T. Lunttila, M. Juvela, A. Nordlund, M.L. Norman, S.D. Ustyugov, MHD turbulence in star-forming clouds, in *American Institute of Physics Conference Series*,

vol. 1242, ed. by G. Bertin, F. de Luca, G. Lodato, R. Pozzoli, M. Romé (2010), pp. 219–230. doi:10.1063/1.3460128

P.P. Papadopoulos, W.F. Thi, F. Miniati, S. Viti, Extreme cosmic ray dominated regions: a new paradigm for high star formation density events in the Universe. Mon. Not. R. Astron. Soc. **414**, 1705–1714 (2011). doi:10.1111/j.1365-2966.2011.18504.x, 1009.2496

E.N. Parker, Sweet's mechanism for merging magnetic fields in conducting fluids. J. Geophys. Res. **62**, 509–520 (1957). doi:10.1029/JZ062i004p00509

E.N. Parker, *Cosmical Magnetic Fields: Their Origin and Their Activity* (Clarendon Press, Oxford/Oxford University Press, New York, 1979), 858 pp

J.C. Perez, J. Mason, S. Boldyrev, F. Cattaneo, On the energy spectrum of strong magnetohydrodynamic turbulence. Phys. Rev. X **2**(4), 041005 (2012). doi:10.1103/PhysRevX.2.041005, 1209.2011

D. Radice, L. Rezzolla, Universality and intermittency in relativistic turbulent flows of a hot plasma. Astrophys. J. Lett. **766**, L10 (2013). doi:10.1088/2041-8205/766/1/L10, 1209.2936

A.B. Rechester, M.N. Rosenbluth, Electron heat transport in a Tokamak with destroyed magnetic surfaces. Phys. Rev. Lett. **40**, 38–41 (1978). doi:10.1103/PhysRevLett.40.38

G. Rocha da Silva, D. Falceta-Gonçalves, G. Kowal, E.M. de Gouveia Dal Pino, Ambient magnetic field amplification in shock fronts of relativistic jets: an application to GRB afterglows. Mon. Not. R. Astron. Soc. **446**, 104–119 (2015). doi:10.1093/mnras/stu2104, 1410.2776

R. Santos-Lima, A. Lazarian, E.M. de Gouveia Dal Pino, J. Cho, Diffusion of magnetic field and removal of magnetic flux from clouds via turbulent reconnection. Astrophys. J. **714**, 442–461 (2010). doi:10.1088/0004-637X/714/1/442, 0910.1117

R. Santos-Lima, E.M. de Gouveia Dal Pino, A. Lazarian, The role of turbulent magnetic reconnection in the formation of rotationally supported protostellar disks. Astrophys. J. **747**, 21 (2012). doi:10.1088/0004-637X/747/1/21, 1109.3716

R. Santos-Lima, E.M. de Gouveia Dal Pino, A. Lazarian, Disc formation in turbulent cloud cores: is magnetic flux loss necessary to stop the magnetic braking catastrophe or not? Mon. Not. R. Astron. Soc. **429**, 3371–3378 (2013). doi:10.1093/mnras/sts597, 1211.1059

A.A. Schekochihin, S.C. Cowley, W. Dorland, G.W. Hammett, G.G. Howes, E. Quataert, T. Tatsuno, Astrophysical gyrokinetics: kinetic and fluid turbulent cascades in magnetized weakly collisional plasmas. Astrophys. J. Suppl. Ser. **182**, 310–377 (2009). doi:10.1088/0067-0049/182/1/310, 0704.0044

S. Servidio, W.H. Matthaeus, M.A. Shay, P. Dmitruk, P.A. Cassak, M. Wan, Statistics of magnetic reconnection in two-dimensional magnetohydrodynamic turbulence. Phys. Plasmas **17**(3), 032315 (2010). doi:10.1063/1.3368798

M.A. Shay, J.F. Drake, R.E. Denton, D. Biskamp, Structure of the dissipation region during collisionless magnetic reconnection. J. Geophys. Res. **103**, 9165–9176 (1998). doi:10.1029/97JA03528

M.A. Shay, J.F. Drake, M. Swisdak, B.N. Rogers, The scaling of embedded collisionless reconnection. Phys. Plasmas **11**, 2199–2213 (2004). doi:10.1063/1.1705650

Z.S. She, E. Leveque, Universal scaling laws in fully developed turbulence. Phys. Rev. Lett. **72**, 336–339 (1994). doi:10.1103/PhysRevLett.72.336

J.V. Shebalin, W.H. Matthaeus, D. Montgomery, Anisotropy in MHD turbulence due to a mean magnetic field. J. Plasma Phys. **29**, 525–547 (1983). doi:10.1017/S0022377800000933

K. Shibata, S. Tanuma, Plasmoid-induced-reconnection and fractal reconnection. Earth Planets Space **53**, 473–482 (2001). astro-ph/0101008

F.H. Shu, Ambipolar diffusion in self-gravitating isothermal layers. Astrophys. J. **273**, 202–213 (1983). doi:10.1086/161359

C.B. Singh, E.M. de Gouveia Dal Pino, L.H.S. Kadowaki, On the role of fast magnetic reconnection in accreting black hole sources. Astrophys. J. Lett. **799**, L20 (2015). doi:10.1088/2041-8205/799/2/L20, 1411.0883

L. Sironi, A. Spitkovsky, Relativistic reconnection: an efficient source of non-thermal particles. Astrophys. J. Lett. **783**, L21 (2014). doi:10.1088/2041-8205/783/1/L21, 1401.5471

S. Stanimirović, A. Lazarian, Velocity and density spectra of the small magellanic cloud. Astrophys. J. Lett. **551**, L53–L56 (2001). doi:10.1086/319837, astro-ph/0102191
H.R. Strauss, Hyper-resistivity produced by tearing mode turbulence. Phys. Fluids **29**, 3668–3671 (1986). doi:10.1063/1.865798
K. Subramanian, A. Shukurov, N.E.L. Haugen, Evolving turbulence and magnetic fields in galaxy clusters. Mon. Not. R. Astron. Soc. **366**, 1437–1454 (2006). doi:10.1111/j.1365-2966.2006.09918.x, astro-ph/0505144
P.A. Sweet, The topology of force-free magnetic fields. Observatory **78**, 30–32 (1958)
R. Sych, V.M. Nakariakov, M. Karlicky, S. Anfinogentov, Relationship between wave processes in sunspots and quasi-periodic pulsations in active region flares. Astron. Astrophys. **505**, 791–799 (2009). doi:10.1051/0004-6361/200912132, 1005.3594
S.I. Syrovatskii, Pinch sheets and reconnection in astrophysics. Annu. Rev. Astron. Astrophys. **19**, 163–229 (1981). doi:10.1146/annurev.aa.19.090181.001115
I.V. Sytine, D.H. Porter, P.R. Woodward, S.W. Hodson, K.H. Winkler, Convergence tests for the piecewise parabolic method and Navier-Stokes solutions for homogeneous compressible turbulence. J. Comput. Phys. **158**, 225–238 (2000). doi:10.1006/jcph.1999.6416
M. Takamoto, T. Inoue, A new numerical scheme for resistive relativistic magnetohydrodynamics using method of characteristics. Astrophys. J. **735**, 113 (2011). doi:10.1088/0004-637X/735/2/113, 1105.5683
M. Takamoto, T. Inoue, A. Lazarian, Turbulent relativistic reconnection. Astrophys. J. **815**, 16 (2015)
H. Tennekes, J.L. Lumley, *First Course in Turbulence* (MIT Press, Cambridge, 1972)
C. Thompson, O. Blaes, Magnetohydrodynamics in the extreme relativistic limit. Phys. Rev. D **57**, 3219–3234 (1998). doi:10.1103/PhysRevD.57.3219
D.A. Uzdensky, A. Spitkovsky, Physical conditions in the reconnection layer in pulsar magnetospheres. Astrophys. J. **780**, 3 (2014). doi:10.1088/0004-637X/780/1/3, 1210.3346
D.A. Uzdensky, N.F. Loureiro, A.A. Schekochihin, Fast magnetic reconnection in the plasmoid-dominated regime. Phys. Rev. Lett. **105**(23), 235002 (2010). doi:10.1103/PhysRevLett.105.235002, 1008.3330
E.T. Vishniac, A. Lazarian, Reconnection in the interstellar medium. Astrophys. J. **511**, 193–203 (1999). doi:10.1086/306643, astro-ph/9712067
E.T. Vishniac, S. Pillsworth, G. Eyink, G. Kowal, A. Lazarian, S. Murray, Reconnection current sheet structure in a turbulent medium. Nonlinear Process. Geophys. **19**, 605–610 (2012). doi:10.5194/npg-19-605-2012
C. Vogt, T.A. Enßlin, A Bayesian view on Faraday rotation maps Seeing the magnetic power spectra in galaxy clusters. Astron. Astrophys. **434**, 67–76 (2005). doi:10.1051/0004-6361:20041839, astro-ph/0501211
P.G. Watson, S. Oughton, I.J.D. Craig, The impact of small-scale turbulence on laminar magnetic reconnection. Phys. Plasmas **14**(3), 032301 (2007). doi:10.1063/1.2458595
G.R. Werner, D.A. Uzdensky, B. Cerutti, K. Nalewajko, M.C. Begelman, The extent of power-law energy spectra in collisionless relativistic magnetic reconnection in pair plasmas (2014) [ArXiv e-prints], 1409.8262
S. Xu, H. Yan, A. Lazarian, Damping of MHD turbulence in partially ionized plasma: implications for cosmic ray propagation (2015) [ArXiv e-prints], 1506.05585
M. Yamada, R. Kulsrud, H. Ji, Magnetic reconnection. Rev. Mod. Phys. **82**, 603–664 (2010). doi:10.1103/RevModPhys.82.603
S. Zenitani, M. Hoshino, The generation of nonthermal particles in the relativistic magnetic reconnection of pair plasmas. Astrophys. J. Lett. **562**, L63–L66 (2001). doi:10.1086/337972, 1402.7139
S. Zenitani, M. Hoshino, The role of the guide field in relativistic pair plasma reconnection. Astrophys. J. **677**, 530–544 (2008). doi:10.1086/528708, 0712.2016
S. Zenitani, M. Hesse, A. Klimas, Two-fluid magnetohydrodynamic simulations of relativistic magnetic reconnection. Astrophys. J. **696**, 1385–1401 (2009). doi:10.1088/0004-637X/696/2/1385, 0902.2074

B. Zhang, H. Yan, The internal-collision-induced magnetic reconnection and turbulence (ICMART) model of gamma-ray bursts. Astrophys. J. **726**, 90 (2011). doi:10.1088/0004-637X/726/2/90, 1011.1197

W. Zhang, A. MacFadyen, P. Wang, Three-dimensional relativistic magnetohydrodynamic simulations of the Kelvin-Helmholtz instability: magnetic field amplification by a turbulent dynamo. Astrophys. J. Lett. **692**, L40–L44 (2009). doi:10.1088/0004-637X/692/1/L40, 0811.3638

J. Zrake, A.I. MacFadyen, Numerical simulations of driven relativistic magnetohydrodynamic turbulence. Astrophys. J. **744**, 32 (2012). doi:10.1088/0004-637X/744/1/32, 1108.1991

J. Zrake, A.I. MacFadyen, Spectral and intermittency properties of relativistic turbulence. Astrophys. J. Lett. **763**, L12 (2013). doi:10.1088/2041-8205/763/1/L12, 1210.4066

E.G. Zweibel, Ambipolar drift in a turbulent medium. Astrophys. J. **567**, 962–970 (2002). doi:10.1086/338682, astro-ph/0107462

Chapter 12
Radiative Magnetic Reconnection in Astrophysics

D.A. Uzdensky

Abstract In this chapter we review a new and rapidly growing area of research in high-energy plasma astrophysics—radiative magnetic reconnection, defined here as a regime of reconnection where radiation reaction has an important influence on the reconnection dynamics, energetics, and/or nonthermal particle acceleration. This influence be may be manifested via a variety of radiative effects that are critical in many high-energy astrophysical applications. The most notable radiative effects in astrophysical reconnection include radiation-reaction limits on particle acceleration, radiative cooling, radiative resistivity, braking of reconnection outflows by radiation drag, radiation pressure, viscosity, and even pair creation at highest energy densities. The self-consistent inclusion of these effects into magnetic reconnection theory and modeling sometimes calls for serious modifications to our overall theoretical approach to the problem. In addition, prompt reconnection-powered radiation often represents our only observational diagnostic tool available for studying remote astrophysical systems; this underscores the importance of developing predictive modeling capabilities to connect the underlying physical conditions in a reconnecting system to observable radiative signatures. This chapter presents an overview of our recent theoretical progress in developing basic physical understanding of radiative magnetic reconnection, with a special emphasis on astrophysically most important radiation mechanisms like synchrotron, curvature, and inverse-Compton. The chapter also offers a broad review of key high-energy astrophysical applications of radiative reconnection, illustrated by multiple examples such as: pulsar wind nebulae, pulsar magnetospheres, black-hole accretion-disk coronae and hot accretion flows in X-ray Binaries and Active Galactic Nuclei and their relativistic jets, magnetospheres of magnetars, and Gamma-Ray Bursts. Finally, this chapter discusses the most critical open questions and outlines the directions for future research of this exciting new frontier of magnetic reconnection research.

D.A. Uzdensky (✉)
Physics Department, Center for Integrated Plasma Studies, University of Colorado, Boulder, CO 80309, USA
e-mail: uzdensky@colorado.edu

W. Gonzalez, E. Parker (eds.), *Magnetic Reconnection*, Astrophysics and Space Science Library 427, DOI 10.1007/978-3-319-26432-5_12

Keywords Astrophysical plasmas • Curvature radiation • Inverse-Compton radiation • Nonthermal particle acceleration • Pair plasma • Radiation reaction force • Radiative reconnection • Relativistic reconnection • Synchrotron radiation

12.1 Introduction

Magnetic reconnection—a process of rapid rearrangement of magnetic field lines corresponding to a change of magnetic field topology—is widely recognized as one of the most important fundamental plasma physical processes (Biskamp 2000; Zweibel and Yamada 2009; Yamada et al. 2010). It is ubiquitous in laboratory, space, and astrophysical plasmas. As with many other important plasma processes, the reason why it is considered to be important and why researchers are interested in it, is that it is one of the processes controlling the plasma energetics, i.e., energy exchange between the different plasma system constituents. The specific case of reconnection involves the flow of energy from the magnetic field to the charged particles comprising the plasma. This energy conversion is made possible by the relaxation of magnetic field to a lower energy state suddenly made accessible by the breaking of topological constraints in reconnection, in particular, the flux freezing constraint.

Although on the fundamental particle level, the released energy goes to the kinetic energy of individual particles, it is customary to describe the resulting energization of the plasma by splitting it into several parts at the fluid level, such as the thermal heating of plasma and the bulk kinetic energy of the reconnection outflows, plus nonthermal particle acceleration at the kinetic level of plasma description. The question of the partitioning of the dissipated magnetic energy among these different forms of plasma energy (as well as the partitioning of energy between electrons and ions) is considered to be one of the main driving questions in magnetic reconnection research (see, e.g., the chapter by Yamada et al. in this volume). To a large extent, this is because it most directly relates to the observed radiation powered by reconnection in remote astrophysical sources. In fact, one of the main reasons why scientists are interested in reconnection, and especially in its energetics aspects, is that this process is commonly believed to be responsible for some of the most spectacular and energetic phenomena observed in the Universe. In particular, it is believed to be the mechanism for powering many explosive phenomena exhibiting very rapid time variability and impulsive character—various kinds of *flares* and bursts of high-energy (UV, X-ray, and gamma-ray) radiation.

Reconnection is especially important as an energetically dominant mechanism in systems that are magnetically dominated (low plasma-β), that is in tenuous hot coronae and magnetospheres of dense and relatively cold gravitationally stratified objects (Uzdensky 2006). The two most prominent and best-studied, classic examples of reconnection in Nature are solar flares and magnetic substorms in the Earth magnetosphere (see, e.g., the chapters by Shibata & Takasao, by Cassak & Fuselier, and by Petrukovich et al. in this volume). This is the area where reconnection

research has started more than 50 years ago (Sweet 1958; Parker 1957; Dungey 1961; Axford 1967; Vasyliunas 1975) and where the case for reconnection is most convincingly established by observations (Masuda et al. 1994; Shibata 1996; Yokoyama and Shibata 1995; Yokoyama et al. 2001; Tsuneta 1996; Paschmann et al. 2013).

However, in the past couple of decades, reconnection has also been increasingly often proposed (although without such a strong observational evidence as in the above heliospheric examples) as an attractive possible mechanism for powerful flares in many astrophysical systems outside the solar system, especially in high-energy astrophysics. It has been invoked to explain energy dissipation and radiation in pulsar systems (e.g., in pulsar magnetospheres, the striped pulsar winds, and pulsar wind nebulae, PWNe) (Michel 1982; Coroniti 1990; Michel 1994; Lyubarskii 1996, 2000; Lyubarsky and Kirk 2001; Kirk and Skjæraasen 2003; Pétri and Lyubarsky 2007; Contopoulos 2007; Lyutikov 2010; Uzdensky and Cerutti 2011; Bednarek and Idec 2011; Cerutti et al. 2012a, 2013, 2014b,a; Sironi and Spitkovsky 2011; Clausen-Brown and Lyutikov 2012; Arka and Dubus 2013; Uzdensky and Spitkovsky 2014; Philippov and Spitkovsky 2014; Philippov et al. 2015; Cerutti et al. 2015); in gamma-ray bursts (GRBs) (Spruit et al. 2001; Drenkhahn and Spruit 2002; Lyutikov 2006b; Giannios and Spruit 2007; McKinney and Uzdensky 2012); magnetospheres of magnetars (Lyutikov 2003a, 2006a; Masada et al. 2010; Uzdensky 2011; Parfrey et al. 2012, 2013), and in coronae and jets of accreting black holes (BHs) (Galeev et al. 1979; van Oss et al. 1993; de Gouveia dal Pino and Lazarian 2005; Uzdensky and Goodman 2008; Goodman and Uzdensky 2008; de Gouveia Dal Pino et al. 2010; Khiali et al. 2015a; Kadowaki et al. 2015; Singh et al. 2015), including those in active galactic nuclei (AGN) and blazars (Romanova and Lovelace 1992; Di Matteo 1998; Di Matteo et al. 1999; Lesch and Birk 1998; Schopper et al. 1998; Larrabee et al. 2003; Liu et al. 2003; Lyutikov 2003b; Jaroschek et al. 2004b,a; Giannios et al. 2009, 2010; Giannios 2010; Nalewajko et al. 2011; Khiali et al. 2015b).

It is worth noting that in most traditional, solar-system applications of reconnection, including solar flares, Earth magnetosphere, and sawtooth crashes in tokamaks, one rightfully ignores radiation emitted promptly during the reconnection process. This is well justified because in these situations the radiative cooling time of the energetic particles is usually much longer than the time they spend in the reconnection region and, in fact, than the entire duration of the reconnection event.

In contrast, however, in many high-energy astrophysical environments, especially relativistic ones, the ambient magnetic and radiation energy density is so high and the system size is so large that reconnection takes place in the radiative regime. This means that the radiation reaction force on the emitting particles is rather strong and needs to be taken into account because it materially affects the particles' motion. This makes it necessary to understand *radiative magnetic reconnection*, which we define here as a reconnection regime in which radiation back-reaction has an important effect on reconnection dynamics, energetics, and/or particle acceleration. In this regime magnetic dissipation and radiative processes intertwine and influence each other. Understanding how this happens represents an exciting new frontier in

plasma astrophysics. This frontier is only now beginning to being charted and the main goal of this article is to give an overview of the recent progress in this area.

In principle, radiation reaction can exert several effects on reconnection: (1) putting an upper limit on the high-energy extent of nonthermal particle acceleration and hence on the energy of the emitted photons; (2) optically-thin or optically-thick radiative cooling; (3) radiative drag on the current-carrying electrons in the layer (radiative resistivity); (4) radiation drag on the reconnection outflows (manifested as an effective radiation viscosity in the optically-thick case); (5) radiation pressure; (6) pair creation. The main radiative mechanisms in high-energy astrophysical plasmas, especially relativistic ones, are cyclotron/synchrotron emission, curvature emission, and inverse-Compton (IC) scattering.

Apart from its significance to basic plasma physics, the main motivation for exploring radiative reconnection comes from numerous astrophysical applications. Examples of radiative relativistic reconnection in astrophysics include:

1. Accretion flows and accretion disk coronae (ADC) around black holes with accretion rates approaching the Eddington limit, in both stellar-mass galactic X-ray binary (XRB) systems and in supermassive BHs in AGN, e.g., quasars. Here, reconnection processes occur in the presence of a very intense radiation field emitted by the disk, which leads to a very powerful inverse-Compton (IC) cooling of the electrons energized by reconnection (Goodman and Uzdensky 2008; Khiali et al. 2015a,b).
2. Magnetospheres and relativistic winds of pulsars (rapidly rotating magnetized neutron stars), where reconnection should happen in the ballerina-skirt equatorial current sheet outside the pulsar light cylinder (LC). In many cases (e.g., the Crab), the magnetic field at the LC is so high that prompt synchrotron cooling of the plasma heated by reconnection is very strong; it controls the energy balance of the layer and limits the plasma temperature. This radiation may then explain the powerful pulsed high-energy (GeV) γ-ray emission observed in Crab and other pulsars (e.g., Lyubarskii 1996; Uzdensky and Spitkovsky 2014; Fish et al. 2016).
3. Pulsar Wind Nebulae (PWN), including the Crab Nebula; here, although radiative cooling is not strong enough to affect the bulk of the plasma, synchrotron radiation reaction may limit the extreme (PeV) particle acceleration, which has important implications for the γ-ray flares recently discovered in the Crab Nebula (Bednarek and Idec 2011; Uzdensky and Cerutti 2011; Cerutti et al. 2012a, 2013, 2014b,a).
4. Ultra-relativistic jets in blazars where radiative braking and cooling may alter reconnection dynamics and radiation production, e.g., in the context of very rapid TeV flares in several blazar systems (Giannios et al. 2009; Nalewajko et al. 2011; Giannios 2013).
5. Gamma-Ray Bursts (GRBs), where magnetic reconnection has been conjectured to power the main prompt gamma-ray emission (Drenkhahn and Spruit 2002; Giannios and Spruit 2006). Here, reconnection takes place in an environment with high energy density and large optical depth, so that photon resistivity, radi-

ation cooling, and radiation pressure need to be taken into account (McKinney and Uzdensky 2012).

6. Magnetospheres of magnetars (ultra-magnetized neutron stars), where it has been suggested that, by analogy with the solar corona, reconnection may explain the observed powerful gamma-ray flares (e.g., Lyutikov 2006a; Uzdensky 2011; Parfrey et al. 2012, 2013; Yu 2012). The energy density in these systems is extremely high and hence reconnection inevitably leads to relativistically-hot temperatures and copious photon and pair creation (Uzdensky 2011; Uzdensky and Rightley 2014).

One can thus see that the large number and the great diversity of examples of radiative magnetic reconnection in astrophysics strongly motivate advancing this new research frontier.

Another practical reason to study radiative reconnection is that, in astrophysics, remote telescopic observations of the radiation produced in a flare provide our only diagnostic probe for studying the underlying physics. For this reason, the ability to calculate the observable radiation spectrum is critical for testing whether reconnection (or any other given process) can explain observations. Thus, in order to connect our theoretical/numerical reconnection models with the actual observable radiation, we must develop a rigorous method for calculating the produced radiation signatures in detail, such as time-resolved spectra for a given orientation of the observer's line of sight.

Finally, radiative reconnection should also be of potential considerable interest to experimental High-Energy-Density (HED) Physics, a new branch of modern physics that has emerged in recent years. One can anticipate rapid progress in HED reconnection studies facilitated by new experimental capabilities developed in the HED Physics community, e.g., made possible by powerful lasers (such as Omega EP and NIF) and Z-pinches (e.g., Magpie Lebedev et al. 2014; Suttle et al. 2014). In fact, several HED reconnection experiments utilizing laser-produced plasmas with mega-gauss magnetic fields have already been reported (e.g., Nilson et al. 2006; Li et al. 2007; Nilson et al. 2008; Dong et al. 2012; Fox et al. 2011, 2012; Fiksel et al. 2014).

This review chapter is organized as follows. Before embarking on our main discussion of the effects that radiation may exert on reconnection, in Sect. 12.2 we first make some remarks about passive radiative signatures of reconnection (Sects. 12.2.1 and 12.2.2), including applications to hard X-ray bremsstrahlung emission in solar flares (Sect. 12.2.3) and low-frequency radio emission due to coherent plasma motions in reconnecting current sheets (Sect. 12.2.4). We then (in Sect. 12.3) talk about the underlying physics of the radiation reaction force with the focus on a few astrophysically most relevant radiation mechanisms: synchrotron, curvature, and inverse-Compton. After this, we begin a systematic exposition of the different manifestations of the effects that the radiation reaction force can have on reconnection. We begin this program with the discussion of a quintessential kinetic effect of radiation: the limits that radiation reaction places on nonthermal particle acceleration in collisionless magnetic reconnection (Sect. 12.4); and we

specifically touch upon two particularly important astrophysical contexts where this issue plays a central role: the Crab Nebula gamma-ray flares (Sect. 12.4.1) and coronae of accreting black holes (Sect. 12.4.2). Then, we move on to the fluid picture and discuss several fluid-level effects. The first category of such effects concerns the effect of radiation reaction force on random thermal motions of the particles in the reconnection layer; it thus affects the layer's thermodynamics and can be described as radiative cooling (Sect. 12.5); here, one has to distinguish the optically thin (Sect. 12.5.1) and the optically thick regimes (Sects. 12.5.2 and 12.5.3). The second group of radiative effects on fluid-level description of magnetic reconnection deals with the effect of the radiation reaction force on the plasma bulk flows and thus concerns the dynamics and electrodynamics of the process; it constitutes the subject of Sect. 12.6. The main two processes included under this rubric are radiative resistivity (Sect. 12.6.1) and radiative braking of the reconnection outflow (Sect. 12.6.2). Finally, Sect. 12.7 is devoted to a brief discussion of a few other, more exotic effects that take place in optically thick reconnection layers, such as radiation pressure, radiative viscosity, hyper-resistivity, and pair creation. We then summarize the paper and discuss critical open questions and outline the directions for future research in Sect. 12.8.

12.2 Passive Radiative Signatures of Reconnection

12.2.1 General Remarks

Although most of this review is devoted to a discussion of radiative magnetic reconnection, which, once again, is defined here as a situation where various aspects of the reconnection process are significantly affected by radiative energy losses, before we proceed with that discussion we first would like to discuss what one can call *passive* radiative signatures of reconnection. Thus, in this section we address the question of how a reconnection region *looks like*, in the literal sense of the word, even in the case where radiative back reaction on the reconnection process, discussed in the subsequent sections, is not important energetically or dynamically. Technically, this means that the radiative cooling time for the particles energized by the reconnection process is longer than the duration of the reconnection process itself, or at least longer than the characteristic time a typical particle spends inside the reconnection region (which could be taken as the Alfvén transit time along the layer). In contrast to the high-energy astrophysical reconnection discussed in the rest of this article, this non-radiative reconnection situation is the main subject of conventional reconnection research, aimed at traditional applications such as solar flares, magnetospheric substorms, tokamak sawtooth crashes, and dedicated laboratory reconnection experiments. The reasons why radiative signatures of reconnection have so far been neglected in these traditional contexts are that, first, the amount of light produced during these reconnection processes is very

small and often not easily detectable with our current technology, and second, we have other, better diagnostic tools to study these reconnection processes, e.g., with direct measurements. This is especially the case for reconnection in the Earth magnetosphere, where direct in-situ measurements of various plasma properties with spacecraft are available (see, e.g., the chapters by Cassak & Fuselier and by Petrukovich et al. in this volume), and for dedicated laboratory experiments where one can use probe arrays (see the chapter by Yamada et al. in this volume).

In contrast, in many astrophysical situations remote telescopic observations of radiation powered by a reconnection event provide our only diagnostic probe into the physical processes at play in a given system. In other words, we usually have no other tools to measure the plasma properties in remote astrophysical reconnection regions and therefore, in order to make any sense of the observations, it is imperative to build predictive theoretical models that can connect the underlying physics of reconnection with the resulting light that we then can, and do, observe at Earth.

It is interesting to note that this is in fact also true for solar flares, but this case is complicated because the post-reconnection conversion of the particle energy into radiation is neither immediate nor straight-forward, it involves interaction of the accelerated particle beams with the solar surface, chromospheric evaporation, etc.. All these additional processes bring in extra modeling uncertainties and thus, to some degree, complicate the task of using the observed flare radiation to learn something about the underlying reconnection process and about the plasma properties before reconnection. In contrast, however, in many (although not all) astrophysical contexts reconnection happens in a free plasma flow far from any dense bodies, and in this case one can be reasonably certain that the observed radiation is in fact produced by the plasma that has been energized in a reconnection region. Most notable astrophysical examples of such a situation are astrophysical jets and winds, AGN radio-lobes, PWN, interstellar medium (ISM), and intra-cluster medium (ICM). The relative slowness of the radiative cooling time compared with the expected reconnection (and hence particle acceleration) time enables one to disentangle the particle acceleration and radiative cooling processes in this case. Then, a comparison of the observed flare spectrum (and its time evolution due to cooling) with the results of a rather straight-forward spectral modeling calculation can yield an unambiguous information about the energy spectrum of particles accelerated by the reconnection process.

It is worthwhile to comment on what concrete radiative signatures of reconnection are regarded as being of interest. The answer depends on the specific astrophysical context and also on our observational capabilities. In general, it would be interesting to be able to calculate from first principles the actual spatially- and temporally resolved image of the reconnection layer (at different photon frequencies), that is, to produce a simulated picture or a movie of how a reconnection layer looks like. In many cases, however, the flaring region is spatially unresolved with our present technology and thus appears as a point-like source. At the same time, however, we often do have detailed spectral and temporal information. In this situation, one is interested in (time-resolved) photon energy spectra and/or (energy-resolved) light-curves.

As an illustration, in the next section we discuss the recent numerical results on nonthermal particle acceleration in relativistic pair-plasma reconnection and the corresponding radiative (synchrotron) spectral signatures. These expected radiation spectra produced by reconnection events can potentially be compared with real observations of various astrophysical systems, as was done, for example in a series of studies of reconnection-powered synchrotron flares in accreting black holes (both microquasars and AGN) by E. de Gouveia dal Pino and her collaborators (de Gouveia dal Pino and Lazarian 2005; de Gouveia Dal Pino et al. 2010; Khiali et al. 2015a,b; Kadowaki et al. 2015; Singh et al. 2015).

12.2.2 Radiative Signatures of Reconnection-Powered Nonthermal Particle Acceleration

In many high-energy astrophysical sources the observed radiation spectra and thus the energy distributions of the radiating particles are often non-thermal, described by power laws. For this reason, the question of nonthermal particle acceleration is a key problem in modern plasma astrophysics and reconnection is widely seen as one of key candidate mechanisms (see, e.g., Hoshino and Lyubarsky 2012 for review). Particle acceleration in reconnection is usually addressed by means of PIC simulations, together with analytical theory.

A substantial number of non-radiative PIC studies have attacked this problem in the context of relativistic reconnection in pair plasmas (Zenitani and Hoshino 2001, 2005, 2007, 2008; Jaroschek et al. 2004b; Lyubarsky and Liverts 2008; Liu et al. 2011; Bessho and Bhattacharjee 2012; Kagan et al. 2013; Cerutti et al. 2012b; Sironi and Spitkovsky 2011, 2014; Guo et al. 2014; Werner et al. 2014; Nalewajko et al. 2015). In addition, Werner et al. (2013) and Melzani et al. (2014) have explored particle acceleration by relativistic reconnection in electron-ion plasmas, and Jaroschek and Hoshino (2009) and Cerutti et al. (2013, 2014b,a) have investigated the case of relativistic pair plasma reconnection with synchrotron radiation reaction.

It is very encouraging to see that continuing improvement in the available computer power has allowed researchers to tackle this problem in a reliable and systematic way with the adequate and necessary dynamic range (e.g., Sironi and Spitkovsky 2014; Guo et al. 2014; Melzani et al. 2014; Werner et al. 2014). These studies have shown that relativistic reconnection does indeed efficiently generate hard power-law particle distributions, $f(\gamma) \sim \gamma^{-\alpha}$. The power-law index α in general varies with the system size L and the upstream magnetization $\sigma \equiv B_0^2/4\pi h$, where h is the relativistic enthalpy density. For large enough pair-plasma systems, $\alpha(L, \sigma)$ seems to approach an asymptotic value $\alpha_*(\sigma)$ in the limit $L \to \infty$. Viewed as a function of σ, this value can be larger than $\sim$2 for modestly relativistic cases ($\sigma \sim 1$) but then monotonically decreases with σ and asymptotically approaches a finite value $\alpha_* \simeq 1 - 1.2$ in the ultra-relativistic limit $\sigma \gg 1$ (e.g., Sironi and

Spitkovsky 2014; Guo et al. 2014; Werner et al. 2014). This value is consistent with analytical predictions by Larrabee et al. (2003) and with the results of several previous numerical studies, e.g., Jaroschek et al. (2004b), Lyubarsky and Liverts (2008). One of the most important new results is that relativistic non-thermal particle spectra seem to be produced at late times with high efficiency in both 2D and 3D simulations and both with and without a guide magnetic field (Sironi and Spitkovsky 2014; Guo et al. 2014). This is in contradiction with the previous picture proposed by Zenitani and Hoshino (2007, 2008), who suggested that a strong guide field is essential for nonthermal particle acceleration in 3D because it can suppress the relativistic drift-kink instability that leads to strong magnetic dissipation but inhibits nonthermal particle acceleration.

Furthermore, as was shown by Werner et al. (2014) in 2D PIC simulations without a guide field starting with a relatively cold initial background plasma, the resulting final nonthermal power law is truncated at high energies by a combination of two cutoffs:

$$f(\gamma) \sim \gamma^{-\alpha}\, e^{-\gamma/\gamma_{c1}}\, e^{-(\gamma/\gamma_{c2})^2}, \tag{12.1}$$

where the exponential cutoff γ_{c1} and the super-exponential cutoff γ_{c2} are well fit as functions of L and σ by

$$\gamma_{c1} \simeq 4\,\sigma\,, \qquad \gamma_{c2} \simeq 0.1\,L/\rho_0\,. \tag{12.2}$$

Here $\rho_0 \equiv m_e c^2/eB_0$ is the nominal Larmor radius and $\sigma \equiv B_0^2/4\pi n_b m_e c^2$ is the "cold" background plasma magnetization, with B_0 being the reconnecting magnetic field strength and n_b being the total (electrons and positrons) background plasma density, both taken upstream of the layer. Also note that the length-scale L in the above expression is the size of the computational domain (with aspect ratio $L_x/L_y = 1$) and is about twice the actual length of the reconnection layer.

The first of the above two cutoffs can be understood as arising from the typical acceleration time ℓ/c that a given particle spends in an elementary marginally stable current layer of width $\delta \sim \rho(\bar{\gamma}) = \bar{\gamma}\rho_0 \sim \sigma\rho_0$, where $\bar{\gamma} \sim 0.3\sigma$ is the average dissipated energy per particle, and of length $\ell \sim 50 - 100\,\delta$ dictated by the stability condition for secondary tearing. The second cutoff probably arises from the finite time the particle spends in the entire layer of system-size length L. In practice, it is the smaller of the two cutoffs that matters for limiting the extent of the power law (Werner et al. 2014). Their ratio can be expressed as

$$\frac{\gamma_{c2}}{\gamma_{c1}} \simeq \frac{1}{40}\,\frac{L}{\sigma\rho_0} = \frac{1}{40}\cdot\frac{3B_{\rm cl}}{2B_0}\,\tau_T\,, \tag{12.3}$$

where $\tau_T \equiv n_b L \sigma_T$ is the Thomson optical depth along the layer [here, $\sigma_T = (8\pi/3)\,r_e^2$ is the Thomson cross section, $r_e = e^2/m_e c^2 \simeq 2.8\times10^{-13}$ cm is the classical electron radius], and $B_{\rm cl} \equiv e/r_e^2 = m_e^2 c^4/e^3 \simeq 6\times10^{15}$ G is the critical classical magnetic field strength.

The fact that there are two cutoffs allows one to define and distinguish between two different physical regimes: (1) the small-system regime ($L/\sigma\rho_0 \lesssim 40$), in which $\gamma_{c2} < \gamma_{c1}$ and so $\gamma_{c2} \propto L$ determines where the power law ends, and (2) the plasmoid-dominated, large-system regime ($L/\sigma\rho_0 \gtrsim 40$), in which $\gamma_{c1} < \gamma_{c2}$ and so $\gamma_{c1} \propto \sigma$ limits the high-energy extent of the power law, independent of L.

Next, to the extent that we are interested in potentially observable radiation signatures of reconnection, it is interesting to ask what radiation spectra are emitted by the particle distributions described above. If relativistic reconnection indeed produces a power law energy spectrum of electrons with an index $\alpha \simeq 1.2$ in the ultra-relativistic, high-σ regime, then the corresponding synchrotron photon spectrum *immediately after the reconnection event* will be a nearly flat power law with a spectral index of $(\alpha - 1)/2 \sim 0.1$, which in practice would be indistinguishable from a flat spectrum. In terms of the photon-number power-law index $\Gamma_{\rm ph}$, defined by $n_{\rm ph}(\epsilon_{\rm ph}) \sim \epsilon_{\rm ph}^{-\Gamma_{\rm ph}}$, this corresponds to $\Gamma_{\rm ph} = (\alpha+1)/2 \simeq 1.1$. In large systems ($L/\sigma\rho_0 \gtrsim 40$), the power-law synchrotron spectrum is then expected to extend up to the characteristic photon energy of

$$\begin{aligned}\epsilon_{\rm sync,\,max} &= \frac{3}{2}\,\hbar\Omega_{c0}\,\gamma_{c1}^2 = \frac{3}{2}\,\hbar\frac{eB_0}{m_e c}\,\gamma_{c1}^2 = \frac{3}{2}\,\alpha_{\rm fs}^{-1}\,m_e c^2\,\frac{r_e}{\rho_0}\,\gamma_{c1}^2 \\ &= \frac{3}{2}\,\alpha_{\rm fs}^{-1}\,m_e c^2\,\frac{B_0}{B_{\rm cl}}\,\gamma_{c1}^2 \simeq 100\,{\rm MeV}\,\frac{B_0}{B_{\rm cl}}\,\gamma_{c1}^2\,, \end{aligned} \tag{12.4}$$

where $\alpha_{\rm fs} = e^2/\hbar c \simeq 1/137$ is the fine structure constant. Substituting our expression $\gamma_{c1} \simeq 4\sigma$, we find

$$\epsilon_{\rm sync,\,max} \simeq 24\,\alpha_{\rm fs}^{-1}\,m_e c^2\,\frac{B_0}{B_{\rm cl}}\,\sigma^2\,, \tag{12.5}$$

It is interesting to note that this limit grows very rapidly with the magnetic field, namely as B_0^5.

On a longer time scale following a reconnection event, subsequent cooling evolution will, of course, soften the emission spectrum since the highest energy particles have shorter radiation cooling times:

$$\begin{aligned} t_{\rm cool}^{\rm sync} &= \frac{\gamma m_e c^2}{P_{\rm rad}} = \frac{\gamma m_e c^2}{(4/3)\,\sigma_T c B^2/8\pi} = \frac{9}{4}\,(\gamma\,\Omega_{c0})^{-1}\,\frac{\rho_0}{r_e} \\ &= \frac{9}{4}\,(\gamma\,\Omega_{c0})^{-1}\,\frac{B_{\rm cl}}{B} \simeq 7.7\times 10^8\,{\rm s}\,\gamma^{-1}\left(\frac{B}{1\,{\rm G}}\right)^{-2} \simeq 24\,{\rm yr}\,\gamma^{-1}\left(\frac{B}{1\,{\rm G}}\right)^{-2}. \end{aligned} \tag{12.6}$$

Here, $\Omega_{c0} \equiv eB/m_e c \simeq 1.76\times 10^7\,(B/1\,{\rm G})\,{\rm rad/s}$ is the classical electron cyclotron frequency. This results in a time-evolving cooling energy limit $\gamma_{\rm br}$ at the particle energy set by $t = t_{\rm cool}(\gamma_{\rm br})$, above which the particle energy spectrum is cut off sharply.

Next, in the case of a complex system (e.g., a corona) with a large number of independent reconnection events (flares) continuously injecting power-law populations of energetic relativistic electrons, each with an initial power-law index of $\alpha_{\rm inj} = 1.2$, one expects the interplay of this continuous injection and synchrotron radiative cooling to result in a steady-state electron distribution with a power-law index $\alpha_{\rm ss} = 1 + \alpha_{\rm inj} \simeq 2.2$. This corresponds to a photon number index of $\Gamma_{\rm ph} = (1 + \alpha_{\rm ss})/2 = 1.6$. Similar considerations apply in the case of IC emission, resulting in the same photon index of $\Gamma_{\rm ph} = 1.6$ for the IC photons, which is intriguingly close to the hard X-ray photon index of 1.7 often observed in the low-hard state of XRBs (e.g., Remillard and McClintock 2006).

Finally, when thinking about possible observable radiative signatures of relativistic reconnection at highest photon energies (hence produced by the highest-energy accelerated particles), one should take into account a possible anisotropy of the accelerated particle population. As was shown by Cerutti et al. (2012b), the highest energy particles accelerated in a reconnection layer may be focused in a few tight beams that sweep from side to side, while staying mostly in the current sheet plane. This *kinetic beaming* effect is strongly energy-dependent, with the effective solid angle Ω of the particle population decreasing from $\Omega/4\pi \sim 1$ for low- and modest-energy particles to as small as $\Omega/4\pi \sim 10^{-2}$ for the highest-energy ones. This effect potentially has important implications for understanding radiative signatures of reconnection and, especially, for connecting theoretical models with observations since it suggests that the usual isotropic emission assumption may lead to large errors in evaluating the energetic requirements implied by the observed radiation flux. Kinetic beaming is also important for correctly interpreting the very rapid emission variability frequently observed in many relativistic astrophysical sources, such as the Crab PWN and blazar and GRB jets. This is because the radiative flux as seen by an external observer is greatly enhanced (relative to the isotropically-averaged total flux) when one of the beams intersects the observer's line of sight. As a result, the observed signal is strongly intermittent, leading to an enhanced rapid and energy-dependent variability.

12.2.3 Loop-Top Hard X-Ray Emission in Solar Flares

An important example of high-energy radiation produced promptly by the plasma energized in a reconnection event is the hard X-ray (up to about 100 keV) emission at the top of post-reconnected coronal magnetic loops in solar flares. In contrast to the hard X-ray emission produced at the footpoints of the reconnected loops on the solar surface, which is traditionally understood as bremsstrahlung radiation emitted by the electrons accelerated in the coronal reconnection region as they strike a dense cold target (the solar photosphere), the loop-top emission involves only those plasma particles that have gone through, and have been accelerated in, the reconnection region, without the agency of any other plasma. This radiation is also believed to be optically-thin nonthermal bremsstrahlung corresponding to a power-law distribution

of electrons extending up to relativistic (MeV) energies (Krucker et al. 2010), although it can also be modeled as a kappa-distribution (Oka et al. 2013, 2015). The observed X-ray radiative power is so high that it implies an extremely high efficiency of non-thermal particle acceleration, with the number density of energetic particles populating the power-law tail being comparable to the expected density of ambient thermal particles. This challenges traditional flare emission models and strongly suggests that a large fraction of the ambient plasma particles in the flare region are accelerated into the power-law tail (e.g., Krucker et al. 2010; Oka et al. 2013, 2015). However, these challenges may be partially alleviated by noticing that the plasmoid-dominated reconnection regime expected in solar flares naturally leads to strong inhomogeneity of the energized plasma, concentrating it into relatively compact, dense plasmoid cores. Since bremsstrahlung is a collisional process, with radiated power per unit volume proportional to the square of the plasma density, this inhomogeneity can greatly enhance the overall emission power. This effect can be easily tested in PIC simulations and perhaps also in laboratory laser-plasma studies of reconnection.

It is interesting to try to generalize Werner et al.'s (2014) results for the high-energy nonthermal cutoff of particles accelerated by a relativistic pair-plasma reconnection process described in the preceding section to the case of non-relativistic reconnection in electron ion plasmas and to apply them to solar flares. Since the flaring region size in solar flares ($10^9 - 10^{10}$ cm) is many orders of magnitude larger than the ion Larmor radius, one is squarely in the large-system regime. Therefore, one expects that the relevant cutoff is ϵ_{c1}, set by the acceleration in elementary (marginally stable to secondary tearing) current layers, $\epsilon_{c1} \simeq eE_{\rm rec}\ell$. We can estimate the characteristic length of these elementary layers as $\ell \sim 100\,\delta \sim 100\,\rho_{i,\rm layer}$, where the layer thickness δ is taken to be comparable to the Larmor radius of the ions inside the layer $\rho_{i,\rm layer}$. Taking for illustration $B_0 = 100\,$G and the plasma density in the layer $n_e = 10^{10}\,{\rm cm}^{-3}$, and hence $V_A \simeq 2 \times 10^3\,{\rm km/s} \simeq 0.7 \times 10^{-3}\,c$, one can estimate (e.g., from the pressure balance across the layer) the plasma temperature in the layer as $k_B T = B_0^2/(16\pi n_e) \simeq 12\,$keV. This corresponds to an ion Larmor radius, and hence the elementary layer's thickness, of $\delta \sim \rho_{i,\rm layer} \simeq 1\,$m, and hence the elementary layer length of $\ell \sim 100\,$m. Next, since we are dealing with non-relativistic collisionless reconnection, the reconnection electric field can be estimated as $E_{\rm rec} \simeq 0.1\,B_0 V_A/c \simeq 0.07\,$G. Therefore, the expected high-energy cutoff should be $\epsilon_{c1} \simeq eE_{\rm rec}\ell \sim 200\,$kev, corresponding to mildly relativistic electrons.

12.2.4 Coherent Radio Emission

In addition to the production of high-energy radiation through incoherent mechanisms such as synchrotron, IC, and bremsstrahlung radiation, another important radiative aspect of reconnection is the possible generation of coherent low-frequency (e.g., radio or microwave) emission associated with collective plasma

motions. This emission may be driven by various small-scale plasma motions excited inside thin reconnection current layers by various plasma instabilities, such as the secondary tearing, the drift-kink, lower-hybrid instability, ion-acoustic, and/or Buneman instabilities, etc.. The nonlinear development of these instabilities may lead to the production of a broad spectrum of fluctuations, e.g., having the form of plasmoids and flux ropes of different sizes in the case of the secondary tearing instability. These plasmoids exhibit complex dynamics marked by their interaction with each other through mergers. It is then plausible that some of these fluctuations will eventually be converted into low-frequency electromagnetic waves that may escape the system and be observed at Earth. Although the efficiency of conversion of reconnection-released energy into such low-frequency emission can be low, this emission may nevertheless provide an important additional diagnostics window into the reconnection process. The typical frequencies of this radiation are expected to be low, on the scale of a fraction of the plasma frequency and lower, corresponding to radio emission in systems as diverse as the solar corona (Shklovsky 1947) and the Crab pulsar magnetosphere (Uzdensky and Spitkovsky 2014). In coronae of accreting black holes in XRBs, however, the plasma density (and hence the plasma frequency) is much higher and hence the corresponding emission probably falls into the infra-red or even optical range (Goodman and Uzdensky 2008).

12.3 Radiation Reaction Force

The main reason why radiation can sometimes be important in various plasma processes, including reconnection, is that it affects the motion of the plasma particles and thus influences the basic dynamics and energetics of the process in question. The primary effect of radiation can be described by the radiation-reaction drag force $\mathbf{f}_{\rm rad}$ experienced by the individual single particles and, associated with this force, the energy loss term $P_{\rm rad}$ in the particle's energy equation.

The relativistic 4-force representing radiation reaction on an emitting particle, called the Abraham-Lorentz-Dirac (ALD) force, can be written as (Jackson 1975):

$$F^{\mu}_{\rm rad} = \frac{2e^2}{3c^3}\frac{d^2u^{\mu}}{d\tau^2} - \frac{P_{\rm rad}}{c^2}u^{\mu}\,. \tag{12.7}$$

where u^{μ} is the particle's 4-velocity, $\tau = \gamma^{-1}t$ is the particle's proper time, and where the radiative power $P_{\rm rad}$ is given by the Larmor formula, which reads, in relativistically covariant notation (Jackson 1975):

$$P_{\rm rad} = \frac{2}{3}\frac{e^2}{m^2c^3}\frac{dp_{\mu}}{d\tau}\frac{dp^{\mu}}{d\tau}. \tag{12.8}$$

Here, $p^{\mu} = mu^{\mu} = mc(\gamma, \gamma\boldsymbol{\beta})$ is the four-momentum of the particle moving with a 3-velocity $\mathbf{v} = \boldsymbol{\beta}c$. This expression can be recast in terms of the parallel ($a_{\parallel}$) and

perpendicular ($a_\perp$) (with respect to the particle direction of motion) 3-acceleration as (Rybicki and Lightman 1979):

$$P_{\rm rad} = \frac{2}{3}\frac{e^2}{c^3}\gamma^4\,(a_\perp^2 + \gamma^2 a_\parallel^2)\,. \tag{12.9}$$

Furthermore, for a particle moving non-relativistically, this formula reduces to the familiar non-relativistic Larmor formula:

$$P_{\rm rad} = \frac{2}{3}\frac{e^2}{m^2c^3}\,|\dot{\mathbf{p}}|^2 = \frac{2}{3}\frac{e^2a^2}{c^3}\,, \tag{12.10}$$

where a is the particle's 3-acceleration.

Returning to our discussion of radiation reaction, in the more familiar 3D language the radiation reaction enters the relativistic equation of motion of a charged particle as an additional friction force $\mathbf{f}_{\rm rad}$:

$$d\mathbf{p}/dt = q\,(\mathbf{E} + [\mathbf{v}\times\mathbf{B}]/c) + \mathbf{f}_{\rm rad}\,, \tag{12.11}$$

where $\mathbf{p} = m\gamma\mathbf{v}$ is the particle's relativistic 3-momentum. The radiation reaction 3-force is related to the ALD 4-force via $F^\mu_{\rm rad} = (\gamma\mathbf{v}\cdot\mathbf{f}_{\rm rad}/c, \gamma\mathbf{f}_{\rm rad})$.

The first term in expression (12.7) for $F^\mu_{\rm rad}$, called the Schott term, is quite peculiar: it involves the second time derivative of the 4-velocity and hence the third-order time derivative of position, which means that the equation of motion that includes this term becomes a third-order differential equation in time. This term dominates in the non-relativistic case ($|\mathbf{v}| \ll c$, $\gamma \to 1$), in which the radiation reaction force reduces to what is known as the Abraham-Lorentz force (e.g., Landau and Lifshitz 1971):

$$\mathbf{f}_{\rm rad}(\gamma \ll 1) \approx \frac{2e^2}{3c^3}\frac{d^2\mathbf{v}}{dt^2}\,. \tag{12.12}$$

In contrast, in the case of ultra-relativistic motion (of main interest to this review) the Schott term can be shown to be small. Ignoring it, the radiation reaction 3-force on ultra-relativistic particles can be expressed in terms of the radiative power simply as

$$\mathbf{f}_{\rm rad}(\gamma \gg 1) \approx -\frac{P_{\rm rad}}{c}\,\boldsymbol{\beta}\,. \tag{12.13}$$

That is, the radiation reaction force in this case indeed plays a role of a friction force, directed opposite to the particle direction of motion. Furthermore, the magnitude of the radiation reaction force for an ultra-relativistic particle is then simply $|\mathbf{f}_{\rm rad}| \approx P_{\rm rad}/c$. This is consistent with the notion that the rate of work done by the radiation reaction force, $\mathbf{f}_{\rm rad}\cdot\mathbf{v} = -P_{\rm rad}\,v^2/c^2$, becomes equal to the particle's radiative energy loss rate $-P_{\rm rad}$ in the limit $v \to c$.

We shall now apply these general expressions to several specific astrophysically-important radiative processes corresponding to different types of accelerated particle motion that enters the above formulae for $P_{\rm rad}$. In astrophysical plasmas acceleration is usually due to the particle motion in an external electromagnetic field. The most important types of accelerated motion, and the corresponding radiation mechanisms, are: (1) cyclotron gyro-motion in a magnetic field and, correspondingly, the cyclotron/synchrotron emission; (2) parallel motion along a curved magnetic field line and curvature emission; (3) oscillatory motion of a charged particle in the electromagnetic field of an incident electromagnetic wave, resulting in Compton scattering (usually referred to as inverse-Compton (IC) scattering if the energy of incident photons is smaller than that of the scattering particles); in astrophysical studies focussed on production of high-energy radiation by energetic electrons scattering soft seed photons, one sometimes treats IC scattering effectively as an emission process; (4) motion of one charged particle in the electric field of another in a close binary collision and, correspondingly, bremsstrahlung (free-free) radiation emission.

We shall now discuss the radiative power and the radiation reaction force for each one of these mechanisms (except for bremsstrahlung) in more detail.

1. Synchrotron Radiation First, for the cyclotron motion of a particle with a 4-velocity $(\gamma, \boldsymbol{\beta}\gamma)$ in a general electro-magnetic field, the radiative power is (Landau and Lifshitz 1971)

$$P_{\rm rad} \simeq \frac{1}{4\pi}\,\sigma_T c\gamma^2 \left((\mathbf{E} + [\boldsymbol{\beta} \times \mathbf{B}])^2 - (\boldsymbol{\beta} \cdot \mathbf{E})^2 \right). \tag{12.14}$$

This expression is actually only approximate: it is based on a perturbative approach, keeping only the acceleration due to the usual Lorentz 4-force $-(e/c)u_\nu F^{\mu\nu}$ in the Larmor formula, while neglecting the effect of the radiation reaction force itself. However, it is valid in most realistic astrophysical situations.

In the frame of reference in which the electric field vanishes (the so-called Teller-Hoffmann frame), the radiative power of a charged particle spiraling in a magnetic field is

$$P_{\rm rad} = P_{\rm synch} = 2\sigma_T c\,\beta^2\gamma^2\,\frac{B_\perp^2}{8\pi} = \frac{2}{3} r_e^2 c\beta^2\gamma^2\,B^2\,\sin^2\alpha\,, \tag{12.15}$$

where α is the pitch angle of the particle relative to the direction of the magnetic field and $B_\perp \equiv B\sin\alpha$ is the magnetic field component perpendicular to the particle's velocity. This radiation is called synchrotron radiation in the case of ultra-relativistic particles, cyclotron radiation in the case of non-relativistic particles, and gyro-synchrotron radiation for the intermediate case of moderately relativistic particles.

It is important to note that cyclotron gyration is perpendicular to the magnetic field and hence only the perpendicular velocity of the particle is involved in this radiation. Even a very energetic particle in a strong magnetic field produces no

synchrotron radiation if it moves strictly parallel to the field (although it may still produce the so-called curvature radiation if the field lines are curved, see below).

In the ultra-relativistic case $\gamma \gg 1$, the synchrotron radiative power (in the Teller-Hoffmann frame) becomes

$$P_{\rm synch}(\gamma \gg 1) = 2\sigma_T c \gamma^2 \frac{B^2}{8\pi} \sin^2\alpha\,, \tag{12.16}$$

and hence the corresponding synchrotron radiation reaction force is

$$\mathbf{f}_{\rm rad}^{\rm synch} = -\frac{\mathbf{v}}{c^2} P_{\rm synch} = -2\,\boldsymbol{\beta}\,\sigma_T\,\gamma^2\,\frac{B^2}{8\pi}\,\sin^2\alpha\,. \tag{12.17}$$

It is worth noting that $P_{\rm synch}$ is proportional to the square of the particle energy and hence the radiative cooling time, $t_{\rm cool} = \gamma m_e c^2/P_{\rm synch} \sim \gamma^{-1}$, is inversely proportional to the particle energy. Correspondingly, $\mathbf{f}_{\rm rad}^{\rm synch}$ and synchrotron energy losses are is especially important for highest-energy relativistic particles.

It is also important to note that the above simple expressions for $P_{\rm synch}$ and $\mathbf{f}_{\rm rad}^{\rm synch}$ are valid only in the Teller-Hoffmann frame, where electric field vanishes. This reference frame corresponds to the $\mathbf{E}\times\mathbf{B}$ drift, $\mathbf{v}_E = c\,[\mathbf{E}\times\mathbf{B}]/B^2$. An important consequence is that synchrotron emission arises only due to the perpendicular (to $\mathbf{B}$) motion of particles relative to the $\mathbf{E}\times\mathbf{B}$ drift. In particular, this means that a cold ideal-MHD plasma flow with the $\mathbf{E}\times\mathbf{B}$ velocity does not produce synchrotron emission, even if it is highly relativistic as in the case of a pulsar wind.

Also, the Teller-Hoffmann frame exists only if the electric field is weaker than the magnetic field and has no component parallel to $\mathbf{B}$, as can be seen by examining two electromagnetic-field Lorentz invariants, $\mathbf{E}\cdot\mathbf{B}$ and $E^2 - B^2$. If these conditions are not satisfied, then the radiative power and hence the radiation reaction force need to be found from more general expressions for the ALD force.

We finally note that the above formula for synchrotron radiation is valid only if the magnetic field remains smooth on the length scale of radiation formation, which is about $\rho_L/\gamma = \rho_0$. This requirement is usually satisfied in most astrophysical cases, but there are situations where it is violated, namely, when the nominal Larmor radius ρ_0 is larger than the magnetic field reversal scale λ_B. In this case, one has the so-called jitter radiation (Medvedev 2000) instead of synchrotron, which may be relevant for GRB prompt emission. However, although the jitter radiation spectrum differs substantially from that of the classical synchrotron radiation, it turns out that the overall radiative power and hence the radiation reaction force are the same in the two cases.

2. Curvature Radiation In some astrophysical applications, especially involving ultra-relativistic particles moving in a strong magnetic field, e.g., in a pulsar magnetosphere, the particles quickly lose their perpendicular (cyclotron) energy by

synchrotron radiation and fall into their lowest Landau level. Then their subsequent motion becomes essentially one-dimensional (1D), parallel to the magnetic field, and is adequately described as the motion of bids on a wire or train cars running along the rails (Sturrock 1971). However, this does not mean that the motion becomes completely trivial or that radiative effects are not important. In particular, if the magnetic field lines are not straight, the particles still experience centripetal acceleration as they move along the curved field lines, and hence can still radiate according to the Larmor formula (Shklovskii 1960). For relativistic motion along curved magnetic fields lines this radiation is called the curvature radiation and its radiative energy loss rate is given by Shklovskii (1960), Sturrock (1971), Chugunov et al. (1975), Zheleznyakov (1977):

$$P_{\rm rad} = P_{\rm curv} = \frac{2}{3}\,\frac{ce^2}{R_c^2}\,\gamma^4\,, \tag{12.18}$$

where R_c is the field lines' radius of curvature.

Correspondingly, ultra-relativistic particles experience a radiative reaction drag force:

$$\mathbf{f}_{\rm rad}^{\rm curv} = -\frac{2}{3}\,\frac{e^2}{R_c^2}\,\gamma^4\,\boldsymbol{\beta}. \tag{12.19}$$

3. Inverse-Compton Radiation In the case of Compton scattering in an isotropic radiation field, the radiative power $P_{\rm rad}$ entering the above expressions (12.7) and (12.13) for the radiation reaction force for relativistic electrons is given by (e.g., Blumenthal and Gould 1970; Pozdnyakov et al. 1983):

$$P_{\rm rad} = P_{\rm IC} = (4/3)\,\sigma c\,U_{\rm rad}\,\gamma^2\beta^2 \approx (4/3)\,\sigma c\,U_{\rm rad}\,\gamma^2\,, \tag{12.20}$$

corresponding to the radiation reaction force

$$\mathbf{f}_{\rm rad}^{\rm IC} = -\mathbf{v}\,P_{\rm rad}/c^2 = -\,(4/3)\,\sigma\gamma^2\,U_{\rm rad}\,\mathbf{v}/c\,, \tag{12.21}$$

where $U_{\rm rad}$ is the radiation energy density and σ is the applicable scattering cross-section.

In most astrophysical applications the scattering is in the so-called Thomson regime, in which the seed photon's energy in the electron's rest frame, $\epsilon'_{\rm ph} \sim \gamma\epsilon_{\rm ph,\,seed}$, is less than $m_e c^2$; then one can use the simple energy-independent Thomson cross-section, $\sigma = \sigma_T$. In the opposite case, however, one has to use a

more general quantum-mechanical Klein-Nishina expression for the cross-section:

$$\sigma_{\rm KN}(x) = \frac{3}{4}\,\sigma_T \left[\frac{1+x}{x^2} \left(\frac{2(1+x)}{1+2x} - \frac{\ln(1+2x)}{x} \right) + \frac{\ln(1+2x)}{2x} - \frac{1+3x}{(1+2x)^2} \right], \tag{12.22}$$

where $x \equiv \epsilon'_{\rm ph}/m_e c^2$. In the ultra-relativistic limit $x \gg 1$, this expression can be approximated as

$$\sigma_{\rm KN}(x \gg 1) \approx \frac{3}{8}\,\sigma_T\,\frac{\ln 2x + 1/2}{x}\,. \tag{12.23}$$

Since the radiative reaction force on relativistic particles due to both synchrotron and inverse-Compton (in the Thomson regime) mechanisms scales as the square of the particle energy $\epsilon = \gamma mc^2$, the corresponding radiative cooling time, $\tau_{\rm rad} = \epsilon/P_{\rm rad}$ scales inversely with the energy. For curvature radiation the effect is even stronger since $P_{\rm rad}^{\rm curv} \sim \gamma^4$ and hence $\tau_{\rm rad}^{\rm curv} \sim \gamma^{-3}$. This means that for each of these processes radiative losses affect more energetic particles the most. What this implies is that radiative energy losses lead not only to the overall cooling of the plasma but also affect the shape of the particle distribution function. In particular, radiative losses may result in an effective upper energy limit on nonthermal particle acceleration, which may have very important observational consequences, as we discuss in the next section.

12.4 Radiation Effects on the Kinetic Picture of Magnetic Reconnection: Limiting Nonthermal Particle Acceleration

Nonthermal particle acceleration, the hallmark of which is usually considered to be the production of (truncated) power-law particle energy distributions, is an important and ubiquitous phenomenon in collisionless space-, solar-, and astrophysical plasmas. Among plasma-physical processes commonly believed to be responsible for nonthermal particle acceleration, the most popular are collisionless shocks, magnetic reconnection, and MHD turbulence. Whatever the mechanism is, however, a particle's energy can be increased only by the work done by the electric field, since the Lorentz force due to the magnetic field is perpendicular to the particle's direction of motion. It therefore follows that, in the presence of radiative losses, the maximum Lorentz factor $\gamma_{\rm rad}$ that a charged particle accelerated by an electric field E can attain is determined by the balance between the accelerating electric force eE and the radiation reaction force $f_{\rm rad}(\gamma)$, i.e., $f_{\rm rad}(\gamma_{\rm rad}) = eE$. Importantly, the electric field in most astrophysical applications is tied to the magnetic field and is typically of order the motional electric field, $E \lesssim vB/c = \beta B$, where $v \equiv \beta c$ is the plasma 3-velocity.

Thus, it is often useful to parametrize the electric field in terms of the magnetic field, e.g., by introducing a dimensionless parameter $\beta_E = E/B$, which is usually less than unity. In most magnetically dominated systems, the typical flow velocity is of the order of the Alfvén speed, V_A, and so one typically expects $\beta_E \lesssim V_A/c$. For example, in the context of magnetic reconnection, the relevant electric field is usually the main reconnection electric field and B is the reconnecting component of the magnetic field; then, $\beta_E = \beta_{\rm rec} = v_{\rm rec}/c$, where the $v_{\rm rec}$ is the reconnection inflow velocity, typically of order $v_{\rm rec} \sim 0.1 V_A$ for collisionless reconnection (e.g., Birn et al. 2001) and $v_{\rm rec} \sim 0.01 V_A$ for resistive-MHD reconnection in the large-system, plasmoid-dominated regime (Bhattacharjee et al. 2009; Huang and Bhattacharjee 2010; Uzdensky et al. 2010; Loureiro et al. 2012), although it can be higher in the presence of background turbulence (e.g., Lazarian and Vishniac 1999; Kowal et al. 2009; Loureiro et al. 2009; Eyink et al. 2011).

In relativistic plasmas, where $\beta_E \sim 1$, one obtains the following upper limits on relativistic particle acceleration in the presence of the three main radiative mechanisms (synchrotron, IC, and curvature) discussed in Sect. 12.3:

1. **Synchrotron radiation** (Guilbert et al. 1983; de Jager et al. 1996; Lyutikov 2010; Uzdensky and Cerutti 2011):

$$\gamma_{\rm rad}^{\rm sync} = \frac{1}{\sin\alpha}\left[\frac{3\,\beta_E}{2}\,\frac{e}{B r_e^2}\right]^{1/2} = \frac{1}{\sin\alpha}\left[\frac{3\,\beta_E}{2}\,\frac{B_{\rm cl}}{B}\right]^{1/2}, \tag{12.24}$$

   where α is the pitch angle of the particle with respect to the magnetic field (here we assume that the electric field is parallel to the direction of the particle's motion). The corresponding maximum characteristic synchrotron photon energy then is

$$\epsilon_{\rm ph,max}^{\rm sync} = \frac{3}{2}\,(\gamma_{\rm rad}^{\rm sync})^2\,\hbar\Omega_{c0} = \frac{9}{4}\,\alpha_{fs}^{-1}\,m_e c^2\,\beta_E \simeq 160\,{\rm MeV}\,\beta_E\,, \tag{12.25}$$

   where $\alpha_{fs} = e^2/\hbar c \simeq 1/137$ is the fine structure constant.
2. **Curvature radiation** (Sturrock 1971; Chugunov et al. 1975; Lyutikov et al. 2012b):

$$\gamma_{\rm rad}^{\rm curv} = \left(\frac{3E_\parallel R_c^2}{2e}\right)^{1/4}, \tag{12.26}$$

   where $E_\parallel$ is the accelerating parallel (to the magnetic field and to the particle velocity) electric field. This corresponds to a characteristic maximum photon energy that can be achieved by curvature radiation (Lyutikov et al. 2012b) of

$$\epsilon_{\rm ph,max}^{\rm curv} = \left(\frac{3}{2}\right)^{7/4}\hbar c R_c^{1/2}\left(\frac{E_\parallel}{e}\right)^{3/4}, \tag{12.27}$$

which can be recast as

$$\epsilon_{\rm ph,max}^{\rm curv} = \left(\frac{3}{2}\right)^{7/4} m_e c^2\, \alpha_{fs}^{-1} \sqrt{\frac{R_c}{r_e}} \left(\frac{E_\parallel}{B_{\rm cl}}\right)^{3/4}. \tag{12.28}$$

3. **Inverse Compton radiation** (in the Thomson regime):

$$\gamma_{\rm rad}^{\rm IC} = \left[\frac{3}{4}\,\frac{eE}{\sigma_T U_{\rm rad}}\right]^{1/2} = \left[\frac{9\,\beta_E}{32\pi}\,\frac{BB_{\rm cl}}{U_{\rm rad}}\right]^{1/2}. \tag{12.29}$$

These radiation-reaction upper energy limits become important in situations where they are lower than the applicable energy limits that may arise due to other reasons. One such other limit, for example, is due to a finite maximum available voltage drop associated with a given system size L and electric field E: $\gamma_{\rm max} = \epsilon_{\rm max}/mc^2 = eEL/mc^2 = \beta_E\, L/\rho_0$, where, once again, $\rho_0 \equiv m_e c^2/eB$ is the fiducial Larmor radius of a mildly relativistic electron corresponding to a magnetic field B (Hillas 1984; Aharonian et al. 2002). While the condition $\gamma_{\rm rad} < \gamma_{\rm max}$ is usually not satisfied in heliospheric environments, this situation does happen naturally in some of the most important high-energy astrophysical systems. In particular, this happens in pulsar magnetospheres (curvature and synchrotron radiation), in PWN (synchrotron), and in black-hole accretion flows (inverse Compton and synchrotron), as we will discuss in the following two sections. For example, in the case of synchrotron radiation, the condition $\gamma_{\rm rad} < \gamma_{\rm max}$ can be recast (ignoring factors of order unity) as $L > \rho_0\,(\rho_0/r_e)^{1/2} = r_e\,(B/B_{\rm cl})^{-3/2} \simeq 1.3\times 10^{11}\,{\rm cm}\,[B/(1\,{\rm G})]^{-3/2} = 1.3\,{\rm m}\,B_6^{-3/2}$, where $B_6 \equiv B/(1\,{\rm MG})$ is the magnetic field normalized to 1 MG, a value typical for gamma-ray-emitting pulsar magnetospheres near the light cylinder and for accretion disks of stellar-mass black holes in XRBs.

An equivalent way to think about the relative importance of radiation reaction in limiting particle acceleration is to consider relativistic particles moving at the radiation reaction limit $\gamma_{\rm rad}$ and to cast their radiative cooling length, $\ell_{\rm cool} = ct_{\rm cool} \equiv \gamma mc^3/P_{\rm rad}$ in terms of their Larmor radius, $\rho \equiv \gamma mc^2/eB$. Since $\gamma_{\rm rad}$ is determined by the force balance between the radiation reaction force $f_{\rm rad} \approx P_{\rm rad}/c$, and the accelerating electric force $eE = e\beta_E B$, one can immediately see that $\ell_{\rm cool} = \rho B/E = \beta_E^{-1}\rho(\gamma_{\rm rad})$. In particular, in the case of reconnection, the electric field is parametrized in terms of the upstream reconnecting magnetic field B_0 as $E = \beta_{\rm rec} B_0$, where $\beta_{\rm rec}$ is the dimensionless reconnection rate which, in collisionless relativistic systems is of order 0.1. Thus, we see that

$$\ell_{\rm cool}(\gamma_{\rm rad}) \simeq \gamma_{\rm rad} m_e c^2/eE \simeq \beta_{\rm rec}^{-1}\,\rho(\gamma_{\rm rad})\,, \tag{12.30}$$

i.e., only perhaps by a factor of $\beta_{\rm rec}^{-1} \sim 10$ longer than the Larmor radius of these particles. This means that, if one is interested in extreme high-energy nonthermal particle acceleration, one has to take radiation reaction into account once the size of the accelerating region exceeds about $10\rho(\gamma_{\rm rad})$. Once again, this is usually not

a concern in most heliospheric environments, but this situation is ubiquitous in astrophysics.

Finally, we would like to note that the above formulation treats radiation reaction as a continuous force on the particles, ignoring the fact that in reality radiation is emitted in the form of discrete photons. When the energy of the emitted photons becomes comparable to the kinetic energy γmc^2 of the emitting particle, one has to take the quantized, discrete nature of the radiation process into account. For example, for synchrotron radiation this happens when the particle's Lorentz factor approaches $\gamma_Q = \rho_0/l_C = B_Q/B$, where $l_C \equiv \hbar/mc$ is the Compton length scale and $\rho_0 \equiv mc^2/eB$, and $B_Q = \alpha_{\rm fs} B_{\rm cl} \simeq 4.4\times 10^{13}\,{\rm G}$ is the critical quantum magnetic field. Comparing γ_Q with $\gamma_{\rm rad}^{\rm sync}$ and neglecting for simplicity order-unity factors like $\sin\alpha$ and $3\beta_E/2$, we see that $\gamma_{\rm rad}^{\rm sync}/\gamma_Q \sim (B/\alpha_{\rm fs}B_Q)^{1/2}$. Therefore, synchrotron radiation reaction prevents a particle from reaching the quantum-radiation regime (i.e., $\gamma_{\rm rad}^{\rm sync} < \gamma_Q$) under most astrophysically-relevant circumstances, namely, as long as $B \lesssim \alpha_{\rm fs} B_Q \sim 10^{11}\,{\rm G}$. The only class of astrophysical objects for which this inequality is violated is neutron stars and, especially, ultra-magnetized neutron stars called magnetars: typical magnetic fields in normal neutral stars are of order $10^{12}\,{\rm G}$, and in magnetars they routinely reach $10^{15}\,{\rm G}$. This means that when considering energetic plasma processes, such as reconnection, in a close vicinity of these objects, the usual continuous-emission picture for synchrotron radiation is not applicable and one should instead describe it as emission of discrete quanta.

12.4.1 Radiative Relativistic Reconnection and the Crab Nebula Flares

One of the most prominent examples of possible radiative effects on nonthermal particle acceleration is given by the emission produced by the Crab PWN. It has now been reasonably firmly established that most of the baseline steady-state nonthermal continuum emission from the Nebula, spanning from radio, to optical, to X-rays, and high-energy (tens of MeV) gamma-rays, is produced by synchrotron radiation from ultra-relativistic electrons and positrons that populate the Nebula (e.g., Shklovskii 1957, 1966). Then, however, the spectrum is observed to drop rather sharply above about 100 MeV, which is convincingly explained by the above "standard" synchrotron radiation reaction limit, $\epsilon_{\rm ph,max} \simeq (9\hbar c/4e^2)\, m_e c^2 \simeq 160\,{\rm MeV}$, (Guilbert et al. 1983; de Jager et al. 1996; Lyutikov 2010; Uzdensky and Cerutti 2011; Komissarov and Lyutikov 2011). This indicates that the theoretical reasoning behind this limit is solid and the limit is indeed applicable in real situations, at least under normal circumstances.

It turns out, however, that this is not the whole story, the actual situation is far more interesting. The validity of the above standard radiation reaction limit was recently challenged observationally by the discovery, made by the space-based gamma-ray observatories AGILE and FERMI, of short ($\sim$1 day), very intense

100 MeV-1 GeV flares in the Crab Nebula (Abdo et al. 2011; Tavani et al. 2011; Balbo et al. 2011; Striani et al. 2011; Buehler et al. 2012; Bühler and Blandford 2014). For basic energetics reasons, the only viable emission mechanism for the flares is still believed to be synchrotron radiation by PeV electrons in milli-Gauss magnetic fields, but the typical energies of the observed flare photons clearly exceed, by a factor of a few, the "standard" $\lesssim$ 100 MeV synchrotron radiation reaction limit (Abdo et al. 2011; Tavani et al. 2011; see Bühler and Blandford 2014 for recent review). This paradox thus challenges standard theories of high-energy particle acceleration in relativistic astrophysical plasmas and has lead to an intense theoretical effort aimed at resolving it (Uzdensky and Cerutti 2011; Bednarek and Idec 2011; Komissarov and Lyutikov 2011; Yuan et al. 2011; Clausen-Brown and Lyutikov 2012; Cerutti et al. 2012a; Bykov et al. 2012; Sturrock and Aschwanden 2012; Lyutikov et al. 2012a; Lyubarsky 2012; Cerutti et al. 2013, 2014b,a).

One promising idea invokes particle acceleration by magnetic reconnection (Uzdensky and Cerutti 2011; Cerutti et al. 2012a, 2013, 2014b,a; see also Bednarek and Idec 2011). The main idea is based on a specific peculiar property of the reconnection process that allows one to circumvent the usual expectation (on which the standard radiation reaction limit is based) that the accelerating electric field E be weaker than the perpendicular magnetic field $B_\perp$ that causes the particle to radiate and hence lose its energy. Indeed, this expectation is usually well justified almost everywhere in astrophysical plasmas and is related to the applicability of ideal MHD, but intense reconnection layers are precisely the places where ideal MHD reconnection does not apply and hence where one can expect the condition $E < B_\perp$ to break down! In fact, the reconnecting magnetic field vanishes exactly at the X-point at the center of a current layer, whereas the electric field there remains finite. Thus, one may expect that the Crab flare paradox can be resolved if the required particle acceleration to PeV energies takes place deep inside a reconnection layer, where the magnetic field is weak and so the associated synchrotron radiation reaction force is greatly reduced (Uzdensky and Cerutti 2011; Cerutti et al. 2012a). What makes this scenario particularly attractive is that ultra-relativistic particles moving along relativistic Speiser trajectories in a current layer have a natural tendency to focus deeper and deeper into the layer as they gain energy (Kirk 2004; Contopoulos 2007; Uzdensky and Cerutti 2011; Cerutti et al. 2012a). This leads to the formation of discrete highly focused and very intense beams of energetic particles that can be accelerated by the reconnection electric field to energies well above the radiation reaction limit $\gamma_{\rm rad}^{\rm synch}$ associated with the upstream reconnecting magnetic field B_0. Eventually, these particles escape the low-$B_\perp$ accelerating region and enter a finite-$B_\perp$ region where they quickly radiate their energy in an intense short burst of synchrotron radiation above 100 MeV. The plausibility of this picture, first suggested analytically by Uzdensky and Cerutti (2011), has then been tested in both test-particle (Cerutti et al. 2012a) and fully self-consistent numerical simulations using the radiative relativistic PIC code Zeltron (Cerutti et al. 2013, 2014b,a). This latter study was one of the first (second only to Jaroschek and Hoshino (2009)) numerical PIC studies of magnetic reconnection that

incorporated the radiation reaction force, and also the first to compute the observable radiative signatures (photon spectra and light curves) of reconnection.

This example illustrates that, whereas there exist important, high-profile astrophysical phenomena where radiation-reaction effects on particle acceleration are expected to play an important role, how exactly these effects play out, in particular, in the case of reconnection-powered synchrotron radiation, is highly non-trivial and extremely interesting.

12.4.2 Reconnection-Powered Particle Acceleration in Accreting Black Hole Coronae

Another important area in high-energy astrophysics where radiation reaction may play an important role in limiting relativistic electron (and perhaps positron) acceleration by reconnection, with potentially important observational consequences, is represented by accretion disks and their coronae in black hole systems, such as galactic X-ray binaries (XRBs) and AGN. Here, unlike in pulsar systems, the main radiative mechanism is inverse-Compton (IC) scattering of soft (10–100 eV in AGN and $\sim$ 1 keV in XRBs) accretion-disk photons by the energetic electrons accelerated in coronal reconnection events. This is especially so in bright systems accreting at a significant fraction of the Eddington limit, such as quasars and microquasars (in the high-soft state). ADCe in such systems often have Thomson optical depth of order unity and the reconnection layers responsible for the coronal heating and the hard X-ray production is often marginally-collisionless (Goodman and Uzdensky 2008). Importantly though, the ambient soft photon field produced by the underlying accretion disk is so intense that the resulting IC radiation reaction is very strong and needs to be taken into account. In particular, it results in an effective Compton-drag resistivity (see Sect. 12.6.1) which, under some conditions, becomes greater than the Spitzer resistivity due to electron-ion Coulomb collisions (Goodman and Uzdensky 2008). And, relevant to our present discussion, radiation reaction due to both IC and synchrotron mechanisms can affect the high-energy end of the electron distribution function and hence the observable hard X-ray and gamma-ray emission (e.g., Khiali et al. 2015a,b).

As discussed above, the relative importance of radiation reaction in reconnection-driven particle acceleration can be assessed by examining the radiative cooling length for electrons at the radiation reaction limit,

$$\ell_{\rm cool}(\gamma_{\rm rad}) = c t_{\rm cool}(\gamma_{\rm rad}) = \gamma_{\rm rad}\, m_e c^3 / P_{\rm rad}(\gamma_{\rm rad}) \sim \beta_E^{-1}\, \rho(\gamma_{\rm rad})\,, \qquad (12.31)$$

and comparing it with other important length scales in the system. For typical conditions in ADCe of XRB black holes accreting near the Eddington limit, $\gamma_{\rm rad}^{\rm IC}\, m_e c^2$ can to be of the order of 1000 MeV; thus, there should be virtually no electrons with energies much higher than the proton rest mass (perhaps multiplied

by a factor of a few) in these systems. The corresponding cooling length of these energetic electrons is then comparable to (or perhaps somewhat larger than) the fiducial proton Larmor radius $\rho_{i0} \sim m_p c^2/eB_0 = 0.3\,\mathrm{cm}\,B_7^{-1}$. Obviously, this length is much smaller than the typical expected reconnection layer length in ADC, $L \sim R_g$, where $R_g \equiv GM/c^2 \simeq 1.5\,\mathrm{km}\,M/M_\odot$ is the gravitational radius of a black hole of mass M and $M_\odot \simeq 2 \times 10^{33}\,\mathrm{g}$ is the solar mass. For example, for a typical XRB stellar-mass black hole with $M \sim 10M_\odot$, we have $R_g = 15\,\mathrm{km}$, and for a typical large super-massive black hole with $M \sim 10^8 M_\odot$, we have $R_g \sim 1.5 \times 10^8\,\mathrm{km} \approx 1\,\mathrm{AU}$.

Interestingly, $\gamma_{\rm rad}^{IC}\, m_e c^2 \sim 1000\,\mathrm{MeV}$ is also comparable to the average dissipated energy per particle, $\bar{\gamma}\, m_e c^2 \sim B_0^2/(16\pi n_e)$, provided that electrons and ions get comparable amounts of energy and that $\sigma_i \equiv B_0^2/(4\pi n_i m_p c^2) \sim 1$ in the corona. This in turn means that the above radiation reaction energy limit is more or less comparable to Werner et al.'s "natural" cutoff $\gamma_{c1} \sim 10\,\bar{\gamma}$ (see Sect. 12.2.2). Thus, provided that cutoff, discovered in 2D PIC simulations of relativistic pair-plasma reconnection (Werner et al. 2014), also applies to electron-ion plasmas, we see that $\gamma_{\rm rad}^{IC}$ may in fact be the smallest, and hence the governing, cutoff that limits nonthermal electron acceleration in coronae of real black holes accreting matter at high accretion rates (e.g., of XRBs in the high-soft state).

The most important potential observational implication of these findings is the prediction that reconnection events in accretion disk coronae of XRB black holes in the high-soft state should be able to produce power-law high-energy IC radiation spectra extending to photon energies on the order of $\epsilon_{\rm ph,\,max} \sim \epsilon_{\rm ph,\,soft}(\gamma_{\rm rad}^{IC})^2 \sim 10^4 - 10^6\,\epsilon_{\rm ph,\,soft} \sim 10-1000\,\mathrm{MeV}$, where we took $\gamma_{\rm rad}^{IC} \sim 100-1000$ and $\epsilon_{\rm ph,\,soft} \sim 1\,\mathrm{keV}$, a typical energy for the dominant radiation emitted by Shakura and Sunyaev (1973) accretion disks around stellar-mass black holes.

However, because of the high compactness of these systems, most of these high-energy gamma-ray photons probably get absorbed by other photons and create electron-positron pairs before they can escape. This could be the primary process that governs (or at least strongly contributes to) the rate of pair production in black-hole coronae and thus may affect the composition (pairs vs. electron-ion plasma) of black-hole-powered winds and jets. Thus, our ability to calculate from first principles the number of electrons accelerated by reconnection to tens and hundreds of MeV, and hence the number of IC photons at these extreme energies, should give us an important handle on the efficiency of pair production in these systems—a fundamental issue in black-hole astrophysics.

12.5 Reconnection with Radiative Cooling

One of the most important effects that radiative drag force can have on reconnection, and one that often comes into play first in various astrophysical contexts, is its effect on the random thermal motions of average, run-of-the-mill particles in the reconnection layer. We call this effect *radiative cooling*. Here we are particularly

interested in the case of prompt radiative cooling, in which the characteristic cooling time $t_{\rm cool}$ of the hot plasma energized by the reconnection processes is shorter than or comparable to the characteristic time that a given fluid element spends inside the reconnection layer, which is typically the Alfvén transit time along the layer, $\tau_A = L/V_A$. In this regime, which we will call the strong radiative cooling regime, radiative energy losses become important in the overall energy balance of the reconnection process and need to be taken into account. The opposite case was considered in Sect. 12.2.

It is easy to estimate that radiative cooling is not important in most traditional (solar-system) applications of reconnection, i.e., in the environments of solar flares, the Earth magnetosphere, and tokamak fusion devices and dedicated laboratory experiments designed to study reconnection under controlled laboratory conditions. Because of this, there has been relatively little work done on incorporating radiative cooling effects into reconnection models. However, when one tries to think about reconnection in various astrophysical contexts, one often finds, by doing simple estimates, that if magnetic reconnection happens in these environments, it has to take place in the strong radiative cooling regime. This realization has lead to an increased interest in radiative magnetic reconnection in the high-energy astrophysics community, especially in recent years (Dorman and Kulsrud 1995; Lyubarskii 1996; Jaroschek and Hoshino 2009; Giannios et al. 2009; Nalewajko et al. 2011; Uzdensky 2011; Uzdensky and McKinney 2011; McKinney and Uzdensky 2012; Takahashi and Ohsuga 2013, 2015; Uzdensky and Spitkovsky 2014). The importance of radiative cooling effects on reconnection have also been recognized in the context of reconnection in the solar chromosphere (Steinolfson and van Hoven 1984; Leake et al. 2013; Ni et al. 2015).

12.5.1 Reconnection with Radiative Cooling: Optically Thin Case

The first key step to study the effects of strong cooling on reconnection in a systematic way was made recently by Uzdensky and McKinney (2011), who developed a simple but self-consistent Sweet–Parker-like model for a non-relativistic resistive-MHD reconnection layer subject to strong optically thin cooling. It is of course understood that, just like the original Sweet–Parker model, this model should not be expected to provide a complete description of reconnection in real large astrophysical systems, which are often subject to a host of other effects, such as ambient turbulence (Lazarian and Vishniac 1999), secondary current-layer instabilities such as the plasmoid instability (Loureiro et al. 2007), and collisionless effects (e.g., Birn et al. 2001), just to name a few. For these reasons the (Uzdensky and McKinney 2011) model of reconnection with radiative cooling should only be viewed as a toy model which, however, brings out several important physical insights into the problem and provides a useful fundamental building block for future studies.

The main idea of this model was that since radiative cooling limits the rise of the plasma temperature in the layer, in the absence of a guide magnetic field, the plasma inside the layer has to compress in order to maintain the pressure balance with the upstream magnetic pressure. By analyzing carefully the balance between ohmic heating and radiative and advective cooling, together with the cross-layer pressure balance and with the equation of motion along the layer, Uzdensky and McKinney (2011) obtained estimates for the key parameters characterizing the reconnecting system: the plasma compression ratio, the reconnection rate, and the layer thickness, in terms of the general parameters of the radiative cooling function. It was found that the reconnection rate, in the case with no guide field, is enhanced relative to the non-radiative case and that the layer thickness is reduced due to the cooling-related compression; a strong guide field, however, suppresses this effect by preventing strong compression. In addition, for the specific case of Spitzer resistivity $\eta_{\rm Sp}$, reconnection is sped up (with or without a guide field) by radiative cooling even further due to the strong inverse scaling of the resistivity with temperature, $\eta_{\rm Sp} \sim T^{-3/2}$. Furthermore, several specific astrophysically-important radiative mechanisms (bremsstrahlung, cyclotron, and inverse Compton) were considered and the conditions for strong-cooling regime were formulated for each one of them. The theory lead to specific expressions for the reconnection rate and to the prediction of a cooling catastrophe behavior for the case of strong bremsstrahlung cooling. Although this study (Uzdensky and McKinney 2011) focused mostly on optically thin case, many of its ideas, concepts, and conclusions should be valid more broadly; however, analyzing reconnection dynamics in the optically-thick case requires approaching the problem as a radiative-transfer problem, as we discuss in Sect. 12.5.2.

An interesting astrophysical example of reconnection where strong radiative cooling is important is reconnection in the magnetospheres of gamma-ray pulsars (e.g., the Crab), at distances comparable to, but also perhaps somewhat larger than the light cylinder (LC) radius (Uzdensky and Spitkovsky 2014; see also Lyubarskii 1996; Arka and Dubus 2013). The rotating pulsar magnetosphere naturally develops an equatorial current sheet beyond the light cylinder, somewhat similar to the heliospheric current sheet, and magnetic reconnection in this current sheet can dissipate a nontrivial fraction of the overall pulsar spin-down power within a few LC radii.

In some rapidly rotating pulsars, the reversing magnetic field just beyond the light cylinder is so strong (e.g., of order 1 MG for the Crab pulsar) that prompt synchrotron cooling of the heated plasma in the layer inevitably becomes important; it controls the energetics of reconnection and may result in production of observed strong pulsed GeV γ-ray emission (Lyubarskii 1996; Uzdensky and Spitkovsky 2014; Arka and Dubus 2013).

In particular, by combining the conditions of the pressure balance across the current layer (reconnection in pulsar magnetosphere is expected to take place without a guide field) and of the balance between the heating by magnetic energy dissipation and synchrotron cooling, one can obtain simple estimates for key physical parameters of the layer's plasma, such as the temperature, density, and

layer thickness, in terms of the reconnecting upstream magnetic field B_0 (Uzdensky and Spitkovsky 2014). Specifically, one expects the plasma to be heated to roughly the radiation reaction limit $\theta_e \equiv T_e/m_e c^2 \sim \gamma_{\rm rad}^{\rm synch}$ [see Eq. (12.24)] and thus to be compressed to the density $n_e \sim B_0^2/(16\pi \gamma_{\rm rad}^{\rm synch} m_e c^2)$ (in the comoving frame of the relativistic pulsar wind). The corresponding thickness of the small elementary inter-plasmoid current layers is then expected to be comparable to the relativistic Larmor radius of these particles, $\delta \sim \rho_L(\gamma_{\rm rad}^{\rm synch}) = \gamma_{\rm rad}^{\rm synch}\rho_0$. For the particularly important case of the Crab pulsar, one finds: $T_e \sim 10^4\, m_e c^2 \sim 10\,{\rm GeV}$, $n_e \sim 10^{13}\,{\rm cm}^{-3}$, and $\delta \sim 10\,{\rm cm}$. After accounting for the bulk Doppler boosting due to the pulsar wind (with a Lorentz factor of order 100), the synchrotron and inverse-Compton emission from the reconnecting current sheet may plausibly explain the observed Crab's pulsed high-energy (GeV) and VHE ($\sim$ 100 GeV) radiation, respectively, while the rapid motions of the secondary plasmoids in the large-scale current layer may contribute to the production of the pulsar radio emission (Uzdensky and Spitkovsky 2014).

In addition to astrophysical applications, magnetic reconnection in the strong optically thin radiative cooling regime may soon be within reach to laboratory studies utilizing powerful modern laser plasma facilities, such as Omega EP and NIF (Uzdensky et al. 2016, in preparation). The main cooling mechanism in these experiments is collisional bremsstrahlung, perhaps augmented by atomic-line cooling, depending on the plasma composition. Since the bremsstrahlung cooling rate scales strongly with the plasma density (as n_e^2) but only weakly with the temperature (as $T^{1/2}$), in order to reach the desired radiative regime, it is advantageous to configure the laser-target setup towards a higher density, a lower temperature, and a larger illuminated area. In addition, the role of radiative cooling is enhanced if one uses targets made of high-Z materials, such as copper and gold. Overall, preliminary estimates indicate that the strong radiative cooling regime is reachable on NIF and perhaps even on Omega EP when using gold targets. Interestingly, some of the physical parameters achievable in these laser-plasma experiments, e.g., magnetic field strengths, densities, characteristic kinetic plasma length scales, are not that different from the values expected in, e.g., BH accretion disk coronae in XRBs. This points to tantalizing potential prospects of studying in the lab the magnetic reconnection processes in the regimes relevant to these astrophysical environments.

12.5.2 Reconnection with Radiative Cooling: Optically-Thick Case

In the optically-thick radiative cooling case, i.e., when the optical depth τ *across* the layer is large, a self-consistent treatment of radiation calls for serious modifications to our overall theoretical approach to the reconnection problem. Specifically, one has to view the reconnection problem in this case essentially as a radiative transfer problem (Uzdensky 2011). The current layer develops a photosphere, with a

photospheric surface temperature, $T_{\rm ph}$, which in a steady state is related to the temperature T_0 at the center of the reconnection layer via $T_0^4/T_{\rm ph}^4 = \tau \gg 1$. Furthermore, in the strong-cooling regime the basic steady-state energy balance between the Poynting flux entering the layer from upstream with the reconnection inflow, $S = (c/4\pi)\, E_{\rm rec} B_0 = v_{\rm rec}\, B_0^2/4\pi = c\,\beta_{\rm rec} B_0^2/4\pi$, and the outgoing radiative flux emitted by the photosphere, $F_{\rm rad} = \sigma_{\rm SB} T_{\rm ph}^4$, where $\sigma_{\rm SB} = \pi^2 k_B^4/60\hbar^3 c^2 \simeq 5.67 \times 10^{-5}\,{\rm erg\,cm^{-2}\,s^{-1}\,K^{-4}}$ is the Stefan-Boltzmann constant, determines the photospheric temperature in terms of the reconnecting magnetic field:

$$T_{\rm ph} = \left[\frac{c\,\beta_{\rm rec}}{\sigma_{\rm SB}}\,\frac{B_0^2}{4\pi}\right]^{1/4}, \tag{12.32}$$

and hence the central layer temperature for a given τ:

$$T_0 = \tau^{1/4} T_{\rm ph} = \left[\tau\,\frac{c\,\beta_{\rm rec}}{\sigma_{\rm SB}}\,\frac{B_0^2}{4\pi}\right]^{1/4}. \tag{12.33}$$

Next, if there is no guide field and if the pressure inside the layer is dominated by the gas pressure, $P_0 = 2 n_{e,0} k_B T_0$, then one can use the condition of pressure balance across the layer between P_0 inside the layer and the combined magnetic plus plasma pressure in the upstream region outside the layer, $(1 + \beta_{\rm up})\, B_0^2/(8\pi)$, where $\beta_{\rm up}$ is the upstream plasma-β parameter, to obtain the central plasma density:

$$n_{e,0} = \frac{B_0^2}{16\pi}\,\frac{1+\beta_{\rm up}}{k_B T_0}. \tag{12.34}$$

The expressions (12.32)–(12.34) govern the basic thermodynamics of a reconnection layer subject to strong radiative cooling in the optically thick regime.

12.5.3 *Optically-Thick Current Layer: Radiation Pressure Effects*

However, in some important astrophysical phenomena, the reconnecting magnetic field is so strong and hence the total plasma energy density in the layer is so high that the pressure is dominated by radiation pressure. For an optically thick layer, we can assume thermal black-body radiation pressure: $P_{\rm rad,0} = a T_0^4/3$, where $a = 4\sigma_{\rm SB}/c \simeq 7.57 \times 10^{-15}\,{\rm erg\,cm^{-3}\,K^{-4}}$ is the radiation constant. In this case, the cross-layer pressure balance does not involve the plasma density and instead yields, in combination with the steady-state energy balance $S = c\,\beta_{\rm rec} B_0^2/4\pi = F_{\rm rad} = \sigma_{\rm SB} T_{\rm ph}^4 = \tau^{-1}\,\sigma_{\rm SB} T_0^4$, a simple but important relationship between the optical depth and the reconnection rate (Uzdensky 2011):

$$\tau\,\beta_{\rm rec} = \frac{3}{8}. \tag{12.35}$$

The validity of this expression is limited by a few assumptions, namely, by the steady-state assumption and by the assumption of strong cooling. The latter, in particular, implies that the radiative diffusion time across the layer, $t_{\rm diff} \sim \tau\delta/c$ is much shorter than the (Alfvénic) advection time $\tau_A \sim L/V_A$ along the layer, and this imposes a certain condition on the layer's aspect ratio relative to the optical depth: $L/\delta > \tau V_A/c$.

12.6 Radiation Drag on Fluid Flow

Another fluid-level manifestation of the radiative drag force is its direct braking effect on bulk plasma motions expected in a reconnecting system. Thus, in contrast to radiative cooling, which affects the *thermodynamics* of the reconnection process, the radiation effects that we consider in this section influence the *dynamics* and *electrodynamics* of reconnection. Here it is convenient to distinguish two aspects of such action:

1. radiative friction on the current-carrying charged particles moving in the out-of-plane direction and responsible for carrying the current in the reconnection layer, resulting in an effective *radiative resistivity*;
2. radiative friction slowing down the *reconnection outflows* in the direction along the reconnecting magnetic field (the outflow direction).

Although the actual underlying physical mechanism behind these two effects is the same, for practical reasons it is convenient to consider them separately because they play different roles in changing the reconnection dynamics.

12.6.1 Radiative Resistivity

When electrons carrying the electric current in a reconnecting current layer drift through an external radiation field, or perhaps radiate themselves via, e.g., synchrotron radiation, the radiation drag force on the electron flow may produce an effective radiative resistivity, $\eta_{\rm rad}$.

In particular, for non-relativistic electrons, e.g., in applications such as accretion disks and ADCe, equating the radiation drag force given by Eq. (12.21) with the accelerating electric force, one finds the steady-state drift velocity $< \mathbf{v}_e > = -(3/4)(ce/\sigma_T U_{\rm rad})\,\mathbf{E}$. These electrons thus carry an electric current of $\mathbf{j}_e = -en_e < \mathbf{v}_e > = (3/4)\,(cn_e e^2/\sigma_T U_{\rm rad})\,\mathbf{E}$, which corresponds to an effective electron contribution to the electric conductivity of

$$\sigma^{\rm IC}_{e,{\rm rad}} = \frac{3}{4}\,\frac{cn_e e^2}{\sigma_T U_{\rm rad}}\,. \tag{12.36}$$

It is interesting to note that, as was discussed by Goodman and Uzdensky (2008), strictly speaking, Compton drag does not change the steady-state resistivity in an electron-ion plasma; perhaps counter-intuitively, the resistivity actually just remains the Spitzer collisional resistivity. This is because radiation drag essentially affects only the electrons but not the ions (because the Thomson cross-section scales as the inverse square of the particle mass). Therefore, even if the electrons are greatly slowed down by the radiation field, the ions can eventually (if long enough time scales and length scales are available) get accelerated by the applied electric field to carry the necessary current. In many important astrophysical applications, however, including reconnection in BH ADCe, one is interested in processes that take place on such short length scales that the ions may not enough range to get accelerated to the Coulomb-collision-limited steady-state drift velocity. In such situations, one can ignore the ion current and hence cast the effective Ohm's law in terms of an effective Compton-drag resistivity, or a Compton magnetic diffusivity given by

$$\eta_{\rm IC} = \frac{c^2}{4\pi\sigma^{\rm IC}_{e,\rm rad}} = \frac{1}{3\pi}\,\frac{c\sigma_T U_{\rm rad}}{n_e e^2}\,. \tag{12.37}$$

In a pair plasma, of course, both electrons and positrons are subject to radiative drag equally; hence, their conductivities are both given by (12.36) (in the non-relativistic regime) and therefore the total radiative resistivity equals one half of the value given by Eq. (12.37).

As we discussed in Sect. 12.4.2, in astrophysical applications such as coronae of accretion disks of black holes accreting at a large fraction of the Eddington rate L_E, the ambient radiation field, with a radiation energy density $U_{\rm rad} \sim L_E/4\pi R^2 c$, where $R \simeq 10R_g$ is the characteristic size of the bright inner part of the accretion disk, is very intense. Under such conditions, the resulting effective radiative resistivity can be quite high and may dominate over the Spitzer resistivity due to classical Coulomb collisions. It can then seriously affect the reconnection processes that are believed to be responsible for coronal heating and for powering the observed hard X-ray emission from these sources. In particular, enhanced radiative resistivity may alter the analysis of whether the global reconnection layer is in the collisional or collisionless regime (Goodman and Uzdensky 2008) and may thus affect (reduce) the reconnection rate and the hierarchy of secondary plasmoids emerging in the reconnection layer. Needless to say, however, the regime where IC effective resistivity is important probably also implies that radiative cooling is important as well, which may actually speed up reconnection (see Sect. 12.5.1). In this case, it is not yet clear what the overall combined effect of radiation (cooling plus resistivity) on the reconnection rate is.

In the relativistic case, the Compton-drag resistivity was calculated by van Oss et al. (1993). An important point to keep in mind when considering effective resistivity in the relativistic case is that electric current depends only on the 3-velocity of charge carriers and not on their Lorentz factor. Thus, as long as the particles are ultra-relativistic (and thus travel nearly at the speed of light), the current

density they can carry is limited by $en_e c$, independent of the electric field. The effect of radiation drag on the resistivity in this case is diminished.

In addition to black-hole accretion disks and their coronae, radiative resistivity due to various radiative mechanisms may also potentially play a role in reconnection processes in a number of other high-energy astrophysical systems, e.g., in the magnetospheres of pulsars (Uzdensky and Spitkovsky 2014), magnetars (Uzdensky 2011), and GRBs (McKinney and Uzdensky 2012).

12.6.2 Radiative Drag on Reconnection Outflow

Finally, let us discuss the effects of radiative drag on the bulk outflow from the reconnection region. This outflow is an important aspect of the reconnection process; its main role is to evacuate from the reconnection layer the plasma that flows into the layer bringing in fresh unreconnected magnetic flux, and thus to make room for more plasma to enter. The outflow thus represents an important element of the overall stagnation-flow pattern around the magnetic X-points. The outflow is driven by a combination of the pressure gradient force and the magnetic tension force associated with reconnected magnetic field lines. It usually represents the fastest motion found in a reconnecting system, with a speed on the order of the Alfvén speed and hence significantly higher than the reconnection inflow velocity. Importantly, the outflow can usually be described roughly as an ideal-MHD motion as it involves the electrons and ions moving together in the same direction.[1]

In a number of astrophysical applications, including TeV flares in blazar jets (Nalewajko et al. 2011) and black-hole accretion disks, GRB jets, and others, the Compton drag due to ambient radiation may have a substantial effect on the reconnection outflow. It can slow down the outflow, choking the motion of plasma through the reconnection system and thereby reducing the reconnection rate in a manner similar to the effect of a large viscosity. For example, (Takahashi and Ohsuga 2013, 2015), using relativistic resistive MHD simulations that included optically-thick radiation effects, reported that radiative drag on the reconnection outflow lead to a reduction of the reconnection rate for Petschek-like relativistic reconnection.

In addition, as the ambient isotropic radiation field exerts a braking Compton-drag force on the plasma flow, it also extracts its energy and can, under certain circumstances, convert a noticeable fraction of the bulk kinetic energy of the outflow into radiation beamed in the outflow direction.

To illustrate the effect of radiative braking of the outflow on the reconnection rate, let us consider a simple, Sweet-Parker-like toy model of a laminar non-relativistic

[1] Strictly speaking in weakly collisional plasmas this is not quite correct since the electron and ion outflow patterns are somewhat different, which results in an in-plane current circulation responsible for the quadrupole out-of-plane magnetic field.

incompressible resistive-MHD reconnection problem. For illustration, we will only take into account the Compton-drag force in the outflow fluid equation of motion and will ignore other radiative effects such as radiative cooling and resistivity. Since the inflow is generally much slower than the outflow, the effect of the radiative drag on the inflow can also be neglected. We will also ignore the guide magnetic field. Furthermore, we will focus on an extreme case where radiative drag dominates over the plasma inertia in establishing the ultimate outflow velocity. The model is then somewhat similar to the analysis of resistive Hall-MHD reconnection in Uzdensky (2009).

For definiteness, let us choose a system of coordinates with x being the direction of the reconnecting magnetic field (and hence of the reconnection outflow), y being the direction across the layer, and z being the ignorable direction. Then, ignoring the plasma inertia in the outflow (x) equation of motion, the outflow velocity u_x is governed by the balance between the outward pressure gradient force $-dP/dx$ (magnetic tension may give a comparable contribution but we ignore it here for simplicity) and the Compton-drag force (per unit volume), $-(4/3)\, n_e \sigma_T U_{\rm rad}\, u_x/c$. This yields the following estimate for the final outflow speed at the end of the layer of length L:

$$u_{\rm out} \sim c\, \frac{\Delta P}{L}\, \frac{1}{n_e \sigma_T U_{\rm rad}} = c\, \frac{\Delta P}{\tau_T\, U_{\rm rad}}\,, \tag{12.38}$$

where $\tau_T \equiv n_e \sigma_T L$ is the Thomson optical depth along the layer. The drop ΔP of the plasma pressure along the layer can be estimated, as is done in the traditional Sweet-Parker model, by using the condition of pressure balance across the layer, $P_0 = P^{\rm up} + B_0^2/8\pi$, and ignoring the variation of the upstream plasma pressure $P^{\rm up}$ along the layer. Thus, $\Delta P \simeq B_0^2/8\pi$ and we get

$$u_{\rm out} \sim c\, \frac{B_0^2}{8\pi\, \tau_T\, U_{\rm rad}} = c\, \tau_T^{-1}\, \frac{U_{\rm magn}}{U_{\rm rad}}\,. \tag{12.39}$$

One can see that, since we assumed the outflow to be non-relativistic, $u_{\rm out} \ll c$, this result requires that the radiation energy density times the optical depth be sufficiently large compared to the magnetic energy density, i.e., $\tau U_{\rm rad} \gg U_{\rm magn}$, a condition that is indeed satisfied, for example, in the inner parts of black-hole accretion disks. Furthermore, since in this model we neglected the plasma inertia compared to the radiation drag, we must also require that $u_{\rm out} \ll V_A = B_0\, (4\pi\rho)^{-1/2}$. This, in turn, imposes an even more stringent condition than $u_{\rm out} \ll c$, namely, $\tau U_{\rm rad} \gg (U_{\rm magn}\, \rho c^2)^{1/2}$, which, however, can also be satisfied inside black-hole accretion disks.

The rest of the reconnection problem analysis is the same as in the classical Sweet-Parker model. Employing the incompressibility condition, $\delta u_{\rm out} = v_{\rm rec} L$, and the steady-state resistive magnetic induction equation: $\delta v_{\rm rec} = \eta$, where $v_{\rm rec}$ is the reconnection inflow velocity, δ is the layer thickness, and η is the magnetic diffusivity (which may, in general, be due to both Coulomb collisions and radiative

resistivity), one obtains the usual Sweet-Parker scaling for the reconnection rate and for the aspect ratio:

$$\frac{\delta}{L} \sim \frac{v_{\rm rec}}{u_{\rm out}} \sim S_{\rm rad}^{-1/2}\,, \tag{12.40}$$

where, however, the radiation-controlled outflow velocity $u_{\rm out}$ replaces the Alfvén speed in the effective Lundquist number, i.e.,

$$S_{\rm rad} \equiv L\,\frac{u_{\rm out}}{\eta}\,. \tag{12.41}$$

This model, although highly simplified, may provide a useful building block in constructing a more complete theoretical picture of magnetic reconnection in certain radiation-rich astrophysical environments, for example, in the context of high accretion rate black-hole accretion flows in XRBs and AGNs.

12.7 Other Radiation Effects in Optically Thick Plasmas: Radiation Pressure, Radiative Viscosity and Hyper-Resistivity, and Pair Creation

In systems with non-negligible optical depth across the layer some of the photons produced by the reconnection process do not promptly leave the system but may interact with the particles in the layer again by scattering or absorption (or pair creation at higher energies, see below). This interaction can lead to additional effects, such as radiation pressure and radiative viscosity, both of which can affect the reconnection dynamics.

In particular, if the layer is optically thick to scattering, then radiation pressure $P_{\rm rad}$ enters the pressure balance across the layer:

$$P_{\rm gas} + P_{\rm rad} + B^2/8\pi = {\rm const}\,. \tag{12.42}$$

This implies that the plasma pressure at the center of the layer does not need to increase as much as in the case without radiation pressure in order to balance the outside magnetic pressure. For example, if the optical depth is large enough for radiation to reach local thermal equilibrium with the plasma at the local plasma temperature T, then $P_{\rm rad} = aT^4/3$ and hence the pressure balance becomes

$$2nk_BT + aT^4/3 + B^2/8\pi = {\rm const}\,. \tag{12.43}$$

Therefore, the temperature in the layer can be lower than in the case without radiation pressure. The thermodynamic structure of the layer in this case is determined by the radiative transfer problem across the layer. If, however, the optical

depth is modest, $\tau \lesssim 1$, then the effects of radiation pressure are reduced by a factor of τ, but can still be significant under some circumstances.

Because of the very steep dependence of the radiation pressure on temperature, we can see that radiation pressure effects are important mostly only in very hot environments. In addition, since the optical depth must be high enough to ensure a good coupling of the radiation pressure to the plasma, the density must also be high. From this one can deduce that radiation pressure effects on reconnection are expected to be important mostly in high-energy-density systems. Most notable astrophysical examples of such systems include the inner parts of black-hole and neutron-star accretion disks in binary systems; magnetospheres of normal neutron stars, e.g., X-ray pulsars (with "normal" magnetic fields of about 10^{12} G), and magnetars in, e.g., SGR systems (with magnetic fields of order 10^{15} G); and central engines of supernovae (SNe) and GRBs.

In addition to the radiation pressure effects in a reconnection layer of non-negligible optical depth, the momentum extracted by radiation from reconnection outflow (see the discussion of radiative braking in Sect. 12.6.2) can be deposited back to the plasma in other parts of the layer, which results in an effective viscosity mediated by the photons. This radiative viscosity is then expected to affect the basic reconnection dynamics in a manner similar to the usual collisional viscosity caused by the thermal motions of electrons and ions: it should lead to broadening of the layer and to decreasing the reconnection rate.

Likewise, the momentum extracted by radiation from current-carrying electrons in the current layer (which leads to a Compton-drag radiative resistivity, see Sect. 12.6.1) can be deposited to other current-carrying electrons elsewhere in the layer if the optical depth is not negligible. This essentially spreads the electric current, making the layer broader, an effect that can be described as a result of a radiative hyper-resistivity proportional to the optical depth (for $\tau < 1$). Interestingly, this hyper-resistivity should only work in electron-ion plasmas; in pair plasmas, since photons can be scattered or absorbed by both electrons and positrons (which drift in opposite directions), radiative hyper-resistivity just gives way to an enhanced radiative resistivity.

In the most extreme astrophysical systems, such as the magnetospheres of magnetars in SGR systems and GRB and SN central engines, the reconnecting magnetic field B_0 exceeds the quantum critical magnetic field $B_Q \equiv \alpha_{\rm fs} B_{\rm cl} = m_e^2 c^3/e\hbar \simeq 4.4\times 10^{13}$ G. Then, the dissipated magnetic energy density is so high that the pressure of the heated plasma inside the reconnection layer becomes dominated by the radiation pressure and, furthermore, the resulting radiation temperature becomes relativistic, i.e., $T_0 \sim m_e c^2 \, (B_0/B_Q)^{1/2}$ (Uzdensky 2011). In this case, prodigious pair production inevitably results and the current layer gets quickly "dressed" in an optically thick and dense pair coat. Once again, the problem of determining the thermodynamic structure across such a dressed layer becomes a radiative transfer problem, but one in which the pair density at any location in the layer below its pair-creation photosphere is determined by the local thermodynamic equilibrium. In particular, for reconnecting magnetic fields that are not just higher, but much higher than B_Q, e.g., in magnetar systems, one expects ultra-relativistically

hot plasma, $T \gg m_e c^2$; and under these conditions the pair density scales as T^3 and the pair contribution to the total pressure becomes comparable to the radiation pressure (Uzdensky 2011). Magnetic reconnection in this very exotic regime may be the mechanism behind some of the most spectacular, energetic phenomena in the Universe—giant SGR flares, releasing huge amounts of energy in the form of gamma-rays in just a fraction of a second (Uzdensky 2011; Uzdensky and Rightley 2014). This regime can be regarded as the most extreme case of radiative reconnection, because all of the radiative effects discussed in this article—radiation-reaction limits on particle acceleration, strong radiative cooling, radiation pressure, Compton-drag resistivity, etc.—are active in this case.

12.8 Conclusions and Outlook

This chapter presented a review of the physics of radiative magnetic reconnection and its applications to various astrophysical phenomena. Traditional reconnection research, motivated by applications to relatively low-energy-density solar-system and laboratory plasma environments, has historically ignored the possible effects and observational signatures of radiation. In many astrophysical reconnecting systems, however, various radiation effects exert an important influence on the dynamics and energetics of the reconnection process, as well as on the associated nonthermal particle acceleration. These effects ultimately stem from the radiation reaction force on individual particles, which is directly related to the rate of energy losses suffered by the particle (i.e., the particle's radiative power). Since the radiative power is often proportional to the energy density of the external agent field that causes the particle to radiate (e.g., magnetic energy density for synchrotron radiation and ambient radiation energy density for inverse-Compton radiation), we see that the relative importance of the radiation reaction force in the particle equation of motion can usually be traced to the high energy density in astrophysical systems of interest, combined with their large size. The main radiation mechanisms involved in high-energy astrophysical reconnection, especially in relativistic systems, are cyclo/synchrotron radiation, curvature radiation, and inverse-Compton scattering. In addition, bremsstrahlung radiation and pair creation can play a role under some circumstances.

The radiation reaction force can manifest itself via several different radiative effects, the relative importance of which depends on the particular astrophysical context. The first radiative effect that comes in at lowest energy densities is the radiation-reaction limit on relativistic particle acceleration. This is a purely kinetic effect, it is due to the fact that for relativistic particles the radiative power, and hence the radiation reaction force, grow rapidly with the particle's Lorentz factor γ. This means that the radiation back-reaction first affects the most energetic particles, while leaving lower-energy particles less affected. This necessitates a kinetic treatment. One of the most prominent astrophysical examples where this effect has to be taken into account in considering magnetic reconnection is the Crab pulsar wind nebula,

in particular in relation to the recently discovered short and bright gamma-ray (hundreds of MeV) flares that seem to require extreme particle acceleration to PeV energies, overcoming the synchrotron radiation reaction limit. Another important astrophysical example is found in reconnection events powering coronal heating and hard-X-ray emission in accretion disk coronae of black holes, e.g., in galactic X-ray binaries and active galactic nuclei. Here, inverse-Compton radiation drag due to the intense ambient soft photon field emitted by the underlying accretion disk imposes interesting upper limits on the electron acceleration.

Most of the other radiative effects acting in high-energy astrophysical reconnection can be described as fluid-level effects; they affect not just a select few highest energy particles but most of the particle population; thus, they seriously affect the overall dynamics and energy budget of a reconnection process. Correspondingly, these effects require very high energy densities, which implies that they usually become important for reconnection events happening close to the central compact object, such as a neutron star or a black hole. Just to organize our thinking, we can categorize the radiative effects on reconnection according to the different components of the particle motion that are being affected by the radiative drag. Thus, radiative drag on random, "thermal', particle motions, especially in the direction across the current layer, effectively leads to radiative cooling, which is reviewed in Sect. 12.5. It may lead to a substantial plasma compression and speed up the reconnection process. Radiative cooling is important in systems such as reconnecting equatorial current sheet in a pulsar magnetosphere just outside the pulsar light cylinder, perhaps powering the observed pulsed high-energy gamma-ray emission (synchrotron cooling, see Sect. 12.5.1); inner parts of accretion disks and accretion disk coronae of black hole systems (inverse-Compton cooling, see Sect. 12.4.2); reconnection events in magnetospheres of magnetars, perhaps powering giant gamma-ray flares in Soft Gamma Repeaters; and in relativistic jets of gamma-ray bursts.

Next, radiative drag on the bulk collective motions of electrons (and perhaps positrons) may result in: (1) effective radiative (Compton drag) resistivity for the flow of electrons carrying the main electric current in the reconnection current layer, important, e.g., in accreting black hole coronae, magnetar magnetospheres, and central engines of supernovae and gamma-ray bursts; and (2) effective braking of the plasma outflow from the reconnection layer, potentially slowing down the reconnection process; this effect has been explored in the context of TeV flares in blazar jets but may also be important in a number of other systems, including accretion disks around black holes and neutron stars.

Whereas most of the above-mentioned radiative effects can operate in optically thin plasmas, there are some radiation effects that take place in optically thick reconnecting systems. In particular, this may occur at very high plasma densities and energy densities, found, e.g., in systems like the central engines and jets of gamma-ray bursts, magnetar magnetospheres, and perhaps central parts of black hole accretion disks. Reconnection layers in these environments may become optically thick, which allows the photons emitted by the energetic particles in the layer to interact with the layer particles again. This secondary interaction opens

up avenues for additional radiative effects, namely, radiation pressure and effective radiative viscosity (see Sect. 12.7). Furthermore, since most of these plasmas are relativistically hot and compact, there are many gamma-ray photons above the pair-production threshold, which makes a copious pair production not only possible but often inevitable. Intense pair production, in turn, further increases the optical depth and plasma collisionality of the reconnection layer.

Finally, apart from its possible active role in influencing reconnection dynamics and energetics, radiation emitted by a reconnection layer also plays a role of an important (and, quite often in astrophysics, the only) *diagnostic tool* that we can use to study remote astrophysical systems. This applies not only to all of the above-mentioned radiative reconnection systems, but also, arguably, to most astrophysical systems where we believe magnetic reconnection takes place, even when it acts as a purely passive tracer. For this reason, it is particularly important to develop theoretical and computational tools that will enable us to predict, calculate potentially observable radiative signatures of a reconnection process.

One should expect continuing rapid development of the field of radiative magnetic reconnection in the next few years. This optimistic outlook for accelerating progress in this exciting new frontier of plasma astrophysics is justified by the convergence of several factors. First, there is a strong and growing astrophysical motivation for its serious development, based on the increasing recognition by the broad astrophysical community of the importance of magnetic reconnection as a potent mechanism for plasma heating, nonthermal particle acceleration, and high-energy radiation production in numerous astrophysical phenomena. This leads to an increased interest among astrophysicists in magnetic reconnection in general; however, as argued in this chapter, in many, if not most, of the astrophysical phenomena of interest reconnection inevitably takes place in the radiative regime, in which prompt radiative energy losses materially affect the process. In addition, the need to connect reconnection theory to observations, by developing the capability to calculate observable radiative signatures, also contributes to the astrophysical motivation.

The second fundamental reason for expecting rapid progress in radiative reconnection is the emerging ability to study this reconnection regime in the lab, namely, by using modern high-energy-density laser-plasma facilities, such as Omega EP and NIF. By using high-$Z_{\rm eff}$ target materials such as gold, it should be possible to achieve a reconnection regime where bremsstrahlung and perhaps atomic-line radiative cooling become important. In addition, powerful Z-pinch facilities (such as Imperial College's MAGPIE) could also potentially be adapted to laboratory studies of radiative HED reconnection. All these new experimental capabilities that are now becoming available can potentially provide a valuable research tool, a testbed for validating theories and numerical models of radiative reconnection, and also perhaps lead to completely new, unexpected discoveries.

Finally, current and future progress in radiative reconnection is greatly facilitated by the appearance of new computational tools, coupled with analytical theory. The most important new development on this front is the emergence of numerical plasma codes that self-consistently include radiation reaction effects on the plasma and,

simultaneously, compute various observable radiative signatures. One of the most prominent examples of this is the radiative relativistic PIC code Zeltron developed at the University of Colorado (Cerutti et al. 2013, 2014b). In addition, active efforts are now underway to augment various fluid-level (e.g., resistive MHD and two-fluid) codes with radiative modules (Takahashi and Ohsuga 2013; Leake et al. 2013; Sadowski et al. 2014; McKinney et al. 2014; Takahashi and Ohsuga 2015; Ni et al. 2015), which will enable one to study collisional and optically-thick reconnection problems. Importantly, while Zeltron has been developed specifically to study radiative magnetic reconnection, an area in which it has already made important contributions, this code—and, one hopes, other radiative plasma codes that are being developed or will be developed in the near future—is sufficiently versatile and can be employed to study other important problems in radiative plasma physics and astrophysics, such as collisionless shocks and turbulence. In this sense, our research efforts towards better understanding astrophysical radiative reconnection should not only lead to progress in this particular area, but also should benefit the broader fields of plasma physics and plasma astrophysics.

Although a lot of progress in developing new radiative computational capabilities has already been achieved, still more work needs to be done. Among the most important radiation processes that should, and hopefully will, be incorporated into kinetic plasma codes (in addition to synchrotron and inverse-Compton radiation already implemented in Zeltron) are non-relativistic cyclotron radiation, Klein-Nishina effects for Compton scattering, curvature radiation, and the quantum-electrodynamic modifications to various radiation processes in the presence of a magnetar-strength (above B_Q) magnetic field. In addition, there is also strong astrophysical motivation to include collisional and finite optical depth effects such as bremsstrahlung emission and absorption, synchrotron self-absorption, synchrotron-self-Compton (SSC) radiation, and pair creation. All these capabilities will greatly expand our ability to study magnetic reconnection, as well as other important plasma processes, in various high-energy astrophysical contexts and thus ultimately will help us attain a better understanding of this violent, shining, beautiful Universe.

Acknowledgements I am very grateful to the organizers of the Parker Workshop on Magnetic Reconnection in Brazil, March 2014, and especially to Dr. Walter Gonzalez. I am also indebted to Prof. Eugene Parker for being a constant shining inspiration.

I am also grateful to numerous colleagues for many stimulating and insightful conversations over many years on various topics discussed in this chapter. Specifically, I would like to thank M. Begelman, A. Beloborodov, A. Bhattacharjee, B. Cerutti, W. Daughton, E. de Gouveia dal Pino, J. Drake, D. Giannios, J. Goodman, R. Kulsrud, H. Li, N. Loureiro, Yu. Lyubarsky, M. Lyutikov, J. McKinney, M. Medvedev, K. Nalewajko, A. Spitkovsky, and G. Werner.

This work has been supported by NSF Grants PHY-0903851 and AST-1411879 , DOE Grants DE-SC0008409 and DE-SC0008655, and NASA Grants NNX11AE12G, NNX12AP17G, NNX12AP18G, and NNX13AO83G.

References

A.A. Abdo, M. Ackermann, M. Ajello, A. Allafort, L. Baldini, J. Ballet, G. Barbiellini, D. Bastieri, K. Bechtol, R. Bellazzini, B. Berenji, R.D. Blandford, E.D. Bloom, E. Bonamente, A.W. Borgland, A. Bouvier, T.J. Brandt, J. Bregeon, A. Brez, M. Brigida, P. Bruel, R. Buehler, S. Buson, G.A. Caliandro, R.A. Cameron, A. Cannon, P.A. Caraveo, J.M. Casandjian, Ö. Çelik, E. Charles, A. Chekhtman, C.C. Cheung, J. Chiang, S. Ciprini, R. Claus, J. Cohen-Tanugi, L. Costamante, S. Cutini, F. D'Ammando, C.D. Dermer, A. de Angelis, A. de Luca, F. de Palma, S.W. Digel, E. do Couto e Silva, P.S. Drell, A. Drlica-Wagner, R. Dubois, D. Dumora, C. Favuzzi, S.J. Fegan, E.C. Ferrara, W.B. Focke, P. Fortin, M. Frailis, Y. Fukazawa, S. Funk, P. Fusco, F. Gargano, D. Gasparrini, N. Gehrels, S. Germani, N. Giglietto, F. Giordano, M. Giroletti, T. Glanzman, G. Godfrey, I.A. Grenier, M.H. Grondin, J.E. Grove, S. Guiriec, D. Hadasch, Y. Hanabata, A.K. Harding, K. Hayashi, M. Hayashida, E. Hays, D. Horan, R. Itoh, G. Jóhannesson, A.S. Johnson, T.J. Johnson, D. Khangulyan, T. Kamae, H. Katagiri, J. Kataoka, M. Kerr, J. Knödlseder, M. Kuss, J. Lande, L. Latronico, S.H. Lee, M. Lemoine-Goumard, F. Longo, F. Loparco, P. Lubrano, G.M. Madejski, A. Makeev, M. Marelli, M.N. Mazziotta, J.E. McEnery, P.F. Michelson, W. Mitthumsiri, T. Mizuno, A.A. Moiseev, C. Monte, M.E. Monzani, A. Morselli, I.V. Moskalenko, S. Murgia, T. Nakamori, M. Naumann-Godo, P.L. Nolan, J.P. Norris, E. Nuss, T. Ohsugi, A. Okumura, N. Omodei, J.F. Ormes, M. Ozaki, D. Paneque, D. Parent, V. Pelassa, M. Pepe, M. Pesce-Rollins, M. Pierbattista, F. Piron, T.A. Porter, S. Rainò, R. Rando, P.S. Ray, M. Razzano, A. Reimer, O. Reimer, T. Reposeur, S. Ritz, R.W. Romani, H.F.W. Sadrozinski, D. Sanchez, P.M.S. Parkinson, J.D. Scargle, T.L. Schalk, C. Sgrò, E.J. Siskind, P.D. Smith, G. Spandre, P. Spinelli, M.S. Strickman, D.J. Suson, H. Takahashi, T. Takahashi, T. Tanaka, J.B. Thayer, D.J. Thompson, L. Tibaldo, D.F. Torres, G. Tosti, A. Tramacere, E. Troja, Y. Uchiyama, J. Vandenbroucke, V. Vasileiou, G. Vianello, V. Vitale, P. Wang, K.S. Wood, Z. Yang, M. Ziegler, Gamma-ray flares from the Crab Nebula. Science **331**, 739–742 (2011). doi:10.1126/science.1199705

F.A. Aharonian, A.A. Belyanin, E.V. Derishev, V.V. Kocharovsky, V.V. Kocharovsky, Constraints on the extremely high-energy cosmic ray accelerators from classical electrodynamics. Phys. Rev. D **66**(2), 023005 (2002). doi:10.1103/PhysRevD.66.023005

I. Arka, G. Dubus, Pulsed high-energy γ-rays from thermal populations in the current sheets of pulsar winds. Astron. Astrophys. **550**, A101 (2013). doi:10.1051/0004-6361/201220110

W.I. Axford, Magnetic storm effects associated with the tail of the magnetosphere. Space Sci. Rev. **7**, 149–157 (1967). doi:10.1007/BF00215592

M. Balbo, R. Walter, C. Ferrigno, P. Bordas, Twelve-hour spikes from the Crab pevatron. Astron. Astrophys. **527**, L4 (2011). doi:10.1051/0004-6361/201015980

W. Bednarek, W. Idec, On the variability of the GeV and multi-TeV gamma-ray emission from the Crab Nebula. Mon. Not. R. Astron. Soc. **414**, 2229–2234 (2011). doi:10.1111/j.1365-2966.2011.18539.x

N. Bessho, A. Bhattacharjee, Fast magnetic reconnection and particle acceleration in relativistic low-density electron-positron plasmas without guide field. Astrophys. J. **750**, 129 (2012). doi:10.1088/0004-637X/750/2/129

A. Bhattacharjee, Y. Huang, H. Yang, B. Rogers, Fast reconnection in high-Lundquist-number plasmas due to the plasmoid instability. Phys. Plasmas **16**(11), 112102 (2009). doi:10.1063/1.3264103

J. Birn, J.F. Drake, M.A. Shay, B.N. Rogers, R.E. Denton, M. Hesse, M. Kuznetsova, Z.W. Ma, A. Bhattacharjee, A. Otto, P.L. Pritchett, Geospace environmental modeling (GEM) magnetic reconnection challenge. J. Geophys. Res. **106**, 3715–3720 (2001). doi:10.1029/1999JA900449

D. Biskamp, *Magnetic Reconnection in Plasmas* (Cambridge University Press, Cambridge, 2000)

G.R. Blumenthal, R.J. Gould, bremsstrahlung, synchrotron radiation, and compton scattering of high-energy electrons traversing dilute gases. Rev. Mod. Phys. **42**, 237–271 (1970). doi:10.1103/RevModPhys.42.237

R. Buehler, J.D. Scargle, R.D. Blandford, L. Baldini, M.G. Baring, A. Belfiore, E. Charles, J. Chiang, F. D'Ammando, C.D. Dermer, S. Funk, J.E. Grove, A.K. Harding, E. Hays, M. Kerr, F. Massaro, M.N. Mazziotta, R.W. Romani, P.M. Saz Parkinson, A.F. Tennant, M.C. Weisskopf, Gamma-ray activity in the crab Nebula: the exceptional flare of 2011 April. Astrophys. J. **749**, 26 (2012). doi:10.1088/0004-637X/749/1/26

R. Bühler, R. Blandford, The surprising Crab pulsar and its nebula: a review. Rep. Prog. Phys. **77**(6), 066901 (2014). doi:10.1088/0034-4885/77/6/066901

A.M. Bykov, G.G. Pavlov, A.V. Artemyev, Y.A. Uvarov, Twinkling pulsar wind nebulae in the synchrotron cut-off regime and the γ-ray flares in the Crab Nebula. Mon. Not. R. Astron. Soc. **421**, L67–L71 (2012). doi:10.1111/j.1745-3933.2011.01208.x

B. Cerutti, D.A. Uzdensky, M.C. Begelman, Extreme particle acceleration in magnetic reconnection layers: application to the Gamma-ray flares in the Crab Nebula. Astrophys. J. **746**, 148 (2012a). doi:10.1088/0004-637X/746/2/148

B. Cerutti, G.R. Werner, D.A. Uzdensky, M.C. Begelman, Beaming and rapid variability of high-energy radiation from relativistic pair plasma reconnection. Astrophys. J. Lett. **754**, L33 (2012b). doi:10.1088/2041-8205/754/2/L33

B. Cerutti, G.R. Werner, D.A. Uzdensky, M.C. Begelman, Simulations of particle acceleration beyond the classical synchrotron burnoff limit in magnetic reconnection: an explanation of the Crab flares. Astrophys. J. **770**, 147 (2013). doi:10.1088/0004-637X/770/2/147

B. Cerutti, G.R. Werner, D.A. Uzdensky, M.C. Begelman, Gamma-ray flares in the Crab Nebula: a case of relativistic reconnection? Phys. Plasmas **21**(5), 056501 (2014a). doi:10.1063/1.4872024

B. Cerutti, G.R. Werner, D.A. Uzdensky, M.C. Begelman, Three-dimensional relativistic pair plasma reconnection with radiative feedback in the Crab Nebula. Astrophys. J. **782**, 104 (2014b). doi:10.1088/0004-637X/782/2/104

B. Cerutti, A. Philippov, K. Parfrey, A. Spitkovsky, Particle acceleration in axisymmetric pulsar current sheets. Mon. Not. R. Astron. Soc. **448**, 606–619 (2015). doi:10.1093/mnras/stv042

I.V. Chugunov, V.I. Eidman, E.V. Suvorov, The motion of charged particles in a strong electromagnetic field and curvature radiation. Astrophys. Space Sci. **32**, L7–L10 (1975). doi:10.1007/BF00646233

E. Clausen-Brown, M. Lyutikov, Crab Nebula gamma-ray flares as relativistic reconnection minijets. Mon. Not. R. Astron. Soc. **426**, 1374–1384 (2012). doi:10.1111/j.1365-2966.2012.21349.x

I. Contopoulos, The role of reconnection in the pulsar magnetosphere. Astron. Astrophys. **466**, 301–307 (2007). doi:10.1051/0004-6361:20065973

F.V. Coroniti, Magnetically striped relativistic magnetohydrodynamic winds - the Crab Nebula revisited. Astrophys. J. **349**, 538–545 (1990). doi:10.1086/168340

E.M. de Gouveia dal Pino, A. Lazarian, Production of the large scale superluminal ejections of the microquasar GRS 1915+105 by violent magnetic reconnection. Astron. Astrophys. **441**, 845–853 (2005). doi:10.1051/0004-6361:20042590

E.M. de Gouveia Dal Pino, P.P. Piovezan, L.H.S. Kadowaki, The role of magnetic reconnection on jet/accretion disk systems. Astron. Astrophys. **518**, A5 (2010). doi:10.1051/0004-6361/200913462

O.C. de Jager, A.K. Harding, P.F. Michelson, H.I. Nel, P.L. Nolan, P. Sreekumar, D.J. Thompson, Gamma-Ray Observations of the Crab Nebula: a study of the synchro-compton spectrum. Astrophys. J. **457**, 253 (1996). doi:10.1086/176726

T. Di Matteo, Magnetic reconnection: flares and coronal heating in active galactic nuclei. Mon. Not. R. Astron. Soc. **299**, L15 (1998). doi:10.1046/j.1365-8711.1998.01950.x

T. Di Matteo, A. Celotti, A.C. Fabian, Magnetic flares in accretion disc coronae and the spectral states of black hole candidates: the case of GX339-4. Mon. Not. R. Astron. Soc. **304**, 809–820 (1999). doi:10.1046/j.1365-8711.1999.02375.x

Q.L. Dong, S.J. Wang, Q.M. Lu, C. Huang, D.W. Yuan, X. Liu, X.X. Lin, Y.T. Li, H.G. Wei, J.Y. Zhong, J.R. Shi, S.E. Jiang, Y.K. Ding, B.B. Jiang, K. Du, X.T. He, M.Y. Yu, C.S. Liu, S. Wang, Y.J. Tang, J.Q. Zhu, G. Zhao, Z.M. Sheng, J. Zhang, Plasmoid ejection and secondary

current sheet generation from magnetic reconnection in laser-plasma interaction. Phys. Rev. Lett. **108**(21), 215001 (2012). doi:10.1103/PhysRevLett.108.215001
V.L. Dorman, R.M. Kulsrud, One-dimensional merging of magnetic fields with cooling. Astrophys. J. **449**, 777 (1995). doi:10.1086/176097
G. Drenkhahn, H.C. Spruit, Efficient acceleration and radiation in Poynting flux powered GRB outflows. Astron. Astrophys. **391**, 1141–1153 (2002). doi:10.1051/0004-6361:20020839
J.W. Dungey, Interplanetary magnetic field and the auroral zones. Phys. Rev. Lett. **6**, 47–48 (1961). doi:10.1103/PhysRevLett.6.47
G.L. Eyink, A. Lazarian, E.T. Vishniac, Fast magnetic reconnection and spontaneous stochasticity. Astrophys. J. **743**, 51 (2011). doi:10.1088/0004-637X/743/1/51
G. Fiksel, W. Fox, A. Bhattacharjee, D.H. Barnak, P.Y. Chang, K. Germaschewski, S.X. Hu, P.M. Nilson, Magnetic reconnection between colliding magnetized laser-produced plasma plumes. Phys. Rev. Lett. **113**(10), 105003 (2014). doi:10.1103/PhysRevLett.113.105003
J. Fish, G. Werner, D. Uzdensky, Effects of synchrotron cooling on relativistic magnetic reconnection (2016, in preparation)
W. Fox, A. Bhattacharjee, K. Germaschewski, Fast magnetic reconnection in laser-produced plasma bubbles. Phys. Rev. Lett. **106**(21), 215003 (2011). doi:10.1103/PhysRevLett.106.215003
W. Fox, A. Bhattacharjee, K. Germaschewski, Magnetic reconnection in high-energy-density laser-produced plasmas. Phys. Plasmas **19**(5), 056309 (2012). doi:10.1063/1.3694119
A.A. Galeev, R. Rosner, G.S. Vaiana, Structured coronae of accretion disks. Astrophys. J. **229**, 318–326 (1979). doi:10.1086/156957
D. Giannios, UHECRs from magnetic reconnection in relativistic jets. Mon. Not. R. Astron. Soc. **408**, L46–L50 (2010). doi:10.1111/j.1745-3933.2010.00925.x
D. Giannios, Reconnection-driven plasmoids in blazars: fast flares on a slow envelope. Mon. Not. R. Astron. Soc. **431**, 355–363 (2013). doi:10.1093/mnras/stt167
D. Giannios, H.C. Spruit, The role of kink instability in Poynting-flux dominated jets. Astron. Astrophys. **450**, 887–898 (2006). doi:10.1051/0004-6361:20054107
D. Giannios, H.C. Spruit, Spectral and timing properties of a dissipative γ-ray burst photosphere. Astron. Astrophys. **469**, 1–9 (2007). doi:10.1051/0004-6361:20066739
D. Giannios, D.A. Uzdensky, M.C. Begelman, Fast TeV variability in blazars: jets in a jet. Mon. Not. R. Astron. Soc. **395**, L29–L33 (2009). doi:10.1111/j.1745-3933.2009.00635.x
D. Giannios, D.A. Uzdensky, M.C. Begelman, Fast TeV variability from misaligned minijets in the jet of M87. Mon. Not. R. Astron. Soc. **402**, 1649–1656 (2010). doi:10.1111/j.1365-2966.2009.16045.x
J. Goodman, D. Uzdensky, Reconnection in marginally collisionless accretion disk coronae. Astrophys. J. **688**, 555–558 (2008). doi:10.1086/592345
P.W. Guilbert, A.C. Fabian, M.J. Rees, Spectral and variability constraints on compact sources. Mon. Not. R. Astron. Soc. **205**, 593–603 (1983)
F. Guo, H. Li, W. Daughton, Y.H. Liu, formation of hard power laws in the energetic particle spectra resulting from relativistic magnetic reconnection. Phys. Rev. Lett. **113**(15), 155005 (2014). doi:10.1103/PhysRevLett.113.155005
A.M. Hillas, The origin of ultra-high-energy cosmic rays. Annu. Rev. Astron. Astrophys. **22**, 425–444 (1984). doi:10.1146/annurev.aa.22.090184.002233
M. Hoshino, Y. Lyubarsky, Relativistic reconnection and particle acceleration. Space Sci. Rev. **173**, 521–533 (2012). doi:10.1007/s11214-012-9931-z
Y. Huang, A. Bhattacharjee, Scaling laws of resistive magnetohydrodynamic reconnection in the high-Lundquist-number, plasmoid-unstable regime. Phys. Plasmas **17**(6), 062104 (2010). doi:10.1063/1.3420208
J.D. Jackson, *Classical Electrodynamics* (1975)
C.H. Jaroschek, M. Hoshino, Radiation-dominated relativistic current sheets. Phys. Rev. Lett. **103**(7), 075002 (2009). doi:10.1103/PhysRevLett.103.075002

C.H. Jaroschek, H. Lesch, R.A. Treumann, Relativistic kinetic reconnection as the possible source mechanism for high variability and flat spectra in extragalactic radio sources. Astrophys. J. Lett. **605**, L9–L12 (2004a). doi:10.1086/420767

C.H. Jaroschek, R.A. Treumann, H. Lesch, M. Scholer, Fast reconnection in relativistic pair plasmas: analysis of particle acceleration in self-consistent full particle simulations. Phys. Plasmas **11**, 1151–1163 (2004b). doi:10.1063/1.1644814

L.H.S. Kadowaki, E.M. de Gouveia Dal Pino, C.B. Singh, The role of fast magnetic reconnection on the radio and Gamma-ray emission from the nuclear regions of microquasars and low luminosity AGNs. Astrophys. J. **802**, 113 (2015). doi:10.1088/0004-637X/802/2/113

D. Kagan, M. Milosavljević, A. Spitkovsky, A flux rope network and particle acceleration in three-dimensional relativistic magnetic reconnection. Astrophys. J. **774**, 41 (2013). doi:10.1088/0004-637X/774/1/41

B. Khiali, E.M. de Gouveia Dal Pino, M.V. del Valle, A magnetic reconnection model for explaining the multiwavelength emission of the microquasars Cyg X-1 and Cyg X-3. Mon. Not. R. Astron. Soc. **449**, 34–48 (2015a). doi:10.1093/mnras/stv248

B. Khiali, E.M. de Gouveia Dal Pino, H. Sol, Particle acceleration and Gamma-ray emission due to magnetic reconnection in the core region of radio galaxies. ArXiv e-prints (2015b)

J.G. Kirk, Particle acceleration in relativistic current sheets. Phys. Rev. Lett. **92**(18), 181101 (2004). doi:10.1103/PhysRevLett.92.181101

J.G. Kirk, O. Skjæraasen, Dissipation in Poynting-flux-dominated flows: the σ-problem of the Crab pulsar wind. Astrophys. J. **591**, 366–379 (2003). doi:10.1086/375215

S.S. Komissarov, M. Lyutikov, On the origin of variable gamma-ray emission from the Crab Nebula. Mon. Not. R. Astron. Soc. **414**, 2017–2028 (2011). doi:10.1111/j.1365-2966.2011.18516.x

G. Kowal, A. Lazarian, E.T. Vishniac, K. Otmianowska-Mazur, Numerical tests of fast reconnection in weakly stochastic magnetic fields. Astrophys. J. **700**, 63–85 (2009). doi:10.1088/0004-637X/700/1/63

S. Krucker, H.S. Hudson, L. Glesener, S.M. White, S. Masuda, J.P. Wuelser, R.P. Lin, Measurements of the coronal acceleration region of a solar flare. Astrophys. J. **714**, 1108–1119 (2010). doi:10.1088/0004-637X/714/2/1108

L.D. Landau, E.M. Lifshitz, *The Classical Theory of Fields* (1971)

D.A. Larrabee, R.V.E. Lovelace, M.M. Romanova, Lepton acceleration by relativistic collisionless magnetic reconnection. Astrophys. J. **586**, 72–78 (2003). doi:10.1086/367640

A. Lazarian, E.T. Vishniac, Reconnection in a weakly stochastic field. Astrophys. J. **517**, 700–718 (1999). doi:10.1086/307233

J.E. Leake, V.S. Lukin, M.G. Linton, Magnetic reconnection in a weakly ionized plasma. Phys. Plasmas **20**(6), 061202 (2013). doi:10.1063/1.4811140

S.V. Lebedev, F. Suzuki-Vidal, L.A. Pickworth, G.F. Swadling, G. Burdiak, J. Skidmore, G.N. Hall, M. Bennett, S.N. Bland, J.P. Chittenden, P. de Grouchy, J. Derrick, J. Hare, T. Parker, F. Sciortino, L. Suttle, A. Ciardi, R. Rodriguez, J.M. Gil, G. Espinosa, E. Hansen, A. Frank, J. Music, Magnetized jets and shocks in radial foil Z-pinches: experiments and numerical simulations, in *APS Meeting Abstracts*, p. 8107P (2014)

H. Lesch, G.T. Birk, On the origin of extended nonthermal optical emission in extragalactic jets. Astrophys. J. **499**, 167–171 (1998). doi:10.1086/305639

C.K. Li, F.H. Séguin, J.A. Frenje, J.R. Rygg, R.D. Petrasso, R.P.J. Town, O.L. Landen, J.P. Knauer, V.A. Smalyuk, Observation of megagauss-field topology changes due to magnetic reconnection in laser-produced plasmas. Phys. Rev. Lett. **99**(5), 055001 (2007). doi:10.1103/PhysRevLett.99.055001

B.F. Liu, S. Mineshige, K. Ohsuga, Spectra from a magnetic reconnection-heated corona in active galactic nuclei. Astrophys. J. **587**, 571–579 (2003). doi:10.1086/368282

W. Liu, H. Li, L. Yin, B.J. Albright, K.J. Bowers, E.P. Liang, Particle energization in 3D magnetic reconnection of relativistic pair plasmas. Phys. Plasmas **18**(5), 052105 (2011). doi:10.1063/1.3589304

N.F. Loureiro, A.A. Schekochihin, S.C. Cowley, Instability of current sheets and formation of plasmoid chains. Phys. Plasmas **14**(10), 100703 (2007). doi:10.1063/1.2783986

N.F. Loureiro, D.A. Uzdensky, A.A. Schekochihin, S.C. Cowley, T.A. Yousef, Turbulent magnetic reconnection in two dimensions. Mon. Not. R. Astron. Soc. Lett. **399**, L146–L150 (2009). doi:10.1111/j.1745-3933.2009.00742.x

N.F. Loureiro, R. Samtaney, A.A. Schekochihin, D.A. Uzdensky, Magnetic reconnection and stochastic plasmoid chains in high-Lundquist-number plasmas. Phys. Plasmas **19**(4), 042303 (2012). doi:10.1063/1.3703318

Y.E. Lyubarskii, A model for the energetic emission from pulsars. Astron. Astrophys. **311**, 172–178 (1996)

Y.E. Lyubarskii, A model for the energetic emission from pulsars. in *IAU Colloq. 177: Pulsar Astronomy - 2000 and Beyond*, ed. by M. Kramer, N. Wex, R. Wielebinski Astronomical Society of the Pacific Conference Series, vol. 202, p. 439 (2000)

Y.E. Lyubarsky, Highly magnetized region in pulsar wind nebulae and origin of the Crab gamma-ray flares. Mon. Not. R. Astron. Soc. **427**, 1497–1502 (2012). doi:10.1111/j.1365-2966.2012.22097.x

Y. Lyubarsky, J.G. Kirk, Reconnection in a striped pulsar wind. Astrophys. J. **547**, 437–448 (2001). doi:10.1086/318354

Y. Lyubarsky, M. Liverts, Particle acceleration in the driven relativistic reconnection. Astrophys. J. **682**, 1436–1442 (2008). doi:10.1086/589640

M. Lyutikov, Explosive reconnection in magnetars. Mon. Not. R. Astron. Soc. **346**, 540–554 (2003a). doi:10.1046/j.1365-2966.2003.07110.x

M. Lyutikov, Role of reconnection in AGN jets. New Astron. Rev. **47**, 513–515 (2003b). doi:10.1016/S1387-6473(03)00083-6

M. Lyutikov, Magnetar giant flares and afterglows as relativistic magnetized explosions. Mon. Not. R. Astron. Soc. **367**, 1594–1602 (2006a). doi:10.1111/j.1365-2966.2006.10069.x

M. Lyutikov, The electromagnetic model of gamma-ray bursts. New J. Phys. **8**, 119 (2006b). doi:10.1088/1367-2630/8/7/119

M. Lyutikov, A high-sigma model of pulsar wind nebulae. Mon. Not. R. Astron. Soc. **405**, 1809–1815 (2010). doi:10.1111/j.1365-2966.2010.16553.x

M. Lyutikov, D. Balsara, C. Matthews, Crab GeV flares from the corrugated termination shock. Mon. Not. R. Astron. Soc. **422**, 3118–3129 (2012a). doi:10.1111/j.1365-2966.2012.20831.x

M. Lyutikov, N. Otte, A. McCann, The very high energy emission from pulsars: a case for inverse compton scattering. Astrophys. J. **754**, 33 (2012b). doi:10.1088/0004-637X/754/1/33

Y. Masada, S. Nagataki, K. Shibata, T. Terasawa, Solar-type magnetic reconnection model for magnetar giant flares. Publ. Astron. Soc. Jpn. **62**, 1093– (2010)

S. Masuda, T. Kosugi, H. Hara, S. Tsuneta, Y. Ogawara, A loop-top hard X-ray source in a compact solar flare as evidence for magnetic reconnection. Nature **371**, 495–497 (1994). doi:10.1038/371495a0

J.C. McKinney, D.A. Uzdensky, A reconnection switch to trigger gamma-ray burst jet dissipation. Mon. Not. R. Astron. Soc. **419**, 573–607 (2012). doi:10.1111/j.1365-2966.2011.19721.x

J.C. McKinney, A. Tchekhovskoy, A. Sadowski, R. Narayan, Three-dimensional general relativistic radiation magnetohydrodynamical simulation of super-Eddington accretion, using a new code HARMRAD with M1 closure. Mon. Not. R. Astron. Soc. **441**, 3177–3208 (2014). doi:10.1093/mnras/stu762

M.V. Medvedev, Theory of "Jitter" radiation from small-scale random magnetic fields and prompt emission from Gamma-ray burst shocks. Astrophys. J. **540**, 704–714 (2000). doi:10.1086/309374

M. Melzani, R. Walder, D. Folini, C. Winisdoerffer, J.M. Favre, The energetics of relativistic magnetic reconnection: ion-electron repartition and particle distribution hardness. Astron. Astrophys. **570**, A112 (2014). doi:10.1051/0004-6361/201424193

F.C. Michel, Theory of pulsar magnetospheres. Rev. Mod. Phys. **54**, 1–66 (1982). doi:10.1103/RevModPhys.54.1

F.C. Michel, Magnetic structure of pulsar winds. Astrophys. J. **431**, 397–401 (1994). doi:10.1086/174493

K. Nalewajko, D. Giannios, M.C. Begelman, D.A. Uzdensky, M. Sikora, Radiative properties of reconnection-powered minijets in blazars. Mon. Not. R. Astron. Soc. **413**, 333–346 (2011). doi:10.1111/j.1365-2966.2010.18140.x

K. Nalewajko, D.A. Uzdensky, B. Cerutti, G.R. Werner, M.C. Begelman, On the distribution of particle acceleration sites in plasmoid-dominated relativistic magnetic reconnection. ArXiv e-prints (2015)

L. Ni, B. Kliem, J. Lin, N. Wu, Fast magnetic reconnection in the solar chromosphere mediated by the plasmoid instability. Astrophys. J. **799**, 79 (2015). doi:10.1088/0004-637X/799/1/79

P.M. Nilson, L. Willingale, M.C. Kaluza, C. Kamperidis, S. Minardi, M.S. Wei, P. Fernandes, M. Notley, S. Bandyopadhyay, M. Sherlock, R.J. Kingham, M. Tatarakis, Z. Najmudin, W. Rozmus, R.G. Evans, M.G. Haines, A.E. Dangor, K. Krushelnick, Magnetic reconnection and plasma dynamics in two-beam laser-solid interactions. Phys. Rev. Lett. **97**(25), 255001–+ (2006). doi:10.1103/PhysRevLett.97.255001

P.M. Nilson, L. Willingale, M.C. Kaluza, C. Kamperidis, S. Minardi, M.S. Wei, P. Fernandes, M. Notley, S. Bandyopadhyay, M. Sherlock, R.J. Kingham, M. Tatarakis, Z. Najmudin, W. Rozmus, R.G. Evans, M.G. Haines, A.E. Dangor, K. Krushelnick, Bidirectional jet formation during driven magnetic reconnection in two-beam laser-plasma interactions. Phys. Plasmas **15**(9), 092701 (2008). doi:10.1063/1.2966115

M. Oka, S. Ishikawa, P. Saint-Hilaire, S. Krucker, R.P. Lin, Kappa distribution model for hard X-ray coronal sources of solar flares. Astrophys. J. **764**, 6 (2013). doi:10.1088/0004-637X/764/1/6

M. Oka, S. Krucker, H.S. Hudson, P. Saint-Hilaire, Electron energy partition in the above-the-looptop solar hard X-ray sources. Astrophys. J. **799**, 129 (2015). doi:10.1088/0004-637X/799/2/129

K. Parfrey, A.M. Beloborodov, L. Hui, Twisting, reconnecting magnetospheres and magnetar spindown. Astrophys. J. Lett. **754**, L12 (2012). doi:10.1088/2041-8205/754/1/L12

K. Parfrey, A.M. Beloborodov, L. Hui, Dynamics of strongly twisted relativistic magnetospheres. Astrophys. J. **774**, 92 (2013). doi:10.1088/0004-637X/774/2/92

E.N. Parker, Sweet's mechanism for merging magnetic fields in conducting fluids. J. Geophys. Res. **62**, 509–520 (1957)

G. Paschmann, M. Øieroset, T. Phan, In-Situ observations of reconnection in space. Space Sci. Rev. **178**, 385–417 (2013). doi:10.1007/s11214-012-9957-2

J. Pétri, Y. Lyubarsky, Magnetic reconnection at the termination shock in a striped pulsar wind. Astron. Astrophys. **473**, 683–700 (2007). doi:10.1051/0004-6361:20066981

A.A. Philippov, A. Spitkovsky, Ab Initio pulsar magnetosphere: three-dimensional particle-in-cell simulations of axisymmetric pulsars. Astrophys. J. Lett. **785**, L33 (2014). doi:10.1088/2041-8205/785/2/L33

A.A. Philippov, A. Spitkovsky, B. Cerutti, Ab Initio pulsar magnetosphere: three-dimensional particle-in-cell simulations of oblique pulsars. Astrophys. J. Lett. **801**, L19 (2015). doi:10.1088/2041-8205/801/1/L19

L.A. Pozdnyakov, I.M. Sobol, R.A. Syunyaev, Comptonization and the shaping of X-ray source spectra - Monte Carlo calculations. Astrophys. Space Phys. Rev. **2**, 189–331 (1983)

R.A. Remillard, J.E. McClintock, X-ray properties of black-hole binaries. Annu. Rev. Astron. Astrophys. **44**, 49–92 (2006). doi:10.1146/annurev.astro.44.051905.092532

M.M. Romanova, R.V.E. Lovelace, Magnetic field, reconnection, and particle acceleration in extragalactic jets. Astron. Astrophys. **262**, 26–36 (1992)

G.B. Rybicki, A.P. Lightman, *Radiative Processes in Astrophysics* (Wiley, New York, 1979)

A. Sadowski, R. Narayan, J.C. McKinney, A. Tchekhovskoy, Numerical simulations of super-critical black hole accretion flows in general relativity. Mon. Not. R. Astron. Soc. **439**, 503–520 (2014). doi:10.1093/mnras/stt2479

R. Schopper, H. Lesch, G.T. Birk, Magnetic reconnection and particle acceleration in active galactic nuclei. Astron. Astrophys. **335**, 26–32 (1998)

N.I. Shakura, R.A. Sunyaev, Black holes in binary systems. Observational appearance. Astron. Astrophys. **24**, 337–355 (1973)

K. Shibata, New observational facts about solar flares from YOHKOH studies - evidence of magnetic reconnection and a unified model of flares. Adv. Space Res. **17**, 9–18 (1996). doi:10.1016/0273-1177(95)00534-L

I.S. Shklovskii, On the nature of the optical emission from the Crab Nebula. Sov. Astron. **1**, 690 (1957)

I.S. Shklovskii, Cosmic radio waves (1960)

I.S. Shklovskii, Remarks on the synchrotron-radiation spectrum of the Crab Nebula. Sov. Astron. **10**, 6 (1966)

J.S. Shklovsky, Emission of radio-waves by the galaxy and the sun. Nature **159**, 752–753 (1947). doi:10.1038/159752a0

C.B. Singh, E.M. de Gouveia Dal Pino, L.H.S. Kadowaki, On the role of fast magnetic reconnection in accreting black hole sources. Astrophys. J. Lett. **799**, L20 (2015). doi:10.1088/2041-8205/799/2/L20

L. Sironi, A. Spitkovsky, Acceleration of particles at the termination shock of a relativistic striped wind. Astrophys. J. **741**, 39 (2011). doi:10.1088/0004-637X/741/1/39

L. Sironi, A. Spitkovsky, Relativistic reconnection: an efficient source of non-thermal particles. Astrophys. J. Lett. **783**, L21 (2014). doi:10.1088/2041-8205/783/1/L21

H.C. Spruit, F. Daigne, G. Drenkhahn, Large scale magnetic fields and their dissipation in GRB fireballs. Astron. Astrophys. **369**, 694–705 (2001). doi:10.1051/0004-6361:20010131

R.S. Steinolfson, G. van Hoven, Radiative tearing - magnetic reconnection on a fast thermal-instability time scale. Astrophys. J. **276**, 391–398 (1984). doi:10.1086/161623

E. Striani, M. Tavani, G. Piano, I. Donnarumma, G. Pucella, V. Vittorini, A. Bulgarelli, A. Trois, C. Pittori, F. Verrecchia, E. Costa, M. Weisskopf, A. Tennant, A. Argan, G. Barbiellini, P. Caraveo, M. Cardillo, P.W. Cattaneo, A.W. Chen, G. De Paris, E. Del Monte, G. Di Cocco, Y. Evangelista, A. Ferrari, M. Feroci, F. Fuschino, M. Galli, F. Gianotti, A. Giuliani, C. Labanti, I. Lapshov, F. Lazzarotto, F. Longo, M. Marisaldi, S. Mereghetti, A. Morselli, L. Pacciani, A. Pellizzoni, F. Perotti, P. Picozza, M. Pilia, M. Rapisarda, A. Rappoldi, S. Sabatini, P. Soffitta, M. Trifoglio, S. Vercellone, F. Lucarelli, P. Santolamazza, P. Giommi, The Crab Nebula superflare in 2011 April: extremely fast particle acceleration and Gamma-ray emission. Astrophys. J. Lett. **741**, L5 (2011). doi:10.1088/2041-8205/741/1/L5

P.A. Sturrock, A model of pulsars. Astrophys. J. **164**, 529 (1971). doi:10.1086/150865

P. Sturrock, M.J. Aschwanden, Flares in the Crab Nebula driven by untwisting magnetic fields. Astrophys. J. Lett. **751**, L32 (2012). doi:10.1088/2041-8205/751/2/L32

L. Suttle, S. Lebedev, G. Swadling, F. Suzuki-Vidal, G. Burdiak, M. Bennett, J. Hare, D. Burgess, A. Clemens, N. Niasse, J. Chittenden, R. Smith, S. Bland, S. Patankar, N. Stuart, An experimental investigation of the collision of counter-streaming magnetized plasma flows with oppositely aligned embedded magnetic fields, in *APS Meeting Abstracts*, p. 5007 (2014)

P.A. Sweet, The neutral point theory of solar flares, in *Electromagnetic Phenomena in Cosmical Physics*, ed. by B. Lehnert. IAU Symposium, vol. 6, p. 123 (1958)

H.R. Takahashi, K. Ohsuga, A numerical treatment of anisotropic radiation fields coupled with relativistic resistive magnetofluids. Astrophys. J. **772**, 127 (2013). doi:10.1088/0004-637X/772/2/127

H.R. Takahashi, K. Ohsuga, Numerical study of relativistic magnetohydrodynamic reconnection and its radiative effects, in *Thirteenth Marcel Grossmann Meeting: On Recent Developments in Theoretical and Experimental General Relativity, Astrophysics and Relativistic Field Theories*, ed. by K. Rosquist, pp. 2344–2345 (2015). doi:10.1142/9789814623995_0437

M. Tavani, A. Bulgarelli, V. Vittorini, A. Pellizzoni, E. Striani, P. Caraveo, M.C. Weisskopf, A. Tennant, G. Pucella, A. Trois, E. Costa, Y. Evangelista, C. Pittori, F. Verrecchia, E. Del Monte, R. Campana, M. Pilia, A. De Luca, I. Donnarumma, D. Horns, C. Ferrigno, C.O. Heinke, M. Trifoglio, F. Gianotti, S. Vercellone, A. Argan, G. Barbiellini, P.W. Cattaneo, A.W. Chen, T. Contessi, F. D'Ammando, G. DeParis, G. Di Cocco, G. Di Persio, M. Feroci, A. Ferrari,

M. Galli, A. Giuliani, M. Giusti, C. Labanti, I. Lapshov, F. Lazzarotto, P. Lipari, F. Longo, F. Fuschino, M. Marisaldi, S. Mereghetti, E. Morelli, E. Moretti, A. Morselli, L. Pacciani, F. Perotti, G. Piano, P. Picozza, M. Prest, M. Rapisarda, A. Rappoldi, A. Rubini, S. Sabatini, P. Soffitta, E. Vallazza, A. Zambra, D. Zanello, F. Lucarelli, P. Santolamazza, P. Giommi, L. Salotti, G.F. Bignami, Discovery of powerful gamma-ray flares from the Crab Nebula. Science **331**, 736– (2011). doi:10.1126/science.1200083

S. Tsuneta, Structure and dynamics of magnetic reconnection in a solar flare. Astrophys. J. **456**, 840 (1996). doi:10.1086/176701

D.A. Uzdensky, Magnetic reconnection in astrophysical systems. ArXiv Astrophysics e-prints (2006)

D.A. Uzdensky, On the physical interpretation of Malyshkin's (2008) model of resistive Hall magnetohydrodynamic reconnection. Phys. Plasmas **16**(4), 040702 (2009). doi:10.1063/1.3125819

D.A. Uzdensky, Magnetic reconnection in extreme astrophysical environments. Space Sci. Rev. **160**, 45–71 (2011). doi:10.1007/s11214-011-9744-5

D.A. Uzdensky, B. Cerutti, M.C. Begelman, Reconnection-powered linear accelerator and Gamma-ray flares in the Crab Nebula. Astrophys. J. Lett. **737**, L40 (2011). doi:10.1088/2041-8205/737/2/L40

D.A. Uzdensky, J. Goodman, Statistical description of a magnetized corona above a turbulent accretion disk. Astrophys. J. **682**, 608–629 (2008). doi:10.1086/588812

D.A. Uzdensky, J.C. McKinney, Magnetic reconnection with radiative cooling. I. Optically thin regime. Phys. Plasmas **18**(4), 042105 (2011). doi:10.1063/1.3571602

D.A. Uzdensky, S. Rightley, Plasma physics of extreme astrophysical environments. Rep. Prog. Phys. **77**(3), 036902 (2014). doi:10.1088/0034-4885/77/3/036902

D.A. Uzdensky, A. Spitkovsky, Physical conditions in the reconnection layer in pulsar magnetospheres. Astrophys. J. **780**, 3 (2014). doi:10.1088/0004-637X/780/1/3

D.A. Uzdensky, N.F. Loureiro, A.A. Schekochihin, Fast magnetic reconnection in the plasmoid-dominated regime. Phys. Rev. Lett. **105**(23), 235002 (2010). doi:10.1103/PhysRevLett.105.235002

R.F. van Oss, G.H.J. van den Oord, M. Kuperus, Accretion disk flares in energetic radiation fields - A model for hard X-rays from black hole candidates. Astron. Astrophys. **270**, 275–287 (1993)

V.M. Vasyliunas, Theoretical models of magnetic field line merging. I. Rev. Geophys. Space Phys. **13**, 303–336 (1975). doi:10.1029/RG013i001p00303

G. Werner, M. Begelman, B. Cerutti, K. Nalewajko, D. Uzdensky, The effect of mass ratio in relativistic, collisionless electron-ion reconnection, in *APS Meeting Abstracts*, p. 5003 (2013)

G.R. Werner, D.A. Uzdensky, B. Cerutti, K. Nalewajko, M.C. Begelman, The extent of power-law energy spectra in collisionless relativistic magnetic reconnection in pair plasmas. ArXiv e-prints (2014)

M. Yamada, R. Kulsrud, H. Ji, Magnetic reconnection. Rev. Mod. Phys. **82**, 603–664 (2010). doi:10.1103/RevModPhys.82.603

T. Yokoyama, K. Shibata, Magnetic reconnection as the origin of X-ray jets and Hα surges on the Sun. Nature **375**, 42–44 (1995). doi:10.1038/375042a0

T. Yokoyama, K. Akita, T. Morimoto, K. Inoue, J. Newmark, Clear evidence of reconnection inflow of a solar flare. Astrophys. J. Lett. **546**, L69–L72 (2001). doi:10.1086/318053

C. Yu, Magnetar giant flares—flux rope eruptions in multipolar magnetospheric magnetic fields. Astrophys. J. **757**, 67 (2012). doi:10.1088/0004-637X/757/1/67

Q. Yuan, P.F. Yin, X.F. Wu, X.J. Bi, S. Liu, B. Zhang, A statistical model for the γ-ray variability of the Crab Nebula. Astrophys. J. Lett. **730**, L15 (2011). doi:10.1088/2041-8205/730/2/L15

S. Zenitani, M. Hoshino, The generation of nonthermal particles in the relativistic magnetic reconnection of pair plasmas. Astrophys. J. Lett. **562**, L63–L66 (2001). doi:10.1086/337972

S. Zenitani, M. Hoshino, Three-dimensional evolution of a relativistic current sheet: triggering of magnetic reconnection by the guide field. Phys. Rev. Lett. **95**(9), 095001 (2005). doi:10.1103/PhysRevLett.95.095001

S. Zenitani, M. Hoshino, Particle acceleration and magnetic dissipation in relativistic current sheet of pair plasmas. Astrophys. J. **670**, 702–726 (2007). doi:10.1086/522226
S. Zenitani, M. Hoshino, The role of the guide field in relativistic pair plasma reconnection. Astrophys. J. **677**, 530–544 (2008). doi:10.1086/528708
V.V. Zheleznyakov, Electromagnetic waves in cosmic plasma. Generation and propagation (1977)
E.G. Zweibel, M. Yamada, Magnetic reconnection in astrophysical and laboratory plasmas. Annu. Rev. Astron. Astrophys. **47**, 291–332 (2009). doi:10.1146/annurev-astro-082708-101726

Chapter 13
Annihilation of Quantum Magnetic Fluxes

W.D. Gonzalez

Abstract After introducing the concepts associated with the Aharonov and Bohm effect and with the existence of a quantum of magnetic flux (QMF), we briefly discuss the Ginzburg-Landau theory that explains its origin and fundamental consequences. Also relevant observations of QMFs obtained in the laboratory using superconducting systems (vortices) are mentioned. Next, we describe processes related with the interaction of QMFs with opposite directions in terms of the gauge field geometry related to the vector potential. Then, we discuss the use of a Lagrangian density for a scalar field theory involving radiation in order to describe the annihilation of QMFs, claimed to be responsible for the emission of photons with energies corresponding to that of the annihilated magnetic fields. Finally, a possible application of these concepts to the observed variable dynamics of neutron stars is briefly mentioned.

Keywords Aharonov-Bohm effect • Dual-slit interference • Gauge-field interaction • Ginzburg-Landau energy equations • Magnetic annihilation • Neutron star cores • Quantum magnetic fluxes • Superconducting vortices • Vector potential

13.1 Introduction

The concept of a quantum of magnetic flux had an indirect origin in the study of quantized Landau levels of electrons orbiting magnetic fields (Landau 1930), with a more direct study done by Aharonov and Bohm much later, in 1959. Since then, the "Aharonov and Bohm effect", showing the existence of a quantum of magnetic flux associated with a phase shift in the electron wave function due to the presence of the vector potential around a non-directly sensed magnetic field, has been extensively studied theoretically as well as in the laboratory, referring especially to superconducting systems (e.g., Peshkin and Tonomura 1989).

W.D. Gonzalez (✉)
National Institute for Space Research (INPE), São José dos Campos, São Paulo 12227-010, Brazil
e-mail: walter.gonzalez@inpe.br

W. Gonzalez, E. Parker (eds.), *Magnetic Reconnection*, Astrophysics and Space Science Library 427, DOI 10.1007/978-3-319-26432-5_13

In this Chapter, after reviewing briefly the Aharonov and Bohm effect and some related observations, we discuss two phenomenological approaches related with the dynamics of quantum magnetic fluxes, especially associated with the interaction and the annihilation of quantum magnetic fluxes.

Thus, in this review we have tried to present a synthesis of five fundamental aspects related with research on quantum magnetic fluxes (QMFs), namely:

- The Aharonov and Bohm effect predicting the existence of QMFs (Sect. 13.2).
- The Ginzburg-Landau energy equations explaining the origin and some consequences of QMFs, in connection with Laboratory observations of QMFs (vortices) using superconducting systems (Sect. 13.3).
- The Treumann et al. (2012) quantum mechanical study of the interaction of QMFs due to the gauge field of their vector potential (Sect. 13.4).
- A quantum field theory approach to study the energetics and emitted radiation related to the annihilation of QMFs (Sects. 13.5 and 13.6).
- A possible application of the physics of QMFs to the study of some observed dynamics in neutron stars (Sect. 13.7).

13.2 The Aharonov–Bohm Effect

The concept involving the Aharonov-Bohm effect is illustrated in Figs. 13.1 and 13.2. Consider the famous dual-slit experiments, where electrons enter from the left and are diffracted by the two slits. Beyond the diffracting slab there is a screen with a movable detector. The detector measures the rate I at which the electrons arrive on the screen at a distance x from the axis of symmetry. This rate is proportional to the probability that an individual electron reaches the detector from the source. This probability has the distribution shown at the right of Fig. 13.1, which is associated with the interference of two amplitudes, one from each slit.

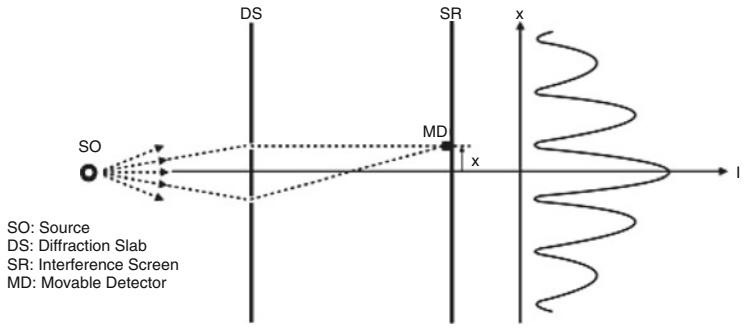

Fig. 13.1 Dual-slit interference experiment with electrons

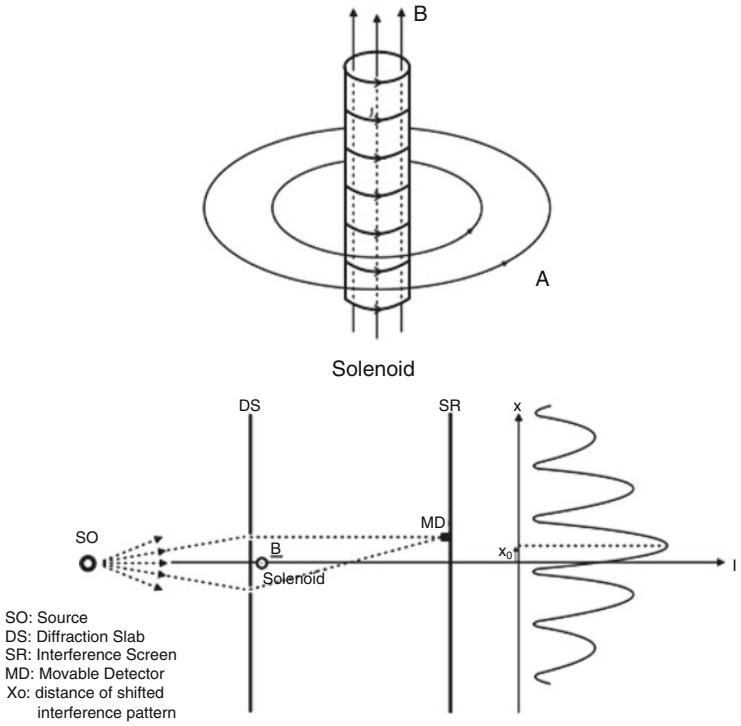

Fig. 13.2 (*Bottom*) Same as Fig. 13.1 showing the Aharonov-Bohm effect. (*Top*) a solenoid with magnetic field **B** and the vector potential **A**

This interference depends on the phase difference between the paths travelled by the electron passing through the two slits.

Next, consider that a very long solenoid with a small diameter is placed just behind the diffraction slab and between the two slits, as shown in Fig. 13.2. The diameter of the solenoid needs to be much smaller than the distance between the slits to avoid the electrons passing too close to the solenoid. For this type of experiment, Aharonov and Bohm (1959) predicted a shift in the interference pattern due to the presence of the solenoid. This effect was experimentally demonstrated initially by Chambers (1960) and later by several other people (e.g., Tonomura et al. 1986).

For a long solenoid carrying an electric current, as shown in Fig. 13.2, there is a B-field inside but not outside, whereas the vector potential **A** does circulate outside the solenoid. For electrons passing through the vector potential region, and not feeling directly the influence of the B-field, Aharonov and Bohm predicted a shift in the phase difference of the electrons proportional to the circulation of **A** outside the solenoid!. They found that the entire interference pattern shifted by an amount x_o, proportional to the intensity of the magnetic flux inside the solenoid.

The Hamiltonian H and the time-independent wave function Ψ for the system illustrated in Fig. 13.2 are (e.g., Peshkin and Tonomura 1989):

$$H = \frac{1}{2m}(-i\hbar\nabla + (e/c)\mathbf{A})^2$$
$$\Psi = \Psi_0 \exp(-iS/\hbar)$$

where $\mathbf{A}(x)$ is the vector potential and $S(x) = -(e/c)\int \mathbf{A}(x')\cdot d\mathbf{x}'$ is the Action line integral along the arm of the interferometer containing the point x. Ψ_0 is the wave function in the absence of the excluded magnetic field.

Let $\Psi = \Psi_0 \exp(-i\delta)$ be the electron wave function, and $\delta = S/\hbar$ the phase difference between the two paths in Fig. 13.2. Since $S = (e/c)\int \mathbf{v}\times\mathbf{A}dt = (e/c)\int \mathbf{A}\cdot d\mathbf{l} = (e/c)\int \mathbf{B}\cdot d\mathbf{A} = (e/c)\phi$, with ϕ: the magnetic flux enclosed by the line integral, then, $\delta = (e/c)\phi/\hbar$.

This phase difference between the two electron paths in Fig. 13.2, which together form a closed path, needs to be a multiple of 2π in order to be a periodic function, with $(e/c)\phi/\hbar = 2\pi n$.

Thus,

$$\phi = nch/e = n\phi_0, \tag{13.1}$$

ϕ_0 is the elementary quantum of magnetic flux and is a **constant of nature**, equal to 4×10^{-7} gauss·cm^2. For a given value of **B**, this quantum of flux, with cross sectional area A_o, has an associated radius $R_o = (ch/\pi eB)^{1/2}$. For example, for the case of the Earth's magnetic field at its surface, $B = 0.5$ gauss, the radius of the associated quantum of flux is about 10^{-2} mm.

13.3 Flux Quantization in Superconductors

The existence of quantized magnetic fluxes (vortices) in superconductors of type II was initially predicted by Abrikosov (1957) and experimentally demonstrated by Deaver and Fairbank (1961) and by Doll and Näbauer (1961). Later, Tonomura et al. (1986), Matsuda et al. (1989) and Harada et al. (1996) obtained much more refined results, showing even the features of individual vortices.

A phenomenological theory describing several aspects of superconductors was proposed by Ginzburg and Landau (1950), from which one can derive the Meissner effect for the expulsion of the magnetic field from superconductors as well as the origin of the Abrikosov vortex involving the unit of magnetic flux quantum ϕ_0.

From the Ginzburg-Landau energy equation in terms of the vector potential **A** and the electron wave function ψ, minimizing it in terms of the vector potential,

one gets (e.g., Kleinert 1989):

$$\frac{1}{4\pi}(\nabla^2\mathbf{A} - \nabla(\nabla\cdot\mathbf{A})) = -\frac{\hbar q}{2m}\frac{1}{2i}(\psi^\dagger(\nabla - \frac{iq}{\hbar c}\mathbf{A})\psi - (\nabla - \frac{iq}{\hbar c}\mathbf{A})\psi^\dagger\psi) \quad (13.2)$$

in which, the expression at the right is Noether's current $\mathbf{j}$:

$$\begin{aligned}\mathbf{j} &= \frac{1}{2i}(\psi^\dagger(\nabla - \frac{iq}{\hbar c}\mathbf{A})\psi - (\nabla - \frac{iq}{\hbar c}\mathbf{A})\psi^\dagger\psi) \\ &= \frac{1}{2i}(\psi^\dagger\nabla\psi - \psi\nabla\psi^\dagger) - \frac{q}{\hbar c}\mathbf{A}|\psi|^2\end{aligned}$$

Note that the Ginzburg-Landau related equations are invariant under the gauge transformation:

$$\begin{aligned}\mathbf{A}(x) &\to \mathbf{A}(x) + \nabla\Lambda(x) \\ \psi(x) &\to e^{\frac{iq}{\hbar c}\Lambda(x)}\psi(x)\end{aligned}$$

Thus providing a phase for the electron wave function. From Eq. (13.2) one can obtain the Meissner effect, for the expulsion of the magnetic flux from the superconducting region, (Ashcroft and Mermin 1976), as:

$$\nabla\times\nabla\times\mathbf{B}(r) = -\frac{1}{\lambda^2}\mathbf{B}(r) \to \mathbf{B}(r) \propto e^{-\frac{\lambda}{r}} \ \ldots$$

where $\lambda = \sqrt{\frac{mc^2}{4\pi nq^2}}$ is the London penetration depth and $q = 2e$ is the Cooper pair.

From expression (13.2) one can also get for the vector potential (Lifshitz and Pitaevskii 1980) the following expression:

$$\mathbf{A} = -\frac{\hbar c}{q}\frac{\mathbf{j}}{|\psi|^2} + \frac{hc}{q}\frac{1}{2i}\frac{1}{|\psi^2|}(\psi^\dagger\nabla\psi - \psi\nabla\psi^\dagger)$$

For regions with $\mathbf{j} = 0$, one can recover the expression for the flux quantization described above,

$$\mathbf{A} = \frac{\hbar c}{q}\nabla\Lambda(x)$$

Integrating $\mathbf{A}$ on a closed contour around the vortex leads to the quantization condition,

$$\oint\mathbf{A}\cdot d\mathbf{l} = \frac{\hbar c}{q}\oint\nabla\Lambda(x)\cdot d\mathbf{l} = \frac{hc}{q}2\pi n$$

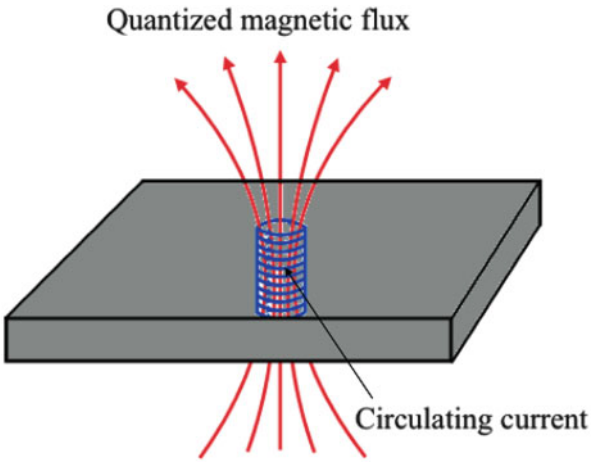

Fig. 13.3 Illustration of a quantum magnetic flux in a superconductor

where n is an integer. We can use Stokes theorem to see that the contour integral of $\mathbf{A}$ is also the flux through the surface:

$$\oint \mathbf{A} \cdot d\mathbf{l} = \int \nabla \times \mathbf{A} \cdot d\mathbf{S} = \int \mathbf{B} \cdot d\mathbf{S} = \phi$$

Equating the last two expressions, one gets the quantized flux, with quantum number n, as given in Eq. (13.1), namely:

$$\phi = n\phi_0, \quad \text{with} \quad \phi_0 = \frac{2\pi\hbar c}{q}$$

Figure 13.3 illustrates an Abrikosov vortex, idealized from vortex structures observed at the Tonomura facility in Japan, using a Field Emission Transmission Electron Microscope (EFTEM), as reviewed by Harada (2013).

Figure 13.4 is an example of an interference micrograph of magnetic fluxes penetrating a superconductor, reproduced from Matsuda et al. (1989). In Fig. 13.4 one can observe, (top) the magnetic field of single vortices penetrating the thin film superconductor with flux ϕ_0, and (bottom) a bundle of vortices penetrating a thicker superconducting film with a flux equal to n times ϕ_0. Since a supercooled superconductor behaves as a "macroscopic" quantum system, one can say that the quantum magnetic flux initially studied by Aharonov and Bohm only through the phase shift in the wave function of the interfering electrons, here the quantum flux becomes a real object!

Figure 13.4, reproduced from Matsuda et al. (1989), shows the changing magnetic fluxes at the superconductor/vacuum boundary, going from their quantized character inside the superconductor to a continuous/classical flux regime outside, within a range of a few London penetration lengths. This is shown by the magnetic field topology outside the superconductor which becomes broader and

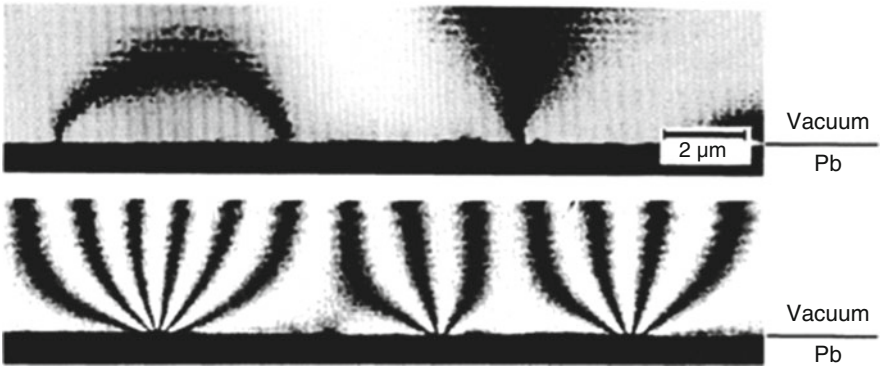

Fig. 13.4 (*Top*) isolated QMFs/vortices. (*Bottom*) bundle of QMFs/vortices (From Matsuda et al. 1989)

more continuous the more distant it gets from the superconductor. At the top-left of this Figure one can see two vortices with opposite polarities, which are stationary and connected outside, also showing a field distribution that becomes more continuous the farther it gets from the superconductor.

The QMFs are associated with the existence of super currents around them in the superconducting Pb slab in Fig. 13.4 and can extend outside only over a few London penetration lengths. Thus, when vortices annihilate with oppositely directed ones (see next Section), the super currents also disappear and, therefore, no extension of the QMFs can be expected outside the superconductor.

13.4 Gauge-Field Geometry and the Interaction of Quantum Magnetic Fluxes

Classically there is no answer to the question of how the force is transmitted across the field-free space between QMFs. No magnetic field exists outside the field flux except for the gauge field associated with the vector potential $\mathbf{A} = \nabla \Lambda$, which does not directly contribute to any magnetic field. It is, in fact, the gauge field which takes care of the absence of magnetic fields outside the flux tube, keeping external space clean of magnetic fields.

From the fact that, for a single isolated flux tube, $\nabla \Lambda$ has only an azimuthal component (Aharonov and Bohm 1959), Λ is proportional to the azimuthal angle θ, as illustrated in Fig. 13.5 (Treumann et al. 2012):

$$\Lambda(\theta) = \frac{\theta}{2\pi}\phi_0 = \frac{c\hbar}{e}\theta$$

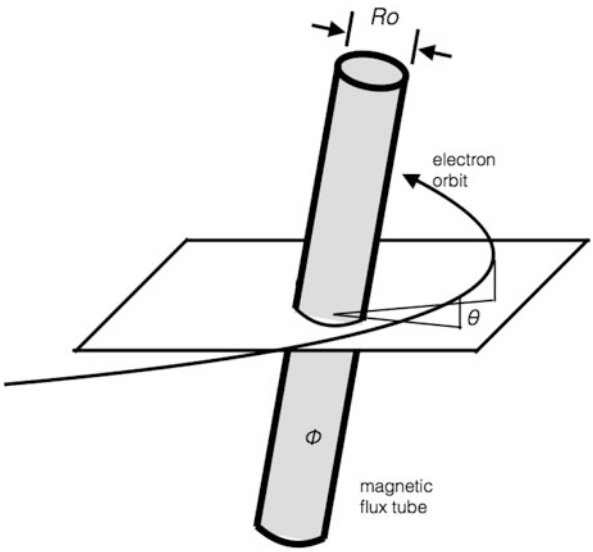

Fig. 13.5 A QMF tube with radius R_o and a circulating electron

Thus, the gauge field Λ is constant in the radial direction, meaning that the radii are gauge-field 'equipotentials' as shown by the black radials emanating from the two circles representing flux tubes in Figs. 13.6 and 13.7. Analytically one can add up the two gauge fields $\Lambda_1(\theta)$ of flux tube 1 and $\Lambda_2(\theta')$ of flux tube 2. The angles θ, θ' are measured in the respective proper frames of flux tube 1 and 2, the origin of the latter being displaced along the x-axis by the distance d from the origin of the former. Thus the total gauge field is a potential field which is additive, being the sum

$$\Lambda = \Lambda_1(\theta) \pm \Lambda_2(\theta') = \frac{\phi_0}{2\pi}(\theta \pm \theta'),$$

where the $+$ sign refers to parallel flux tubes and the $-$ sign to anti-parallel flux tubes. The angle θ' is to be transformed into the proper frame of flux tube 1 such that $\theta'(\theta, r; d)$ becomes a function of distance d (in units R_o) between the flux tubes, angle θ (in radians), and radius r (also in units R_o). The angle θ' maps to an angle θ via the relation:

$$\tan\theta' = \frac{R\sin\theta}{R\cos\theta - 1}, \quad R = \frac{r}{d},$$

which when used in the above sum yields the expression (Treumann et al. 2012):

$$\Lambda(\theta, R) = \frac{\phi_0}{2\pi}\left[\theta \mp \tan^{-1}\left(\frac{R\sin\theta}{1 - R\cos\theta}\right)\right], \quad d > R_o, \tag{13.3}$$

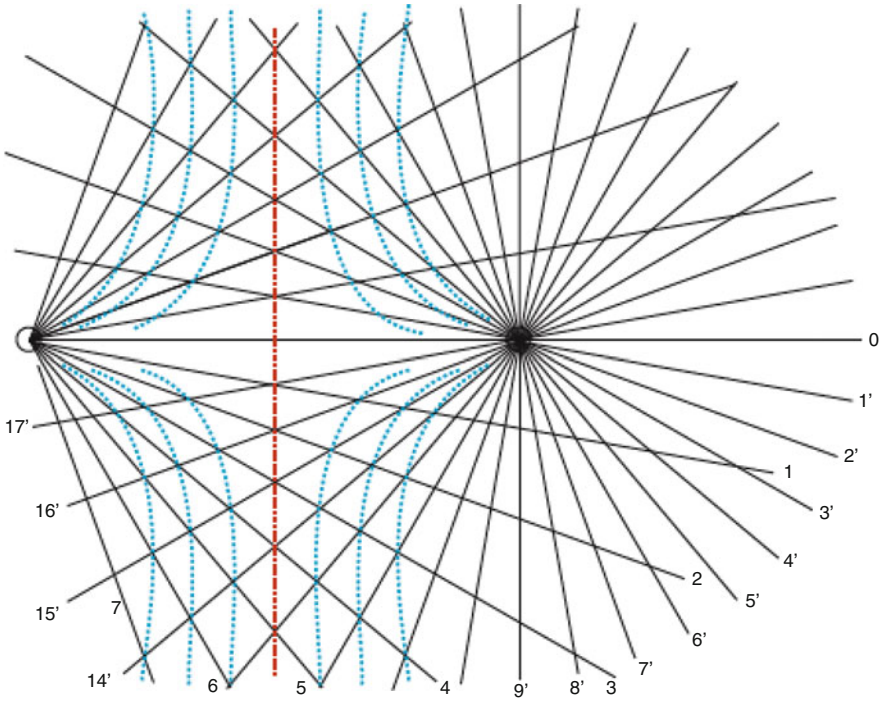

Fig. 13.6 Superposition of the equi-gauge potential lines $\Lambda = \text{const}$ of two parallel elementary flux tubes. Equi-gauge potentials are exactly radial. The flux tubes are shown in their cross sections and point out of the plane. They are separated in space by a distance d. The equi-gauge potentials are clockwise numbered consecutively with the equi-gauge potentials of the right flux tube indicated by primes on the numbers. Since potentials add the superposition of the equipotentials, generating the dashed repulsive potential pattern in the space between the flux tubes, indicates that the interaction between a pair of parallel flux tubes is subject to repulsion (adapted from Treumann et al. 2012)

for the quantum-mechanically total gauge field in the space external to the two flux tubes. The R and θ dependence of the second term in the brackets destroys the strictly radial pattern of equi-gauge potentials, with the main region of interest being $R < 1$. The gauge field equipotentials are obtained by holding expression (13.3) constant. This yields the equi-gauge equation:

$$R(\theta, \tilde{\Lambda}) = \frac{\tan(\theta - \tilde{\Lambda})}{\cos\theta[\tan(\theta - \tilde{\Lambda}) \pm \tan\theta]}$$

$$\tilde{\Lambda} \equiv \frac{2\pi}{\phi_0}\Lambda = const.$$

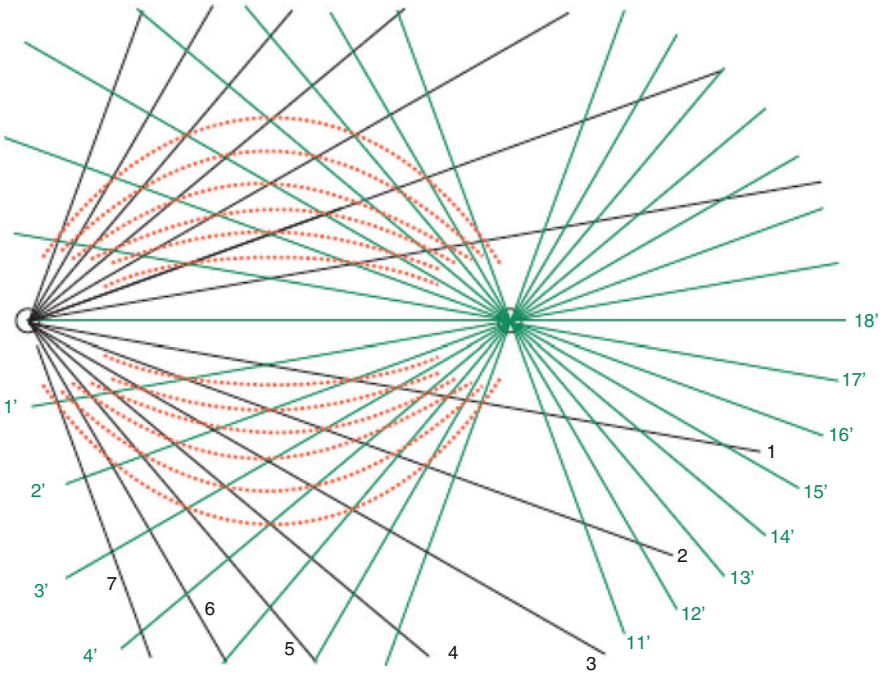

Fig. 13.7 Superposition of the equi-gauge potential lines $\Lambda = \text{const}$ of two anti-parallel flux tubes. The field lines are shown in their cross sections with the left flux tube pointing out of the plane and the right pointing into the plane, being spatially separated by a distance d. The equi-gauge potentials are again clockwise numbered consecutively. Because of the opposite direction of the field in the right flux tube, the primed equi-gauge potentials are numbered anti-clockwise. Addition of the equi-gauge potentials yields the dashed equi-gauge superposition pattern of connected equi-gauge potentials in the region between the flux tubes. Such a pattern indicates attraction between the oppositely directed flux tubes mediated by the gauge fields (adapted from Treumann et al. 2012)

Varying $\tilde{\Lambda}$ and calculating $R(\theta, \tilde{\Lambda})$ for each fixed value of $\tilde{\Lambda}$ produces a pattern of equi-gauge potentials which now has become dependent of radius R. This dependence is enforced by the mere presence of another flux tube at distance $r = d$. Clearly, if the distance d between the flux tubes is large, i.e. $d \gg r$, this pattern degenerates to the original radial pattern of one isolated flux tube. Again, the + (-) signs apply to parallel and anti-parallel flux tubes.

One can geometrically construct the shape of the equi-gauge potentials by superposition (Treumann et al. 2012). This is shown schematically in Figs. 13.6 and 13.7 for the two respective cases of parallel and anti-parallel flux tubes, with the equi-gauge potentials plotted for two (stretched) flux tubes in the perpendicular plane under the condition that each flux tube would be isolated in space and no other flux tubes would be present. In the parallel case the solitary patterns of both flux tubes are of course identical, being numbered clockwise. In the antiparallel

case they are numbered in opposite order (i.e. the anti-parallel flux tube radials are numbered anti-clockwise). Superposing the two gauge fields produces the dashed curves in these figures.

An important and intuitive observation is that for parallel flux tubes half way between the two flux tubes, the superposition of the gauge fields creates a separation barrier in the gauge potential, which forces the superimposed gauge field equipotential flux tubes to deviate up to 90° from their radial directions. This enforces a pronounced radial dependence of the gauge equipotential field. *The pattern is similar to the equipotentials produced by two electric charges of equal sign causing repulsion of the charges.* Extrapolating to our case of two interacting parallel field fluxes, we may conclude that it is the repulsive action of the gauge fields between the two parallel magnetic flux tubes which keeps the parallel field fluxes separate. When several parallel QMFs interact, one expects a lattice structure among them (Treumann et al. 2012).

Figure 13.7 shows the plot of the equi-gauge potentials for the case when the magnetic fields are anti-parallel. In this case the left flux tube points out of the drawing plane and the right tube points into the plane. By having turned the right flux tube by 180° into the plane, the rotational sense and thus the counting of the equi-gauge potentials is reversed. When superimposed with the equi-gauge potentials of the left flux tube, the picture of the dashed lines is obtained in this case. It is seen now that the equi-gauge potentials of the two flux tubes connect and an attractive gauge-potential structure is obtained. *The pattern is similar to the equipotentials produced by two electric charges of opposite sign causing attraction of the charges.*

Even though the physical implication of the repulsive and attractive equi-gauge potentials is not quite clear in the ordinary quantum mechanical treatment given qualitatively here, we can conclude that the interaction between two flux tubes is mediated by the presence of gauge fields. Parallel magnetic flux tubes cause repulsive gauge field potentials, while anti-parallel flux tubes are subject to attractive gauge field potentials. Clarification of the physical content awaits a treatment in terms of the quantum electrodynamic solution of the Aharonov-Bohm problem involving the interaction of two flux tubes. Anticipating the solution, we boldly conclude from the electrodynamic analogy that the physical implication confirms the expectation that parallel QMFs reject each other while anti-parallel QMFs attract each other, even though the space between them is void of any magnetic fields. It is, however, filled with gauge fields which are responsible for the interaction.

This theory is based on the notion of the additivity of the gauge potentials spanned by each of the QMFs. As long as there is no other known interaction between magnetic flux quanta, superposition of the gauge fields is well justified. It will, however become distorted if some interaction potential has to be included. For the time being no such interaction potentials are known, at least to our knowledge.

13.5 Annihilation Energy of QMFs

For the annihilation of two QMFs, the Ginzburg-Landau approach gives, in zeroth order (e.g., Speight 1997), the following expression:

$$E = \frac{1}{4\pi}\phi_0 BL, \tag{13.4}$$

with L = length of flux tube, and $\phi_0 = 2 \times 10^{-7}$ gauss $\cdot$ cm^2.

Thus, for a field $B = 0.1$ gauss and $L = 0.1$ mm, the annihilation energy amounts approximately to 10^{-11} ergs. Also, since $\phi_0 = A_0 B = (\pi R_o^2)B$, with the cross sectional radius of the flux tube R_o being typically of order $2\pi\lambda$, where λ is the London penetration depth, Eq. (13.4) for the energy leads to an expression of the annihilation energy per unit length of $(\phi_0/4\pi^2\lambda)^2$.

13.6 Flux Annihilation and Photon Emission

Since the Ginzburg-Landau and the Treumann et al. (2012) approaches to study the dynamics of QMFs/vortices do not explicitly involve radiation, in order to study the radiation emitted during the annihilation of a vortex-antivortex system, one needs to use a full quantum field theory approach as described, for example, by Hecht and DeGrand (1990) and by Gleiser and Thorarinson (2007). For this study, Hecht and DeGrand (1990) used a scalar field theory approach (e.g., Zee 2012) with the Lagrangian density:

$$L = \frac{1}{2}(\partial_\mu \phi^*)(\partial^\mu \phi) - \frac{\lambda}{4}(\phi^*\phi - \eta^2)^2.$$

where λ is the scalar field coupling parameter and the field function ϕ is expressed in terms of the superconductor density ρ and the wave phase δ, describing an isolated vortex, in 2D, as

$$\phi(x, y, t) = \rho(x, y, t)e^{i\delta(x,y,t)}.$$

η is the magnetic flux vorticity in terms of the quantum of magnetic flux. Using an equation of motion for the vortex derived from a complex Lagrangian density, including vector fields, Gleiser and Thorarinson (2007) studied the evolution of the interacting vortex-antivortex system and found that above a threshold of the semiconductor parameter range the vortex and antivortex annihilate fast, radiating photons with energies proportional to the external magnetic field energy of the vortex-antivortex pair, whereas below such a threshold they found that the annihilated energy goes first into an oscillatory radiation, called oscillons, before transmitting its energy to the system. Figure 13.8 shows a computer simulation

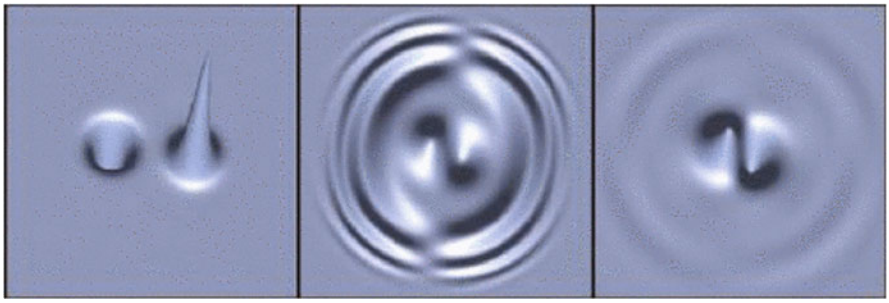

Fig. 13.8 Magnetic field intensities of a vortex-antivortex pair (*left*), of their annihilated radiation wavefront (*middle*) and of their oscillating dipole (*right*). From Gleiser and Thorarinson (2007)

obtained by Gleiser and Thorarinson (2007) for the latter process, in which one can see the magnetic field intensities of the vortex-antivortex pair (at the left), of the wavefront of the radiation (at the center) and of the oscillating dipole (at the right).

13.7 QMFs and Superconducting Neutron Star Cores

It has been implied long ago (Migdal 1959) that the interior of neutron stars can involve superfluid and superconducting states. More recently, Page et al. (2011) studied the neutron star in the supernova remnant of Cassiopeia A, and found that its proton core could exist in a superconducting state at about a few million degrees kelvin, in contrast to the near absolute-zero temperatures required for superconducting at Earth. Cas A is the remnant of a huge star that was observed to explode about 330 years ago (Fig. 13.9). The neutron star is about 11,000 light-years away, in the constellation Cassiopeia. It was found by Page et al. (2011) that this neutron star has cooled by about 4 % over a 10-year period!

Among several important questions related to the dynamics of neutron stars is that concerning the issue about how they cool. For this question, the neutron star in Cassiopeia has both a well established age, and a well known surface temperature of about 2 million degrees. For this scenario, one could consider models with mixtures of condensates developing a description that accounts for the presence of rotating magnetic flux tubes of the type of QMFs, that have been argued to exist in the proton component of the superconducting neutron star core (e.g., Shaham 1981). One also needs to model the forces that impede the motion of flux tubes and understand how these forces act on the condensates. Page et al. (2011) dealt with the development of such a model for the outer core of a neutron star, where such a condensate with magnetic flux tubes is expected to exist. They discuss the hydrodynamics of this system, focusing on the role of the magnetic field, the vortex/flux tube tension and the dissipative mutual friction forces. The results of their study can be directly applied to a number of interesting issues, such as those associated with neutron star

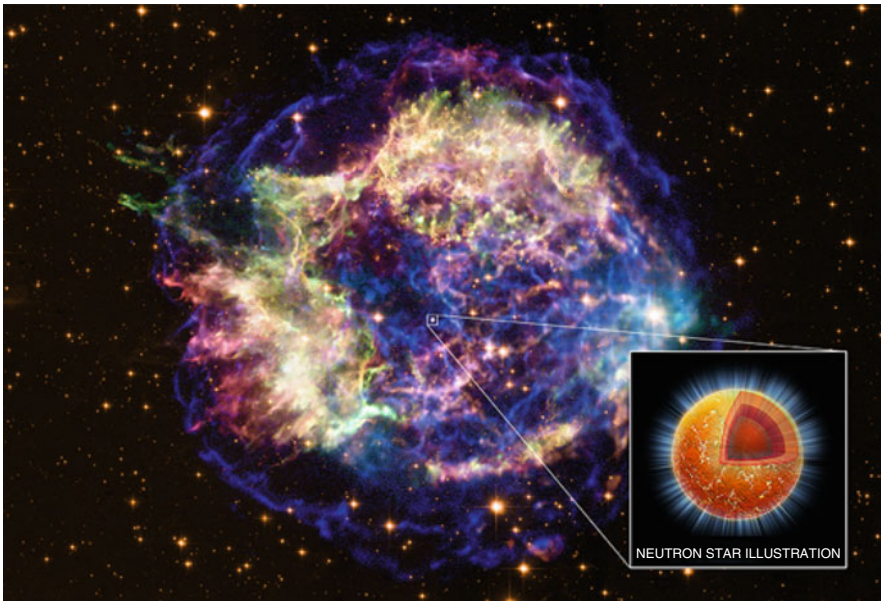

Fig. 13.9 Composite image of X-rays from Chandra (*red*, *green*, and *blue*) and optical data from Hubble (*gold*) of Cassiopeia A, the remains of a massive star that exploded in a supernova. *Inset*: A cutout of the interior of the neutron star, where densities increase from the crust (*orange*) to the core (*red*) and to the region where the superfluid and superconducting region exist (*inner red*). Credit: X-ray: NASA/CXC/xx; Optical: NASA/STScI; Illustration: NASA/CXC/M.Weiss

oscillations and with fast changes in their rotational period (neutron star glitches), as discussed by Muslimov and Tsygan (1985).

13.8 Summary

In this chapter we have briefly reviewed the concept of a phase shift in the electron wave function when passing outside a thin and long solenoid, at a region not containing a magnetic field, as predicted by Aharonov and Bohm (1959) and observed in the laboratory first by Chambers (1960) and later by several other people (e.g., Tonomura et al. 1986). That phase shift was found to exist associated with the presence of the vector potential circling the magnetic field of the solenoid and leading to the existence of a quantum of magnetic flux, $\phi_o = ch/e$, now regarded a constant of nature. Then we showed in Sect. 13.3 that the origin and some consequences of QMFs can be described by the semiclassical and phenomenological Ginzburg-Landau energy equations.

We have also discussed about some observations of QMFs in superconducting systems (vortices), as done by the Tonomura research group in Japan, in which

they were able to observe single and multiple vortices as well as the annihilation of oppositely directed vortices (Matsuda et al. 1989). Since superconductors behave as "macroscopic" quantum systems, one can say that the quantum magnetic flux initially studied by Aharonov and Bohm only through the phase shift in the wave function of the interfering electrons, in superconductors of type II the quantum magnetic flux becomes a real object!

We have later discussed the interaction of QMFs by assuming that such an interaction is carried by the gauge field associated with the vector potential, as described by Treumann et al. (2012). This description leads to an understanding of a Coulomb-type of interaction, namely with two QMFs behaving as in the Coulomb interaction of two electrons, as illustrated in Figs. 13.6 and 13.7 .

Then, because the Ginzburg-Landau and the Treumann et al. approaches to study the interaction of oppositely directed QMFs do not treat the expected emission of radiation, we have briefly mentioned a QFT approach followed by Hecht and DeGrand (1990) and by Gleiser and Thorarinson (2007), who have tried to study the type of radiation that results from the vortex-antivortex annihilation. Gleiser and Thorarinson (2007) found two types of radiation associated with the annihilation, a fast one leaving the system and a more delayed one, going first into an oscillatory behavior (oscillons) and then into a dipole type of radiation. The energy of the radiated photons is expected to have the energy of the annihilated magnetic fluxes.

Finally, due to the discovery that the core of neutron stars can involve superfluid and superconducting states, such as in Cassiopeia A (e.g., Page et al. 2011), even at very high temperatures, one can try to apply to such scenarios the concept and consequences of annihilating QMFs. With that application, one can try to explain some observed phenomena in neutron stars, such as neutron star glitches and rotational anomalies (e.g., Muslimov and Tsygan 1985).

Appendix I

Although the proper way to study the radiation emitted by annihilating QMFs is using tools from quantum field theory, as those followed by Hecht and DeGrand (1990) and by Gleiser and Thorarinson (2007) and briefly mentioned in Sect. 13.6, an indication of the presence of radiation in the interaction of QMFs can already be visualized from the Treumann et al. (2012) approach, as outlined below.

A heuristic argument about the force between the flux tubes of Figs. 13.6 and 13.7 can be put forward as follows. The gauge field $\nabla \Lambda = \mathbf{A}$ causes an electric potential:

$$U = -\partial \Lambda / \partial t.$$

(cf., Jackson 1975, pp. 220–223) being of pure gauge nature. It is clear that the gauge field around an isolated flux tube is stationary, and $U = 0$. In the presence of another flux tube, however, information is exchanged between the flux tubes, requiring time. The gauge field becomes nonstationary, acquiring time dependence;

the equivalent induced electrostatic potential is non-zero. The time dependence of the gauge field in the Lorentz gauge is taken care of by the wave equation for Λ:

$$\nabla^2 \Lambda - \frac{1}{c^2} \frac{\partial^2 \Lambda}{\partial^2 t} = 0$$

of which the solution Λ is subject to the boundary conditions on the surfaces of the two flux tubes. These prescribe that $\nabla \Lambda = \mathbf{A}$ on both surfaces.

Formally, the potential caused by the gauge field gives rise to a *gauge-Coulomb force*

$$\mathbf{F} = e \nabla U = -e \frac{\partial \nabla \Lambda}{\partial t} = -\frac{2\pi c \hbar}{\phi_0} \frac{\partial \nabla \Lambda(\theta, r, t)}{\partial t},$$

which in the presence of another flux tube evolves a radial component, the sign of which depends on the mutual orientation of the flux tubes. Formally, QMFs behave like electric charges of value $2\pi c\hbar/\phi_0$. However, there are no massive charged particles involved on which the force could act in the empty space between the flux tubes. Hence the force must be experienced by the flux tubes only, where for tow flux tubes $\Lambda(\theta, r)$ is given by expression (13.3) for a given time interval. This force causes acceleration and displacement of a flux tube in the presence of another one at distance d.

Appendix II

Since the topic of this Book is Magnetic Reconnection, there is in my opinion an apparently interesting related issue in the material discussed in this chapter, which remains to be explored.

It refers to a possible reconnection scenario associated with the classical magnetic fluxes pervading the space outside the superconducting medium, such as that illustrated in Fig 13.4, when that space is (somehow) filled with plasma.

We assume that externally created magnetic fluxes with opposite directions meet at the middle of the superconducting slab forming vortices and antivortices that can annihilate, as described by Harada et al. (1996). Thus, the region where the annihilation occurs would resemble a "diffusion" region of reconnection, whereas the "cutted" classical magnetic field existing outside the superconductor could be regarded as a "reconnected" field. Therefore, one may tentatively say hat such "reconnected fluxes" would propagate externally as Alven waves carrying magnetic energy, which eventually could be measured in the laboratory.

Thus, the radiation emitted by the annihilating QMFs from the superconductor, together with the classical magnetic energy carried by the Alfven waves outside, would energetically represent the main outcome from the combined annihilation/reconnection system.

As mentioned in this Chapter, the quantum character of the annihilating magnetic fluxes in the superconductor extends outside only over a few London penetration lengths, and further than that one expects to have a classical magnetic flux, as that illustrated in Figure 13.4.

If this scenario turns out to be confirmed by further research, one could apply our knowledge on magnetic reconnection to possible related superconducting/plasma systems, as those associated with the superconducting core and the external magnetized plasma of neutron stars, in which the superconducting core is expected to have a large volume of annihilating QMFs, as described in the last section of this chapter. Thus, from the discussion given above, one may expect that the external reconnected field would propagate in the magnetosphere of the neutron star carrying substantial amount of magnetic energy and perhaps leading into some interesting magnetospheric dynamics that could be studied.

Acknowledgements W.D. Gonzalez would like to thank the 'Conselho Nacional de Pesquisas, CNPq' of Brazil for support, through the Project PQ-303329/2011-4. The author has benefited from extensive discussions with Prof. Rudolf Treumann and also from additional discussions with Prof. Eugene Parker, Prof. Murray Peshkin, Prof. Anthony Zee, Prof. Ken Harada, Prof. Marcelo Gleiser, Dr. Golibjon Berdiyorov, Dr. Denis Vodolazov, and Dr. Clovis Wotzasek.

References

A.A. Abrikosov, Zh. Eksp. Teor. Fiz. **32**, 1442 (1957) [English translation: Sov. Phys. J. Exp. Theor. Phys. **5**, 1174 (1957)]
Y. Aharonov, D. Bohm, Phys. Rev. **115**, 485–491 (1959)
N.W. Ashcroft, N.D. Mermin, *Solid State Physics* (Thompson Learning, London, 1976)
R.G. Chambers, Phys. Rev. Lett. **5**, 3–5 (1960)
B.S. Deaver Jr., W.M. Fairbank, Phys. Rev. Lett. **7**, 43–46 (1961)
R. Doll, M. Näbauer, Phys. Rev. Lett. **7**, 51–52 (1961)
V.L. Ginzburg, L.D. Landau, Zh. Eksp. Teor. Fiz. **20**, 1064 (1950) [English translation: L.D. Landau, *Collected Papers* (Pergamon Press, Oxford, 1965), p. 546]
M. Gleiser, J. Thorarinson, Phys. Rev. D (2007). doi:10.1103/PhysRevD.76.041701
K. Harada, Microscopy (Tokyo) (2013). doi:10.1093/jmicro/dft013
K. Harada et al., Phys. Rev. B **53**, 9400 (1996)
M.W. Hecht, T.A. DeGrand, Phys. Rev. D **42**, 519 (1990)
J.D. Jackson, *Classical Electrodynamics* (Wiley, New York, 1975)
H. Kleinert, *Gauge Fields in Condensed Matter*. Superflow and Vortex Lines, vol. I (World Scientific, Singapore, 1989)
L.D. Landau, Z. Phys. (1930). doi:10.1007/BF01397213
E.M. Lifshitz, L.P. Pitaevskii, *Statistical Physics*, Part 2 (Elsevier, New York, 1980)
T. Matsuda et al., Phys. Rev. Lett. **62**, 2519 (1989)
A.B. Migdal, Zh. Eksp. Teor. Fiz. **37**, 249 (1959) [English translation: Sov. Phys. J. Exp. Theor. Phys. **10**, 176 (1990)]
A.G. Muslimov, A.I. Tsygan, Astrophys. Space Sci. **115**, 43 (1985)
D. Page et al., Phys. Rev. Lett. (2011). doi:10.1103/PhysRevLett.106.081101
M. Peshkin, A. Tonomura, *The Aharonov-Bohm Effect*. Lecture Notes in Physics, vol. 340 (Springer, Berlin, 1989)
J. Shaham, *Proceedings of the 5th Göttingen-Jerusalem Symposium on Astrophysics*. Abh. Akad. Wiss., Göttingen Math-Phys., Kl, vol. 33, 1981, p. 211

J.M. Speight, Phys. Rev. D **55**, 3830 (1997)
A. Tonomura et al., Phys. Rev. Lett. **56**, 792–795 (1986)
R.A. Treumann, W. Baumjohann, W.D. Gonzalez, Ann. Geophys. (2012). doi:10.5194/angeo-30-1515-2012
A. Zee, *Quantum Field Theory in a Nutshell* (Princeton University Press, Princeton, 2012)

Index

W. Gonzalez, E. Parker (eds.), *Magnetic Reconnection*, Astrophysics and Space Science Library 427, DOI 10.1007/978-3-319-26432-5